



*Diana Faiella*

THE INTERMEDIATE-ISOLATION SYSTEM FOR NEW  
AND EXISTING BUILDINGS: SEISMIC BEHAVIOR  
AND DESIGN CRITERIA

*Tesi di Dottorato in*  
Ingegneria Strutturale, Geotecnica e Rischio Sismico

*XXX ciclo*

*Il Tutor*  
*Prof.ssa Ing. Elena MELE*

*Il Coordinatore*  
*Prof. Ing. Luciano ROSATI*



# CONTENT

<b>CONTENT .....</b>	<b>i</b>
<b>1. INTRO .....</b>	<b>1</b>
1.1. Motivation of the thesis work.....	1
1.2. Research objectives and methods.....	4
1.2.1. Research objectives .....	4
1.2.2. Methods .....	4
1.3. Outline of the thesis .....	5
<b>2. BIS, TMD, IIS – THEORETICAL BASIS .....</b>	<b>9</b>
2.1. Introduction.....	9
2.2. Base Isolation Systems (BIS).....	10
2.2.1. Base Isolation Theory for 2DOF Systems .....	10
2.2.1.1. Governing equations of motion .....	11
2.2.1.2. Modal Analysis of the simplified model .....	12
2.2.1.3. Response to sinusoidal input.....	20
2.2.1.4. Response to a generic seismic input.....	24
2.2.1.5. Isolation of very flexible structures .....	27
2.2.1.6. Rigid structure vs. Flexible structure with respect to the isolation system .....	30
2.2.2. Base Isolation Theory for MDOF Systems.....	34
2.3. Tuned Mass Damper Systems (TMD).....	40
2.3.1. Tuned Mass Damper Theory for SDOF Systems .....	40
2.3.1.1. Undamped Structure: Undamped TMD.....	40
2.3.1.2. Undamped Structure: Damped TMD .....	43

---

Sinusoidal external force .....	49
Harmonic ground acceleration .....	51
2.3.1.3.    Damped Structure: Damped TMD .....	58
2.3.2.    Tuned Mass Damper Theory for MDOF Systems .....	65
2.4.    Inter-story Isolation Systems (IIS) .....	70
2.4.1.    Inter-Story Isolation Theory for 3DOF and 2DOF Systems	70
2.4.1.1.    Simplified modeling.....	70
2.4.1.2.    Governing equations of motion .....	70
2.4.1.3.    Comparison among the equations of motion of the	
different simplified models.....	72
<b>3.    DESIGN PRACTICE AND APPLICATIONS .....</b>	<b>75</b>
3.1.    Inter-story Isolated Structure .....	75
3.2.    IIS real buildings .....	79
3.2.1.    IIS for new building .....	79
3.2.1.1.    Iidabashi 1 <sup>st</sup> Building - JAPAN .....	79
3.2.1.2.    Shiodome Sumitomo building - JAPAN .....	88
3.2.1.3.    Festival Tower Osaka - JAPAN.....	99
3.2.1.4.    Tekko Building - JAPAN.....	109
3.2.2.    IIS for existing building.....	121
3.2.2.1.    China Basin 185 Berry Street Building - USA.....	121
3.3.    Observations .....	134
<b>4.    LITERATURE OVERVIEW AND DISCUSSION.....</b>	<b>137</b>
4.1.    Dynamic Behavior of Intermediate Isolation Systems.....	137
4.2.    Modeling of Intermediate Isolation System (IIS) .....	138
4.3.    Parametric Analyses.....	140
4.3.1.    Design parameters.....	141
4.3.2.    Design criteria and relevant response parameters .....	145



---

4.4.	Overview of the major papers on intermediate isolation systems	146
4.4.1.	Threefold approach (energy dissipation, isolation, mass damping)	146
4.4.2.	Isolation Approach [Wang et al. 2011, 2012, 2013; Kobayashi & Koh 2008; Ryan & Earl 2010]	151
4.4.2.1.	Parametric analyses by Wang et al. [2011, 2012, 2013]	153
4.4.2.2.	Modal Coupling Effect – MCE [Wang et al. 2011, 2012, 2013]	154
4.4.2.3.	Modal Coupling Effect – MCE [Kobayashi & Koh 2008]	156
4.4.2.4.	Experimental campaigns	158
4.4.2.5.	Parametric analysis by Kobayashi and Koh [Kobayashi & Koh 2008]	167
4.4.2.6.	Parametric analysis by Ryan and Earl [Ryan & Earl 2010]	168
4.4.3.	Mass Damper Approach [De Angelis et al. 2012; Villaverde 1985, 2002; Sadek et al. 1997; Chey et al. 2013; Miranda et al. 2013; Reggio & De Angelis 2014, 2015]	170
4.4.4.	Concentrated energy dissipation systems [Murakami et al. 2000, Murakami 2001, Sueoka et al. 2004, Tsuneki et al. 2008-2009]	179
4.5.	Analytical Formulations in the Current Literature	183
4.5.1.	Isolation Approach	183
4.5.1.1.	Modal Analysis of the simplified 3DOF IIS model	183
4.5.1.2.	Modal Analysis of the simplified 3DOF IIS model	189
4.5.2.	Mass Damping Approach	192
4.5.2.1.	Approaches of [Sadek et al. 1997], [Miranda et al. 2012], [Chey et al. 2010], [Wang et al. 2017]	192
	Approach of [Moutinho et al. 2012]	193

---

Approach of [Chey et al. 2010].....	194
Approach of [Wang et al. 2017].....	194
4.5.2.2.    Approaches of [De Angelis et al. 2012], [Reggio & De Angelis 2014, 2015].....	194
4.5.3.    Concentrated Energy Dissipation.....	200
4.5.3.1.    Energy Input Concept.....	200
4.5.3.1.    Energy Balance concept in seismic isolated structures	206
BIS.....	207
IIS.....	208
4.5.3.2.    Shear coefficient distribution .....	217
IIS.....	220
4.6.    Observations and results .....	225
<b>5.    ANALYSIS OF REAL IIS BUILDINGS .....</b>	<b>227</b>
5.1.    Introduction .....	227
5.2.    The case studies: brief description .....	227
5.3.    Simplified modeling and dynamic properties .....	228
5.4.    Modal Analyses .....	235
5.4.1.    RB models .....	237
5.4.2.    RB+D models.....	238
5.4.3.    Mode Coupling Effect.....	239
5.5.    Theory and design practice: Isolation and Mass Damping Approaches vs. IB & SSB .....	241
5.5.1.    Isolation Approach: Wang and Kobayashi vs. IB & SSB	242
5.5.1.1.    Design parameters and comparison to IB and SSB	243
5.5.1.2.    Analysis results – mode coupling effect and comparison to IB and SBB.....	245
5.5.2.    Isolation approach: Kelly vs. IB and SSB .....	249

---

5.5.3.	Theory and practice: Mass Damping Approach vs. IB and SSB	250
5.6.	Time History Analyses .....	260
5.6.1.	Hysteresis loops .....	261
5.6.2.	Maximum story drifts .....	263
5.6.3.	Maximum story accelerations .....	266
5.6.4.	Time histories of story accelerations .....	268
5.6.5.	Maximum story shear forces.....	268
5.6.6.	Seismic indices .....	273
5.6.7.	Maximum story shear coefficient.....	275
5.6.8.	Energy components distribution.....	277
5.7.	Theory and practice: Murakami et. al vs. IB and SSB .....	279
5.8.	Conclusive remarks and design implications .....	285
<b>6.</b>	<b>PARAMETRIC ANALYSIS .....</b>	<b>287</b>
6.1.	Introduction.....	287
6.2.	Simplified Parametric Analysis and dynamic properties .....	288
6.2.1.	Model definition .....	288
6.2.1.1.	10DOF FB model.....	293
6.2.1.2.	10DOF ISO model.....	295
6.3.	Modal Analysis .....	296
6.3.1.1.	Modal expansion of the inertial forces.....	307
6.3.1.2.	Mode Coupling Effect (MCE) .....	310
6.4.	Time History Analysis.....	331
6.5.	Conclusive remarks and design implications .....	334
<b>7.</b>	<b>IIS FOR RETROFIT .....</b>	<b>337</b>
7.1.	Introduction.....	337
7.2.	Simplified 3DOF model.....	338
7.3.	Case Study.....	339
7.4.	Simplified parametric analysis .....	341

---

7.4.1.	Design parameters.....	341
7.4.1.1.	Distribution of the isolated mass between the US and ISO system	342
7.4.1.2.	Flexibility of the structural portions.....	344
7.4.2.	Modeling of damping.....	346
7.4.3.	Modal Analysis.....	347
7.4.3.1.	Natural modes of vibration .....	347
7.4.3.1.1.	Modal Coupling Effect (MCE) .....	352
7.4.3.2.	Complex modes of vibration.....	355
7.4.4.	Response spectrum analysis.....	357
7.4.4.1.	Story Shear Force .....	357
7.4.4.2.	Story displacement.....	364
7.4.4.3.	Base Shear .....	366
7.4.5.	Comparison between two 3DOF IIS models .....	368
7.4.5.1.	Modeling of the isolators bearings by bilinear modeling	368
7.4.5.2.	Response Spectrum Analysis (RSA) .....	371
7.4.5.3.	Time History Analysis (THA) .....	374
7.5.	Choice of the design configuration for the upper structure and the isolation system.....	378
7.6.	Three-dimensional analysis .....	380
7.6.1.	Modal Analysis.....	380
7.6.2.	Response spectrum Analysis.....	382
7.6.3.	Time History Analysis.....	383
7.7.	Conclusive remarks and design implications.....	385
<b>8.</b>	<b>CONCLUSIONS .....</b>	<b>387</b>
8.1.	Summary .....	387
8.2.	Major Results.....	390
8.3.	Design implications .....	394

---

<b>REFERENCES .....</b>	<b>397</b>
<b>APPENDIX A: IIS for retrofit .....</b>	<b>405</b>
A.1. Modal Analysis .....	405
A.2. Response Spectrum Analysis.....	424
A.3. Time History Analysis .....	430
<b>APPENDIX B: Design Implications .....</b>	<b>435</b>
B.1. Influence of periods of the structural portions and of the isolation system.....	435
B.1.1. $T_{ISO}$ vs. $T_{US}$ .....	435
B.1.2. $T_{ISO}$ vs. $T_{LS}$ .....	436
B.1.3. $T_{ISO}$ vs. $T_{US}$ and $T_{LS}$ .....	437
B.2. “Perfect” and “Non-perfect” Isolation.....	437
B.2.1. Perfect isolation.....	437
B.2.2. Non-perfect isolation .....	438
B.3. Mode Coupling Effect (MCE) .....	439
B.3.1. MCE + perfect isolation.....	439
B.3.2. MCE + non-perfect isolation.....	440
B.3.3. MCE parameter: $\beta$ .....	440
B.3.4. 3DOF IIS vs. MDOF IIS.....	441
B.4. Mass ratio, IIS robustness, untuned IIS effect .....	443
B.5. Mass and stiffness distributions .....	444
B.6. Damping.....	444



---

---

Ai miei genitori



# 1. INTRO

## 1.1. MOTIVATION OF THE THESIS WORK

Seismic isolation is today a mature design strategy, thoroughly studied by the international scientific community since the '80s, consolidated by more than thirty years of design practice, and characterized by a diffusion of applications with a high gradient. Thanks to the growing confidence in the seismic performance achievable by isolated buildings, as observed at the occurrence of severe earthquakes [Nakashima et al. 2004, Miyazaki 2008, Kani et al. 2006, Nakamura et al. 2011, Saito et al. 2011, Takayama et al. 2012], new fields of application of the isolation principle have recently emerged, somehow pushing the boundaries of the well established original concept and posing new challenging design issues (Fig 1.1). Among these recent trends, the use of intermediate story isolation systems (IIS, also appointed as mid-story isolation), is currently spreading and gaining significant popularity, mainly in Japan, both for the seismic design of new buildings [Murakami et al. 2000, Sueoka et al. 2004, Tsuneki et al. 2008 - 2009, Okada et al. 2014, Nakagawa et al. 2015, Tamari et al. 2017], and for vertical addition in and /or retrofit of existing buildings [Dutta et al. 2009]. A recent study by [Kobayashi & Sasaki 2009] refers to more than 60 buildings equipped with IIS, realized starting from the late 90s.

Shifting the position of the isolation system from the base of the building to a certain level along elevation, strongly enhances the feasibility of the isolation strategy in several situations, like in the case of densely populated areas [Wang et al. 2012], when the planning and urban restraints at the base of a building do not allow for the introduction of the gap in the case of classical base isolation systems; further IIS is an advantageous solution for mixed-use buildings, where the different occupancies along elevation give rise to different architectural plans, structural systems, and grid layouts, thus identifying a level of structural discontinuity, or even of transfer structure, that can be ideally utilized for placing the isolation system [Murakami et al. 2000, Tsuneki et al. 2008-2009, Okada & Yoshida 2014, Zhou et al. 2016]; also tall buildings can become good candidates

for seismic isolation thanks to the introduction of an optimally placed IIS [Zhou et al. 2016], that can remarkably improve the response of both structural parts above and below the isolation system. Finally, the vertical addition of new floors, isolated on the top of existing buildings, is a retrofit strategy that allows the increase of usable area and real estate value without increasing the seismic demand, thanks to the so-called “mass damper effect” exerted by the upper part on the existing substructure. [Chey et al. 2013, Dutta et al. 2009, Ryan & Earl 2010, Tsuneki et al. 2008-2009].

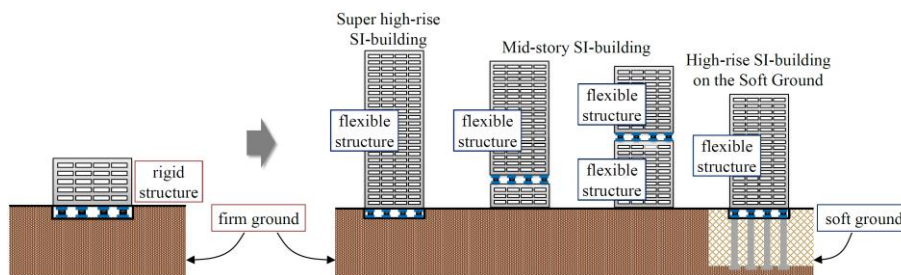


**Fig. 1.1. Expansion of the scope of application of seismic isolated buildings [Moriizumi & Kobayashi 2012]**

However, while the design concept of base isolation is today highly mature and several thousands of applications have been realized, for the IIS not a single, fully shared design approach is defined but multiple approaches. It is worth noticing that the concept itself of base isolation, and the dynamics of the base isolated buildings, are by far more straightforward and simpler than in the case of IIS. It is quite intuitive that the building substructure, with its own flexibility, may affect the response of the isolated superstructure; furthermore, the choice of the location of the isolation system along the building elevation, determines the ratio of upper to lower mass, which, as well, strongly affects the resulting vibration characteristics and dynamic response of the single upper and lower portions, and of the structural complex.

Considering that, in general terms, isolation is “a means to change dynamic characteristics of a vibrating system”, while the base isolation practically reduces a multi-degree of freedom (MDOF) structure to a single-degree of freedom (SDOF) system, the mid-story isolation changes one MDOF system into another MDOF with different vibration characteristics [Ziyacifar & Noguchi 1998]. An additional important difference between BIS and IIS is related to the need and importance of energy dissipation in

the two isolation systems: while the first vibration mode of BI buildings is characterized by large mass participation and period falling in the less intensive zone of the earthquake spectra, in a IIS the first mode only activates a smaller mass fraction, and the higher modes, with considerable amount of mass, can be close to the high-energy zone of the spectra, thus the total input energy can be comparable to, or even higher than conventional buildings [Ziyaeifar & Noguchi 1998]. Therefore, while BIS deflects earthquake energy through the dynamics of the system [Naeim & Kelly 1999] and does not need significant energy dissipation, in the IIS the component of energy dissipation is an important attribute required to the isolation system.

The overview of the main scientific contributions on this topic provided in the inherent literature reflects the variety of approaches, both in the formulation of the problem and in the definition of the design objectives and parameters. Basically, three major conceptual approaches can be clearly identified, each mainly focusing on one single aspect of the three ones related to IIS, namely: energy dissipation, isolation, mass damping.

Some papers, coming from the Japanese research community, also including the designers of important buildings with IIS [Murakami et al. 2000, Sueoka et al. 2004, Tsuneki et al. 2008-2009], mainly deal with the IIS as a “concentrated energy dissipation” design problem, and assume the dampers yielding force as the major design parameters for achieving the performance objective of the structural complex.

Other studies [Wang et al. 2011, Moriizumi & Kobayashi 2012, Ryan & Earl 2010], on the contrary, pay more attention to the isolation aspect. In particular [Wang et al. 2011] adopt the frequency and mass ratios as the major design parameters and analyze how these parameters affect the dynamic behavior, modes coupling effect and seismic performance, explicitly excluding the cases of ‘mass absorber’ and ‘building mass damper’, which are regarded as irrelevant for the isolation technology. [Schellenberg et al. 2016] carry out an experimental campaign for the simulation of buildings with IIS, through a real-time hybrid simulation system combined with a shaking table; the major focus of the paper is the hybrid shake table testing method rather than the IIS, and having fixed the isolation and superstructure period, the effect of varying the period of the lower structure is assessed, without any specific considerations on the definition of the design parameters and with only some final recommendations on the period ratio. [Ryan & Earl 2010] examine the

effectiveness of IIS as a function of its location along the building elevation, basically adopting the design criteria of BIS.

Finally, some papers [De Angelis et al. 2012 and 2015, Chang et al. 2012, Chey et al 2013] mainly focus the attention just on the mass damper effect, appointed as non conventional or building tuned mass damper: in particular [De Angelis et al. 2015] investigates the behavior of IIS through a reduced order 2DOF model (SDOF lower structure +TMD system), and define the optimal TMD parameter, namely the frequency ratio, which minimizes the displacement response of the structure. [Chey et al 2013], as well, investigate the “added stories isolation system” as a TMD optimally tuned according to the procedure proposed by [Sadek et al 1997].

## **1.2. RESEARCH OBJECTIVES AND METHODS**

### **1.2.1. Research objectives**

In view of the foregoing, the major research objectives of the thesis work are:

- to compare the three different approaches of isolation, dissipation and mass damper effect, and merging together the precious design guidelines coming from each of them, covering all the range of actual and potential applications of IIS;
- to identify the predominant role among the three behavioral aspects of isolation, mass damping and energy dissipation, in different ranges of IIS application;
- to define design criteria both for new and existing buildings.

### **1.2.2. Methods**

In a first step of research the analysis of two real building case-studies representative of the wide IIS applicability, has been carried out, in order to interpret the latest design practice in the light of approaches and indications coming from the world of research.

Hence, starting from the precious outcomes of the analyses, two parametric analyses have been carried out, considering both new and

existing buildings. In the first parametric analysis, developed on 1D-MDOF inter-story isolated models, the influence of different locations of the isolation system along the building height, and of different mass and stiffness distributions, has been investigated. In the second parametric analysis, carried out on 1D-3DOF inter-story isolated models, the response of an IIS vertical addition for retrofitting an existing masonry building, has been investigated, with the aim of identifying the optimal superstructure configuration; then, a 3D FEM model is adopted for the detailed analysis of the IIS structure.

### 1.3. OUTLINE OF THE THESIS

The thesis is composed of the following chapters and appendices:

*Chapter 2: “BIS, TMD, IIS – theoretical basis”* – In this chapter, in order to grasp the dynamic behavior of structures with isolation systems, base isolation (BIS), tuned mass damping (TMD) and intermediate isolation (IIS) strategies are firstly examined separately; and, secondly, the equations of motion of simplified two and three degrees-of-freedom IIS (2 and 3 DOF IIS) models are compared to the two degrees-of-freedom BIS (2DOF BIS) and single degrees-of-freedom with TMD (SDOF + TMD) models.

*Chapter 3: “Design practice and applications”* – An overview of the main real applications of IIS, both for new building and for vertical addition in the retrofit of existing buildings, is provided in this chapter; in particular the exam of IIS real buildings refers to four new buildings and one retrofitted building.

*Chapter 4: “Literature overview and discussion”* – In this chapter the review of the scientific literature is presented, focusing the attention on: modeling approaches, problem formulation, identification of the design parameters, results of parametric analyses, design criteria, experimental tests. The major outcomes and observations coming from the literature review and the relevant design implications are discussed.

*Chapter 5: “Analysis of real IIS buildings”* – Two real-world applications of IIS are chosen as case studies and thoroughly analyzed, in order to

interpreting the latest design practice in the light of approaches and indications coming from the world of research. In the chapter the buildings are described, and the major data obtained from publications and communication with the designers are presented and utilized for an approximate prediction of, and a preliminary discussion on the dynamic properties of the three structural parts of each building, and, consequently, on their expected dynamic interaction; in addition, a straightforward comparison between the anticipated dynamic behavior of the two buildings is presented. Modal and time history analyses are then carried out on the MDOF models of the two buildings; the main results are reported and design implications are discussed, in the light of the previous observations and of the provisions suggested in the inherent scientific literature.

*Chapter 6: “Parametric analysis”* – The modal properties of the inter-story isolation system (IIS) structures are explored in this chapter, with particular attention to the mode coupling effect of the higher modes (MCE).

Multi-degree-of-freedom isolated models, representative of a 10-story building, are considered, and the influence of different placements of the isolation system, as well as of different mass and stiffness distributions are investigated. Multi-degree-of-freedom fixed-base models are also considered for comparison. In this framework an analytical formulation for avoiding MCE is derived for MDOF systems, and, then, extended to 3DOF IIS models.

*Chapter 7: “IIS for retrofit”* – This chapter explores the effectiveness and the feasibility of the inter-story isolation system (IIS) as a seismic retrofit strategy; a case study is selected for this purpose, an existing three-story masonry structure that has large safety margin with respect to gravity load condition. Firstly, a simplified 3DOF parametric analysis is proposed to identify the optimal superstructure isolated configuration, i.e. the one that minimizes the seismic response. Hence, a 3D FEM model is adopted for the detailed analysis of the IIS structure, carrying out linear and non-linear dynamic analyses. Finally, a comparison between the results obtained with the simplified 3DOF model and the more refined 3D FEM model is provided.

*Chapter 8: “Conclusions”* – This chapter has assessed the effectiveness and the feasibility of the inter-story isolation system on the basis of the literature review, the analysis of real applications of IIS, and the results of the parametric analyses carried out on new and existing buildings.

*Appendix A: “IIS for retrofit”* – This appendix provides insights about Chapter 7 in terms of modal, response spectrum and time history analyses, carried out on simplified 3DOF IIS models.

*Appendix B: “Design implications”* – This appendix shows the main design implications for IIS buildings.





## 2. BIS, TMD, IIS – THEORETICAL BASIS

### 2.1. INTRODUCTION

A IIS structure can be ideally divided in two portions, an upper and lower structure above and below the isolation layer.

Shifting the position of the isolation layer from the base to a generic level along the height of the building, it is quite intuitive that the building substructure, with its own flexibility, may affect the response of the isolated superstructure.

From a dynamic point of view, the flexible interface combines seismic isolation and mass damping strategies: isolation reduces input energy transmitted to the structure by lengthening its fundamental period; mass damping reduces the response dynamics of the structure by transferring vibration energy from the main structure to the auxiliary mass, called to dissipate it.

Therefore, on the one hand the isolation interface acts as a filter for the inertia forces rising to the upper structure, on the other the lower structure shows a reduced response thanks to the mass damping effect exerted by the isolated superstructure.

In the scientific literature, the IIS technique is addressed by focusing both on the aspects of seismic isolation and mass damping, using simplified lumped 2 degrees-of-freedom models, 1D-3DOF IIS ([Villaverde 1985-2002, Sadek et al. 1999, Murakami 2001, Murakami et al. 2001, Murakami & Sueoka, Qi et al. 2006, Ping et al. 2008-2016, De Angelis et al. 2012, Moutinho 2012, Chey et al. 2013, Reggio & De Angelis 2015, Zhou et al. 2016]), and 3 degrees-of-freedom models, 1D-3DOF IIS, ([Kobayashi & Koh 2008, Wang et al. 2011, 2012a-b, 2013, Moriizumi & Kobayashi 2012]).

The 1D-2DOF IIS models are often based on the premise that the isolated superstructure behaves as a rigid body under earthquake excitations. This assumption is considered accurate when the flexibility of the isolated portion is mainly concentrated at the isolation layer; and the upper structure is very rigid, both with respect to the isolation system and to the

lower structure; consequently, the mass of the upper structure and isolation is characterized by one lumped mass supported by the isolator; the lower part of the structure below the isolation story is represented by another lumped mass.

In order to capture the effect of the flexibility of the upper structure on the response of base isolated buildings Kelly developed a 2DOF (the so-called “isolated single DOF”) where the isolation and the upper stories are modeled as two lumped-mass models [Kelly 1990]. Analogously, in a mid-story isolation system, the representation of the upper part flexibility leads to a 3DOF model.

In the present chapter, in order to grasp the dynamic behavior of mid-story structures, base isolation (BIS), tuned mass damping (TMD) and intermediate isolation (IIS) strategies are firstly examined separately, and, secondly, the equations of motion of 2-3 DOF IIS models are compared to the corresponding ones of 2DOF base-isolated structure (2DOF BIS) and SDOF with TMD (SDOF + TMD).

## **2.2. BASE ISOLATION SYSTEMS (BIS)**

### **2.2.1. Base Isolation Theory for 2DOF Systems**

An elementary analysis for the purpose of gaining insight into the behavior of isolated buildings is developed by J. M. Kelly [Kelly 1990, Naeim & Kelly 1999] using a simple linear two-degree of freedom (2DOF) model, with linear springs and linear viscous damping. Since most isolation systems are intrinsically non-linear this analysis will be only approximate for such systems, and effective stiffness and damping will have to be estimated by some equivalent linearization process.

The kinematic parameters that characterize the absolute motion of the 2DOF BIS model are (Fig. 2.1):

$u_g$ : ground displacement

$u_b$ : absolute displacement of the isolation system

$u$ : absolute displacement of the main structure

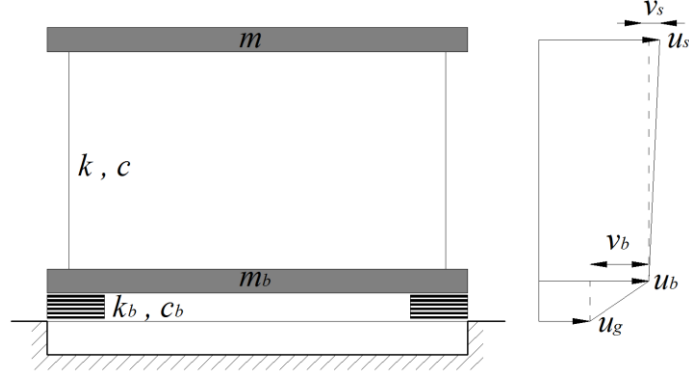


Fig. 2.1. 2DOF BIS model

### 2.2.1.1. Governing equations of motion

The absolute equations of motion are:

$$m\ddot{u} = -c(\dot{u} - \dot{u}_b) - k(u - u_b) \quad (2.1)$$

$$m_b\ddot{u}_b = -c_b(\dot{u}_b - \dot{u}_g) - k_b(u_b - u_g) \quad (2.2)$$

It is convenient to work with relative displacements (Fig. 2.2):

$$v_s = u - u_b \quad (2.3)$$

$$v_b = u_b - u_g \quad (2.4)$$

from which the absolute displacement of the main structure can be written as:

$$u = v_s + v_b + u_g \quad (2.5)$$

and the Eqs. (2.1) - (2.2) become:

$$m\ddot{v}_b + m\ddot{v}_s + c\dot{v}_s + kv_s = -m\ddot{u}_g \quad (2.6)$$

$$(m + m_b)\ddot{v}_b + m\ddot{v}_s + c_b\dot{v}_b + k_bv_b = -(m + m_b)\ddot{u}_g \quad (2.7)$$

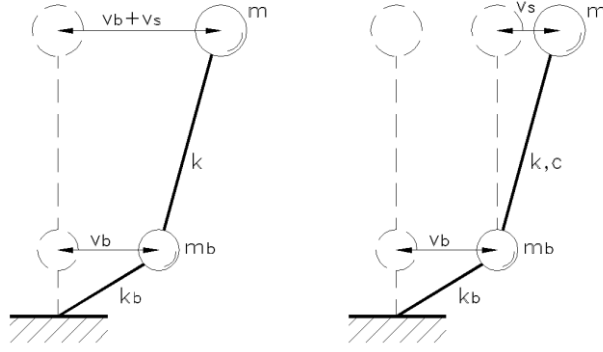


**Fig. 2.2. Absolute vs. relative displacement**

It is easy to see that if the relative motion between the structure and the base, expressed by  $v_s$ , is suppressed, Eq. (2.7) becomes the equation of a single-degree-of-freedom equivalent to the base isolation system:

$$M\ddot{v}_b + c_b\dot{v}_b + k_b v_b = -M\ddot{u}_g \quad (2.8)$$

where  $M$  is the total mass of the building plus that of the isolation layer (isolators and concrete slab). If  $v_b$  is suppressed, the Eq. (2.6) becomes the usual equation for a fixed-base single-degree-of-freedom system:

$$m\ddot{v}_s + c\dot{v}_s + kv_s = -m\ddot{u}_g \quad (2.9)$$

### 2.2.1.2. Modal Analysis of the simplified model

This two-degree-of-freedom system of equations can be solved directly or through modal decomposition. A modal analysis provides insight into the response of isolated systems and the results will be applicable to more elaborate models. To develop the modes, frequencies and participation factors of the system, the Eqs. (2.6) - (2.7) can be rewritten in the matrix form:

$$\mathbf{M}\ddot{\mathbf{v}} + \mathbf{C}\dot{\mathbf{v}} + \mathbf{K}\mathbf{v} = -\mathbf{M}\mathbf{r}\ddot{u}_g \quad (2.10)$$

where  $\mathbf{M}$ ,  $\mathbf{C}$  and  $\mathbf{K}$  are the mass, damping and stiffness matrices respectively corresponding to

$$\mathbf{M} = \begin{bmatrix} \mathbf{M} & \mathbf{m} \\ \mathbf{m} & \mathbf{m} \end{bmatrix}; \quad \mathbf{C} = \begin{bmatrix} \mathbf{c}_b & 0 \\ 0 & \mathbf{c} \end{bmatrix}; \quad \mathbf{K} = \begin{bmatrix} \mathbf{k}_b & 0 \\ 0 & \mathbf{k} \end{bmatrix} \quad (2.11)$$

and the vectors  $\mathbf{v}$  and  $\mathbf{r}$  are

$$\mathbf{v} = \begin{Bmatrix} \mathbf{v}_b \\ \mathbf{v}_s \end{Bmatrix}; \quad \mathbf{r} = \begin{Bmatrix} 1 \\ 0 \end{Bmatrix} \quad (2.12)$$

Defining the mass ratio  $\gamma$  as:

$$\gamma = \frac{\mathbf{m}}{\mathbf{m} + \mathbf{m}_b} = \frac{\mathbf{m}}{\mathbf{M}} \quad (2.13)$$

and the nominal frequencies  $\omega_s$ ,  $\omega_b$  and the damping factors  $\xi_s$ ,  $\xi_b$  (respectively corresponding to the structure and the isolation system) as:

$$\omega_s = \sqrt{\frac{\mathbf{k}}{\mathbf{m}}}, \quad \omega_b = \sqrt{\frac{\mathbf{k}_b}{\mathbf{M}}} \quad (2.14)$$

$$\xi_s = \frac{\mathbf{c}}{2\mathbf{m}\omega_s}, \quad \xi_b = \frac{\mathbf{c}_b}{2\mathbf{M}\omega_b} \quad (2.15)$$

the following order of magnitude are assumed for:

- i)  $\mathbf{m}_b < \mathbf{m}$  (i.e.  $\gamma < 1$ ) but of the same order of magnitude
- ii)  $\omega_s \gg \omega_b$ , and, defining  $\varepsilon = \left( \frac{\omega_b}{\omega_s} \right)^2$ , the ratio  $\varepsilon = O(10^{-2})$ ;
- iii)  $\xi_s$  and  $\xi_b$  of the same order of magnitude as  $\varepsilon$ .

In terms of these quantities, the Eqs. (2.6) - (2.7) become:

$$\ddot{\mathbf{v}}_s + \ddot{\mathbf{v}}_b + 2\omega_s \xi_s \dot{\mathbf{v}}_s + \omega_s^2 \mathbf{v}_s = -\ddot{\mathbf{u}}_g \quad (2.16)$$

$$\gamma \ddot{\mathbf{v}}_s + \ddot{\mathbf{v}}_b + 2\omega_b \xi_b \dot{\mathbf{v}}_b + \omega_b^2 \mathbf{v}_b = -\ddot{\mathbf{u}}_g \quad (2.17)$$

The eigenvalues and the eigenvectors problem associated to Eq. (2.10) is

$$(\mathbf{K} - \omega_n^2 \mathbf{M}) \boldsymbol{\phi}^n = \mathbf{0} \quad (2.18)$$

where  $\omega_n$  is the frequency of the system and  $\boldsymbol{\phi}^n = \{\phi_b^n, \phi_s^n\}^T$  is the corresponding modal shape, with  $n = 1, 2$ . The characteristic equation for this system can be expressed in the following explicit polynomial form:

$$(1 - \gamma)\omega_n^4 - (\omega_b^2 + \omega_s^2)\omega_n^2 + \omega_b^2\omega_s^2 = 0 \quad (2.19)$$

The lower of the two roots of this equation ( $\omega_1$  and  $\omega_2$ ) will be denoted by  $\omega_b^*$ , which represents the shifted isolation frequency, and the higher root by  $\omega_s^*$ , which represents the structural frequency modified by the presence of the isolation system. The exact roots are given by:

$$\omega_{1,2}^2 = \frac{1}{2(1-\gamma)} \left\{ (\omega_s^2 - \omega_b^2) \mp \left[ (\omega_s^2 + \omega_b^2)^2 - 4(1-\gamma)\omega_s^2\omega_b^2 \right]^{1/2} \right\} \quad (2.20)$$

Accounting for the fact that  $\omega_b \ll \omega_s$  ( $\varepsilon = O(10^{-2})$ ) and rewriting the radical in the form:

$$(\omega_s^2 + \omega_b^2)^2 \left( 1 + 4\gamma \frac{\omega_s^2\omega_b^2}{\omega_s^2 + \omega_b^2} \right) \quad (2.21)$$

and then expanding this binomial series, the roots  $\omega_1^2$  and  $\omega_2^2$ , of the same order of  $\varepsilon$ , are given by:

$$\omega_1^2 = \omega_b^{*2} = \omega_b^2 \left( 1 - \gamma \frac{\omega_b^2}{\omega_s^2} \right) = \omega_b^2 (1 - \gamma\varepsilon) \quad (2.22)$$

$$\omega_2^2 = \omega_s^{*2} = \frac{\omega_s^2}{1 - \gamma} (1 + \gamma\varepsilon) \quad (2.23)$$

In many cases it may be sufficiently accurate to take as approximations for  $\omega_b^{*2}$ ,  $\omega_s^{*2}$  the first terms:

$$\omega_b^{*2} = \omega_b^2 \quad (2.24)$$

$$\omega_s^{*2} = \frac{\omega_s^2}{(1-\gamma)} \quad (2.25)$$

This indicates that the isolation frequency is only slightly changed by flexibility in the structure (the change is of order  $\varepsilon$ ), while the structural frequency is significantly increased by the addition of the base mass. The separation between the isolation frequency and the fixed-base structural frequency is increased by combining the two elements.

The undamped natural modes of the system  $\boldsymbol{\phi}^n = \{\phi_b^n, \phi_s^n\}^T$  with  $n=1,2$ , are given by the two equations:

$$\begin{aligned} &(-\omega_n^2 + \omega_b^2)\phi_b^n + (-\gamma\omega_n^2)\phi_s^n = 0 \\ \text{or} \\ &(-\omega_n^2)\phi_b^n + (-\omega_n^2 + \omega_b^2)\phi_s^n = 0 \end{aligned} \quad (2.26)$$

in which the roots  $\omega_n^2$  ( $\omega_1^2 = \omega_b^{*2}$  and  $\omega_2^2 = \omega_s^{*2}$ ) are computed by Eqs. (2.22) - (2.23).

The first mode shape  $\boldsymbol{\phi}^1$ , setting  $\phi_b^1 = 1$  and retaining terms of order  $\varepsilon$ , is given by:

$$\boldsymbol{\phi}^1 = \begin{Bmatrix} 1 \\ \varepsilon \end{Bmatrix} \quad (2.27)$$

Analogously, the second mode  $\boldsymbol{\phi}^2$  is:

$$\boldsymbol{\phi}^2 = \begin{Bmatrix} 1 \\ -\frac{1}{\gamma}[1-(1-\gamma)\varepsilon] \end{Bmatrix} \quad (2.28)$$

These are sketched in Fig. 2.3 and show that  $\boldsymbol{\phi}^1$  is approximately a rigid structure mode, whereas  $\boldsymbol{\phi}^2$  involves both structural deformation and

isolation system deformation. The displacement of the top of the structure is of the same order as the base displacement, but opposite direction.

Considering  $\varepsilon = O(10^{-2})$ , the eigenvectors have the following approximate expression:

$$\phi^1 \approx \begin{Bmatrix} 1 \\ 0 \end{Bmatrix}, \quad \phi^2 \approx \begin{Bmatrix} 1 \\ -1/\gamma \end{Bmatrix} \quad (2.29)$$

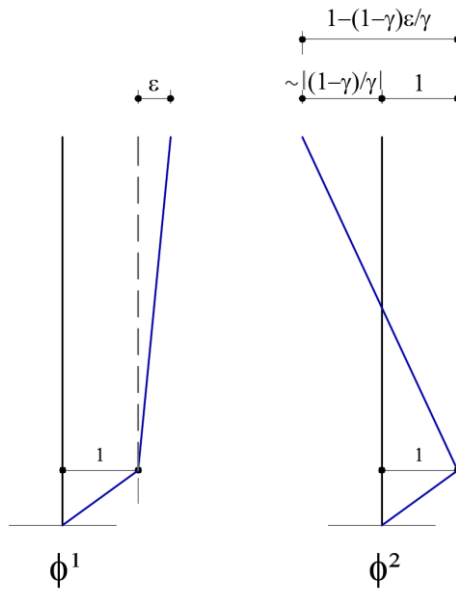


**Fig. 2.3. Mode Shapes of the 2DOF BIS model**

The vectors  $\phi^1$  and  $\phi^2$  form a complete base and they are used to uncouple the equations of motion (2.10), writing

$$\mathbf{v} = \begin{Bmatrix} v_b \\ v_s \end{Bmatrix} = q_1 \phi^1 + q_2 \phi^2 \quad (2.30)$$

where  $q_1$  and  $q_2$  are the unknown time-dependent modal coefficients.

From Eq. (2.30), the relative displacements  $v_b$  and  $v_s$  can be expressed in the scalar form as:



$$\mathbf{v}_b = \mathbf{q}_1 \boldsymbol{\phi}_b^1 + \mathbf{q}_2 \boldsymbol{\phi}_b^2 \quad (2.31)$$

$$\mathbf{v}_s = \mathbf{q}_1 \boldsymbol{\phi}_s^1 + \mathbf{q}_2 \boldsymbol{\phi}_s^2 \quad (2.32)$$

Substituting Eq. (2.30) into Eq. (2.10) and considering the orthogonality properties of the modal matrix  $\boldsymbol{\Phi} = [\boldsymbol{\phi}^1 \ \boldsymbol{\phi}^2]$  with respect to the mass  $\mathbf{M}$ , the stiffness  $\mathbf{K}$  and damping matrix  $\mathbf{C}$ , we obtained

$$\ddot{\mathbf{q}}_1 + 2\omega_b^* \xi_b^* \dot{\mathbf{q}}_1 + \omega_b^{*2} \mathbf{q}_1 = -\mathbf{L}_1 \ddot{\mathbf{u}}_g \quad (2.33)$$

$$\ddot{\mathbf{q}}_2 + 2\omega_s^* \xi_s^* \dot{\mathbf{q}}_2 + \omega_s^{*2} \mathbf{q}_2 = -\mathbf{L}_2 \ddot{\mathbf{u}}_g \quad (2.34)$$

where it is implicitly assumed that the damping in the system is light enough to retain the orthogonality of the modes.

In these equations the following notations are used:

$$2\omega_n^* \xi_n^* = \frac{\boldsymbol{\phi}^{nT} \mathbf{C} \boldsymbol{\phi}^n}{\boldsymbol{\phi}^{nT} \mathbf{M} \boldsymbol{\phi}^n}, \quad \omega_n^{*2} = \frac{\boldsymbol{\phi}^{nT} \mathbf{K} \boldsymbol{\phi}^n}{\boldsymbol{\phi}^{nT} \mathbf{M} \boldsymbol{\phi}^n}, \quad \mathbf{L}_n = \frac{\boldsymbol{\phi}^{nT} \mathbf{M} \mathbf{r}}{\boldsymbol{\phi}^{nT} \mathbf{M} \boldsymbol{\phi}^n} \quad (2.35)$$

with  $\xi_n^*$  and  $\mathbf{L}_n$  the damping ratio and the participation factor of the  $n$ -th mode, respectively.

The computation of the first participating factor  $\mathbf{L}_1$  involves the following matrix multiplications:

$$\mathbf{L}_1 \tilde{\mathbf{m}}_1 = \boldsymbol{\phi}^{1T} \mathbf{M} \mathbf{r} = \begin{bmatrix} 1 & \varepsilon \end{bmatrix} \begin{bmatrix} \mathbf{M} & \mathbf{m} \\ \mathbf{m} & \mathbf{m} \end{bmatrix} \begin{bmatrix} 1 \\ 0 \end{bmatrix} = \mathbf{M} + \mathbf{m}\varepsilon \quad (2.36)$$

where

$$\tilde{\mathbf{m}}_1 = \boldsymbol{\phi}^{1T} \mathbf{M} \boldsymbol{\phi}^1 = \begin{bmatrix} 1 & \varepsilon \end{bmatrix} \begin{bmatrix} \mathbf{M} & \mathbf{m} \\ \mathbf{m} & \mathbf{m} \end{bmatrix} \begin{bmatrix} 1 \\ \varepsilon \end{bmatrix} = \mathbf{M} + 2\mathbf{m}\varepsilon + \mathbf{m}\varepsilon^2 \quad (2.37)$$

Retaining only terms to order  $\varepsilon$ , it is obtained:

$$\mathbf{L}_1 = 1 - \gamma\varepsilon \quad (2.38)$$

For the second participation factor  $\mathbf{L}_2$ , the same computations give:

$$\mathbf{L}_2 \tilde{\mathbf{m}}_2 = \boldsymbol{\phi}^{2T} \mathbf{M} \mathbf{r} = \mathbf{M} + m\mathbf{a} \quad (2.39)$$

where

$$\tilde{\mathbf{m}}_2 = \boldsymbol{\phi}^{2T} \mathbf{M} \boldsymbol{\phi}^2 = \mathbf{M} + 2m\mathbf{a} + m\mathbf{a}^2 \quad (2.40)$$

and

$$\mathbf{a} = -\frac{1}{\gamma} [1 - (1 - \gamma)\boldsymbol{\varepsilon}] \quad (2.41)$$

Since  $\gamma = \frac{m}{M}$

$$\mathbf{L}_2 \tilde{\mathbf{m}}_2 = \mathbf{M}(1 - \gamma)\boldsymbol{\varepsilon} \quad (2.42)$$

and

$$\tilde{\mathbf{m}}_2 = \mathbf{M} \frac{(1 - \gamma)[1 - 2(1 - \gamma)\boldsymbol{\varepsilon}]}{\gamma} \quad (2.43)$$

Thus

$$\mathbf{L}_2 = \gamma\boldsymbol{\varepsilon} \quad (2.44)$$

Together with the shift in the frequencies, these results reveal why the seismic isolation system is effective.

The participation factor for the first mode,  $\mathbf{L}_1$ , is, according to the assumptions on the order of magnitude of  $\gamma$  and  $\boldsymbol{\varepsilon}$ , almost equal to 1.

The participation factor for the second mode,  $\mathbf{L}_2$ , which is the mode that involves structural deformation, is of order  $\boldsymbol{\varepsilon}$ , and if the original frequencies  $\omega_b$  and  $\omega_s$  are well separated, this could be very small. In addition, the frequency of this mode is shifted to a higher value than the original-fixed base frequency and if the earthquake input has large spectral accelerations at the original structural frequency, shifting it higher could shift it out of the range of strong earthquake motion.

However, since the participation factor for this mode is very small, this mode is orthogonal to the earthquake input characterized by  $\mathbf{M}\ddot{\mathbf{r}}_g$ . This means that even if earthquake does have energy at this frequency, the ground motion will not be transmitted into the structure. This is the real

effectiveness of a seismic isolation system. It does not absorb energy; it deflects energy through this property of orthogonality.

Energy absorption is of course an important part of the behavior of an isolation system and in this simple model it is represented by linear viscous damping considering uncoupled equations of motion.

For what concerns the damping factors  $\xi_b^*$  and  $\xi_s^*$ , respectively corresponding to the isolation system and the main mass, it is possible to make very good estimates in each element when treated separately.

An isolation system, composed by laminated rubber bearings, will provide a degree of damping in the range of  $10 \div 20\%$  of the critical damping. The structure will have somewhat less, probably of the order of  $2\%$ . In conventional structural analyses it is generally assumed that the damping in a structure will be about  $5\%$  of critical damping, assuming some degree of damage in the design.

A base-isolated system aims to reduce the forces experienced by the structure to such a level that no damage will occur to the structure or to nonstructural elements such as partitions, thus, a lower value for the structural damping is appropriate.

Normally, this large difference in damping between the two components would lead to a coupling of the equations of motion, and a complex modal analysis should be used to correctly analyze the system; however, using such an approach, the simplicity that allow to develop an intuitive grasp of the system's behavior could be lost. Therefore, an approximate form will be used by neglecting the off-diagonal terms of  $\phi^{nT} \mathbf{C} \phi^n$ , which would couple the equations of motion.

From Eqs. (2.22), (2.23) and (2.35), recalling that:

$$\omega_b^* = \omega_b (1 - \gamma \epsilon)^{1/2}, \quad \omega_s^* = \omega_s \frac{(1 + \gamma \epsilon)^{1/2}}{(1 - \gamma)^{1/2}}, \quad 2\omega_n^* \xi_n^* = \frac{\phi^{nT} \mathbf{C} \phi^n}{\phi^{nT} \mathbf{M} \phi^n}$$

and utilizing the previous results for  $\tilde{m}_1$  and  $\tilde{m}_2$ , it is found that:

$$2\omega_b^* \xi_b^* = 2\omega_b \xi_b (1 - 2\gamma \epsilon) \tag{2.45}$$

$$2\omega_s^* \xi_s^* = \frac{2\omega_s \xi_s + \gamma 2\omega_b \xi_b}{1 - \gamma} \tag{2.46}$$

Thus, the damping factors  $\xi_b^*$  and  $\xi_s^*$  are given by:

$$\xi_b^* = \frac{\xi_b (1 - 2\gamma\epsilon)}{(1 - \gamma\epsilon)^{1/2}} = \xi_b \left( 1 - \frac{3}{2} \gamma\epsilon \right) \quad (2.47)$$

$$\xi_s^* = \left( \frac{\xi_s}{(1 - \gamma)^{1/2}} + \gamma \frac{\xi_b \epsilon^{1/2}}{(1 - \gamma)^{1/2}} \right) \cdot \left( 1 - \frac{1}{2} \gamma\epsilon \right) \quad (2.48)$$

Combining the structure and the isolation system, from Eq. (2.47) can be noticed that the damping  $\xi_b^*$  is almost equal to  $\xi_b$ ; conversely, Eq. (2.48) shows that the structural damping is increased by the damping in the bearings to the order of  $\epsilon^{1/2}$ ; the product of  $\xi_b$  and  $\epsilon^{1/2}$  may be a significant addition to the term  $\xi_s$  and could be important if  $\xi_s$  is very small. This shows that high damping in the rubber bearings can provide significant damping to the structural mode.

### 2.2.1.3. Response to sinusoidal input

With these results for  $L_1$ ,  $L_2$ ,  $\xi_1$ ,  $\xi_2$ , we are able to estimate the response of the system to any dynamic input. Let us consider first the response to sinusoidal input and look at the amplification factor defined by the magnitude of the ratio of relative displacement to ground displacement. We denote:

$$A_s = \left| \frac{v_s}{\hat{u}_g} \right| ; \quad A_b = \left| \frac{v_b}{\hat{u}_g} \right| \quad (2.49)$$

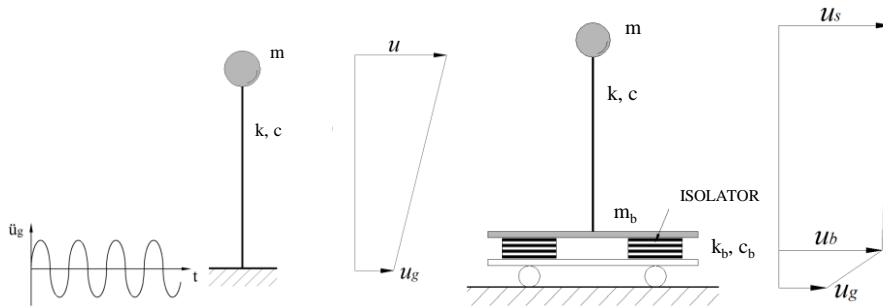


Fig. 2.4. Mode Shapes of the 2DOF BIS model

and set:

$$\ddot{\mathbf{u}}_g = \Omega^2 \hat{\mathbf{u}}_g e^{i\Omega t} \quad (2.50)$$

in the modal equations, considering the sinusoidal force periodic of  $\Omega$ . We then have:

$$\mathbf{A}_s = \left| \frac{\mathbf{v}_s}{\hat{\mathbf{u}}_g} \right| = \left| \phi_s^1 \frac{L_1 \Omega^2}{(\omega_b^{*2} - \Omega^2) + i2\omega_b^* \Omega \xi_b^*} + \phi_s^2 \frac{L_2 \Omega^2}{(\omega_s^{*2} - \Omega^2) + i2\omega_s^* \Omega \xi_s^*} \right| \quad (2.51)$$

and:

$$\mathbf{A}_b = \left| \frac{\mathbf{v}_b}{\hat{\mathbf{u}}_g} \right| = \left| \phi_b^1 \frac{L_1 \Omega^2}{(\omega_b^{*2} - \Omega^2) + i2\omega_b^* \Omega \xi_b^*} + \phi_b^2 \frac{L_2 \Omega^2}{(\omega_s^{*2} - \Omega^2) + i2\omega_s^* \Omega \xi_s^*} \right| \quad (2.52)$$

Although these expressions can be written out as algebraic functions of  $\Omega$  without imaginary parts, it is more instructive to look at the form that they take for specific values of  $\omega$ . We focus the attention to three frequencies, namely the fixed-base frequency  $\omega_s$  and the two isolated frequencies  $\omega_b^*, \omega_s^*$ .

When  $\Omega = \omega_b^*$ , we have:

$$\mathbf{A}_s = \left| \varepsilon \frac{(1 - \gamma \varepsilon) \omega_b^{*2}}{i2\omega_b^{*2} \xi_b^*} - \frac{1}{\gamma} \frac{[1 - (1 - \gamma) \varepsilon] \gamma \varepsilon \omega_b^{*2}}{(\omega_s^{*2} - \omega_b^{*2}) + i2\omega_s^* \omega_b^* \xi_s^*} \right| \quad (2.53)$$

Retaining terms to the first order in  $\varepsilon$ , this gives:

$$\mathbf{A}_s = \frac{\varepsilon}{2\xi_b^*} \quad (2.54)$$

For the amplification of the base motion we have:

$$A_b = \left| \frac{1 - \gamma \varepsilon}{2\xi_b^*} + \frac{\gamma \varepsilon^2}{(1 - \varepsilon) + i\varepsilon} \right| \quad (2.55)$$

which, to the same order in  $\varepsilon$ , is:

$$A_b = \frac{1 - \gamma \varepsilon}{2\xi_b \left(1 - \frac{3}{2}\gamma \varepsilon\right)} = \frac{1}{2\xi_b} \left(1 + \frac{1}{2}\gamma \varepsilon\right) \quad (2.56)$$

When  $\omega = \omega_s^*$  we find (by means of the same manipulations) that:

$$A_s = (1 - (1 - \gamma)\varepsilon) \frac{\varepsilon}{2\xi_s^*} \quad (2.57)$$

and:

$$A_b = 1 + \frac{1}{2} \frac{\gamma^2 \varepsilon^2}{(2\xi_s^*)^2} \quad (2.58)$$

The values of the amplification factors  $A$ ,  $A_b$ ,  $A_s$ , for the forcing frequency  $\Omega$  respectively equal to the two isolated frequencies  $\omega_b^*$ ,  $\omega_s^*$ , and the fixed-base frequency  $\omega_s$  are provided in Tab. 2.1; in addition, a schematic representation of the three conditions by comparing the fixed-base and the base-isolated structures, is depicted in Fig. 2.5.

**Table 2.1. Order of magnitude for the structural response**

$\Omega$	$A$	$A_s$	$A_b$
$\omega_b^*$	$\varepsilon$	1	$1/\varepsilon$
$\omega_s^*$	1	1	1
$\omega_s$	$1/\varepsilon$	$\varepsilon$	1

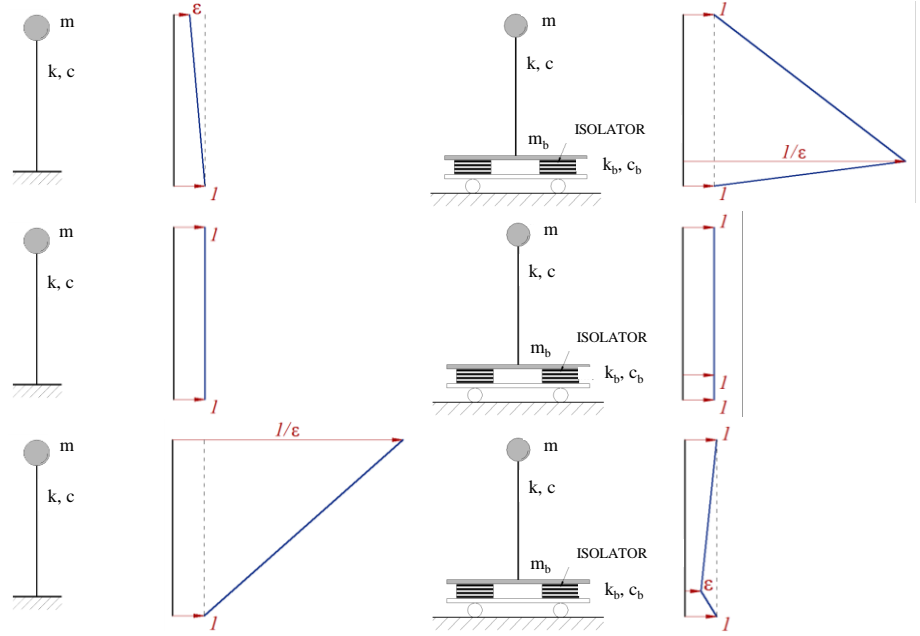


Fig. 2.5. Amplification factors: (a)  $\Omega = \omega_b^*$ , (b)  $\Omega = \omega_s^*$ , (c)  $\Omega = \omega_s$

From Fig. 2.5 and Tab. 2.1 can be observed that, the most favorable situation corresponds to a harmonic motion close to the building frequency  $\omega_s$ . In this case, the amplification factor  $A_s$  for an isolated building is  $\varepsilon$  which is much lower than the one corresponding to a fixed-base structure, equal to  $1/\varepsilon$ . The amplification factor for the base is  $A_b$  which in this case has an order of magnitude 1. Furthermore, the amplification factors  $A_b$  and  $A_s$  corresponding to the second mode also have an order of magnitude 1.

The exact expressions for all values of  $\Omega$  are:

$$A_s = \Omega^2 \varepsilon \left[ \frac{(\omega_s^{*2} - \omega_b^{*2})^2 + \Omega^2 (2\omega_s^* \xi_s^* - 2\omega_b^* \xi_b^*)^2}{[(\omega_b^{*2} - \Omega^2)^2 + 4\omega_b^{*2} \Omega^2 \xi_b^{*2}] \cdot [(\omega_s^{*2} - \Omega^2)^2 + 4\omega_s^{*2} \Omega^2 \xi_s^{*2}]} \right]^{1/2} \quad (2.59)$$

$$A_b = \Omega^2 \left[ \frac{(\omega_s^{*2} - \omega_b^{*2})^2 + \gamma \varepsilon \Omega^2 (2\omega_s^* \xi_s^* - 2\omega_b^* \xi_b^*)^2}{\left[ (\omega_b^{*2} - \Omega^2)^2 + 4\omega_b^{*2} \Omega^2 \xi_b^{*2} \right] \cdot \left[ (\omega_s^{*2} - \Omega^2)^2 + 4\omega_s^{*2} \Omega^2 \xi_s^{*2} \right]} \right]^{1/2} \quad (2.60)$$

These expression have been evaluated for a few choices of the parameters  $\gamma$ ,  $\varepsilon$ ,  $\xi_b$ ,  $\xi_s$  and the results are shown in Fig. 2.6.

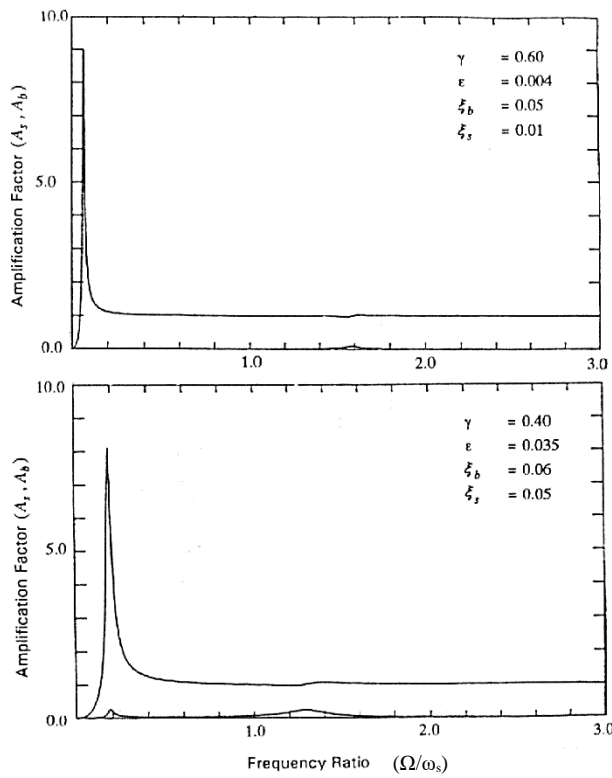


Fig. 2.6. Amplification Factors for the 2DOF BIS subjected to sinusoidal excitation

#### 2.2.1.4. Response to a generic seismic input

If the time history of the ground motion  $\ddot{u}_g(t)$  is known, the modal components  $q_1$  and  $q_2$  can be computed from:



$$q_1 = -\frac{L_1}{\omega_b^*} \int_0^t \ddot{u}_g(t-\tau) e^{-\omega_b^* \xi_b^* \tau} \sin \omega_b^* \tau d\tau \quad (2.61)$$

$$q_2 = -\frac{L_2}{\omega_s^*} \int_0^t \ddot{u}_g(t-\tau) e^{-\omega_s^* \xi_s^* \tau} \sin \omega_s^* \tau d\tau \quad (2.62)$$

and estimates of the maximum values of  $q_1$  and  $q_2$  are given by:

$$|q_1|_{\max} = L_1 S_D(\omega_b^*, \xi_b^*) \quad (2.63)$$

$$|q_2|_{\max} = L_2 S_D(\omega_s^*, \xi_s^*) \quad (2.64)$$

where  $S_D(\omega, \xi)$  is the displacement response spectrum for the ground motion  $\ddot{u}_g(t)$  at frequency  $\omega$  and the damping factor  $\xi$ .

Generally, for design purposes, a design damped acceleration response spectrum is given. In this case, the predicted maximum displacements will be:

$$|v_s|_{\max} = \left\{ \left( \phi_s^1 q_{1,\max} \right)^2 + \left( \phi_s^2 q_{2,\max} \right)^2 \right\}^{1/2} \quad (2.65)$$

$$|v_b|_{\max} = \left\{ \left( \phi_b^1 q_{1,\max} \right)^2 + \left( \phi_b^2 q_{2,\max} \right)^2 \right\}^{1/2} \quad (2.66)$$

where now:

$$q_{1,\max} = L_1 \frac{1}{\omega_b^{*2}} S_A(\omega_b^*, \xi_b^*) \quad (2.67)$$

$$q_{2,\max} = L_2 \frac{1}{\omega_s^{*2}} S_A(\omega_s^*, \xi_s^*) \quad (2.68)$$

with  $S_A(\omega, \xi)$  the acceleration design spectrum at  $\omega$  and  $\xi$ . Thus, substituting Eqs. (2.67) - (2.68) into Eqs. (2.65) - (2.66), it is obtained:

$$|v_s|_{\max} = \left\{ \left[ \varepsilon^2 (1-\gamma\varepsilon)^2 \frac{S_A^2(\omega_b^*, \xi_b^*)}{\omega_b^{*4}} \right] + \left[ \frac{1}{\gamma^2} (1-(1-\gamma)\varepsilon)^2 \gamma^2 \varepsilon^2 \frac{S_A^2(\omega_s^*, \xi_s^*)}{\omega_s^{*4}} \right] \right\}^{1/2} \quad (2.69)$$

$$|v_b|_{\max} = \left\{ \left[ (1-\gamma\varepsilon)^2 \frac{S_A^2(\omega_b^*, \xi_b^*)}{\omega_b^{*4}} \right] + \left[ \gamma^2 \varepsilon^2 \frac{S_A^2(\omega_s^*, \xi_s^*)}{\omega_s^{*4}} \right] \right\}^{1/2} \quad (2.70)$$

Many design spectra are approximately constant velocity spectra and in such cases the values of  $S_A$  for different frequencies, neglecting variations due to damping, are related by:

$$S_A(\omega, \beta) = \omega S_v \quad (2.71)$$

where  $S_v$  is a constant. For such design spectra the maximum displacements are:

$$|v_s|_{\max} = \varepsilon \left\{ (1-\gamma\varepsilon)^2 \frac{\omega_b^{*2}}{\omega_b^{*4}} (1-(1-\gamma)\varepsilon)^2 \frac{\omega_s^{*2}}{\omega_s^{*4}} \right\}^{1/2} S_v = \frac{\omega_b S_v}{(1-\gamma)\omega_s^2} \quad (2.72)$$

$$|v_b|_{\max} = \left\{ (1-\gamma\varepsilon)^2 \frac{\omega_b^{*2}}{\omega_b^{*4}} \gamma^2 \varepsilon^2 \frac{\omega_s^{*2}}{\omega_s^{*4}} \right\}^{1/2} S_v = \frac{S_v}{\omega_b} = S_D(\omega_b, \xi_b) \quad (2.73)$$

The design base shear coefficient  $C_s$  is defined by:

$$C_s = \frac{k_s v_s}{m} = \omega_s^2 v_s \quad (2.74)$$

For a fixed-base structure this is:

$$C_s = \omega_s^2 S_D(\omega_b, \xi_b) = S_A(\omega_b, \xi_b) \quad (2.75)$$

When the structure is isolated this becomes:

$$C_s = \omega_s^2 \left\{ \frac{\varepsilon^2 (1 - \gamma \varepsilon)^2 S_A^2(\omega_b^*, \xi_b^*)}{\omega_b^{*4}} + \frac{\varepsilon^2 [1 - (1 - \gamma) \varepsilon]^2 S_A^2(\omega_s^*, \xi_s^*)}{\omega_s^{*4}} \right\} \quad (2.76)$$

Substituting Eqs. (2.22) - (2.23) into Eq. (2.76), the base shear coefficient for the isolated structure assumes the form:

$$\begin{aligned} C_s &= \varepsilon \left\{ \frac{(1 - \gamma \varepsilon)^2 S_A^2(\omega_b^*, \xi_b^*)}{(1 - \gamma \varepsilon)^2 \varepsilon^2} + \frac{[1 - (1 - \gamma) \varepsilon]^2 S_A^2(\omega_s^*, \xi_s^*)}{\frac{(1 + \gamma \varepsilon)^2}{(1 - \gamma)^2}} \right\} = \\ &= \left\{ S_A^2(\omega_b^*, \xi_b^*) + \varepsilon^2 (1 - \gamma)^2 (1 - 2\varepsilon) S_A^2(\omega_s^*, \xi_s^*) \right\} \end{aligned} \quad (2.77)$$

Although the second term is multiplied by  $\varepsilon^2$ , it can be of the same order as the first term. This will be the case if the spectrum is a constant displacement spectrum. If the spectrum is either constant velocity or constant acceleration, the second term is negligible. These results indicate that for small  $\varepsilon$  and a typical design spectrum, the isolation system can be designed at least in the initial phase for a relative base displacement  $S_D(\omega_b, \xi_b)$  and the building for a base shear coefficient of  $S_A(\omega_b, \xi_b)$ . The reduction in base shear as compared with a fixed-base structure where  $C_s = S_A(\omega_s, \xi_s)$  is given by:

$$\frac{S_A(\omega_b, \xi_b)}{S_A(\omega_s, \xi_s)} \quad (2.78)$$

Which for a constant velocity spectrum is  $\omega_b / \omega_s$  or roughly of order  $\varepsilon^{1/2}$ , and this underestimates the reduction since  $\xi_b$  will in general be larger than  $\xi_s$ .

#### 2.2.1.5. Isolation of very flexible structures

The isolation of very flexible structure is here proposed for both new and existing buildings; the first case refers to IIS applications while the second one to both BIS and IIS technologies.

In new IIS applications the flexibility of the upper structure may affects the response of the overall structure leading to a possible detrimental amplification of the response of both upper and lower structures (see Chapter 6); in retrofit applications the isolation is proposed for existing buildings that are deficient in seismic resistance but with relatively long fixed-base periods.

In particular, the retrofit by means of inter-story isolation is realized introducing the isolation interface between the original configuration and its vertical addition, leading to a reduced response of the existing structure thanks to the mass damper effect exerted by the isolated upper structure; in addition, the isolation acts as a filter for the inertial forces transmitted to the upper structure, thanks to the isolation effect (see Chapter 7).

On the contrary, in retrofit BIS applications, a cut at the base of pillars is made to insert the isolation layer; a reduction in the seismic load is provided due to the isolation effect.

In order to illustrate both the benefits and limitations of this approach, it is useful to consider the special case when both the fixed-base period,  $\omega_s$ , and the isolation frequency,  $\omega_b$ , are the same. In this case, the characteristic equation for  $\omega_n$  in Eq. (2.19) for the two frequencies of the composite system becomes

$$(1 - \gamma)\omega_n^4 - 2\omega_0^2\omega_n^2 + \omega_0^4 = 0 \quad (2.79)$$

where  $\omega_0 = \omega_b = \omega_s$ .

The two frequencies are given by:

$$\omega_b^{*2} = \frac{1 - \gamma^{1/2}}{1 - \gamma} \omega_0^2 \quad (2.80)$$

$$\omega_s^{*2} = \frac{1 + \gamma^{1/2}}{1 - \gamma} \omega_0^2 \quad (2.81)$$

Combining the structure and the isolation system, from Eq. (2.80) can be noticed that the frequency  $\omega_b^*$  is larger than  $\omega_b$ ; conversely, Eq. (2.81) shows that the structural frequency is lower than the frequency  $\omega_s$ .

The mode shapes  $\phi^1$  and  $\phi^2$ , corresponding to these are

$$\phi^1 = \begin{Bmatrix} 1 \\ \frac{1-\sqrt{\gamma}}{\sqrt{\gamma}-\gamma} \end{Bmatrix} = \begin{Bmatrix} 1 \\ \frac{1}{\sqrt{\gamma}} \end{Bmatrix} \quad (2.82)$$

$$\phi^2 = \begin{Bmatrix} 1 \\ \frac{1+\sqrt{\gamma}}{-(\sqrt{\gamma}+\gamma)} \end{Bmatrix} = \begin{Bmatrix} 1 \\ \frac{1}{-\sqrt{\gamma}} \end{Bmatrix} \quad (2.83)$$

These are sketched in Fig. 2.7 and show that in both the mode shapes the relative modal displacement of the structure with respect to the isolation layer is equal to  $|\gamma^{-1/2}|$ .

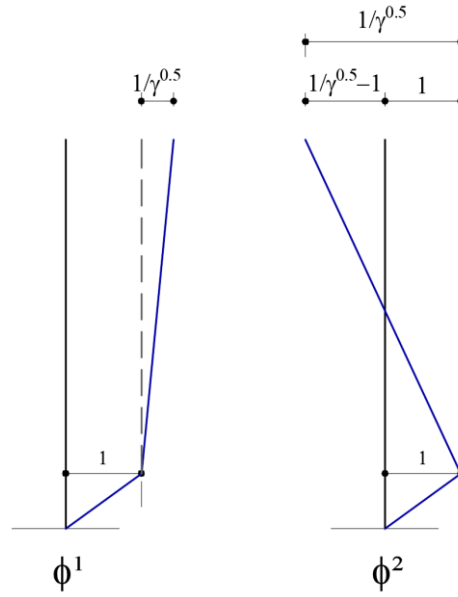


**Fig. 2.7. Mode Shapes of the 2DOF BIS model with isolation of very flexible structure**

The participation factors for each mode, calculated from Eq.(2.35), with the appropriate results for  $\omega_n$  and  $\phi^n$ , are:

$$L_1 = \frac{1}{2} \quad (2.84)$$

$$L_2 = \frac{1}{2} \quad (2.85)$$

and, since the higher mode participates with the same fraction of mass than the fundamental mode, its effect is not negligible.

Using the same approximations for modal damping as given by Eqs. (2.47) and (2.48), the damping factors for the two modes are:

$$\xi_b^* = \frac{\xi_b + \xi_2}{2} \left( \frac{1}{1 - \gamma^{1/2}} \right)^{1/2} \quad (2.86)$$

$$\xi_s^* = \frac{\xi_b + \xi_s}{2} \left( \frac{1}{1 + \gamma^{1/2}} \right)^{1/2} \quad (2.87)$$

Combining the structure and the isolation system, from Eq. (2.86) can be noticed that the damping  $\xi_b^*$  is larger than  $\xi_b$ ; conversely, Eq. (2.87) shows that the structural damping is almost equal to the damping in the bearings to the order of  $\epsilon^{1/2}$ ; the product of  $\xi_b$  and  $\epsilon^{1/2}$  may be a significant addition to the term  $\xi_s$  and could be important if  $\xi_s$  is very small. This shows that high damping in the rubber bearings can provide significant damping to the structural mode.

### ***2.2.1.6. Rigid structure vs. Flexible structure with respect to the isolation system***

A comparison between rigid and flexible structures with respect to the isolation system is proposed in the following numerical example.

- *Rigid structure with respect to the isolation system –  $I = 5$*

*Data:*

$$T_s = 0.4 \text{ s}; \quad \omega_s = 15.708 \text{ rad / s}$$

$$T_b = 2 \text{ s}; \quad \omega_b = 3.142 \text{ rad / s}$$

$$\gamma = \frac{m_b}{m_s + m_b} = 0.6$$

$$\xi_s = 0.02$$

$$\xi_b = 0.10$$

*Results:*

According to the data, the drift ratio,  $\varepsilon$ , is:

$$\varepsilon = \left( \frac{\omega_b}{\omega_s} \right)^2 = \left( \frac{T_s}{T_b} \right)^2 = \left( \frac{1}{I} \right)^2 = \left( \frac{0.4}{2} \right)^2 = 0.04$$

and, a period ratio  $I$ , defined as the ratio of the nominal period of the isolation system,  $T_b$ , to the nominal period of the structure,  $T_s$ , is equal to:

$$I = \frac{T_b}{T_s} = \frac{2}{0.4} = 5$$

From Eqs. (2.22) and (2.23), the circular frequencies of the base isolated structure are:

$$\omega_1 = \omega_b^* = \omega_b \sqrt{1 - \gamma \varepsilon} = 3.142 \sqrt{1 - 0.6 \cdot 0.04} = 3.104 \text{ rad / s}; \quad T_1 = 2.024 \text{ s}$$

$$\omega_2 = \omega_s^* = \omega_s \sqrt{\frac{1 + \gamma \varepsilon}{1 - \gamma}} = \omega_s \sqrt{\frac{1 + \gamma \varepsilon}{1 - \gamma}} = 15.708 \sqrt{\frac{1 + 0.6 \cdot 0.04}{1 - 0.6}} = 25.133 \text{ rad / s};$$

$$T_2 = 0.25 \text{ s}$$

From Eqs. (2.47) and (2.48), the damping ratios of the base isolated structure are:

$$\xi_1 = \xi_b^* = \xi_b \left( 1 - \frac{3}{2} \gamma \varepsilon \right) = 0.10 \left( 1 - \frac{3}{2} 0.6 \cdot 0.04 \right) = 0.0964$$

$$\begin{aligned}\xi_2 = \xi_s^* &= \left( \frac{\xi_s}{(1-\gamma)^{1/2}} + \gamma \frac{\xi_b \varepsilon^{1/2}}{(1-\gamma)^{1/2}} \right) \cdot \left( 1 - \frac{1}{2} \gamma \varepsilon \right) = \\ &= \left( \frac{0.02 + 0.6 \cdot 0.10 \cdot 0.04^{1/2}}{(1-0.6)^{1/2}} \right) \cdot \left( 1 - \frac{1}{2} 0.6 \cdot 0.04 \right) = 0.05\end{aligned}$$

Therefore, combining the isolation system and the structure it can be noticed that: the first period  $T_1$  increases almost of 1.2% with respect to the nominal isolation period  $T_b$ , while the second period  $T_2$  decreases of the 37.5% with respect to the nominal period of the structure  $T_s$ ; the first damping ratio  $\xi_1$  decreases of the 3.6% with respect to the nominal isolation period  $\xi_b$ , while the second period  $\xi_2$  increases of the 150% with respect to the nominal period of the structure  $\xi_s$ .

- *Flexible structure with respect to the isolation system –  $I = 5$*

*Data:*

$$T_s = T_b = 2.0 \text{ s}; \quad \omega_s = \omega_b = 3.142 \text{ rad / s}$$

$$\gamma = \frac{m_b}{m_s + m_b} = 0.6$$

$$\xi_s = 0.02$$

$$\xi_b = 0.10$$

*Results:*

According to the data, the drift and period ratios,  $\varepsilon$  and  $I$ , are:

$$\varepsilon = \left( \frac{\omega_b}{\omega_s} \right)^2 = \left( \frac{T_s}{T_b} \right)^2 = \left( \frac{1}{1} \right)^2 = \left( \frac{2}{2} \right)^2 = 1$$

$$I = \frac{T_b}{T_s} = \frac{2}{2} = 1$$

It is worth noticing that when the structure has the same flexibility of the isolation system, the drift and isolation periods are equal to 1.

From Eqs. (2.80) and (2.81), the circular frequencies of the base isolated structure are:



$$\omega_1 = \omega_b^* = \omega_0 \sqrt{\frac{1-\gamma^{1/2}}{1-\gamma}} = 3.142 \sqrt{\frac{1-0.6^{1/2}}{1-0.6}} = 2.359 \text{ rad / s}; \quad T_1 = 2.663 \text{ s}$$

$$\omega_2 = \omega_s^* = \omega_0 \sqrt{\frac{1+\gamma^{1/2}}{1-\gamma}} = 3.142 \sqrt{\frac{1+0.6^{1/2}}{1-0.6}} = 6.618 \text{ rad / s}; \quad T_2 = 0.949 \text{ s}$$

From Eqs. (2.86) and (2.87), the damping ratios of the base isolated structure are:

$$\xi_1 = \xi_b^* = \frac{\xi_s + \xi_b}{2} \left( \frac{1}{1-\gamma^{1/2}} \right)^{1/2} = \frac{0.02+0.10}{2} \left( \frac{1}{1-0.6^{1/2}} \right)^{1/2} = 0.126$$

$$\xi_2 = \xi_b^* = \frac{\xi_s + \xi_b}{2} \left( \frac{1}{1+\gamma^{1/2}} \right)^{1/2} = \frac{0.02+0.10}{2} \left( \frac{1}{1+0.6^{1/2}} \right)^{1/2} = 0.045$$

Therefore, combining the isolation system and the structure it can be noticed that: the first period  $T_1$  increases almost of 33.1% with respect to the nominal isolation period  $T_b$ , while the second period  $T_2$  decreases of the 52.5% with respect to the nominal period of the structure  $T_s$ ; the first damping ratio  $\xi_1$  increases of the 26% with respect to the nominal isolation period  $\xi_b$ , while the second period  $\xi_2$  increases of the 125% with respect to the nominal period of the structure  $\xi_s$ .

With reference to the above, the drift ratio  $\varepsilon$  is inverse proportional to the isolation ratio  $I$ , but when the structure possesses the same flexibility of the isolation,  $\varepsilon$  and  $I$  are equal.

Looking at the periods of the rigid and flexible structures, the first period is respectively almost equal (2.026 s), and larger than (2.664 s), the nominal isolation period (2.0 s); the second period in both cases is less than the nominal structural period (0.25 s vs. 0.4s and 0.949 s vs. 2 s).

Instead, considering the damping ratios of the rigid and flexible structures, the first damping ratio is respectively almost equal (0.096), and larger than (0.123), the isolation damping ratio (0.1); the second damping ratio in both cases is larger than the structural damping ratio (0.05 s and 0.045 vs. 0.02).

### 2.2.2. Base Isolation Theory for MDOF Systems

The foregoing two-degree-of-freedom analysis of a simple linear model can be applied to the case of a building with several stories. The structural system of this building may be represented by a mass matrix  $\mathbf{M}_s$ , a damping matrix  $\mathbf{C}_s$ , and a stiffness matrix  $\mathbf{K}_s$ . If the structure were conventionally based, the relative displacement  $\mathbf{u}_s$  of each degree of freedom with respect to the ground would be given by:

$$\mathbf{M}_s \ddot{\mathbf{u}}_s + \mathbf{C}_s \dot{\mathbf{u}}_s + \mathbf{K}_s \mathbf{u}_s = -\mathbf{M}_s \mathbf{r}_s \ddot{u}_g \quad (2.88)$$

Where  $\mathbf{r}_s$  is a vector that couples each degree of freedom to the ground motion. When this structural model is superposed on a base isolation system with base mass  $m_b$ , stiffness  $k_b$  and damping  $c_b$ , this equation is replaced by:

$$\mathbf{M}_s \ddot{\mathbf{v}}_s + \mathbf{C}_s \dot{\mathbf{v}}_s + \mathbf{K}_s \mathbf{v}_s = -\mathbf{M}_s \mathbf{r}_s (\ddot{u}_g + \ddot{v}_b) \quad (2.89)$$

where  $v_b$  is the relative displacement of the base slab to the ground. The overall equation of motion for the combined building and base slab is:

$$\mathbf{r}_s^T \mathbf{M}_s (\ddot{\mathbf{v}}_s + \mathbf{r}_s \ddot{v}_b + \mathbf{r}_s \ddot{u}_g) + m_b (\ddot{u}_g + \ddot{v}_b) + c_b \dot{v}_b + k_b v_b = 0 \quad (2.90)$$

which can be written in the form:

$$\mathbf{r}_s^T \mathbf{M}_s \ddot{\mathbf{v}}_s + (m + m_b) \ddot{v}_b + c_b \dot{v}_b + k_b v_b = -(m + m_b) \ddot{u}_g \quad (2.91)$$

In this equation we have identified  $\mathbf{r}_s^T \mathbf{M}_s \mathbf{r}_s$  as the total mass of the building so that  $m + m_b$  is the total mass carried on the isolation system. The matrix form of these equations is:

$$\mathbf{M} \ddot{\mathbf{v}} + \mathbf{C} \dot{\mathbf{v}} + \mathbf{K} \mathbf{v} = -\mathbf{M} \mathbf{r}_s \ddot{u}_g \quad (2.92)$$

where:

$$\mathbf{M} = \begin{bmatrix} m + m_b & \mathbf{r}_s^T \mathbf{M}_s \\ \mathbf{M}_s \mathbf{r}_s & \mathbf{M}_s \end{bmatrix}; \quad \mathbf{C} = \begin{bmatrix} c_b & 0 \\ \mathbf{0} & \mathbf{C}_s \end{bmatrix} \quad (2.93)$$

and:

$$\mathbf{K} = \begin{bmatrix} \mathbf{k}_b & \mathbf{0} \\ \mathbf{0} & \mathbf{K}_s \end{bmatrix}; \quad \mathbf{r} = \begin{bmatrix} 1 \\ \mathbf{0} \end{bmatrix} \quad (2.94)$$

with:

$$\mathbf{v} = \begin{bmatrix} \mathbf{v}_b \\ \mathbf{v}_s \end{bmatrix} \quad (2.95)$$

The natural modes of the fixed-base structure are assumed known and denoted by  $\phi_s^i$  where  $i=1$  to  $N$ . in terms of these, the displacement of each degree of freedom of the superstructure can be represented as:

$$\mathbf{v}_s = \sum_{i=1}^N q_{s,i} \phi_s^i \quad (2.96)$$

The natural frequencies  $\omega_{s,n}^2$  are given by:

$$\mathbf{M}_s \phi_s^n \omega_{s,n}^2 = \mathbf{K}_s \phi_s^n \quad (2.97)$$

and we assume that  $\phi_s^n \mathbf{C}_s \phi_s^m = 0$  if  $n \neq m$ .

The matrix equations of motion reduce to the  $N+1$  equations:

$$\mathbf{r}_s^T \mathbf{M}_s \phi_s^i \ddot{q}_{s,i} + (m + m_b) \ddot{v}_b + c_b \dot{v}_b + k_b v_b = -(m + m_b) \ddot{u}_g \quad (2.98)$$

and:

$$\ddot{q}_{s,i} + 2\omega_{s,i} \xi_{s,i} \dot{q}_{s,i} + \omega_{s,i}^2 q_{s,i} = -L_{s,i} (\ddot{u}_g + \ddot{v}_b), \quad i=1 \text{ to } N \quad (2.99)$$

where  $L_{s,i}$  are the participation factors of the fixed-base modes, i.e.:

$$L_{s,i} = \frac{\phi_s^{iT} \mathbf{M}_s \mathbf{r}_s}{\phi_s^{iT} \mathbf{M} \phi_s^i} \quad (2.100)$$

The fixed-base modal masses, stiffnesses and damping constants are:

$$\tilde{m}_{s,i} = \boldsymbol{\phi}_s^{iT} \mathbf{M}_s \boldsymbol{\phi}_s^i; \quad \tilde{k}_{s,i} = \boldsymbol{\phi}_s^{iT} \mathbf{K}_s \boldsymbol{\phi}_s^i; \quad \tilde{c}_{s,i} = \boldsymbol{\phi}_s^{iT} \mathbf{C}_s \boldsymbol{\phi}_s^i \quad (2.101)$$

and we can write these equations in the form:

$$\sum_{i=1}^N \frac{L_{s,i} \tilde{m}_{s,i}}{m + m_b} \ddot{q}_{s,i} + \ddot{v}_b + 2\omega_b \xi_b \dot{v}_b + \omega_b^2 v_b = -\ddot{u}_g \quad (2.102)$$

and:

$$L_{s,i} \ddot{v}_b + \ddot{q}_{s,i} + 2\omega_{s,i} \xi_{s,i} \dot{q}_{s,i} + \omega_{s,i}^2 q_{s,i} = -L_{s,i} \ddot{u}_g, \quad i = 1 \text{ to } N \quad (2.103)$$

Comparing the Eqs. (2.102) - (2.103) with the previous set of the 2DOF isolated model, i.e. Eqs. (2.17) - (2.16), the equations can be made to correspond if we replace  $v_b$  in the elementary analysis with  $L_1 v_b$ ,  $\ddot{u}_g$  with  $L_1 \ddot{u}_g$ , and

$$\gamma = \frac{m}{m + m_b}$$

by:

$$\gamma = \frac{L_{s,1}^2 \tilde{m}_{s,1}}{m + m_b} \quad (2.104)$$

giving:

$$\frac{L_{s,1}^2 \tilde{m}_{s,1}}{m + m_b} \ddot{q}_{s,i} + L_{s,1} \ddot{v}_b + 2\omega_b \xi_b L_{s,1} \dot{v}_b + \omega_b^2 L_{s,1} v_b = -L_{s,1} \ddot{u}_g \quad (2.105)$$

$$L_{s,1} \ddot{v}_b + \ddot{q}_{s,i} + 2\omega_{s,i} \xi_{s,i} \dot{q}_{s,i} + \omega_{s,i}^2 q_{s,i} = -L_{s,1} \ddot{u}_g \quad (2.106)$$

If this is done,  $q_{s,i}$  will be given by the solution for  $v_s$ .

The basic results for the single-degree-of-freedom structure, namely that:

$$|v_b|_{\max} = \frac{1}{\omega_b^2} S_A(\omega_b, \xi_b) \quad (2.107)$$

and:

$$C_s = S_A^2(\omega_b^*, \xi_b^*) + \varepsilon^2 (1 - \gamma) S_A^2(\omega_s^*, \xi_s^*)^{(1/2)} \quad (2.108)$$

are replaced as follow. The maximum relative base displacement is given by:

$$|L_{s,l} v_b|_{\max} = \frac{1}{\omega_b^2} L_{s,l} S_A(\omega_b, \xi_b) \quad (2.109)$$

and, since  $L_i$  appears on both sides, the elementary result is unchanged. In order to obtain the base shear we have:

$$|q_{s,l}|_{\max} = \left\{ \frac{\varepsilon^2 L_{s,l}^2 S_A^2(\omega_b^*, \xi_b^*)}{\omega_b^{*4}} + \frac{\varepsilon^2 L_{s,l}^2 S_A^2(\omega_s^*, \xi_s^*)}{\omega_s^{*4}} \right\}^{1/2} \quad (2.110)$$

where now  $\omega_s^*, \xi_s^*$  are calculated using the earlier transformations, and

$$\varepsilon = \frac{\omega_b^2}{\omega_1^2} \quad (2.111)$$

The relative displacement vector  $\mathbf{v}_s$  is given by:

$$\mathbf{v}_s = \mathbf{q}_{s,l} \boldsymbol{\phi}_s^1 \quad (2.112)$$

and the inertial force on each element, neglecting damping contributions, is

$$\mathbf{F}_s = \mathbf{K}_s \mathbf{v}_s = \mathbf{q}_{s,l} \mathbf{K}_s \boldsymbol{\phi}_s^1 = \mathbf{q}_{s,l} \mathbf{M}_s \boldsymbol{\phi}_s^1 \omega_{s,l}^2 \quad (2.113)$$

the total horizontal force on the superstructure is:

$$\mathbf{r}_s^T \mathbf{F}_s = \mathbf{q}_{s,l} \omega_{s,l}^2 L_{s,l} \tilde{\mathbf{m}}_l \quad (2.114)$$

and this is the turn expressed in terms of the base shear coefficient  $C_s$  through:

$$\mathbf{C}_s \mathbf{m} = \mathbf{r}_s \mathbf{F}_s \quad (2.115)$$

Thus:

$$\begin{aligned} C_s &= \frac{L_{s,l}^2 \tilde{\mathbf{m}}_{s,l}}{m} \left\{ L_{s,l}^2 S_A^2(\omega_b, \xi_b) + (1-\gamma)^2 \varepsilon^2 L_{s,l}^2 S_A^2(\omega_b^*, \xi_b^*) \right\}^{1/2} = \\ &= \frac{L_{s,l}^2 \tilde{\mathbf{m}}_{s,l}}{m} \left\{ S_A^2(\omega_b, \xi_b) + (1-\gamma)^2 \varepsilon^2 S_A^2(\omega_b^*, \xi_b^*) \right\}^{1/2} \end{aligned} \quad (2.116)$$

In the standard equivalent lateral force procedure, the building considered as a fixed-base structure is designed to resist the lateral seismic base shear  $V$  given by  $V = C_s W$ , where  $W$  is the total weight. The value of  $C_s$  is derived from a formula such as:

$$C_s = \frac{1.2 A_v S}{R T^{2/3}} \quad (2.117)$$

With  $A_v$  a code-specified acceleration,  $S$  a factor to represent soil type,  $T$  the period of the building and  $R$  a ductility factor. Alternatively, the value of  $C_s$  can be derived from a spectrum.

The lateral seismic shear force  $F_x$  at any level denoted by  $x$  is given by:

$$F_x = C_{v_x} V \quad (2.118)$$

where

$$C_{v_x} = \frac{W_x h_x^j}{\sum_i W_i h_i^j} \quad (2.119)$$

In this formula the terms  $W_i$ ,  $W_x$  are the weights of levels  $i$ -th and  $x$ ,  $h_i$ ,  $h_x$  the heights of levels  $i$  and  $x$ , and  $j$ -th an exponent which is taken to be

1 if the period is 0.5 seconds or less and 2 if it is 2.5 seconds or more. This reflects the fact that a stiff, low building will respond predominantly in shear with a roughly linear first mode and a tall, flexible building in bending with a quadratic first mode. The exponent  $j$  may be selected by linear interpolation between 1 and 2.

The seismic shear force at any level  $x$  is calculated from:

$$V_x = \sum_{i=1}^N F_i \quad (2.120)$$

For an isolated building the distribution of shear force should be given by the shape of the first isolated mode, namely  $\{1, \epsilon L_1 \phi\}^T$ , or, if we neglect the  $\epsilon$  terms, the distribution should be uniform. Then:

$$F_x = C_{V_x} V \quad (2.121)$$

and:

$$C_{V_x} = \frac{W_x}{W} \quad (2.122)$$

and:

$$V_x = \sum_{i=x}^N C_{V_i} V = V \sum_{i=x}^N \frac{W_i}{W} = C_s \sum_{i=x}^N W_i \quad (2.123)$$

Therefore, in design we estimate  $C_s$  from the design spectrum and design the superstructure at each level for a shear force equal to  $C_s$  times the weight above. If appropriate, the ductility factor  $R$  can be taken into account, but the reduction factor varies from 1 to 8 depending in the structural system used and represents the intuitive feeling that many structural forms have substantial reserves of strength beyond their elasticity capacity.

## 2.3. TUNED MASS DAMPER SYSTEMS (TMD)

### 2.3.1. Tuned Mass Damper Theory for SDOF Systems

#### 2.3.1.1. Undamped Structure: Undamped TMD

Fig. 2.8 shows an undamped SDOF + TMD model composed by a main system with a mass  $m$  and a spring stiffness  $k$ , and a tuned mass damper attached to the primary mass with a mass  $m_d$  and a stiffness  $k_d$ .

The various displacement measures are:  $u_g$ , the absolute ground motion;  $v_s$ , the relative motion between the primary mass and the ground; and  $v_d$ , the relative displacement between the damper and the primary mass. Considering the primary mass subjected to both external forcing and ground motion, the governing equations take the form

$$m_d(\ddot{v}_d + \ddot{v}_s) + k_d v_d = -m_d \ddot{u}_g \quad (2.124)$$

$$m\ddot{v}_s + k v_s - k_d v_d = -m\ddot{u}_g + p \quad (2.125)$$

where  $\ddot{u}_g$  is the absolute ground acceleration and  $p$  is the force loading applied to the primary mass.

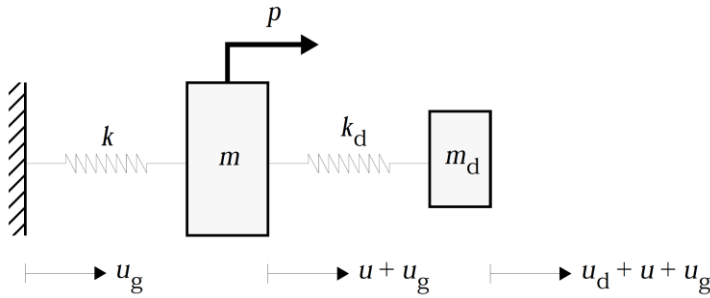


Fig. 2.8. Undamped SDOF system coupled with an undamped TMD system

Considering both excitations periodic, of frequency  $\Omega$ , i.e.:

$$\ddot{u}_g = \hat{\ddot{u}}_g \sin \Omega t \quad (2.126)$$

$$p = \hat{p} \sin \Omega t \quad (2.127)$$



expressing the response as

$$v_s = \hat{v}_s \sin \Omega t \quad (2.128)$$

$$v_d = \hat{v}_d \sin \Omega t \quad (2.129)$$

and substituting for these variables, the equilibrium equations are transformed into:

$$(-m_d \Omega^2 + k_d) \hat{v}_d - m_d \Omega^2 \hat{v}_s = -m_d \hat{\ddot{u}}_g \quad (2.130)$$

$$-k_d \hat{v}_d + (-m \Omega^2 + k) \hat{v}_s = -m \hat{\ddot{u}}_g + \hat{p} \quad (2.131)$$

The solutions for  $\hat{v}_s$  and  $\hat{v}_d$  are given by

$$\hat{v}_s = \frac{\hat{p}}{k} \left( \frac{1 - \rho_d^2}{D_1} \right) - \frac{m \hat{\ddot{u}}_g}{k} \left( \frac{1 + \alpha - \rho_d^2}{D_1} \right) \quad (2.132)$$

$$\hat{v}_d = \frac{\hat{p}}{k_d} \left( \frac{\alpha \cdot \rho^2}{D_1} \right) - \frac{m \hat{\ddot{u}}_g}{k_d} \left( \frac{\alpha}{D_1} \right) \quad (2.133)$$

where

$$D_1 = (1 - \rho^2)(1 - \rho_d^2) - \alpha \cdot \rho^2 \quad (2.134)$$

$\alpha$  is the mass ratio equal to

$$\alpha = \frac{m_d}{m} \quad (2.135)$$

$\rho$ ,  $\rho_d$  are dimensionless frequency ratios, given by

$$\rho = \frac{\Omega}{\omega_s} = \frac{\Omega}{\sqrt{k/m}} \quad (2.136)$$

$$\rho_d = \frac{\Omega}{\omega_d} = \frac{\Omega}{\sqrt{k_d/m_d}} \quad (2.137)$$

with  $\omega_s$  and  $\omega_d$  the frequencies of the primary mass and the absorber, respectively.

Selecting the mass ratio and the damper frequency ratio such that

$$1 + \alpha - \rho_d^2 = 0 \quad (2.138)$$

reduces the solutions (2.132) and (2.133) to

$$\hat{v}_s = \frac{\hat{p}}{k} \quad (2.139)$$

$$\hat{v}_d = -\frac{\hat{p}}{k_d} \rho^2 + \frac{m \hat{u}_g}{k_d} \quad (2.140)$$

This choice isolates the primary mass from ground motion and reduces the response due to external force to the pseudo-static value  $\hat{p}/k$ . A typical range for  $\alpha$  is  $0.01 \div 0.1$ . Then, the *optimal* damper frequency is very close to the forcing frequency. The exact relationship follows from Eq. (2.138) and is given by:

$$\omega_d|_{\text{opt}} = \frac{\Omega}{\sqrt{1+\alpha}} \quad (2.141)$$

The corresponding damper stiffness is

$$k_d|_{\text{opt}} = \left( \omega_d|_{\text{opt}} \right)^2 m_d = \frac{\Omega m \alpha}{1+\alpha} \quad (2.142)$$

Finally, substituting for  $k_d$ , Eq. (2.140) takes the following form

$$\hat{v}_d = \frac{1+\alpha}{\alpha} \left( \left| \frac{\hat{p}}{k} \right| + \left| \frac{\hat{u}_g}{\Omega^2} \right| \right) \quad (2.143)$$

One specifies the amount of relative displacement for the damper and determines  $\alpha$  with Eq.(2.143). Given  $\alpha$  and  $\Omega$ , the stiffness is found

using Eq. (2.142). It should be noted that this stiffness applies for a particular forcing frequency. Once the mass damper properties are defined, Eqs. (2.132) and (2.133) can be used to determine the response for a *different* forcing frequency. The primary mass will move under ground motion excitation in this case.

### 2.3.1.2. Undamped Structure: Damped TMD

Fig. 2.9 shows an undamped SDOF + damped TMD model composed by a main system with a mass  $m$  and a spring stiffness  $k$ , a tuned mass damper attached to the primary mass with a mass  $m_d$ , a stiffness  $k_d$  and a viscous damper  $c_d$ .

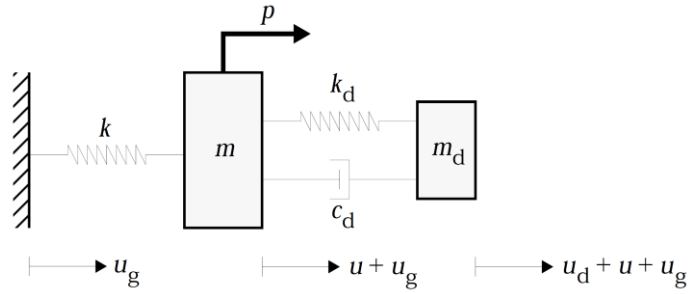


Fig. 2.9. Undamped SDOF system coupled with a damped TMD system

Considering the primary mass subjected to both external forcing  $p$  and ground motion  $\ddot{u}_g$ , the governing equations take the form

$$m_d(\ddot{v}_d + \ddot{v}_s) + c_d \dot{v}_d + k_d v_d = -m_d \ddot{u}_g \quad (2.144)$$

$$m \ddot{v}_s + k v_s - c_d \dot{v}_d - k_d v_d = -m \ddot{u}_g + p \quad (2.145)$$

The inclusion of the damping terms in Eqs. (2.144) - (2.145) produces a phase shift between the period excitation and the response. It is convenient to work initially with the solution expressed in terms of complex quantities. The excitation is expressed as

$$\ddot{u}_g = \hat{u}_g e^{i\Omega t} \quad (2.146)$$

$$p = \hat{p} e^{i\Omega t} \quad (2.147)$$

where  $\hat{\mathbf{u}}_g$  and  $\hat{p}$  are real quantities. The response is taken as

$$\mathbf{v}_s = \hat{\mathbf{v}}_s e^{i\Omega t} \quad (2.148)$$

$$\mathbf{v}_d = \hat{\mathbf{v}}_d e^{i\Omega t} \quad (2.149)$$

where the complex amplitudes,  $\hat{\mathbf{v}}_s$  and  $\hat{\mathbf{v}}_d$  are considered to be complex quantities. The real and the imaginary parts of  $\hat{\mathbf{u}}_g$  correspond to cosine and sinusoidal input. Then, the corresponding solution is given by either the real (for cosine) or imaginary (for sine) parts of  $\mathbf{v}_s$  and  $\mathbf{v}_d$ . Substituting Eqs. (2.148) - (2.149) in the set of governing equations and canceling  $e^{i\Omega t}$  from both sides results in

$$(-m_d \Omega^2 + i c_d \Omega + k_d) \hat{\mathbf{v}}_d - m_d \Omega^2 \hat{\mathbf{v}}_s = -m_d \hat{\mathbf{u}}_g \quad (2.150)$$

$$-(i c_d \Omega + k_d) \hat{\mathbf{v}}_d + (-m \Omega^2 + k) \hat{\mathbf{v}}_s = -m \hat{\mathbf{u}}_g + \hat{p} \quad (2.151)$$

The solution of the governing equations is

$$\hat{\mathbf{v}}_s = \frac{\hat{p}}{k D_2} (f^2 - \rho^2 + i 2 \xi_d \rho f) - \frac{m \hat{\mathbf{u}}_g}{k D_2} [(1 + \alpha) f^2 - \rho^2 + i 2 \xi_d \rho f (1 + \alpha)] \quad (2.152)$$

$$\hat{\mathbf{v}}_d = \frac{\hat{p} \rho^2}{k D_2} - \frac{m \hat{\mathbf{u}}_g}{k D_2} \quad (2.153)$$

where

$$D_2 = (1 - \rho^2)(f^2 - \rho^2) - \alpha \rho^2 f^2 + i 2 \xi_d \rho f [1 - \rho^2 (1 + \alpha)] \quad (2.154)$$

with

$$f = \frac{\omega_d}{\omega_s} \quad (2.155)$$

the frequency ratio between the mass damper and the main structure, and  $\rho$  was defined earlier as the ratio of  $\Omega$  to  $\omega_s$  (see Eq. (2.136)).

Converting the complex solutions to polar form leads to the following expressions

$$\hat{v}_s = \frac{\hat{p}}{k} H_1 e^{i\delta_1} - \frac{m\hat{u}_g}{k} H_2 e^{i\delta_2} \quad (2.156)$$

$$\hat{v}_d = \frac{\hat{p}}{k} H_3 e^{-i\delta_3} - \frac{m\hat{u}_g}{k} H_4 e^{-i\delta_3} \quad (2.157)$$

where the  $H_i$  factors define the amplification of the pseudo-static responses, and the  $\delta$  terms are the phase angles between the response and the excitation. The various  $H_i$  and  $\delta_i$  expressions are listed below

$$H_1 = \frac{\sqrt{(f^2 - \rho^2)^2 + (2\xi_d \rho f)^2}}{|D_2|} \quad (2.158)$$

$$H_2 = \frac{\sqrt{[(1 + \alpha)f^2 - \rho^2]^2 + [2\xi_d \rho f(1 + \alpha)]^2}}{|D_2|} \quad (2.159)$$

$$H_3 = \frac{\rho^2}{|D_2|} \quad (2.160)$$

$$H_4 = \frac{1}{|D_2|} \quad (2.161)$$

$$|D_2| = \sqrt{[(1 - \rho^2)(f^2 - \rho^2) - \alpha \rho^2 f^2]^2 + 4\xi_d^2 \rho^2 f^2 [1 - \rho^2(1 + \alpha)]^2} \quad (2.162)$$

Also

$$\delta_1 = \alpha_1 - \delta_3 \quad (2.163)$$

$$\delta_2 = \alpha_2 - \delta_3 \quad (2.164)$$

$$\tan \delta_3 = \frac{2\xi_d \rho f [1 - \rho^2(1 + \alpha)]}{(1 - \rho^2)(f^2 - \rho^2) - \alpha \rho^2 f^2} \quad (2.165)$$

$$\tan \alpha_1 = \frac{2\xi_d \rho f}{f^2 - \rho^2} \quad (2.166)$$

$$\tan \alpha_2 = \frac{2\xi_d \rho f(1+\alpha)}{(1+\alpha)f^2 - \rho^2} \quad (2.167)$$

From Eqs. (2.158) - (2.159) can be seen that the amplification factors  $H_1$  and  $H_2$  depend on four essential variables, i.e.  $\alpha$ ,  $\xi_d$ ,  $f$  and  $\rho$ .

In what follows, both the solutions corresponding to external forcing ( $H_1$ ) and ground motion ( $H_2$ ) are examined and optimal values for the loading conditions are established.

Figs. 2.10 - 2.11 shows the variation of the amplitudes  $H_1$  and  $H_2$  with the frequency ratio  $\rho$  for specific values of damper mass  $\alpha$  and frequency ratio  $f$ , and various values of the damper damping ratio,  $\xi_d$ ; in particular, with dotted lines are depicted the curves with damping equal to 0 and  $\infty$ , with continuous lines are drawn the curves with different not null damping values.

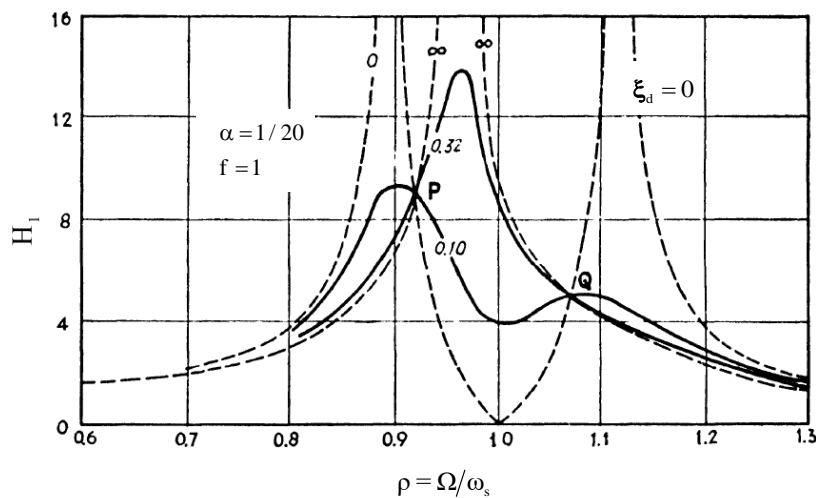


Fig. 2.10.  $H_1$  vs.  $\rho$  [Den Hartog 1940]

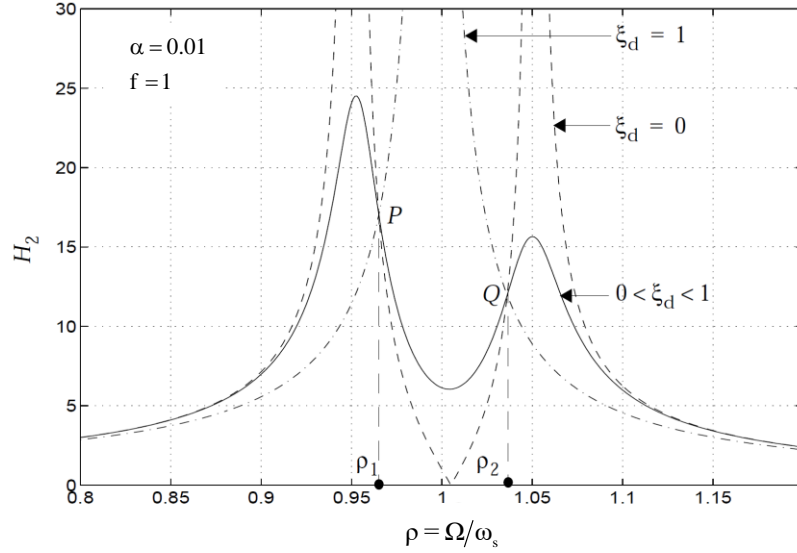


Fig. 2.11.  $H_2$  vs.  $\rho$  [Connor & Laflamme 2014]

From Figs. 2.10 - 2.11 the following observations can be made:

for  $\xi_d = 0$  the case of the damper absorber falls into the case of the undamped TMD and there are two infinite peaks located on each side of  $\rho = 1$ ;

for  $\xi_d = \infty$  the two masses are virtually damped together into a single degree of freedom system with a total mass  $m + m_d$  and there is a single infinite peak located at  $\rho \approx 1$ ;

damping factors in between 0 and  $\infty$  produce finite resonant peak;

all the curves pass through the point P and Q independently by the damping.

The values of  $\xi_d$  equal to 0 and  $\infty$  can be physically explained as follows [Den Hartog 1947]. “It was seen that damping energy is dissipated, i.e., converted into heat. When the damping force does considerable work, the amplitude remains small at resonance. This is a relation that holds for more complicated systems also. The work done by the damping force is given by the force times the displacements through which it operates. In our case the displacement is the relative motion between the two masses or also the extension of the damper spring.

If  $\xi_d = 0$ , the damping force is zero, no work is done, and hence the resonant amplitude is infinite. But when  $\xi_d = \infty$ , the two masses are locked

each other, their relative displacement is zero and again no work is done. Somewhere in between 0 and  $\infty$  there is a damping for which the product of damping force and displacement becomes a maximum, and then the resonant amplitude will be small.”

The goal to be pursued is to reduce the resonant peak of the amplitude down to its lowest possible value.

Since all the curves pass through the points **P** and **Q** independently on the damping value, the problem is solved by the calculation of their location. The most favorable curve is the one that passes with a horizontal tangent through the highest of the two fixed points **P** or **Q**. Therefore, the best obtainable resonant amplitude (at optimum damping) is the ordinate of that point.

In addition, by changing the frequency ratio  $f$  of the damper with respect to the main system, **P** and **Q** can be shifted up and down the curve for  $\xi_d = 0$ . By changing  $f$  one point goes up and the other goes down.

Clearly, the most favorable case is such that, first by a proper choice of  $f$  the fixed points are adjusted to equal height, and second by a proper choice of  $\xi_d$  the curve is adjusted to pass with a horizontal tangent through one of them.

From the above considerations, the amplification factors  $H_1$  and  $H_2$  can be written as

$$H_{1,2} = \sqrt{\frac{a_1^2 + \xi_d^2 a_2^2}{a_3^2 + \xi_d^2 a_4^2}} = \frac{a_2}{a_4} \sqrt{\frac{a_1^2 / a_2^2 + \xi_d^2}{a_3^2 / a_4^2 + \xi_d^2}} \quad (2.168)$$

where the  $a$  terms are functions of  $\alpha$ ,  $\rho$  and  $f$ . Then, for  $H_1$  and  $H_2$  to be independent of  $\xi_d$ , the following condition must be satisfied

$$\left| \frac{a_1}{a_2} \right| = \left| \frac{a_3}{a_4} \right| \quad (2.169)$$

The corresponding values for  $H_1$  and  $H_2$  are



$$H_{1,2}|_{P,Q} = \left| \frac{a_2}{a_4} \right| \quad (2.170)$$

Starting from this point, two loading conditions, i.e. sinusoidal force and harmonic ground motion, are separately examined as follows.

***Sinusoidal external force***

An in-depth treatment of the external forcing case is contained in Den Hartog's text [Den Hartog 1940]; the main features are reported in the following.

Substituting the  $a_1$ ,  $a_2$ ,  $a_3$ ,  $a_4$  terms of the amplification factor  $H_1$  for the sinusoidal external force, (2.158),

$$\begin{aligned} a_1 &= (f^2 - \rho^2)^2, \\ a_2 &= 4\rho^2 f^2, \\ a_3 &= [(1 - \rho^2)(f^2 - \rho^2) - \alpha\rho^2 f^2]^2, \\ a_4 &= 4\rho^2 f^2 [1 - \rho^2(1 + \alpha)]^2, \end{aligned}$$

in Eq. (2.169), i.e.:

$$(f^2 - \rho^2)^2 = \frac{[(1 - \rho^2)(f^2 - \rho^2) - \alpha\rho^2 f^2]^2}{[1 - \rho^2(1 + \alpha)]^2} \quad (2.171)$$

a quadratic equation for  $\rho^2$  is obtained:

$$\rho^4 - 2 \frac{1 + f^2 + \alpha f^2}{2 + \alpha} \rho^2 + \frac{2f^2}{2 + \alpha} = 0 \quad (2.172)$$

The two positive roots,  $\rho_1$  and  $\rho_2$ , are the frequency ratios corresponding to the abscissa of the points **P** and **Q**.

Similarly, Eq. (2.170) expands to

$$H_1|_{P,Q} = \frac{1}{|1 - \rho_{1,2}^2(1 + \alpha)|} \quad (2.173)$$

### *Optimal tuning frequency*

From Eq. (2.172), substituting the two roots into Eq. (2.173) and equating the two expressions, the same ordinate for the points P and Q is derived. By simple algebra manipulations, the *optimal tuning frequency*  $f_{\text{opt}}$  is given by:

$$f_{\text{opt}} = \frac{1}{1 + \alpha} \quad (2.174)$$

Thus, the corresponding optimum damper frequency is

$$\omega_d|_{\text{opt}} = f_{\text{opt}} \omega_s \quad (2.175)$$

and the corresponding roots and optimal amplification factors are

$$\rho_{1,2}|_{\text{opt}} = \sqrt{\frac{1}{1 + \alpha} \left( 1 \mp \sqrt{\frac{\alpha}{2 + \alpha}} \right)} \quad (2.176)$$

$$H_1|_{\text{opt}} = \sqrt{1 + \frac{2}{\alpha}} \quad (2.177)$$

with coordinates of the fixed points equal to  $P, Q \equiv (\rho_{1,2}|_{\text{opt}}; H_1|_{\text{opt}})$ .

### *Optimal damping*

The *optimal damping*  $\xi_d|_{\text{opt}}$  at the optimal tuning frequency  $f_{\text{opt}}$  can be derived substituting Eq. (2.174) into Eq. (2.158) and writing the resulting expression in terms of damping, as follows.

$$\xi_d^2 = \frac{(f^2 - \rho^2)^2 - H_1^2 \left[ (1 - \rho^2)(f^2 - \rho^2) - \alpha \rho^2 f^2 \right]^2}{4f^2 \rho^2 \left[ 1 - H_1^2 \rho^2 (1 + \alpha) \right]^2} \quad (2.178)$$

Differentiating Eq. (2.178) with respect to  $\rho$ , thus finding the slope of the curve, and equating it to zero, for both the points P and Q, the expressions of  $\xi_d$  can be calculated, leading to:

$$\xi_d^2 = \frac{\alpha(3 \mp \sqrt{\alpha/(\alpha+2)})}{8(1+\alpha)^2} \quad (2.179)$$

A useful average value between the two gives the optimal damping  $\xi_d|_{\text{opt}}$  at the optimal tuning frequency:

$$\xi_d|_{\text{opt}} = \sqrt{\frac{3\alpha}{8(1+\alpha)^2}} \quad (2.180)$$

A graphical representation of the optimal condition is depicted in Fig. 2.12.

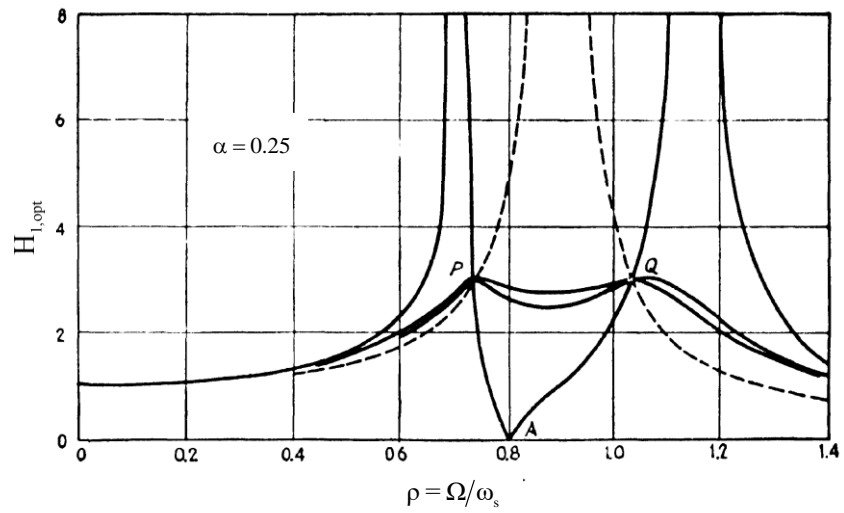


Fig. 2.12.  $H_1$  vs.  $\rho$  for  $f_{\text{opt}}$  [Den Hartog 1940]

### **Harmonic ground acceleration**

Substituting the  $a_1$ ,  $a_2$ ,  $a_3$ ,  $a_4$  terms of the amplification factor  $H_2$  for the harmonic ground acceleration, (2.159),

$$\begin{aligned}
a_1 &= \left[ (1 + \alpha) f^2 - \rho^2 \right]^2, \\
a_2 &= 4 \rho^2 f^2 (1 + \alpha)^2, \\
a_3 &= \left[ (1 - \rho^2) (f^2 - \rho^2) - \alpha \rho^2 f^2 \right]^2, \\
a_4 &= 4 \rho^2 f^2 \left[ 1 - \rho^2 (1 + \alpha) \right]^2,
\end{aligned}$$

in Eq. (2.169), i.e.:

$$\frac{\left[ (1 + \alpha) f^2 - \rho^2 \right]^2}{(1 + \alpha)^2} = \frac{\left[ (1 - \rho^2) (f^2 - \rho^2) - \alpha \rho^2 f^2 \right]^2}{\left[ 1 - \rho_{1,2}^2 (1 + \alpha) \right]^2} \quad (2.181)$$

a quadratic equation for  $\rho^2$  is obtained:

$$\rho^4 - \left[ (1 + \alpha) f^2 + \frac{1 + 0.5\alpha}{1 + \alpha} \right] \rho^2 + f^2 = 0 \quad (2.182)$$

The two positive roots,  $\rho_1$  and  $\rho_2$ , are the frequency ratios corresponding to the abscissa of the points **P** and **Q**.

Similarly, Eq. (2.170) expands to

$$H_2|_{P,Q} = \frac{1 + \alpha}{\left[ 1 - \rho_{1,2}^2 (1 + \alpha) \right]} \quad (2.183)$$

#### *Optimal tuning frequency*

From Eq. (2.182), substituting the two roots into Eq. (2.183) and equating the two expressions, the same vertical coordinate for the points **P** and **Q** is derived.

By simple algebra manipulations, the *optimal tuning frequency*  $f_{\text{opt}}$  is given by:

$$f_{\text{opt}} = \frac{\sqrt{1 - 0.5\alpha}}{1 + \alpha} \quad (2.184)$$

Thus, the corresponding optimum damper frequency is

$$\omega_d|_{\text{opt}} = f_{\text{opt}} \omega_s \quad (2.185)$$

and the corresponding roots and optimal amplification factors are

$$\rho_{1,2}|_{\text{opt}} = \sqrt{\frac{1 \pm \sqrt{0.5\alpha}}{1 + \alpha}} \quad (2.186)$$

$$H_2|_{\text{opt}} = \frac{1 + \alpha}{\sqrt{0.5\alpha}} \quad (2.187)$$

with coordinates of the fixed points equal to  $P, Q \equiv (\rho_{1,2}|_{\text{opt}}; H_2|_{\text{opt}})$ .

#### *Optimal damping*

The *optimal damping*  $\xi_d|_{\text{opt}}$  at the optimal tuning frequency  $f_{\text{opt}}$  can be derived substituting Eq. (2.184) into Eq. (2.159) and writing the resulting expression in terms of damping.

Differentiating this resulting expression with respect to  $\rho$ , thus finding the slope of the curve, and equating that slope to zero respectively for the point P and Q, the expressions of  $\xi_d$  can be calculated.

The expression for the optimal damping at the optimal tuning frequency is

$$\xi_d|_{\text{opt}} = \sqrt{\frac{\alpha(3 - \sqrt{0.5\alpha})}{8(1 + \alpha)(1 - 0.5\alpha)}} \quad (2.188)$$

Figs 2.13 ÷ 2.18 show the variation of the optimal parameters (i.e.:  $f_{\text{opt}}$ ,

$\rho_{1,2}|_{\text{opt}}$ ,  $\xi_d|_{\text{opt}}$ ,  $H_2|_{\text{opt}}$ ,  $H_4|_{\text{opt}}$ ,  $H_4 / H_2$ ) with the mass ratio,  $\alpha$ .

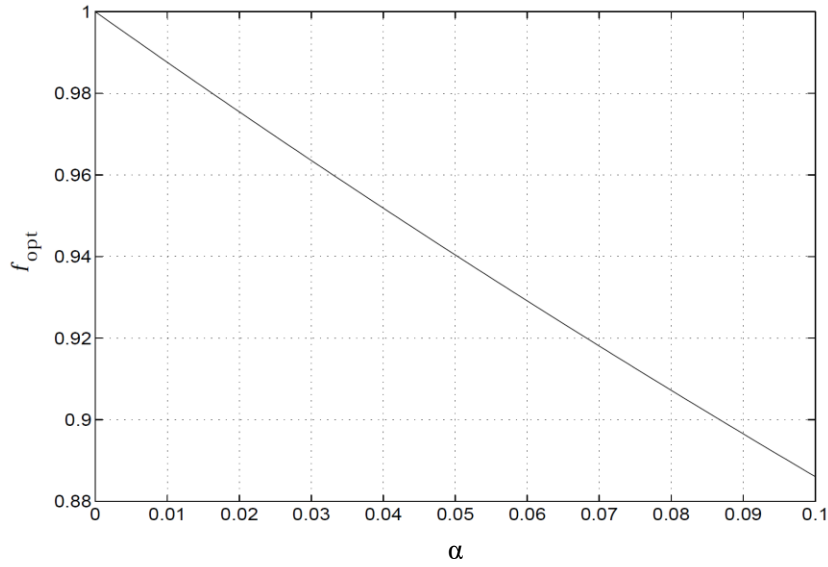


Fig. 2.13. Optimum tuning frequency ratio,  $f_{\text{opt}}$  [Connor & Laflamme 2014]

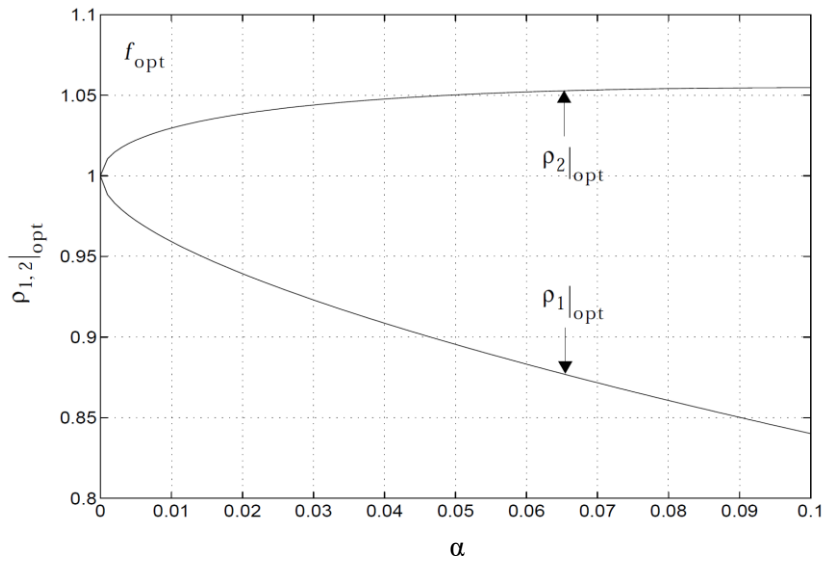


Fig. 2.14. Input frequency ratios at which the response is independent of damping [Connor & Laflamme 2014]

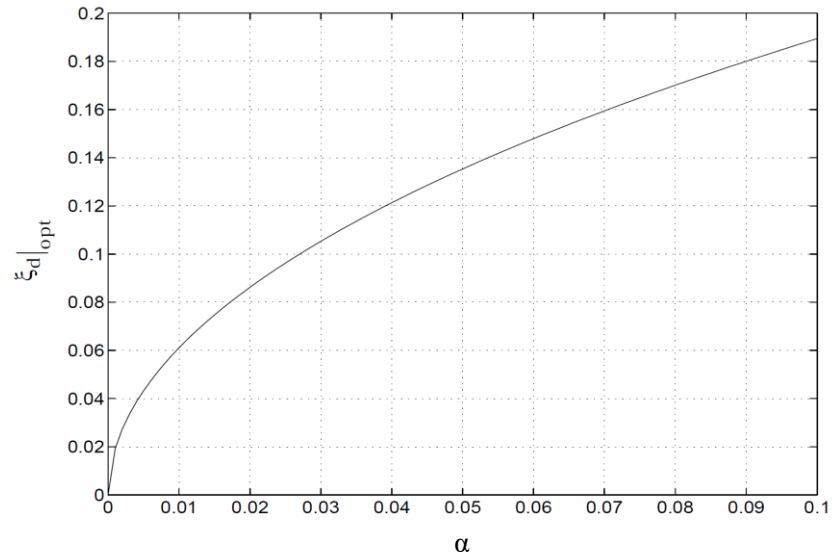


Fig. 2.15. Optimal damping ratio for TMD [Connor & Laflamme 2014]

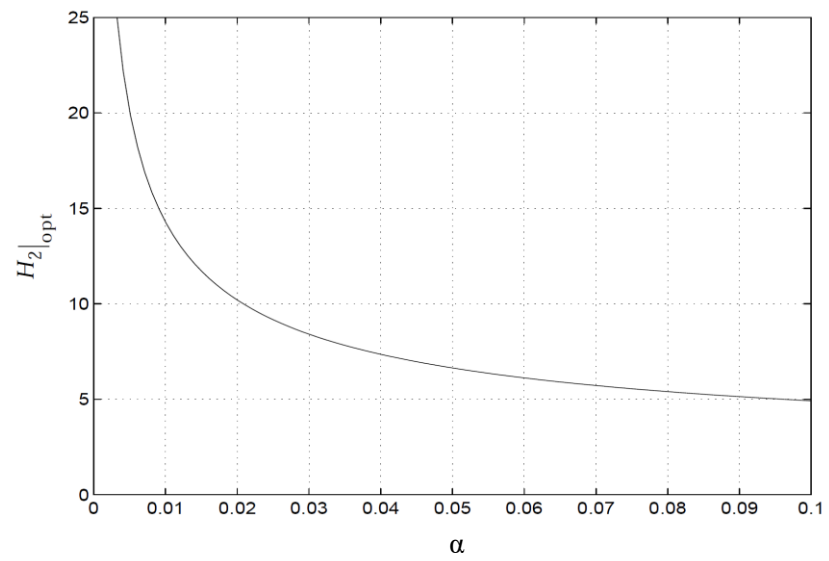


Fig. 2.16. Maximum dynamic amplification factor for SDOF system (optimal tuning and damping) [Connor & Laflamme 2014]

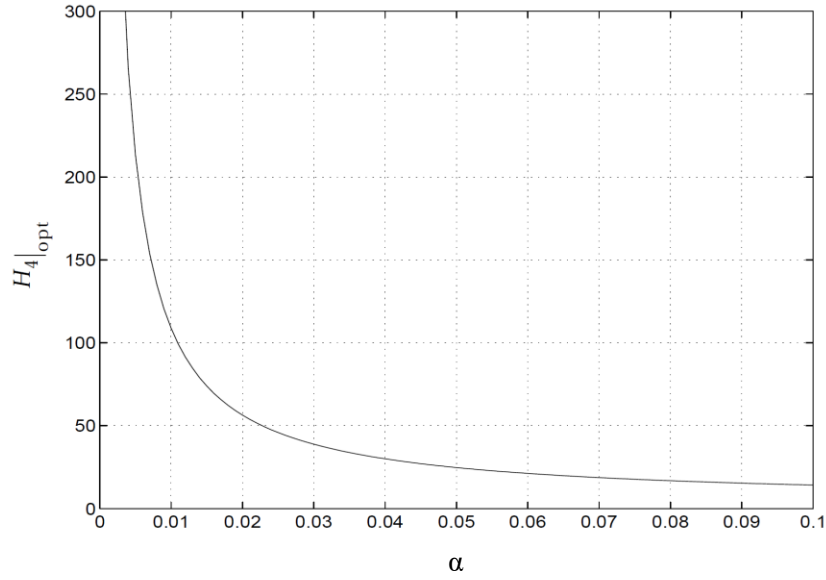


Fig. 2.17. Maximum dynamic amplification factor for TMD [Connor & Laflamme 2014]

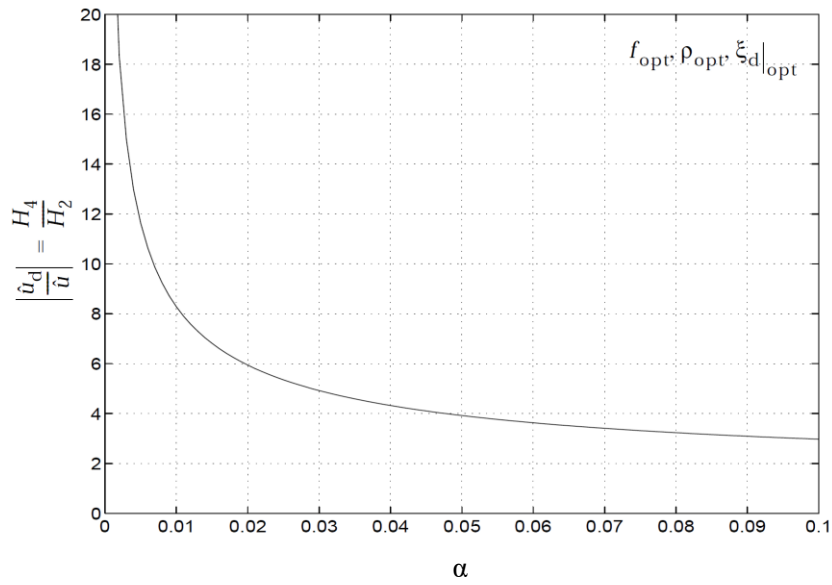
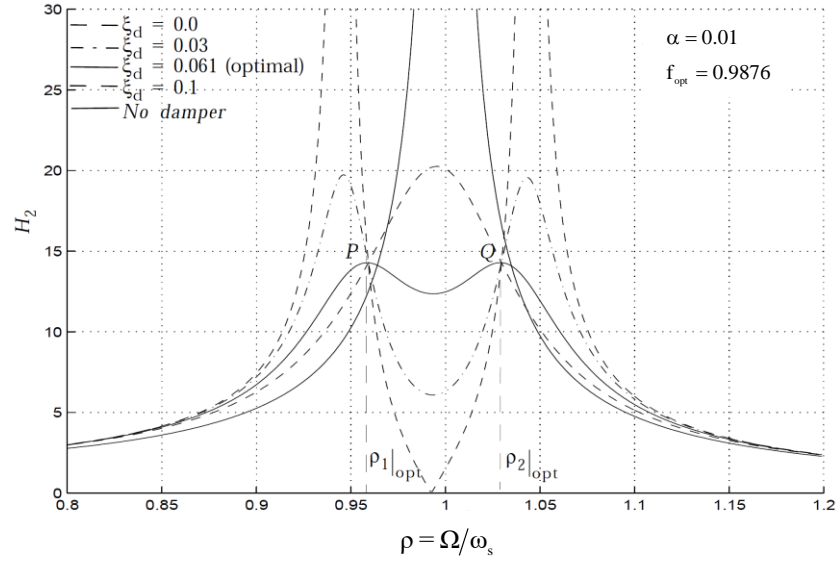


Fig. 2.18. Ratio of maximum TMD amplitude to maximum system amplitude [Connor & Laflamme 2014]



Lastly, response curve for a typical mass ratio,  $\alpha = 0.01$ , and optimal tuning is plotted in Fig. 2.19.



**Fig. 2.19.**  $H_2$  vs.  $\rho$  for  $f_{opt}$  [Connor & Laflamme 2014]

The response for no damper is also plotted in the graph. One observes that the effect of the damper is to limit the motion in a frequency range centered on the natural frequency of the primary mass and extending about  $0.15\omega_s$ . Outside of this range, the motion is not significantly influenced by the damper.

Since the maximum amplification for a damped SDOF system without a TMD, undergoing harmonic excitation, is given by [Chopra 2000]:

$$H_{max} = \frac{1}{2\xi\sqrt{1-\xi^2}} \quad (2.189)$$

considering that  $\xi$  is small, a reasonable approximation of (2.189) is

$$H_{max} \approx \frac{1}{2\xi} \quad (2.190)$$

Expressing the optimal  $H_2$  in a similar form provides a measure of the equivalent damping ratio  $\xi_e$  for the primary mass, i.e.:

$$\xi_e \approx \frac{1}{2H_2|_{\text{opt}}} \quad (2.191)$$

Fig. 2.20 shows the variation of  $\xi_e$  with the mass ratio  $\alpha$ ; for example, according to the graph for a mass ratio of 0.02,  $\xi_e$  is equivalent to about 5% of damping in the primary system.

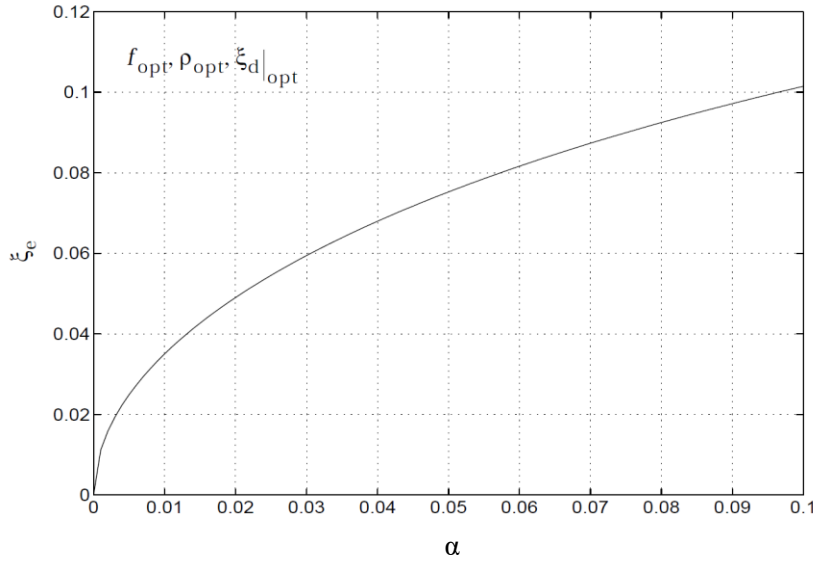


Fig. 2.20. Equivalent damping ratio  $\xi_e$  for optimally tuned TMD [Connor & Laflamme 2014]

### 2.3.1.3. Damped Structure: Damped TMD

Real systems always contain some damping. Although an absorber is likely to be added only to a lightly damped system, assessing the effect of damping in the real system on the optimal tuning of the absorber is an important design consideration.

Fig. 2.21 shows a damped SDOF + TMD model composed by a main system with a mass  $m$ , spring stiffness  $k$  and viscous damper  $c$ , and a tuned mass damper attached to the primary mass, with a mass  $m_d$ , stiffness  $k_d$  and viscous damper  $c_d$ .

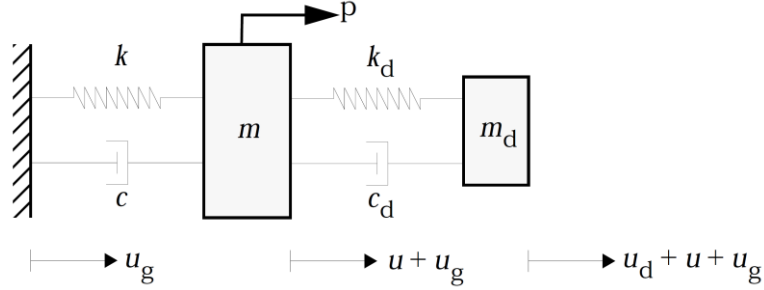


Fig. 2.21. Damped SDOF system coupled with a damped TMD system

Considering the system subjected to both external forcing and ground excitation, the equations of motions are

$$m_d(\ddot{v}_d + \ddot{v}_s) + c_d \dot{v}_d + k_d v_d = -m_d \ddot{u}_g \quad (2.192)$$

$$m\ddot{v}_s + c\dot{v}_s + kv_s - c_d \dot{v}_d - k_d v_d = -m\ddot{u}_g + p \quad (2.193)$$

Proceeding in the same way as for the undamped case (see Eqs. (2.146) ÷ (2.149)), the governing equations can be rewritten as

$$(-m_d \Omega^2 + ic_d \Omega + k_d) \hat{v}_d - m_d \Omega^2 \hat{v}_s = -m_d \hat{\ddot{u}}_g \quad (2.194)$$

$$-(ic_d \Omega + k_d) \hat{v}_d + (-m \Omega^2 + ic \Omega + k) \hat{v}_s = -m \hat{\ddot{u}}_g + \hat{p} \quad (2.195)$$

and the solution is

$$\hat{v}_s = \frac{\hat{p}}{kD_3} (f^2 - \rho^2 + i2\xi_d \rho f) - \frac{m \hat{\ddot{u}}_g}{kD_3} [(1 + \alpha)f^2 - \rho^2 + i2\xi_d \rho f (1 + \alpha)] \quad (2.196)$$

$$\hat{v}_d = \frac{\hat{p}\rho^2}{kD_3} - \frac{m \hat{\ddot{u}}_g}{kD_3} (1 + i2\xi_d \rho) \quad (2.197)$$

where

$$D_3 = \left[ (1 - \rho^2)(f^2 - \rho^2) - \alpha \rho^2 f^2 - 4\xi_s \xi_d f \rho^2 \right] + i2 \left\{ \xi_d \rho f [1 - \rho^2 (1 + \alpha)] + \xi_s \rho (f^2 - \rho^2) \right\} \quad (2.198)$$

Converting the complex solutions to polar form leads to the following expressions

$$\hat{v}_s = \frac{\hat{p}}{k} H_5 e^{i\delta_5} - \frac{m\hat{u}_g}{k} H_6 e^{i\delta_6} \quad (2.199)$$

$$\hat{v}_d = \frac{\hat{p}}{k} H_7 e^{-i\delta_7} - \frac{m\hat{u}_g}{k} H_8 e^{-i\delta_8} \quad (2.200)$$

The various  $H$  and  $\delta$  expressions are listed below

$$H_5 = \frac{\sqrt{(f^2 - \rho^2)^2 + (2\xi_d \rho f)^2}}{|D_3|} \quad (2.201)$$

$$H_6 = \frac{\sqrt{[(1 + \alpha)f^2 - \rho^2]^2 + [2\xi_d \rho f(1 + \alpha)]^2}}{|D_3|} \quad (2.202)$$

$$H_7 = \frac{\rho^2}{|D_3|} \quad (2.203)$$

$$H_8 = \frac{\sqrt{1 + (2\xi_s \rho)^2}}{|D_3|} \quad (2.204)$$

$$|D_3| = \sqrt{[(1 - \rho^2)(f^2 - \rho^2) - \alpha \rho^2 f^2 - 4\xi_s \xi_d f \rho^2]^2 + 4\{\xi_d \rho f[1 - \rho^2(1 + \alpha)] + \xi_s \rho(f^2 - \rho^2)\}^2} \quad (2.205)$$

$$\delta_5 = \alpha_1 - \delta_7 \quad (2.206)$$

$$\delta_6 = \alpha_2 - \delta_7 \quad (2.207)$$

$$\delta_8 = \alpha_3 - \delta_7 \quad (2.208)$$

$$\tan \delta_7 = 2 \frac{\xi_d \rho f[1 - \rho^2(1 + \alpha)] + \xi_s \rho(f^2 - \rho^2)}{(1 - \rho^2)(f^2 - \rho^2) - \alpha \rho^2 f^2 - 4\xi_s \xi_d f \rho^2} \quad (2.209)$$

$$\tan \alpha_3 = 2\xi_s \rho \quad (2.210)$$

The terms  $\alpha_1$  and  $\alpha_2$  are defined by Eqs (2.166) - (2.167).

In what follows, the case of an external force applied to the primary mass is considered. Since  $|D_3|$  involves  $\xi_s$ , one cannot establish analytical expressions for the optimal tuning frequency and optimal damping ratio

in terms of the mass ratio only; in this case, these parameters also depend on  $\xi_s$ . Numerical simulations can be carried out to evaluate  $H_5$  and  $H_7$  for an appropriate range of  $\rho$ , given the values for  $\alpha$ ,  $\xi_s$ ,  $f$ , and  $\xi_d$ . Starting with specific values for  $\alpha$  and  $\xi_s$ , plots of  $H_5$  versus  $\rho$  can be generated for a range of  $f$  and  $\xi_d$ . Each  $H_5$  -  $\rho$  plot has a peak value of  $H_5$ . The combination of  $f$  and  $\xi_d$  that correspond to the *lowest* peak value of  $H_5$  is taken as the *optimal* state. Repeating this process for different values of  $\alpha$  and  $\xi_s$  produces the behavioral data needed to design the damper system.

Fig. 2.22 shows the variation of the maximum value of  $H_5$  for the optimal state. The corresponding response of the damper,  $H_7$ , is plotted in Fig. 2.23. Adding damping to the primary mass has an appreciable effect for small value of  $\alpha$ . Noting Eqs. (2.203) and (2.201), the ratio of damper displacement to primary mass displacement is given by

$$\left| \frac{\hat{v}_d}{\hat{v}_s} \right| = \frac{H_7}{H_5} = \frac{\rho^2}{\sqrt{(f^2 - \rho^2)^2 + (2\xi_d \rho f)^2}} \quad (2.211)$$

Since the damping ratio  $\xi_s$  is small, the ratio  $H_7/H_5$  is essentially independent of  $\xi_s$ . Fig. 2.34 confirms this statement.

The optimal values of the frequency and damping ratios, i.e.  $f_{\text{opt}}$  and  $\xi_d|_{\text{opt}}$ , generated through simulation are plotted in Figs. 2.25 - 2.26.

Lastly, using Eq. (2.191),  $H_5|_{\text{opt}}$  can be converted to an equivalent damping ratio for the primary system (Fig. 2.27), i.e.:

$$\xi_e = \frac{1}{2H_5|_{\text{opt}}} \quad (2.212)$$

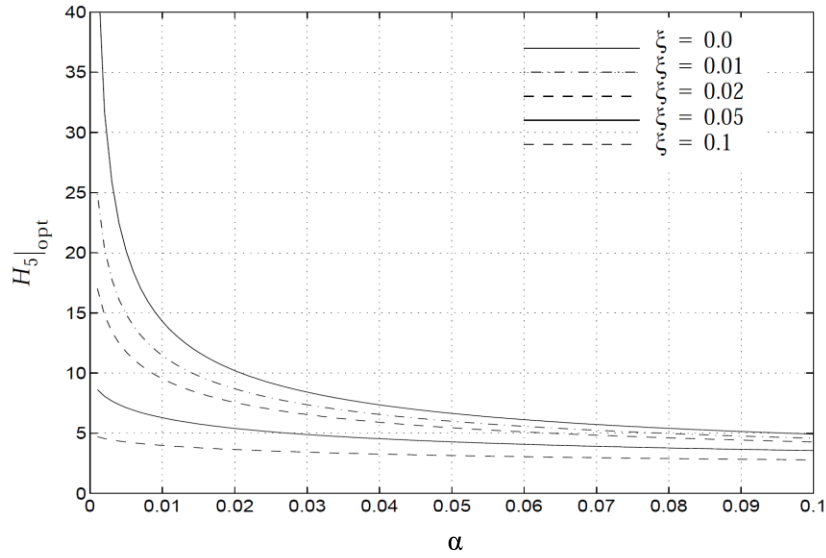


Fig. 2.22. Maximum dynamic amplification factor for damped SDOF system [Connor & Laflamme 2014]

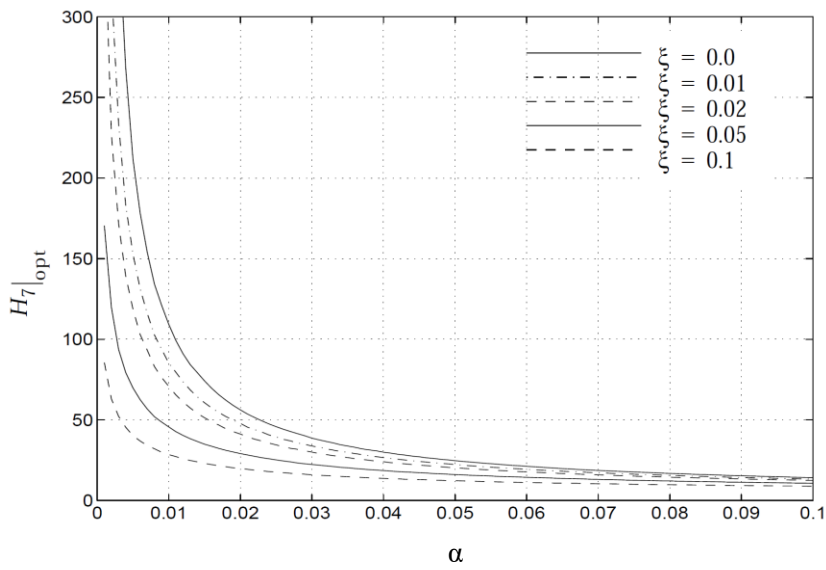


Fig. 2.23. Maximum dynamic amplification factor for TMD [Connor & Laflamme 2014]

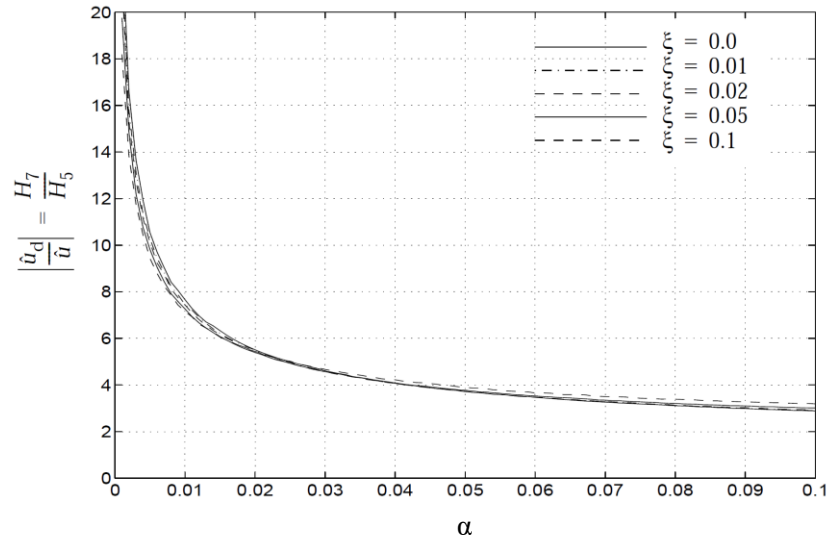


Fig. 2.23. Ratio of maximum TMD amplitude to maximum system amplitude [Connor & Laflamme 2014]

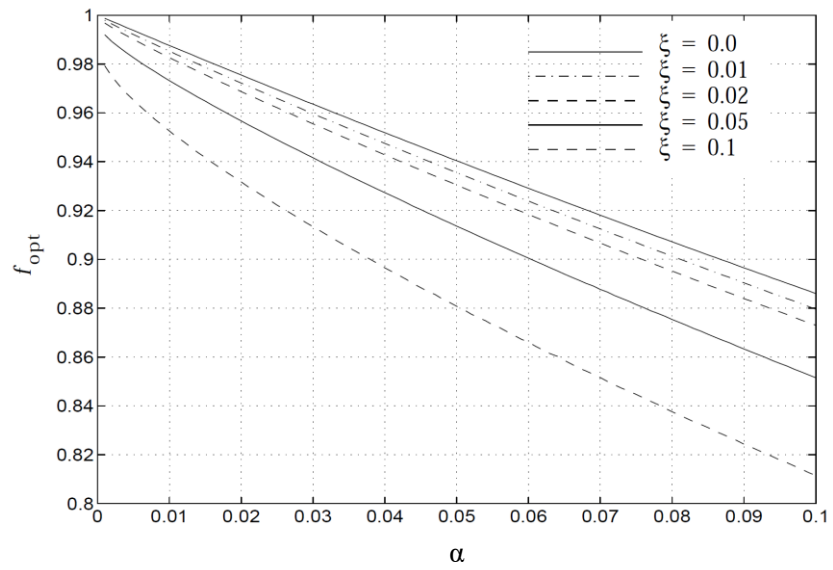


Fig. 2.25. Optimum tuning frequency ratio for TMD,  $f_{opt}$  [Connor & Laflamme 2014]

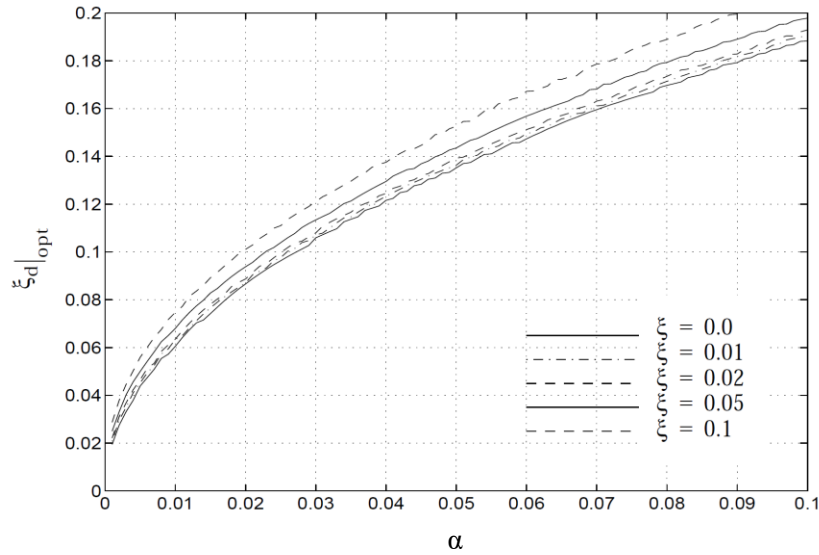


Fig. 2.26. Optimal damping ratio for TMD,  $\xi_d|_{opt}$  [Connor & Laflamme 2014]

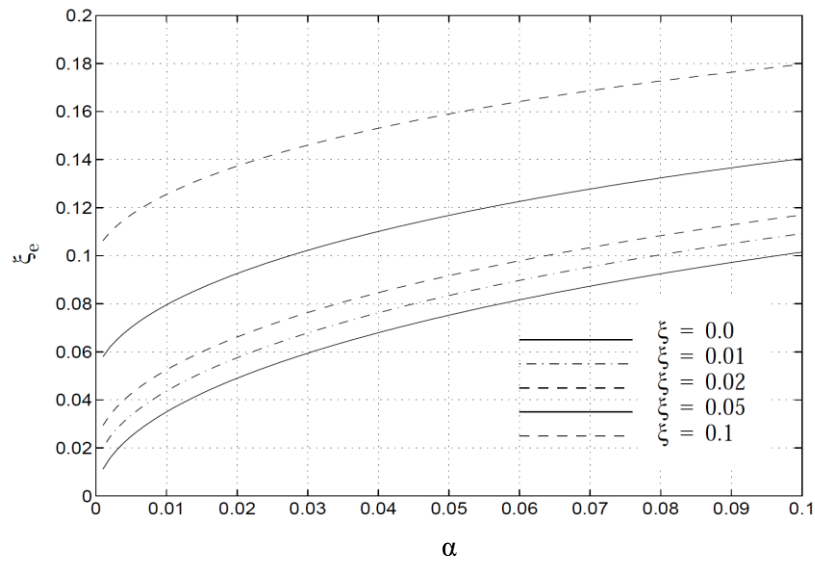


Fig. 2.27. Equivalent damping ratio for optimally tuned TMD,  $\xi_e$  [Connor & Laflamme 2014]



### 2.3.2. Tuned Mass Damper Theory for MDOF Systems

The theory of a SDOF system can be extended to deal with a MDOF system having a number of tuned mass damper located throughout the structure.

Fig. 2.28 shows a damped 2DOF + TMD model composed by a main system with masses  $m_1$  and  $m_2$ , spring stiffnesses  $k_1$  and  $k_2$  and viscous dampers  $c_1$  and  $c_2$ , and a tuned mass damper attached to the primary mass with mass  $m_d$ , stiffness  $k_d$  and viscous damper  $c_d$ .

Considering the primary masses  $m_1$  and  $m_2$  subjected to both external forcing  $p_1$  and  $p_2$ , respectively, and ground motion  $\ddot{u}_g$ , the governing equations take the form

$$m_1 \ddot{v}_1 + c_1 \dot{v}_1 + k_1 v_1 - c_2 (\dot{v}_2 - \dot{v}_1) - k_2 (v_2 - v_1) = -m_1 \ddot{u}_g + p_1 \quad (2.213)$$

$$m_2 \ddot{v}_2 + c_2 (\dot{v}_2 - \dot{v}_1) + k_2 (v_2 - v_1) - c_d \dot{v}_d - k_d v_d = -m_2 \ddot{u}_g + p_2 \quad (2.214)$$

$$m_d \ddot{v}_d + c_d \dot{v}_d + k_d v_d = -m_d (\ddot{u}_g + \ddot{v}_2) \quad (2.215)$$

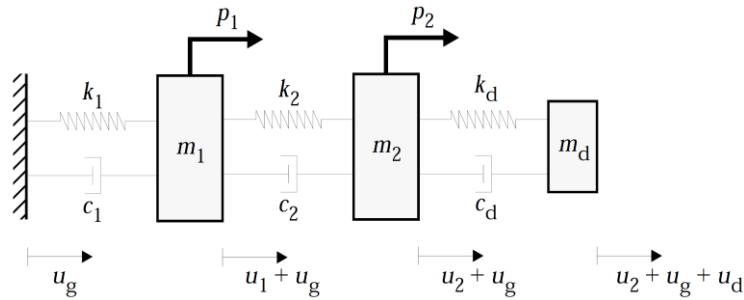


Fig. 2.28. Damped 2DOF system coupled with a damped TMD system

It is convenient to reduce the primary 2DOF system into an equivalent SDOF system, thus Eqs. (2.213) - (2.214) can be combined in a form similar to SDOF case defined by (2.193).

The approach followed here is based on transforming the original matrix equation to scalar modal equations. Introducing matrix notation, Eqs. (2.213) - (2.214) are written as

$$\mathbf{M}_s \ddot{\mathbf{v}}_s + \mathbf{C}_s \dot{\mathbf{v}}_s + \mathbf{K}_s \mathbf{v}_s = \begin{bmatrix} -m_1 \ddot{u}_g + p_1 \\ -m_2 \ddot{u}_g + p_2 \end{bmatrix} + \begin{bmatrix} 0 \\ -c_d \dot{v}_d - k_d v_d \end{bmatrix} \quad (2.216)$$

where the displacement vector  $\mathbf{v}_s$  and the mass  $\mathbf{M}_s$ , stiffness  $\mathbf{K}_s$  and damping  $\mathbf{C}_s$  matrices are

$$\mathbf{v}_s = \begin{bmatrix} v_1 \\ v_2 \end{bmatrix}, \quad \mathbf{M}_s = \begin{bmatrix} m_1 & 0 \\ 0 & m_2 \end{bmatrix}, \quad \mathbf{K}_s = \begin{bmatrix} k_1 + k_2 & -k_2 \\ -k_2 & k_2 \end{bmatrix}, \quad \mathbf{C}_s = \begin{bmatrix} c_1 + c_2 & -c_2 \\ -c_2 & c_2 \end{bmatrix} \quad (2.217)$$

The vector  $\mathbf{v}_s$  can be expressed in terms of modal coordinates as

$$\mathbf{v}_s = \boldsymbol{\phi}_s^1 q_{s,1} + \boldsymbol{\phi}_s^2 q_{s,2} \quad (2.218)$$

The modal vectors satisfy the following orthogonality relations

$$\boldsymbol{\phi}_s^{jT} \mathbf{K}_s \boldsymbol{\phi}_s^i = \delta_{ij} \omega_{sij}^2 \boldsymbol{\phi}_s^{iT} \mathbf{M}_s \boldsymbol{\phi}_s^i \quad (2.219)$$

Defining modal mass, stiffness and damping terms

$$\tilde{m}_{s,j} = \boldsymbol{\phi}_s^{jT} \mathbf{M}_s \boldsymbol{\phi}_s^j, \quad \tilde{k}_{s,j} = \boldsymbol{\phi}_s^{jT} \mathbf{K}_s \boldsymbol{\phi}_s^j = \tilde{m}_{s,j} \omega_{s,j}^2, \quad \tilde{c}_{s,j} = \boldsymbol{\phi}_s^{jT} \mathbf{C}_s \boldsymbol{\phi}_s^j, \quad (2.220)$$

expressing the elements of  $\boldsymbol{\phi}_s^j$  as

$$\boldsymbol{\phi}_s^j = \begin{bmatrix} \phi_{s,1}^j \\ \phi_{s,2}^j \end{bmatrix} \quad (2.221)$$

and assuming damping proportional to stiffness

$$\mathbf{C}_s = a_p \mathbf{K}_s \quad (2.222)$$

with  $a_p$  a proportional coefficient, a set of uncoupled equations for  $q_1$  and  $q_2$  is obtained as follows

$$\tilde{m}_{s,j} \ddot{q}_{s,j} + \tilde{c}_{s,j} \dot{q}_{s,j} + \tilde{k}_{s,j} q_{s,j} = \phi_{s,1}^j (-m_1 \ddot{u}_g + p_1) + \phi_{s,2}^j (-m_2 \ddot{u}_g + p_2 + c_d \dot{v}_d + k_d v_d) \quad (2.223)$$

with  $j = 1, 2$ .

With this assumption, the modal damping ratio is given by

$$\xi_{s,j} = \frac{\tilde{c}_{s,j}}{2\tilde{m}_{s,j}\omega_{s,j}^2} = \frac{a_p \omega_{s,j}}{2} \quad (2.224)$$

Since a TMD is effective for a narrow frequency range, we have to decide on which modal resonant response is to be controlled with the TMD. Once this decision is made, the analysis can proceed using the selected modal equation and the initial equation for the TMD, i.e. Eq. (2.215). Considering the first modal response is to be controlled, Eq. (2.223) for  $j=1$  becomes:

$$\tilde{m}_{s,1}\ddot{q}_{s,1} + \tilde{c}_{s,1}\dot{q}_{s,1} + k_{s,1}q_{s,1} = \phi_{s,1}^1 p_1 + \phi_{s,2}^1 p_2 - (m_1 \phi_{s,1}^1 + m_2 \phi_{s,2}^1) \ddot{u}_g + \phi_{s,2}^1 (c_d \dot{v}_d + k_d v_d) \quad (2.225)$$

In general,  $v_2$  is obtained by superposing the modal contributions

$$v_{s,2} = \phi_{s,2}^1 q_{s,1} + \phi_{s,2}^2 q_{s,2} \quad (2.226)$$

However, when the external forcing frequency is close to  $\omega_1$ , the first mode response will dominate, and it is reasonable to assume

$$v_{s,2} = \phi_{s,2}^1 q_{s,1} \quad (2.227)$$

Solving for  $q_1$

$$q_{s,1} = \frac{v_{s,2}}{\phi_{s,2}^1} \quad (2.228)$$

and then substituting in Eq. (2.225), the equation is rewritten as

$$\tilde{m}_{le} \ddot{v}_{s,2} + \tilde{c}_{le} \dot{v}_{s,2} + k_{le} v_{s,2} = c_d \dot{v}_d + k_d v_d + \tilde{p}_{le} - L_{le} \tilde{m}_{le} \ddot{u}_g \quad (2.229)$$

where  $\tilde{m}_{1e}$ ,  $\tilde{k}_{1e}$ ,  $\tilde{c}_{1e}$ ,  $L_{1e}$  and  $\tilde{p}_{1e}$  represent the equivalent SDOF parameters for the combination of mode 1 and mass 2, (the mass at which the TMD is attached) and, respectively correspond to:

$$\tilde{m}_{1e} = \frac{\tilde{m}_{s,1}}{\phi_{s,2}^1}, \quad \tilde{k}_{1e} = \frac{\tilde{k}_{s,1}}{\phi_{s,2}^1}, \quad \tilde{c}_{1e} = a_p \tilde{k}_{1e} \quad (2.230)$$

$$\tilde{p}_{1e} = \frac{\phi_{s,1}^1 p_1 + \phi_{s,2}^1 p_2}{\phi_{s,2}^1} = \frac{\tilde{p}_1}{\phi_{s,2}^1} \quad (2.231)$$

$$L_{1e} = \frac{\phi_{s,2}^1}{\tilde{m}_{s,1}} (m_1 \phi_{s,1}^1 + m_2 \phi_{s,2}^1) \quad (2.232)$$

Eqs. (2.215) and (2.229) are similar in form to the SDOF equations treated in the previous section, i.e. Eqs. (2.192) and (2.193).

Given the mass damper  $m_d$ , the mass ratio  $\alpha$  is defined in terms of the equivalent SDOF mass  $\tilde{m}_{1e}$

$$\alpha = \frac{m_d}{\tilde{m}_{1e}} \quad (2.233)$$

The damper parameters are

$$m_d = \alpha \tilde{m}_{1e}, \quad \omega_d = f_{opt} \omega_1, \quad c_d = 2\xi_d \Big|_{opt} \omega_d m_d \quad (2.234)$$

This derivation can be readily generalized to allow for tuning on the  $i$ -th modal frequency. Thus, Eq. (2.228) can be written as

$$q_{s,i} = \frac{v_{s,2}}{\phi_{s,2}^i} \quad (2.235)$$

where  $i$  is either 1 or 2. The equivalent SDOF mass  $\tilde{m}_{ie}$ , force  $\tilde{p}_{ie}$  and modal participation factor  $L_{ie}$  are

$$\tilde{m}_{ie} = \frac{\tilde{m}_{s,i}}{\phi_{s,2}^i}, \quad \tilde{k}_{ie} = \frac{\tilde{k}_{s,i}}{\phi_{s,2}^i}, \quad \tilde{c}_{ie} = a_p \tilde{k}_{ie} \quad (2.236)$$

$$\tilde{p}_{ie} = \frac{\phi_{s,1}^i p_1 + \phi_{s,2}^i p_2}{\phi_{s,2}^i} = \frac{\tilde{p}_i}{\phi_{s,2}^i} \quad (2.237)$$

$$L_{ie} = \frac{\phi_{s,2}^i}{\tilde{m}_{s,i}} (m_1 \phi_{s,1}^i + m_2 \phi_{s,2}^i) \quad (2.238)$$

The general case of a MDOF system with a tuned mass damper connected to the  $n$ -th degree of freedom is reported in the following. With the same notation defined above, the  $j$ -th modal equation can be expressed as

$$\tilde{m}_{s,j} \ddot{q}_{s,j} + \tilde{c}_{s,j} \dot{q}_{s,j} + k_{s,j} q_{s,j} = \tilde{p}_j + \phi_{s,n}^j (c_d \dot{v}_d + k_d v_d) \quad j=1,2,\dots,N \quad (2.239)$$

where  $\tilde{p}_j$  denotes the modal force due to ground motion and external forcing, and  $\phi_{s,n}^j$  is the element of  $\boldsymbol{\phi}_s^j$  corresponding to the  $n$ -th displacement variable. To control the  $i$ -th response, by setting  $j = i$  in Eq. (2.239) and introducing the approximation

$$q_{s,i} = \frac{v_{s,n}}{\phi_{s,n}^i} \quad (2.240)$$

Eq. (2.239) can be written in terms of  $v_{s,n}$  as follows.

$$\tilde{m}_{ie} \ddot{v}_{s,n} + \tilde{c}_{ie} \dot{v}_{s,n} + k_{ie} v_{s,n} = c_d \dot{v}_d + k_d v_d + \tilde{p}_{ie} \quad (2.241)$$

where

$$\tilde{m}_{ie} = \frac{\tilde{m}_{s,i}}{\phi_{s,n}^{i^2}} = \frac{\boldsymbol{\phi}_i^T \mathbf{M} \boldsymbol{\phi}_i}{\phi_{s,n}^{i^2}}, \quad \tilde{k}_{ie} = \frac{\tilde{k}_{s,i}}{\phi_{s,n}^{i^2}} = \omega_{s,i}^2 \tilde{m}_{ie}, \quad \tilde{c}_{ie} = a_p \tilde{k}_{ie} \quad (2.242)$$

$$\tilde{p}_{ie} = \frac{\tilde{p}_i}{\phi_{s,n}^i} \quad (2.243)$$

$$m_d = \alpha \tilde{m}_{ie}, \quad \omega_d = f_{opt} \omega_{s,i}, \quad c_d = 2 \xi_d \Big|_{opt} \omega_d m_d \quad (2.244)$$

The optimal mass damper for mode  $i$  is obtained by selecting  $n$  such that  $\phi_{s,n}^i$  is the maximum element in  $\boldsymbol{\phi}_s^i$ .

## 2.4. INTER-STORY ISOLATION SYSTEMS (IIS)

### 2.4.1. Inter-Story Isolation Theory for 3DOF and 2DOF Systems

#### 2.4.1.1. Simplified modeling

The equations of motion of simplified two and three degrees-of-freedom IIS (2DOF IIS and 3DOF IIS) models are compared to the corresponding ones of 2DOF base-isolated structure (2DOF BIS) and SDOF with TMD (SDOF + TMD), examined previously in §2.2 - 2.3.

A graphical representation of the four simplified lumped mass models (3DOF IIS, 2DOF IIS, 2DOF BIS, SDOF+TMD) is given in Fig. 2.29.

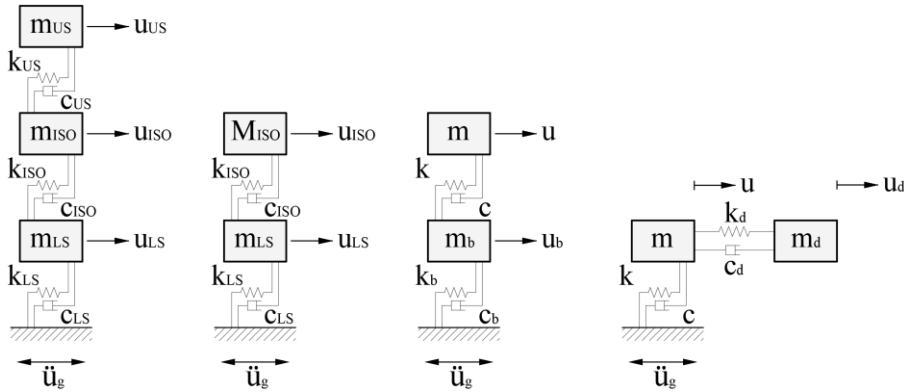


Fig. 2.29. Simplified models: (a) 3DOF IIS, (b) 2DOF IIS, (c) 2DOF BIS, (d) SDOF+TMD

#### 2.4.1.2. Governing equations of motion

The governing equations of motion for the four models considered herein are described as follows.

##### 3DOF IIS Model

The equations of motion for the 3DOF IIS model concerning the inter-story isolation system are given by:

$$\mathbf{m}_{\text{US}} (\ddot{\mathbf{v}}_{\text{US}} + \ddot{\mathbf{v}}_{\text{ISO}} + \ddot{\mathbf{v}}_{\text{LS}}) + \mathbf{c}_{\text{US}} \dot{\mathbf{v}}_{\text{US}} + \mathbf{k}_{\text{US}} \mathbf{v}_{\text{US}} = -\mathbf{m}_{\text{US}} \ddot{\mathbf{u}}_{\text{g}} \quad (2.245)$$

$$\mathbf{m}_{\text{ISO}} (\ddot{\mathbf{v}}_{\text{ISO}} + \ddot{\mathbf{v}}_{\text{LS}}) + \mathbf{c}_{\text{ISO}} \dot{\mathbf{v}}_{\text{ISO}} + \mathbf{k}_{\text{ISO}} \mathbf{v}_{\text{ISO}} = -\mathbf{m}_{\text{ISO}} \ddot{\mathbf{u}}_{\text{g}} \quad (2.246)$$

$$\mathbf{m}_{\text{LS}} \ddot{\mathbf{v}}_{\text{LS}} + \mathbf{c}_{\text{LS}} \dot{\mathbf{v}}_{\text{LS}} + \mathbf{k}_{\text{LS}} \mathbf{v}_{\text{LS}} = -\mathbf{m}_{\text{LS}} \ddot{\mathbf{u}}_{\text{g}} + \mathbf{c}_{\text{ISO}} \dot{\mathbf{v}}_{\text{ISO}} + \mathbf{k}_{\text{ISO}} \mathbf{v}_{\text{ISO}} \quad (2.247)$$

in which:  $\mathbf{m}$ ,  $\mathbf{c}$  and  $\mathbf{k}$  are the masses, the viscous damping constants and the stiffnesses;  $\mathbf{v}$  and  $\mathbf{u}$  are the relative and the absolute displacements of the dofs. In Eqs. (2.245) ÷ (2.247) the subscripts **US**, **ISO**, **LS** and **g** respectively correspond to upper structure, isolation level, lower structure and ground.

#### 2DOF IIS Model

The equations of motion for the 2DOF IIS model concerning the inter-story isolation system are given by:

$$(\mathbf{m}_{\text{US}} + \mathbf{m}_{\text{ISO}})(\ddot{\mathbf{v}}_{\text{ISO}} + \ddot{\mathbf{v}}_{\text{LS}}) + \mathbf{c}_{\text{ISO}} \dot{\mathbf{v}}_{\text{ISO}} + \mathbf{k}_{\text{ISO}} \mathbf{v}_{\text{ISO}} = -\mathbf{m}_{\text{ISO}} \ddot{\mathbf{u}}_{\text{g}} \quad (2.248)$$

$$\mathbf{m}_{\text{LS}} \ddot{\mathbf{v}}_{\text{LS}} + \mathbf{c}_{\text{LS}} \dot{\mathbf{v}}_{\text{LS}} + \mathbf{k}_{\text{LS}} \mathbf{v}_{\text{LS}} = -\mathbf{m}_{\text{LS}} \ddot{\mathbf{u}}_{\text{g}} + \mathbf{c}_{\text{ISO}} \dot{\mathbf{v}}_{\text{ISO}} + \mathbf{k}_{\text{ISO}} \mathbf{v}_{\text{ISO}} \quad (2.249)$$

where the sum  $\mathbf{m}_{\text{US}} + \mathbf{m}_{\text{ISO}}$  represents the total isolated mass above the isolation layer, i.e.  $\mathbf{M}_{\text{ISO}}$ .

#### 2DOF BIS Model

The equations of motion for the 2DOF BIS model concerning the base isolation system, given by Eqs. (2.6) and (2.7), are recalled here for completeness:

$$\mathbf{m} \ddot{\mathbf{v}}_{\text{b}} + \mathbf{m} \ddot{\mathbf{v}}_{\text{s}} + \mathbf{c} \dot{\mathbf{v}}_{\text{s}} + \mathbf{k} \mathbf{v}_{\text{s}} = -\mathbf{m} \ddot{\mathbf{u}}_{\text{g}} \quad (2.6)$$

$$(\mathbf{m} + \mathbf{m}_{\text{b}}) \ddot{\mathbf{v}}_{\text{b}} + \mathbf{m} \ddot{\mathbf{v}}_{\text{s}} + \mathbf{c}_{\text{b}} \dot{\mathbf{v}}_{\text{b}} + \mathbf{k}_{\text{b}} \mathbf{v}_{\text{b}} = -(\mathbf{m} + \mathbf{m}_{\text{b}}) \ddot{\mathbf{u}}_{\text{g}} \quad (2.7)$$

in which  $\mathbf{m}$ ,  $\mathbf{m}_{\text{b}}$ ,  $\mathbf{c}$ ,  $\mathbf{c}_{\text{b}}$ ,  $\mathbf{k}$ ,  $\mathbf{k}_{\text{b}}$  are the masses, the damping constants and the stiffnesses respectively corresponding to the main structure and the isolation system;  $\mathbf{v}$ ,  $\mathbf{v}_{\text{b}}$  are the relative displacements of the same dofs.

#### SDOF+TMD Model

The equations of motion for the SDOF+TMD model concerning the tuned mass damper system, given by Eqs. (2.192) and (2.193), are recalled

here for completeness (neglecting the contribution of the external force  $p$ ):

$$m_d(\ddot{v}_d + \ddot{v}_s) + c_d \dot{v}_d + k_d v_d = -m_d \ddot{u}_g \quad (2.192)$$

$$m\ddot{v}_s + c\dot{v}_s + kv_s - c_d \dot{v}_d - k_d v_d = -m\ddot{u}_g \quad (2.193)$$

where  $m$ ,  $m_d$ ,  $c$ ,  $c_d$ ,  $k$ ,  $k_d$  are the masses, the damping constants and the stiffnesses respectively corresponding to the main structure and the TMD;  $v$ ,  $v_d$  are the relative displacements of the same dofs.

### 2.4.1.3. *Comparison among the equations of motion of the different simplified models*

Observing Eqs. (2.245) ÷ (2.247) of the 3DOF IIS model it is possible to subdivide the system in two schemes: the first one is a 2DOF model, analogous to the 2DOF BIS model ([Kelly 1990]); the second one is analogous to the SDOF+TMD model ([Connor & Laflamme 2014]).

By setting:

$$m_{US} = m, \quad c_{US} = c, \quad k_{US} = k,$$

$$u_{US} = u, \quad v_{US} = v,$$

$$\text{since } \ddot{v}_{US} + \ddot{v}_{ISO} + \ddot{v}_{LS} + \ddot{u}_g = \ddot{u}_{US} \text{ and } \ddot{v}_s + \ddot{v}_b + \ddot{u}_g = \ddot{u},$$

the analogy between Eqs. (2.245) and (2.6), respectively corresponding to the upper structure of IIS and IIS, is provided; i.e.:

$$\begin{cases} m_{US} \ddot{u}_{US} + c_{US} \dot{v}_{US} + k_{US} v_{US} = 0 \\ m \ddot{u} + c \dot{v}_s + kv_s = 0 \end{cases} \quad (2.250)$$

By setting:

$$m_{ISO} = m_b, \quad c_{ISO} = c_b, \quad k_{ISO} = k_b,$$

$$u_{ISO} = u_b, \quad v_{ISO} = v_b,$$

$$\text{since } \ddot{v}_{ISO} + \ddot{v}_{LS} + \ddot{u}_g = \ddot{u}_{ISO} \text{ and } (m + m_b)(\ddot{v}_b + \ddot{u}_g) + m\ddot{v}_s = m\ddot{u} + m_b\ddot{u}_b,$$

the analogy between Eqs. (2.246) and (2.7), respectively corresponding to the isolation system of IIS and BIS, is provided; i.e.:



$$\begin{cases} m_{\text{ISO}} \ddot{u}_{\text{ISO}} + c_{\text{ISO}} \dot{v}_{\text{ISO}} + k_{\text{ISO}} v_{\text{ISO}} = c_{\text{US}} \dot{v}_{\text{US}} + k_{\text{US}} v_{\text{US}} \\ m_b \ddot{u}_b + c_b \dot{v}_b + k_b v_b = c \dot{v}_s + k v_s \end{cases} \quad (2.251)$$

By setting:

$$m_{\text{LS}} = m, \quad c_{\text{LS}} = c, \quad k_{\text{LS}} = k,$$

$$v_{\text{LS}} = v, \quad v_{\text{ISO}} = v_d,$$

the analogy between Eqs. (2.247) and (2.193), respectively corresponding to the lower structure of IIS and the main structure with TMD, is immediately verified, i.e.:

$$\begin{cases} m_{\text{LS}} \ddot{v}_{\text{LS}} + c_{\text{LS}} \dot{v}_{\text{LS}} + k_{\text{LS}} v_{\text{LS}} = -m_{\text{LS}} \ddot{u}_g + c_{\text{ISO}} \dot{v}_{\text{ISO}} + k_{\text{ISO}} v_{\text{ISO}} \\ m \ddot{v}_s + c \dot{v}_s + k v_s = -m \ddot{u}_g + c_d \dot{v}_d + k_d v_d \end{cases} \quad (2.252)$$

In addition, comparing the 3DOF IIS and SDOF+TMD models, by setting:

$$m_{\text{ISO}} = m_d, \quad c_{\text{ISO}} = c_d, \quad k_{\text{ISO}} = k_d,$$

$$v_{\text{ISO}} = v_d, \quad v_{\text{LS}} = v_s,$$

Eq. (2.246) is comparable to Eq. (2.192), i.e.:

$$\begin{cases} m_{\text{ISO}} (\ddot{v}_{\text{ISO}} + \ddot{v}_{\text{LS}}) + c_{\text{ISO}} \dot{v}_{\text{ISO}} + k_{\text{ISO}} v_{\text{ISO}} = -m_{\text{ISO}} \ddot{u}_g \\ m_d (\ddot{v}_d + \ddot{v}_s) + c_d \dot{v}_d + k_d v_d = -m_d \ddot{u}_g \end{cases} \quad (2.253)$$

or even, comparing the 2DOF IIS and SDOF+TMD models, by setting:

$$M_{\text{ISO}} = m_d, \quad c_{\text{ISO}} = c_d, \quad k_{\text{ISO}} = k_d,$$

$$v_{\text{ISO}} = v_d, \quad v_{\text{LS}} = v_s,$$

Eq. (2.248) is comparable to Eq. (2.192), i.e.:

$$\begin{cases} M_{\text{ISO}} (\ddot{v}_{\text{ISO}} + \ddot{v}_{\text{LS}}) + c_{\text{ISO}} \dot{v}_{\text{ISO}} + k_{\text{ISO}} v_{\text{ISO}} = -M_{\text{ISO}} \ddot{u}_g \\ m_d (\ddot{v}_d + \ddot{v}_s) + c_d \dot{v}_d + k_d v_d = -m_d \ddot{u}_g \end{cases} \quad (2.254)$$

The comparison between the equations of motion of the four models (3DOF IIS, 2DOF IIS, 2DOF BIS, SDOF + TMD) confirm that intermediate isolation systems combine the strategies of isolation and mass damping.

Therefore, the dynamics of IIS is more complex than that of BIS and TMD; for this reason, the evaluation of the vibrational behavior of such systems can be addressed from different points of view.

In Chapter 4 is provided the overview of the scientific literature on this topic, which reflect a variety of approach both in the formulation of the problem and in the definition of the design criteria.

### **3. DESIGN PRACTICE AND APPLICATIONS**

#### **3.1. INTER-STORY ISOLATED STRUCTURE**

The use of intermediate story isolation systems (IIS, also appointed as mid-story isolation), is currently spreading and gaining significant popularity, mainly in Japan, both for the seismic design of new buildings, and for vertical addition in the retrofit of existing buildings. A recent study by [Kobayashi & Sasaki 2009] refers to more than 60 buildings equipped with IIS, realized starting from the late 90s.

The main information provided in the paper by [Kobayashi & Sasaki 2009] refer to:

- Building height per year (Fig. 3.1a);
- Equivalent first period per year (Fig. 3.1b);
- Structural types of the upper and lower structure (Fig. 3.1c);
- Location of the isolation layer along the height of the building (Fig. 3.1d);
- Types and combination of isolators and types of damper (Fig. 3.1e, f);
- drift in the structural portions and deformation of the isolation system (Fig. 3.2);
- story shear coefficient of upper and lower structures and of the isolation systems (Fig. 3.3);
- Main differences between IIS and BIS buildings (Table 3.1).

As can be seen from Fig. 3.1a, b the structural types considered are reinforced concrete, steel and mixed steel-reinforced concrete (RC, S, SRC) structures or other types. In particular, for the upper (U) and lower (L) structure the same or different structural types can be used.

During the period 1995 ÷ 2007 an improvement of the building height, with an average value of 60 m, was observed (52 data). The major height

was reached with RC buildings with a maximum value of 130 m in 2007, followed by RC and SRC respectively for the upper and lower structures, or other types.

In addition, from Fig. 3.1c it is also noticed that RC buildings and U+L RC + SRC are the structural types more frequent with the 78% and 8%, respectively, followed by S or mixed structures with 2%.

Looking at the equivalent 1<sup>st</sup> period for the II earthquake level, Fig.3.1b shows an improvement during the period 1995 ÷ 2007 with average growth of 0.09 s per year and a mean value of 3.81 s.

The height of 60 m was used as reference for defining the location of the isolation level along the height of the building. From Fig. 3.1d can be seen that for building height less than 60 m, the isolation level was placed at the lower levels with the 51%, while for building height larger than 60 m up to the second floor with the 20%.

From Fig. 3.1e can be seen that the isolator types are natural rubber bearing (NRB), lead rubber bearing (LRB), high damping rubber bearing (HDRB). More frequently was used LRB with the 40% or a combination of LRB and NRB with the 26%.

From Fig. 3.1f can be seen that the damper types are steel damper (SD) , lead damper (LD), oil damper (OD); more frequently were used SD and LS with the 39% and 33%, respectively.

Looking at the interstory drift, in Fig. 3.2 can be observed that the upper and lower structure show the same range of values ( $1/1600 \div 1/200$ ) with more frequent values of  $1/400 - 1/200$  and  $1/1600$ , respectively; the more frequent displacement of the isolation layer is 40 cm. Kobayashy & Sasaki provided also the average values corresponding to  $1/387$  and  $1/487$  respectively for upper and lower structures, and an average displacement of the isolation equal to 32.98 cm.

In terms of shear coefficient, in Fig. 3.3 can be observed that the upper structure and isolation (ISO) system show the same range of values ( $0.06 \div 0.15$ ) with more frequent values of  $0.09 \div 0.12$ ; the lower structure shows values between  $0.1 \div 0.4$  with more frequent values of  $0.2 \div 0.3$ . Kobayashy & Sasaki provided also the average values corresponding to 0.11 and 0.23 respectively for the upper structure and isolation, and the for lower structure.

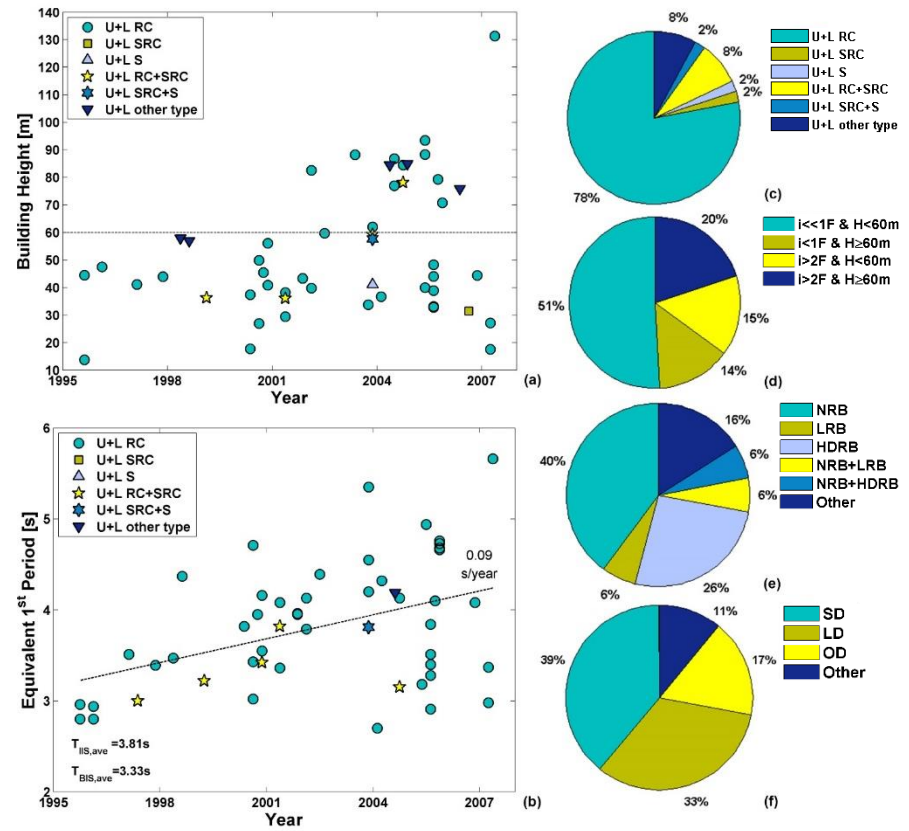


Fig. 3.1. (a) building height per year (52 data), (b) equivalent 1<sup>st</sup> period per year (521 data), (c) structural types (59 data), (d) isolation level (60 data), (e) types and combination of isolators (31 data), (f) types of dampers (18 data). [redrawn from Kobayashi & Sasaki 2009]

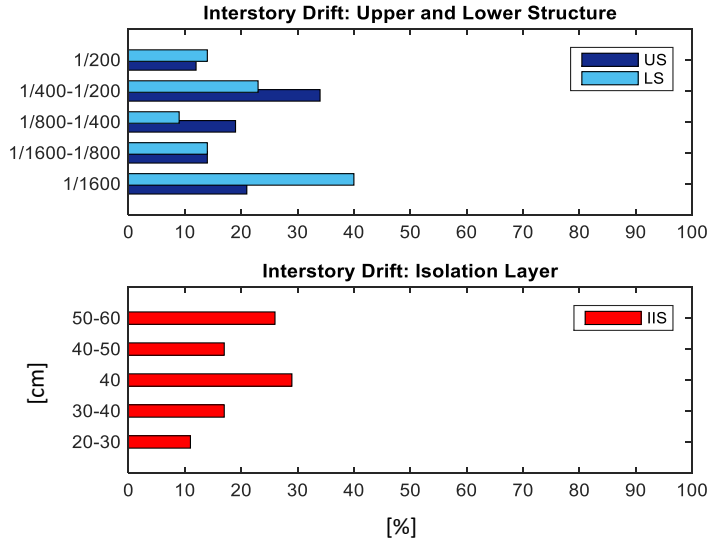


Fig. 3.2. (a) interstory drifts of U and L structures (U:118 data, L: 22 data), (b) interstory drifts of isolation layer (114 data), (c) schematic representation of the drift distribution [redrawn from Kobayashi & Sasaki 2009]

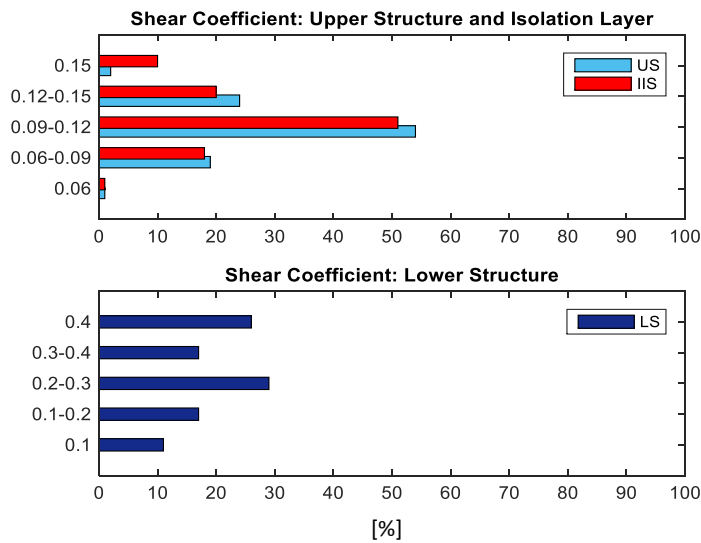


Fig. 3.3. (a) shear coefficient of the U structure and isolation layer (U: 98 data, ISO: 114 data), (b) shear coefficient of the lower structure (23 data), (c) schematic representation of the shear coefficient distribution [redrawn from Kobayashi & Sasaki 2009]

In the paper by [Kobayashi & Sasaki 2009] a comparison between the average values of the maximum response of mid-story and base isolated structure is provided (Tab. 3.1). The average values refer to the first equivalent period, peak roof acceleration, maximum story drift, base shear coefficient and maximum displacement.

Generally, in the mid-story isolated structure are observed larger values than the base isolated structure counterparts due to the interaction between upper and lower structures.

**Table 3.1 Average values of the maximum response**

Structure	$T_{1,eq}$ [s]	Peak roof acc. [cm/s <sup>2</sup> ]	Max story drift [-]	Base shear coef. [-]	Max displ. [cm]
IIS	3.81	254.2	1/387	0.11	32.98
BIS	3.33	221	1/1742	0.12	26.9

### 3.2. IIS REAL BUILDINGS

An overview of the main real applications of IIS, both for new building and for vertical addition in and /or retrofit of existing buildings, is provided in the following.

In particular the IIS real buildings refer to four new buildings, i.e. the Iidabashi 1<sup>st</sup> Building [Tsuneki et al. 2008 - 2009, Murakami et al. 2000], the Shiodome Sumito Building [Suoeka et al. 2004, Tsuneki et al. 2008 - 2009], Nakanoshima Festival Tower [Nikken Journal 14 – 2013, Okada et al. 2014, Nakagawa et al. 2015], Tekko Building [Tamari et al. 2017]; one retrofitted building, i.e. China Basin Berry Street Building [Sumnicht 2008, China Basin Addition 2008, Dutta et al. 2009].

#### 3.2.1. IIS for new building

##### 3.2.1.1. *Iidabashi 1<sup>st</sup> Building - JAPAN*

The building, located in Tokyo, has been designed by Nikken Sekkei and completed in the year 2000, Fig. 3.4.

It is a mixed-use building with 14 stories above ground (height  $H=59$  m), two stories below ground and one-story penthouse. The elevation is divided in two portions (Fig. 3.5 d) by an isolation layer located between

the 9<sup>th</sup> and 10<sup>th</sup> floor. The two portions are different for plan dimensions, space occupancy, and structural system: the lower part, with a plan 130 x 40 m (Fig. 3.5 c), extends for nine stories and reaches 38 m of height, is devoted to office space, and has a mixed structure, made of shear walls and steel reinforced concrete (SRC) frame; the upper part, with a much narrower plan 130x15m (Fig. 3.5 a), is made by five stories and reaches 59 m above ground, has retails/condominium occupancy, and present shear wall reinforced concrete (RC) structure.



**Fig. 3.4. Iidabashi 1<sup>st</sup> building [Murakami et al. 2000]**

The isolation system is composed by 40 laminated natural rubber bearings (RB), with diameter equal to 800 mm, and 212 lead dampers (LD), 180 mm in diameter; the grid of the isolators, 6.4 x 16.35 m (Fig. 3.5b), replicates the main floor grid of the lower structure. An interior view of the isolation layer is provided in Fig. 3.6.



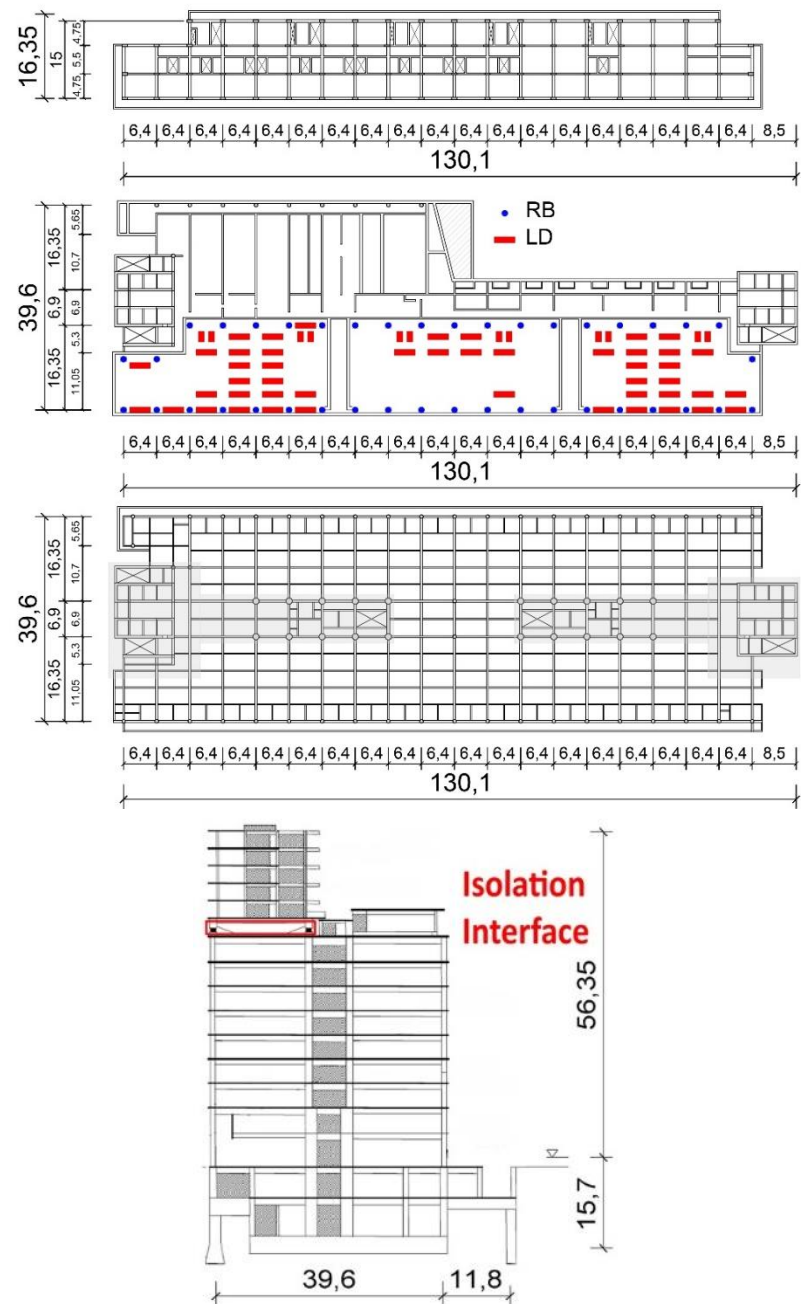


Fig. 3.5. Iidabashi 1<sup>st</sup> building: Plans and Sections (a) upper typical floor, (b) isolation floor, (c) lower typical floor, (d) Transversal section (dimension in meters) [redrawn from Murakami et al. 2000, Murakami 2001]



Fig. 3.6. Interior view of the isolation layer [Murakami et al. 2000, Murakami 2001]

### Simplified analysis

#### *Simplified model*

A simplified lumped masses multi-degree of freedom (MDOF) model was utilized for the vibration analysis of the building.

The Iidabashi 1<sup>st</sup> building is represented by 15 lumped masses, 9 in the lower part, 1 in the intermediate isolation layer and 5 in the upper part.

A graphical representation of the MDOF vibration analysis model of the buildings with the corresponding values of the lumped masses and of the story horizontal stiffness, is given in Fig. 3.7.

Tab. 3.2 shows the secant stiffness of rubber bearings; the first stiffness and yield shear force of dampers,  $F_{y,tot}$ ; the ratio of the total damper yield force  $F_{y,tot}$  to the total building weight  $W_{tot}$ .

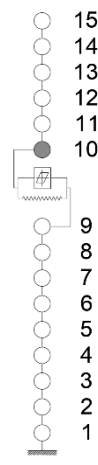
In the MDOF models, viscous damping equal to 2% is assumed in the upper and lower structures, and 0% for the rubber bearings in the seismic isolation interface, where the major source of dissipation is given by the hysteretic response of the lead units, explicitly accounted for by means of the bi-linear force-displacement model of the isolation system.

From Fig. 3.7, can be easily derived that the mass of the upper part of the building was about 22% of the total mass above ground.

Table 3.2 Characteristics of the dampers

Device	secant stiffness (RB), 1 <sup>st</sup> stiffness (LD) [GN/m]	$F_{y,tot}$ [kN]	$\alpha_s' = \frac{F_{y,tot}}{W_{tot}}$
RB	0.0530	-	-
LD	1.6251	13544	2%

RB (Rubber Bearing), LD (Lead Damper)



Node	Mass [kNs <sup>2</sup> /m]	Stiffness [GN/m]
15	1657.9	9.4
14	2305.4	16.6
13	2305.4	20.1
12	2315.2	22.9
11	2315.2	34.4
10	4022.1	*
9	12704.0	7.2
8	4914.8	7.5
7	4914.8	8.0
6	5091.4	8.5
5	5179.7	9.1
4	5189.5	9.8
3	5209.1	11.0
2	5532.8	12.8
1	5434.7	12.3

\* see Table 3.2

**Fig. 3.7. Vibration analysis model**

#### *Energy dissipation*

[Murakami et al. 2000] deal with the IIS as a “concentrated energy dissipation” design problem, and assume the dampers yielding force as the major design parameters for achieving the performance objective of the structural complex.

An artificial seismic wave is used to simulate the level-2 earthquake motion (large earthquake motion). The artificial seismic wave is made setting the velocity response spectra in the long period range at  $S_v=100$  cm/s ( $\xi=0.05$ ).

The relation between the amount of seismic input energy under the level-2 earthquake motion (large earthquake motion) and the amount of energy absorption in each structural portion (LS, ISO and US), varying the damper volume, is provided in Fig. 3.8. The variation of the damper volume is represented by the ratios  $\alpha_s$ , i.e. the yield strength of the damper/ to the weight of the upper stories, and  $\alpha'_s$ , i.e. the yield strength of the damper to the total weight.

With an increase in the damper volume, about the 70 – 80% of seismic input energy is absorbed by hysteretic damping of the isolation story (dampers). The amount of energy absorbed by internal viscous damping of the upper stories is as small as 0.1 – 0.3% with respect to the amount

of seismic input energy in the same case of ordinary base-isolated buildings. With an increase in the volume of the damper, the amount of energy absorbed by internal viscous damping of the lower stories is as small as 20 – 30% of seismic input energy and stable.

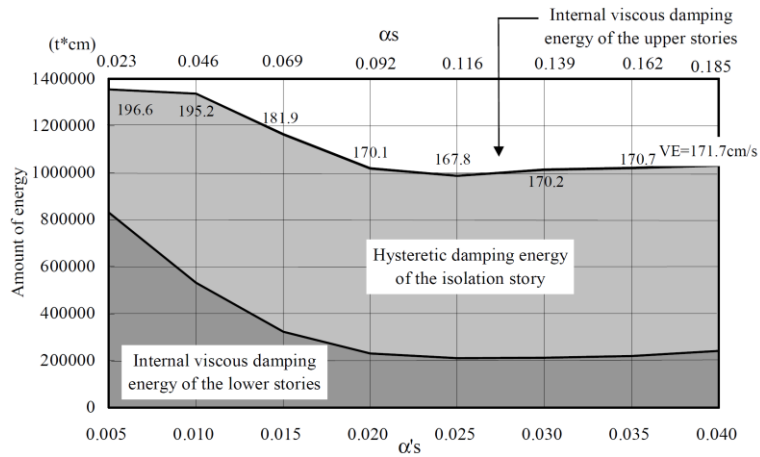


**Fig. 3.8. Relation between the damper volume and the amount of energy of each portion**

Fig. 3.9 shows the maximum deformation of the isolation story in changing the volume of the damper. From Fig. 3.9 can be noticed that the maximum deformation of the isolation story decreases with increase in the volume of the damper and that it gets steady at about  $\alpha's=0.02 - 0.025$  ( $\alpha_s=0.09 - 0.12$ ).

It is worth to noticing that with  $\alpha's=0.02 - 0.025$  ( $\alpha_s=0.09 - 0.12$ ) both the amount of energy absorbed by hysteretic damping of the isolation story and the maximum deformation of the isolation story are stable.

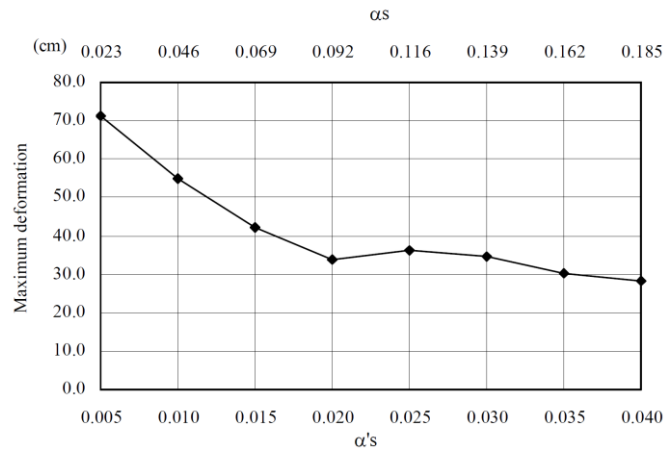


**Fig. 3.9.** Relation between the damper volume and the maximum deformation of the isolation story

### Three-dimensional analysis

More detailed studies also were made by earthquake response analysis using a 3-dimensional analysis model of a total of 15 stories including nine stories of lower stories, one story of isolation story and five stories of upper stories.

#### *Modal analysis*

Tab. 3.3 gives the natural period of the 3-D analysis model respectively.

**Table 3.3.** Natural period of the analysis space model

Model	$T_1$ [s]	$T_2$ [s]	$T_3$ [s]
3D IIS - RB+LD	1.35	1.35	1.21
3D IIS - RB	3.47	3.45	3.20
3D US	0.29	0.24	0.21

#### *Time history analysis*

The seismic motion wave forms used in the analysis were three actually measured wave forms (El Centro NS, Taft EW, Hachinohe NS) and an artificial seismic motion wave form (ARTWAVE474), each with a maximum velocity of 50cm/sec. The artificial seismic motion wave form was produced using the phase characteristics of measured seismic wave motion wave forms, setting the acceleration response spectrum shape in the long period region so that in the velocity response spectrum  $S_v = 80$

cm/s ( $\xi = 0.05$ ). The earthquake response spectrum for the seismic input wave considered herein is provided in Fig. 3.10 ( $\xi = 0.05$ ).

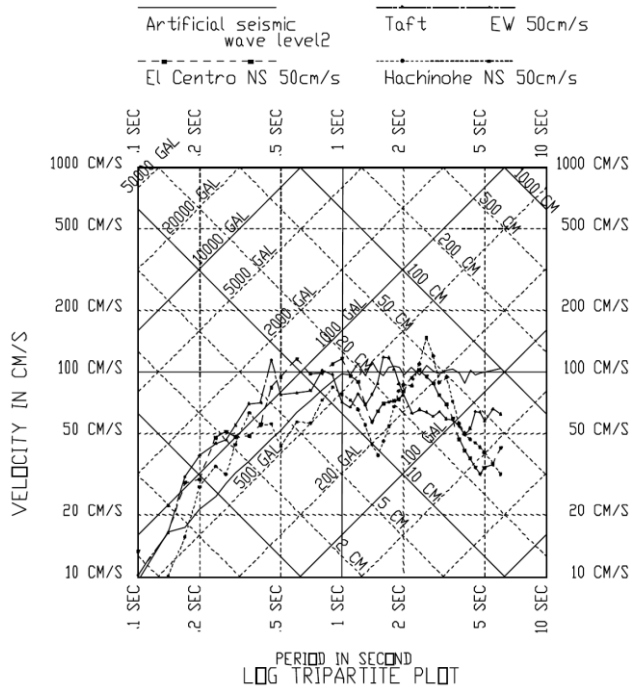


**Fig. 3.10. Pseudo-velocity response spectrum**

Therefore, design of the building was made to provide  $\alpha'_s = 0.02 - 0.03$  setting the design target of the isolation story at 40 cm or below in the maximum deformation in the level-2 earthquake.

Fig. 3.11 shows the results of response analysis in the level-2 earthquake in the direction of the short side of the building. The graph on the left refers to the maximum story deflection, while the graph on the right refers to the maximum shear force.

From Fig. 3.11a can be observed that the deformation of the building is mainly concentrated in the isolation story with a maximum deformation of 32.6 cm within the target value.

The peak drift of the US stories is 0.20 cm, i.e. about 1/1530 of the story height, and the peak drift of the LS stories is 2.1 cm, i.e. about 1/195 of

the story height. Both the peak drifts of US and LS stories are remarkably small as compared with ordinary earthquake-resistant buildings. From Fig. 3.11b can be observed that the maximum shear forces of the US and LS stories are below the elastic limit strength and have excellent earthquake resisting performance. The maximum response story shear force in the building is about 1/5 in the US and 1/2 in the LS with respect to the corresponding counterparts in a reference fixed-base structures.

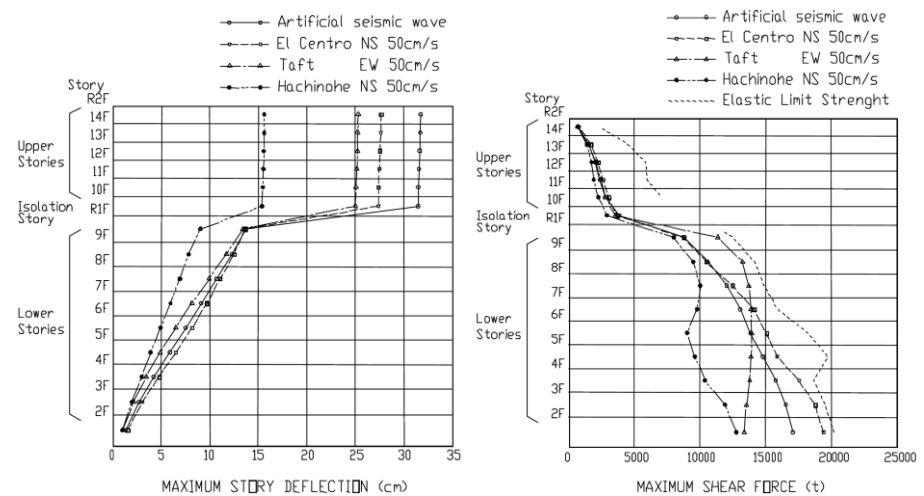


Fig. 3.11. (a) maximum story drift, (b) maximum shear force

#### Energy dissipation

Fig. 3.12 shows the relation between the amount of seismic energy absorption on each story under the artificial seismic wave. From Fig. 3.12 can be seen that almost the 80% of the seismic energy is absorbed the lead damper in the isolation story. This distribution confirm that the inter-story isolation system can be seen as a “concentrated type” of energy dissipation system, different from the common approach of distributed energy dissipation systems, where the dampers are spread throughout the building structure.

Iidabashi 1<sup>st</sup> building has been chosen as case study and the is thoroughly analyzed in Chapter 5, in order to evaluate the dynamics of real mid-story isolated building in the light of approaches and indications coming from the world of research.

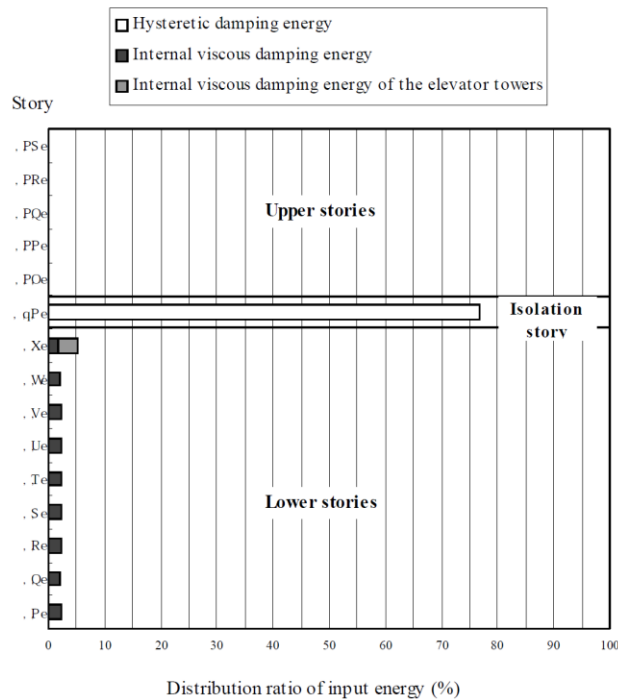


Fig. 3.12. Input distribution of seismic energy to each story of the building

### 3.2.1.2. Shiodome Sumitomo building - JAPAN

The building, designed by Nikken Sekkei as well, and completed in 2004, is located at Shiodome, in Tokyo, Fig. 3.13.

It is a mixed-use tall building, with 3 basement levels and 25 stories above ground, reaching the height of 126.1 m; the plan is approximately 110 x 40 m, with a floor area of 4339 m<sup>2</sup> (Fig. 3.14 a, b, c).

The isolation layer is located between the 11<sup>th</sup> and 12<sup>th</sup> floor, approximately at 50 m height, and divides the building in two portions (Fig. 3.14 a, b), only distinguished for the occupancy, i.e. hotel and office space in the lower and upper structure, respectively. A peculiarity of the building is the presence of a large atrium, about 40 m of height, which is located on the North side of the lower structure (Fig. 3.14 c). The structural system is a steel (S) frame, both for the upper and lower parts.

The atrium covers the 10 hotel's floors in height and the halved hotel floor area in plan. Therefore, the most important proposition for this building from a structural planning aspect was how to achieve the building above the large atrium maintaining high structural performance.



The section column is hexagonal, and it is consisted of welded steel plates (thickness is 36mm and 70mm).

These columns, about 40 m long, support large vertical permanent load (about 20000 kN). Thus, to prevent buckling, the top and bottom of column is steel casting, the wide of top section is smaller than center section, the bottom of column is pin (Fig. 3.15b).

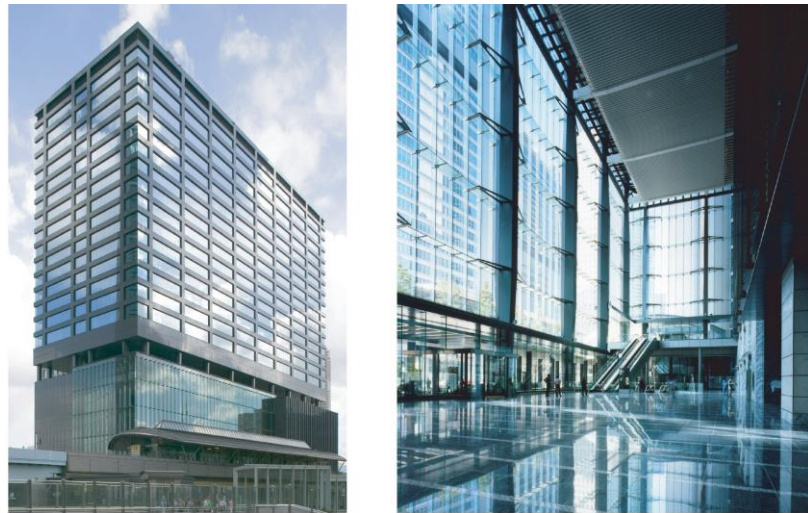


**Fig. 3.13.** (a) external view of the building, (b) atrium internal view [Sueoka et al. 2004]

The isolation system is composed by 41 laminated natural rubber bearings (RB) of different diameter, namely: 13  $\phi$  1300 mm, 19  $\phi$  1100 mm, 9  $\phi$  1000 mm, plus 100 lead dampers (LD) and 14 steel dampers (SD). Three alignments of isolators, two perimeter and one interior, can be observed in the plan longitudinal direction of the isolation floor (Fig. 3.14 b), with device spacing equal to 12.8 m and 6.4 m; the distribution of isolators and dampers in plan suggests the need of balancing the different mass distributions in the upper and lower parts.

A view of the isolation layer and of the atrium columns during the construction is provided in Fig. 3.16.

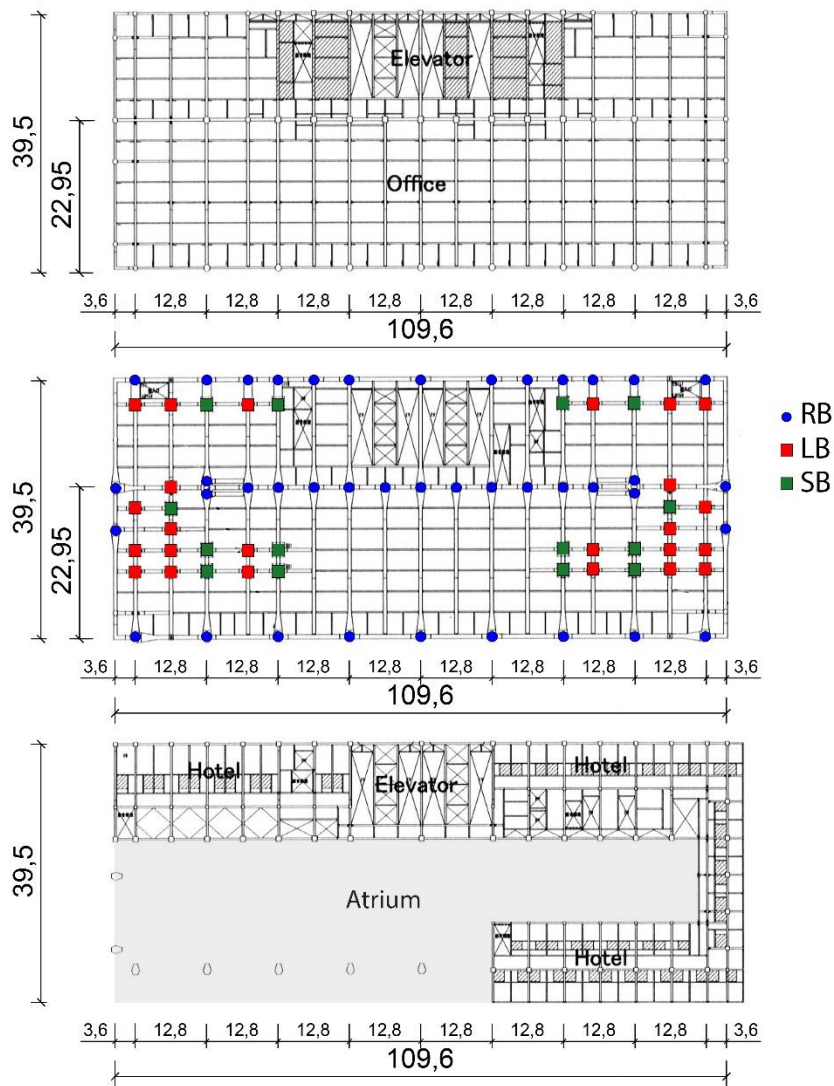


Fig. 3.14. Shiodome Sumitomo building: Plans (a) upper typical floor, (b) isolation floor, (c) lower typical floor, (dimension in meters) [Sueoka et al. 2004]

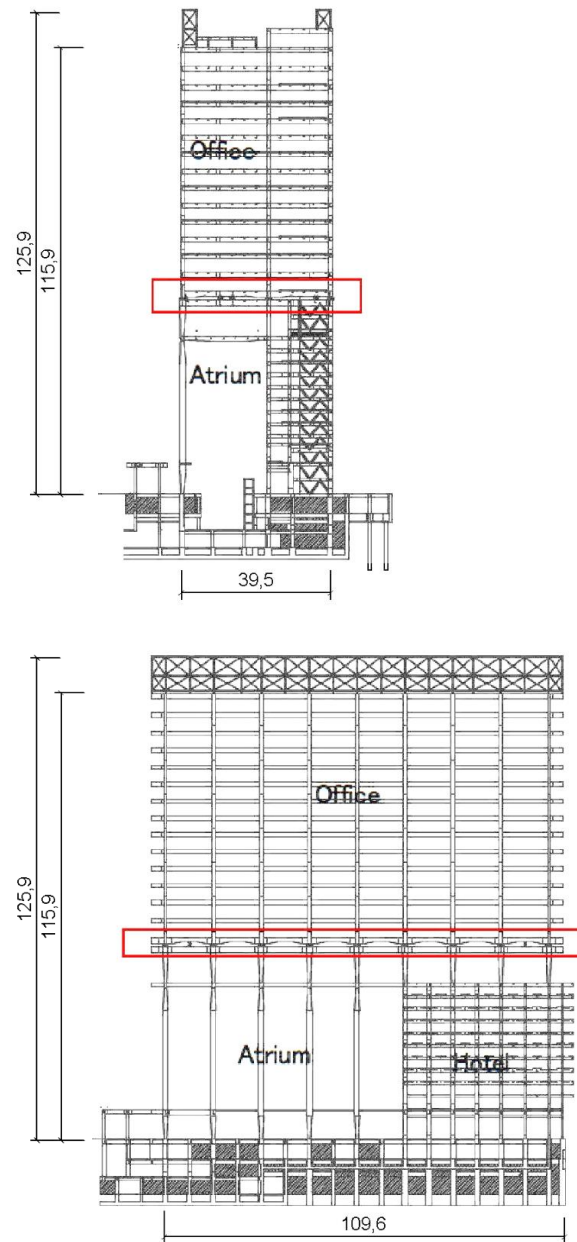


Fig. 3.15. Shiodome Sumitomo building: Sections (a) transversal, (b) Longitudinal, (dimension in meters) [Sueoka et al. 2004]



**Fig. 3.16. Shiodome Sumitomo building: Sections (a) construction of the isolation layer, (b) construction of the atrium columns [Sueoka et al. 2004]**

### Simplified analysis

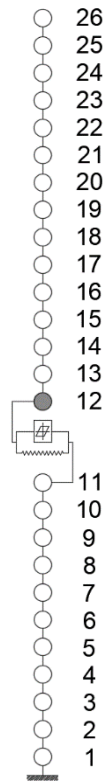
#### *Simplified model*

A simplified lumped masses multi-degree of freedom (MDOF) model was utilized for the vibration analysis of the building.

A graphical representation of the MDOF vibration analysis model of the buildings with the corresponding values of the lumped masses and of the story horizontal stiffness, is given in Fig. 3.16.

The Shiodome Sumitomo building is represented by 26 masses, 11 in the lower part, 1 in the intermediate isolation layer and 14 in the upper part.

Tab. 3.4 shows the secant stiffness of rubber bearings; the first and second stiffness and yield shear force of dampers,  $F_{y,tot}$ ; the ratio of the total damper yield force  $F_{y,tot}$  to the total building weight  $W_{tot}$ .



Story	Mass [kNs <sup>2</sup> /m]	Stiffness [kN/mm]	
		X	Y
26	5767.6	2.1	1.5
25	3460.8	2.4	1.7
24	3446.5	2.9	2.1
23	3075.4	3.0	2.2
22	3083.6	3.0	2.2
21	3093.8	3.1	2.3
20	3116.2	3.3	2.5
19	3167.2	3.3	2.5
18	3169.2	3.4	2.6
17	3124.4	3.3	2.6
16	3131.5	3.4	2.7
15	3139.7	3.4	2.6
14	3185.5	3.0	2.3
13	3566.8	4.0	3.1
12	4029.6	*	*
11	3127.4	1.3	1.1
10	3126.4	5.6	4.5
9	1720.7	5.3	4.8
8	1697.2	5.2	5.0
7	1717.6	5.3	5.2
6	1714.6	5.4	5.4
5	1715.6	5.6	5.7
4	1732.9	5.7	5.9
3	1725.8	6.1	6.3
2	2582.1	2.3	2.7
1	3079.5	2.7	3.2

\* see Table 3.4

Fig. 3.16. Vibration analysis model [Sueoka et al. 2004]

Table 3.4. Characteristics of the isolation interface

Device	secant stiffness (RB), 1 <sup>st</sup> stiffness (LD) [GN/m]	2 <sup>nd</sup> stiffness [kN/cm]	F <sub>y,tot</sub> [kN]	$\alpha'_s = \frac{F_{y,tot}}{W_{tot}}$
RB	0.0807	-	-	-
LD	2.65	-	22000	3%
SD	6.78	0.0022	3500	3%

RB (Rubber Bearing), LD (Lead Damper), SD (Steel Damper)

In the MDOF models, viscous damping equal to 2% is assumed in the upper and lower structures, and 0% for the rubber bearings in the seismic isolation interface, where the major source of dissipation is given by the

hysteretic response of the lead and steel units, explicitly accounted for by means of the bi-linear force-displacement model of the isolation system. From Fig. 3.16, can be easily derived that the mass of the upper part of the building was about 68% of the total mass above ground.

#### *Modal Analysis*

The natural vibration periods of the 26DOF IIS model considering both isolators and dampers are provided in Tab. 3.5. In particular in the table are given the period values taking into account either the secant stiffness of the isolation system or the elastic stiffness of only isolators.

The vibration modes of the 26DOF IIS model are depicted in Fig. 3.18; the graph on the left refers to the initial stiffness of both isolators and dampers, while the graph on the right refers to the secant stiffness of isolators.

**Table 3.5. Characteristics of the isolation interface**

Mode	Direction	Natural period [s]	Modal Participation Factor
1	X	5.95 (3.26)	7.47 (7.97)
	Y	6.04 (3.42)	7.45 (-7.82)
2	X	1.06 (1.06)	3.16 (2.44)
	Y	1.17 (1.15)	-1.56 (2.57)
3	X	0.96 (0.65)	2.60 (-1.76)
	Y	0.96 (0.70)	3.77 (1.87)
4	X	0.52 (0.48)	-0.11 (0.98)
	Y	0.60 (0.53)	-0.17 (-1.31)

The value in ( ) shows the values at the initial stiffness

A first, quite trivial consideration is that, taking into account only isolators a much longer first period is obtained than in the case of both isolators and dampers.

In Fig. 3.18b the 1<sup>st</sup> mode involves deformation mainly concentrated at the isolation level, with almost no deformations in the US and only slight deformations in the LS; on the contrary the 2<sup>nd</sup> and 3<sup>rd</sup> modes show comparable displacements for both US and LS, and the 4<sup>th</sup> and 5<sup>th</sup> modes display negligible deformations in the US. Similar considerations can be done for the vibration modes in Fig. 3.18a; however, the reduced 1<sup>st</sup> period leads to a minor deformation in the isolation layer and major deformations



in the US in the fundamental mode; the higher modes (from the 2<sup>nd</sup> to the 5<sup>th</sup>) show displacements in both US and LS.

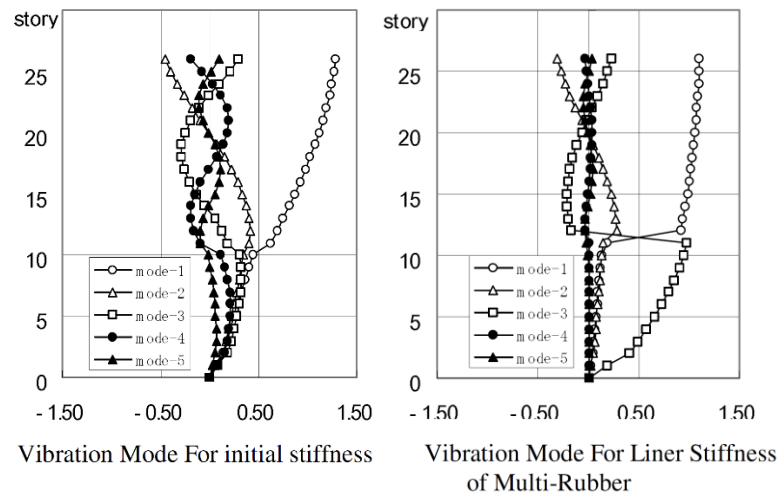


**Fig. 3.18. Vibration modes (a) initial stiffness of both dampers and isolators, (b) linear stiffness of isolators [Sueoka et al. 2004]**

#### *Time history Analysis*

The seismic waves used for the response analysis are three simulated seismic waves, i.e. Hachinohe EW (K1-wave), Tohoku NS (K2-wave) and Kobe NS (K3-wave). The pseudo-velocity response spectra of each wave are shown in Fig. 3.19.

The story drift and acceleration envelopes obtained from the time history analyses of the 26DOF IIS model of the Shiodome Sumitomo buildings are shown in Fig. 3.20.

The distribution of maximum displacement is similar to the shape of first vibration mode, when only isolators are considered (Fig. 3.18). The maximum displacement of isolation interface is about 30 cm, the peak drift of the other floors is within  $1 \div 3$  cm, i.e. below  $1/200$  of story deformation angle. The maximum acceleration is observed in the floor below the isolation layer; the upper floors show a reduction of the story acceleration thanks to the isolation effect.

The story shear force envelope obtained from the time history analyses of the 26DOF IIS model of the Shiodome Sumitomo buildings is shown in Fig. 3.21. The upper floors show the larger reduction of the shear force thanks to the isolation effect.

A comparison of the peak story shear force under K3-wave between the isolated model and a reference fixed-based model is also provided in Fig. 3.22.

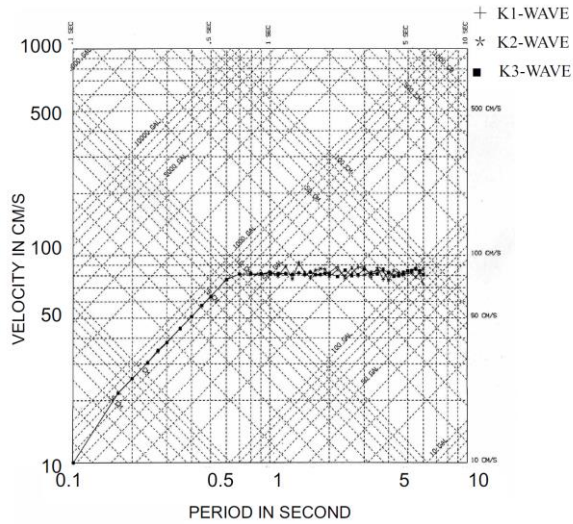


Fig. 3.19. Pseudo-velocity response spectrum

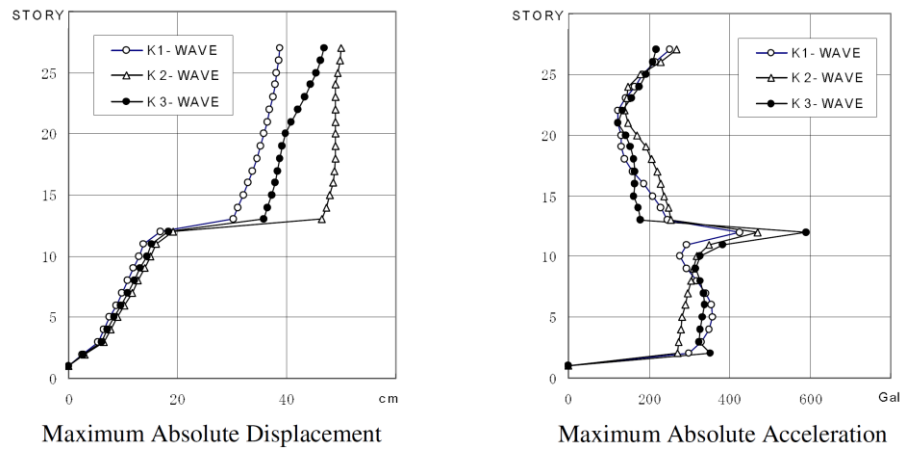
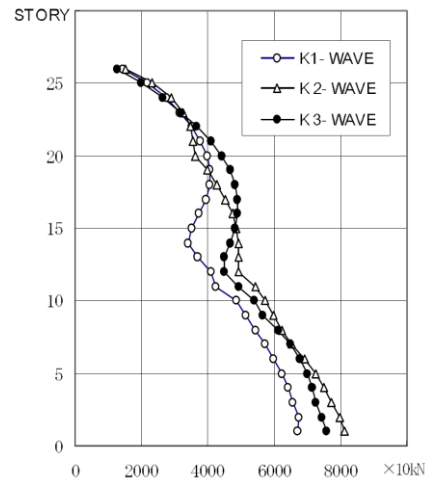


Fig. 3.20. (a) maximum absolute displacement, (b) maximum absolute acceleration

It can be observed that the maximum shear forces of the US and LS stories are below the elastic limit strength and have excellent earthquake resisting



performance. The maximum response story shear force in the building is about 1/3 - 1/2 in the US and 1/2 in the LS with respect to the corresponding counterparts in a reference fixed-base structures.



Maximum Shear Force

Fig. 3.21. Maximum shear force

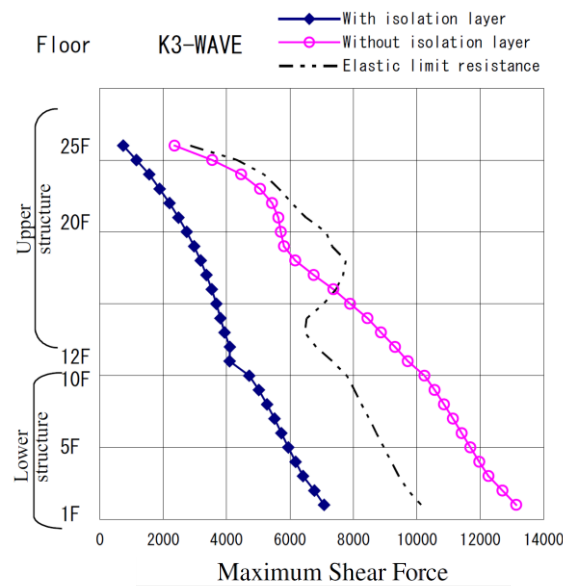


Fig. 3.22. Isolated vs. fixed-base models - shear force under K3-Wave

### Energy dissipation

The distributions of the energy components obtained from the time history analyses of the 26DOF model of Shiodome Sumitomo building subjected to a specific seismic input (Hachinohe, Tohoku, Kobe) is shown in Fig. 3.23. In each graph are provided the time histories of the Input Energy, the Inertia Energy, the Internal Viscous Damping Energy and the Hysteretic Energy.

From the figure, it is possible to notice that a large amount of the seismic input energy is dissipated through the hysteretic response of the dampers within the isolation system; the share of hysteretic energy is between  $70 \div 80\%$ .

This distribution confirm that the inter-story isolation system can be seen as a “concentrated type” of energy dissipation system, different from the common approach of distributed energy dissipation systems, where the dampers are spread throughout the building structure.

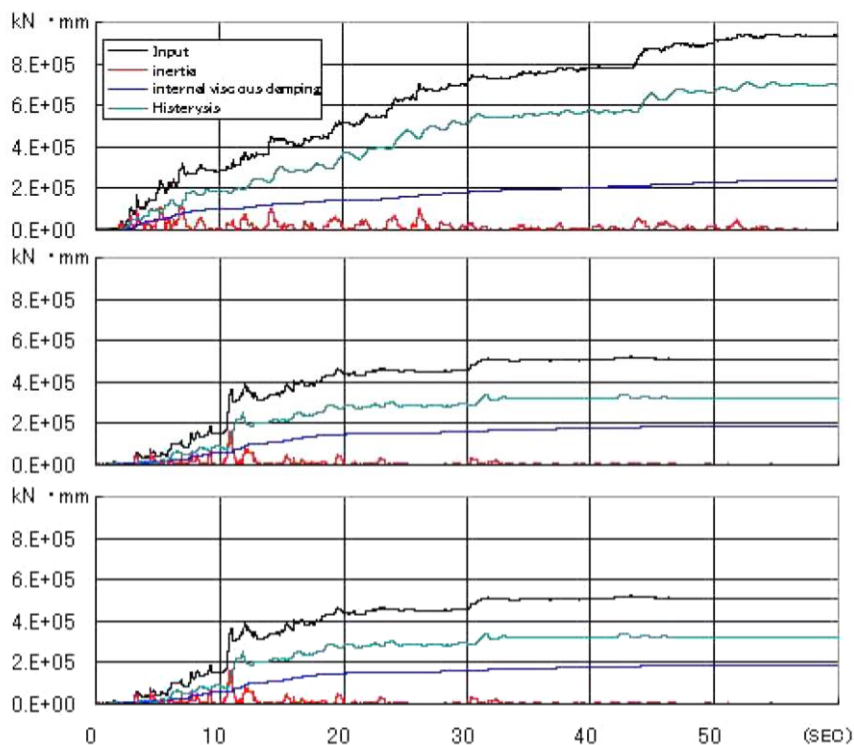


Fig. 3.23. Time histories of the energy components: (a) Hachinohe EW, (b) Tohoku NS, (c) Kobe NS

Shiodome Sumitomo building has been chosen as case study and the is thoroughly analyzed in Chapter 5, in order to evaluate the dynamics of real mid-story isolated building in the light of approaches and indications coming from the world of research.

### **3.2.1.3. Festival Tower Osaka - JAPAN**

The original Festival Hall in Osaka was constructed in 1958. The hall boasted 2,700 seats and was characterized by excellent acoustics, referred to as “sound from the heavens”. However, in December 2008, it was torn down on its 50th anniversary, to be rebuilt as a new hall.

Nakanoshima Festival Tower (Fig. 3.24), designed by Nikken Sekkei, and completed in 2012, is located in Osaka.



**Fig. 3.24. View of the building**

It is a mixed-use tall building, with 3 underground levels and 39 stories above ground, reaching the height of 200 m.

The building is comprised of 3 broad sections, i.e. the lower-level floors from the 8<sup>th</sup> floor and below including the hall (Fig. 3.25), the intermediate-level floors from the 9<sup>th</sup> floor directly above the hall to the 12<sup>th</sup> floor, and the upper-level floors from the 13<sup>th</sup> floor which includes the Sky Lobby (Fig. 3.26). The new hall occupies floors 3 through 8 of the

lower-level floors. It is a large-scale hall with the same maximum seating capacity of 2700 seats as the old hall.

The architectural basic floor plans and the architectural cross section of the building are depicted in Fig. 3.27, a structural cross section is provided in Fig. 3.28.

The isolation layer is located immediately above the new Festival Hall between the lower-level and middle-level floors, and divides the building in two portions (Fig. 3.28), only distinguished for the occupancy, i.e. hotel and office space in the lower and upper structure (Fig. 3.27 a, c), respectively. A peculiarity of the building is the presence of a large hall, which covers 7 floors (2<sup>nd</sup> through 8<sup>th</sup> floors) and all the plan (Fig. 3.27 c, e and Fig. 3.28).

The lower-level floors of the Nakanoshima Festival Tower are steel-reinforced concrete (SRC) and the middle-level (9<sup>th</sup> to 12<sup>th</sup>) and the upper-level floors (14<sup>th</sup> and above) are steel (S) frame (Fig. 3.28).

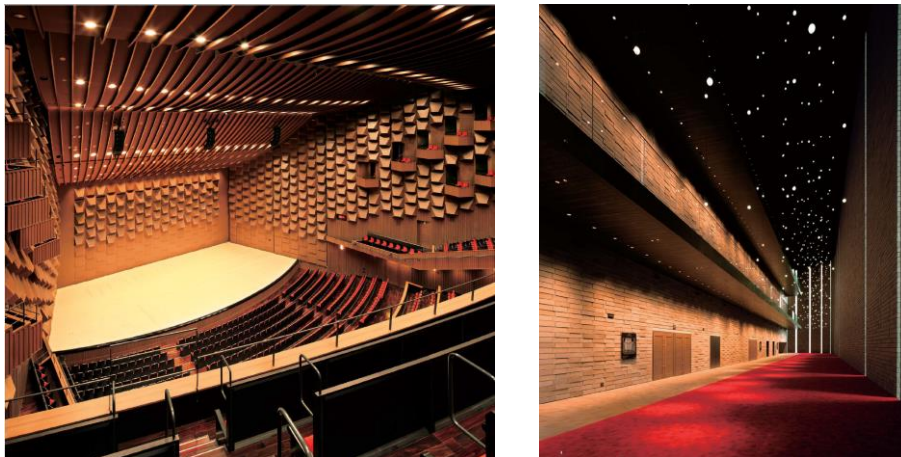


Fig. 3.25. (a) Interior of Festival Hall, (b) Interior of the three-floor atrium



**Fig. 3.26. (a) Sky Lobby on the 13<sup>th</sup> floor, ceiling height is 9.6 m, (b) Mega-truss members visible in the Sky Lobby**

The most important proposition for this building from a structural planning aspect was how to achieve the building up of center-core high-rise offices above the large 2700-seat capacity hall while maintaining high structural performance. In order to implement this proposition, the following two points that characterize the structural plan of this building were employed:

- Giant trusses to transfer the load of upper-level floors to the perimeter of the hall and secure the large open space of the hall;
- Mid-story seismic isolation system to create a seismic isolation layer in the boundary between the hall and the office floors.

Rigidity and strength are obtained for the upper-level floors (Fig. 3.29a) from the earthquake resistant brace assembly of the center core frame and the perimeter frame surrounding the building with 128 H-shaped steel columns spaced at 1.8 m, forming a bearing wall-like perimeter framework (outer-framed tube). CFT (concrete filled tube) is employed for the 9 columns of the core, and oil dampers are implemented to reduce motion by either seismic force or wind force. The top of the building has a “hat-truss” that reduces warping of the building as a whole.

Between the upper and middle levels of the building, corresponding to the 13<sup>th</sup> to 15<sup>th</sup> floors, are two major trusses; a mega-truss and a belt-truss (Fig.

3.30). The mega-truss is a huge three-dimensional structure 20 meters high; it supports the column axial force of the upper level core (38000 t) and transmits the load of the upper floors to the 16 big columns, namely “big columns, with a cross section of 3 x 1.5 m, directly below the outer perimeter of the upper-level floors. The belt-truss is a two dimensional truss around the outside of the 14<sup>th</sup> floor. It serves to distribute the force of the 128 perimeter steel columns around the upper-level floors to the big columns, each column supports a total load of 6000t. The big columns support the entire load of the building from the 13<sup>th</sup> floor up, and the two huge trusses make possible the vast space obtained for the hall in the lower part of the building (Fig. 3.29b).

The framing plan and framing elevations for the mega trusses and prime columns are shown in Fig. 3.31. The mega-trusses are comprised of the 13th floor girders (Fig. 3.31a) which are the lower chord members, the girders inside the core on the 15th floor (inside the core in Fig. 3.31b) which are the upper chord members, and the diagonals which connect them with a distance of approximately 27 m between nodes (outside the core in Fig. 3.31b). The long-term load supported by each diagonal is approximately 3000 t.

The various members of the mega-trusses and the prime columns contend three-dimensionally (Fig. 3.32), and a maximum of 8 members converge on a single node.

### 3. Design practice and applications

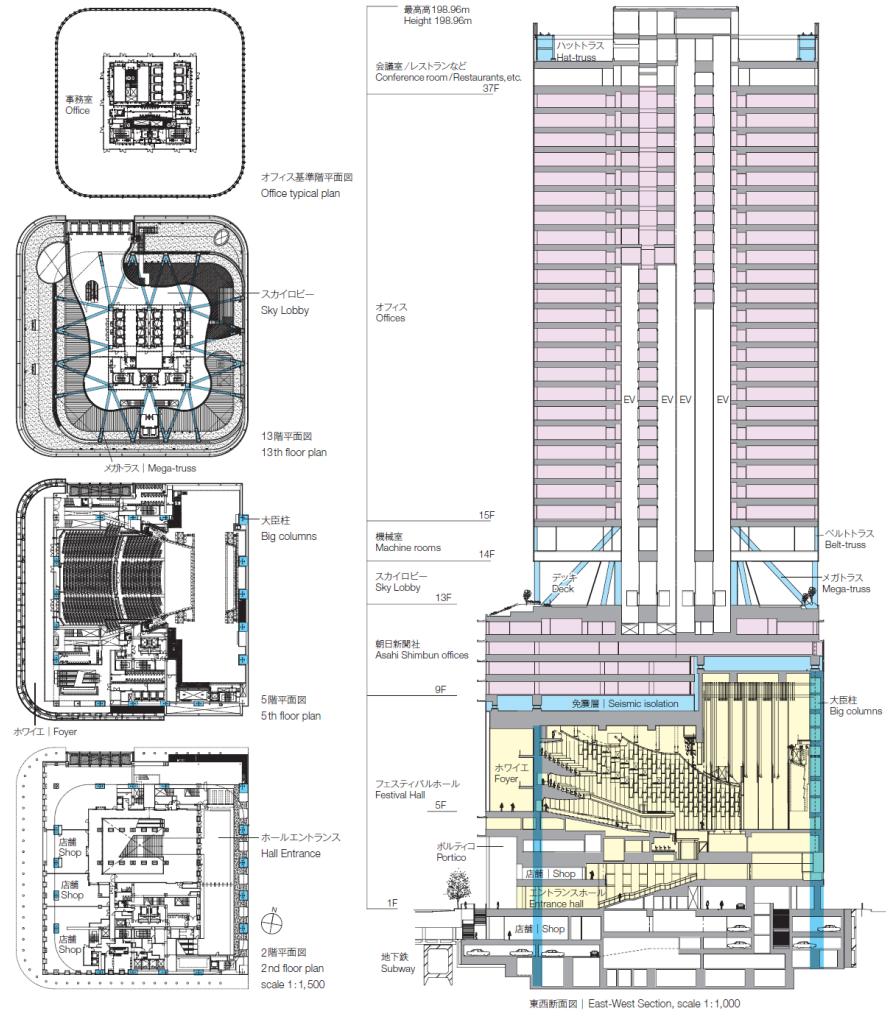


Fig. 3.27. Floor plans: (a) upper typical floor, (b) 13<sup>th</sup> floor, (c) 5<sup>th</sup> floor, (d) 2<sup>nd</sup> floor, (e) cross section of the building

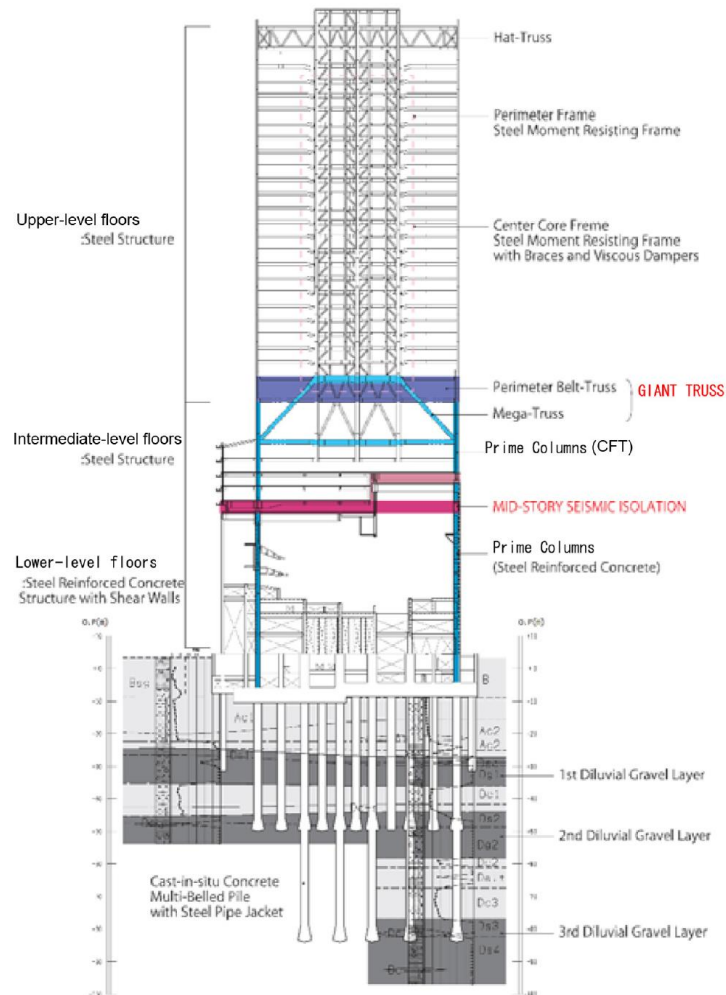


Fig. 3.28. Cross section



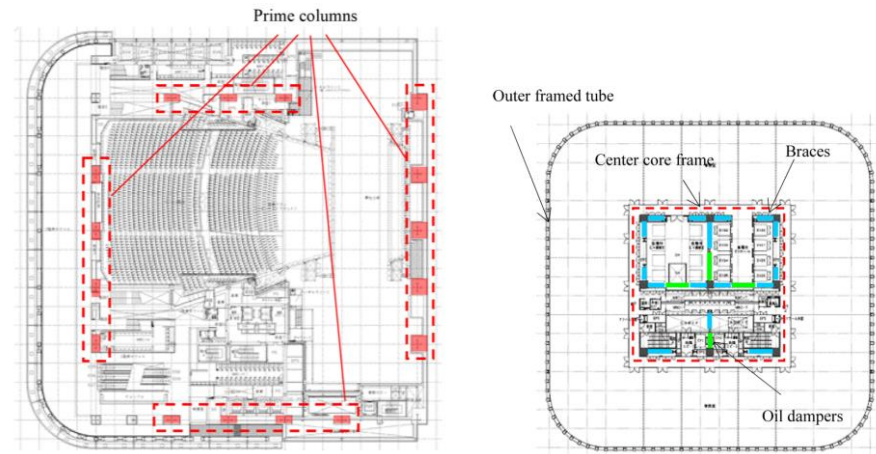


Fig. 3.29. (a) basic floor layout of upper-level floors, (b) basic floor layout of lower-level floors

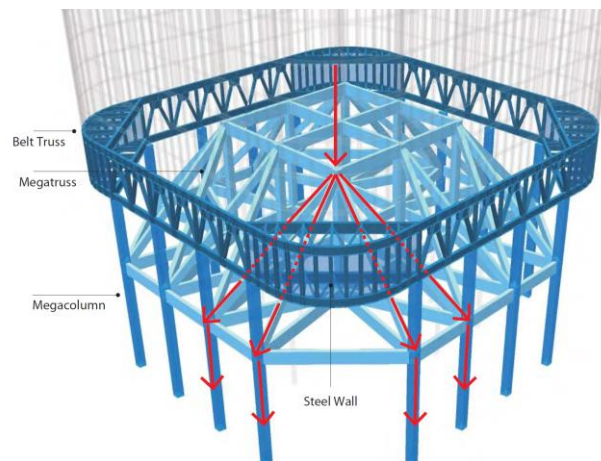


Fig. 3.30. Outline of mega-trusses and belt trusses between the 13<sup>th</sup> and 15<sup>th</sup> floors

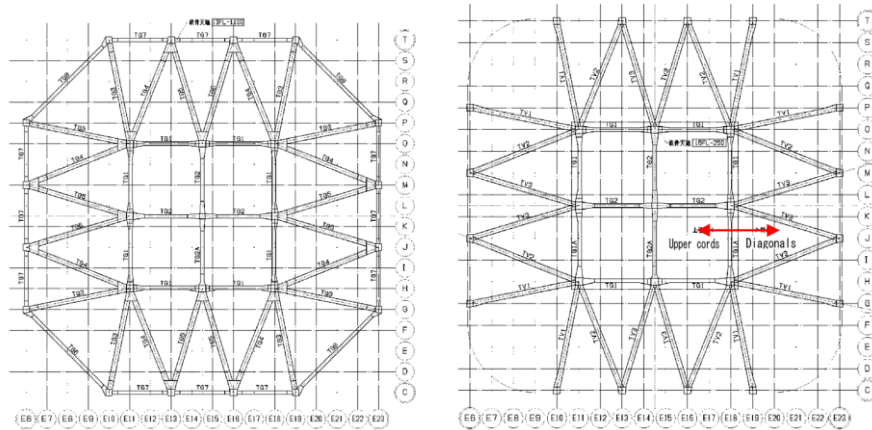


Fig. 3.31. (a) 13<sup>th</sup> floor framing plan, (b) 15<sup>th</sup> floor framing plan

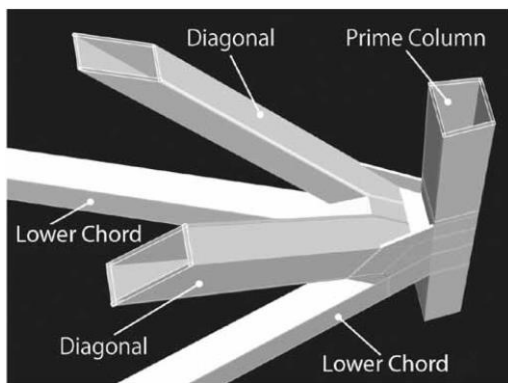


Fig. 3.32. Schematic diagram of Mega-truss connection

The isolation system is composed by 66 lead rubber bearings (LRB), subdivided in 32 square LRB 1500 x 1500 mm and in 34 circular LRB of different diameter between  $\phi$  800 ÷ 1000 mm, plus 24 oil dampers (OD), 12 for each direction. A view of the isolators and damping devices is provided in Fig. 3.34.

The layout of the seismic isolation layer and a view of the isolators and damping devices are shown in Figs. 3.33 and 3.34, respectively. The oil dampers are employed as energy-absorbing elements and each damper offers a maximum resistance of 1000 t; the large square LRBs are set to support the prime columns which bear 95% of the building weight above (each couple of square LRBs support the weight of each prime column, i.e. 6000 t); the remaining 5% weight is supported by the circular LRBs.

In order to avoid crashing, the clearance between the object isolated side and the object fixed side is secured as 650 mm. In addition, since the seismic isolation layer of this building is installed directly above the hall, the area of the upper section of the stage called the fly tower becomes a staggered seismic isolation layer which is 2 stories higher and the clearance between the structural components of isolated side and the fly tower are secured as 750 mm at least.

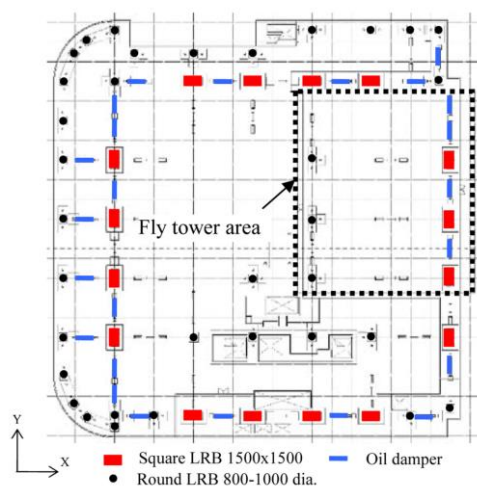


Fig. 3.33. Schematic layout of seismic isolation floor



Fig. 3.34. (a) view of the square LRBs, (c) view of the OD

### Three-dimensional model

#### *Time history analysis*

The seismic performance of the mid-story seismic isolation system is verified through series of dynamic response analyses using two levels of

variation of earthquakes set created in accordance with Japanese law. The intensity of the motion is set as “rare” earthquake for Level 1 and “extremely rare” earthquake for Level 2. Dynamic response analyses were performed using six to ten varieties of earthquakes including recorded motion data and artificially generated motion considering geological properties of the specific site.

This building's seismic-resistant design criteria are shown in Tab.3.6.

**Table 3.6. Target performance of seismic design**

Earthquake scale		Level 1 earthquake	Level 2 earthquake
U floors	Member stress	Short-term allowable stress or less	
I floors	Story drift angle	$\leq 1/300$	$\leq 1/150$
ISO	Deformation level	1/2 stable def. or less	stable def. or less
	Deformation	$\leq 200$ mm	$\leq 400$ mm
L floors	Member stress	Short-term allowable stress or less	
	Story drift angle	$\leq 1/800$	$\leq 1/400$
Foundation	Member stress	Short-term allowable stress or less	
	Support strength	Short-term allowable bearing capacity or less	

U (Upper), I (Intermediate), ISO (Isolation), L (Lower)

The peak drift angle and floor acceleration responses are provided respectively in Fig.3.35 a and b.

From Fig. 3.35 can be observed that, since the lower-level floors are SRC construction as rather rigid structure, seismic force is largely amplified at the top of the hall. Mid-story seismic isolation layer reduces the acceleration into the intermediate-level floors to around 25% thanks to the isolation effect. The maximum story drift of the upper level floors is more than 30% smaller than that of general high-rise office buildings.

It is worth noticing that Nakanoshima Festival Tower has a most efficient structural system to avoid the rubber bearings subjected to tensile force because of application of mega-trusses. Since the building weight is concentrated to the large square LRBs which are laid out along perimeter line of the upper-level floors, the uplift force caused by overturning moment is theoretically minimized.

Therefore, by employing this mid-story seismic isolation structure, the building is able to achieve the high seismic safety required of the headquarters of a news company.

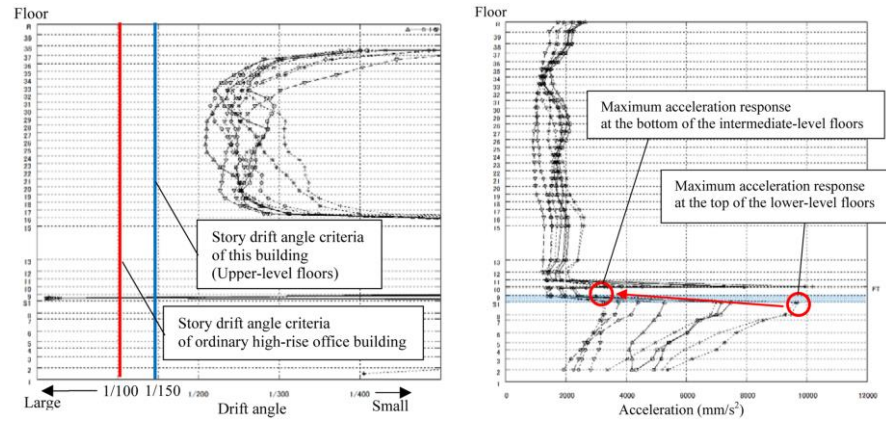


Fig. 3.35. (a) peak drift angle response, (b) peak floor acceleration response

#### 3.2.1.4. Tekko Building - JAPAN

The building, located on a narrow site more than 200m long near Tokyo station, has been designed by Mitsubishi Jisho Sekkei Inc. and completed in 2015, Fig. 3.36.



Fig. 3.36. East view of the building

It is a mixed-use tall building, consisting of 2-seismic isolated buildings on an integrated lower part, i.e. a Main Building (office building) located on the north side of the site, and a South Tower (lively facilities building) located on the south side. The building layout is provided in Fig. 3.37.



The Main Building is 3 basement levels, 26 stories above ground and 2 stories penthouse, reaching the height of 136.9 m; the plan is approximately 114.5 x 28 m, with a floor area of 3206 m<sup>2</sup>. The South Tower is 3 basement levels, 19 stories above ground and 1 story penthouse, reaching the height of 99.2 m (Figs. 3.38 – 3.39); the plan is approximately 38.3 x 28 m, with a floor area of 1072.4 m<sup>2</sup>. The main structure is a steel (S) frame above ground and a steel framed reinforced concrete (SRC) below ground.

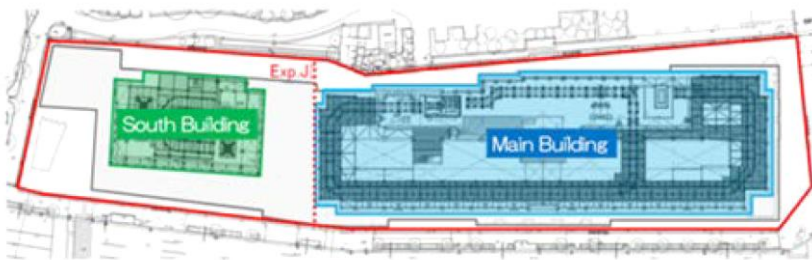
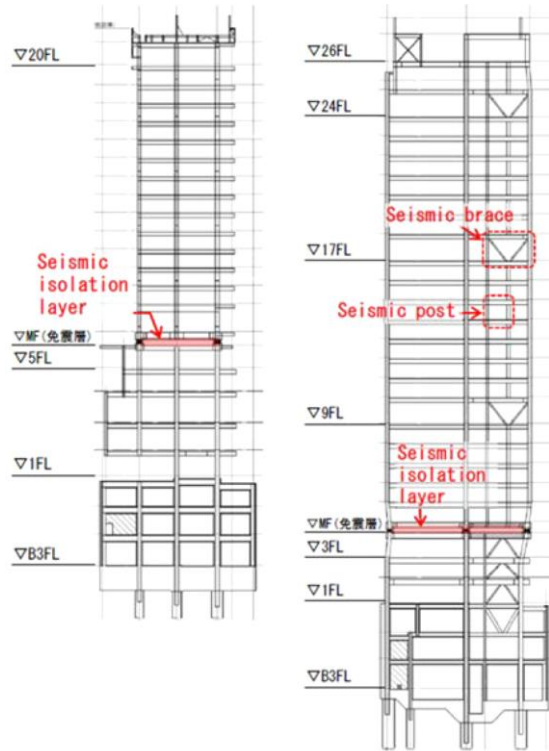


Fig. 3.37. Building layout



Fig. 3.38. Longitudinal section of the building



**Fig. 3.39. Transversal section: (a) South Building, (b) Main Building**

The isolation layer is located below the 4<sup>th</sup> and 6<sup>th</sup> floor of the Main Building and the South Tower, respectively, and divides the building in two portions (Figs. 3.38 – 3.39), only distinguished for the occupancy in the tower, i.e. commercial facilities and apartments in the lower and upper structure, respectively.

The isolation system of the Main Building is composed by 48 laminated natural rubber bearings (RB) of diameter  $\phi$  1000 ÷ 1500 mm, plus 30 u-shape steel dampers (LD) and 40 oil dampers (OD) with 8 units with locking mechanism. Three main alignments of isolators, two perimeter and one interior, can be observed in the plan longitudinal direction of the isolation floor (Fig. 3.40), with device spacing equal to 16.8 m and 7.2 m. The isolation system of the South Tower is composed by 10 laminated natural rubber bearings (RB) of diameter  $\phi$  800 ÷ 1200 mm, plus 8 oil dampers (OD). Two perimeter alignments of isolators can be observed in

the plan longitudinal direction of the isolation floor (Fig. 3.41), with device spacing equal to 28 m and 7.2 m.

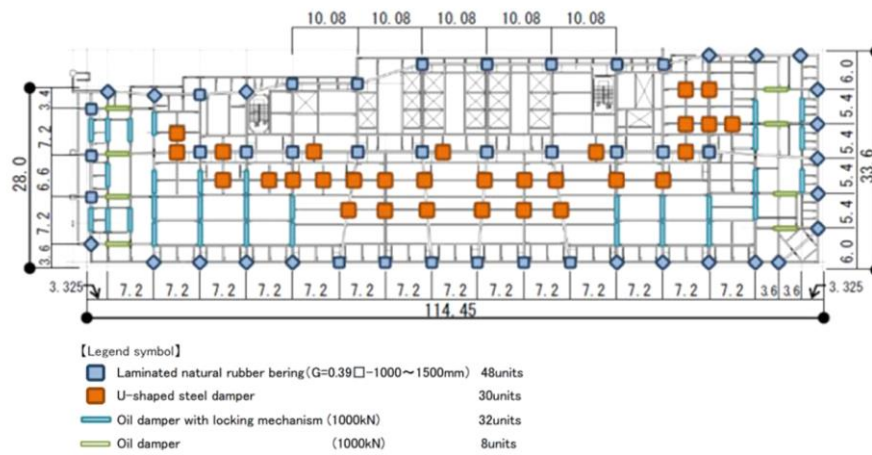


Fig. 3.40. Seismic isolation plan of Main Building

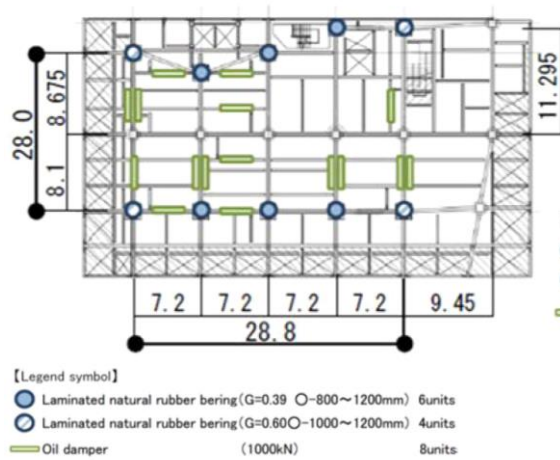


Fig. 3.41. Seismic isolation plan of South Building

## Seismic design

### *Simplified analysis*

#### *Simplified model*

A coupled lumped-mass analysis model in which 2 buildings are arranged in parallel with a boundary below them is adopted for the vibration



response analysis, as the building is configured with 2 buildings and an integrated lower part.

In the model, the B3 floor is assumed to be fixed on the earth with no displacement and each of the mass of the 3 basement floors is assumed to be integrated.

The masses of the floors of 3 parts, the Main building, the South Tower and the boundary, from 1st to 3rd floor are arranged in parallel and the three of them are assumed to be rigid floor with the same displacement. The seismic isolation layers of the Main Building and the South Tower are placed below the 4<sup>th</sup> floor and 6<sup>th</sup> floor, respectively.

Above those, the structure of the Main Building and the South Tower is modeled as 23 lumped masses and 16 lumped masses, respectively, with bending-shear spring.

A graphical representation of the coupled - MDOF vibration analysis model of the buildings is given in Fig. 3.42.

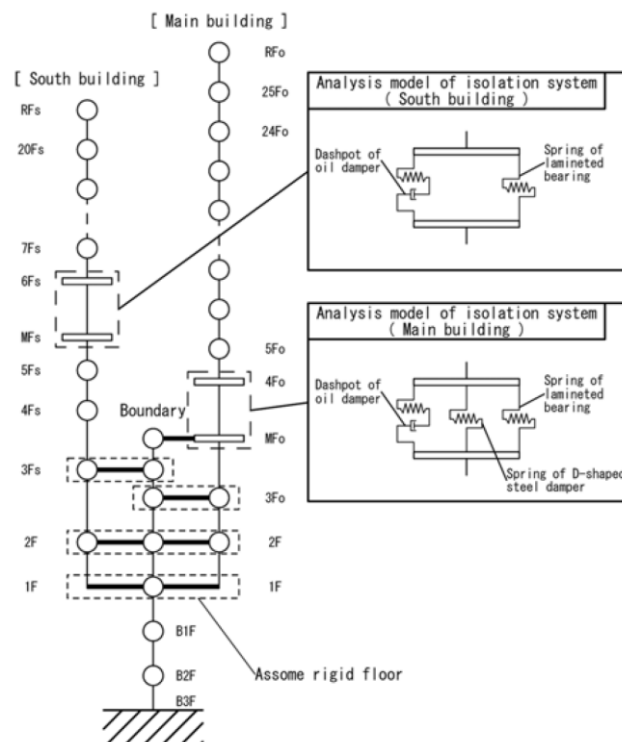


Fig. 3.42. Vibration Analysis Model

### Modal Analysis

The natural vibration periods of the building are shown in Tab. 3.7 considering both the initial stiffness and the deformation of the isolation system at the time of 30 cm. From Tab. 3.7 can be noticed that the 1<sup>st</sup> period of the South Tower is 5.68 s in both the cases considered while the 1<sup>st</sup> period of the Main Building is equal to 4.24 s and 5.38 s, respectively for the initial state and the state at the time of 30 cm.

Parametric studies were carried out to investigate amplification of the response caused by resonance due to a coupling effect or variation in the level of the input seismic motions or equivalent stiffness, as the seismically isolated periods of the 2 buildings are close.

**Table 3.7. Natural vibration periods of the building**

Direction	Mode	Natural period [s]	
		Initial state	Deformation at the time of 30 cm
X	1 <sup>st</sup> (SB, 1 <sup>st</sup> )	5.68	5.68
	2 <sup>nd</sup> (MB, 1 <sup>st</sup> )	3.79	5.06
	3 <sup>rd</sup> (MB, 2 <sup>nd</sup> )	1.32	1.53
	4 <sup>th</sup> (SB, 2 <sup>nd</sup> )	1.21	1.21
	5 <sup>th</sup> (MB, 3 <sup>rd</sup> )	0.79	0.84
Y	1 <sup>st</sup> (SB, 1 <sup>st</sup> )	5.66	5.66
	2 <sup>nd</sup> (MB, 1 <sup>st</sup> )	4.24	5.38
	3 <sup>rd</sup> (MB, 2 <sup>nd</sup> )	1.44	1.71
	4 <sup>th</sup> (SB, 2 <sup>nd</sup> )	1.11	1.11
	5 <sup>th</sup> (MB, 3 <sup>rd</sup> )	0.84	0.90

MB (Main Building), SB (South Building), ( ) number of mode in the MB and SB as standalone structures

### Time History analysis

Time history analysis was carried out including 3 measured waves from the past (El Centro 1940 NS, Taft 1952 EW, and Hachinohe 1968 NS); 3 waves prescribed by the notification (Hachinohe, Kobe, and random phase), each of which were defined for Level 1 and Level 2; two waves unique to the site were examined, assuming the Kanto earthquake and the Tokai/Tonankai /Nankai (three coupled) earthquakes.

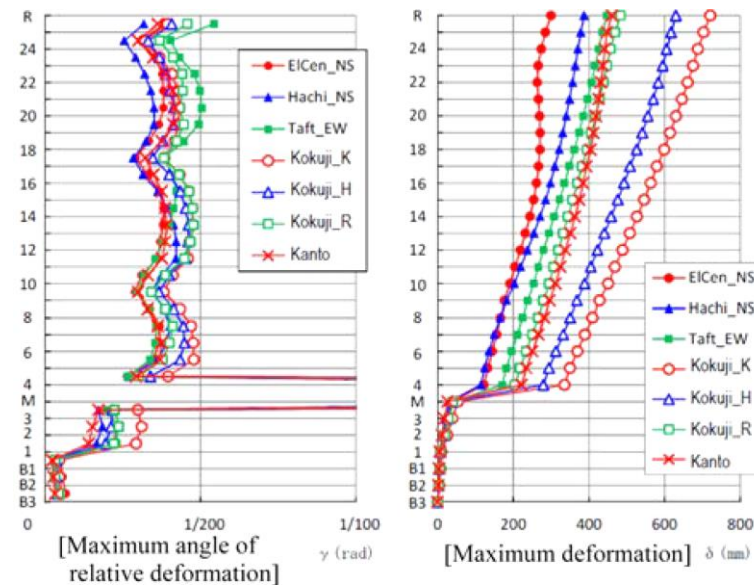
The target performance of the seismic design under the Level 1 (rarely occurring seismic motion) and Level 2 (extremely rarely occurring seismic motion) is shown in Tab. 3.8.

**Table 3.8. Target performance of seismic design**

	Level 1 Earthquake Rare	Level 2 Earthquake Extremely rare
U and L floors	Short-term allowable stress or less Story drift $\leq 1/200$	Short-term allowable stress or less Story drift $\leq 1/100$
ISO	Bearing Shear strain 200% No tensile force	Bearing Shear strain $\leq 267\%$ Tensile stress $\leq 1 \text{ N/mm}^2$ Short-term allowable surface pressure or less
Basement	Short-term allowable stress or less	Elastic limit stress or less
Foundation	Short-term allowable stress or less	Ultimate stress or less

U (Upper), I (Intermediate), ISO (Isolation), L (Lower)

The results of the time history analysis in terms of maximum angle of the relative deformation and of maximum deformation are depicted in Figs. 3.43 - 3.44, respectively for the Main Building and the South Tower. From Figs. 3.43 - 3.44 can be noticed that the maximum story drift under the level 2 was  $1/184$  and  $1/173$  for the Main and South Buildings, respectively; the maximum displacement of the isolation layer was 33.6 cm and 25.1 cm for the Main and South Buildings, respectively.

**Fig. 3.43. Results of the vibrational analysis (Main Building)**

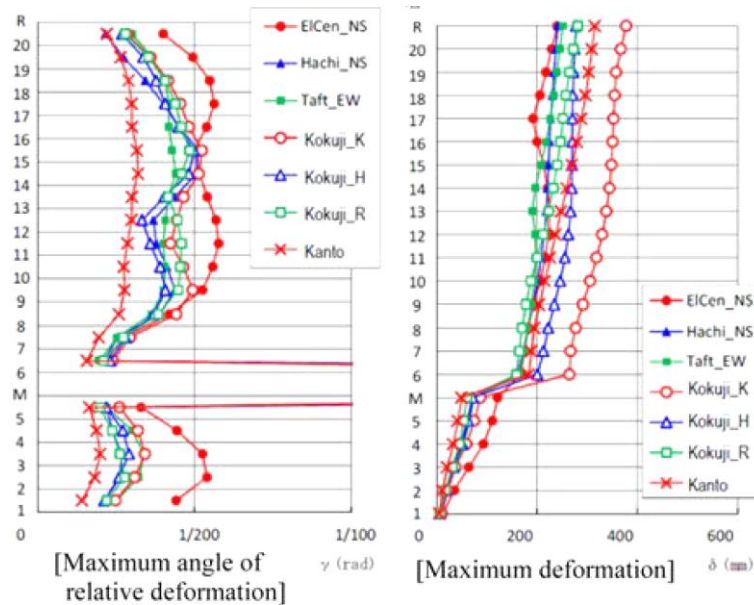


Fig. 3.44. Results of the vibrational analysis (South Building)

### Wind design

In the design of the building against wind, an analysis was carried out for 2 levels of wind loading.

The target performance of the wind design under the Level 1 and Level 2 for the structural frames and the isolation system is shown in Tabs. 3.9 – 3.10.

Table 3.9. Target wind performance of the structural frame

Load level	Story drift	Stress in structural frame members
Level 1	$\leq 1/200$	Equal to the short term
Level 2		allowable stress or less

Table 3.10. Target wind performance of the seismic isolation layer

Load level	Seismic isolation layer
Level 2	Deformation of the ISO $\leq$ seismic isolation clearance
	No uplift on the seismic isolation bearings
	No fatigue failure of steel dampers
	Integrity of oil dampers

From the wind loading response analysis results, it was confirmed that the responses shear force for both the Main Building and the South Tower were less than the design shear force, and the shear stresses under the Level 2 wind load were less than the short term allowable stresses.

### **Locking mechanism for oil dampers**

The elevators, which pass through the seismic isolation layer in the Main Building, will stop when a large displacement occurs in the seismic isolation layer.

Under normal conditions the oil dampers with a locking mechanism (Fig.3.45) function as normal oil dampers without locking, but during strong winds the oil dampers are locked using a solenoid valve.

In the Main Building the oil dampers with locking mechanism are locked under wind loads with a return period of 4-5 years (wind velocity at the top of the building of 25 m/s), the strong wind warning level of the Japan Meteorological Agency, based on measurements by a wind direction anemometer installed on the top of the building (Fig.3.46).

The locking mechanism is released using a timer, so that the locking mechanism is released at a certain time after the locking mechanism has been activated, and also can be controlled manually.

When an earthquake occurs while the locking system is activated, there is a system whereby the lock is released based on accelerometer measurements.

In addition, in order to verify safety, seismic response analysis has also been carried out using the stiffness of the seismic isolation layer when locked, assuming a case in which the lock release function did not work normally.



**Fig. 3.45. Damper with a locking mechanism**

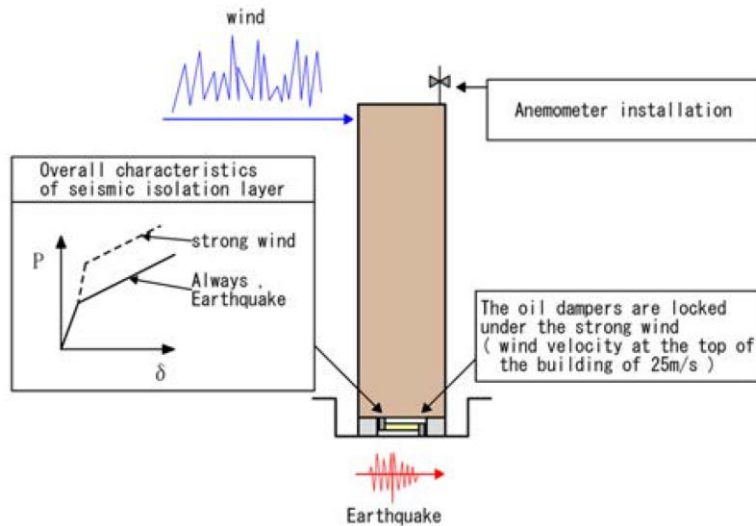


Fig. 3.46. Use of damper with a locking mechanism

### Monitoring of building under seismic and wind loads

After completion of the construction of the building, measurements of the building were carried out under seismic and wind load for a year.

#### *Building measurement during earthquakes*

During this period, earthquakes of seismic intensity 3 were measured twice, and in each earthquake the seismic isolation effect was confirmed. In particular, the first one was an M5.5 earthquake on 16<sup>th</sup> May 2016 with an epicenter in the south of Ibaraki Prefecture and the second one was an M7.4 earthquake on 22<sup>nd</sup> November 2016 with an epicenter in the sea off Fukushima. Going from the level below to the level above the isolation interface, a reduction of the acceleration response equal to 31% and 62% (32.2 gal  $\rightarrow$  9.9 gal and 18.3.2 gal  $\rightarrow$  11.4 gal) for the Main Building, and of 17% and 32% (29.5 gal  $\rightarrow$  4.9 gal and 19.2 gal  $\rightarrow$  6.2 gal) for the South Building were observed respectively for the two earthquakes, Fig. 3.47.

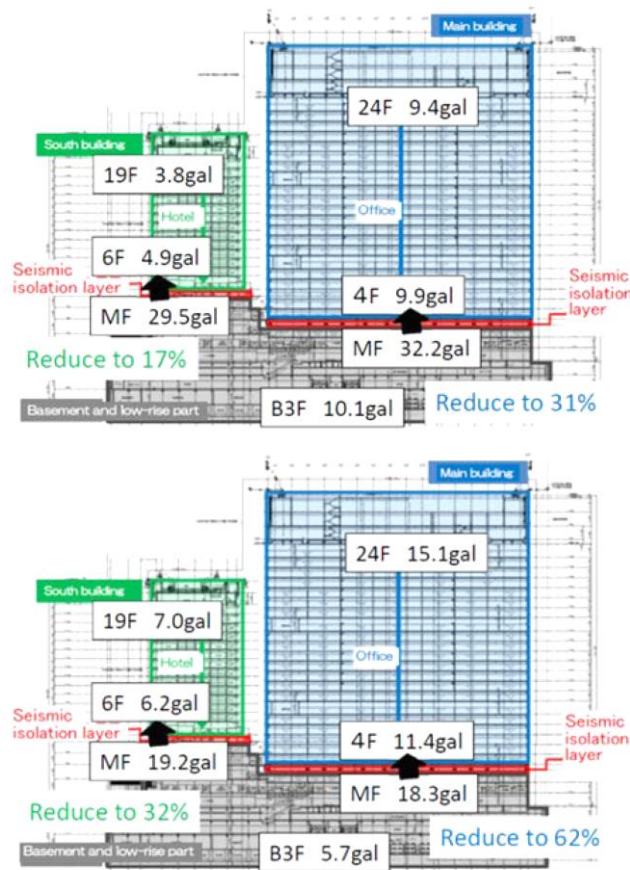


Fig. 3.47. Observed maximum accelerations: (a) May 16, 2016, (b) Nov 22, 2016

#### *Building measurement during strong winds*

In the wind measurements in the 1 year after completion of construction, instantaneous maximum wind velocity exceeding 25 m/s on the top of the building was measured on 2 days, 2017/4/17 and 2017/4/29, during which the locking mechanism of the oil dampers was activated.

In the wind measurements on 2017/4/29 it was found that the instantaneous maximum wind velocity exceeded 25 m/s twice, with measured values of 30 m/s and 26 m/s (Fig. 3.48).

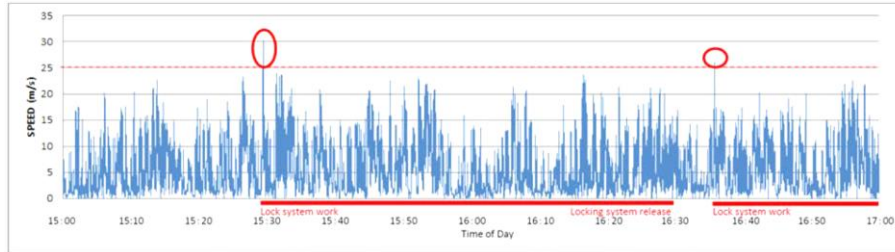


Fig. 3.48. Observed maximum accelerations, Apr 29, 2017

When the locking mechanism of the oil dampers was activated, the acceleration response increased below the seismic isolation layer due to the wind pressure acting above the seismic isolation layer. As a result, it was confirmed that the oil damper locking mechanism was activated properly; in both the Main and South buildings excellent habitability less than the H-10 was observed on the roof floor (Figs. 3.49 – 3.50).

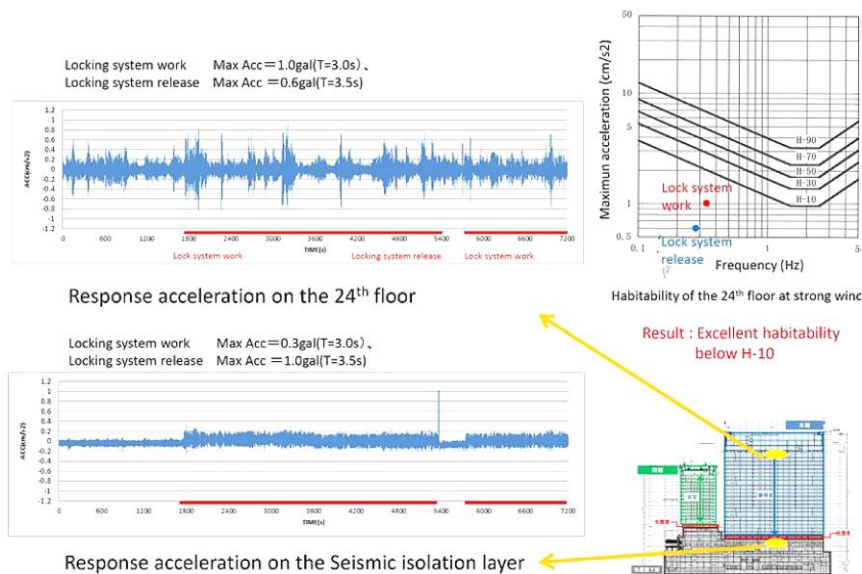


Fig. 3.49. Response situation during strong wind (Main Building)



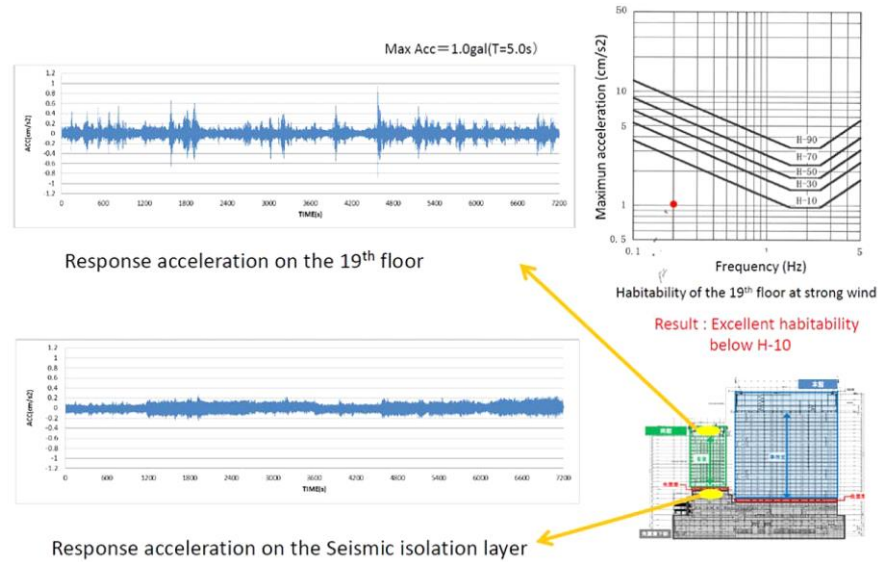


Fig. 3.50. Response situation during strong wind (South Building)

Therefore, the validity of the design was confirmed by the measurements.

### 3.2.2. IIS for existing building

#### 3.2.2.1. China Basin 185 Berry Street Building - USA

The 185 Berry Street building at China Basin (Fig. 3.51) was originally designed in the mid-1980s and opened in 1991. With the construction of Pac Bell Park just to the east, and the new University of California at San Francisco (UCSF) Mission Bay campus to the west, office space and life science space in this portion of the City became highly desirable.



Fig. 3.51. View of the building [“On the Grid”, JohnSumnicht 2008]

The existing building is a three-story, about 274.3 m long and 30.5 m wide concrete frame structure with post-tensioned flat slabs and two expansion joints at approximately the third of the length (Fig. 3.52).

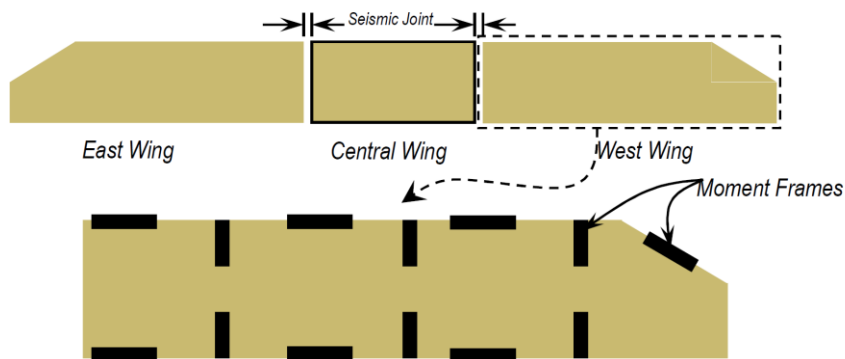


Fig. 3.52. Plan View of the China Basin Building

Development manager McCarthy Cook & Co wanted to expand this structure adding as much new rentable space as possible. In its existing condition, approximately 7432 mq of additional space could be added on top of the existing building with light-weight steel framing without implementing a seismic upgrade to the existing structure. In order to add

the desired two new floors conventional upgrade approaches involved building new reinforced concrete shear walls within the existing occupied structure. This would have been highly disruptive to the bio-science laboratories operated by UCSF, a major existing tenant in the building. Despite the fact that the University desired to expand its presence at China Basin, it could not tolerate the disruption of its existing operations that seismic retrofit construction would have entailed.

The San Francisco office of Simpson Gumpertz and Heger (SGH) proposed that the two new stories be constructed on seismic isolation bearings placed on top of the existing structure. This mid-level isolation concept had never previously been implemented in any building in the United States. In initial feasibility studies, SGH demonstrated that using this technique, the new construction atop the isolation bearings would act like a giant tuned, 244 m long mass damper. During strong earthquake shaking, the new stories addition would move laterally to counteract and dampen the motions of the existing building and actually reduce the amount of earthquake force and displacement demand on the existing structure. This not only permitted the new space to be constructed without requiring a structural upgrade but also improved the seismic performance capability of the existing building. Most importantly, it eliminated the need for an intrusive and disruptive seismic retrofit of the nearly, fully occupied building below.

The final solution allowed the maximum addition of added floor area with respect to retrofitting conventional methods (13500 mq vs. 8400 mq) without the introduction of seismic joints (Fig. 3.53). In addition the project scale of China Basin (252 m) is comparable to the Transamerica Building (260 m) and to Bank of America Building (241 m) project scale (Fig. 3.54).

It is worth noticing that the retrofitted “*impressive project, and unique application of b.i. technology, ..., really very challenging*” of the Berry Street won the “SEAONC Awards – Excellence in Structural Engineering 2008”; the Jury comment was: “*The design solution was highly ingenious, requiring innovative use of cutting-edge technology.*”

Some pictures of the China Basin elevation under construction are provided in Fig. 3.55.

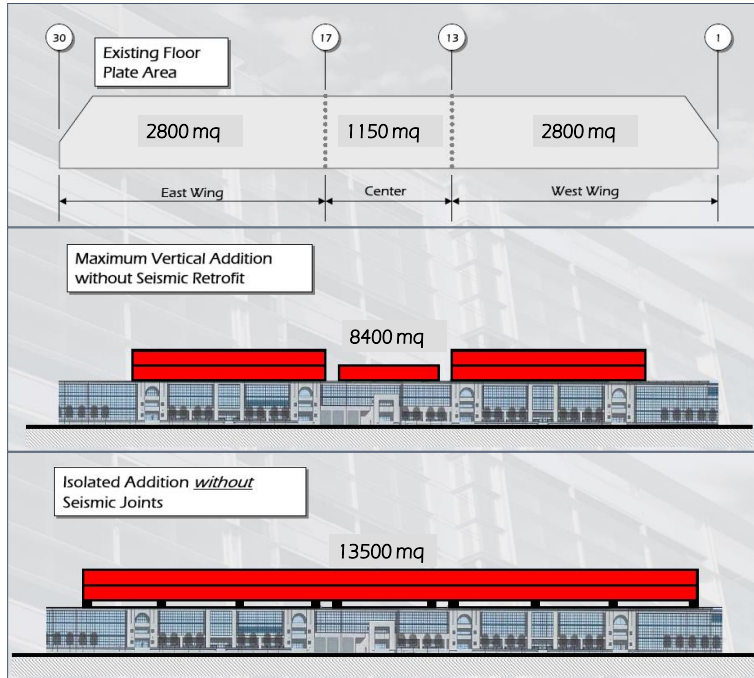


Fig. 3.53. (a) Existing floor plate area, (b) maximum addition with conventional methods, (c) vertical addition on isolators

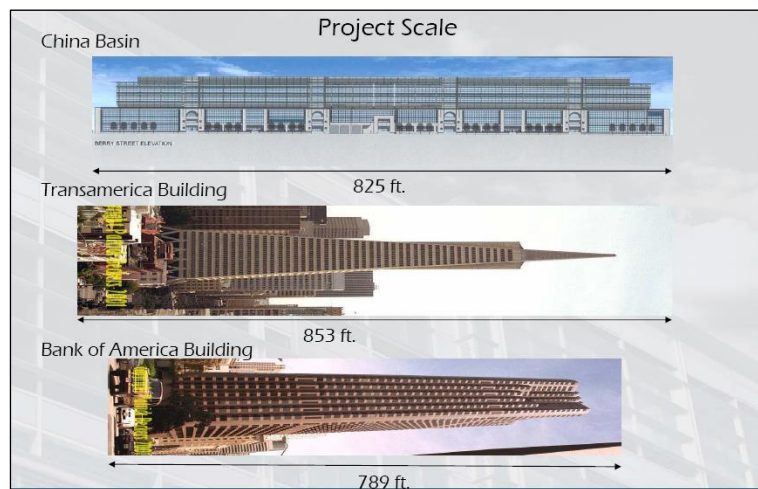


Fig. 3.54. Project scale: (a) China Basin, (b) Transamerica Building, (c) Bank of America Building

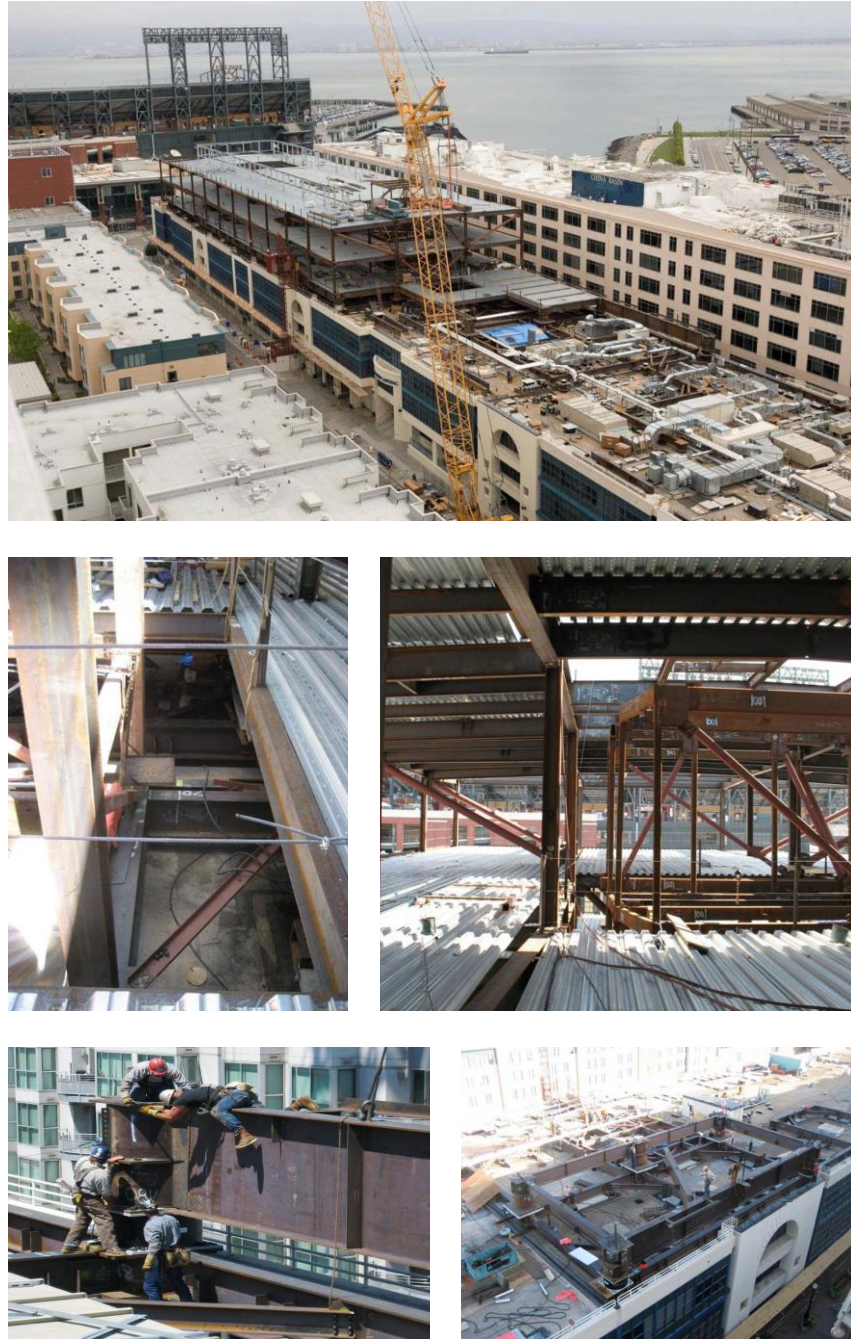


Fig. 3.55. (a) elevation under construction, (b) – (c) view of the seismic joints, (d) – (e) steel beam installation



The design of the isolation system was a real challenge because a relatively light superstructure had to be isolated and the isolators were required to be stable at a displacement of  $\pm 1.14$  m which was approximately 1.5 times the code required maximum displacement of  $\pm 76$  cm (average of seven maximum credible earthquakes).

For this reason, a system composed of 87 seismic isolators, including 33 lead rubber bearings (LRBs), and 54 sliders in series with an elastomeric bearing (EBs), was designed.

The number and location of the two devices were optimized to give the correct balance of stiffness and displacement demand in the isolated structure. The LRB's were placed along the exterior lines in order to maximize the torsional resistance while the ESB's were placed in the interior lines (Fig. 3.56).

The main dimensions of the LRBs are: 1156 mm diameter with 0.361 m of rubber and a 0.152 m lead core.

The elastomeric slider (ESB) consisted of a 1829 mm stainless steel sliding plate on top of a 0.61 m diameter elastomeric bearing with a 0.127 m lead core and a 0.305 m diameter PTFE sliding surface.

A detail of the LRB and the steel girders of the isolation layer is depicted in Fig. 3.57; a view of the isolator devices is provided in Fig. 3.58.

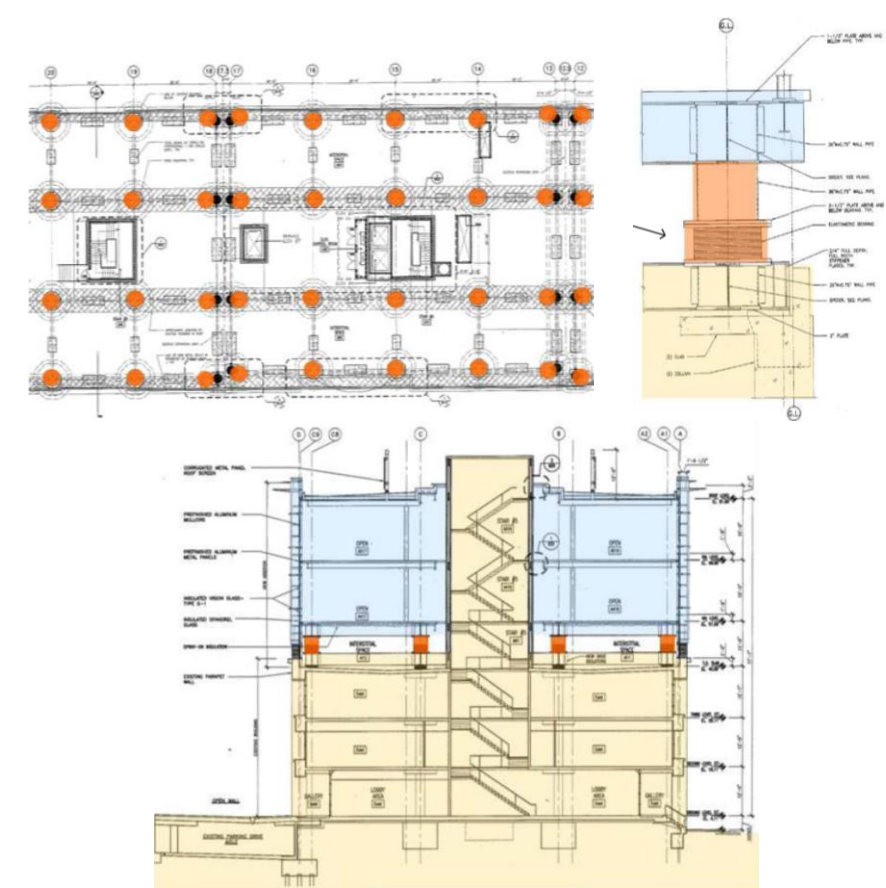


Fig. 3.56. (a) Seismic isolation plan, (b) detail of the elastomeric bearing, (c) Cross-section of the building

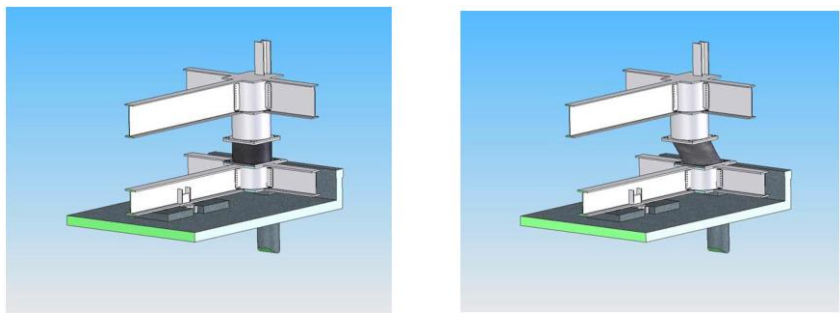
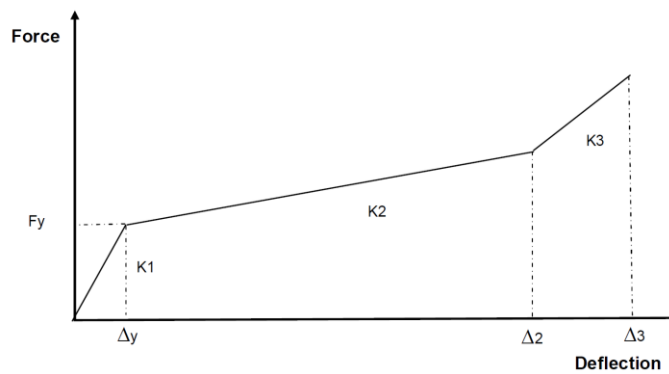


Fig. 3.57. Detail of the elastomeric bearing and the steel girder of the isolation system



Fig. 3.58. (a) rubber bearing, (b) elastomeric sliders

The isolation system is characterized by a tri-linear restoring force characteristic model, the isolation system design properties are shown in Fig. 3.59. An example of the results of the prototype test on the LRB and ESB are provided in Figs. 3.60 – 3.61, respectively.



Design Properties

Device	$F_y$ or $\mu$ [Kips]	$K_1$ [k/in]	$\Delta_y$ [in]	$K_2$ [k/in]	$\Delta_2$ [in]	$K_3$ [k/in]	$\Delta_3$ [in]	K beyond $\Delta_3$
LRB	36	70	0.51	7	35	10.5	44+/-	>0
Slider	0.1	22	$\mu D/22$	0	31.5	8	42	16-20 to 45"

Fig. 3.59. Isolation System Design Properties [Dutta et al. 2009]



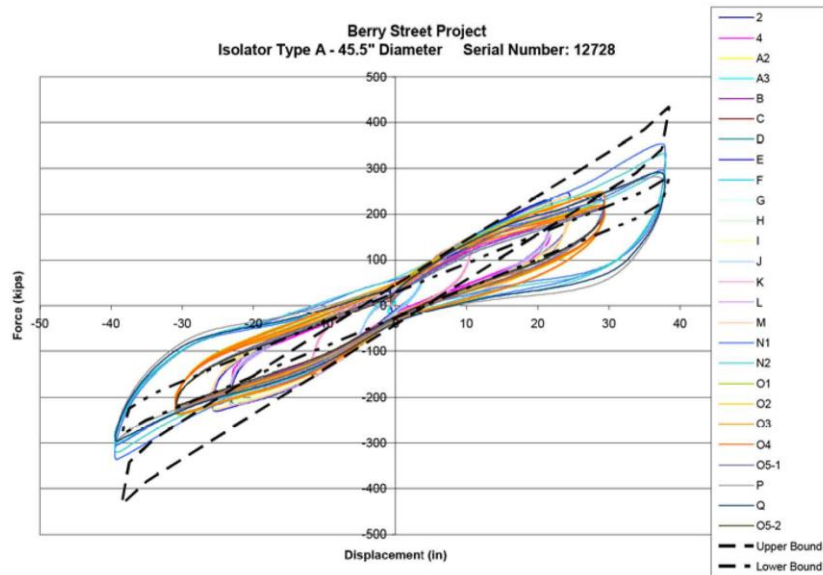


Fig. 3.60. Hysteresis Loops of the Lead Rubber Bearings [Dutta et al. 2009]

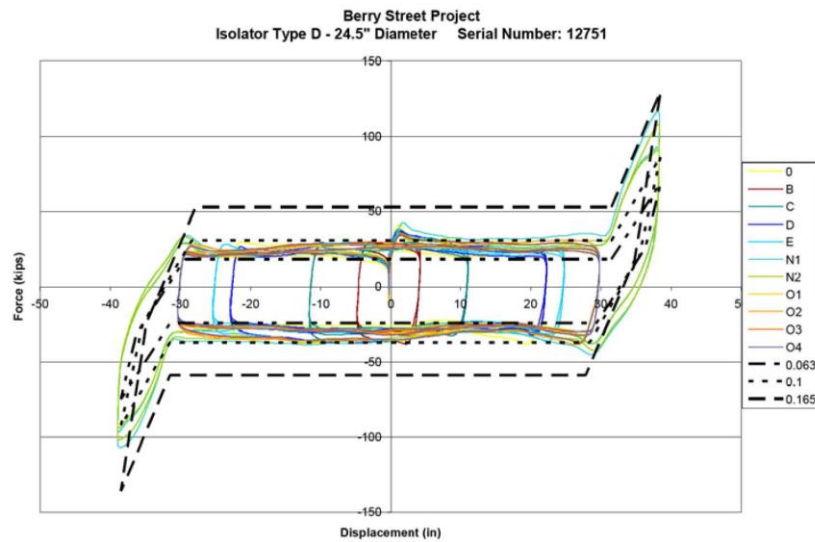


Fig. 3.61. Hysteresis Loops of the Elastomeric Sliders [Dutta et al. 2009]

### Three-dimensional analysis

SGH developed a highly detailed analytical model of the structure that represented the nonlinear characteristics of the existing structure, the seismic isolators, the new addition, and even the existing foundation piles

beneath the structure. Analyses were further complicated by the fact that the existing building is actually three separate structures, formed by the presence of two expansion joints located at approximately the 1/3 points of the 252 meters long structure. SGH modeled the structure so that the effects of pounding between the three separate structures could be explored. Eventually, SGH decided to place viscous dampers at the joints between the separate structures, to dissipate some of the energy transferred between the separate pieces as they collide, much as such devices are used to cushion the forces associated with berthing large ships at marine terminals.

A full three dimensional non linear model of the three wings was constructed in RAM Perform.

#### *Time history analysis*

SGH performed a sophisticated non linear time history analysis to justify that the base isolated addition was not detrimental to the existing structure.

Time history analysis were carried out under two different sets of 7 ground motions with two orthogonal components. The first set (Fig. 3.62 and Tab. 3.11), representative of the ground shaking at the ground surface, is scaled to a consensus MCE (Maximum Considered Earthquake) level spectrum developed by the geotechnical engineer of record with review by the Peer Review Panel. The second set was used for analyses of the structure considering the lateral flexibility of the piles. Lateral flexibility of the piles was determined by performing a nonlinear static analysis of a typical pile modeled using nonlinear beam and soil spring elements.

**Table 3.11. Ground Shaking Records Used to Develop Surface Motions [Dutta et al. 2009]**

<b>Earthquake</b>	<b>Record</b>
1940 Imperial Valley	El Centro
1995 Kobe	Amagasaki
1999 Kocaeli	Duzce
1992 Landers	Yermo
2002 Denali	Pump Station 10
1992 Landers	North Palm Springs
1987 Superstition Hills	Imperial County Center

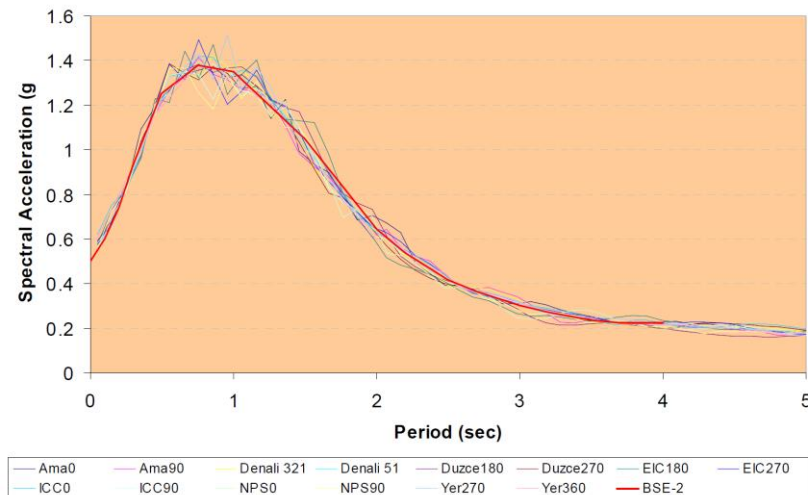


**Fig. 3.62. Spectra for suite of spectrally matched ground surface motions used in analyses [Dutta et al. 2009]**

#### *Reliability Analysis*

The peer review team requested to demonstrate that the building along with the addition possessed the necessary toughness of a code compliant structure. To prove that, the SGH performed a reliability analysis using the results from Incremental Dynamic Analyses (IDAs) in order to estimate a confidence level associated with the existing building's ability to resist global collapse at MCE level shaking.

In these analyses, the records previously used for the MCE analyses were progressively amplitude scaled up from 1.0 to a maximum multiplier of 2.2 on the MCE spectrum. The end point of most of the analyses was due to convergence failure caused by excessive deformation in one or a group of elements, suggesting occurrence of collapse. The amplitude scale increment was scaled immediately preceding that point as the collapse capacity of the structure for the particular record.

The scalar ground motion multiplier is depicted in Figs. 3.63 ÷ 3.65 as a function of the peak displacement at the center of the roof in the west, center, east x and y direction, respectively. From Figs. 3.63 ÷ 3.65 can be observed that the retrofitted structure was able to withstand motions up to a multiplier of 1.5 for all the curves except for Yermo record.

The maximum multiplier that did not produce any non-convergence for the Yermo record was 1.2. Based on this, it can be concluded that a global instability will ensue if the structure is subjected to approximately 1.5 times the MCE level ground motion, for most records.

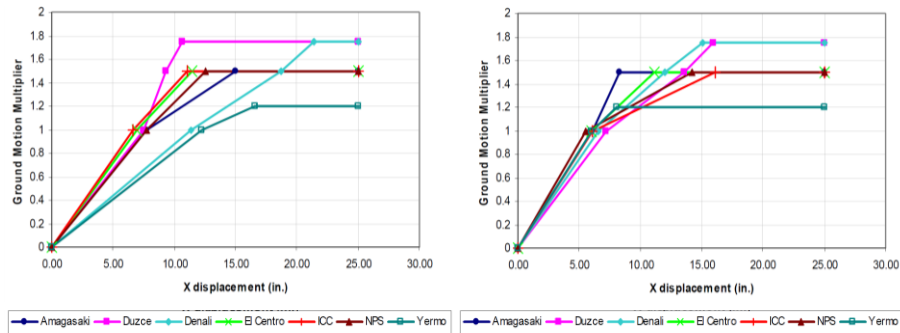


Fig. 3.63. Displacements of the IDA: (a) X-West, (b) Y-West [Dutta et al. 2009]

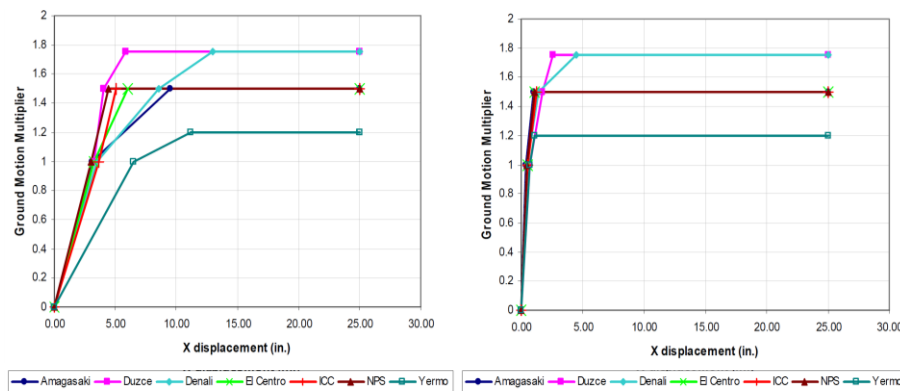


Fig. 3.64. Displacements of the IDA: (a) X-Center, (b) Y-Center [Dutta et al. 2009]

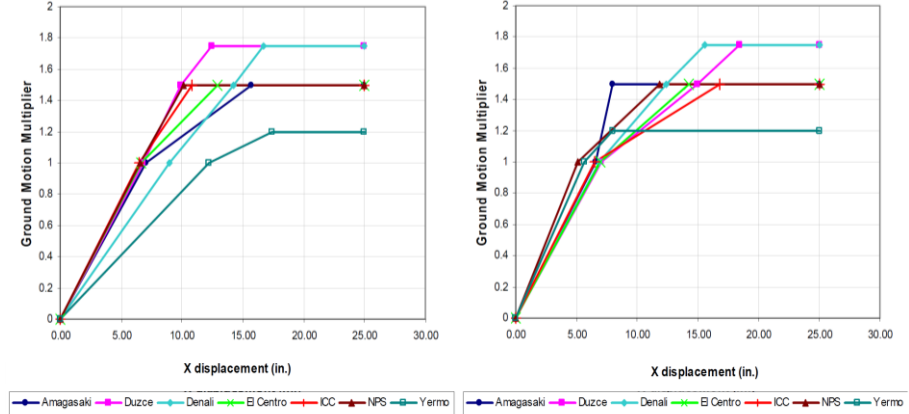


Fig. 3.65. Displacements of the IDA: (a) X-East, (b) Y-East [Dutta et al. 2009]

The results of the IDA are satisfactory and in conformance with the recommendations of FEMA 356 which requires that a pushover analysis be continued to 1.5 times the target displacement to capture any undesirable collapse modes that might be triggered in the vicinity of the expected response displacement.

Using the results of the IDAs, SGH determined the confidence level, as the reliability,  $R$ , as defined by Benjamin and Cornell and as further explained below.

The numerical formulation of the reliability  $R$  is obtained using the total probability theorem. Assuming that the displacement capacity for the structure is represented by the random variable  $C$  and the demand by random variable  $D$ , reliability  $R$  is given by the probability that the capacity is greater than the demand. Mathematically this can be written as:

$$R = 1 - P(C > D) \quad (3.1)$$

which for this project, is evaluated at the MCE ground shaking intensity level, using statistical distributions for the random variables  $C$  and  $D$ , respectively obtained from IDAs at MCE level shaking.

Assuming that the capacity  $C$  and the demand  $D$  are independent random variables, the probability of failure at a given displacement value  $\Delta$ ,  $P(C > D|\Delta)$ , can be calculated as the product of the conditional probability of the demand equaling displacement  $\Delta$ ,  $P(D = \Delta)$ , and the probability

that the structure's displacement capacity is less than  $\Delta$ ,  $P(C < \Delta)$ . Finally, the total reliability can be calculated by integrating Eq. (3.1) over the entire range of displacement values,  $\Delta$ . Therefore, formula (3.1) can be rewritten as:

$$R = 1 - \int_0^{\infty} P(D = \Delta) \cdot P(C < \Delta) d\Delta \quad (3.2)$$

The reliability of the existing building and the retrofitted building with the isolated addition is depicted in Fig. 3.66 in terms of the maximum displacements in West and East X and Y (WX, WY, EX, EY) directions. The histograms show that the base isolated addition has a higher reliability than the base structure without the addition. This clearly illustrates that the beneficial effect isolation has on the overall performance of the China Basin building.

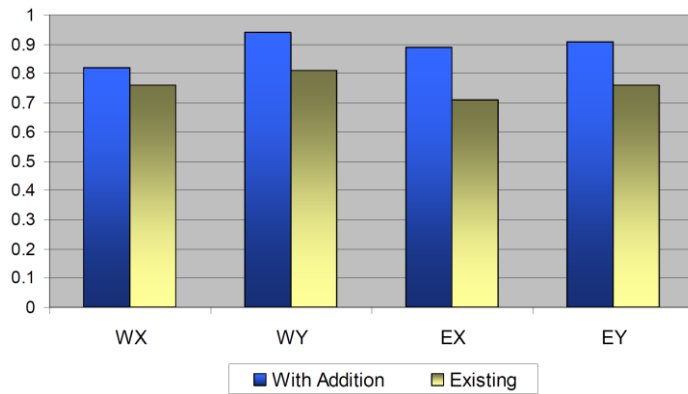


**Fig. 3.66. Comparison of Reliability of the Original and the Building with Isolated Addition**

### 3.3. OBSERVATIONS

The seismic database of more than 60 Japanese buildings equipped with IIS and realized starting from the late 90s, has demonstrate the growing confidence in the seismic performance achievable by this technique, representing a valid option for structural designers to ensure superior seismic performance to new buildings or in order to retrofit existing ones.

For this reason, the overview of the main real applications of IIS, both for new buildings and for vertical addition in the retrofit of existing buildings, is provided in this chapter.

In particular five IIS buildings, four new and one retrofitted, are selected for the representativeness of the wide applicability of mid-story isolation in the current design practice. In fact, typical and atypical configurations are examined; design solutions are provided to overcome particular issues related mainly to the flexibility of IIS structures both from architectural - functional and structural points of view.

In the chapter are also provided some differences between BIS and IIS structures.

Generally, in mid-story isolated structures are observed larger values than base isolated structures counterparts due to the interaction between upper and lower structures. In addition, the building as a whole is affected by higher mode vibrations, thus, the vibration characteristics of the building are governed not only by the stiffness of the isolation layer and the number of dampers, but also by the stiffness of the upper and the lower structures, and the weight ratio of the upper and lower structures. Moreover, the dynamic behavior of the structural depends not only on the location of the isolation layer, which defines the mass and stiffness ratios between superstructure and substructure, but also on the distribution of the mass and stiffness along the height of the building, which may affect the response of upper and lower structures and of the overall structure. It is a consequence of the architectural and functional flexibility of IIS.

From the exam of the buildings it is observed a typical case in which the upper structure is very stiff and shows a minor number of floors with respect to the lower structure.

In other atypical cases the upper structure is heavier and more flexible than the lower structure counterparts due to the larger number of floors with respect to the substructure and to a partial or almost total emptying of the lower structure. In this context, seismic performance has been ensured by creating ad hoc structural systems: a system of perimeter columns which cover the entire height of the lower structure, paying more attention to buckling; or giant truss to transfer the load from the upper structure to the perimeter lower structure through a mega-columns system. In addition, since in these cases the superstructure has many floors, the overturning moment due to horizontal loads could cause traction in isolators; thus, thanks to the transfer structure the isolators are

always under compression, and placing the isolators along the perimeter, the uplift force is minimized.

Moreover, a twin inter-story structure is considered; the designers carried out analyses to avoid resonance effects at the seismic isolation periods of the coupled buildings. A locking mechanism by means of oil dampers is implemented to reduce the displacement of the seismic isolation layer during strong winds. After completion of construction, the effectiveness of inter-story isolation was confirmed by measurements of the buildings carried out during earthquakes and wind.

Looking at the existing building, the vertical addition by means of inter-story isolation has demonstrate the feasibility and the effectiveness of IIS technique for retrofitting existing buildings.

The overview of the IIS applications has also shown the variety of approaches, both in the formulation of the problem and in the definition of the design objectives and parameters. The conceptual approaches of isolation, mass damping and energy dissipation are clearly identified.



## **4. LITERATURE OVERVIEW AND DISCUSSION**

### **4.1. DYNAMIC BEHAVIOR OF INTERMEDIATE ISOLATION SYSTEMS**

Shifting the position of the isolation system (ISO) from the base to a generic level of the building, the isolation interface divides the structure in two portions, an upper structure (US) and a lower structure (LS), respectively above and below the isolation layer.

The intermediate seismic isolation (IIS) combines the strategies of isolation and mass damping. In fact, the set of US and ISO can be seen analogous to a base isolation system (BIS) and as a mass damper (TMD) for the LS.

This statement derived from the comparison of the equations of motion of the simplified models of BIS, TMD and IIS reported in Chapter 2 (see Eqs. (2.6) - (2.7); (2.192) - (2.193); (2.245) ÷ (2.249)).

It is quite intuitive that the upper and lower structures not only can be studied separately, but also the interaction between the two portions can be considered, leading to two main problems: effect of the higher modes and energy dissipation.

Generally speaking, in IIS systems the first mode represents the mode of the isolation while the higher modes correspond to the modes of the isolated US and LS. If the US is sufficiently stiff with respect to the isolation system, the higher modes of the isolated US are negligible, since the combination of US + ISO behaves as a BIS. Instead, the higher modes of LS are effective since, no matter how flexible the isolation is, the dynamic of the LS cannot directly enjoy from this flexibility. In addition, the higher modes can be characterized by a higher fraction of participating mass. Therefore, since these modes show periods like that of a conventional fixed-base structure, the input energy of IIS and fixed-base structures can be comparable. Furthermore, the energy dissipation represents an important feature for the IIS effectiveness.

The peculiarities of IIS explain why the design approach for such systems is not well established and uniquely shared.

For these reasons, in the current scientific literature on this topic, it is possible to define three major conceptual approaches, each mainly focusing on one single aspect of the three ones related to IIS, namely: energy dissipation, isolation, mass damping.

With this purpose, in the present chapter the review of the main scientific contributions is presented focusing the attention on modeling approaches, problem formulation and identification of the governing design parameters, results of parametric analyses and design criteria derived from the analyses and tests. Then, the main analytical formulations for the three approaches are analyzed. Finally, the major outcomes and observations coming from the literature review and the relevant design implications are discussed.

## **4.2. MODELING OF INTERMEDIATE ISOLATION SYSTEM (IIS)**

In order to evaluate the effect of a mid-story isolation system on the dynamic behavior a multistory building, it is necessary that a complete model of the system accurately incorporates the details of the building and the isolation system properties.

Simplified lumped mass models and more refined three-dimensional (1D and 3D) models, accounting for the linear and/or non-linear restoring force characteristics of the isolation system, have been commonly adopted in literature.

Whereas multi-degree-of-freedom lumped-mass (1D-MDOF) models are adopted for a detailed guess of the dynamic behavior of IIS systems, two- and three- lumped-mass (1D-2DOF and 1D-3DOF) models are used to simply examine the impact of the design parameters, once established the correspondence between the reduced-order 2DOF or 3DOF and MDOF models. In fact, these simplified lumped-mass models can be very helpful in preparing and planning an initial design solution; then, the effectiveness of the design solutions can be finally evaluated by more refined 3D MDOF models.

1D-MDOF models are composed of all the degrees of freedom of the upper and lower portions, considered as standalone structures, and of the

isolation system. Many researchers adopt multi-lumped-mass model to grasp the global dynamic behavior of the mid-story buildings, paying more attention on the effect of the flexibility of the upper part of the isolated structure on the system response, and on the impact of the dynamic interaction between substructure and isolated superstructure.

1D-MDOF models are utilized by the following researchers, within widely differentiated scopes and with different research objectives.

[Murakami et al. 2000-2001, Sueoka et al. 2004, Tsuneki et al. 2008-2009] utilize MDOF models to describe the behavior of real new “flexible-stiff mixed-used” and retrofitted existing buildings; [Zhou et al. 2004, Hu et al. 2004] study the effectiveness of mid-story isolation as a retrofitting strategy in a real mixed-used public building. [Sadek et al. 1999] employ IIS technique for new and existing buildings and extend the method to the vibration control system proposed by [Feng & Mita 1995], the so-called “mega-sub configuration”, for tall buildings. With the aim of retrofitting existing buildings, [Villaverde 2002] studies an aseismic roof isolation system and [Chey et al. 2013] investigate the performance of “added stories” isolation system. [Moutinho 2012], [Matta & De Stefano 2007] and [Tian et al 2007] exploit a roof isolation system to reduce seismic vibration of the whole building. [Reggio & De Angelis 2015], [Ryan & Earl 2010] and [Champis et al. 2012] examine the effectiveness of inter-story isolation systems as a function of their location; in particular [Ryan & Earl 2010] and [Champis et al. 2012] include both single-story and every-story isolation. [Kobayashi et al. 2003, Kobayashi & Koh 2008] investigate on the effect of the dynamic interaction between upper and lower structures in intermediate isolated systems.

The 1D-2DOF models of IIS are often based on the premise that the isolated superstructure behaves as a rigid body under earthquake excitations. This assumption is considered accurate when the flexibility of the isolated portion is mainly concentrated at the isolation layer; and the upper structure is very rigid, both with respect to the isolation system and to the lower structure; consequently, the mass of the upper structure and isolation is characterized by one lumped mass supported by the isolator; the lower part of the structure below the isolation story is represented by another lumped mass.

For instance, [Villaverde 1985], [Murakami 2001, Murakami et al. 2001, Murakami & Sueoka], [Qi et al. 2006] and [Zhou et al. 2009] utilize the total masses of the lower part of the isolated structure as the bottom mass of the two-mass model; [Sadek et al. 1999], [Villaverde 2002], [Ping et al

2008-2016], [De Angelis et al. 2012], [Moutinho 2012], [Chey et al.2013] and [Reggio & De Angelis 2015] incorporate the modal characteristics of the lower part to determine the bottom mass.

It is worth noticing that, also the “dual isolation systems”, in which isolation layers are placed both at the base and at a mid-story, can be represented by a 2DOF model. In this case the two-lumped masses respectively correspond to the base and the mid-story isolation layer, thus, assuming that each isolated superstructure behaves as a rigid body. [Becker & Ezazi 2016].

In order to capture the effect of the flexibility of the upper structure on the response of base isolated buildings Kelly developed a 2DOF (the so-called “isolated single DOF”) where the isolation and the upper stories are modeled as two lumped-mass models [Kelly 1990]. Analogously, in a mid-story isolation system, the representation of the upper part flexibility leads to a 3DOF model.

Such three-lumped mass models are used by [Kobayashi & Koh 2008, Moriizumi & Kobayashi 2012] and [Wang et al. 2011, 2012a-b, 2013], to study the impact of modal interaction on the substructure and isolated superstructure response; in particular [Wang et al. 2011, 2012a, 2013] adopt 3DOF models to identify the range of lower and upper structure frequencies where modal interaction and coupling can adversely affect the performance of the isolation system; however, in [Kobayashi & Koh 2008, Moriizumi & Kobayashi 2012] and [Wang et al. 2011, 2012a, 2013] the mass of the upper and lower structure is equal to the corresponding reactive mass, in [Wang et al. 2012a] the concept of generalized mass is adopted for the modal definition.

### **4.3. PARAMETRIC ANALYSES**

In the existing literature on IIS parametric analyses have been carried out by varying:

- the location of the isolation system, having fixed mass and stiffness distributions and the damping ratios of the structural portions [Ping et al. 2008, Zhou et al. 2016, Wang et al. 2013, Reggio & De Angelis 2015];

- the mass and stiffness distributions in the upper and lower structures, having fixed the damping ratios of the structural portions and the location of the isolation system [Chey et al. 2013];
- the location of the isolation system and the mass and stiffness distributions, having fixed the damping ratios of the structural portions [Zhou et al. 2016, Wang et al. 2012a, Kobayashi & Koh 2008, Ryan & Earl 2012];
- the damping ratios of upper and lower structures, having fixed mass and stiffness distributions of the structural portions and the location of the isolation system [Reggio & De Angelis 2015].

#### 4.3.1. Design parameters

The design parameters governing the dynamic behavior of intermediate isolation system are:

- mass ratios;
- frequency ratios;
- nominal isolation period;
- nominal period of the structural portion;
- damping of the isolation system;
- damping ratios of the structural portions;
- ratio of the damper yield force to total above-ground mass.

Some of those parameters are specifically addressed for exploiting either the isolation effect or the mass damper effect; others can be used for both purposes.

In the following the design parameters are expressed according to the notation used in the present work.

In terms of mass, the following parameters have been used:

- the ratios of masses of the upper and lower structure to the isolation mass  $r_{US} = m_{US} / m_{ISO}$  and  $r_{LS} = m_{LS} / m_{ISO}$  [Wang et al. 2011, 2012a, 2013];
- the ratio between the masses of the upper and lower structures, i.e.  $m_{US} / m_{LS}$  [Wang et al. 2011, 2012a, 2013; Kobayashi & Koh 2008; Ryan & Earl 2010];

- the ratio between the total isolated mass, equal to the mass of the upper structure and isolation system, and the lower mass, i.e.  $\alpha = (m_{US} + m_{ISO}) / m_{LS}$  [Ping et al. 2008, Zhou et al. 2016, Kobayashi & Koh 2008, Sadek et al. 1997, Chey et al. 2013, De Angelis et al. 2012, Reggio & De Angelis 2015];
- the ratio between the total isolated mass and the total mass, i.e.  $R_m = (m_{US} + m_{ISO}) / M_{tot}$  [Murakami et al. 2000, Sueoka et al. 2004, Tsuneki et al. 2008-2009].

In terms of frequency, the following parameters have been used:

- the ratio between the frequencies of the upper or lower structure and the isolation system, i.e.  $\omega_{US} / \omega_{ISO}$  and  $\omega_{LS} / \omega_{ISO}$ , for exploiting the isolation effect [Wang et al. 2011, 2012a, 2013];
- the ratio between the frequencies of the isolation system and the lower structure, i.e.  $f = \omega_{ISO} / \omega_{LS}$ , for exploiting the mass damper effect [Ping et al. 2008, Zhou et al. 2016, Sadek et al. 1997, Chey et al. 2013, De Angelis et al. 2012, Reggio & De Angelis 2015].

The nominal isolation period,  $T_{ISO}$ , has been used by [Wang et al. 2011, 2012a, 2013; Kobayashi & Koh 2008; Ryan & Earl 2010], the nominal period of the substructure,  $T_{LS}$ , has been adopted by [Kobayashi & Koh 2008] and the nominal period of the superstructure,  $T_{US}$ , has been assumed by [Ryan & Earl 2010].

The damping ratio of the isolation system,  $\xi_{ISO}$ , and of the substructure,  $\xi_{LS}$ , have been used by [Ping et al. 2008; Zhou et al. 2016; Wang et al. 2011, 2012a, 2013; Kobayashi & Koh 2008; Ryan & Earl 2010; Sadek et al. 1997; Chey et al. 2013; De Angelis et al. 2012; Reggio & De Angelis 2015], and the damping ratio of the of the superstructure,  $\xi_{US}$ , has been assumed by [Wang et al. 2011, 2012a, 2013; Kobayashi & Koh 2008; Ryan & Earl 2010; Chey et al. 2013; Reggio & De Angelis 2015].

The ratio of the damper yield force to total above-ground mass,  $\alpha'_s$ , has been adopted by [Murakami et al. 2000, Sueoka et al. 2004, Tsuneki et al. 2008-2009].

The ranges of values adopted for the design parameters defined above by the authors of the major papers on IIS are reported in Tab. 4.1; in addition,

the value assumed for each conceptual approach are reported and discussed in §4.5.

**Table 4.1. Values adopted for the design parameters**

Design Parameters	Total range of values	Range of values		
		IS	MD	ED
$r_{US}$	$0 \div 15$	$0 \div 15$		
$r_{LS}$	$0 \div 12$	$0 \div 12$		
$m_{US} / m_{LS}$	$0 \div 5$	$0 \div 5$		
$\alpha$	$0 \div 10$	$0.2 \div 6$	$0 \div 10$	
$R_m$	$0.1 \div 1$	$0.2 \div 1$		$0.1 \div 0.8$
$\omega_{US} / \omega_{ISO}$	$3 \div 40$	$3 \div 40$		
$\omega_{LS} / \omega_{ISO}$	$3 \div 40$	$3 \div 40$		
$f$	$0 \div 10$	$0.025 \div 0.3$	$0 \div 10$	
$\xi_{ISO}$	$0 \div 1$	$0 \div 0.7$	$0 \div 1$	
$\xi_{US}$	$0.02 \div 0.05$	$0.02$		
$\xi_{LS}$	$0 \div 0.05$	$0.02$	$0 \div 0.05$	
$T_{ISO}$	$1 \div 4$	$1 \div 4$		
$T_{US}$	$0.05 \div 0.7$	$0.05 \div 0.7$		
$T_{LS}$	$0.05 \div 0.7$	$0.05 \div 0.7$		
$\alpha_s$	$0.005 \div 0.08$			$0.005 \div 0.08$

IS = Isolation, MD = Mass Damping, ED = Energy Dissipation

Although those parameters spread in a wide range, the analyses carried out for each approach are more restricted and, however, characterized by some variability.

In order to provide an overall picture for understanding the dynamics of IIS structures, a preliminary discussion on the design parameters adopted is provided. In Tab. 4.1, starting from the values assumed for each approach, the values derived for the other control strategies are marked in italics.

For what concerns the *isolation approach*, the major parameters considered are the mass ratios  $r_{US}$ ,  $r_{LS}$ ,  $m_{US} / m_{LS}$ ; the frequency ratios  $\omega_{US} / \omega_{ISO}$  and  $\omega_{LS} / \omega_{ISO}$ ; the damping ratios  $\xi_{ISO}$ ,  $\xi_{LS}$ ,  $\xi_{US}$ ; the nominal periods  $T_{ISO}$ ,  $T_{LS}$ ,  $T_{US}$ . Considering the *mass damping approach*, the major parameters considered are the mass ratio  $\alpha$ ; the frequency ratio  $f$ ; the damping ratios

$\xi_{ISO}$  and  $\xi_{LS}$ . In terms of the *energy dissipation approach*, the major parameters considered are the mass ratio  $R_m$  and the shear coefficient of the dampers  $\alpha_s'$ .

In all the control strategies the range of values in terms of mass ratios are more extended for exploring, from a theoretical point of view, all the possibilities. However, in practice these values are more restricted.

In general, increasing the values of  $r_{US}$ ,  $r_{LS}$ ,  $m_{US} / m_{LS}$ ,  $\alpha$  and  $R_m$  the level of the isolation layer moves from the top to base of the building. In addition, these values can represent a different mass distribution of the upper and lower structures. For example, one structural portion could be characterized by more stories and a great emptying for architectural needs.

The nominal periods, explicitly addressed in the isolation approach, represent in a synthetic way the ratio of the mass and stiffness of the single portion or, in addition, the interaction between different mass and stiffness distributions. In fact, the same value can correspond to a portion more flexible and lighter or stiff and heavy in equal measure, or even different their combinations.

The frequency ratios  $\omega_{US} / \omega_{ISO}$  and  $\omega_{LS} / \omega_{ISO}$  are assumed as design parameters in the isolation approach. The structural frequencies are chosen such that the isolation represents a flexible interface with respect to both upper and lower structures.

The frequency ratio  $f$ , addressed in the mass damping approach, is the inverse of the ratio  $\omega_{LS} / \omega_{ISO}$ . Lower values of  $f$  lead to a rigid LS with respect to the isolation layer; larger values of  $f$  represent a quite rigid or flexible LS with respect to the isolation. It is worth noting that, while the LS can be more flexible than the isolation system, if this happens for the US, the combination of US + ISO does not behave as a BIS and the overall behavior of the IIS changes, leading to a fixed-based isolated structure.

The damping ratios are greater for the mass damping approach. In general, the damping ratio of the structural portions can be neglected, since it is small compared to that of the isolation. This leads to a reduced computational complexity. However, since the damping ratio of the structural portions is lower than the one of the isolation, the system is characterized by non-proportional damping. For this reason, the assumption of proportional damping commonly adopted in design practice could not be adequate to grasp the behavior of IIS systems.

The shear coefficient of the dampers  $\alpha_s'$  is utilized in the energy dissipation approach by the Japanese school of researchers. It represents



the shear distribution at the isolation layer of the dampers normalized with respect to the weight of the building. Increasing the ratio  $\alpha_s$ , the energy dissipated by the isolation system increases; however, excessive values of the shear coefficient does not lead to a significant improvement in the response of the building.

#### **4.3.2. Design criteria and relevant response parameters**

The main design criteria implemented for reducing the response in mid-story isolated structure consist in:

- minimizing the base shear force [Ping et al 2008, Zhou et al 2016, Wang et al. 2011, 2012a, 2013; Kobayashi & Koh 2008; Ryan & Earl 2010];
- minimizing the displacements of the upper structure, lower structure, or both upper and lower structures [Wang et al. 2011, 2012a, 2013; Kobayashi & Koh 2008; De Angelis et al. 2012];
- equalizing both damping ratios and frequencies of the main structure and TMD in the complex mode of vibrations [Sadek et al. 1997, Chey et al. 2013];
- maximizing the energy dissipated by the isolation system [Murakami et al. 2000, Sueoka et al. 2004, Tsuneki et al. 2008-2009, Reggio & De Angelis 2014, 2015].

In order to achieve the effectiveness of such systems, some indices which represent the response of the controlled structure normalized with respect to the uncontrolled configuration were defined, expressed in terms of:

- the displacement of the main structure;
- the relative displacement between the structure and the device mass;
- the absolute acceleration of both the main system and the TMD.

#### 4.4. OVERVIEW OF THE MAJOR PAPERS ON INTERMEDIATE ISOLATION SYSTEMS

The overview of the main papers on IIS related to the three major conceptual approaches, i.e. isolation, mass damping and energy dissipation, is provided in the following.

##### 4.4.1. Threefold approach (energy dissipation, isolation, mass damping)

The papers by [Ping et al 2008] and [Zhou et al 2016] provide an overview of the optimal design parameters covering the range of all the three design approaches; in addition, this range of values of the threefold approach is shown in Tab. 4.2.

[Ping et al. 2008] consider a 2DOF reduced-order model, and employ an optimization procedure based on the minimization of the base shear variance assuming earthquake excitation as a stationary stochastic process with zero mean. The optimal design parameters are the frequency ratio  $f$  and the damping ratio  $\xi_{iso}$ . The ratios  $f$  and  $\xi_{iso}$  respectively vary in the interval  $0.05 \div 1$  and  $0 \div 0.7$ , by varying the mass ratios  $\alpha$  in the range of  $0.01 \div 10$ . It is worth noticing that the lower limit of the frequency ratio  $f$  is selected to avoid excessive drift of the isolation layer, as a design “rule”, while the upper value corresponds to the fact that the optimum frequency ratio is usually less than 1; the lower and upper limits of the mass ratio  $\alpha$  respectively correspond to conventional TMD ( $\alpha = 0.1$ ) and BIS ( $\alpha = 10$ ) systems; the upper limit of the damping ratio  $\xi_{iso}$  refers to technical considerations. [Ping et al. 2008] show that increasing the mass ratio, the optimal frequency ratio  $f_{opt}$  decreases while the corresponding damping ratio  $\xi_{iso,opt}$  increases. The optimal parameters  $f_{opt}$  and  $\xi_{iso,opt}$  vary in the following ranges, respectively: for the tuning zone, in which  $\alpha$  is less than 1, they are  $0.5 \div 0.9$  and  $0.1 \div 0.3$ ; for mid-story isolation zone, in which  $\alpha$  is between 1 and 4, they are  $0.05 \div 0.5$  and  $0.3 \div 0.7$ ; for base isolation zone, in which  $\alpha$  is greater than 4, they are 0.05 and  $0.5 \div 0.7$  (Figs. 4.1  $\div$  4.3).

Therefore, it exists an optimal damping ratio of the isolation layer in the tuning frequency zone and the base isolation zone; however, in the mid-story isolation zone whose control mechanism is isolation and energy

dissipation, the higher damping level results in a better control performance.

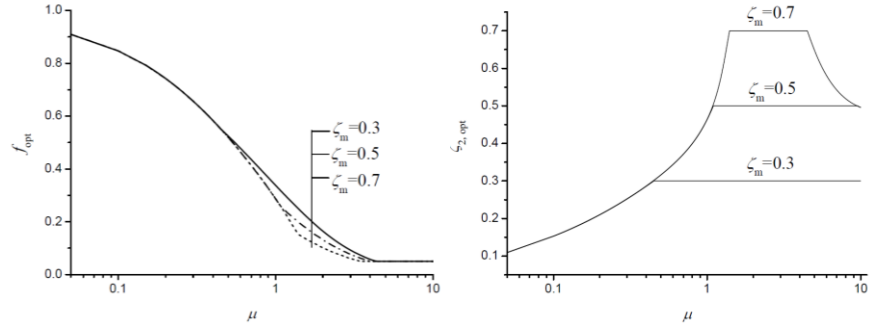


**Fig. 4.1. Optimal design parameters: (a) optimal frequency ratio vs. mass ratio (b) optimal damping ratio vs. mass ratio**  
[Ping et al. 2008]

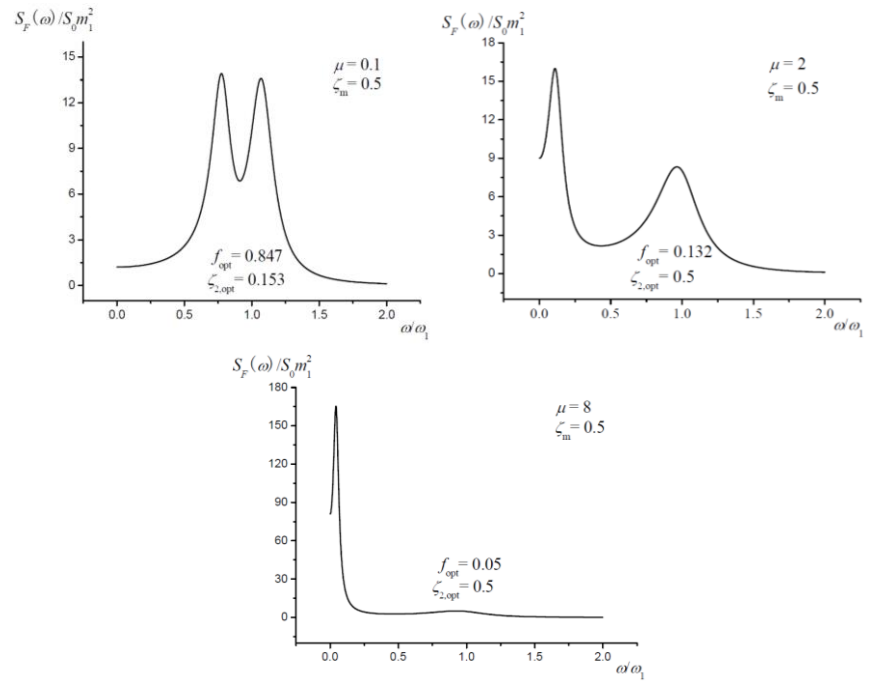


**Fig. 4.2. Power spectral density function of base shear for optimal design parameters: (a)  $\alpha = 0.1$ , (b)  $\alpha = 2$ , (c)  $\alpha = 8$**   
[Ping et al. 2008]

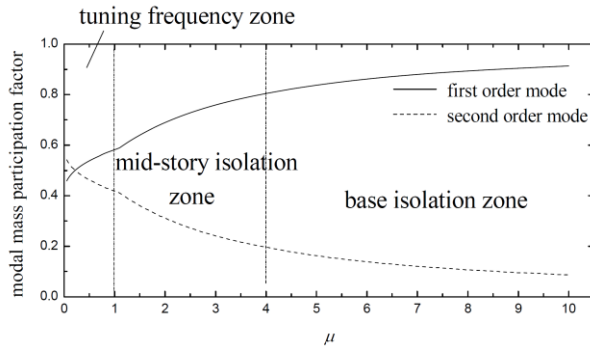


**Fig. 4.3. modal mass participation factor vs. mass ratio [Ping et al. 2008]**

[Zhou et al. 2016] utilize a mode synthesis-based approach to define a 2DOF reduced-order model which accurately described the complete structure behavior.

The authors define an optimization criterion which consists in minimizing the total base shear thanks to the mid-story isolators to limit the complexity of optimization. In particular, two base shear-based performance objectives are considered for deriving the optimal isolation parameters (frequency ratio  $f$  and damping ratio  $\xi_{\text{ISO}}$ ): the maximum base shear for any harmonic excitation, and the variance of the base shear for a band limited white noise (representing the excitations with energies in a range of frequencies). The behavior of the isolation system is assumed linear.

Since the damping in the main structure is relatively small compared to the isolation system, the damping of the original structure is ignored in order to simplify analytical formulation. Zhou et al. suggested that this assumption was, however, not expected to produce highly suboptimal isolators.

Varying the mass ratio  $\alpha$  between  $0 \div 10$ , the design parameters frequency ratio  $f$  and damping ratio  $\xi_{\text{ISO}}$  were varied in the range  $0.05 \div 1$  and  $0 \div 0.5$ , respectively. The lower and upper limits of the mass ratio were respectively chosen to represent conventional TMD and BIS systems; the upper and lower limits of the frequency ratio were respectively selected to prevent large story drift of isolators and to consider that optimum frequency ratio is usually less than 1; the upper limit of the damping ratio was selected for technical considerations, in fact, in order to increase the damping, additional damping devices are necessary.

It is worth noticing that the optimization criterion and the range of interest of the design parameters used by Zhou et al. are remarkably similar to the ones used by Ping. et al.

Similar values for the optimal isolation parameters were provided for both the base shear-based performance objectives.

Zhou et al. find that increasing the mass ratio, the optimal frequency ratio  $f_{opt}$  decreases while the corresponding damping ratio  $\xi_{ISO,opt}$  increases. The optimal parameters  $f_{opt}$  and  $\xi_{ISO,opt}$  were varied in the following ranges, respectively: for the tuning zone, in which  $\alpha$  is less than 1, they were  $0.3 \div 1$  and  $0.1 \div 0.5$ ; for mid-story isolation zone, in which  $\alpha$  is between 1 and 6, they were  $0.05 \div 0.3$  and 0.5; for base isolation zone, in which  $\alpha$  is greater than 6, they are 0.05 and 0.5, Fig. 4.4. Thus, for mass ratios larger than 1 the damping ratio is always 0.5.

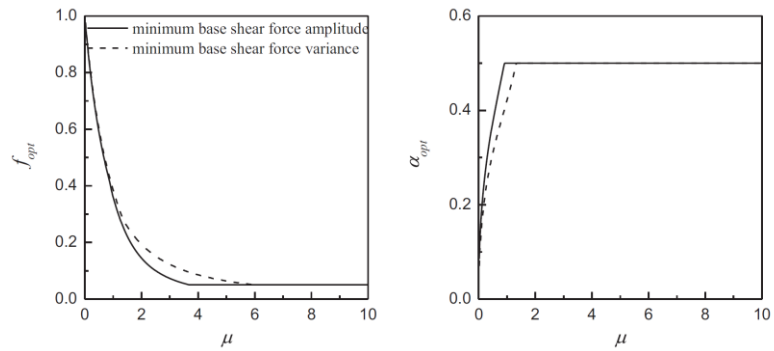


**Fig. 4.4. Optimal design parameters, minimum base shear amplitude vs. minimum base shear variance: (a) frequency ratio vs. mass ratio, (b) damping ratio vs. mass ratio [Zhou et al. 2016]**

The methods of Zhou et al. and Ping et al. are comparable; however, increasing the mass ratio, the different upper bound for the optimal damping ratio provides quite different optimal parameters.

The optimization procedure based on the minimization of the base shear variance was implemented by Zhou et al. in two buildings very different from each other.

The first building is an ideal 16-story building modeled as shear structure with uniform mass and stiffness distributions; 16DOF IIS models are developed changing the placement of the isolation level at every story from the 2<sup>nd</sup> to the 16<sup>th</sup> level. The second building, “likely to be encountered in an urban setting”, is a 11-story building composed of two

underground floors and nine floors above ground; different mass and stiffness characteristics are chosen and the isolation system is placed at the first level above ground.

In both buildings, viscous dampers are included in each story to introduce a damping ratio equal to 0.05.

Re-arranging the floor mass values of both the buildings, the range of the mass ratios and a comparison between the mass of the structural portion and of the overall structure are reported in the following.

For the first 16-story building the mass values and ratios for the extreme placement of the isolation level, i.e. the 16<sup>th</sup> and 2<sup>nd</sup> floors, are:

$m_{US} = 0 \div 14000$  kg,  $m_{ISO} = 1000$  kg,  $m_{LS} = 15000 \div 0$  kg,  $M_{tot} = 16000$  kg,  $r_{US} = 0 \div 14$ ,  $r_{LS} = 15 \div 1$ ,  $m_{US} / m_{LS} = 0 \div 14$ ,  $\alpha = 0.07 \div 15$ ,  $R_m = 0.06 \div 0.94$ .

For the second 11-story building the mass values and ratios are:

$m_{US} = 9037.9$  kg,  $m_{ISO} = 960.1$  kg,  $m_{LS} = 15673.5$  kg,  $M_{tot} = 25671.5$  kg,  $r_{US} = 9.4$ ,  $r_{LS} = 16.3$ ,  $m_{US} / m_{LS} = 0.58$ ,  $\alpha = 0.64$ ,  $R_m = 0.4$ .

In order to assess the effectiveness of mid-story isolated structure, performance indices, which represent the rms response of the controlled structure normalized with respect to the uncontrolled configuration, are defined in terms of base shear and roof accelerations.

Under El Centro motion, in the 16MDOF IIS models the ratio of the base shear varies in the range  $0.2 \div 0.6$  and increases by increasing the location of the isolation system; the ratio of the roof acceleration varies in the range  $0.2 \div 1.2$  and increases by increasing the location of the isolation system, being larger than 1 only for the roof isolation system. Considering the same input wave, in the 11DOF IIS model, the ratio of the base shear is equal to 0.524 while the ratio of the roof acceleration is equal to 0.360.

Comparing the values of the indices derived in 11DOF IIS model and in 16DOF models, the following consideration can be done: in terms of base shear, the same values are obtained placing the isolation system between 15<sup>th</sup> and 16<sup>th</sup> levels; in terms of roof acceleration, the same values are obtained placing the isolation system between 12<sup>th</sup> and 13<sup>th</sup> levels; considering the same placement of the isolation layer, the 11DOF IIS model shows higher values; considering the same mass ratios of 11DOF IIS model, the isolation system should be placed between the 11<sup>th</sup> and 12<sup>th</sup> levels.

From the contributions of Ping et al. and Zhou et al. emerge that moving the isolation layer from the roof to the bottom of the structure, the control

mechanism changes going from tuning frequency, isolation and energy dissipation to base isolation. In addition, the performance of both lower and isolated upper structures depends not only on the location of the isolation layer, which defines the mass and stiffness ratios between the upper and lower structures, but also on the distribution of the mass and stiffness along the height of the building, which may affect the response of these structural portions and of the overall structure.

**Table 4.2. Threefold approach: mass damping, energy dissipation and isolation**

Design Parameters	Ping et al. 2008			Zhou et al. 2016		
	MD	IIS	BIS	MD	IIS	BIS
$\alpha$	$0 \div 1$	$1 \div 4$	$4 \div 10$	$0 \div 1$	$1 \div 6$	$6 \div 10$
$\xi_{LS}$	0.05	0.05	0.05	0	0	0
$f$	$0.05 \div 1$	$0.05 \div 1$	$0.05 \div 1$	$0.05 \div 1$	$0.05 \div 1$	$0.05 \div 1$
$\xi_{ISO}$	$0 \div 0.7$	$0 \div 0.7$	$0 \div 0.7$	$0 \div 0.5$	$0 \div 0.5$	$0 \div 0.5$
$f_{opt}$	$0.3 \div 0.9$	$0.05 \div 0.3$	0.05	$0.3 \div 1$	$0.05 \div 0.3$	0.05
$\xi_{ISO,opt}$	$0.1 \div 0.3$	$0.3 \div 0.7$	$0.5 \div 0.7$	$0.1 \div 0.5$	0.5	0.5

MD = Mass Damping, IIS = Intermediate Isolation System, BIS = Base Isolation System

#### 4.4.2. Isolation Approach [Wang et al. 2011, 2012, 2013; Kobayashi & Koh 2008; Ryan & Earl 2010]

Along this direction, the conceptual approach of the isolation provides precious insights into the overall dynamic behavior of mid-story isolated structures, and the impact of the dynamic interaction between substructure and isolated superstructure, the effect of the flexibility of the upper isolated structure, the influence of the higher modes, the effect of coupling of the higher modes on the seismic performance of structural portions.

In this framework, some major contributions are provided by [Wang et al. 2011, 2012, 2013], [Kobayashi & Koh 2008], [Ryan & Earl 2010]; in addition, the range of values of the isolation approach is shown in Tabs. 4.3 – 4.4; in the tables the values of the design parameters derived starting from the data in each paper are marked in italics.

In particular [Wang et al. 2011, Kobayashi & Koh 2008] investigate the dynamic behavior of mid-story isolated structures, describing the main theoretical results of analyses carried out on 3DOF models, that simply suggest the impact of the major design parameters; thereafter, on the basis of the theoretical formulation of the problem, the results of two experimental campaigns are proposed [Wang et al. 2012, Wang. et al. 2013]; then, the study is extended to MDOF models which are more able to describe the interaction of the structural portions [Kobayashi & Koh 2008, Ryan & Earl 2010].

**Table 4.3. Isolation approach – Wang et al.**

Design Parameters	Wang et al.			TOT.
	2011	2012	2013	
$r_{US}$	5	2.4	4.7	$2.4 \div 5$
$r_{LS}$	1,-,2	1.2,-,2.4	1.7	$1 \div 2.4$
$m_{US} / m_{LS}$	2.5,-,5	1,-,2	2.8	$1 \div 5$
$\alpha$		1.42,-,2.83	5.7	$1.42 \div 5.7$
$R_m$		0.59,-,0.74,-,1	0.77	$0.59 \div 1$
$k_{US} / k_{LS}$	$0.1 \div 5^*$	0.25,-,0.87	0.098,-,0.5	$0.1 \div 5$
$k_{US} / k_{ISO}$		34.59	8.97	$9 \div 35$
$k_{LS} / k_{ISO}$		39.71,-,141.35	17.89,-,92.14	$18 \div 141$
$T_{ISO}$ [s]	2	2	1	$1 \div 2$
$T_{US}$ [s]	$0.05 \div 0.67$	0.29	0.30	$0.05 \div 0.67$
$T_{LS}$ [s]	$0.05 \div 0.67$	0.1,-,0.27	0.056,-,0.13	$0.05 \div 0.67$
$\omega_{US} / \omega_{ISO}$	$3 \div 40$	7	3.3	$3 \div 40$
$\omega_{LS} / \omega_{ISO}$	$3 \div 40$	7.5,-,20	7.8,-,17.7	$3 \div 40$
$f$	$0.025 \div 0.33$	$0.05 \div 0.13$	$0.056 \div 0.13$	$0.025 \div 0.33$
$\xi_{ISO}$	0.2	0.2	0.2	0.2
$\xi_{US}$	0.02	0.02	0.02	0.02
$\xi_{LS}$	0.02	0.02	0.02	0.02

\*practical range



Table 4.4. Isolation approach – Kobayashi &amp; Koh, Ryan &amp; Earl

Design Parameters	Kobayashi & Koh 2008			Ryan & Earl 2010
	3DOF	MDOF	TOT.	
$r_{US}$		$3 \div 15$	$3 \div 15$	$0 \div 4.54$
$r_{LS}$		$0 \div 12$	$0 \div 12$	$0 \div 4.54$
$m_{US} / m_{LS}$		$0.25 \div 2.75$	$0.25 \div 2.75$	$0 \div 4$
$\alpha$	0.5,-,1,-,3	$0.33 \div 3$	$0.33 \div 3$	$0.22 \div 5.1$
$R_m$		$0.25 \div 1$	$0.25 \div 1$	$0.18 \div 1$
$k_{US} / k_{LS}$				
$k_{US} / k_{ISO}$		100	100	
$k_{LS} / k_{ISO}$	21.33,-,64,-,13	100	21.33÷ 128	
$T_{ISO}$ [s]	4	$2.5 \div 3.4$	$2.5 \div 4$	2.5
$T_{US}$ [s]				0.5
$T_{LS}$ [s]	0.5		0.5	
$\omega_{US} / \omega_{ISO}$				5
$\omega_{LS} / \omega_{ISO}$	8		8	
$f$	0.13		0.13	0.2
$\xi_{ISO}$	0.2	0.2	0.2	0
$\xi_{US}$	0.02	0.02	0.02	0.02
$\xi_{LS}$	0.02	0.02	0.02	0.02

#### 4.4.2.1. Parametric analyses by Wang et al. [2011, 2012, 2013]

The papers by [Wang et al. 2011, 2012, 2013] propose a simplified analyses of mid-story isolated structures by means of 3DOF models, composed by LS, ISO and US. The authors identify the parameters governing the dynamic response of the structure and the mode coupling effect, namely: the ratios of masses of the upper and lower structure to the isolation mass  $r_{US} = m_{US}/m_{ISO}$  and  $r_{LS} = m_{LS}/m_{ISO}$ ; and the ratios of the frequency of the upper and lower structure to the isolation frequency, i.e.  $\omega_{US}/\omega_{ISO}$  and  $\omega_{LS}/\omega_{ISO}$ .

The mass ratios considered in the analysis always correspond to the case of superstructure heavier than the substructure; further, the frequency ratios are defined by a lower bound equal to 3, which ensures an isolation period at least three times the US period (according to the rule commonly adopted for base isolated structures), and an upper bound, equal to 40, that corresponds to very stiff LS and US.

Starting from the above design parameters, the ratio of the dynamic stiffness of the US and LS, i.e.  $k_{US}/k_{LS}$ , can be derived considering that:

$k_{US} = \omega_{US}^2 m_{US}$  and  $k_{LS} = \omega_{LS}^2 m_{LS}$ ; the ratio  $r_{US}/r_{LS}$  varies between 2.5 and 5; the frequency ratios vary between 3 and 40. The range of the stiffness ratios between the US and LS are:  $k_{US}/k_{LS} = [(3 \div 40)/(3 \div 40)]^2 \cdot 2.5$  and  $k_{US}/k_{LS} = [(3 \div 40)/(3 \div 40)]^2 \cdot 5$ .

Considering the possible combinations between minimum and maximum values, the ranges of the stiffness ratio  $k_{US}/k_{LS}$  are  $0.014 \div 444$  and  $0.028 \div 889$ ; however, a more restricted practical range of  $0.1 \div 5$  seems to be adequate in order to take into account more stiff or flexible US than LS.

#### **4.4.2.2. Modal Coupling Effect – MCE [Wang et al. 2011, 2012, 2013]**

Considering the range of the design parameters described above, and in particular  $\omega_{US}/\omega_{ISO}$  and  $\omega_{LS}/\omega_{ISO}$ , [Wang et al. 2011, 2012, 2013] have investigated the effect of the higher modes on the dynamic behavior of a mid-story isolated structures.

Basically, it is recognized that the dynamics of structures with mid-story isolation is affected by the vibration characteristics of the US and LS, and that, depending on these characteristics, two different scenarios for the dynamic behavior of the global structure are found: a major influence of one of the higher modes (either the 2<sup>nd</sup> or the 3<sup>rd</sup> mode), or a coupling effect of the 2<sup>nd</sup> and 3<sup>rd</sup> modes.

Coupled higher modes are detrimental for the dynamic response of the structure, since amplification in the LS or US are expected.

The results of the parametric analysis carried out on 3DOF models are shown in Fig. 4.5 where the effect of higher modes and the potential of modal coupling effect in mid-story isolated structures are provided as a function of the couples of frequency ratios  $\omega_{US}/\omega_{ISO}$  and  $\omega_{LS}/\omega_{ISO}$ . In particular the graph is divided into three parts, which represent the two regions where either the 2<sup>nd</sup> or the 3<sup>rd</sup> mode prevails, and the bandwidth, marked by dashed lines, where coupling of the 2<sup>nd</sup> and the 3<sup>rd</sup> modes occurs.

From the Fig. 4.5 it can be observed that contemporary low values of both frequency ratios  $\omega_{US}/\omega_{ISO}$  and  $\omega_{LS}/\omega_{ISO}$  cause a mode coupling effect, while large values of both parameters not only exclude a dynamic coupling between the US and LS, but also allow for remarkable simplifications from

a design point of view, namely the first frequency and mode damping are approximately equal to the isolation system counterparts, i.e.  $\omega_1 \approx \omega_{ISO}$  and  $\xi_1 \approx \xi_{ISO}$ .

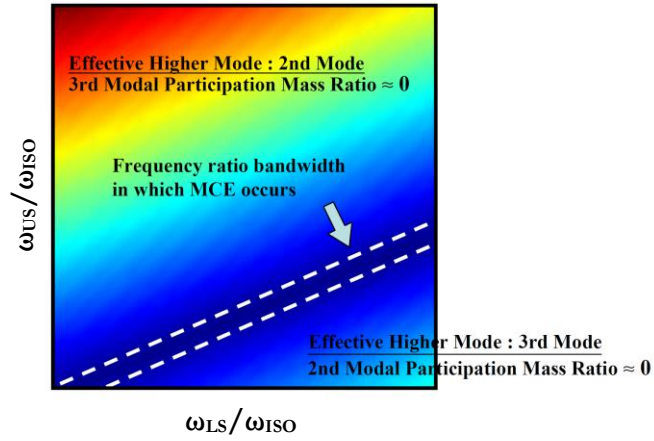


Fig. 4.5. Summarized dynamic characteristics of higher modes in 3DOF IIS model [Wang et al. 2013]

However, according to the graph, in order to exclude a coupling effect is sufficient to have quite different values for the two frequency ratios  $\omega_{US}/\omega_{ISO}$  and  $\omega_{LS}/\omega_{ISO}$ . In particular, when the value of  $\omega_{US}/\omega_{ISO}$  is large (say, larger than 20), even though  $\omega_{LS}/\omega_{ISO}$  is small, the effect of the 2<sup>nd</sup> mode is predominant, the second modal frequency is approximately equal to the frequency of the substructure, i.e.  $\omega_2 \approx \omega_{LS}$ , and the participating mass ratio of the 3<sup>rd</sup> mode,  $\Gamma_3$ , is equal to zero. When  $\omega_{LS}/\omega_{ISO}$  is large, say, larger than 20, if  $\omega_{US}/\omega_{ISO}$  is smaller than 8, the effect of the 3<sup>rd</sup> mode is predominant, the third modal frequency is approximately equal to the frequency of the substructure, i.e.  $\omega_3 \approx \omega_{LS}$ , and the participating mass ratio of the 2<sup>nd</sup> mode,  $\Gamma_2$ , is equal to zero; for  $\omega_{LS}/\omega_{ISO}$  equal to 20, instead, the effect of the 2<sup>nd</sup> mode is predominant if  $\omega_{US}/\omega_{ISO}$  is larger than 11, while for  $\omega_{LS}/\omega_{ISO}$  larger than 20, no coupling effect is predicted if  $\omega_{US}/\omega_{ISO}$  is, as well, larger than 20. In all cases, since [Wang et al. 2011] consider a rigid US, the effect of the higher modes are only related to the motion of the LS. When there is a coupling effect, both frequencies  $\omega_2$  and  $\omega_3$  are almost equal and far from the frequency  $\omega_{LS}$  and both participating mass ratios  $\Gamma_2$  and  $\Gamma_3$  are different from zero.

On the bases of the above results, the paper by [Wang et al. 2013] demonstrates analytically the adverse effect arising from the coupling of the higher modes on the seismic response of mid-story isolated structures. The condition in which MCE occur (i.e.  $\omega_2 \approx \omega_3$ ) is investigated solving the eigenvalue problem of a simplified 3DOF mid-story isolated model and making some reasonable assumptions, namely: the fundamental modal frequency  $\omega_1$  is assumed approximately equal to the nominal frequency of the isolation system  $\omega_{ISO}$  and well separated from the higher modal frequencies  $\omega_2$  and  $\omega_3$ ; this means that the two structural portions are sufficiently stiff with respect to the isolation system and both the square of the frequency ratios  $(\omega_{US}/\omega_{ISO})^2$  and  $(\omega_{ISO}/\omega_{LS})^2$  are more less than 1, typically of order  $O(10^{-1})$ .

With some algebraic manipulations, Wang et al. derive simple linear expressions for addressing MCE, either in terms of frequency or stiffness and mass ratios:

$$(\omega_{LS} / \omega_{ISO}) = (\omega_{US} / \omega_{ISO}) \sqrt{1 + r_{US}} \quad \text{or} \quad \omega_{LS} = \omega_{US} \sqrt{1 + r_{US}} \quad (4.1)$$

$$k_{LS} = k_{US} \left( \frac{m_{LS}}{m_{US}} + \frac{m_{LS}}{m_{ISO}} \right) \quad (4.2)$$

Observing the MCE expression, the design parameters which govern the occurrence of this undesirable condition are  $\omega_{US}$ ,  $\omega_{LS}$  and  $r_{US}$ ; this means that the MCE occurrence is independent on  $\omega_{ISO}$ , thus, irrelevant to different types, mechanical properties, and deformation extent (linear or nonlinear behavior) of seismic isolation bearings.

Even though the expression derived by Wang et al for addressing MCE is very simple and useful to implement, the physical meaning of the frequency  $\omega_{US} \sqrt{1 + r_{US}}$  is not explicitly given.

#### **4.4.2.3. Modal Coupling Effect – MCE [Kobayashi & Koh 2008]**

The dynamic interaction between the upper and lower structures of mid-story isolated building and the detrimental effect of the coupled higher modes are also investigated by Kobayashi and Koh in [Kobayashi & Koh 2008], where the dynamics of IIS structure is analyzed by means of a 3DOF model and different parameters are selected for understanding the

impact of the dynamic interaction between substructure and isolated superstructure.

The design parameters are the nominal period of the isolation,  $T_{ISO}$ , and of the lower structure,  $T_{LS}$ , which are set respectively equal to 4 s and 0.5 s; and the mass ratio  $\alpha$  which is set equal to 0.5, 1.0 and 3.0.

On the basis of the results of [Ping et. al 2008], it can be stated that the mass ratios considered herein spread from the tuning to the mid-story isolation zone; therefore, different placements of the isolation layer are implicitly considered. However, the long value of  $T_{ISO}$  oriented the research of [Kobayashi & Koh 2008] to the conceptual approach of isolation rather than the dissipation or mass damper effect.

For analyzing the higher modes effect, Kobayashi and Koh employed the method outlined by [Skinner 1993] for defining the contribution of the higher modes to earthquake response of base isolated structures. In fact Skinner has revealed the influence of the higher mode to earthquake response of base isolation buildings, that consists in sweeping the modal response with free-free mode shape vectors.

In the paper [Kobayashi & Koh 2008], the same method is applied to mid-story isolation buildings. The free-free 3DOF IIS model (ff-3DOF IIS) is obtained by setting the stiffness of seismic isolation layer equal to zero (i.e. ideal isolation). Solving the eigenvalues problem, it can be observed that the perfect isolation allows to consider the dynamic behavior of the ff-3DOF IIS system as a combination of the base isolated US, with the stiffness of seismic isolation layer equal to zero (ff-2DOF ISO+US), and the fixed-base LS (SDOF LS). In this framework, the MCE can be expressed by a parameter  $\beta$ , being:

$$\beta = \frac{\omega_{US+ISO,2}}{\omega_{LS}} \quad (4.3)$$

i.e. the ratio between the second frequency of the ff-2DOF ISO+US model,  $\omega_{US+ISO,2}$ , and the frequency of the SDOF LS model,  $\omega_{LS}$ . The parameter  $\beta$  can be rewritten in terms of the nominal frequencies of the US and LS as follows:

$$\beta = \frac{\omega_{US} \sqrt{1 + r_{US}}}{\omega_{LS}} \quad (4.4)$$

and can be easily calculated, showing that when it is equal or very close to one, the MCE occurs.

Comparing the (4.4) and the (4.1), it can be stated that the analytical formulations derived by [Wang et al. 2013] and [Kobayashi & Koh 2008] for addressing MCE are exactly the same (quite trivially, equate  $\omega_{LS}$  and  $\omega_{US}\sqrt{1+\Gamma_{US}}$  means that the ratio between those frequencies is equal to one).

Therefore, a simple design rule can be derived: *no MCE arises if the second frequency of the base-isolated US is far from the frequency of the fixed-base LS.*

#### **4.4.2.4. Experimental campaigns**

On the basis of the above theoretical formulation of the problem, Wang et al. perform two experimental campaigns described in detail in the papers [Wang et al. 2012] and [Wang et al. 2013]. In [Wang et al. 2012] the differences between the dynamic behaviors in base-isolated and mid-story isolated buildings are investigated by fixing the dynamic characteristic of the upper structure of two inter-story isolated structures, with a base isolated model also considered for comparison. In [Wang et al. 2012] the effect of the coupling of the higher modes (MCE) is specifically explored by fixing the dynamic characteristic of the upper structure of two inter-story structures, which respectively simulate the dynamic behavior of a building with and without MCE. The main design parameters and results of the two experimental campaigns are given in the following.

In the first experimental campaign the authors perform shaking table tests on three scaled down structural models, namely: Specimen A, Specimen B and Specimen C, depicted in Figs. 4.6 ÷ 4.8. The isolation system is composed of high damping rubber bearings.

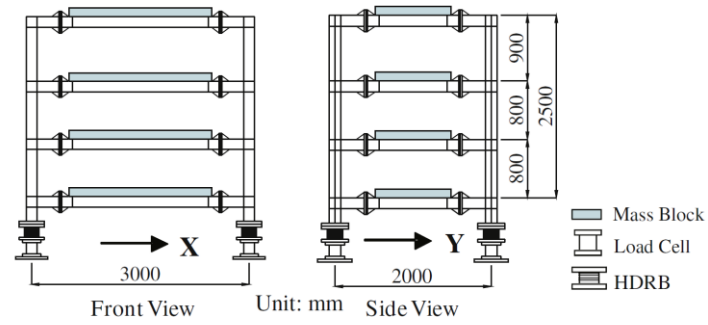


Fig. 4.6. Design drawing and installation photo of Specimen A [Wang et al. 2012]

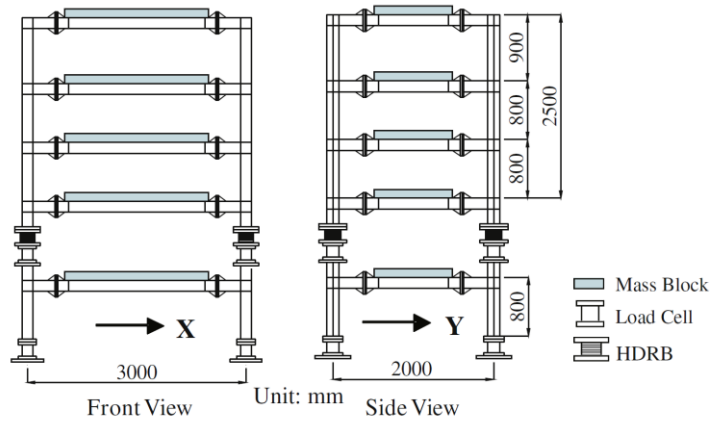
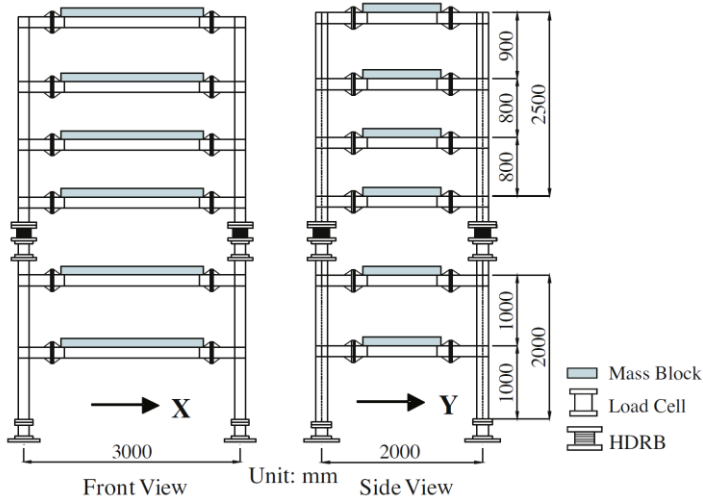


Fig. 4.7. Design drawing and installation photo of Specimen B [Wang et al. 2012]



**Fig. 4.8. Design drawing and installation photo of Specimen C [Wang et al. 2012]**

The seismic reactive mass per floor assigned at the upper and lower structures is respectively  $4 \text{ kNs}^2/\text{m}$  and  $6 \text{ kNs}^2/\text{m}$ , the isolation story mass is  $5 \text{ kNs}^2/\text{m}$ .

From the above values the mass ratios can be derived, i.e.:

Specimen A:  $R_m = 1$ ;

Specimen B:  $r_{US} = 2.4$ ,  $r_{LS} = 1.2$ ,  $m_{US}/m_{LS} = 2.0$ ,  $R_m = 0.74$  and  $\alpha = 2.83$ ;

Specimen C:  $r_{US} = 2.4$ ,  $r_{LS} = 2.4$ ,  $m_{US}/m_{LS} = 1.0$ ,  $R_m = 0.59$  and  $\alpha = 1.42$ .

Comparing these values with the corresponding counterparts of the parametric analysis carried out on [Wang et al. 2011], i.e.  $r_{LS} = 1, 2$  and  $r_{US} = 5$ , it can be noted that in Specimens B and C the mass ratio  $r_{US}$  is halved; recalling the results of [Ping et al. 2008], a mass ratio  $\alpha$  in the range of  $1 \div 4$  places Specimens B and C in the mid-isolation zone.

The nominal isolation period  $T_{ISO}$  is not specified in the paper; however, it is reasonable to assume a value of  $2 \text{ s}$  (or likewise, a nominal isolation frequency  $\omega_{ISO}$  equal to  $\pi$ ) utilized in the previous paper by the same authors [Wang et al. 2011]. With this assumption, the frequency ratios ( $\omega_{LS}/\omega_{ISO}$ ,  $\omega_{US}/\omega_{ISO}$ ) for Specimen B are around  $(20, 7)$  and for Specimen C are around  $(7.5, 7)$ .

Starting from the above values for the design parameters, the nominal frequencies (or periods) of the structural portions, as standalone



structures, and the stiffness ratios between the structural portions can be derived and compared with the values assumed in the parametric analysis. Specimen B,  $\omega_{LS} = 62.832 \text{ rad/s}$  ( $T_{LS} = 0.10 \text{ s}$ ) and  $\omega_{US} = 21.991 \text{ rad/s}$  ( $T_{US} = 0.286 \text{ s}$ );  $k_{US}/k_{LS} \approx 0.35$ .

Specimen C,  $\omega_{LS} = 23.562 \text{ rad/s}$  ( $T_{LS} = 0.267 \text{ s}$ ) and  $\omega_{US} = 21.991 \text{ rad/s}$  ( $T_{US} = 0.286 \text{ s}$ );  $k_{US}/k_{LS} \approx 1.23$ .

It is noted that Specimen C simulates an “extreme and practically rare” mid-story isolated structure in which the lower structure is not sufficiently stiff, but still not comparable to the flexibility of the isolation system.

The value of the MCE parameters for Specimen B and C is given by

$$\beta_B = \left( \frac{\omega_{US} \sqrt{1 + r_{US}}}{\omega_{LS}} \right)_B = \frac{21.991 \sqrt{1 + 2.4}}{68.832} = \frac{40.549}{68.832} = 0.59 \ll 1.0 \quad (4.5)$$

$$\beta_C = \left( \frac{\omega_{US} \sqrt{1 + r_{US}}}{\omega_{LS}} \right)_C = \frac{21.991 \sqrt{1 + 2.4}}{23.562} = \frac{40.549}{23.562} = 1.72 \gg 1.0 \quad (4.6)$$

Both Specimens B and C are far from MCE. Observing the results for Specimen C, the almost equal frequencies of structural portions ( $\omega_{LS} = 23.562 \text{ rad/s}$  vs.  $\omega_{US} = 21.991 \text{ rad/s}$ , scatter of 7%) are not able to give rise to MCE, since the mass ratio  $r_{US}$  is always greater than 1 in design practice; thus,  $\beta$  is at least 1.41 (assuming  $\omega_{LS} = \omega_{US}$  and  $r_{US} = 1$ ).

Observing the identified modal characteristics and shapes of test specimens subjected to 1999 Chi-Chi earthquake (Taiwan) provided in Fig. 4.9, the following considerations can be done.

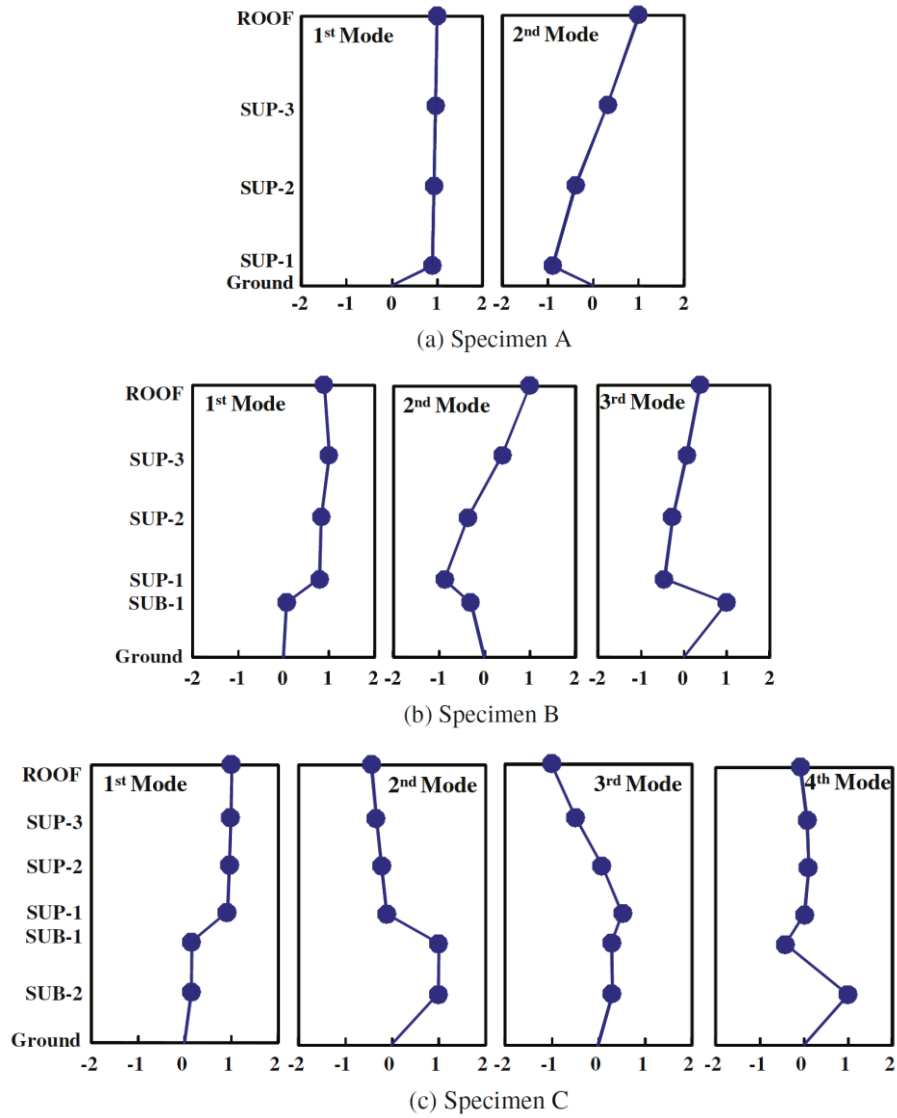


**Fig. 4.9.** Identified mode shapes of test specimens subjected to 1999 Chi-Chi earthquake with PGA of 1.19 g: (a) Specimen A, (b) Specimen B, (c) Specimen C [Wang et al. 2012]

Specimen A shows the typical mode shapes of base isolated buildings with a negligible participation of the higher modes. The first mode shape of Specimens B and C shows displacement mainly in the isolation layer and

minor deformation in both the structural portions; the first participating mass ratio of Specimens B and C is almost equal to the mass ratio  $R_m$  (with scatter respectively equal to 4.3% and 14.6%) and it is lower in Specimen C. The higher mode shapes of Specimens B and C show deformation mainly concentrated at either upper or lower structure; the effective higher mode for Specimens B and C (i.e. the one possesses not negligible participating mass ratio) is the third and the second mode, respectively. Looking at the modal damping ratios, the mid-story isolated structures show lower values than the base isolated structure counterpart; furthermore, increasing the mass and the flexibility of the lower structure (i.e. Specimen C), the first modal damping ratio decreases.

It is noticeable that, with the same design of the isolated upper structure, the mid-story isolation design (i.e. both Specimens B and C) has more significant participation of the higher modes, longer fundamental modal period and smaller fundamental modal damping ratio than the base isolation design (i.e. Specimen A). This is particularly evident when the isolation system is designated at a higher level of the building (the lower structure possesses a larger mass), or when the lower structure is more flexible (i.e. Specimen C).

These considerations support the results of [Wang et al. 2011] which demonstrate experimentally that the first modal damping ratio and the first modal participation mass ratio of a mid-story isolated building are significantly affected by the mass and stiffness of the lower structure.

Observing the displacement and acceleration response histories and the peak of the shear force response, it can be noticed that: the response of base isolated structure is less than the response of mid-story isolated structures; however, depending on the frequency content of the earthquake, the unusual mass and stiffness distributions of Specimen C cause larger peak values of base shear and relative displacements both in the lower and in the upper structures, with respect to Specimen B.

In order to simulate intermediate isolated structures with and without MCE, shaking table tests are performed in the second experimental campaign by [Wang, et al. 2013] on two scaled down structural models, appointed as Specimen D and Specimen E, depicted in Figs. 4.10 – 4.11. Both models are equipped with mid-story isolation system composed of lead rubber bearings and located on the top of the first floor.

Specimen D refers to an inter-story isolated building where the mass and frequency ratios between the lower and upper structures are chosen to

avoid MCE, while Specimen E refers to a building where the dynamic characteristics of the structural portions give rise to MCE.

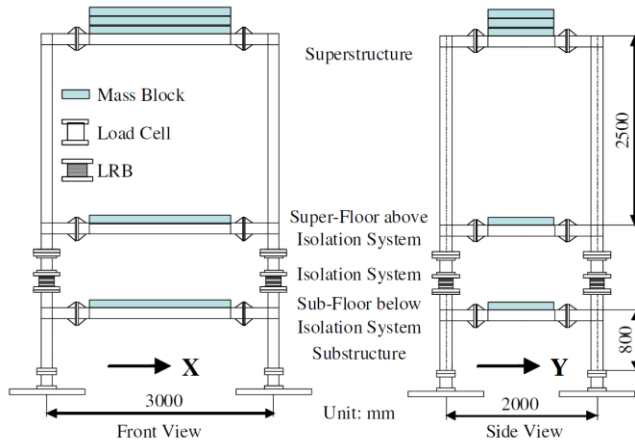


**Fig. 4.10. Design drawing and installation photo of Specimen D [Wang et al. 2013]**

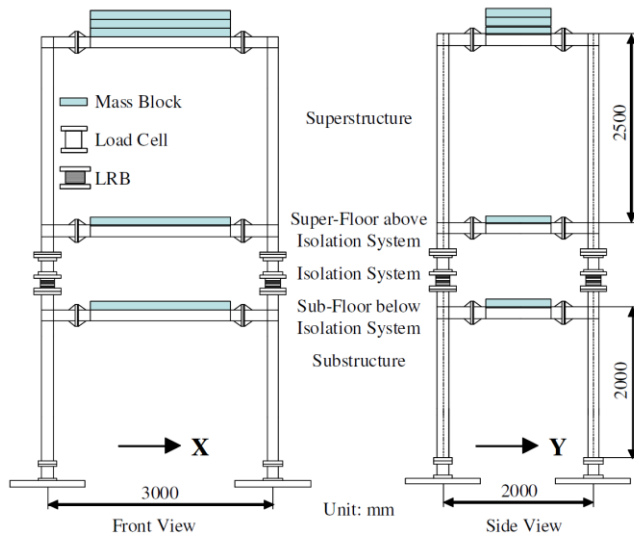


**Fig. 4.11. Design drawing and installation photo of Specimen E [Wang et al. 2013]**

The main design parameters of Specimen D and E are mass and frequency ratios, specified as follows.

For both models, the seismic reactive masses assigned to the lower structure, isolation level and upper structure respectively correspond to 5

kNs<sup>2</sup>/m, 3 kNs<sup>2</sup>/m and 14 kNs<sup>2</sup>/m, leading to mass ratios  $r_{LS}$  and  $r_{US}$  equal to 1.7 and 4.7. These values agree with the mass ratios assumed in the authors' parametric analysis, i.e.  $r_{LS} = 1, 2$  and  $r_{US} = 5$ . The nominal isolation period  $T_{ISO}$  is set equal to 1 s, or likewise, the nominal isolation frequency  $\omega_{ISO}$  is equal to  $2\pi$ .

From the above parameters the other mass ratios can be derived, e.g.  $m_{US}/m_{LS} = 2.8$ ,  $R_m = 0.77$  and  $\alpha = 5.7$ . Recalling the results of [Ping et al. 2008], a mass ratio  $\alpha$  equal to 5.7 places the models in the base isolation zone; however, setting  $T_{ISO} = 1$  s seems not enough long to ensure the isolation effect, particularly if compared to the corresponding value used in other research papers, such as the work of [Kobayashi & Koh 2008], where  $T_{ISO} = 4$  s.

The frequency ratios ( $\omega_{LS}/\omega_{ISO}$ ,  $\omega_{US}/\omega_{ISO}$ ) for Specimen D are (17.7, 3.3) and for Specimen E are (7.8, 3.3); thus, the unique difference between the two models is the stiffness of the upper structure.

Starting from the above design parameters, the nominal frequencies (or periods) of the structural portions, as standalone structures, and the stiffness ratios between the structural portions can be derived and compared with the values assumed in the parametric analysis.

For Specimen D,  $\omega_{LS} = 111.213$  rad/s ( $T_{LS} = 0.0564$  s) and  $\omega_{US} = 20.734$  rad/s ( $T_{US} = 0.303$  s);  $k_{US}/k_{LS} \approx 0.1$ . For Specimen E,  $\omega_{LS} = 49.009$  rad/s ( $T_{LS} = 0.128$  s) and  $\omega_{US} = 20.734$  rad/s ( $T_{US} = 0.303$  s);  $k_{US}/k_{LS} \approx 0.5$ .

The values for the MCE parameter for Specimen D and E are given by:

$$\beta_D = \left( \frac{\omega_{US} \sqrt{1 + r_{US}}}{\omega_{LS}} \right)_D = \frac{20.734 \sqrt{1 + 4.7}}{111.213} = \frac{49.502}{111.213} = 0.44 \ll 1.0 \quad (4.7)$$

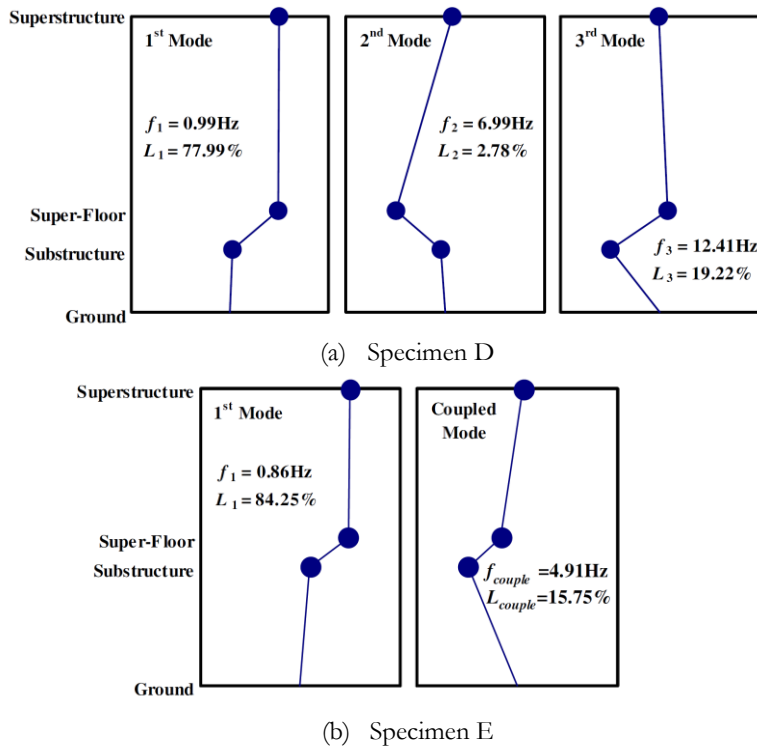
$$\beta_E = \left( \frac{\omega_{US} \sqrt{1 + r_{US}}}{\omega_{LS}} \right)_E = \frac{20.734 \sqrt{1 + 4.7}}{49.009} = \frac{49.502}{49.009} = 1.01 \quad (4.8)$$

Since only  $\beta_E$  is close to 1, MCE is expected to occur in Specimen E.

Useful information can be derived by observing the mode shapes, modal frequencies and participating mass ratio of the two structures after dynamic identification, Fig. 4.12.

The first modal shape for both Specimen D and E shows displacement mainly in the isolation layer and minor deformation in the LS. Also in terms of period and participating mass, it can be observed that the first period is coincident with the isolation period, and the participating mass

is very close to the mass ratio  $R_m$ . Those results suggest that the first mode is representative of the isolation mode. Some differences between the two structures arise looking at the higher modes. The second and the third modes of the Specimen D respectively correspond to the mode of the isolated upper structure with almost no deformation in the LS, and of the mode of the lower structure, with almost no deformation in the US. On the contrary, for Specimen E it is shown the coupled mode shape obtained as a combination of the identified second and third mode shapes according to their identified participation mass ratios. This mode shows deformation in both the lower and isolated upper structures.



$f_1, f_2, f_3, f_{\text{couple}}$ : First, Second, Third and Coupled Modal Natural Frequencies

$L_1, L_2, L_3, L_{\text{couple}}$ : First, Second, Third and Coupled Modal Participation Mass Ratios

**Fig. 4.12.** Identified mode shapes of test specimens subjected to 1999 Chi-Chi earthquake with PGA of 0.32 g: (a) Specimen D, (b) Specimen E [Wang et al. 2013]

Observing the story drift and acceleration response histories it can be noticed that: the condition in which MCE occurs is independent of the design of isolation bearings and on the intensity of earthquake excitation; MCE results in the amplified seismic responses at both upper and lower structures; depending on the frequency content of the earthquake, going from the upper to the lower structure the peak displacement of Specimen E grow from 20% to 430% and the peak acceleration from 10% to 200% with respect to the Specimen D counterparts.

**4.4.2.5. *Parametric analysis by Kobayashi and Koh [Kobayashi & Koh 2008]***

[Kobayashi & Koh 2008] describe the vibration characteristics of mid-story isolated buildings based on the results of eigenvalue analyses and time history analyses, paying more attention on the modal coupling effect of the higher modes, which may cause a detrimental amplification of the upper structure response.

For this purpose, the dynamic response of MDOF fixed-base and mid-story isolated models is compared. The fixed-base model is a 16DOF shear model, with uniform mass distribution and stiffness distribution that gives rise to uniformly inter-story drift; the fundamental period and the damping ratio are set to 1 s and 0.02, respectively. Six 16DOF isolated models are considered, shifting the position of the isolation system from the 1<sup>st</sup>, 5<sup>th</sup>, 8<sup>th</sup>, 9<sup>th</sup>, 10<sup>th</sup> to the 13<sup>th</sup> story; the mass and stiffness distributions are the same of the conventional system except for the isolation layer in which the stiffness of isolators is adjusted to 1/100 of the corresponding counterpart in the uncontrolled configuration. Therefore, the first natural period in the controlled configuration goes from 3.4 s and 2.5 s for the extreme 1<sup>st</sup> isolated story and 13<sup>th</sup> isolated story 16DOF models. The isolation system is composed of isolators, hysteresis and viscous dampers; the damping ratio of the isolators and structural portions are equal to 0.2 and 0.02, respectively.

Under El Centro NS motion; the acceleration and story shear coefficient of the upper structure in the 8<sup>th</sup> story isolation model are remarkably large compared with other models. This is caused by modal coupling effect; thus, the ratio between the mass and the stiffness of the structural portions may strongly affect the response of the structure, mainly of the isolated superstructure.

#### 4.4.2.6. Parametric analysis by Ryan and Earl [Ryan & Earl 2010]

[Ryan & Earl 2010] examine the effectiveness of inter-story and multi-story isolation systems. The seismic response of different isolated systems is compared to reference fixed-base and base-isolated models.

The fixed-base structure is modeled as 6-story shear frame (infinitely rigid beams) with a uniform mass distribution and a segmented stiffness distribution. In particular, the story stiffnesses  $k_i$ , for  $i = (1, \dots, 6)$  going from the bottom to the top story, are equal to  $k_1 = k_2 = k$ ,  $k_3 = k_4 = 7/8 k$ ,  $k_5 = k_6 = 3/4 k$  where  $k$  is scaled to give a fundamental period of 0.5 s. Five 6-single-story isolation and two multi-story isolation frames are considered: in the first group the isolation layer is placed at the base and on the top of the 1<sup>st</sup>, 2<sup>nd</sup>, 3<sup>rd</sup> and 6<sup>th</sup> story; in the second group the isolation layers are placed at the base and on the top of the 3<sup>rd</sup> story, and at every story, Fig. 4.13.

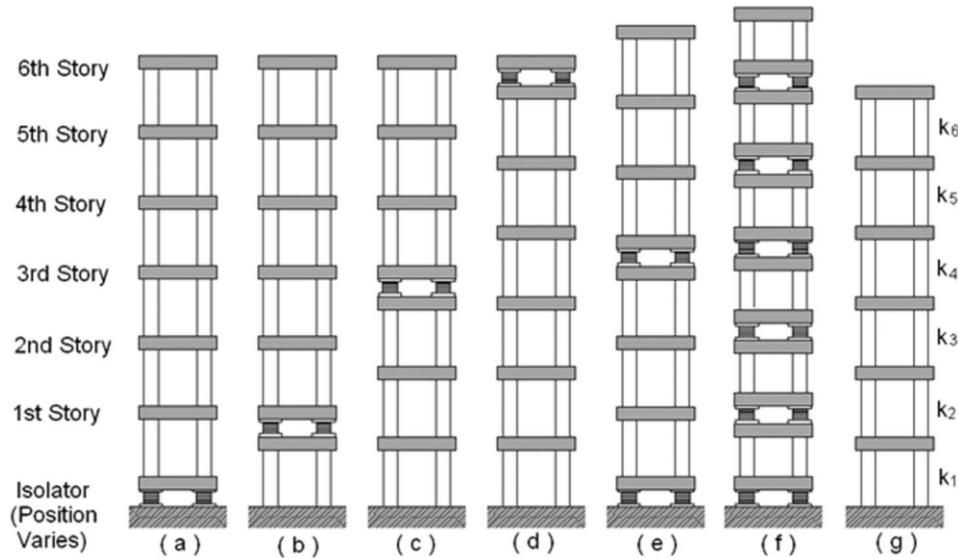


Fig. 4.13. Inter-story isolation systems to be evaluated include single-story isolation at: (a) base, (b) top of the first story, (c) mid-height, (d) roof; and multi-story isolation at: (e) base and mid-height, and (f) every story ;(g) reference fixed base model [Ryan & Earl 2010]

The total mass at the isolation level exceeds the story mass of the un-isolated level of 10%; the stiffness of the isolation system is selected to obtain a first natural period of 2.5 s for all the isolated models. A damping



ratio of 0.02 is assigned in the fixed-base frame while no damping is included in all the isolation systems.

Time history analyses are performed to select the optimum design deformation of non-linear inter-story and multi-story isolators; the authors recommend to determine the design deformation as the median deformation observed from linear response history analysis of the system with nominal isolation properties under a suite of selected ground motions.

On the basis of time history analyses in terms of story drifts and base shear (Fig. 4.14), it is observed that: the single-story isolation is effective in mitigating the force demands above the isolation system but less effective in mitigating lower-level forces, the better performance is shown decreasing the isolation level (in agreement with the results of [Reggio & De Angelis 2014, 2015]); no improvements are observed locating the isolation level at the top of the first floor or inserting the isolation system at every story with respect to base isolation; the roof isolation is the least effective inter-story system, since the design parameters have been selected to exploit the isolation effect and not the mass damper effect for which the roof isolation is commonly designed (see [Sadek et al. 1997, Villaverde 2002, Villaverde et al. 2005, Matta & De Stefano 2009, De Angelis et al. 2012, Moutinho 2012]).

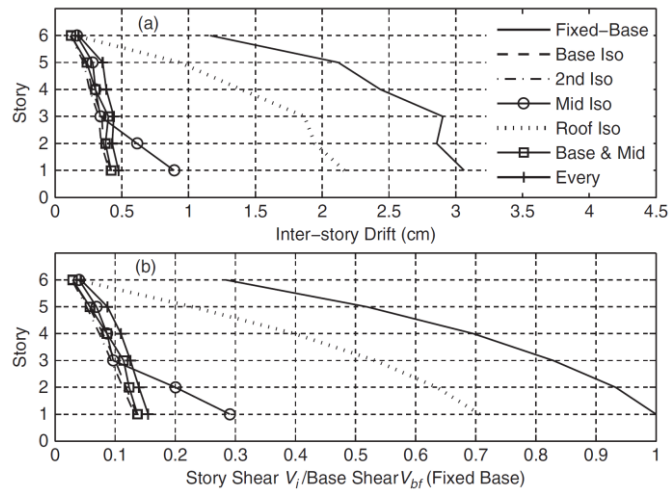


**Fig. 4.14. (a) Inter-story drifts and (b) ratio of inter-story shear to base shear of the fixed-base building compared for different inter- and multi-story isolation systems [Ryan & Earl 2010]**

#### **4.4.3. Mass Damper Approach [De Angelis et al. 2012; Villaverde 1985, 2002; Sadek et al. 1997; Chey et al. 2013; Miranda et al. 2013; Reggio & De Angelis 2014, 2015]**

Considering the mass damper effect, it is well established that small tuned mass dampers (TMDs) attached to structure are very effective in reducing excessive harmonic vibrations induced by external loads like wind but are not equally interesting within the content of earthquake engineering problems.

Three inherent limitations to the seismic effectiveness of the TMD can be found ([De Angelis et al. 2012]): the lack of robustness against deviations in design parameters; a high dependence on earthquake frequency content; and the impulsive character of the earthquake excitation.

In order to overcome these limitations, TMDs should require relatively large mass and, hence, large space for the installation; furthermore, since by design the mass is set in resonance with the supporting structure, it usually experiences large displacements with respect to the main structure, and, as a result, large clearance is required to accommodate such large displacements. Lastly, the mass need to be mounted on a smooth surface to minimize friction forces and facilitate the free motion ([Villaverde 2002]).

Recent studies have proposed a new, non-conventional configuration, the so-called non-conventional TMD, in which masses already present in the structure to be protected are converted into tuned masses, retaining structural and architectural functions beyond the mere control function ([De Angelis et al. 2012]). The implementation of a flexible isolation layer at an intermediate level of the structure simultaneously provides a large mass, represented by the upper isolated structure, and allows to accommodate large displacements at the isolation floor. Therefore, a non-conventional TMD realized by means of a mid-story isolation system seems the logical solution to enhance the effectiveness of TMD under seismic excitation.

Along this research direction, [Villaverde 1985] implements a heavily-damped vibration absorber to increase the damping of a building and reduce its response to earthquake. Villaverde finds that TMDs performs best when the first two complex modes of vibration of the main structure

and mass device have approximately the same damping ratio at the average of the damping ratio of the structure and TMD, i.e.

$$\xi_{\text{ISO,opt}} = \frac{\xi_s + \xi_{\text{ISO}}}{2} \quad (4.9)$$

Villaverde observed that this condition can be reached only if the TMD is in resonance with the main structure, i.e.  $f = 1$ .

Afterwards, [Sadek et al. 1997] show that increasing the mass ratio (values greater than 0.005) the design formulae of Villaverde fail in ensuring the equality of modal damping ratios and that the structural response is mainly influenced by the mode with the lower damping; depending on the frequency content of the earthquake, higher TMD displacement response is achieved with respect to the uncontrolled configuration.

In order to extend the validity of the Villaverde methodology, [Sadek et al. 1997] use a SDOF structure - TMD system and select the values of the TMD design parameters that result in equal damping ratios and equal frequencies in the two complex modes of vibration.

The mass ratio is varied in the range of  $0 \div 1$ , the structure damping ratio is set equal to 0, 0.02 and 0.05.

Numerical searching technique based on the complex eigenvalue problem is proposed and, using a curve fitting of the results, closed-form design formulae for the optimal TMD frequency and damping ratios are derived. For the damped structure, the optimal frequency and damping ratios are given by:

$$f_{\text{opt}} = \frac{1}{1+\alpha} \left[ 1 - \xi_s \sqrt{\frac{\alpha}{1+\alpha}} \right]; \quad \xi_{\text{ISO,opt}} = \frac{\xi_s}{1+\alpha} + \sqrt{\frac{\alpha}{1+\alpha}} \quad (4.10)$$

Quite trivially, for the undamped structure the expressions (4.10) assume the following form:

$$f_{\text{opt}} = \frac{1}{1+\alpha}; \quad \xi_{\text{ISO,opt}} = \sqrt{\frac{\alpha}{1+\alpha}} \quad (4.11)$$

Sadek et al. also extend the theory developed for 2DOF systems to MDOF models, finding that the tuning frequency ratio for a MDOF system is nearly equal to the one derived for a SDOF system, with mass ratio  $\alpha\phi$ ,

being  $\phi$  the amplitude of the first mode of vibration for a unit participation factor computed at the location of TMD, i.e.  $f_{\text{MDOF}}(\alpha) = f_{\text{SDOF}}(\alpha\phi)$  and  $\xi_{\text{MDOF}}(\alpha) = \xi_{\text{SDOF}}(\alpha\phi)$ . Therefore, the optimal frequency and damping ratios are given by

$$f_{\text{opt}} = \frac{1}{1 + \alpha\phi} \left[ 1 - \xi_s \sqrt{\frac{\alpha\phi}{1 + \alpha\phi}} \right]; \quad \xi_{\text{ISO,opt}} = \frac{\xi_s}{1 + \alpha\phi} + \sqrt{\frac{\alpha\phi}{1 + \alpha\phi}} \quad (4.12)$$

The control procedure by Sadek et al. is successfully applied and many researchers implement the methods [Chey et al. 2013, Miranda et al. 2013] or use it for comparison [De Angelis et al. 2012, Reggio & De Angelis 2014, 2015].

The paper by [Chey et al. 2013] explore the potentials of an “added stories” (ASI) system as a retrofitting strategy for enhancing the seismic performance of an existing 12-story reinforced concrete frame structure; two and four isolated stories were respectively added on the 12-story model, increasing the mass of 24% and 40%, Fig. 4.15.

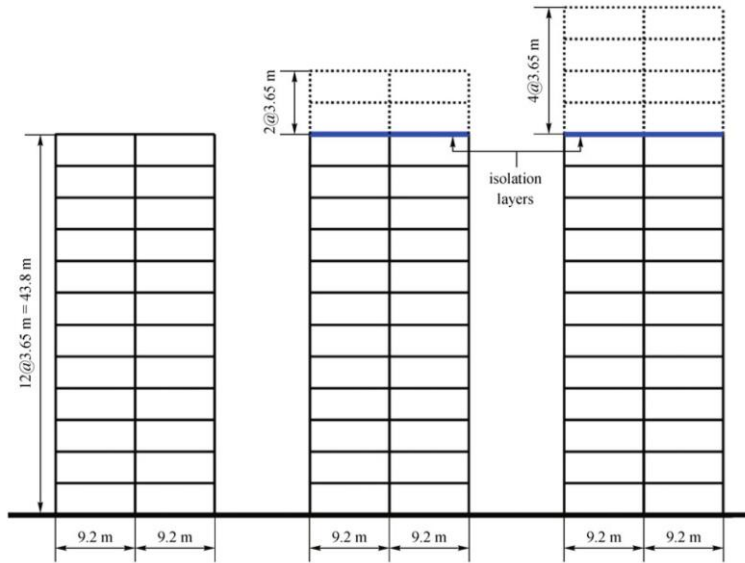


Fig. 4.15. (a) 12-story target model (b) 14-story retrofitted model, (c) 16-story retrofitted model [Chey et al. 2013]

The design procedure for ASI system developed by Chey et al. employs the control method proposed by Sadek et al. for defining the optimal TMD design parameters, i.e. the frequency and damping ratios, for MDOF systems. The authors provide the optimal tuning and damping ratios versus mass ratio values ranging from 0 to 1, with 5% of internal damping for “12 + 2” and “12 + 4” ASI models. It is found that increasing the mass ratio, the optimal tuning ratio decreases while the optimal damping ratio increases; for “12 + 2” ASI model with a mass ratio of 0.31, the optimal frequency and damping ratios respectively correspond to 0.684 and 0.716; for “12 + 4” ASI model with a mass ratio of 0.52, the optimal frequency and damping ratios respectively corresponded to 0.568 and 0.842.

Comparing the approaches presented in the papers by [Chey et al. 2013] and [Ping et al. 2008], it can be noticed that for mass ratios less than 1, which represent the tuning frequency zone, the results are in agreement only in terms of optimal frequency ratio, since the method of Sadek et al. results in much higher damping ratios.

The effectiveness of ASI system is evaluated on the basis of a statistical assessment, by comparing the 50<sup>th</sup> (median) percentile responses under time history records spanning over a range of three seismic levels (low, medium and high suites); of the “12”, “12+2” and “12+4” story models were compared. The assessment indicated that, on average, the ASI system receives considerably more input energy than the original 12-story building; however, the share of structural components of the system from this energy remains small. This is in agreement with the considerations made in the paper by [Ziyaeifar & Noguchi 1998].

Some control indices, which represent the 50<sup>th</sup> percentile response of the controlled structures normalized to the uncontrolled configuration in terms of peak relative displacements, inter-story drift ratios, story shear forces and total accelerations are evaluated.

In general, the indices cover a range of  $0.6 \div 0.85$ ; the lower values, corresponding to the high suite for story shear forces and total accelerations, and to low suite for peak displacements and inter-story drift, are observed for the “12+4” ASI system, thanks to the large mass ratio (Fig. 4.16).

[De Angelis et al. 2012] investigate the dynamic behavior of a non-conventional TMD with large mass ratio implemented via inter-story isolation by means of high damping rubber bearings.

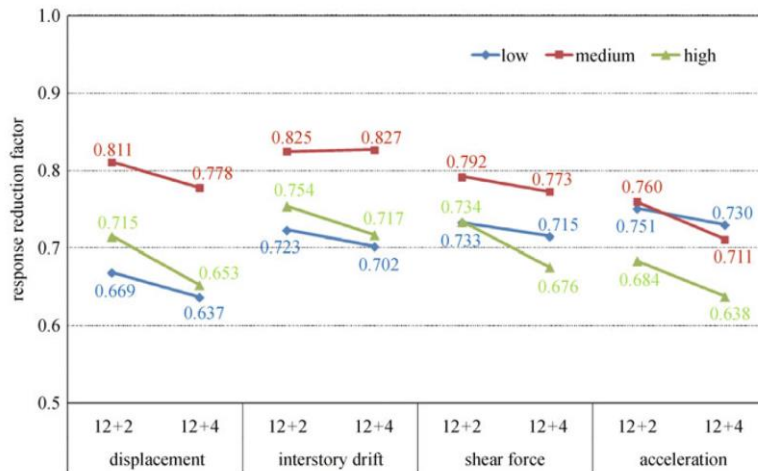


Fig. 4.16. (a) 12-story target model (b) 14-story retrofitted model, (c) 16-story retrofitted model [Chey et al. 2013]

The governing equations are firstly derived for a MDOF proportionally damped structure (a two-story steel frame) equipped with TMD, then a generalized SDOF structure - TMD system is introduced for design purposes.

The optimization criterion consists in a numerical searching technique which minimizes the root-mean-square (rms) displacement response of the damped main structure; a stationary Gaussian stochastic process with zero mean and white noise spectral density is used to model ground acceleration.

The mass ratio  $\alpha$  is set equal to 1.049 to realize the non-conventional TMD; considering the frame response dominated by the first mode, the dynamic properties of the generalized SDOF structure are determined as the frequency of the fundamental mode  $\omega_1 = 33.61 \text{ rad/s}$  ( $T_1 = 0.187 \text{ s}$ ) and the damping ratio  $\xi_1 = 0.02$ . Since the equivalent damping ratio of HDRBs experimentally varies between 0.10 and 0.15 for a target shear strain of 100-150%, the damping ratio in the first complex mode is assumed to be a constant equal to 0.12; consequently, the only design parameter, the frequency ratio  $f$ , is varied in between  $0 \div 1$ .

From the optimization procedure the optimum frequency ratio  $f_{\text{opt}}$  is found equal to 0.42; in addition, some indices which represent the rms response of the controlled structure normalized to the uncontrolled configuration are defined in terms of displacement of the main structure

( $U_1$ ), relative displacement between the structure and the device mass ( $U_{21}$ ), absolute acceleration of both the main system and the TMD ( $A_1$  and  $A_2$ ). At the optimal  $f_{opt}$ , the indices  $A_2$ ,  $A_1$  and  $U_{21}$  are found respectively 0.3, 0.4 and 0.8; therefore, the stroke  $U_{21}$  and the acceleration device  $A_2$  are in allowable range.

Comparing the approaches of [De Angelis et al. 2012] and [Ping et al. 2008], for mass ratios almost equal to 1, which represent the transition between the tuning frequency and mid-story isolation zones, the results are in agreement, since the optimal parameters  $f_{opt}$  belongs to the range  $0.4 \div 0.5$ .

In order to evaluate the novelty of the design procedure, [De Angelis et al. 2012] compare the proposed method with the method of [Sadek et al. 1997]; in particular, a small mass ratio of 0.02 and a large mass ratio of 1.049 are considered to compare both the cases of conventional and non-conventional TMDs, Fig. 4.17.

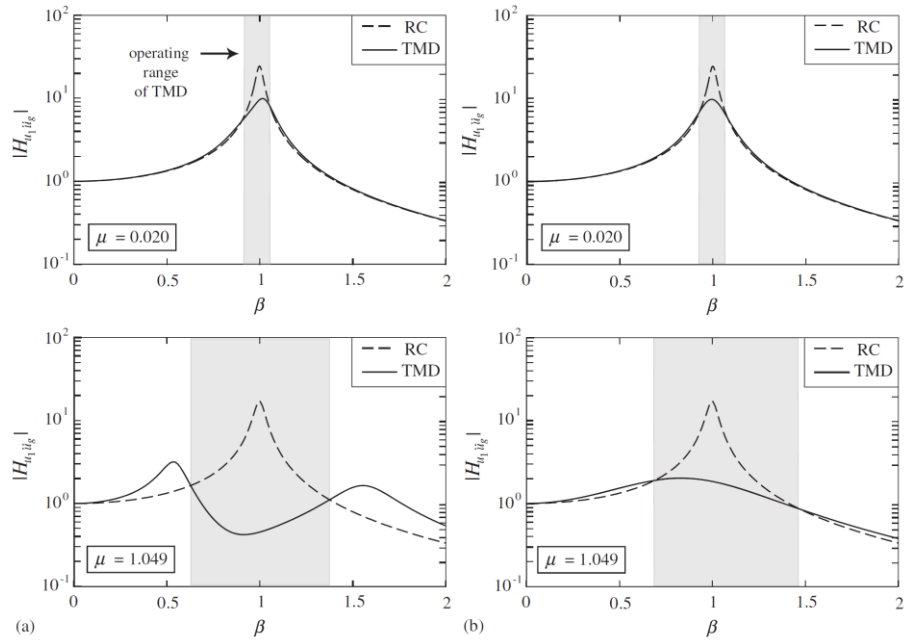


**Fig. 4.17.** Frequency response function of the main structure displacement vs. to ground acceleration in the uncontrolled (RC) and optimally controlled (TMD) configurations. Optimal design of TMD using: (a) the method proposed by De Angelis et al. and (b) the method by Sadek et al. Two mass ratios are considered: 0.020 and 1.049. [De Angelis et al. 2012]

While for the small mass ratio the two methods give rise to similar results, for large mass ratio significant differences emerge both in terms of optimal design parameters and modal properties. The method of Sadek et al. results in much higher damping ratios ( $\xi_2$ : 0.7253 vs. 0.1630) and modal damping ratio ( $\eta_1$ : 0.5226 vs. 0.1200,  $\eta_2$ : 0.5370 vs. 0.1044). It is worth noticing that similar results are not feasible for implementing HDRBs in the isolation layer. Furthermore, the stroke  $U_{21}$  with the method of De Angelis et al. was halved with respect to the one of Sadek et al.

The seismic effectiveness of proposed method was finally evaluated by means of shaking table tests.

The analytical results coupled to experimental evidence show that: a non-conventional TMD with a large mass ratio provides greater reduction of the structural response with respect to a conventional TMD; the large mass ratio leads to a more robust and effective control system; thanks to the TMD robustness, the system becomes less frequency dependent and the reduced response is obtained also for non-optimal configurations.

Sometimes, the boundaries between the different conceptual approaches are overcome, as in the paper by [Reggio & De Angelis 2014, 2015] in which the authors combine the non-conventional TMD and the concentrated energy dissipation approaches.

[Reggio & De Angelis 2014, 2015] propose an energy-based design methodology for non-conventional TMD implemented via inter-story isolation, considering both MDOF and 2DOF reduced-order models which represent the dynamic behavior of a multi-story shear type frame structure equipped with a single-story isolation system. The optimization criterion consists in maximizing an energy performance index (namely: EDI), defined as “the ratio between the incremental energy dissipated in the isolation system and the incremental input energy globally transferred to the two-DOF model”, by assuming the ground acceleration as a stationary Gaussian stochastic process with zero mean and white noise spectral density. The procedure has then been implemented in 5DOF models, shifting the position of isolation layer from the third to the roof level and carrying out seismic analysis under historical accelerograms with different frequency content.

The optimal design parameters are the frequency ratio  $f$  and the damping ratio  $\xi_{ISO}$ , which are greater than 0 and in between  $0 \div 1$ , respectively; the mass ratio  $\alpha$  is set equal to 0.1, 0.5 and 1.0 while the damping ratio of the lower structure is equal to 0.02. It is shown that varying the couple  $f - \xi_{ISO}$ , the energy performance index spreads in between  $10 \div 90\%$ ; however,



increasing the mass ratio the interval in which EDI attains the higher values significantly expands, enhancing the robustness of the control performance, Fig. 4.18. For instance: for  $\alpha = 0.5$  the optimal parameters are  $f_{\text{opt}} = 0.6543$  and  $\xi_{\text{ISO,opt}} = 0.29$ , which correspond to  $\text{EDI}_{\text{max}} = 0.9155$ . In order to investigate the influence of the damping ratio of primary oscillator, the authors consider three different values of the damping ratio, i.e. 0.02, 0.03, 0.05. Fig. 4.19 shows the values of  $\text{EDI}_{\text{max}}$  and of the optimal design parameters, frequency and damping ratios, versus mass ratio by varying the damping ratio of the main structure. From this figure it can be observed that increasing the damping of the primary oscillator the value of  $\text{EDI}_{\text{max}}$  decreases while comparable results are obtained for the optimal parameters.

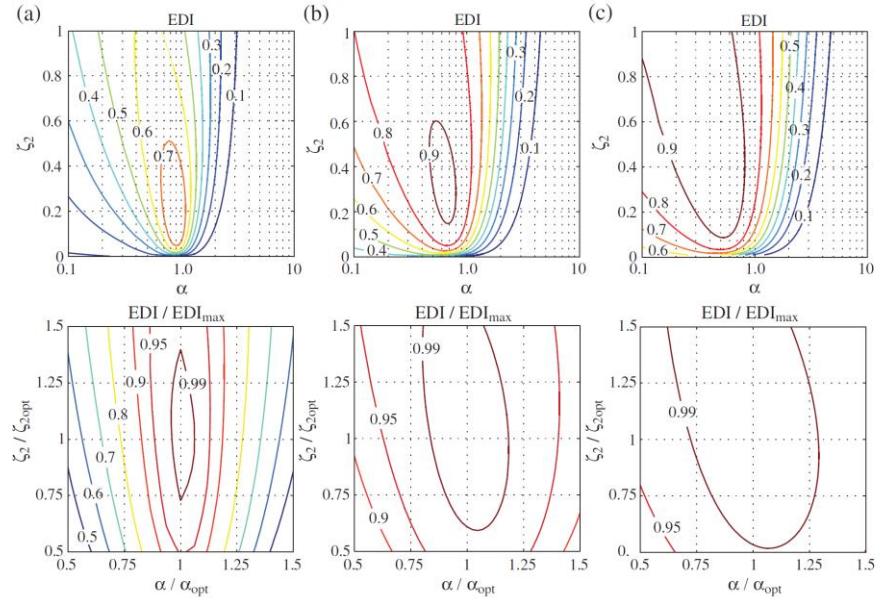


**Fig. 4.18. Reduced-order two-DOF model under stochastic white-noise input, Energy Dissipation Index (EDI) vs. design parameters: frequency ratio, isolation damping ratio and sensitivity of  $\text{EDI} = \text{EDI}_{\text{max}}$  to deviations of the design parameters; Mass ratios: (a) 0.10, (b) 0.50, (c) 1.0; damping ratio in the main structure equal to 0.02. [Reggio & De Angelis 2015]**

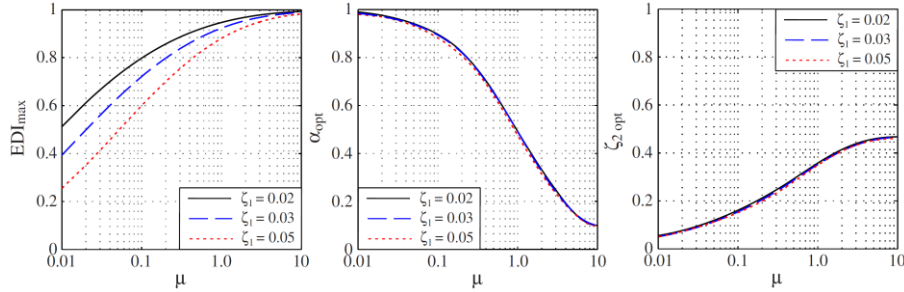


**Fig. 4.19. Reduced-order two-DOF model,  $EDI_{max}$  and optimal design parameters vs. mass ratio for various damping ratios of the primary oscillator, i.e. 0:02; 0:03; 0:05: (a)  $EDI_{max}$ , (b) optimal frequency ratio, (c) optimal damping ratio [Reggio & De Angelis 2015]**

The implementation of the methodology in 5DOF models, with uniform mass and stiffness distributions, has shown a considerable reduction of the structural response in all the controlled structures with respect to the fixed-base configuration; the mid-story isolation system (i.e. the isolation layer placed at the third level) allows the better performance.

Comparing the approaches of [Reggio & De Angelis 2014, 2015] and [Ping et al. 2008], it can be noticed that, although the optimization criteria used are different (the former maximizes an energy performance index and the latter minimizes the base shear variance), for mass ratios less than 1, which represent the tuning frequency zone, the results are in agreement since the optimal parameters  $f_{opt}$  and  $\xi_{iso,opt}$  belong to  $0.5 \div 0.9$  and  $0.1 \div 0.3$ , respectively.

It is worth noticing that, while [Sadek et al. 1997] selected the TMD design parameters by equating both the damping and the frequency ratios in the two complex modes, [Reggio & De Angelis 2014, 2015] found that the maximization of EDI leads to approximately equal damping ratios and different modal frequency. However, Sadek et al. gives optimal parameters that are very difficult to implement and tune in practice.

The range of values of the design parameters adopted for the mass damping approach is shown in Tab. 4.5.

**Table 4.5. Mass Damping Approach**

Design Parameters	Sadek et al. 1997	Chey et al. 2013	De Angelis et al. 2012	Reggio & De Angelis 2015
$\alpha$	$0 \div 0.15$	$0 \div 1$	$0.02, -, 1.049$	$0.01 \div 10$
$\xi_{LS}$	$0, -, 0.02, -, 0.05$	$0.05$	$0.02$	$0.02, -, 0.03, -, 0.05$
$\xi_{US}$		$0.05$		$0.02$
$f$	$0.85 \div 1$	$0 \div 1$	$0 \div 1$	$0.1 \div 10$
$\xi_{ISO}$	$0 \div 0.5$	$0 \div 1$	$0.10 \div 0.15$	$0 \div 1$
$\eta_i$			$0.12$	
EDI				$0.1 \div 1$
$f_{opt}$	$0.85 \div 1$	$0.4 \div 1$	$0.42$	$0.1 \div 1$
$\xi_{ISO,opt}$	$0 \div 0.4$	$0.2 \div 1$		$0.05 \div 0.5$
EDI <sub>opt</sub>	$0 \div 0.4$	$0.2 \div 1$		$0.25 \div 1$

#### 4.4.4. Concentrated energy dissipation systems [Murakami et al. 2000, Murakami 2001, Sueoka et al. 2004, Tsuneki et al. 2008-2009]

Some papers, coming from the Japanese research community, also including the designers of important buildings with IIS [Murakami et al. 2000, Murakami 2001, Sueoka et al. 2004, Tsuneki et al. 2008-2009], mainly deal with the IIS as a “concentrated energy dissipation” design problem, and assume the dampers yielding force as the major design parameters for achieving the performance objective of the structural complex (Tab. 4.6).

The main features of the concentrated energy dissipation approach are reported in the paper by [Tsuneki et al. 2009]:

“In a high-rise building employing a middle-story isolated structural system, the product of the inertial force considering the upper structure to be a rigid body and the horizontal displacement is governed by the elastic strain energy accumulated in the laminated rubber bearings, so the ratio of the mass of the upper structure with respect to the total mass above ground ( $R_m$ ) has a big effect on the response reduction effect on the building as a whole.

In general, the high stiffness and resistance of the lower structure is not necessary, while it is possible that the energy is concentrated in the isolation layer if the stiffness of the lower structure is large compared with

the laminated rubber bearings and its resistance can be ensured general elastic behavior. As almost all the seismic energy input into the building is absorbed by the dampers, it is necessary to ensure the energy absorption capability of the dampers at the base isolation. A response prediction analysis was carried out by an artificial seismic motion, in which the input energy equivalent to the major earthquake motion was converted into a velocity value ( $V_D = 150 \text{ cm/s}$ ). And the ratio of the mass of the upper structure to that of the total above-ground mass ( $R_m$ ) is used as a parameter in this analysis. The maximum shear coefficient in the isolation layer ( ${}_m \alpha$ ) and the response shear coefficient at the first story ( ${}_u \alpha$ ) was plotted respectively against the ratio of the damper yield force ( $\alpha'_s$ ) to total above-ground mass, see Fig. 4.20. From this figure it can be seen that if the mass ratio of the upper structure ( $R_m$ ) is about 0.2 or higher, a mass damper effect can be obtained. When the optimum amount of damping is similar to that of base isolation, the optimum amount of damping increased with the mass ratio, while for a mass ratio of 0.3 or higher, the amount is in the range from 0.03 to 0.05.

With high rise buildings employing a middle-story isolated structural system, it is necessary to carry out a time history response analysis to determine the detailed behavior during an earthquake, but [Murakami 2001] proposes response prediction equations for schematic design for use as a guide. The proposed response prediction equations were obtained from energy balance and a characteristic function obtained from modal analysis of the two-mass model, after checking that a multi-mass middle story isolation structure model could be replaced with the equivalent two-mass middle-story isolation structure model. From this response prediction method, it is possible to numerically evaluate the specific effect of the energy input to the building, the mass ratio of the upper structure, the yield force ratio of the dampers, and the period of the isolated structure on the response shear force and relative deformation of the isolation layer, and the base shear coefficient of the lower structure. By comparing this response prediction method with the vibration response analysis results under the major earthquakes for the “Iidabashi First Building, First Hills Iidabashi,” it was found that the predicted values virtually enveloped the analysis values, so the method is effective as a response prediction method for schematic design. Also, from the results it was found that the optimum ratio of the damper yield force ( $\alpha'_s$ ) to the total above-ground weight was about from 0.025 to 0.03, see Fig. 4.21”.

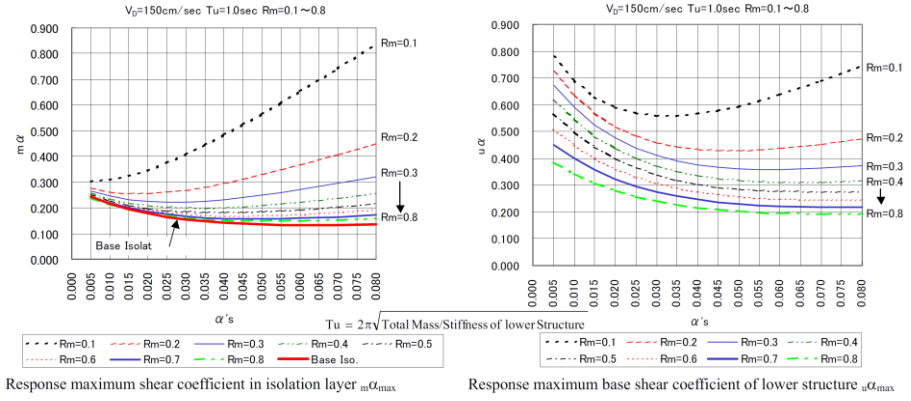


Fig. 4.20. Maximum predicted response value in each part when the velocity conversion value of the energy that contributes to damage is  $V_D = 150 \text{ cm/s}$  [Tsuneki et al. 2009]

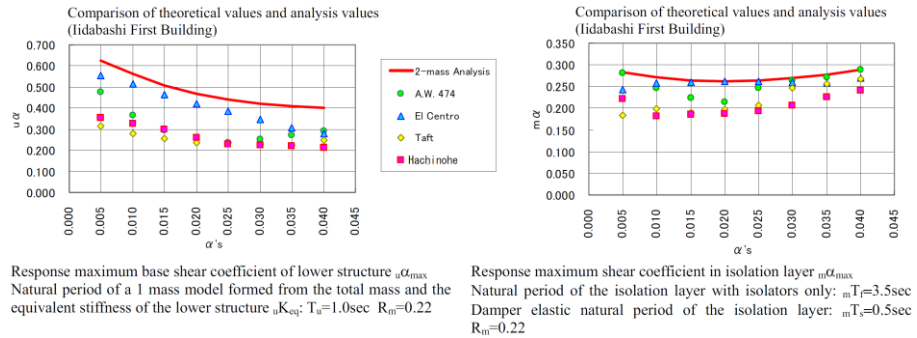


Fig. 4.21. Relationship between quantity of dampers and maximum response values in each part under the major earthquake ( $V_D = 150 \text{ cm/s}$ ) [Tsuneki et al. 2009]

Tabs. 4.6 ÷ 4.8 summarize the values assumed for the three approaches, i.e. isolation, mass damping and energy dissipation, by considering the contributions of all the papers.

**Table 4.6. Global values for the Energy Dissipation Approach**

Design Parameters	Energy Dissipation Approach
$R_m$	$0.1 \div 0.8$
$m \alpha$	$0.1 \div 0.9$
$u \alpha$	$0.1 \div 0.9$
$\alpha_s$	$0.005 \div 0.08$
$\alpha_{s,opt}$	$0.025 \div 0.03$
$m \alpha_{opt}$	$0.15 \div 0.4$
$u \alpha_{opt}$	$0.25 \div 0.58$
<b>CED</b>	$0.7 \div 0.8$

CED = Concentrated Energy dissipation

**Table 4.7. Global values for the Isolation approach**

Design Parameters	Isolation Approach
$r_{US}$	$0 \div 15$
$r_{LS}$	$0 \div 12$
$m_{US} / m_{LS}$	$0 \div 5$
$\alpha$	$0.2 \div 6$
$R_m$	$0.2 \div 1$
$k_{US} / k_{LS}$	$0.1 \div 5$
$k_{US} / k_{ISO}$	$9 \div 100$
$k_{LS} / k_{ISO}$	$18 \div 141$
$T_{ISO}$ [s]	$1 \div 4$
$T_{US}$ [s]	$0.05 \div 0.7$
$T_{LS}$ [s]	$0.05 \div 0.7$
$\omega_{US} / \omega_{ISO}$	$3 \div 40$
$\omega_{LS} / \omega_{ISO}$	$3 \div 40$
$f$	$0.025 \div 0.3$
$\xi_{ISO}$	$0 \div 0.2$
$\xi_{US}$	$0.02$
$\xi_{LS}$	$0.02$

Table 4.8. Global values for the Mass Damping Approach

Design Parameters	Mass Damping Approach
$\alpha$	$0 \div 10$
$\xi_{LS}$	$0 \div 0.05$
$\xi_{US}$	$0.02$
$f$	$0 \div 10$
$\xi_{ISO}$	$0 \div 1$
$\eta_l$	$0.12$
EDI	$0.1 \div 1$
$f_{opt}$	$0.1 \div 1$
$\xi_{ISO,opt}$	$0.05 \div 0.5$
EDI <sub>opt</sub>	$0.25 \div 1$

## 4.5. ANALYTICAL FORMULATIONS IN THE CURRENT LITERATURE

### 4.5.1. Isolation Approach

#### 4.5.1.1. Modal Analysis of the simplified 3DOF IIS model

Considering the 3DOF IIS model, Eqs. (2.245) ÷ (2.247) can be written in matrix form as follows.

$$\mathbf{M}\ddot{\mathbf{v}} + \mathbf{C}\dot{\mathbf{v}} + \mathbf{K}\mathbf{v} = -\mathbf{M}\boldsymbol{\tau}\ddot{u}_g \quad (4.13)$$

where  $\mathbf{v} = \{v_{LS} \quad v_{ISO} \quad v_{US}\}^T$  is the vector of the relative displacement to the ground;  $\boldsymbol{\tau} = \{1 \quad 0 \quad 0\}^T$  is the vector which multiplies the ground acceleration  $\ddot{u}_g$ ; the matrices of mass  $\mathbf{M}$ , of damping  $\mathbf{C}$ , of stiffness  $\mathbf{K}$ , respectively correspond to:

$$\mathbf{M} = \begin{bmatrix} m_{LS} & 0 & 0 \\ m_{ISO} & m_{ISO} & 0 \\ m_{US} & m_{US} & m_{US} \end{bmatrix}; \quad \mathbf{C} = \begin{bmatrix} c_{LS} & -c_{ISO} & 0 \\ 0 & c_{ISO} & -c_{US} \\ 0 & 0 & c_{US} \end{bmatrix}; \quad \mathbf{K} = \begin{bmatrix} k_{LS} & -k_{ISO} & 0 \\ 0 & k_{ISO} & -k_{US} \\ 0 & 0 & k_{US} \end{bmatrix} \quad (4.14)$$

in which  $c_{LS} = 2\xi_{LS}m_{LS}\omega_{LS}$ ,  $c_{US} = 2\xi_{US}m_{US}\omega_{US}$ ,  $c_{ISO} = 2\xi_{ISO}M_{ISO}\omega_{ISO}$  are the damping constants;  $\xi_{LS}$ ,  $\xi_{US}$ ,  $\xi_{ISO}$  are the damping ratios and

$$\omega_{LS} = \sqrt{\frac{k_{LS}}{m_{LS}}}, \quad \omega_{US} = \sqrt{\frac{k_{US}}{m_{US}}}, \quad \omega_{ISO} = \sqrt{\frac{k_{ISO}}{M_{ISO}}} \quad (4.15)$$

the nominal frequencies of the LS, US and ISO.

Solving the eigenvalue problem of Eq. (4.13), the characteristic equation is obtained as follows:

$$\lambda^3 + a\lambda^2 + b\lambda + c = 0 \quad (4.16)$$

where a, b, c are given by:

$$a = -\frac{\omega_{LS}^2(1-R_m)(1-\gamma) + \omega_{ISO}^2(1-R_m\gamma) + \omega_{US}^2(1-R_m)}{(1-R_m)(1-\gamma)} \quad (4.17)$$

$$b = \frac{\omega_{LS}^2\omega_{ISO}^2(1-R_m) + \omega_{LS}^2\omega_{US}^2(1-R_m) + \omega_{ISO}^2\omega_{US}^2}{(1-R_m)(1-\gamma)} \quad (4.18)$$

$$c = -\frac{\omega_{LS}^2\omega_{US}^2\omega_{ISO}^2}{1-\gamma} \quad (4.19)$$

where  $R_m$  is the mass ratio of the isolated mass,  $M_{ISO} = m_{ISO} + m_{US}$ , to the total mass,  $m_{tot} = m_{LS} + m_{ISO} + m_{US}$ , i.e.:

$$R_m = \frac{m_{ISO} + m_{US}}{m_{LS} + m_{ISO} + m_{US}} = \frac{M_{ISO}}{m_{tot}} \quad (4.20)$$

and  $\gamma$  is the mass ratio defined in Chapter 2 (§2.2) for the linear theory developed by Kelly for base-isolated system, i.e.  $\gamma = m/(m_b + m)$ ; in



particular, assuming  $m = m_{US}$  and  $m_b = m_{ISO}$ , the parameter  $\gamma$  assumes the form:

$$\gamma = \frac{m_{US}}{m_{ISO} + m_{US}} = \frac{m_{US}}{M_{ISO}} \quad (4.21)$$

Employing Eqs. (4.20) and (4.21), the  $n$ -th mode shape vector  $\phi_n$  ( $n = 1, 2, 3$ ) is given by:

$$\phi_n = \begin{Bmatrix} \phi_{LSn} \\ \phi_{ISON} \\ \phi_{USn} \end{Bmatrix} = \begin{Bmatrix} 1 \\ \frac{1-R_m}{R_m} \cdot \frac{\omega_{LS}^2 - \omega_n^2}{\omega_{ISO}^2} \\ \frac{1-R_m}{R_m} \cdot \frac{\omega_{LS}^2 - \omega_n^2}{\omega_{US}^2 - (1-\gamma)\omega_n^2} \end{Bmatrix} \quad (4.22)$$

where  $\phi_{LSn}$ ,  $\phi_{ISON}$ ,  $\phi_{USn}$  are the  $n$ -th mode shapes of story drifts of the lower structure, isolation layer and upper structure, respectively (Fig. 4.22).

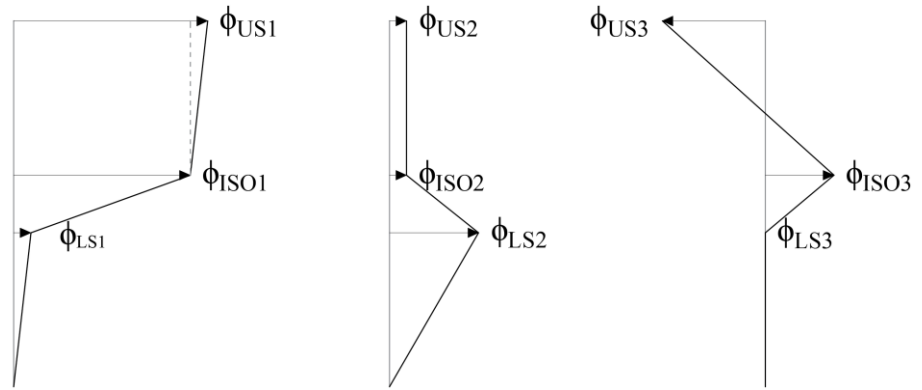


Fig. 4.22. Mode Shapes of the 3DOF IIS model

The fundamental (or isolated) modal natural frequency  $\omega_1$  may be very close to the isolated frequency  $\omega_{ISO}$ , and is well separated from the residual modal natural frequencies if the elastic lateral stiffnesses of the substructure and superstructure are much greater than the effective lateral stiffness of the isolation system.

Defining  $\varepsilon_1 = \omega_{\text{ISO}}^2 / \omega_{\text{LS}}^2$  and  $\varepsilon_2 = \omega_{\text{ISO}}^2 / \omega_{\text{US}}^2$ , and assuming that  $\varepsilon_1$  and  $\varepsilon_2$  are of an order equal to or less than  $10^{-1}$ , the first mode shape of story drifts can be approximated by substituting  $\omega_{\text{ISO}}$  for  $\omega_1$ . Therefore, the first mode shape of story drifts is obtained from Eq. (4.22) as follows:

$$\phi_1 = \begin{Bmatrix} \phi_{\text{LS1}} \\ \phi_{\text{ISO1}} \\ \phi_{\text{US1}} \end{Bmatrix} = \begin{Bmatrix} 1 \\ \frac{1 - R_m}{R_m} \cdot \frac{1 - \varepsilon_1}{\varepsilon_1} \\ \frac{1 - R_m}{R_m} \cdot \frac{\omega_{\text{LS}}^2 (1 - \varepsilon_1)}{\omega_{\text{US}}^2 [1 - (1 - \gamma)\varepsilon_2]} \end{Bmatrix} = \begin{Bmatrix} 1 \\ \frac{1}{\alpha} \cdot \frac{\omega_{\text{LS}}^2}{\omega_{\text{ISO}}^2} \\ \frac{1}{\alpha} \cdot \frac{\omega_{\text{LS}}^2}{\omega_{\text{US}}^2} \end{Bmatrix} \quad (4.23)$$

where  $\alpha$  is the mass ratio of the isolated mass,  $M_{\text{ISO}} = m_{\text{ISO}} + m_{\text{US}}$ , to the lower mass,  $m_{\text{LS}}$ , i.e.:

$$\alpha = \frac{M_{\text{ISO}}}{m_{\text{LS}}} \quad (4.24)$$

and  $\phi_{\text{LS1}}$ ,  $\phi_{\text{ISO1}}$ ,  $\phi_{\text{US1}}$  are the 1<sup>st</sup> mode shapes of story drifts of the lower structure, isolation layer and upper structure, respectively.

Neglecting the high-order terms of  $\omega_{\text{ISO}} / \omega_{\text{LS}}$  and  $\omega_{\text{ISO}} / \omega_{\text{US}}$ , the first modal damping ratio  $\xi_1$  can be obtained based on the classical damping assumption in which the off-diagonal terms of the modal damping matrix are neglected. In particular,  $\xi_1$  is given by:

$$\xi_1 = \frac{\xi_{\text{ISO}}}{1 + 2\alpha \left( \frac{\omega_{\text{ISO}}}{\omega_{\text{LS}}} \right)^2 + 4\gamma^2 \left( \frac{\omega_{\text{ISO}}}{\omega_{\text{US}}} \right)^2} \quad (4.25)$$

and the first modal participation mass ratio  $L_1$  can be determined by:

$$L_1 = \frac{\frac{m_{\text{tot}}}{m_{\text{ISO}}} \left( \frac{\omega_{\text{ISO}}}{\omega_{\text{LS}}} \right)^2 + \frac{m_{\text{LS}}}{m_{\text{ISO}}} \left[ 1 + 2\gamma \left( \frac{\omega_{\text{ISO}}}{\omega_{\text{US}}} \right)^2 \right]}{\frac{m_{\text{tot}}}{m_{\text{ISO}}} \left[ \frac{1}{\alpha} + 2 \left( \frac{\omega_{\text{ISO}}}{\omega_{\text{LS}}} \right)^2 + 2 \frac{\gamma}{\alpha} \left( \frac{\omega_{\text{ISO}}}{\omega_{\text{US}}} \right)^2 \right]} \quad (4.26)$$

From Eq. (4.25), it is seen that the first modal damping ratio may be significantly affected by the masses and stiffnesses of the upper and lower structure.

If the elastic lateral stiffness of the substructure and superstructure is much greater than the effective lateral stiffness of the isolation system, such that  $\omega_{\text{ISO}} / \omega_{\text{LS}}$  and  $\omega_{\text{ISO}} / \omega_{\text{US}}$  are sufficiently small, it is reasonable to assume that the first vibration mode is the isolation mode and the effective damping ratio is equal to the first modal damping ratio.

However, the damping ratios of the structural portions, i.e.  $\xi_{\text{US}}$ ,  $\xi_{\text{LS}}$ , generally differ from the damping ratio of the isolation system  $\xi_{\text{ISO}}$ . Therefore, assuming different values of the damping ratios for the three DOFs, the IIS model is characterized by non-proportional damping.

A *non-classical* or *non-proportional viscous damped system* is characterized by complex-valued natural modes, and does not satisfy the Caughey and O' Kelly identity:  $\mathbf{C}\mathbf{M}^{-1}\mathbf{K} = \mathbf{K}\mathbf{M}^{-1}\mathbf{C}$  [Veletsos & Ventura 1986].

The common design assumption of proportional damping, which leads to real-valued natural modes of vibration identical to the ones of the associated undamped system, and allows for neglecting the off-diagonal terms of the damping matrix  $\mathbf{C}$  (i.e. the Caughey and O' Kelly identity is satisfied) could not be adequate to grasp the actual dynamic behavior of the system.

Furthermore, when  $\mathbf{C}$  is an arbitrary symmetric positive definite matrix, the expansion in terms of the eigenvectors for the undamped system and real modal coordinates does not lead to uncoupled modal equations. In this case, we have to work with an expansion involving complex modal coordinates and complex state eigenvectors [Connor & Laframme 2014]. Therefore, rather than working with second-order equations, it is more

convenient to transform the system provided in Eq. (4.13) to a set of first-order equations which represent the state space formulation, i.e.:

$$\dot{\mathbf{z}}(t) = \mathbf{A}\mathbf{z}(t) + \mathbf{B}_g \ddot{\mathbf{u}}_g(t) \quad (4.27)$$

where the state space matrix  $\mathbf{A}$  ( $2n \times 2n$ ), the input matrix  $\mathbf{B}_g$  ( $2n \times 1$ ) and the state space vector  $\mathbf{z}(t)$  ( $2n \times 1$ ) are given by:

$$\mathbf{A} = \begin{bmatrix} \mathbf{0} & \mathbf{I} \\ -\mathbf{M}^{-1}\mathbf{K} & -\mathbf{M}^{-1}\mathbf{C} \end{bmatrix}_{2n \times 2n} \quad \mathbf{A} = \begin{bmatrix} \mathbf{0} & \mathbf{I} \\ -\mathbf{M}^{-1}\mathbf{K} & -\mathbf{M}^{-1}\mathbf{C} \end{bmatrix}_{2n \times 2n} \quad (4.28)$$

$$\mathbf{B}_g = \begin{Bmatrix} \mathbf{0} \\ -\boldsymbol{\tau} \end{Bmatrix}_{2n \times 1} \quad (4.29)$$

$$\mathbf{z} = \begin{Bmatrix} \mathbf{u} \\ \dot{\mathbf{u}} \end{Bmatrix}_{2n \times 1} \quad (4.30)$$

$\mathbf{I}$  ( $n \times n$ ) the unit matrix.

Considering the absolute displacement with respect to the ground, the matrices  $\mathbf{M}$ ,  $\mathbf{C}$ ,  $\mathbf{K}$  and the vector  $\boldsymbol{\tau}$  respectively correspond to:

$$\mathbf{M} = \begin{bmatrix} m_{LS} & 0 & 0 \\ 0 & m_{ISO} & 0 \\ 0 & 0 & m_{US} \end{bmatrix}; \quad \mathbf{C} = \begin{bmatrix} c_{LS} + c_{ISO} & -c_{ISO} & 0 \\ -c_{ISO} & c_{ISO} + c_{US} & -c_{US} \\ 0 & -c_{US} & c_{US} \end{bmatrix}; \quad (4.31)$$

$$\mathbf{K} = \begin{bmatrix} k_{LS} + k_{ISO} & -k_{ISO} & 0 \\ -k_{ISO} & k_{ISO} + k_{US} & -k_{US} \\ 0 & -k_{US} & k_{US} \end{bmatrix}$$

$$\boldsymbol{\tau} = \{1 \ 1 \ 1\}_{n \times 1}^T$$

Considering the non-classically damped IIS, the eigenvalue problem of Eq. (4.32):

$$\mathbf{A}\mathbf{u}_i = \lambda_i \mathbf{u}_i \quad (4.32)$$

is solved to obtain the  $i$ -th complex eigenvalue,  $\lambda_i$ , and eigenvector,  $\mathbf{u}_i$ . The  $i$ -th frequency and damping ratio are:

$$f_i = 2\pi|\lambda_i| \quad (4.33)$$

$$\eta_i = -\mathbf{Re}(\lambda_i)/|\lambda_i| \quad (4.34)$$

where

$$|\lambda_i| = \sqrt{\mathbf{Re}(\lambda_i)^2 + \mathbf{Im}(\lambda_i)^2} \quad (4.35)$$

is the modulus of the  $i$ -th eigenvalue;  $\mathbf{Re}(\lambda_i)$  and  $\mathbf{Im}(\lambda_i)$  are the real and complex conjugate pair of  $\lambda_i$ .

#### 4.5.1.2. Modal Analysis of the simplified 3DOF IIS model

Considering the 2DOF IIS model, Eqs. (2.248) - (2.249) can be written in the same matrix form as (4.13), in which the  $\mathbf{v}$  and  $\boldsymbol{\tau}$  are:

$$\mathbf{v} = \{v_{LS} \quad v_{ISO}\}^T \text{ and } \boldsymbol{\tau} = \{1 \quad 0\}^T;$$

the matrices of mass  $\mathbf{M}$ , of damping  $\mathbf{C}$ , of stiffness  $\mathbf{K}$ , respectively correspond to:

$$\mathbf{M} = \begin{bmatrix} m_{LS} & 0 \\ M_{ISO} & M_{ISO} \end{bmatrix}; \quad \mathbf{C} = \begin{bmatrix} c_{LS} & -c_{ISO} \\ 0 & c_{ISO} \end{bmatrix}; \quad \mathbf{K} = \begin{bmatrix} k_{LS} & -k_{ISO} \\ 0 & k_{ISO} \end{bmatrix} \quad (4.36)$$

Solving the eigenvalue problem of Eq. (4.13), the characteristic equation is obtained as follows:

$$a\lambda^2 + b\lambda + c = 0 \quad (4.37)$$

where  $a$ ,  $b$ ,  $c$  are given by:

$$a = m_{LS}M_{ISO} \quad (4.38)$$

$$b = -[(m_{LS}k_{ISO}) + M_{ISO}(k_{LS} + k_{ISO})] \quad (4.39)$$

$$c = k_{LS}k_{ISO} \quad (4.40)$$

Therefore, the  $n$ -th mode shape vector  $\phi_n$  ( $n = 1, 2$ ) is given by:

$$\phi_n = \begin{Bmatrix} \phi_{LSn} \\ \phi_{ISO n} \end{Bmatrix} = \begin{Bmatrix} 1 \\ \frac{1}{\alpha} \cdot \frac{\omega_{LS}^2 - \omega_n^2}{\omega_{ISO}^2} \end{Bmatrix} \quad (4.41)$$

A graphical representation of the two mode shapes is provided in Fig. 4.23.

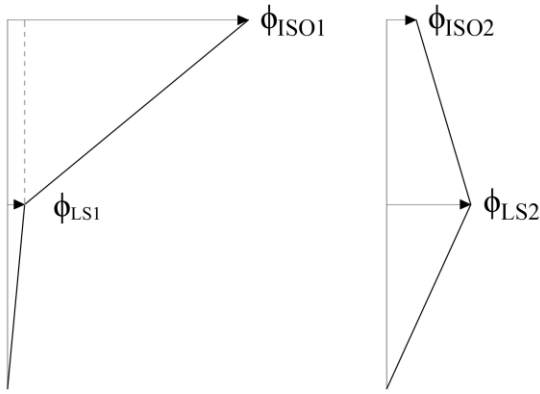


**Fig. 4.23. Mode Shapes of the 3DOF IIS model**

Considering the ratio  $\varepsilon_1 = \omega_{ISO}^2 / \omega_{LS}^2$  of an order equal to or less than  $10^{-1}$ , and  $\omega_1$  approximately equal to  $\omega_{ISO}$ , the first mode shape obtained from Eq. as follows:

$$\phi_1 = \begin{Bmatrix} \phi_{LS1} \\ \phi_{ISO1} \end{Bmatrix} = \begin{Bmatrix} 1 \\ \frac{1}{\alpha} \cdot \frac{1 - \varepsilon_1}{\varepsilon_1} \end{Bmatrix} \cong \begin{Bmatrix} 1 \\ \frac{1}{\alpha} \cdot \frac{\omega_{LS}^2}{\omega_{ISO}^2} \end{Bmatrix} \quad (4.42)$$

Considering the non-classically damped IIS, the eigenvalue problem is the same described in § 4.6.1.1.

***Frequency Response Function (FRF)***

The  $H_{y,j}(i\omega)$  as a frequency response function of  $j$ -th story displacement under sinusoidal excitation:

$$\ddot{y}_g = e^{i\omega t} \quad (4.43)$$

is evaluated as follows:

$$\mathbf{H}_y(i\omega) = -(-\omega^2 \mathbf{M} + i\omega \mathbf{C} + \mathbf{K})^{-1} \mathbf{M} \mathbf{r}, \quad \mathbf{r} = \{1 \quad 1 \quad \dots\}^T \quad (4.44)$$

$$\mathbf{H}_y(i\omega) = \{H_{y,1}(i\omega) \quad H_{y,2}(i\omega) \quad \dots \quad H_{y,j}(i\omega) \quad \dots\}^T \quad (4.45)$$

The  $H_{A,j}(i\omega)$  as a frequency response function of  $j$ -th story absolute acceleration, and  $H_{r,j}(i\omega)$  as that of inter-story drift of the  $j$ -th story are evaluated by  $H_{y,j}(i\omega)$  as follows:

$$H_{A,j}(i\omega) = 1 - \omega^2 H_{y,j}(i\omega) \quad (4.46)$$

$$H_{r,j}(i\omega) = H_{y,j}(i\omega) - H_{y,j-1}(i\omega), \quad H_{r,1}(i\omega) = H_{y,1}(i\omega) \quad (4.47)$$

The  $\sigma_x$  as root-mean-square (RMS) value of a random variable response  $X$  to  $S(\omega)$  as power spectrum ground acceleration is expressed by using the frequency response function  $H_x(i\omega)$  as Eq. (4.48). When the power spectrum  $S(\omega)$  is assumed as white noise which is a constant value for  $\omega$ , the  $\sigma_m/\sigma_n$  as RMS value ratio of random vibration response  $m$  and  $n$  is evaluated by Eq. (4.49).

$$\sigma_x^2 = \int_0^\infty |H_x(i\omega)|^2 S(\omega) d\omega \quad (4.48)$$

$$\sigma_m/\sigma_n = \sqrt{\int_0^\infty |H_m(i\omega)|^2 d\omega / \int_0^\infty |H_n(i\omega)|^2 d\omega} \quad (4.49)$$

### 4.5.2. Mass Damping Approach

#### 4.5.2.1. Approaches of [Sadek et al. 1997], [Miranda et al. 2012], [Chey et al. 2010], [Wang et al. 2017] Approach of [Sadek et al. 1997]

For a SDOF with TMD, the state matrix  $\mathbf{A}$  in terms of the natural frequency and damping ratio ( $\omega_{LS}$  and  $\xi_{LS}$ ) of the structure, and the mass, frequency, and damping ratio ( $\alpha$ ,  $f$  and  $\xi_{ISO}$ ) of the TMD is given as follows.

$$\mathbf{A} = \begin{bmatrix} 0 & 0 & 1 & 0 \\ 0 & 0 & 0 & 1 \\ -\omega_{LS}^2 f^2 & \omega_{LS}^2 f^2 & -2\omega_{LS}\xi_{ISO}f & 2\omega_{LS}\xi_{ISO}f \\ \omega_{LS}^2 \alpha f^2 & -\omega_{LS}^2 (1 + \alpha f^2) & 2\omega_{LS}\xi_{ISO}\alpha f & -2\omega_{LS}(\xi_{ISO}\alpha f + \xi_{LS}) \end{bmatrix} \quad (4.50)$$

The eigenvalue problem  $|\mathbf{A} - \lambda \mathbf{I}|$  results in the following four-order equation:

$$\begin{aligned} & \left( \frac{\lambda}{\omega_{LS}} \right)^4 + [2f\xi_{ISO}(1 + \alpha) + 2\xi_{LS}] \left( \frac{\lambda}{\omega_{LS}} \right)^3 + \\ & + [1 + f^2(1 + \alpha) + 4f\xi_{LS}\xi_{ISO}] \left( \frac{\lambda}{\omega_{LS}} \right)^2 + 2f(\xi_{ISO} + \alpha\xi_{LS}) \left( \frac{\lambda}{\omega_{LS}} \right) + f^2 = 0 \end{aligned} \quad (4.51)$$

The solution of Eq. (4.51) gives the complex eigenvalues of the system matrix, which are in the following form:

$$\lambda_{j,j+1} = \omega_{jj}\xi_{jj} \pm i\omega_{jj}\sqrt{1 - \xi_{jj}^2} \quad (4.52)$$

where  $\lambda_{j,j+1}$  are the pair of conjugate eigenvalues associated with the  $j$ -th vibration mode, which are related to its circular frequency  $\omega_{jj}$  and the modal damping ratio  $\xi_{jj}$ .

The eigenvectors associated with eigenvalues are generally complex entities, and, thus, the vibration modes are non-classically damped.



It is worth noticing that, the eigenvalue in Eq. (4.51) are normalized with respect to the frequency  $\omega_{LS}$ .

It means that the optimal parameters,  $(f_{opt}$  and  $\xi_{ISO,opt}$ ), are independent of the entity of the natural frequency of the main structure.

[Sadek et al 1997] proposed a numerical searching technique for the optimum parameters  $f_{opt}$  and  $\xi_{ISO,opt}$ . In particular, for a given damping ratio  $\xi_{LS}$  and for each mass ratio  $\alpha$ , the values of  $f$  and  $\xi_{ISO}$  are varied, matrix  $\mathbf{A}$  is formed, and its eigenvalues are computed.

The optimum values are obtained for approximately equal damping and frequency ratios of the complex modes, i.e.  $\xi_{11} = \xi_{22}$  and  $\omega_{11} = \omega_{22}$ .

For design purpose, a curve fitting of the data is used for both damped and undamped structures. The formulations introduced in the previous section for the SDOF + TMD system as well as of the MDOF + TMD are recalled for completeness:

$$f_{opt} = \frac{1}{1+\alpha} \left[ 1 - \xi_{LS} \sqrt{\frac{\alpha}{1+\alpha}} \right]; \quad \xi_{ISO,opt} = \frac{\xi_{LS}}{1+\alpha} + \sqrt{\frac{\alpha}{1+\alpha}} \quad (4.10)$$

$$f_{opt} = \frac{1}{1+\alpha}; \quad \xi_{ISO,opt} = \sqrt{\frac{\alpha}{1+\alpha}} \quad (4.11)$$

$$f_{opt} = \frac{1}{1+\alpha\phi} \left[ 1 - \xi_s \sqrt{\frac{\alpha\phi}{1+\alpha\phi}} \right]; \quad \xi_{ISO,opt} = \frac{\xi_s}{1+\alpha\phi} + \sqrt{\frac{\alpha\phi}{1+\alpha\phi}} \quad (4.12)$$

with  $f_{MDOF}(\alpha) = f_{SDOF}(\alpha\phi)$ ,  $\xi_{MDOF}(\alpha) = \xi_{SDOF}(\alpha\phi)$ ,  $\phi$  the amplitude of the first mode of vibration for a unit participation factor computed at the location of TMD.

#### ***Approach of [Moutinho et al. 2012]***

[Moutinho et al. 2012] define the optimum parameters  $f_{opt}$  and  $\xi_{ISO,opt}$  starting from the methodology proposed by [Sadek et a. 1997] (Eqs. (4.50) ÷ (4.52)) but defining different objectives. The optimum parameters are found by selecting the parameters that simultaneously meet the condition  $\xi_{11} = \xi_{22}$  and are in correspondence with the minimum value of the

maximum FRF amplitude associated with the response of the primary mass.

#### ***Approach of [Chey et al. 2010]***

[Chey et al. 2010] define the optimum parameters  $f_{opt}$  and  $\xi_{ISO,opt}$  starting from the formulation proposed by [Sadek et al. 1997] for MDOF, i.e. Eqs. (4.12). On the basis of these optimum parameters, the stiffness and damping constant of the isolation system are defined. Then, the effectiveness of the TMD with large mass ratio is verified by carrying out time history analyses for different suites of earthquake with a statistical method.

#### ***Approach of [Wang et al. 2017]***

Even though Wang et al. belong to the school of the isolation approach, recently they have investigated also the mass damping approach. Wang et al., drawing upon the insight of isolation, consider the 3DOF IIS model, without neglecting the interaction between the upper and lower structures. The authors define the optimum parameters of both the upper structure and the isolation system starting from the results of Sadek et al. in terms of the equality of the damping ratios, i.e.  $\xi_{11} = \xi_{22} = \xi_{33}$  in the complex modes. Based on the proposed objective function with given  $\omega_{LS}$ ,  $\alpha_{ISO}$ ,  $\alpha_{US}$ ,  $\xi_{LS}$ , and  $\xi_{US}$ , the optimum design parameters for  $f_{ISO}$ ,  $f_{US}$  and  $\xi_{ISO}$ , i.e.  $f_{ISO,opt}$ ,  $f_{US,opt}$  and  $\xi_{ISO,opt}$ , respectively, can be determined. The procedure is validated by an experimental campaign with shaking table tests.

#### ***4.5.2.2. Approaches of [De Angelis et al. 2012], [Reggio & De Angelis 2014, 2015]***

[De Angelis et al. 2012] propose the optimal design of structures with large mass ratio TMD, considering a reduced-order SDOF + TMD:

$$\ddot{u}_{LS} + 2\xi_{LS}\omega_{LS}\dot{u}_{LS} + \omega_{LS}^2 u_{LS} = -\ddot{u}_g + \frac{p}{m_{LS}} \quad (4.53)$$

$$\alpha\ddot{u}_{ISO} = -\alpha\ddot{u}_g - \frac{p}{m_{LS}} \quad (4.54)$$

$$\frac{p}{m_{LS}} = \alpha f^2 \omega_{LS}^2 v_{ISO} + 2\alpha f \xi_{ISO} \omega_{LS} \dot{v}_{ISO} \quad (4.55)$$

In order to consider the probabilistic nature of earthquake, ground acceleration is modeled as a Gaussian random process having zero mean and white noise power spectral density.

This choice seems to be adequate to a design phase, although it neglects the dependency on the excitation frequency content.

Being the input process stationary with zero mean, such is assumed to be the system response and the following non-dimensional variables are introduced:

$$U_{LS} = \frac{\sigma_{u_{LS,TMD}}}{\sigma_{u_{LS,RC}}}, \quad V_{ISO} = \frac{\sigma_{v_{ISO,TMD}}}{\sigma_{u_{ISO,RC}}}, \quad A_{LS} = \frac{\sigma_{a_{LS,TMD}}}{\sigma_{a_{LS,RC}}}, \quad A_{ISO} = \frac{\sigma_{a_{ISO,TMD}}}{\sigma_{a_{ISO,RC}}} \quad (4.56)$$

In Eqs. (4.56), standard deviation  $\sigma_{\bullet}$  coincides with the RMS  $\sqrt{E[(\bullet)^2]}$ , where the symbol  $E[\bullet]$  denotes the expected value operator.

#### *Optimization*

An optimization problem was defined which consists in minimizing the RMS ratio  $U_{LS}$  of the main structure displacement with respect to  $f$ . The equation

$$\frac{\partial U_{LS}(f)}{\partial f} = 0 \quad (4.57)$$

was solved through a numerical search algorithm.

It is worth noticing that the parameter  $\xi_{ISO}$  is here assumed constant for implementing high damping rubber bearing in the isolation interface. In fact, these devices are characterized by equivalent damping ratios in the range of 0.1 ÷ 0.15 for a target shear strain of 100% ÷ 150%. For this reason, the damping ratio  $\xi_{ISO}$  is fixed to obtain a first modal complex damping ratio equal to 0.12.

In addition, in order to compare the response of the uncontrolled (RC) and controlled (TMD) configurations, the frequency response function  $H_{u_{LS}}(\rho)$  of the main structure displacement with respect to ground acceleration is derived as follows.

$$H_{u_{LS,RC}}(\rho) = -\frac{1}{1-\rho^2 + \frac{2i\rho\xi_{LS}}{\sqrt{1+\alpha}}} \quad (4.58)$$

$$H_{u_{LS,TMD}}(\rho) = -\frac{C_0(\rho)}{1+\alpha - \rho^2 C_0(\omega) + 2i\rho\xi_{LS}\sqrt{1+\alpha}} \quad (4.59)$$

where

is the ratio between the input frequency and the natural frequency of the system in the RC configuration

$$C_0(\rho) = 1 + \alpha \frac{f^2(1+\alpha) + 2i\rho f\xi_{ISO}\sqrt{1+\alpha}}{f^2(1+\alpha) - \rho^2 + 2i\rho f\xi_{ISO}\sqrt{1+\alpha}} \quad (4.60)$$

[Reggio & De Angelis 2014, 2015] propose an optimal energy-based seismic design of non-conventional TMD implemented via inter-story isolation.

The probabilistic nature of seismic excitation is taken into account by modeling the ground acceleration as a stationary Gaussian stochastic process with zero mean and white noise power spectral density.

Writing the equations of motion (4.53) ÷ (4.55) in the first-order state space form (4.27), and assuming a zero mean stationary input process and zero initial conditions, response  $\mathbf{z}(t)$  is in turn a zero mean stationary process whose complete description is given by its covariance matrix  $\mathbf{G}_{zz} = E[\mathbf{z}\mathbf{z}^T]$  which satisfies the following differential equation

$$\dot{\mathbf{G}}_{zz} = \mathbf{A}\mathbf{G}_{zz} + \mathbf{G}_{zz}\mathbf{A}^T + 2\pi\mathbf{S}_0\mathbf{B}\mathbf{B}^T \quad (4.61)$$

which however reduces to an algebraic equation

$$\mathbf{A}\mathbf{G}_{zz} + \mathbf{G}_{zz}\mathbf{A}^T + 2\pi\mathbf{S}_0\mathbf{B}\mathbf{B}^T = \mathbf{0} \quad (4.62)$$

When  $\dot{\mathbf{G}}_{zz} = \mathbf{0}$  due to the stationarity of  $\mathbf{z}(t)$ . Eq. (4.62) is in the form of a Lyapunov equation and can be solved numerically to determine  $\mathbf{G}_{zz}$ .

#### *Energy balance*

The equation of relative energy balance [24], derived by considering one DOF at a time, is used to characterize the dynamic behavior of the reduced-order two-DOF model from an energy-based point of view.

The equation of motion of the primary oscillator, Equation (1a), is first considered. The equation of relative energy balance is obtained by multiplying both members by  $\mathbf{P} \mathbf{u}_1$ , the velocity of the primary oscillator relative to ground, and then integrating over time, yielding

$$E_{k,LS}(t) + E_{d,LS}(t) + E_{e,LS}(t) = E_{i,LS}(t) + E_f(t) \quad (4.63)$$

Where  $E_{k,LS}(t)$  is the relative kinetic energy;  $E_{d,LS}(t)$  is the energy dissipated by viscous damping;  $E_{e,LS}(t)$  is the elastic strain energy;  $E_{i,LS}(t)$  is the relative input energy; and  $E_f(t)$  is the energy flowing from the secondary to the primary oscillator through the isolation system.

Being the design input a stochastic process, Eq. (4.63) can be formulated in terms of expected values as

$$E[E_{k,LS}] + E[E_{d,LS}] + E[E_{e,LS}] = E[E_{i,LS}] + E[E_f] \quad (4.64)$$

In a time increment  $\Delta t$ , Eq. (4.64) is given for the energy increments as

$$E[\Delta E_{d,LS}] - E[\Delta E_f] = E[\Delta E_{i,LS}] \quad (4.65)$$

because  $E[\Delta E_{k,LS}] - E[\Delta E_{e,LS}] = 0$  due to the conservation of mechanical energy.

The equation of motion of the secondary oscillator, Eq.(4.54), is subsequently considered. By multiplying both members by the velocity  $\dot{\mathbf{u}}_{ISO}$  of the secondary oscillator relative to ground

$$\alpha \ddot{u}_{\text{ISO}} \dot{u}_{\text{ISO}} = -\alpha \ddot{u}_g \dot{u}_{\text{ISO}} - \frac{p}{m_{\text{LS}}} \dot{u}_{\text{ISO}} \quad (4.66)$$

rewriting Eq. (4.66) in the form

$$\alpha \ddot{u}_{\text{ISO}} \dot{u}_{\text{ISO}} = -\alpha \ddot{u}_g \dot{u}_{\text{ISO}} - \frac{p}{m_{\text{LS}}} \dot{u}_{\text{LS}} - \frac{p}{m_{\text{LS}}} \dot{v}_{\text{ISO}} \quad (4.67)$$

and integrating over time, the equation of relative energy balance is obtained as

$$E_{k,\text{ISO}}(t) = E_{i,\text{ISO}}(t) - E_f(t) - E_{d,\text{ISO}}(t) - E_{e,\text{ISO}}(t) \quad (4.68)$$

where  $E_{k,\text{ISO}}(t)$  is the relative kinetic energy;  $E_{i,\text{ISO}}(t)$  is the relative input energy;  $E_{e,\text{ISO}}(t)$  is the elastic strain energy;  $E_{d,\text{ISO}}(t)$  is the energy dissipated by viscous damping and  $E_f(t)$  is the energy flowing from the secondary to the primary oscillator as in Eq. (4.64). By formulating Eq. (4.68) in stochastic terms

$$E[E_{k,\text{ISO}}] = E[E_{i,\text{ISO}}] - E[E_f] - E[E_{d,\text{ISO}}] - E[E_{e,\text{ISO}}] \quad (4.69)$$

and considering the energy increments corresponding to a time increment  $\Delta t$ , it follows:

$$E[\Delta E_{d,\text{ISO}}] + E[\Delta E_f] = E[\Delta E_{i,\text{ISO}}] \quad (4.70)$$

as  $E[\Delta E_{k,\text{ISO}}] + E[\Delta E_{e,\text{ISO}}] = 0$  consistently with the conservation of mechanical energy.

#### *Optimization problem*

Within the set of parameters that govern the response of the reduced-order two-DOF model, mass ratio  $\alpha$  and dynamic properties  $\omega_{\text{LS}}$  and  $\xi_{\text{LS}}$  are known data, depending on the properties of the structure provided with inter-story isolation, while frequency ratio  $f$  and damping ratio  $\xi_{\text{ISO}}$

are the design parameters of the isolation system, to be determined through an optimization problem.

An energy-based approach to the optimization problem is here proposed as it can deal, in a synthetic and effective way, with the different response quantities influenced by inter-story isolation.

With the aim of achieving the global protection of both the structural portions separated by the isolation system, or, in other words, of reducing the seismic response of both the substructure and the isolated superstructure in the meantime, the following energy performance index, named *Energy Dissipation Index* (EDI)

$$EDI = \frac{E[\Delta E_{d,ISO}]}{E[\Delta E_{i,LS}] + E[\Delta E_{i,ISO}]} \quad (4.71)$$

is defined. Referring to the stochastic relative energy balance, it represents the ratio, in terms of expected values, between the incremental energy dissipated in the isolation system and the incremental input energy globally transferred to the two-DOF model in a time increment  $\Delta t$ . The former is given by

$$E[\Delta E_{d,ISO}] = 2\alpha f_{ISO} \omega_{LS} E[(\dot{v}_{ISO})^2] \Delta t \quad (4.72)$$

while the latter is computed by substituting Eqs. (4.65) and (4.70) as

$$\begin{aligned} E[\Delta E_{i,LS}] + E[\Delta E_{i,ISO}] &= E[E_{d,LS}] + E[E_{d,ISO}] = \\ &= 2\xi_{LS} \omega_{LS} E[(\dot{u}_{LS})^2] \Delta t + 2\alpha f_{ISO} \omega_{LS} E[(\dot{v}_{ISO})^2] \Delta t \end{aligned} \quad (4.73)$$

By virtue of the zero mean input assumption, the expected values  $E[(\dot{u}_{LS})^2]$  and  $E[(\dot{v}_{ISO})^2]$  in Eqs. (4.72) and (4.73) are equal to the variances  $\sigma_{u_{LS}}^2$  and  $\sigma_{v_{ISO}}^2$  of velocities  $\dot{u}_{LS}$  and  $\dot{v}_{ISO}$ , respectively.

Variances  $\sigma_{u_{LS}}^2$  and  $\sigma_{v_{ISO}}^2$  are derived from the covariance matrix  $\mathbf{G}_{zz}$ , which is determined by solving Eq. (4.62).

A single-objective optimization problem is then formulated by requiring the objective function, or EDI, to be maximized over the space of the design parameters ( $f$ ,  $\xi_{\text{ISO}}$ ):

$$\text{find } \max_{f, \xi_{\text{ISO}}} [\text{EDI}(f, \xi_{\text{ISO}})] \quad \text{subject to } f > 0 \quad \text{and} \quad 0.0 \leq \xi_{\text{ISO}} \leq 1.0 \quad (4.74)$$

The maximum value  $\text{EDI}_{\text{max}}$  and the corresponding optimal values  $f_{\text{opt}}$  and  $\xi_{\text{ISO, opt}}$  of the design parameters are found through a numerical search algorithm, with  $f$  and  $\xi_{\text{ISO}}$  spanning their ranges with increments of  $10^{-4}$  to reach the desired accuracy. The optimal design parameters  $f_{\text{opt}}$  and  $\xi_{\text{ISO, opt}}$  are hence used to determine the engineering design parameters of the isolation system, the stiffness  $k_{\text{ISO, opt}}$  and the damping  $c_{\text{ISO, opt}}$  coefficients:

$$k_{\text{ISO, opt}} = M_{\text{ISO}} f_{\text{opt}}^2 \omega_{\text{LS}}^2 \quad (4.75)$$

$$c_{\text{ISO, opt}} = 2\xi_{\text{ISO, opt}} \sqrt{M_{\text{ISO}} k_{\text{ISO, opt}}} \quad (4.76)$$

### 4.5.3. Concentrated Energy Dissipation

#### 4.5.3.1. Energy Input Concept

Considering a single-mass oscillatory system subjected to uni-directional horizontal ground motion, the equation of motion is expressed as follows [Akiyama 1985].

$$M\ddot{y} + C\dot{y} + F(y) = F_e \quad (4.77)$$

where  $M$  is the mass;  $C\dot{y}$  the damping force;  $F(y)$  the restoring force,  $F_e = -M\ddot{u}_g$  the seismic force, with  $\ddot{u}_g$  the ground acceleration;  $y$  the displacement of the mass relative to the ground.

Multiplied by  $dy = \dot{y}dt$  on both sides, and integrated over the entire duration of an earthquake,  $t_0$ , Eq. (4.77) assumes the following form:

$$M \int_0^{t_0} \ddot{y} \dot{y} dt + C \int_0^{t_0} \dot{y}^2 dt + \int_0^{t_0} F(y) \dot{y} dt = \int_0^{t_0} F_e \dot{y} dt \quad (4.78)$$



where

$\int_0^{t_0} F_e \dot{y} dt = E$  represents the total amount of energy exerted by an earthquake, namely: input energy;

$C \int_0^{t_0} \dot{y}^2 dt = W_h$  expresses the energy consumed by the damping mechanism;

$M \int_0^{t_0} \ddot{y} dt = M \dot{y}_{t=t_0}^2 / 2$  expresses the kinetic energy at the instant when the motion vanishes;

$\int_0^{t_0} F(y) \dot{y} dt$  expresses the strain energy deposited in the spring system, which consists of cumulative plastic energy,  $W_p$ , and elastic strain energy at the instant when the earthquake motion fades away.

The kinetic energy and the elastic strain energy constitute the elastic vibrational energy,  $W_e$ .

Therefore, Eq. (4.78) can be rewritten as follows.

$$W_E + W_p + W_h = E \quad (4.79)$$

The elastic vibrational energy  $W_E$  has a range of

$$0 \leq W_E \leq \frac{Q_Y}{\delta_Y} \quad (4.80)$$

with  $Q_Y$  and  $\delta_Y$  respectively corresponding to the horizontal force and the displacement at the elastic limit.

$W_p$  is the accumulated effect of the plastic deformation of the spring system and it is defined as the damage to the structure to an earthquake.

Akiyama considers the assumption of Housner to define the elastic-plastic vibrational systems:

$$W_E + W_p \leq E_H \quad (4.81)$$

where

$E_H = MV_{\max}^2 / 2$  is the energy input attributable to damage;  
 $V_{\max}$  is the maximum velocity response of the elastic systems (velocity response spectrum)

Denoting

$$W_E + W_P = E_D \quad (4.82)$$

being  $E_D$  the energy input attributable to damage, the following relation holds, since  $E_H$  represent the maximum vibration energy during an earthquake:

$$E_D \leq E_H \quad (4.83)$$

Observing Eqs. (4.79) and (4.82), it is possible to notice that in an undamped system the energy  $W_h$  is null and, consequently,  $E$  is equal to  $E_D$ ; instead in a damped system,

$$E_D + W_h = E \quad (4.84)$$

and

$$W_E + W_P = E \frac{1}{\left(1 + 3\xi_s + 1.2\sqrt{\xi_s}\right)^2} \quad (4.85)$$

where

$1/\left(1 + 3\xi_s + 1.2\sqrt{\xi_s}\right)$  is a coefficient obtained by comparing the input energies  $E$  and  $E_D$  as a function of the period  $T$  of the structure under El Centro input motion, and by considering a damped system with elastic-perfectly plastic restoring force characteristics;  
 $\xi_s$  is the structural damping ratio.

Therefore, the energy absorption due to miscellaneous damping is

$$W_h = E - E_D \quad (4.86)$$

A seismic input can be described in terms of pseudo-velocity converted from the total energy exerted by an earthquake,  $V_E$ . Therefore, the equivalent velocity is defined as follows

$$V_E = \sqrt{\frac{2E}{M}} \quad (4.87)$$

In the same manner the equivalent velocity that contributes to the damage is defined as follows.

$$V_D = \sqrt{\frac{2E_D}{M}} \quad (4.88)$$

According to Eqs. (4.85), (4.87) and (4.88), the ratio between the equivalent velocity that contributes to the damage,  $V_D$ , and the equivalent input velocity,  $V_E$ , is defined as

$$\frac{V_D}{V_E} = \frac{1}{(1 + 3\xi_s + 1.2\sqrt{\xi_s})} \quad (4.89)$$

Varying the damping ratio  $h$  in the range of  $0.02 \div 0.03$ , and substituting these value into Eq. (4.89), the equivalent velocity that contributes to the damage assumes the following values.

$$\xi_s = 0.02 \rightarrow V_D = 0.81V_E$$

$$\xi_s = 0.03 \rightarrow V_D = 0.77V_E$$

An energy spectrum can be considered to check the ultimate strength of structures against the earthquake motion.

The energy spectrum, represented by the  $V_E - T$  relationship, is built considering one-mass system with 10% of damping constant [Akiyama 1985, 1988].

A design energy spectrum can be simply expressed by two line segments which envelop the energy spectrum, as can be seen in Fig. 4.24. One is the line that represents the energy input in the range of the shorter natural periods, which must go through the origin of the  $V_E - T$  diagram. The other is the line for greater natural period, which is parallel to the  $T$ -axis. The two lines are expressed as follows [Akiyama 1994]:

$$\begin{aligned} &\text{for } T \leq T_G \quad (\text{shorter period range}) \\ &V_E = \frac{V_{EM} T}{T_G} \end{aligned} \quad (4.90)$$

$$\begin{aligned} &\text{for } T > T_G \quad (\text{longer period range}) \\ &V_E = V_{EM} \end{aligned} \quad (4.91)$$

where

- $T_G$  is the transient period which separates the range of period;
- $V_{EM}$  is the level of  $V_E$  in the longer period range;
- $T$  is the fundamental natural period in the elastic range.

Considering the elongation of substantial period of vibration due to plastification of structure, the energy spectrum for design use must be modified by introducing a magnification factor  $a_s$  as follows.

$$V_E = a_s \frac{V_{EM} T}{T_G} \quad (4.92)$$

The value of  $a_s$  depends on the restoring force characteristics and the extent of plastification of the structure and lies in the range of 1.2 to 1.5 for practical structures.

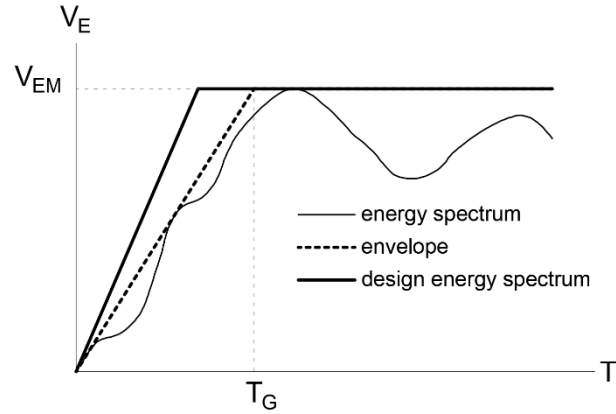


Fig. 4.24. Energy spectrum

For design purpose, the  $V_E - T$  curve can be built as a function of the soil class (Fig. 4.25). In the Japanese building code the ground is classified in four categories, going from the Class-I for ground consisting of bedrock to Class-IV for the softest soil. The values of the ground period  $T_G$  and of the pseudo-velocity  $V_E$  are reported as follows.

$T_G = 0.4 \text{ s},$	$V_E = 120 \text{ cm/s}$	for Class-I ground,
$T_G = 0.6 \text{ s},$	$V_E = 150 \text{ cm/s}$	for Class-II ground,
$T_G = 0.8 \text{ s},$	$V_E = 200 \text{ cm/s}$	for Class-III ground,
$T_G = 1.0 \text{ s},$	$V_E = 250 \text{ cm/s}$	for Class-IV ground.

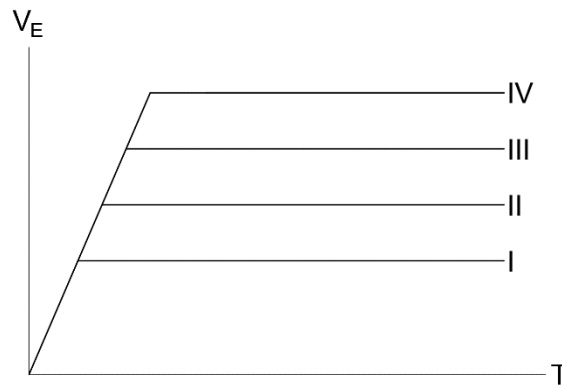


Fig. 4.25. Forms of the  $V_E - T$  relationships

In general, for a preliminary analysis, it is possible to choose the following values for the equivalent velocities:

$$\begin{aligned} V_E &= 200 \text{ cm/s} \\ V_D &= 150 \text{ cm/s} \end{aligned} \quad (4.93)$$

Therefore, the equivalent velocity ratio is equal to

$$\frac{V_D}{V_E} = 0.75 \quad (4.94)$$

#### 4.5.3.1. Energy Balance concept in seismic isolated structures

In isolated structures, most of the seismic energy input is absorbed by isolators and dampers installed in the isolation story.

In practical design, the most fundamental issue is related to the structural characteristics of the isolation story, which are summarized as follows [Yamaguchi et al. 1993].

- 1) The stiffness of isolators can be expressed by the first natural period  $T_f$  of the building, assuming that the horizontal load is supported by isolators only;
- 2) The damping characteristics can be expressed by the coefficient of the yield shear force of dampers  $\alpha_s$ , which is equal to ratio of the yield strength of the damper to weight of the upper stories;
- 3) The deformation limit of isolators and dampers  $\delta_{\max}$ .

Considering the non-linear restoring force characteristics of isolators without hysteresis loop and the perfect elastic-plastic characteristics of the dampers, the energy stored by the isolation system is shown in Fig. 4.26.

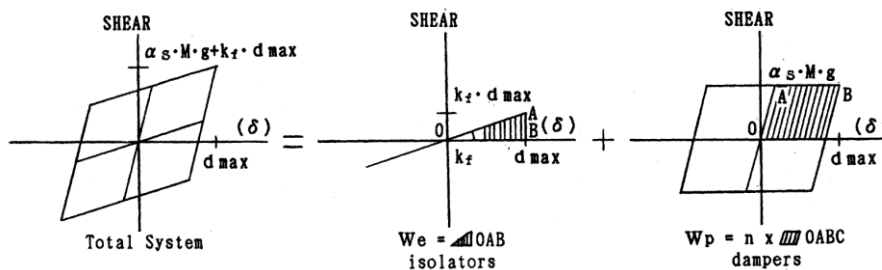


Fig. 4.26. Energy stored by the isolation system [Yamaguchi et al. 1993]

**BIS**

According to the Recommendation for the Design of Base-Isolated Buildings of the AIJ's subcommittee, the energy stored by the isolation story is equal to the sum of the elastic energy stored by isolators,  $W_E$ , and the accumulated energy stored by dampers,  $W_P$ , i.e.:

$$W_E = \frac{K_f \delta_{\max}^2}{2} = \frac{4\pi^2 M}{2T_f^2} \delta_{\max}^2 \quad (4.95)$$

$$W_P = \kappa \alpha_s M g_m \delta_{\max} \quad (4.96)$$

where  $\kappa$  is a damage concentration index, which depends on the characteristics of the isolation story and input seismic wave. Based on the results of the parametric dynamic analysis, [Akiyama 1989, 1992] proposed  $\kappa = 8$ .

The seismic capacity of the isolation interface in terms of equivalent velocity converted from the accumulated energy is:

$$V_D = \sqrt{V_{De}^2 + V_{Dp}^2} \quad (4.97)$$

where  $V_{De}$  and  $V_{Dp}$  represent the equivalent velocity of the energy stored by the isolators and dampers, respectively, i.e.:

$$V_{De} = \sqrt{\frac{2W_E}{M}} = \frac{2\pi}{T_f} \delta_{\max} \quad (4.98)$$

$$V_{Dp} = \sqrt{\frac{2W_P}{M}} \cong 4\sqrt{\alpha_s g \delta_{\max}} \quad (4.99)$$

Therefore, from Eq. (4.88) can be derived the energy attributable to damage as follows.

$$E_D = \frac{M V_D^2}{2} \quad (4.100)$$

### IIS

In a BI structure isolators and dampers are installed at the base of the building. The isolation and damping devices alone absorbed the seismic input energy while the structure does not play a part in energy dissipation. In a IIS structure not only the isolation interface but also the lower structure contribute to the energy dissipation.

In this section the study of [Murakami et al. 2001, Murakami & Sueoka 2004] is provided to define the energy balance concept for the intermediate isolation systems.

#### 1D-2DOF IIS model

Starting from a MDOF IIS model, in order to predict the response of a mid-story isolated building a reduced-order 2DOF IIS model is considered. A graphical representation of the MDOF and 2DOF IIS models is shown in Fig. 4.27.

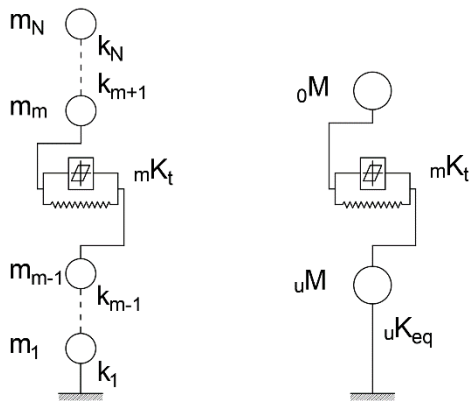


Fig.4.27. 1D MDOF IIS vs. 1D 2DOF IIS

In the MDOF IIS model, the total number of degrees of freedom is  $N$ ; the dofs of the lower structures are  $m - 1$  and the dofs of the upper structure are  $N - m$ , with  $m$  the dof of the isolation story.

In the reduced-order 2DOF IIS model the upper lumped-mass represents the total mass of the isolated US,  ${}_0M$ ; the lower lumped-mass represent the total lower mass,  ${}_uM$ . The equivalent stiffness of the LS is obtained taking into account the mass total mass,  $M_{TOT} = {}_0M + {}_uM$  and the first natural period of the MDOF LS,  $T_u$ , considered as a standalone structure.



$${}_u k_{eq} = \frac{4\pi^2 M_{TOT}}{T_u^2} \quad (4.101)$$

The stiffness of the isolation system is equal to the sum of the stiffness of isolators and dampers, i.e.:

$${}_m K_t = {}_m K_f + {}_m K_s \quad (4.102)$$

With the subscripts 0, m, u, are generally indicated the upper structure, the mid-story isolation and the lower structure, respectively.

The same restoring force characteristics for isolators and dampers of BIS are assumed for the IIS structure, see Fig. 4.28.

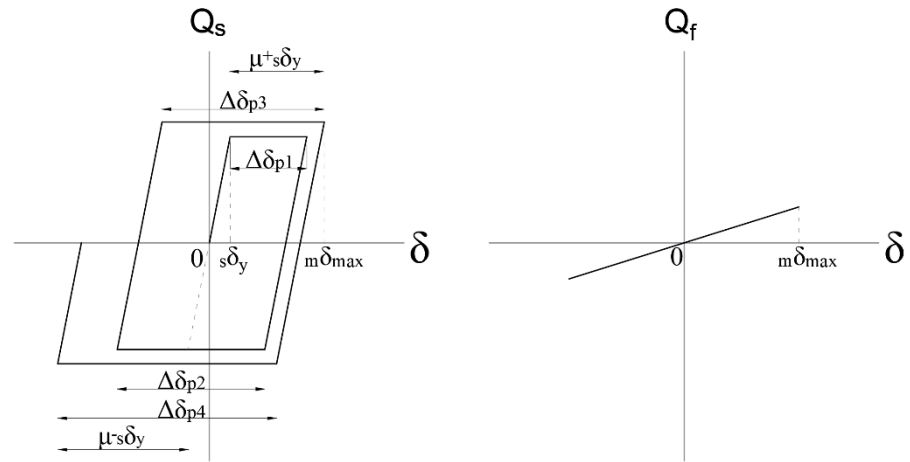


Fig.4.28. Restoring force characteristics: (a) Dampers, (b) Rubber Bearings

The energy balance in Eq. (4.79) can be rewritten as:

$$({}_0 W_E + {}_0 W_P + {}_0 W_h) + ({}_m W_E + {}_m W_P + {}_m W_h) + ({}_u W_E + {}_u W_P + {}_u W_h) = E \quad (4.103)$$

Furthermore, the aliquots which take part in the energy balance are: the elastic strain energy of the isolation system,  ${}_m W_E$ , and of the lower structure,  ${}_u W_E$ ; the cumulative inelastic strain energy of the isolation system,  ${}_m W_P$ ; the energy absorption due to miscellaneous damping of the lower structure,  ${}_u W_h$ . Therefore, Eq. (4.103) assumes the form:

$${}_mW_E + {}_mW_P + {}_uW_E + {}_uW_h = E \quad (4.104)$$

Therefore, the total elastic strain energy,  $W_E$ , the total cumulative inelastic strain energy,  $W_P$ , and the total energy absorption due to miscellaneous damping,  $W_h$ , are respectively equal to:

$$W_E = {}_mW_E + {}_uW_E \quad (4.105)$$

$$W_P = {}_mW_P \quad (4.106)$$

$$W_h = {}_uW_h \quad (4.107)$$

*Total cumulative inelastic strain energy*

The cumulative inelastic strain energy  ${}_mW_P$  is equal to:

$${}_mW_P = Q_y {}_s\delta_p \quad (4.108)$$

where

$Q_y$  is the yield strength considering of dampers;

${}_s\delta_p$  is the cumulative inelastic deformation of dampers.

The cumulative inelastic deformation  ${}_s\delta_p$  is equal to the sum of the  $i$ -th positive and  $j$ -th negative plastic deformation contributes, i.e.  $\Delta\delta_{pi}^+$  and  $\Delta\delta_{pj}^-$ , respectively (Fig. 4.28a):

$${}_s\delta_p = \sum_{i=1}^n \Delta\delta_{pi}^+ + \sum_{j=1}^m \Delta\delta_{pj}^- = {}_s\delta_p^+ + {}_s\delta_p^- \quad (4.109)$$

where the total positive and negative cumulative plastic deformations,  ${}_s\delta_p^+$  and  ${}_s\delta_p^-$ , are respectively equal to:

$${}_s\delta_p^+ = \sum_{i=1}^n \Delta\delta_{pi}^+, \quad {}_s\delta_p^- = \sum_{j=1}^m \Delta\delta_{pj}^- \quad (4.110)$$

The cumulative inelastic deformation  ${}_s\delta_p$  can be expressed in terms of the yield displacement of dampers,  ${}_s\delta_y$ , by introducing the cumulative inelastic deformation ratio,  ${}_m\eta$ , being  ${}_m\eta$  the ratio of  ${}_s\delta_p$  to  ${}_s\delta_y$ , i.e.:

$${}_m\eta = \frac{{}_s\delta_p}{{}_s\delta_y} \quad (4.111)$$

Defining the kinematic ductility  ${}_m\mu_{\max}$  as:

$${}_m\mu_{\max} = \frac{{}_m\delta_{\max} - {}_s\delta_y}{{}_s\delta_y} \quad (4.112)$$

in which  ${}_m\delta_{\max}$  is the maximum deformation of the isolation system, the relationship between the ratio  ${}_m\eta$  and the ductility  ${}_m\mu_{\max}$  can be expressed as:

$${}_m\eta = \kappa {}_m\mu_{\max} \quad (4.113)$$

where  $\kappa$  it is still assumed equal to 8, according to the value proposed by [Akiyama 1989, 1992].

Therefore, the displacement  ${}_m\delta_{\max}$  is given by:

$${}_m\delta_{\max} = (1 + {}_m\mu_{\max}) {}_s\delta_y = \left(1 + \frac{{}_m\eta}{\kappa}\right) {}_s\delta_y \quad (4.114)$$

Substituting Eq. (4.111) into Eq. (4.108), the energy  ${}_mW_p$  can be rewritten as:

$${}_mW_p = {}_m\eta Q_y {}_s\delta_y = {}_m\eta \frac{Q_y^2}{{}_mK_t} \quad (4.115)$$

where  ${}_s\delta_y = Q_y / {}_mK_t$ .

Introducing the yield shear coefficient of dampers  $\alpha_s$ , being  $\alpha_s$  the ratio of the yield strength,  $Q_y$ , to the total weight of the upper structure,  ${}_uMg$ , i.e.

$$\alpha_s = \frac{Q_y}{{}_0Mg} = \frac{Q_y}{R_m M_{TOT} g} \quad (4.116)$$

where  $R_m$  is the mass ratio of the upper structure to the whole structure, i.e.:

$$R_m = \frac{{}_0M}{{}_0M + {}_uM} = \frac{{}_0M}{M_{TOT}} \quad (4.117)$$

the expression (4.115) becomes:

$${}_mW_p = {}_m\eta \frac{\alpha_s^2 R_m^2 M_{TOT}^2 g^2}{{}_mK_t} \quad (4.118)$$

Then, from Eq. (4.101) recalling the total mass  $M_{TOT}$  can be written as:

$$M_{TOT} = \frac{T_u^2 {}_uK_{eq}}{4\pi^2} \quad (4.119)$$

Eq. (4.118) becomes:

$${}_mW_p = {}_m\eta \frac{M_{TOT} g^2 T_u^2 \alpha_s^2}{{}_mK_t} {}_m c \quad (4.120)$$

where  ${}_m c = \frac{{}_uK_{eq} R_m^2}{{}_mK_t}$ .

Finally, substituting Eq. (4.114), expressed in terms of  ${}_m\eta$ , into Eq. (4.120), and recalling Eq. (4.106), the total cumulative inelastic strain energy,  $W_p$ , assumes the form:

$$W_P = {}_m W_P = \left( \kappa \frac{\delta_{\max}}{\delta_y} - 1 \right) \frac{M_{\text{TOT}} g^2 T_u^2 {}_u K_{\text{eq}} \alpha_s'^2}{4\pi^2 {}_m K} \quad (4.121)$$

*Total elastic strain energy*

The elastic strain energy of isolators  ${}_m W_E$  is given by (Fig. 4.28b):

$${}_m W_E = \frac{{}_m K_f {}_m \delta_{\max}^2}{2} \quad (4.122)$$

The elastic strain energy of dampers  ${}_u W_E$  is given by (Fig. 4.28a):

$${}_u W_E = \frac{{}_u K_{\text{eq}} {}_u \delta_{\text{eq}}^2}{2} = \frac{{}_u K_{\text{eq}} ({}_u \delta_w + {}_u \delta_f)^2}{2} \quad (4.123)$$

in which

$${}_u \delta_w = \psi {}_s \delta_y \quad (4.124)$$

$${}_u \delta_f = \zeta {}_m \delta_{\max} \quad (4.125)$$

$$\psi = \frac{{}_u \mathbf{u}_w}{{}_m \mathbf{u}_w - {}_u \mathbf{u}_w} \quad (4.126)$$

$$\zeta = \sqrt{\frac{(\beta_{f1} \cdot {}_u \mathbf{u}_{f1})^2 + (\beta_{f2} \cdot {}_u \mathbf{u}_{f2})^2 \left( \frac{T_{f2}}{T_{f1}} \right)^2}{[\beta_{f1} ({}_m \mathbf{u}_{f1} - {}_u \mathbf{u}_{f1})]^2 + [\beta_{f2} ({}_m \mathbf{u}_{f2} - {}_u \mathbf{u}_{f2})]^2 \left( \frac{T_{f2}}{T_{f1}} \right)^2}} \quad (4.127)$$

where

${}_u \delta_w$  is the relative modal displacement of the lower structure, considering both isolators and dampers under elastic behavior;

${}_u \delta_f$  is the relative modal displacement of the lower structure, considering only isolators;

$\psi, \zeta$  are drift ratios;

${}_m \mathbf{u}_w, {}_u \mathbf{u}_w$  are the first modal displacements considering both isolators and dampers under elastic behavior;

${}_m \mathbf{u}_f, {}_u \mathbf{u}_f, \beta_f$  are the modal displacements and participation factors of the two modes of vibration, considering only isolators

Solving the square of binomial and considering Eqs. (4.124) and (4.125), Eq. (4.123) becomes:

$${}_u W_E = \frac{{}_u K_{eq} \zeta_m^2 \delta_{max}^2}{2} + {}_u K_{eq} \zeta_m \delta_{max} \psi_s \delta_y + \frac{{}_u K_{eq} \psi_s^2 \delta_y^2}{2} \quad (4.128)$$

Therefore, substituting Eqs. (4.122) and (4.128) into Eq. (4.105), the total elastic strain energy assumes the following form:

$$W_E = \frac{({}_m K_f + {}_u K_{eq} \zeta^2) {}_m \delta_{max}^2}{2} + {}_u K_{eq} \zeta \psi_s \delta_y {}_m \delta_{max} + \frac{{}_u K_{eq} \psi_s^2 \delta_y^2}{2} \quad (4.129)$$

The mode shapes of the 2DOF IIS models considering only isolators or both isolators and dampers are depicted in Figs. 4.29 – 4.30, respectively. From the figures can be seen that when only isolators are considered, the first mode shows the same shape as in a BIS structure, in which the displacements are mainly concentrated in the isolation layer; when also the dampers are taken into account, the displacement of the lower structure increases while that of the isolation layer decreases with respect to the presence of only the isolation devices.

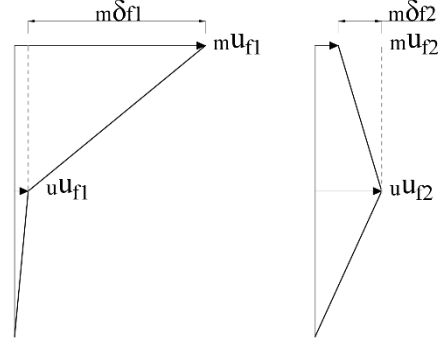


Fig.4.29. Mode shapes of the 2DOF IIS model considering only isolators

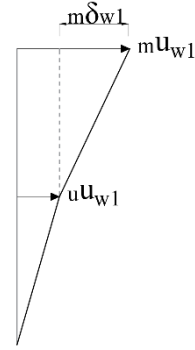


Fig.4.30. First mode shape of the 2DOF IIS model considering both isolators and dampers

*Total energy absorption due to miscellaneous damping*

The energy absorption due to miscellaneous damping,  $W_h$ , is due to the contribution of only the lower structure, i.e.:

$$W_h = {}_u W_h = E - E_D \quad (4.130)$$

where the energy attributable to damage,  $E_D$ , is obtained substituting Eqs. (4.121) and (4.129) into Eq.(4.82), as follows.

$$\begin{aligned}
E_D = & \frac{(\kappa_m K_f + \kappa_u K_{eq} \zeta^2) \delta_{max}^2}{2} + \\
& + \kappa_u K_{eq} \zeta \psi_s \delta_y \delta_{max} + \frac{\kappa_u K_{eq} \psi_s^2 \delta_y^2}{2} + \left( \kappa \frac{\delta_{max}}{\delta_y} - 1 \right) \frac{M_{TOT} g^2 T_u^2 \kappa_{eq} \alpha_s'^2}{4\pi^2 \kappa_m K}
\end{aligned} \quad (4.131)$$

*Maximum displacement of the isolation system*

Recalling Eq. (4.88),  $E_D$  can be written in terms of the pseudo-velocity attributable to damage,  $V_D$ , i.e.:

$$E_D = \frac{M_{TOT} V_D^2}{2} \quad (4.132)$$

Equating Eqs. (4.131) and (4.132), the maximum displacement of the isolation system,  $\delta_{max}$ , can be derived as a function of the energy balance. The procedure is reported in the following.

$$\begin{aligned}
E_D = \frac{M_{TOT} V_D^2}{2} = & \frac{(\kappa_m K_f + \kappa_u K_{eq} \zeta^2) \delta_{max}^2}{2} + \\
& + \kappa_u K_{eq} \zeta \psi_s \delta_y \delta_{max} + \frac{\kappa_u K_{eq} \psi_s^2 \delta_y^2}{2} + \left( \kappa \frac{\delta_{max}}{\delta_y} - 1 \right) \frac{M_{TOT} g^2 T_u^2 \kappa_{eq} \alpha_s'^2}{4\pi^2 (\kappa_m K_f + \kappa_m K_s)}
\end{aligned} \quad (4.133)$$

$$\begin{aligned}
& (\kappa_m K_f + \kappa_u K_{eq} \zeta^2) \delta_{max}^2 + 2 \left\{ \kappa_u K_{eq} \zeta \psi_s \delta_y + \frac{\kappa M_{TOT}^2 g^2 \alpha_s'^2}{(\kappa_m K_f + \kappa_m K_s) \delta_y} \right\} \delta_{max} + \\
& + \kappa_u K_{eq} \psi_s^2 \delta_y^2 - \left( \frac{2M_{TOT}^2 g^2 \alpha_s'^2}{\kappa_m K_f + \kappa_m K_s} + M_{TOT} V_D^2 \right) = 0
\end{aligned} \quad (4.134)$$

$$\delta_{max} = \frac{-b + \sqrt{b^2 - AC}}{A} \quad (4.135)$$

$$A = (\kappa_m K_f + \kappa_u K_{eq} \zeta^2) \quad (4.136)$$



$$b = {}_u K_{eq} \zeta \psi_s \delta_y + \frac{\kappa M_{TOT}^2 g^2 \alpha_s'^2}{({}_m K_f + {}_m K_s)_s \delta_y} \quad (4.137)$$

$$C = {}_u K_{eq} \psi_s^2 \delta_y^2 - \left( \frac{2 M_{TOT}^2 g^2 \alpha_s'^2}{{}_m K_f + {}_m K_s} + M_{TOT} V_D^2 \right) \quad (4.138)$$

$$\begin{aligned} {}_m \delta_{max} = & \frac{-{}_m K({}_u K + \kappa {}_m K_s) M_{TOT} g \alpha_s'}{{}_m K_s \cdot {}_m K_t \cdot K_e} + \\ & + \frac{\sqrt{\left\{ \left( {}_u K {}_m K + \kappa {}_m K_s^2 \right)^2 + {}_m K_t \cdot K_e \left( 2 {}_m K_s^2 - {}_u K {}_m K_t \psi \right) \right\} M_{TOT}^2 g^2 \alpha_s'^2 + {}_m K_s^2 {}_m K_t^2 M_{TOT} V_D^2}}{{}_m K_s \cdot {}_m K_t \cdot K_e} \end{aligned} \quad (4.139)$$

where

$${}_m K_f + {}_m K_s = {}_m K_t, \quad {}_m K_t \zeta = {}_m K, \quad {}_m K_f + {}_u K_{eq} \zeta^2 = K_e, \quad {}_u K_{eq} \psi = {}_u K.$$

#### 4.5.3.2. Shear coefficient distribution

Earthquake ground motions exert seismic forces to buildings. These seismic forces can have different shapes due to the stiffness distribution considered (Fig.4.31) [Ishiyama 2011].

If the building moves as a rigid body along with the ground motion, seismic forces and seismic coefficients become uniform from the top to the base as shown in Fig.4.31 a. The seismic forces of the upper stories are transmitted to lower stories and finally to the ground through the foundation, and the seismic shear forces are the sum of seismic forces of upper stories. In case the seismic forces are uniformly distributed, the seismic shear forces increase linearly from top to base (Fig.4.31 d). This distribution (Fig.4.31 a, d) is called (1) uniform distribution of seismic forces.

Since the building is not rigid, the upper stories are subjected to larger seismic forces. If the response displacements increase linearly from the base to the top, so as the seismic forces (Fig.4.31 b). Then the distribution of seismic shear forces becomes as a parabola where the vertex locates at

the bottom or which opens to the left (Fig.4.31 e). This distribution (Fig.4.31 b, e) is called (2) inverted triangle distribution of seismic forces. For high-rise buildings, the seismic forces of upper stories become very large, and the distribution of the seismic forces can be shown as Fig.4.31 c. Then the seismic shear forces distribute as a parabola where the vertex is at the top or which opens downwards (Fig.4.31 f).

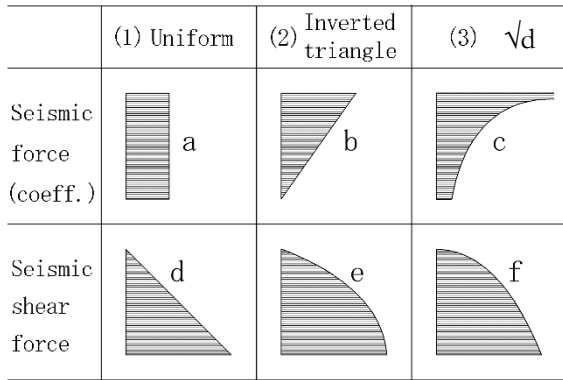


**Fig.4.31. Distributions of seismic forces (coefficients) and seismic shear forces [Ishiyama 2011]**

Defining the normalized weight  $d_i$ , cf. Eq. (4.141) as the weight above the level concerned divided by the total weight above the base, the distribution of the seismic shear forces is proportional to  $\sqrt{d}$ . Therefore, this distribution can be called (3) “ $\sqrt{d}$  distribution” (Fig.4.31 f). Incidentally the distribution of seismic forces is proportional to  $1/\sqrt{d}$  (Fig.4.31 c).

The seismic shear force at the level concerned divided by the weight above the level is called “seismic shear coefficient”. In the seismic code of Japan, the distribution of the seismic shear coefficients is given by so-called  $A_i$  distribution as follows.

$$A_i = 1 + \left( \frac{1}{\sqrt{d_i}} - d_i \right) \frac{2T}{1 + 3T} \quad (4.140)$$

where,  $T$  (s) is the fundamental natural period of the building, and  $d_i$  is the normalized weight of the  $i$ -th level that is defined as follows.

$$d_i = \frac{\sum_{j=i}^N w_j}{\sum_{j=1}^N w_j} \quad (4.141)$$

where,  $N$  is the number of stories above the base,  $i$  and  $j$  indicate the story number, and  $w_j$  is the weight of the  $j$ -th story.

The ratio  $d_i$  becomes unity (1.0) at the first story and converges to zero at upper stories, but never becomes zero. This normalized weight is very convenient to express the distributions of seismic forces and shear forces, although only Japanese code adopts the normalized weight as a seismic force parameter.

$A_i$  distribution includes the three distributions indicated in Fig.4.31, i.e. (1) uniform distribution of seismic forces, (2) inverted triangular distribution of seismic forces, and (3)  $\sqrt{d_i}$  distribution.

$A_i$  distribution converges to the distribution (1) when the natural period becomes shorter for low-rise buildings, and the effects of the distributions (2) and (3) becomes larger for high-rise buildings.

The  $A_i$  distribution is also shown in Fig. 4.32.

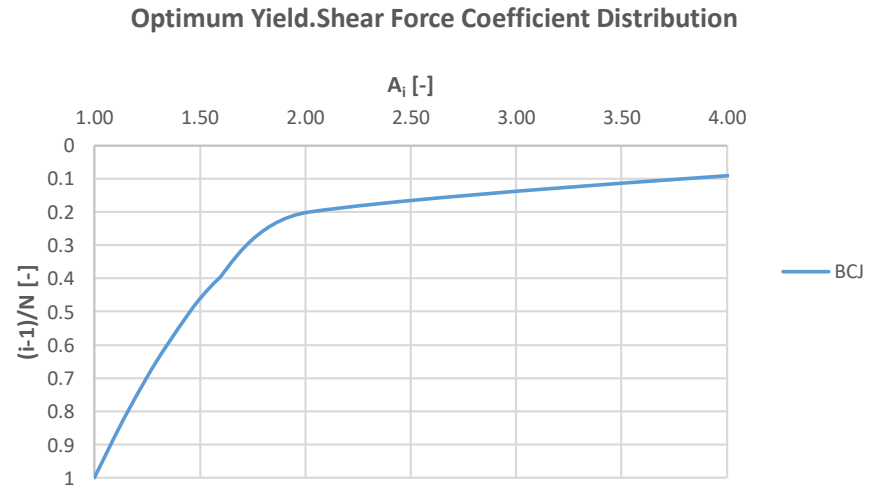


Fig. 4.32.  $A_i$  distribution for BIS

**IIS**

Considering the simplified 2DOF IIS described above, [Murakami et al. 2001, Murakami & Suoeka 2004] propose a simplified method for the prediction of response of mid-story isolated buildings extending the optimum shear coefficient distribution for BIS to IIS structures.

Therefore, considering the upper isolated structure of the IIS model behaving as a BIS structure, the shear coefficient distribution is the same for the upper structure of BIS and IIS. Then, the procedure is extended to the lower structure.

*Isolation Story*

The shear coefficient of the isolation story,  ${}_m\alpha$ , is provided as follows:

$${}_m\alpha = \alpha_f + \alpha_s \quad (4.142)$$

where the shear coefficient of isolators,  $\alpha_f$ , and dampers,  $\alpha_s$ , are respectively given by:

$$\alpha_f = \frac{Q_f}{R_m M_{TOT} g} = \frac{{}_m K_f {}_m \delta_{max}}{R_m M_{TOT} g} \quad (4.143)$$

$$\alpha_s = \frac{{}_s Q_y}{R_m M_{TOT} g} = \frac{{}_m K_s {}_m \delta_y}{R_m M_{TOT} g} \quad (4.144)$$

*Upper Structure*

The shear coefficient of the  $i$ -th story of the upper structure ( $i=m+1, \dots, N$ ),  ${}_0\alpha_i$ , is defined as the ratio of the maximum shear force of the  $i$ -th upper story,  ${}_0 Q_{i,max}$ , to the total weight above the story considered, i.e.:

$${}_0\alpha_i = \frac{{}_0 Q_{i,max}}{\sum_{j=i}^N m_j g} \quad (4.145)$$

Furthermore,  ${}_0\alpha_i$  can be expressed as follows [AIJ 1993].

$${}_0\alpha_i = \alpha_f + {}_0\alpha_{si} \quad (4.146)$$

where

$$\alpha_f = \frac{Q_f}{R_m M_{TOT} g} = \frac{{}_m K_f \delta_{max}}{R_m M_{TOT} g} \quad (4.147)$$

is the shear coefficient of isolators;

$${}_0\alpha_{si} = {}_0a_i {}_0\alpha_{opt} \alpha_s \quad (4.148)$$

is the shear coefficient of the  $i$ -th story considering only dampers, where:

${}_0\alpha_{opt}$	is the optimal shear coefficient distribution;
${}_0a_i$	is a coefficient which increases along the height of the building with a linear distribution;
${}_0a_{opt}$	is an optimum coefficient.

In particular,  ${}_0\alpha_{opt}$  can be assumed equal to the  $A_i$  distribution of the  $i$ -th upper story,  ${}_0A_i$ ; from Eqs. (4.140) and (4.141) it is given by:

$${}_0A_i = 1 + \left( \frac{1}{\sqrt{{}_0d_i}} - {}_0d_i \right) \frac{2{}_0T_1}{1 + 3{}_0T_1} \quad (4.149)$$

with

$${}_0d_i = \frac{\sum_{j=m+1}^N m_j}{R_m M_{TOT}} \quad (4.150)$$

where  ${}_0M = R_m M_{TOT}$ .

Considering that  ${}_0a_i$  is equal to 1 at the isolation level and to  ${}_0a_{opt}$  at the top story, it can be expressed as:

$${}_0a_i = \frac{{}_0a_{\text{opt}} - 1}{N - m} (i + 1 - m) + \frac{N - {}_0a_{\text{opt}}}{N - m} \quad (4.151)$$

In addition, the optimum coefficient  ${}_0a_{\text{opt}}$  can be expressed in terms of a stiffness ratio  ${}_0b_s$ , between the stiffness of the first upper story,  ${}_0k_{m+1}$ , and that of the dampers,  ${}_mk_s$ , i.e. :

$${}_0b_s = \frac{{}_0k_{m+1}}{{}_mk_s} \quad (4.152)$$

$${}_0a_{\text{opt}} = 3.1238 - 0.1238{}_0b_s, \quad \text{for } 1 \leq {}_0b_s < 10 \quad (4.153)$$

$${}_0a_{\text{opt}} = 2.0127 - 0.0127{}_0b_s, \quad \text{for } 10 \leq {}_0b_s < 80 \quad (4.154)$$

$${}_0a_{\text{opt}} = 1, \quad \text{for } {}_0b_s \geq 80 \quad (4.155)$$

Moreover, the range of these equations is set to  $0.01 < \alpha_s < 0.06$  and  $1 \leq {}_0b_s$  in a basic isolated structure. However, the authors have assumed expression (4.153), even if it is  $1 < {}_0b_s$ .

When the stiffness ratio  ${}_0b_s$  becomes 100 or more, the shear coefficient distribution of the upper structure is shown typically in the Fig. 4.33.

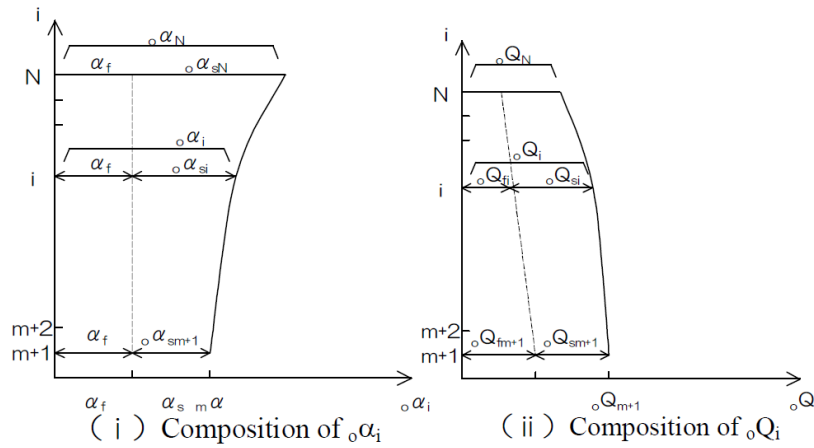


Fig.4.33. Conceptual diagram of response distribution of the upper structure [Murakami & Sueoka 2004]

### Lower Structure

The shear force produced by the mode in which the lower structure mainly moves when only the stiffness of the isolators at the isolation story is considered is given as follows.

$${}_u Q_i = R_m M_{TOT} g_m \alpha + \frac{d_i - R_m}{1 - R_m} {}_u A_i ({}_u \alpha - R_m \alpha) M_{TOT} g \quad (4.156)$$

where

$$d_i = \frac{\sum_{j=1}^N m_j}{M_{TOT}} \quad (4.157)$$

is the normalized weight of the  $i$ -th story considering the whole structure,

$${}_u \alpha_i = \frac{1}{d_i} \left[ R_m \alpha + \frac{d_i - R_m}{1 - R_m} {}_u A_i ({}_u \alpha - R_m \alpha) \right] \quad (4.158)$$

is the shear coefficient of the  $i$ -th lower story, with  $i = 1, \dots, m - 1$ .

In particular the  ${}_u A_i$  distribution considering only the lower structure is provided as follows.

$${}_u A_i = 1 + \left( \frac{1}{\sqrt{{}_l d_i}} - {}_l d_i \right) \frac{2 {}_u T_l}{1 + 3 {}_u T_l} \quad (4.159)$$

where

$${}_u d_i = \frac{\sum_{j=1}^{m-1} m_j}{(1 - R_m) M_{TOT}} \quad (4.160)$$

is the normalized weight of the  $i$ -th story considering only the lower structure,

and

$${}_u\alpha = \frac{{}_m\delta_{\max}\zeta_u K_{eq}}{M_{TOT}g} + \frac{{}_uK_{eq}\psi\alpha'_s}{{}_mK_s} \quad (4.161)$$

is the maximum shear coefficient of the lower structure.

The shear coefficient distribution of the lower structure is shown typically in the Fig. 4.34.

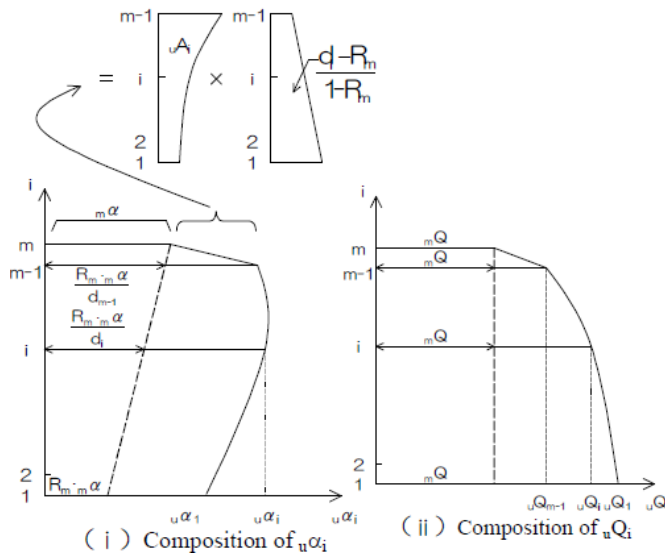


Fig.4.34. Conceptual diagram of response distribution of the lower structure  
[Murakami & Sueoka 2004]



#### 4.6. OBSERVATIONS AND RESULTS

Shifting the position of the isolation system from the base to a generic level along the height of the building, the dynamics of IIS become more complex than that of BIS. In fact, the IIS technology combines the strategies of isolation, mass damping and energy dissipation.

For this reason, in the current literature a variety of approaches both in the formulation of the problem and in the definition of design parameters and criteria is observed. Each school of thought focus the attention on one of the aspects related to IIS (isolation, mass damping and energy dissipation).

In this chapter the overview of the main papers on this topic is presented to define the design parameters and characteristics which influence the dynamic behavior of such systems as well as the design criteria adopted.

The main features of the three approaches and some observations on dynamic and design issues coming from the overview of papers on IIS are provided in the following.

Considering the *isolation approach*, the impact of the dynamic interaction between upper and lower structures (US and LS), the effect of the higher modes and its possible modal coupling (MCE) are investigated.

Basically, it is recognized that the dynamic of structures with mid-story isolation is affected by the vibration characteristics of the US and LS.

When the dynamic characteristics of the structural portions (US and LS) are similar, the MCE is expected. This detrimental effect consists in undesirable amplifications in the response of upper and lower structures. However, from the results of the analyses it is noticed that, the MCE is independent on the characteristic of the isolation system and it can be prevented by a careful design.

Looking at the *mass damping* approach, the IIS is implemented by converting masses already present on the structure into tuned masses, retaining their structural function in addition to the control function. For this reason, these systems are also appointed as “non-conventional” or “building” tuned mass damper.

From the results of parametric analyses, it is shown that a non-conventional TMD with a large mass ratio provides greater reduction of the structural response. Consequently, its major robustness leads to a

system less dependent on the frequency content and on the optimal configuration.

With the *energy dissipation* approach, the isolation interface is designed as a concentrated energy dissipation system. It was observed that increasing the mass ratio, the maximum energy dissipated by the isolation system reaches values of  $70 \div 80\%$ ; however, increasing the damping of the structural portions the dissipated energy decreases.

In this context, in order to evaluate the dynamic behavior of IIS buildings, parametric analyses have been carried out in the current literature by adopting simplified (1D) and more refined (3D) models. Multi or 2 - 3 lumped-mass (1D MDOF or 2-3DOF) models are used to provide a good prediction of the dynamic response of the structure, while three-dimensional (3D MDOF) models are considered for a global assessment of the seismic behavior of the building.

The design parameters commonly adopted in the papers refer to: mass and frequency ratios between either the structural portions or the structural portions and the isolation system; damping ratios of upper and lower structures and of the isolation system; ratio of the yield strength of dampers to the total above-ground weight.

The design criteria available in the main papers on this topic consist in reducing the base shear and the displacement of the structural portions or in maximizing the energy dissipated by the isolation system.

From the results of the analyses it is stated that the position of the isolation level, the mass and stiffness distributions and the higher modes influence the dynamic behavior of such systems. Moving the isolation layer from the top to the bottom of the structure, the control mechanism changes going from tuning frequency, isolation and energy dissipation to base isolation.

From the overview of the current literature emerges the necessity of merging the precious outcomes coming from each conceptual approach for a more complete understanding of the design problem.

## **5. ANALYSIS OF REAL IIS BUILDINGS**

### **5.1. INTRODUCTION**

In this chapter two real-world applications of IIS are chosen as case studies and thoroughly analyzed, in order to interpreting the latest design practice in the light of approaches and indications coming from the world of research. In the following the buildings are described, and the major data obtained from publications and communication with the designers are presented and utilized for an approximate prediction of, and a preliminary discussion on the dynamic properties of the three structural parts of each building, and, consequently, on their expected dynamic interaction; in addition, a straightforward comparison between the anticipated dynamic behavior of the two buildings is presented. Modal and time history analyses are then carried out on the MDOF models of the two buildings; the main results are reported and design implications are discussed, in the light of the observations and of the provisions suggested in the inherent scientific literature.

### **5.2. THE CASE STUDIES: BRIEF DESCRIPTION**

Starting from the overview of the main real-world applications of IIS provided in Chapter 3, two high-rise buildings, i.e. Iidabashi 1<sup>st</sup> Building and Shiodome Sumitomo Building [Murakami et al. 2000, Sueoka et al. 2004, Tsuneki et al. 2008-2009], are herein chosen as case studies. The buildings are selected on the basis of two criteria: availability of data and representativeness of the full range of IIS applications in the current design practice. A view of the buildings; the framing elevation and the typical plan of the upper, intermediate and lower structure; the arrangement of the isolators and dampers; are shown in Figs. 3.4 - 3.5 for Iidabashi 1<sup>st</sup> Building and in Figs. 3.13 ÷ 3.15 for Shiodome Sumitomo Building. The general description of the two buildings are also reported in

Chapter 3. The major data of the two buildings are given in Tab. 5.1 for completeness.

**Table 5.1. Major data of the buildings**

	<b>IB</b>	<b>SSB</b>
No. stories	14 + penthouse	25
Plan dimension [mxm]	130.1 x 39.6 (off.), 130.1x15.0 (apart.)	109.6 x 39.5 (off. and hotel)
Floor area [m <sup>2</sup> ]	5152.0 (off.), 1951.5 (apart.)	4339 (off. and hotel)
Tot. floor area [m <sup>2</sup> ]	43324	108475
Height [m]	59.0	126.1
Interstory height [m]	4.1 (off.), 3.05 (apart.)	4.2
Structure	SRC + RC + S	S
Isolation System	40 RBs (Φ800) 212 LDs Φ180	41 RBs (Φ1300, Φ1100, Φ1000) 100 LDs + 14 SDs

IB (Iidabashi 1<sup>st</sup> Building), SSB (Shiodome Sumitomo Building)

SRC (Steel Reinforced Concrete), RC (Reinforced Concrete), S (Steel)

RB (Rubber Bearing), LD (Lead Damper), SD (Steel Damper)

### 5.3. SIMPLIFIED MODELING AND DYNAMIC PROPERTIES

Simplified lumped masses multi-degree of freedom (MDOF) models are developed and utilized for an in depth analysis and discussion of the buildings dynamics. In particular for both buildings, three different MDOF models are considered, namely: RB, RB+D and FB models (RB = Rubber Bearing, D = Damper, FB = Fixed-Base). In the RB models the isolation layer is only represented by the isolators, while in the RB+D model both isolators and dampers are taken into account; finally, the FB models for each building are composed by the degrees of freedom of the lower and upper structures, without the one corresponding to the isolation system.

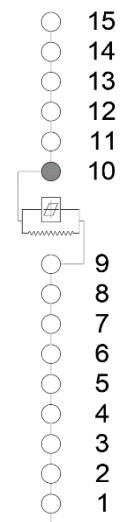
For the modal analyses carried out in the next paragraph, two different RB+D models are considered, respectively appointed as RB+D<sup>(1)</sup> and RB+D<sup>(2)</sup>; in both models the parallel combination of isolators and dampers are considered, with the global initial stiffness in the RB+D<sup>(1)</sup> models, and the global secant stiffness, computed at the design displacement, in the RB+D<sup>(2)</sup> models.

The data necessary for the construction of the MDOF models, i.e. the floor mass values, the interstory structural stiffness distribution, the characteristics of the isolators and dampers, are all derived from the papers [Murakami et al. 2000, Sueoka et al. 2004] (Chapter 3) and/or have been kindly provided by the designer through personal communication [K. Murakami, personal communication, 2015].

The Iidabashi 1<sup>st</sup> Building is represented by 15 lumped masses, 9 in the lower part, 1 in the intermediate isolation layer and 5 in the upper part; the Shiodome Sumitomo Building is represented by 26 masses, 11 in the lower part, 1 in the intermediate isolation layer and 14 in the upper part.

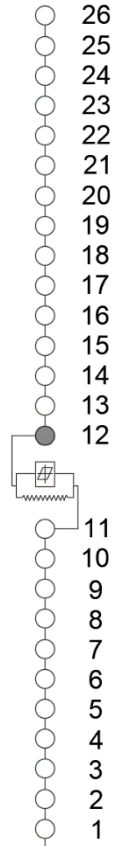
A graphical representation of the MDOF RB+D models of the two buildings, with the corresponding values of the lumped masses and of the story horizontal stiffness, are given in Figs. 5.1 – 5.2.

The structure horizontal stiffness at each level is represented by an equivalent linear shear spring, while the stiffness of the isolation interface is represented by means of two springs working in parallel: an equivalent linear elastic spring, which describes the global behavior of the rubber bearings, and an elastic-plastic spring with bi-linear restoring force characteristic, which represents the total contribution of the hysteretic dampers.



Node	Mass [kNs <sup>2</sup> /m]	Stiffness [GN/m]
15	1657.9	9.4
14	2305.4	16.6
13	2305.4	20.1
12	2315.2	22.9
11	2315.2	34.4
10	4022.1	RB 0.053 RB+D <sup>(1)</sup> 1.653 RB+D <sup>(2)</sup> 0.087
9	12704.0	7.2
8	4914.8	7.5
7	4914.8	8.0
6	5091.4	8.5
5	5179.7	9.1
4	5189.5	9.8
3	5209.1	11.0
2	5532.8	12.8
1	5434.7	12.3

Fig. 5.1. Vibration analysis model of Iidabashi 1<sup>st</sup> Building



Node	Mass [kNs <sup>2</sup> /m]	Stiffness [GN/m]
26	5767.6	1.5
25	3460.8	1.7
24	3446.5	2.1
23	3075.4	2.2
22	3083.6	2.2
21	3093.8	2.3
20	3116.2	2.5
19	3167.2	2.5
18	3169.2	2.6
17	3124.4	2.6
16	3131.5	2.7
15	3139.7	2.6
14	3185.5	2.3
13	3566.8	3.1
12	4029.6	RB 0.081
		RB+D <sup>(1)</sup> 2.849
		RB+D <sup>(2)</sup> 0.134
11	3127.4	1.1
10	3126.4	4.5
9	1720.7	4.8
8	1697.2	5.0
7	1717.6	5.2
6	1714.6	5.4
5	1715.6	5.7
4	1732.9	5.9
3	1725.8	6.3
2	2582.1	2.7
1	3079.5	3.2

Fig. 5.2. Vibration analysis model of Shiodome Sumitomo Building

The total stiffness  $K_{D,tot}$ , and yield shear force of dampers,  $F_{y,tot}$ , as well as the ratio of the total damper yield force  $F_{y,tot}$  to the total building weight  $W_{tot}$ , appointed as  $\alpha'_s$ , are given in Tab. 5.2.

In the MDOF models, viscous damping equal to 2% is assumed in the upper and lower structures, and 0% for the rubber bearings in the seismic isolation interface, where the major source of dissipation is given by the hysteretic response of the lead and steel units, explicitly accounted for by means of the bi-linear force-displacement model of the isolation system.

**Table 5.2 Characteristics of the dampers for the two buildings**

Building	Device	$K_{D,tot}$ [GN/m]	$F_{y,tot}$ [kN]	$\alpha_s' = \frac{F_{y,tot}}{W_{tot}}$
<b>IB</b>	LD	1.6	13544	2%
<b>SSB</b>	LD	2.7	22000	3%
	SD	0.068/0.0022*	3500	

IB (Iidabashi 1<sup>st</sup> Building), SSB (Shiodome Sumitomo Building)

RB (Rubber Bearing), LD (Lead Damper), SD (Steel Damper)

\* 2<sup>nd</sup> stiffness

It is worth noticing that the assumption of null value for the damping ratio of rubber bearings seems to be adequate, since it is negligible with respect to the dampers counterpart. In the cases in which the source of dissipation is given only by isolators, the damping ratio is necessary different from zero. However, in order to compare RB and RB+D models, when only isolators are taken into account the viscous damping is still assumed equal to 0%.

In the following text, for the sake of brevity, the Iidabashi 1<sup>st</sup> Building and the Shiodome Sumitomo Building are respectively appointed as IB and SSB; in addition, upper and lower structures (also appointed as superstructure and substructure) are often identified as US and LS.

Considering the MDOF systems represented in Figs. 5.1 – 5.2, the equations of motion, expressed in matrix form, are given by:

$$\mathbf{M}\ddot{\mathbf{x}} + \mathbf{C}\dot{\mathbf{x}} + \mathbf{K}\mathbf{x} = -\mathbf{M}\mathbf{r}\ddot{x}_g \quad (5.1)$$

where  $\mathbf{M}$ ,  $\mathbf{C}$ ,  $\mathbf{K}$  are the (N x N) mass, damping and stiffness matrices of IB and SSB, with N the total number of dofs of RB and RB+D models, i.e. 15 for IB and 26 for SSB;  $\mathbf{x}(t)$  is the (N x 1) displacement vector of the structures with respect to the ground,  $\mathbf{r}$  is the (N x 1) unit vector that multiplies the ground acceleration  $\ddot{x}_g(t)$ .

Quite trivially, considering the FB models of the two buildings, in Eq. (5.1) the matrices and vectors have dimensions respectively equal to (N-1 x N-1) and (N-1 x 1).

The major global data utilized for the models of the Iidabashi and Shiodome buildings are shown and compared in Tab. 5.3 and Tab. 5.4.

In the Tab. 5.3 are provided mass, stiffness and period values; in particular: the total masses of the whole building ( $M_{TOT}$ ), of the lower structure ( $m_{LS}$ ), of the upper structure ( $m_{US}$ ), and of the isolation level ( $m_{ISO}$ ); the global stiffness parameters of the lower and upper structure, and of the isolation system, i.e.:  $k_{LS,st}$  and  $k_{LS,dyn}$ ,  $k_{US,st}$  and  $k_{US,dyn}$  and,  $k_{ISO,RB}$  and  $k_{ISO,RB+D}^{(2)}$ ; the natural period values of the upper and lower structures considered as standalone structures ( $T_{LS}$ ,  $T_{US}$ ), of the fixed base structure ( $T_{FB}$ ), and of the isolation layer ( $T_{ISO,RB}$  and  $T_{ISO,RB+D}^{(2)}$ ).

It is worth spending some words for specifying the assumptions made in the simplified calculation of the global values of the stiffness parameters for the upper and lower structures, provided in the Tab. 5.3 and appointed as  $k_{LS,st}$  and  $k_{LS,dyn}$ ,  $k_{US,st}$  and  $k_{US,dyn}$ , as well as in the calculation of the stiffness of the isolation system,  $k_{ISO,RB}$  and  $k_{ISO,RB+D}^{(2)}$ . From a static point of view, the global stiffness of the upper and lower structures  $k_{US,st}$  and  $k_{LS,st}$  are defined by combining in series the shear spring constants of the relevant stories, i.e. :

$$k_{US(LS),st} = \frac{1}{\sum_{u(l)} \frac{1}{k_{u(l)}}} \quad (5.2)$$

where U and L represent the degrees of freedom of the US and LS, respectively. From a dynamic point of view, equivalent one lumped mass (SDOF) models are defined for the LS and the US, and on the basis of the total mass and the first natural period, the so-called dynamic stiffness parameters,  $k_{US,dyn}$  and  $k_{LS,dyn}$ , are derived:

$$k_{US(LS),dyn} = \frac{4\pi^2 m_{US(LS)}}{T_{1,US(LS)}^2} \quad (5.3)$$

It is worth noticing that the dynamic stiffness values of both the upper and lower structure are slightly larger than the static counterparts, since the dynamic values are derived from the formula (5.3), where the actual distribution of stiffness and masses in the structure is taken into account through the period value.



Concerning the stiffness of the isolation system,  $k_{\text{ISO,RB}}$  is the global stiffness only given by the rubber bearings, while  $k_{\text{ISO,RB+D}}^{(2)}$  is the secant stiffness given by the parallel combination of rubber bearings and dampers at the design displacement, respectively equal to 40 cm for the IB and 50 cm for the SSB. Analogously, two values of the isolation period are reported in the Tab. 5.3, namely  $(T_{\text{ISO,RB}})$  and  $(T_{\text{ISO,RB+D}}^{(2)})$ , both derived considering a SDOF model, with mass equal to  $m_{\text{US}} + m_{\text{ISO}}$ , and stiffness respectively given by  $k_{\text{ISO,RB}}$  and  $k_{\text{ISO,RB+D}}^{(2)}$ .

Starting from the data of Tab. 5.3, in Tab. 5.4 are also given, for the IB and the SSB: the mass ratio  $m_{\text{US}}/m_{\text{LS}}$ , the stiffness ratio  $(k_{\text{US}}/k_{\text{LS}})_{\text{st,dyn}}$ , the period ratios  $T_{\text{ISO}}/T_{\text{US}}$  and  $T_{\text{ISO}}/T_{\text{LS}}$ , computed both for the RB and RB+D models. In the last column of both Tab. 5.3 and Tab. 5.4, each couple of parameter values determined for the IB and SSB is directly compared.

The values provided in Tab. 5.3 and Tab. 5.4 allow for an approximate guess of, and a preliminary discussion on the dynamic properties of the three structural parts of each building, and, consequently, on their expected dynamic interaction. In addition, a straightforward comparison between the anticipated dynamic behavior of the two buildings is possible.

**Table. 5.3. Mass, Natural Period and Stiffness values; comparison between IB and SSB**

		<b>IB</b>	<b>SSB</b>	<b>IB vs. SSB</b>
$M_{\text{TOT}}$	[kNs <sup>2</sup> /m]	69092	75498	1 : 1.1
$m_{\text{US}}$		10899	47528	1 : 4.4
$m_{\text{ISO}}$		4022	4030	1 : 1
$m_{\text{LS}}$		54171	23940	2.3 : 1
$T_{\text{FB}}$	[s]	1.17	3.27	1 : 2.8
$T_{\text{US}}$		0.21	2.18	1 : 10.4
$T_{\text{ISO,RB}}$		3.33	5.02	1 : 1.5
$T_{\text{ISO,RB+D}}^{(2)}$		2.60	3.90	1 : 1.5
$T_{\text{LS}}$		0.98	1.06	1 : 1.1
$k_{\text{US,st}}$	[GN/m]	3.46	0.163	21.2 : 1
$k_{\text{US,dyn}}$		9.76	0.39	24.7 : 1
$k_{\text{ISO,RB}}$		0.053	0.081	1 : 1.5
$k_{\text{ISO,RB+D}}^{(1)}$		1.653	2.849	1 : 1.7
$k_{\text{ISO,RB+D}}^{(2)}$		0.087	0.134	1 : 1.5
$k_{\text{LS,st}}$		1.02	0.32	3.2 : 1
$k_{\text{LS,st}}$		2.23	0.84	2.6 : 1

**Table. 5.4. Mass, stiffness and frequency ratios; comparison between IB and SSB**

	IB	SSB	IB vs. SSB
$m_{US}/m_{LS}$	0.2	2.0	1 : 9.9
$(k_{US}/k_{LS})_{st}$	3.4	0.5	6.7 : 1
$T_{ISO,RB} / T_{US}$	15.9	2.3	6.9 : 1
$T_{ISO,RB} / T_{LS}$	3.4	4.7	1 : 1.4
$T_{ISO,RB+D}^{(2)} / T_{US}$	12.4	1.8	6.9 : 1
$T_{ISO,RB+D}^{(2)} / T_{LS}$	2.7	3.7	1 : 1.4
$(k_{US}/k_{LS})_{dyn}$	4.4	0.5	9.3 : 1

As can be seen from Tab. 5.3 and Tab. 5.4, the two buildings, despite the different height (59.0 vs. 126.1 m) and number of stories (14 vs. 25), have quite similar total masses, only 10% larger in the SSB, where the large atrium in the LS covers about 40 m of height and approximately 50% of the plan area. The upper structure in IB has a weight equal to 20% of the lower structure, while in SSB the US is approximately 2 times heavier than the LS.

In terms of dynamic stiffness ratios, it can be noticed that the US of the IB is 4.4 times more rigid than the LS, while in the SSB the US has a lateral stiffness approximately halved with respect to the LS. Comparing the two buildings it is possible to notice that the upper and lower structures of IB are more rigid than the SSB counterparts, of 25 and 2.6 times, respectively.

On the basis of both mass and stiffness comparison, it results that the US of the IB is lighter and more rigid than the US in the SSB; in fact, as a standalone structure, the IB superstructure has a natural period 10 times shorter than the SSB one (0.21 sec versus 2.18 s). The LS of IB is heavier and more rigid than the SSB LS, but the ratio between the mass and the stiffness are quite similar, so the natural period of the two substructures is comparable (0.98 vs. 1.06 s), with a slight scatter of 8%. Globally, IB is slightly lighter (10%) and much more rigid than SSB, thus the first natural period of the IB overall structure, considered as a fixed-base structure ( $T_{FB}$ , neglecting the presence of the isolation layer) is quite shorter (approximately 40%) than the SSB counterpart.

Looking at the isolation system in the two buildings, very similar mass values can be (quite trivially) observed. The global stiffness given by the isolators only ( $k_{ISO,RB}$ ) and by the combination in parallel of isolators plus dampers ( $k_{ISO,RB+D}^{(2)}$ ), are respectively 1.5 and 1.6 larger in the SSB than in IB, while the yield shear coefficient  $\alpha'_s$  is equal to 2% for IB, and of 3%

for SSB. However, being the upper part of the SSB approximately 4.4 times heavier the IB counterpart, the isolation period values ( $T_{\text{ISO,RB}}$ ) and ( $T_{\text{ISO,RB+D}}^{(2)}$ ) are much longer for SSB than IB, namely 5.02 vs. 3.33 s, and 3.90 vs. 2.60 s.

#### 5.4. MODAL ANALYSES

Modal analyses are carried out on the MDOF models (RB, RB+D<sup>(1)</sup>, RB+D<sup>(2)</sup>, and FB) of the two buildings; the main results are reported and discussed, in the light of the previous observations and of the design provisions suggested in the inherent scientific literature.

The first three natural vibration modes obtained for the four MDOF models of the Iidabashi and Shiodome buildings are depicted in Fig. 5.3 and Tab. 5.5. The three graphs on the left refer to the results obtained for the IB, while the ones on the right refer to SSB; the values of periods and participating mass ratios for the four models are also provided in Tab. 5.5.

**Table 5.5. Vibration modes: (a) Iidabashi 1<sup>st</sup> building, (b) Shiodome Sumitomo building**

Building	Model	1 <sup>st</sup> mode		2 <sup>nd</sup> mode		3 <sup>rd</sup> mode	
		T [s]	$\Gamma$ [%]	T [s]	$\Gamma$ [%]	T [s]	$\Gamma$ [%]
IB	RB	3.43	26.4	0.954	58.1	0.341	9.3
	RB+D <sup>(1)</sup>	1.30	77.2	0.521	10.1	0.319	6.8
	RB+D <sup>(2)</sup>	2.74	29.8	0.938	54.9	0.341	9.3
	FB	1.17	80.9	0.375	11.9	0.215	3.8
SSB	RB	5.97	73.4	1.18	3.2	0.960	18.8
	RB+D <sup>(1)</sup>	3.43	80.7	1.17	9.0	0.701	4.6
	RB+D <sup>(2)</sup>	5.08	75.2	1.18	4.7	0.911	15.5
	FB	3.27	80.6	1.10	9.0	0.677	5.0

A first, quite trivial consideration is that in the RB models the first natural period is much longer than in the RB+D<sup>(1)</sup> models, since the flexible interface in RB models only accounts for the isolators; however the RB+D<sup>(2)</sup> models, where the design secant stiffness of the isolation system is considered in lieu of the initial stiffness, the periods lengthen again, and closely approach the values given in Tab. 5.3.

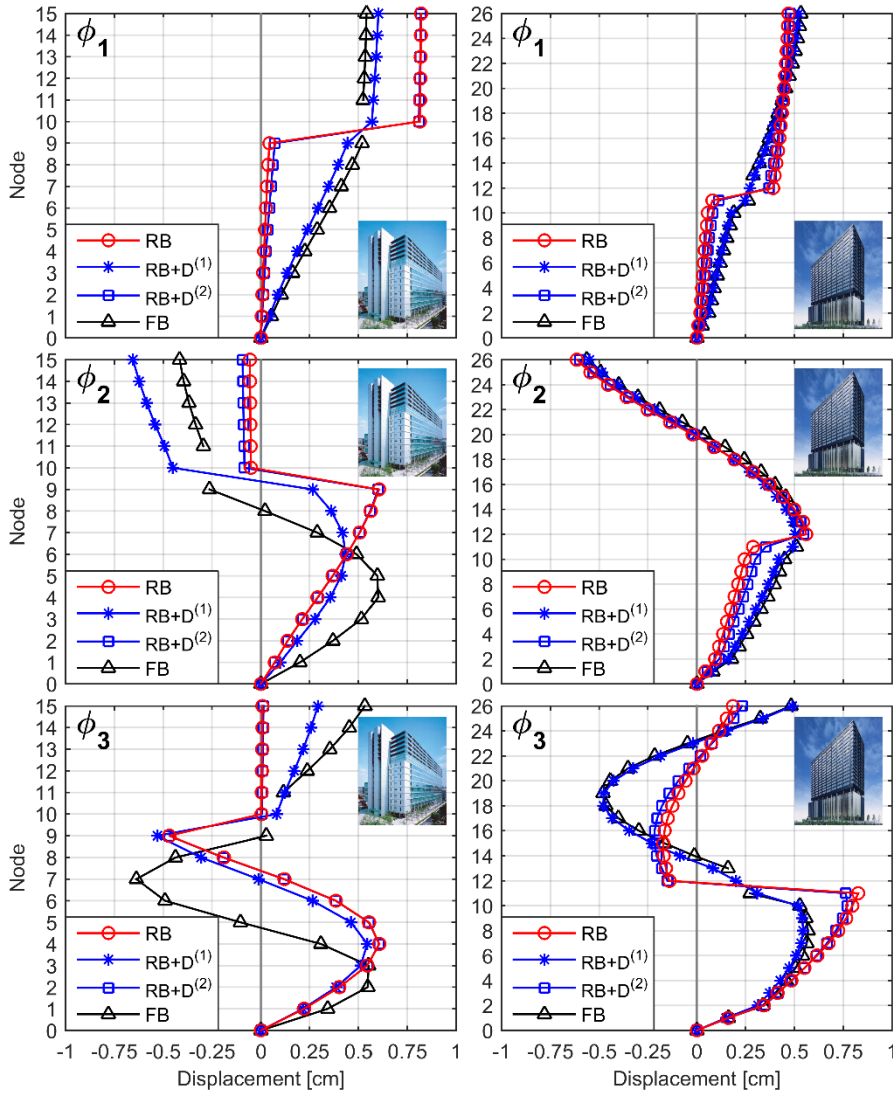


**Fig. 5.3. Vibration modes: (a) Iidabashi 1<sup>st</sup> building, (b) Shiodome Sumitomo building**

The first period of the overall building structures, both in the case of the RB and RB+D<sup>(1)</sup> models are very close to the values obtained by the designers with more refined three-dimensional models and provided in the papers [Murakami et al. 2000, Sueoka et al. 2004]; in particular, for the IB, the periods herein calculated are 3.43 s (RB) and 1.30 s (RB+D<sup>(1)</sup>), that

are practically coincident with 3.47 s and 1.35 s given by the designers; for the SBB, as well, the values of 5.97 s (RB) and 3.43 s (RB+D<sup>(1)</sup>) closely match 6.04 s and 3.42 s, respectively.

In the following, the results from the RB models and the RB+D models are separately examined, since the RB models allow to understand the dynamics of the isolated buildings, while the RB+D models show how this dynamic behavior is modified by the introduction of the dampers.

#### 5.4.1. RB models

Looking at the RB models, it is worth noticing that, in both buildings, the first mode involves deformation mainly concentrated at the isolation level, with almost no deformations in the US and only slight deformations in the LS.

In the case of the IB, the first period  $T_{RB,1}$  is practically coincident with the SDOF isolation period  $T_{ISO,RB}$  (3.43 vs. 3.33 s), and the participating mass ratio,  $\Gamma_{RB,1}$ , equal to 26.4%, is quite close to the ratio  $(m_{US} + m_{ISO}) / M_{TOT}$  (21.6%).

For the SSB RB model, as well, the comparison  $T_{RB,1}$  vs.  $T_{ISO,RB}$  (5.97 vs. 5.02 s) and  $\Gamma_{RB,1}$  vs.  $(m_{US} + m_{ISO}) / M_{TOT}$  (73.4% vs. 68.3%) basically confirms the above general considerations; in this case the large value of the participating mass associated to the first mode is directly related to the US mass value, 2 times the LS one. These observations suggest that the RB models of both buildings apparently behave like a base isolation system of the superstructure.

Larger differences between the two buildings arise considering the second and third modes: while for the IB these modes mainly involve deformations in the LS and isolation system, with negligible deformations in the US, for the SSB, both US and LS show comparable displacements. The second period of the IB RB model is very close to the natural period of the LS considered as a standalone structure ( $T_{RB,2} = 0.95$  s vs.  $T_{LS} = 0.98$  s), and also the large value of the participating mass ratio,  $\Gamma_{RB,2}$ , equal to 58.1%, is related to the large mass of the LS ( $m_{LS} / M_{TOT} = 78.4\%$ ). The third mode of the IB RB model reminds the second mode of the LS, and is characterized by a lower mass participating ratio (9.3%).

On the contrary, in the SSB, both the second and third modes of the RB model show displacements in the US and LS; the second mode shape

appears similar to the fixed-base one, is characterized by a very small participating mass (3.2%) and period  $T_{RB,2} = 1.18$  s, while the third mode involves a larger mass (18.8%) with a period  $T_{RB,3} = 0.96$  s, and again exhibits deformations throughout the elevation, though more concentrated in the LS and isolation system. It is worth noticing that the equivalent period of the lower structure,  $T_{LS}$ , equal to 1.06 s, is an average value between  $T_{RB,2}$  and  $T_{RB,3}$ .

Summing up, the first mode of both RB models represents the first mode of the US isolated at the base, with minor deformations in the LS. In the IB RB model, the second and third modes are representative of the first and second mode of the LS, with almost no deformation in the US. In SSB RB model, the second and third modes involves displacements both in the US and LS, suggesting a mode coupling effect.

#### 5.4.2. RB+D models

The RB+D<sup>(1)</sup> and FB models show, for both buildings, very close values of natural period and displacements in the first mode. This is true for both buildings; in the Shiodome building the closeness of modal displacements and period values between the RB+D<sup>(1)</sup> and FB models is also preserved in the 2<sup>nd</sup> and the 3<sup>rd</sup> mode. On the contrary, for the Iidabashi building, larger differences between the two models can be observed in the higher modes: in the second mode the behavior of the LS in the RB+D<sup>(1)</sup> model is intermediate between the RB and FB models, with also the period value, equal to 0.521, intermediate between the RB and FB ones (0.954 s and 0.375 s, respectively); in the third mode, the LS displacements closely match the RB model counterparts, while also US displacements can be observed, contrarily to the RB model; in this case the period ( $T_{RB+D,3}^{(1)} = 0.319$  s), is closer to RB than FB counterpart ( $T_{RB,3} = 0.341$  s vs.  $T_{FB,3} = 0.215$  s). Generally, also the modal participating mass ratios of RB+D<sup>(1)</sup> and FB models are very similar, for both buildings.

The RB+D<sup>(2)</sup> models, instead, provide results very similar to the RB counterparts, with almost overlapping displacement distributions for both buildings in the three modes, and close values of natural period; the largest difference between the two models can be observed with reference to the first period, for both buildings, going from  $T_{RB,1} = 3.43$  s to  $T_{RB+D,1}^{(2)} = 2.74$  s for the Iidabashi Building, and from  $T_{RB,1} = 5.97$  s to  $T_{RB+D,1}^{(2)} = 5.08$  s for the Shiodome Building. On the basis of this close matching of

vibration characteristics, the discussion on the modal analysis results made in the previous sub-paragraph with reference to the RB models, is also valid for the RB+D<sup>(2)</sup> counterparts.

#### 5.4.3. Mode Coupling Effect

From the previous exam of the building modal characteristics it clearly emerges that almost no mode coupling was evident for the Iidabashi building in the RB and RB+D<sup>(2)</sup> models, while a slight coupling could be observed in the RB+D<sup>(1)</sup>. On the contrary, the three Shiodome Building models, RB and RB+D<sup>(1)</sup> and RB+D<sup>(2)</sup>, all show coupling of the US and LS in the higher modes; for the RB+D<sup>(1)</sup>, even the first mode show displacements both in the US and LS.

This coupling effect of the higher modes, which can produce an amplification in the seismic response of the structure, has been explicitly addressed in some papers on mid-story isolation [Wang et al. 2011, 2012, 2013; Kobayashi & Koh 2008]; basically, it is recognized that the dynamics of structures with mid-story isolation is affected by the vibration characteristics of the US and LS, and that, depending on these characteristics, two different scenarios for the dynamic behavior of the global structure are found: a major influence of one of the higher modes (either the 2<sup>nd</sup> or the 3<sup>rd</sup> mode), or a coupling effect of the 2<sup>nd</sup> and 3<sup>rd</sup> modes.

In the next paragraph, the vibration characteristics of the buildings are interpreted through the lens of the theoretical framework established by [Wang et al.]. By now, let's consider that, from a physical point of view, a mode coupling effect implies that the US and the LS structures move together. Observing the 2<sup>nd</sup> and the 3<sup>rd</sup> mode shapes of the RB and RB+D<sup>(2)</sup> models (Fig. 5.3), in the IB only the LS displays deformations, while in the SSB comparable deformations are exhibited by both the US and LS. For a more detailed assessment, all vibration modes of the RB models, i.e. 15 for IB and 26 for SSB, are considered and the relevant structural parts involved in the modal displacements (LS, ISO, US, or coupled LS+US), are provided in Fig. 5.4, along with participating mass ratios.

From the IB graph of Fig. 5.4, it is possible to recognize: 1 mode for the intermediate isolation layer, 9 and 5 modes, respectively, for the lower and upper structures; these mode distributions among the three structural parts exactly reflects the number of the degrees of freedom of the ISO (1),

LS (9) and US (5). The cumulative participating mass ratios for the three parts are equal to 26.4%, 73.6% and 0.0% for the ISO, LS and US, respectively. In this perspective, the IB appears as a paradigmatic example of ideal middle-story isolation, where the US is designed in order to be very stiff with respect to the LS, and the predominant modes, beyond the isolation one, are the modes of the LS.

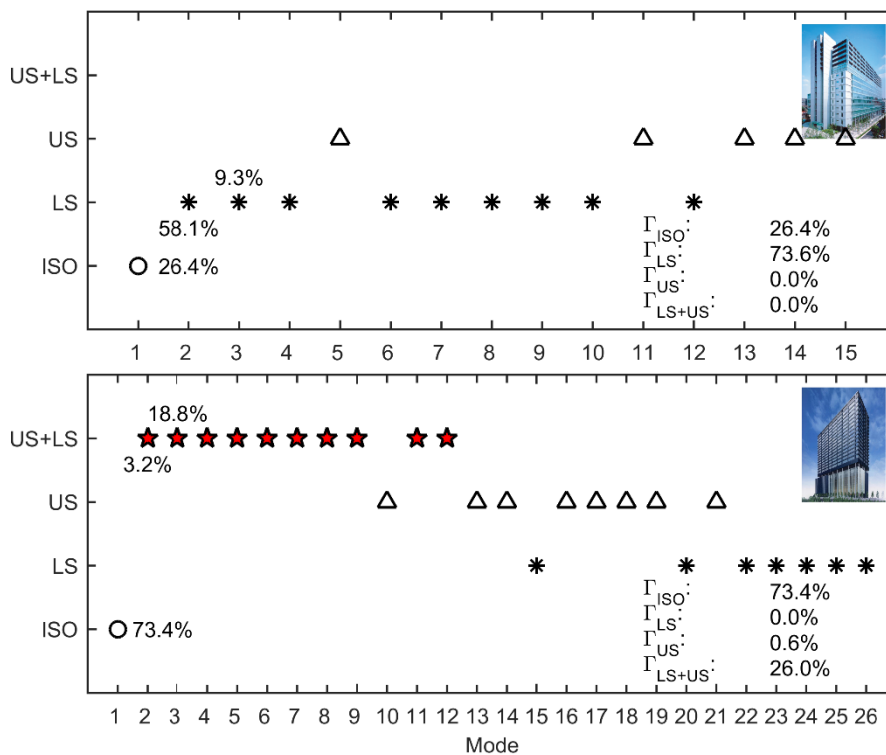


**Fig. 5.4. Vibration modes: (a) Iidabashi 1st building, (b) Shiodome Sumitomo building**

On the contrary, the upper structure of the SSB is more flexible; therefore, from the SSB graph of Fig. 5.4 can be clearly individuated: 1 mode for the ISO, 8 modes for the US (instead of 14, number of degrees of freedom in the upper structure), and 7 modes for the LS (instead of 11, number of degrees of freedom in the lower structure). Therefore, 10 modes are coupled. The cumulated participating mass are equal to 73.4%, 0.0%, 0.6%, respectively for ISO, LS, US, and 26.0% for the coupled LS - US. It is worth noticing that a little percentage of the mass is related to the US



only, as well as all modes only involving the LS have null participating mass.

### 5.5. THEORY AND DESIGN PRACTICE: ISOLATION AND MASS DAMPING APPROACHES VS. IB & SSB

In order to compare the dynamic response of the two real case studies in the light of the isolation and mass damping approaches, currently adopted in the inherent scientific literature, reduced single degree of freedom models for the LS, US and isolation system are considered.

It is worth highlight that, until now, the equivalent reduced-order SDOF models of the three parts have been defined as a function of the total mass and the fundamental mode of each part, see § 5.3.

In this section, in lieu of the total masses and the equivalent stiffnesses of the structural portions and the isolation system, the modal masses, stiffnesses and damping constants are considered, still taking into account the fundamental mode of each part.

For reducing the order of the LS MDOF part, as can be seen in Chapter 2 (§ 2.3), the lower structure can be assumed analogous to a structure with attached a TMD, i.e. the isolated US. The modal mass, stiffness and damping constant of the LS are given by Eq. (2.220), i.e.:

$$\tilde{m}_{LS} = \tilde{m}_{LS,1} = \boldsymbol{\phi}_{LS,1}^T \mathbf{M}_{LS} \boldsymbol{\phi}_{LS,1} \quad (5.4)$$

$$\tilde{k}_{LS} = \tilde{k}_{LS,1} = \boldsymbol{\phi}_{LS,1}^T \mathbf{K}_{LS} \boldsymbol{\phi}_{LS,1} \quad (5.5)$$

$$\tilde{c}_{LS} = \tilde{c}_{LS,1} = \boldsymbol{\phi}_{LS,1}^T \mathbf{C}_{LS} \boldsymbol{\phi}_{LS,1} \quad (5.6)$$

where  $\mathbf{M}_{LS}$ ,  $\mathbf{K}_{LS}$ ,  $\mathbf{C}_{LS}$  are the ( $L \times L$ ) LS mass, stiffness and damping matrices of IB and SSB, with  $L$  the total number of the LS dofs, i.e. 9 for IB and 11 for SSB;  $\boldsymbol{\phi}_{LS,1}$  is the first mode shape of the LS, obtained assuming equal to 1 the modal displacement of the mass at which the TMD (the isolated US) is attached, i.e. the top one.

For reducing the order of the US+ISO MDOF part, as can be seen in Chapter 2 (§ 2.2), the isolated upper structure can be assumed analogous to a base isolated structure. The modal mass, stiffness and damping constant of the US are given by Eq. (2.101), i.e.:

$$\tilde{m}_{US} = \tilde{m}_{US,1} = \boldsymbol{\phi}_{US,1}^T \mathbf{M}_{US} \boldsymbol{\phi}_{US,1} \quad (5.7)$$

$$\tilde{\mathbf{k}}_{\text{US}} = \tilde{\mathbf{k}}_{\text{US},1} = \boldsymbol{\phi}_{\text{US},1}^T \mathbf{K}_{\text{US}} \boldsymbol{\phi}_{\text{US},1} \quad (5.8)$$

$$\tilde{\mathbf{c}}_{\text{US}} = \tilde{\mathbf{c}}_{\text{US},1} = \boldsymbol{\phi}_{\text{US},1}^T \mathbf{C}_{\text{US}} \boldsymbol{\phi}_{\text{US},1} \quad (5.9)$$

where  $\mathbf{M}_{\text{US}}$ ,  $\mathbf{K}_{\text{US}}$ ,  $\mathbf{C}_{\text{US}}$  are the (U x U) US mass, stiffness and damping matrices of IB and SSB, with U the total number of the US dofs, i.e. 5 for IB and 14 for SSB;  $\boldsymbol{\phi}_{\text{US},1}$  is the first mode shape of the US.

The modal mass, stiffness and damping constant of the isolation system are respectively given by:

$$\tilde{\mathbf{m}}_{\text{ISO}} = \frac{1-\gamma}{\gamma} \tilde{\mathbf{m}}_{\text{US}} \quad (5.10)$$

$$\tilde{\mathbf{k}}_{\text{ISO}} = \tilde{\mathbf{M}}_{\text{ISO}} \omega_{\text{ISO}}^2 \quad (5.11)$$

$$\tilde{\mathbf{c}}_{\text{ISO}} = 2\xi_{\text{ISO}} \tilde{\mathbf{M}}_{\text{ISO}} \omega_{\text{ISO}} \quad (5.12)$$

where the mass ratio  $\gamma$ , given by Eq. (2.104), is equal to:

$$\gamma = \frac{L_1^2 \tilde{\mathbf{M}}_{\text{ISO}}}{\mathbf{M}_{\text{ISO}}} = \frac{\Gamma_{\text{US+ISO},1}}{\mathbf{M}_{\text{ISO}}} \quad (5.13)$$

with  $L_{\text{US+ISO},1}$  and  $\Gamma_{\text{US+ISO},1}$  the first participation factor and participating mass of the isolated US,  $\tilde{\mathbf{M}}_{\text{ISO}} = \tilde{\mathbf{m}}_{\text{US}} + \tilde{\mathbf{m}}_{\text{ISO}}$  the total modal isolated mass. The values adopted for the reduced-order single degree of freedom of the three parts are provided in Tab. 5.6.

### 5.5.1. Isolation Approach: Wang and Kobayashi vs. IB & SSB

In order to grasp the dynamic behavior of structures with middle-story isolation through the lens of the isolation approach, a brief description on the main research contributions is provided in the following. In particular, the studies carried out by [Wang et al. 2011, 2012, 2013], [Kobayashi & Koh 2008] for IIS and by [Kelly 1997] for BIS are briefly introduced and the relevant design provisions are discussed with reference to the IB and SSB case studies.

**Table. 5.6. Dynamic characteristics of LS, US and ISO SDOF models**

Parameters	IB	SSB
$\tilde{m}_{LS}$ [t]	26963	11502
$\tilde{k}_{LS}$ [kN/m]	1112880	404910
$\tilde{c}_{LS}$ [kN s/m]	6929	2730
$\xi_{LS}$	0.02	0.02
$\tilde{m}_{US}$ [t]	4688	23125
$\tilde{k}_{US}$ [kN/m]	4278073	191045
$\tilde{c}_{US}$ [kN s/m]	5665	2659
$\xi_{US}$	0.02	0.02
$\gamma$	0.589	0.750
$\tilde{m}_{ISO}$ [t]	3276	7692
$\tilde{M}_{ISO}$ [t]	7964	30817
$\tilde{k}_{ISO}$ [kN/m]	28275	48236
$\tilde{c}_{ISO}$ [kN s/m]	6003	15422
$\xi_{ISO}$	0.20	0.20

#### 5.5.1.1. *Design parameters and comparison to IB and SSB*

The paper by [Wang et al. 2011 - 2013] proposes a simplified analyses of mid-story isolated structures by means of 3DOF models, composed by LS, ISO and US. The authors identify the parameters governing the dynamic response of the structure and the mode coupling effect, namely (adopting the symbols utilized in the thesis): the ratios of masses of the upper and lower structure to the isolation mass  $r_{US} = \tilde{m}_{US} / \tilde{m}_{ISO}$  and  $r_{LS} = \tilde{m}_{LS} / \tilde{m}_{ISO}$ ; and the ratios of the frequency of the upper and lower structure to the isolation frequency, i.e.  $\omega_{US} / \omega_{ISO}$  and  $\omega_{LS} / \omega_{ISO}$ .

A parametric analysis is carried out with 3DOF models, by setting an isolation period equal to 2 s and varying the above design parameters, i.e. adopting for the mass ratios the value couples  $(r_{LS}, r_{US}) = (1, 5)$  and  $(r_{LS}, r_{US}) = (2, 5)$ , while the frequency ratios  $\omega_{US} / \omega_{ISO}$  and  $\omega_{LS} / \omega_{ISO}$  vary in the range  $3 \div 40$ . In the analysis, both the US and LS have inherent viscous damping ratio of 5%, while for the isolation system an equivalent damping ratio of 20% is assumed.

The mass ratios considered in the analysis always correspond to the case of superstructure heavier than the substructure; further, the frequency ratios are defined by a lower bound equal to 3, which ensures an isolation period at least three times the US period (according to the rule commonly adopted for base isolated structures), and an upper bound, equal to 40, that corresponds to very stiff LS and US.

Starting from the above design parameters, the ratio of the dynamic stiffness of the US and LS,  $k_{US} / k_{LS}$ , can be derived and compared to the corresponding values of the case studies considered in this paper; for this purpose, derived the ratio  $r_{US} / r_{LS}$ , which varies between 2.5 and 5, and varying both the frequency ratios between 3 and 40, the range of the stiffness ratios between the US and LS are computed. As can be seen in Chapter 4 (§ 4.4.2), the range for the ratio  $k_{US} / k_{LS}$  is equal to  $0.1 \div 5$ ; thus, both stiffer and more flexible US than LS are considered. The ranges of the design parameters selected by [Wang et al. 2011 - 2013], namely the mass ratios ( $r_{US}$ ,  $r_{LS}$ ,  $\tilde{m}_{US} / \tilde{m}_{LS}$ ), the period ratios ( $T_{ISO} / T_{US}$ ,  $T_{ISO} / T_{LS}$ ), the stiffness ratios ( $k_{US} / k_{LS}$ ), are compared to the corresponding values of the Iidabashi and Shiodome buildings in Tab. 5.7.

**Table. 5.7. Comparison of design parameters: [Wang et al 2011 - 2013] vs. IB and SSB**

	Wang et al.	IB	SSB
$r_{US}$	5	1.4	3.0
$r_{LS}$	$1 \div 2$	8.2	1.5
$\tilde{m}_{US} / \tilde{m}_{LS}$	$2.5 \div 5$	0.2	2.0
$T_{ISO,RB} / T_{US}$	$3 \div 40$	15.9	2.3
$T_{ISO,RB} / T_{LS}$	$3 \div 40$	3.4	4.7
$T_{ISO,RB+D}^{(2)} / T_{US}$	$3 \div 40$	12.5	1.8
$T_{ISO,RB+D}^{(2)} / T_{LS}$	$3 \div 40$	2.7	3.7
$(k_{US} / k_{LS})_{dyn}$	$0.1 \div 5$	4.4	0.5

From the comparison with the parameter ranges, it is possible to observe that: the US mass ratio,  $r_{US}$ , is smaller than 5, the reference upper bound set by [Wang et al. 2011 - 2013], for both the buildings; the LS mass ratio,  $r_{LS}$ , in IB is larger and in SSB is smaller than 2, the maximum value defined by [Wang et al. 2011 - 2013]; the US-LS mass ratio,  $\tilde{m}_{US} / \tilde{m}_{LS}$ , is smaller than 2.5, the minimum value adopted by Wang, for both buildings.

With regard to the period ratios, i.e.  $T_{ISO} / T_{US}$  and  $T_{ISO} / T_{LS}$ , both fall within the range  $3 \div 40$  for the IB; in the SSB only  $T_{ISO} / T_{LS}$  is within the

range, while  $T_{ISO} / T_{US}$  is much smaller than the lower bound. Finally, the stiffness ratio  $k_{US} / k_{LS}$  of both the buildings are within the Wang range  $0.1 \div 5$ .

Summing up, in both buildings the mass ratios (US and LS to ISO) fall outside the range defined by Wang (except for the ratio  $r_{LS}$  in SSB), while the ratio between the two masses of US and LS is smaller in IB than in SSB, and only the latter is within the considered range. In IB both the frequency and stiffness ratios belong to the range set by Wang, while in SSB only  $T_{ISO} / T_{LS}$  is approximately equal to the lower bound of the range. The value that mainly seems to affect the dynamic behavior of SSB, as already seen in the previous paragraphs, is the stiffness ratio  $k_{US} / k_{LS}$ , that is very small.

#### **5.5.1.2. Analysis results – mode coupling effect and comparison to IB and SBB**

Considering the range of the design parameters described above, and in particular  $\omega_{US} / \omega_{ISO}$  and  $\omega_{LS} / \omega_{ISO}$ , [Wang et al. 2011 - 2013] have investigated the effect of the higher modes on the dynamic behavior of a mid-story isolated structure. The results of the parametric analysis carried out on 3DOF models are shown in Fig. 5.5, where the effect of higher modes and the potential of modal coupling effect in mid-story isolated structures are provided as a function of the couples of frequency ratios  $\omega_{US} / \omega_{ISO}$  and  $\omega_{LS} / \omega_{ISO}$ .

In particular the graph is divided into three parts, which represent the two regions where either the 2<sup>nd</sup> or the 3<sup>rd</sup> mode prevails, and the bandwidth, marked by continuous lines, where coupling of the 2<sup>nd</sup> and the 3<sup>rd</sup> modes occurs.

In particular, the dotted line in the MCE bandwidth is obtained considering the following formula derived by [Wang et al. 2011 - 2013; Kobayashi & Koh 2008] for addressing the coupling, described in Chapter 4 and recalled here for completeness, i.e.:

$$\frac{\omega_{LS}}{\omega_{ISO}} = \frac{\omega_{US}}{\omega_{ISO}} \sqrt{1 + r_{US}} \quad (4.1)$$

In Fig. 5.5, the bandwidth is built up considering a deviation from Eq. (4.1) of  $\pm 15\%$ .

From the Fig. 5.5 it can be observed that quite different values of the frequency ratios cause a mode coupling effect; on the contrary, equal or very different values of  $\omega_{US} / \omega_{ISO}$  and  $\omega_{LS} / \omega_{ISO}$  avoid MCE. Large values of both parameters not only exclude a dynamic coupling between the US and LS, but also allow for remarkable simplifications from a design point of view, namely the first frequency and mode damping are approximately equal to the isolation system counterparts, i.e.  $\omega_1 \cong \omega_{ISO}$  and  $\xi_1 \cong \xi_{ISO}$ .

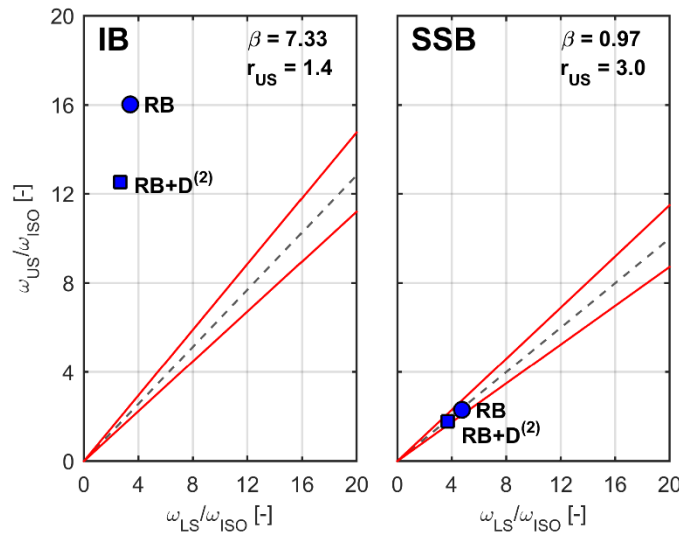


Fig. 5.5. Effect of the higher modes

According to the graph, when the value of  $\omega_{US} / \omega_{ISO}$  is large (say, larger than 16), even though  $\omega_{LS} / \omega_{ISO}$  is small, the effect of the 2<sup>nd</sup> mode is predominant, the second modal frequency is approximately equal to the frequency of the substructure, i.e.  $\omega_2 \approx \omega_{LS}$ , and the participating mass ratio of the 3<sup>rd</sup> mode,  $\Gamma_3$ , is equal to zero. When  $\omega_{LS} / \omega_{ISO}$  is large, say, larger than 16, if  $\omega_{US} / \omega_{ISO}$  is smaller than 8 in IB and 6 in SSB, the effect of the 3<sup>rd</sup> mode is predominant, the third modal frequency is approximately equal to the frequency of the substructure, i.e.  $\omega_3 \approx \omega_{LS}$ , and the participating mass ratio of the 2<sup>nd</sup> mode,  $\Gamma_2$ , is equal to zero; for  $\omega_{LS} / \omega_{ISO}$  equal to 20, instead, the effect of the 2<sup>nd</sup> mode is predominant if  $\omega_{US} / \omega_{ISO}$  is larger than 15 in IB and 12 in SSB, while for whatever value of  $\omega_{LS} / \omega_{ISO}$  larger than 16, no coupling effect is predicted if  $\omega_{US} / \omega_{ISO}$  is,

as well, larger than 16. In all cases, since [Wang et al. 2011 - 2013] consider a rigid US with respect to the isolation system, the effect of the higher modes are only related to the motion of the LS. When there is a coupling effect, both frequencies  $\omega_2$  and  $\omega_3$  are far from the frequency  $\omega_{LS}$  and both participating mass ratios  $\Gamma_2$  and  $\Gamma_3$  are different from zero.

In addition, from Eq. (4.1), the term  $1/\sqrt{1+r_{US}}$  represents the slope of the dotted lines in Fig. 5.5. When this term is equal to 0.63, i.e.  $\omega_{US}/\omega_{ISO}$  is 0.63 times  $\omega_{LS}/\omega_{ISO}$ , the MCE occurs in IB; when it is equal to 0.50, i.e.  $\omega_{US}/\omega_{ISO}$  is 0.50 times  $\omega_{LS}/\omega_{ISO}$ , the MCE arises in SSB.

Considering the two building case studies, it is possible to represent in the diagram of Fig. 5.5 the couples of values  $(\omega_{LS}/\omega_{ISO}, \omega_{US}/\omega_{ISO})$ , respectively for RB and RB+D<sup>(2)</sup> models, i.e.: (3.4, 16.0) and (2.7, 12.5) for the IB; (4.7, 2.3) and (3.7, 1.8) for the SSB.

In the IB, at quite large values of  $\omega_{US}/\omega_{ISO}$  correspond low values of  $\omega_{LS}/\omega_{ISO}$ ; while in the RB model both the values fall within the parametric range ( $3 \div 40$ ), in the RB+D<sup>(2)</sup> model the parameter  $\omega_{LS}/\omega_{ISO}$  is lower than the lower bound. In the SSB, on the contrary, the couples are composed by quite low values, and in particular  $\omega_{US}/\omega_{ISO}$  are smaller than the lower bound of the range. Therefore, a predominant effect of the 2<sup>nd</sup> mode is expected in the IB, while a modal coupling effect should occur in the SSB. The above predictions on dynamic characteristics and higher mode effects in the two buildings fully agree with the results of the modal analysis carried out on the RB MDOF models, already provided in Fig. 5.3. In fact, for the IB RB model, the second period,  $T_{RB,2}$  is 0.95 s, which closely matches the equivalent period of the LS,  $T_{LS}$ , equal to 0.98 s; according to [Wang et al. 2011 - 2013], when  $T_{RB,2} \approx T_{LS}$  and the frequency ratios are quite distant, as in the IB case, the vibration characteristics of the building are mainly affected by the 2<sup>nd</sup> mode and the third mode effect is negligible, as confirmed by the participating mass ratio,  $\Gamma_{RB,2}$  and  $\Gamma_{RB,3}$ , respectively equal to 58.1% and 9.3%. In the SSB RB model  $T_{RB,2}$  and  $T_{RB,3}$  are equal to 1.183 s and 0.96 s, and the equivalent period of the LS,  $T_{LS}$ , equal to 1.06 s, is an average value between  $T_{RB,2}$  and  $T_{RB,3}$ ; further, considering that the frequency ratios are very similar, a coupling effect of the higher modes is expected, as can be clearly observed looking at the second and third mode shapes of Fig. 5.3, and as also confirmed by Fig. 5.4, where, considering all higher modes, 10 over 26 are coupled modes, with displacements occurring both in the LS and US.

Similar considerations can be done taking into account the IB and SSB RB+D<sup>(2)</sup> models.

In addition, recalling the MCE parameter  $\beta$  introduced in Chapter 4 for 3DOF IIS models (see [Wang et al. 2011 - 2013; Kobayashi & Koh 2008]):

$$\beta = \frac{\omega_{US} \sqrt{1 + r_{US}}}{\omega_{LS}} = \frac{T_{LS}}{T_{US}} \sqrt{1 + r_{US}} \quad (4.4)$$

the MCE occurs when it is equal or very close to one.

Therefore, the MCE parameter  $\beta$  for IB and SSB, also provided in Fig. 5.5, is respectively equal to

$$\beta_{IB} = \frac{0.98}{0.21} \sqrt{1 + 1.4} = 7.33 \gg 1.0; \quad \beta_{SSB} = \frac{1.06}{2.18} \sqrt{1 + 3.0} = 0.97 \approx 1.0$$

For IB a value of  $\beta$  equal to 7.33 (very far from 1) indicates no coupling of the higher modes, while for SSB a value of 0.97 (close to 1) suggests MCE.

Observing each term in the formula for both IB and SSB, while the periods  $T_{LS}$  are comparable (0.98 s vs. 1.06 s), the periods  $T_{US}$  (0.21 s vs. 2.18 s) and the US mass ratio  $r_{US}$  (1.4 vs. 3.0) are far away from each other. Therefore, the dynamic characteristics (mass and stiffness) of the US lead to a deeply different dynamic behavior of the two buildings, suggesting modal coupling only in SSB.

Approximately, from the analysis of the two buildings, the MCE is avoided if the periods of the US and LS are well separated, at least 1:5.

It is worth noticing that this formulation is still valid for MDOF models since the MCE occurs between the first mode of the US isolated at the base and of the LS. If the modal coupling arises for modes higher than the first of those two portions, the parameter  $\beta$  so defined is not able to keep the global behavior of the model.

These results seem to confirm the previous preliminary guess of the MCE implying US and LS structures move together.



### 5.5.2. Isolation approach: Kelly vs. IB and SSB

An additional insight into the behavior of the mid-story isolated structures can be done by checking if the structural complex made by the US and ISO can be considered dynamically equivalent to a base isolated structure. For this purpose, a comparison is carried out with reference to the linear theory formulated by [Kelly 1997, Naeim and Kelly 1999], detailed described in Chapter 2 (§ 2.2).

According to Kelly's linear theory, a base isolated structure is mainly affected by the first mode, with a mode shape  $\{\phi_1\}^T = \{1, \varepsilon\}^T$  (Eq. (2.27)), where the parameter  $\varepsilon$  represents the amplification of the displacement in the US with respect to the isolation layer.

The parameter  $\varepsilon$  can be estimated as the square of the ratio between the frequencies of the base isolated system,  $\omega_b$ , and of the fixed base structure,  $\omega_s$ , or, equivalently, between the period  $T_s$  and  $T_b$ , i.e.:

$$\varepsilon_{BIS} = \left( \frac{\omega_b}{\omega_s} \right)^2 = \left( \frac{T_s}{T_b} \right)^2 \quad (5.14)$$

In the case of a mid-story isolated structure, we can substitute  $T_s$  and  $T_b$  with  $T_{US}$  and  $T_{ISO}$ , respectively, in order to obtain an estimate of  $\varepsilon$ :

$$\varepsilon_{ISO} = \left( \frac{T_{US}}{T_{ISO}} \right)^2 \quad (5.15)$$

For a base isolated structure, with  $T_s = 0.4$  sec,  $T_b = 2.0$  sec, and a mass ratio  $\gamma$  equal to 0.6 (being  $\gamma = m / (m + m_b)$ , Eq. (2.13)), the parameter  $\varepsilon$  is equal to 0.04. Typically, for base isolated buildings with well separated fixed-base and isolation frequencies,  $\varepsilon$  is of the order of  $10^{-2}$ .

In the Iidabashi and Shiodome buildings, the values of  $\varepsilon$  calculated according to the formula (5.15), are equal to 0.004 and 0.19, i.e. one order of magnitude smaller and larger, respectively, than the typical value of a base isolated structure. Considering the MDOF models, it is also possible to estimate  $\varepsilon$  as a function of the modal characteristics, i.e.:

$$\varepsilon = \Delta_{TOP,US} / u_{ISO} \quad (5.16)$$

where  $\Delta_{\text{TOP,US}}$  is the modal relative top-bottom displacement of the US and  $u_{\text{ISO}}$  is the modal displacement of the isolation. The values of  $\varepsilon$  computed according to the formula (5.16) are: for the Iidabashi building 0.008, and for the Shiodome building 0.20.

Therefore, the prediction of the first mode shape according to the linear theory of Kelly for base isolated structures is also valid for mid-storey isolated buildings, considering the upper structure and the intermediate isolation system. With respect to typical base isolated structures, a wider variation of the values of  $\varepsilon$  (of two orders of magnitude) can be observed as a function of the upper structure flexibility in the case studies here considered. The values of  $\varepsilon$  computed according to the formula (5.16) are of the same order of magnitude as the ones obtained according to the definition (5.15). The order of magnitude of  $10^{-1}$  derived from (5.15) and (5.16) for the SSB, confirm the peculiar, non typical behavior of this building.

On the basis of the above observations, the parameter  $\varepsilon$ , computed according to the formula (5.15) on the basis of the US and isolation periods, can be used in a preliminary design of the superstructure in order to have the order of magnitude of the expected relative displacements, i.e. as a prediction of the value given by the formula (5.16).

### 5.5.3. Theory and practice: Mass Damping Approach vs. IB and SSB

In order to apply the optimal formulations provided in the current literature for the mass damping approach, a controlled 2DOF reduced-order model is considered by neglecting the contribution of dampers (2DOF RB model) for the sake of simplicity.

Considering the 2DOF RB model, in Eq. (5.1) the matrices  $\mathbf{M}$ ,  $\mathbf{C}$ ,  $\mathbf{K}$  and the vectors  $\mathbf{x}$ ,  $\mathbf{r}$  have  $2 \times 2$  and  $2 \times 1$  dimensions, respectively.

In particular the first and the second degree of freedom are characterized by masses, stiffnesses and damping constants respectively equal to  $\tilde{m}_{\text{LS}}$ ,  $\tilde{k}_{\text{LS}}$ ,  $\tilde{c}_{\text{LS}}$ , and  $\tilde{M}_{\text{ISO}}$ ,  $\tilde{k}_{\text{ISO}}$ ,  $\tilde{c}_{\text{ISO}}$ .

The mass ratio  $\alpha$ , defined as the ratio between the isolated mass and the lower mass, i.e.  $\alpha = \tilde{M}_{\text{ISO}} / \tilde{m}_{\text{LS}}$ , the real value of  $f$ , a variation of the isolation damping ratio  $\xi_{\text{ISO}}$  between  $0.1 \div 0.5$  are provided in Tab. 5.8 for the two buildings.

The values of the frequency and damping ratios,  $f$  and  $\xi_{iso}$ , adopted for IB and SSB, are compared to the optimal values,  $f_{opt}$  and  $\xi_{iso,opt}$ , derived from the papers [Sadek et al. 1997, Reggio & De Angelis 2015, Zhou et al. 2016, Ping et al. 2008, Ayorinde & Warburton 1980, Moutinho 2012, Hoang et al. 2007] and are provided in Tab. 5.9.

**Table 5.8. Real values of  $\alpha$ ,  $f$ ,  $\xi_{iso}$  of the two buildings 2DOF RB models**

Parameters	IB	SSB
$\alpha$	0.295	2.679
$f$	0.293	0.211
$\xi_{iso}$	$0.10 \div 0.50$	$0.10 \div 0.50$

**Table 5.9. Optimal values in the current literature**

Paper	IB		SSB	
	$f_{opt}$ [-]	$\xi_{iso,opt}$ [-]	$f_{opt}$ [-]	$\xi_{iso,opt}$ [-]
Sadek et al. 1997	0.765	0.493	0.267	0.859
Reggio & De Angelis 2015	0.762	0.246	0.275	0.432
Zhou et al. 2016	0.745	0.500	0.408	0.500
Ping et al. 2008	0.666	0.250	0.094	0.500
Ayorinde & Warburton 1980	0.713	0.249	-	-
Feng & Mita 1995	0.713	0.299	-	-
Moutinho 2012	0.765	0.298	-	-
Hoang et al. 2007	0.716	0.209	-	-

From Tab. 5.9 can be seen that, for IB  $f_{opt}$  varies between  $0.666 \div 0.765$  and  $\xi_{iso,opt}$  between  $0.209 \div 0.500$ ; for SSB  $f_{opt}$  varies between  $0.094 \div 0.408$  and  $\xi_{iso,opt}$  between  $0.432 \div 0.859$ .

Therefore, for both the buildings, a certain variability of the optimal values can be observed. In addition, for SSB, that is characterized by a large mass ratio  $\alpha$  (say, more than 1), many optimal formulae cannot be applied. This suggests that, for the mass damping effect, the mass ratios should be smaller than, or almost equal to, 1.

The formulations or the graphical representation of the optimal values, adopted by the authors of these papers, have been described and discussed in the previous Chapters 2 and 4, and are recalled here for completeness.

- [Sadek et al. 1997]

The optimal parameters defined by Sadek et al. for a SDOF structure - TMD system, resulting in equal damping ratios and equal frequencies in the two complex modes of vibration, are derived by a curve fitting of the results, i.e.:

$$f_{opt} = \frac{1}{1+\alpha} \left[ 1 - \xi_{LS} \sqrt{\frac{\alpha}{1+\alpha}} \right]; \quad \xi_{ISO,opt} = \frac{\xi_{LS}}{1+\alpha} + \sqrt{\frac{\alpha}{1+\alpha}} \quad (4.10)$$

- [Reggio & De Angelis 2015]

Reggio and De Angelis propose an energy-based design methodology for non-conventional TMD, consisting in the maximization of an energy performance index (namely: EDI), defined as the ratio between the energy dissipated in the isolation system and the total input energy, by assuming the ground acceleration as a stationary Gaussian stochastic process with zero mean and white noise spectral density. Considering a SDOF structure - TMD system, for  $\xi_{LS} = 0.02$  the optimal parameters can be derived by Fig. 4.19, recalled here for completeness.

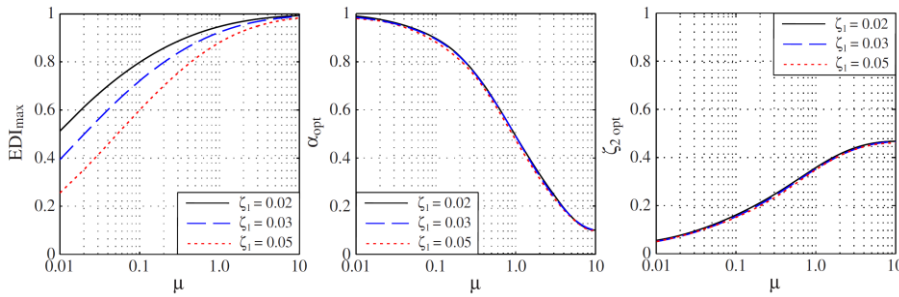


**Fig. 4.19. Reduced-order two-DOF model,  $EDI_{max}$  and optimal design parameters vs. mass ratio for various damping ratios of the primary oscillator, i.e. 0:02; 0:03; 0:05: (a)  $EDI_{max}$ , (b) optimal frequency ratio, (c) optimal damping ratio [Reggio & De Angelis 2015]**

- [Zhou et al. 2016]

Zhou et al. derive the optimal parameters for a 2DOF reduced-order model by minimizing the variance of the base shear for a band limited white noise. Neglecting the structural damping, the following optimal formulae are utilized:

$$f_{\text{opt}} = \sqrt{\frac{\sqrt{C_2^2 + 4L_{\text{LS},1}^2 C_1} - C_2}{2C_1}} \quad (5.17)$$

$$C_1 = 3(\alpha + 1)^2 (L_{\text{LS},1} + \alpha)^2 \quad (5.18)$$

$$C_2 = (L_{\text{LS},1} + \alpha)^2 [4(\alpha + 1)\xi_{\text{ISO,max}}^2 + \alpha] - 2L_{\text{LS},1}(\alpha + 1)(L_{\text{LS},1} + \alpha) \quad (5.19)$$

where  $\xi_{\text{ISO,max}} = 0.5$  and  $L_{\text{LS},1}$  is the participation factor of the LS fundamental mode.

- **[Ping et al. 2008]**

Ping et al. employ an optimization procedure based on the minimization of the base shear variance assuming earthquake excitation as a stationary stochastic process with zero mean. Considering a 2DOF reduced-order model, the optimal parameters can be derived by Fig. 4.1, recalled here for completeness.

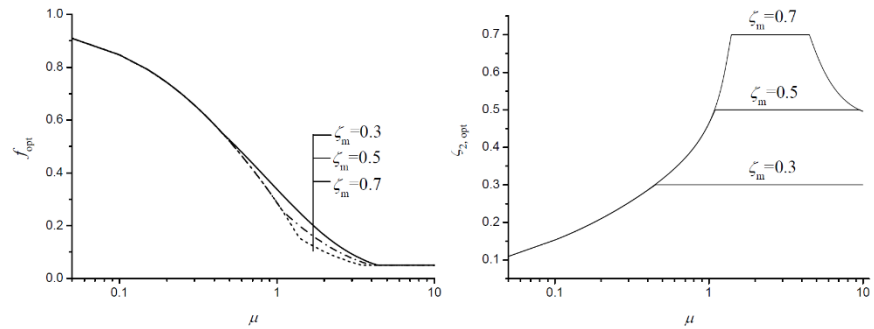


**Fig. 4.1. Optimal design parameters: (a) optimal frequency ratio vs. mass ratio (b) optimal damping ratio vs. mass ratio [Ping et al. 2008]**

- **[Ayorinde & Warburton 1980]**

Ayorinde and Warburton defined the optimum parameters for an undamped 2DOF reduced-order model under a white noise ground excitation, given by:

$$f_{\text{opt}} = \frac{\sqrt{1-\alpha/2}}{1+\alpha}; \quad \xi_{\text{ISO,opt}} = \sqrt{\frac{\alpha(1-\alpha/4)}{4(1+\alpha)(1-\alpha/2)}} \quad (5.20)$$

- **[Feng & Mita 1995]**

Feng and Mita utilized a mega-subconfiguration systems in which the mega-structure represents the main structure, while the substructure the TMD. The authors derived the optimum parameters of a 2DOF reduced-order model by minimizing the mean square values of the displacements of the mega-structure and accelerations of substructures, assuming a ground motion represented by a white noise, i.e.:

$$f_{\text{opt}} = \frac{\sqrt{1-\alpha/2}}{1+\alpha}; \quad \xi_{\text{ISO,opt}} = \frac{1}{2} \sqrt{(1+\alpha)f^4 + f^2 + \frac{1-3(1+\alpha)^2 f^2}{(1+\alpha)^3}} \quad (5.21)$$

- **[Moutinho 2012]**

Moutinho defines the optimum parameters for a 2DOF reduced-order model that simultaneously meet the condition of equal modal damping in the complex modes of vibration, and are in correspondence with the minimum value of the maximum frequency response function (FRF) amplitude associated with the response of the main mass.

The author provides tabulated optimum values as a function of the structural damping ratios and the mass ratios between the TMD and the main structure. A simple parabolic interpolation is used to calculate intermediate values among the values proposed by Moutinho.

- **[Hoang et al. 2007]**

Hoang et al. proposed different optimum parameters by considering the ground motion modeled by a stationary stochastic process with a power spectral density.

They conclude that the ground damping ratio produces negligible effect on the determination of optimal TMD parameters.

For a 2DOF reduced-order model, considering a structural frequency equal to the ground frequency, the optimal parameters are derived by a curve fitting of the results, i.e.:

$$f_{\text{opt}} = \frac{\sqrt{(1-0.6\alpha)(1-\alpha^2)}}{1+\alpha} - 0.7\xi_{\text{LS}}; \quad \xi_{\text{ISO,opt}} = \frac{\sqrt{\alpha(1+2.5\alpha+\alpha^2)}}{2(1+2.7\alpha)} \quad (5.22)$$

In order to compare the real and optimal values of the frequency and damping ratios for IB and SSB, the frequency response function  $H_{u_{\text{LS}}}(\rho)$  of the LS displacement with respect to ground acceleration for the uncontrolled (LS) and controlled (IIS) configurations, described in Chapter 4, is utilized and recalled here for completeness.

$$H_{u_{\text{LS,LS}}}(\rho) = -\frac{1}{1-\rho^2 + \frac{2i\rho\xi_{\text{LS}}}{\sqrt{1+\alpha}}} \quad (4.58)$$

$$H_{u_{\text{LS,IIS}}}(\rho) = -\frac{C_0(\rho)}{1+\alpha - \rho^2 C_0(\omega) + 2i\rho\xi_{\text{LS}}\sqrt{1+\alpha}} \quad (4.59)$$

where

$\rho = \Omega / \omega_{\text{LS}}$  is the ratio between the input frequency,  $\Omega$ , and the LS natural frequency,  $\omega_{\text{LS}}$ .

$$C_0(\rho) = 1 + \alpha \frac{f^2(1+\alpha) + 2i\rho f\xi_{\text{ISO}}\sqrt{1+\alpha}}{f^2(1+\alpha) - \rho^2 + 2i\rho f\xi_{\text{ISO}}\sqrt{1+\alpha}} \quad (4.60)$$

The frequency response function  $H_{u_{\text{LS}}}(\rho)$  of the LS displacement with respect to ground acceleration in the uncontrolled (LS), really and optimally controlled (IIS) configurations are shown in Figs 5.6 ÷ 5.13; each couple of graphs refers to the results obtained for the two buildings 2DOF models. In particular, Figs. 5.6 ÷ 5.9 depict the real configurations of the two buildings for different damping ratios (0.1, 0.2, 0.3, 0.5); Figs. 5.10 ÷ 5.13 show the results for the optimally configurations derived from the papers [Sadek et al. 1997, Reggio & De Angelis 2015, Zhou et al. 2016, Ping et al. 2008].

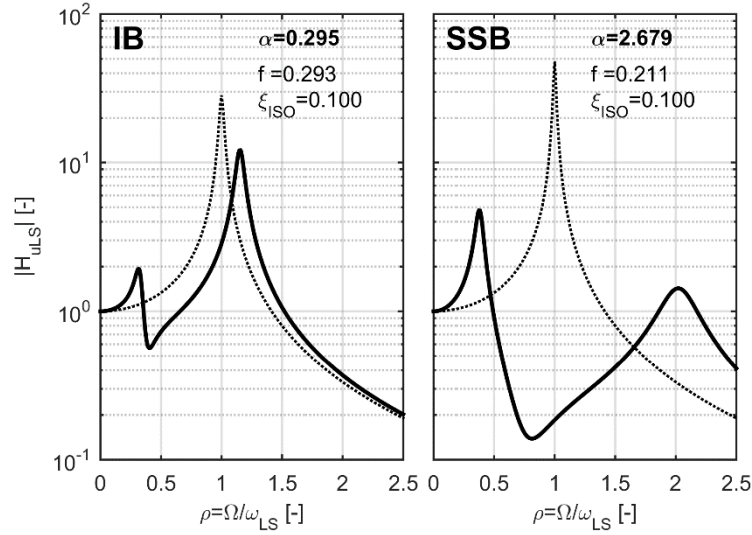


Fig. 5.6. IB vs. SSB: frequency response function of the LS displacement with respect to ground acceleration in the uncontrolled (dotted line) and controlled (continuous line) configurations;  $\xi_{ISO} = 0.1$ .

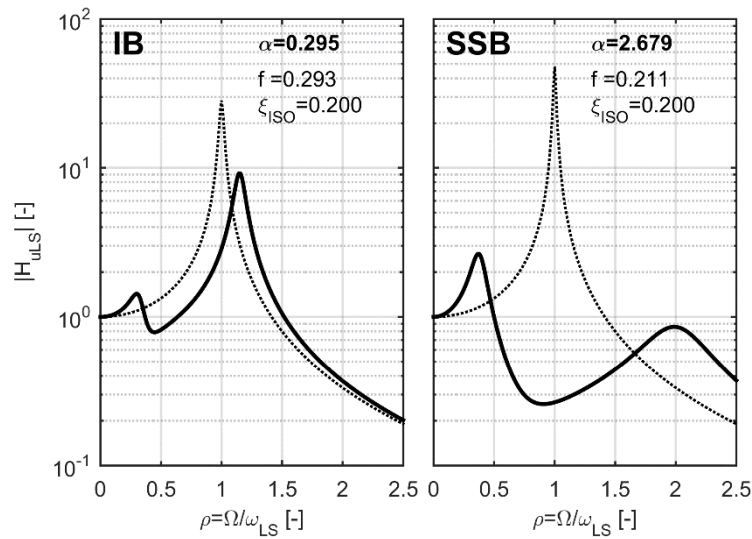


Fig. 5.7. IB vs. SSB: frequency response function of the LS displacement with respect to ground acceleration in the uncontrolled (dotted line) and controlled (continuous line) configurations;  $\xi_{ISO} = 0.2$ .



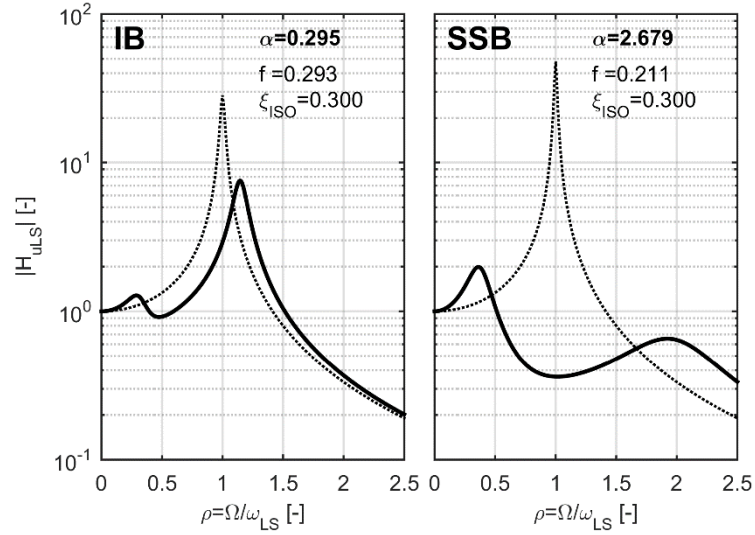


Fig. 5.8. IB vs. SSB: frequency response function of the LS displacement with respect to ground acceleration in the uncontrolled (dotted line) and controlled (continuous line) configurations;  $\xi_{ISO} = 0.3$ .

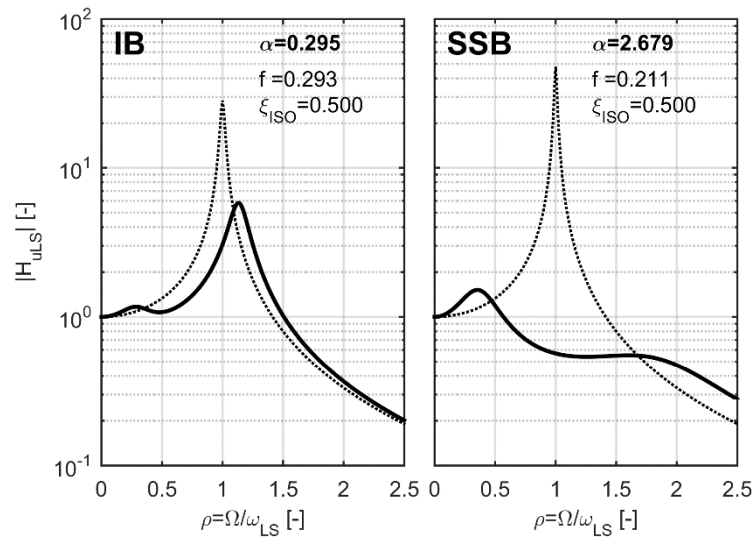


Fig. 5.9. IB vs. SSB: frequency response function of the LS displacement with respect to ground acceleration in the uncontrolled (dotted line) and controlled (continuous line) configurations;  $\xi_{ISO} = 0.5$ .

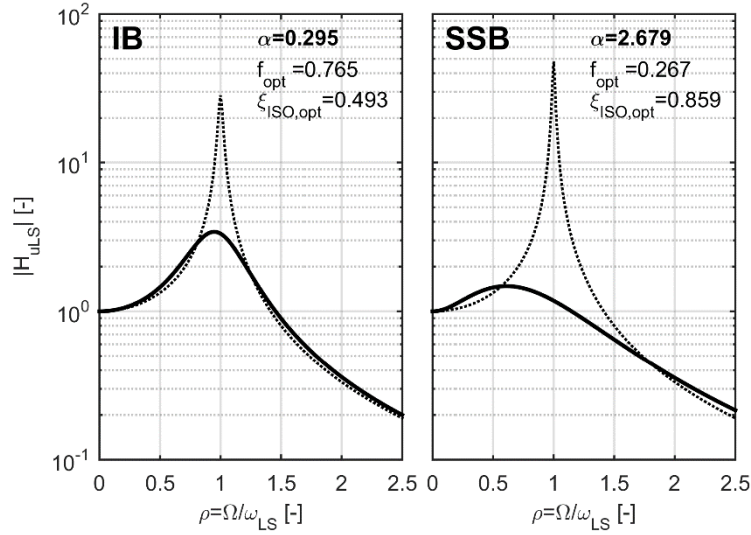


Fig. 5.10. Sadek et al. vs. IB and SSB: frequency response function of the LS displacement with respect to ground acceleration in the uncontrolled (dotted line) and optimally controlled (continuous line) configurations.

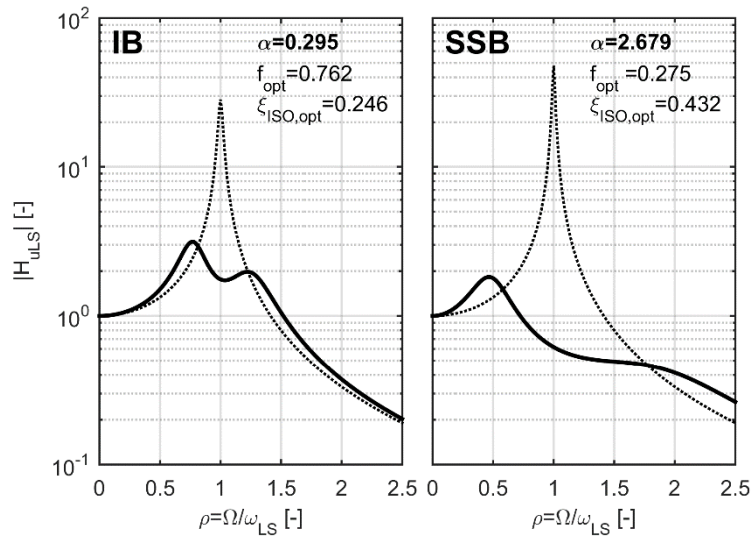


Fig. 5.11. Reggio & De Angelis vs. IB and SSB: frequency response function of the LS displacement with respect to ground acceleration in the uncontrolled (dotted line) and optimally controlled (continuous line) configurations.

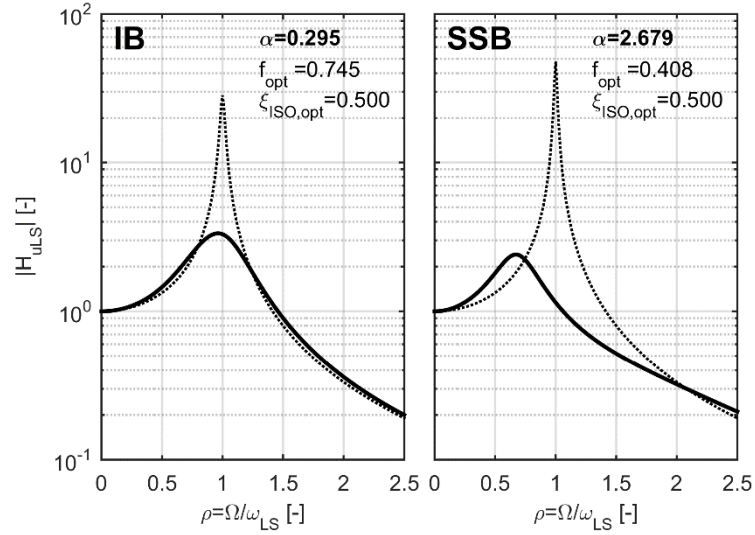


Fig. 5.12. Zohu et al. vs. IB and SSB: frequency response function of the LS displacement with respect to ground acceleration in the uncontrolled (dotted line) and optimally controlled (continuous line) configurations.

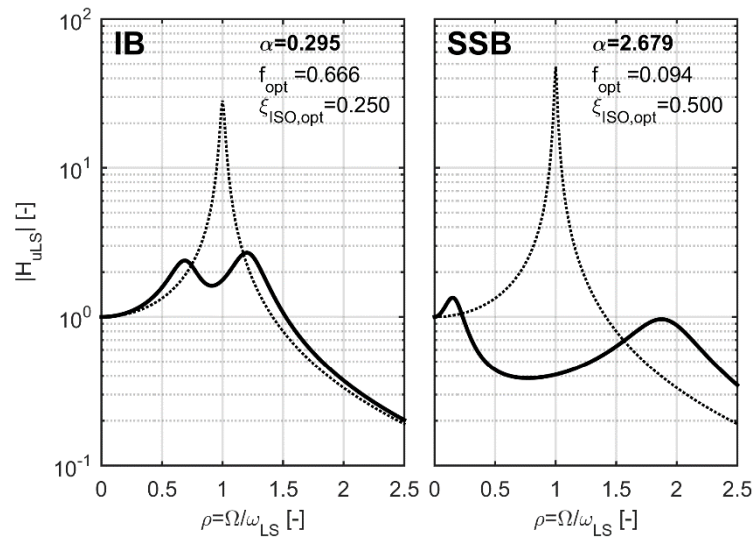


Fig. 5.13. Ping et al. vs. IB and SSB: frequency response function of the LS displacement with respect to ground acceleration in the uncontrolled (dotted line) and optimally controlled (continuous line) configurations.

As can be seen from these figures, the frequency response curves in the LS and IIS configurations intersect at two points, which identify the bandwidth controlled by the TMD (operating range): between these points, the amplitude of the frequency response function is reduced due to the presence of the isolators, elsewhere it is increased.

Comparing the graphs, can be noticed that, in SSB, the large mass ratio  $\alpha$  leads to greater reductions of the LS displacement response over a much broader frequency range, also in the really untuned controlled configuration (Figs. 5.6 ÷ 5.9). Therefore, the large mass ratio increases the robustness of TMD, improving its seismic effectiveness. In fact, the system becomes less dependent on the earthquake frequency content and on the optimal configuration. In addition, observing the real controlled configurations of the two buildings (Figs. 5.6 ÷ 5.9), it is possible noticing that, increasing the damping ratio from 0.1 to 0.5, the LS displacement response increases in the operating range and decreases outside.

## 5.6. TIME HISTORY ANALYSES

In order to assess the response of the two mid-story isolated buildings to seismic inputs, the MDOF RB, RB+D and FB models, already described in paragraphs 5.3 and 5.4, have been utilized for carrying out time history analyses. The RB+D models fully account for the nonlinear behavior of the isolation devices and dampers, while both the US and LS are considered elastic. The seismic waves considered for the analyses are obtained from three ground motion records, El Centro S00E (TH1), Hachinohe NS (TH2) and Taft S69E (TH3), scaled in order to set the maximum velocity to the target value of 50 cm/s, as specified by the Japanese seismic code. Data of the scaled ground motions are given in Tab. 5.10, while in Figs. 5.14 – 5.15 the scaled acceleration input waves and the relevant response spectra in acceleration are provided.

**Table 5.10. Major data of scaled input waves for dynamic analysis**

Input wave for analysis	El Centro S00E	Hachinohe NS	Taft S69E
Max. Acceleration [g]	0.457	0.343	0.515
Max. Velocity [cm/s]	49.98	50.00	50.00
Step Time [s]	0.02	0.01	0.02
Analysis Time [s]	53.78	65.68	54.28

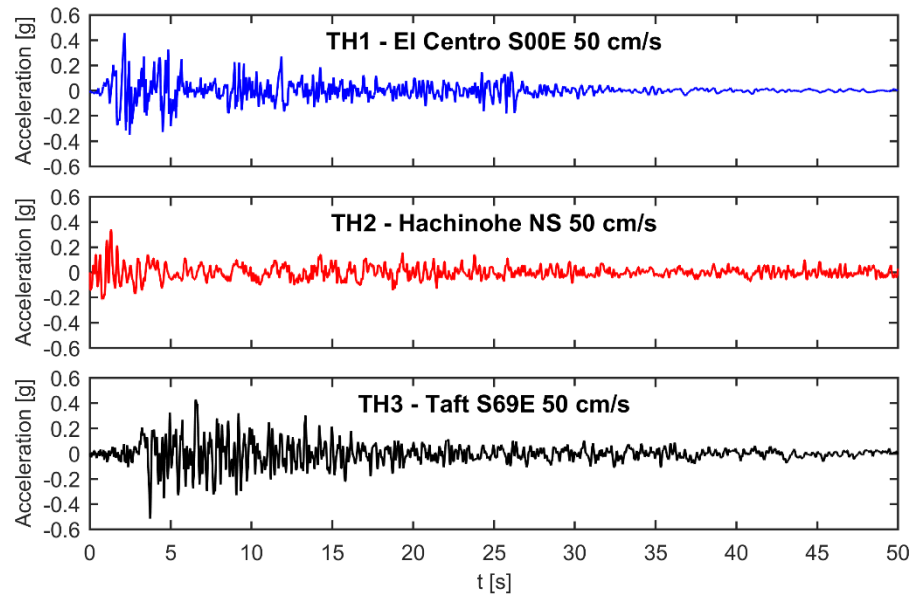


Fig. 5.14. Acceleration records: (a) El Centro S00E, (b) Hachinohe NS, (c) Taft S69E

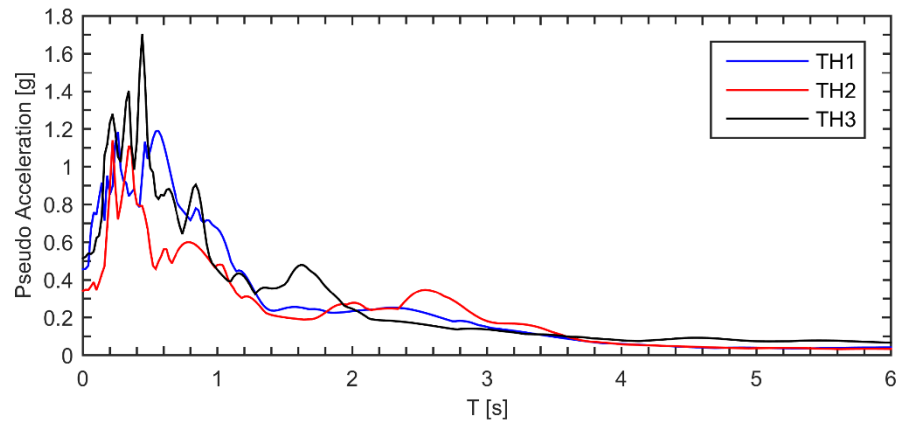
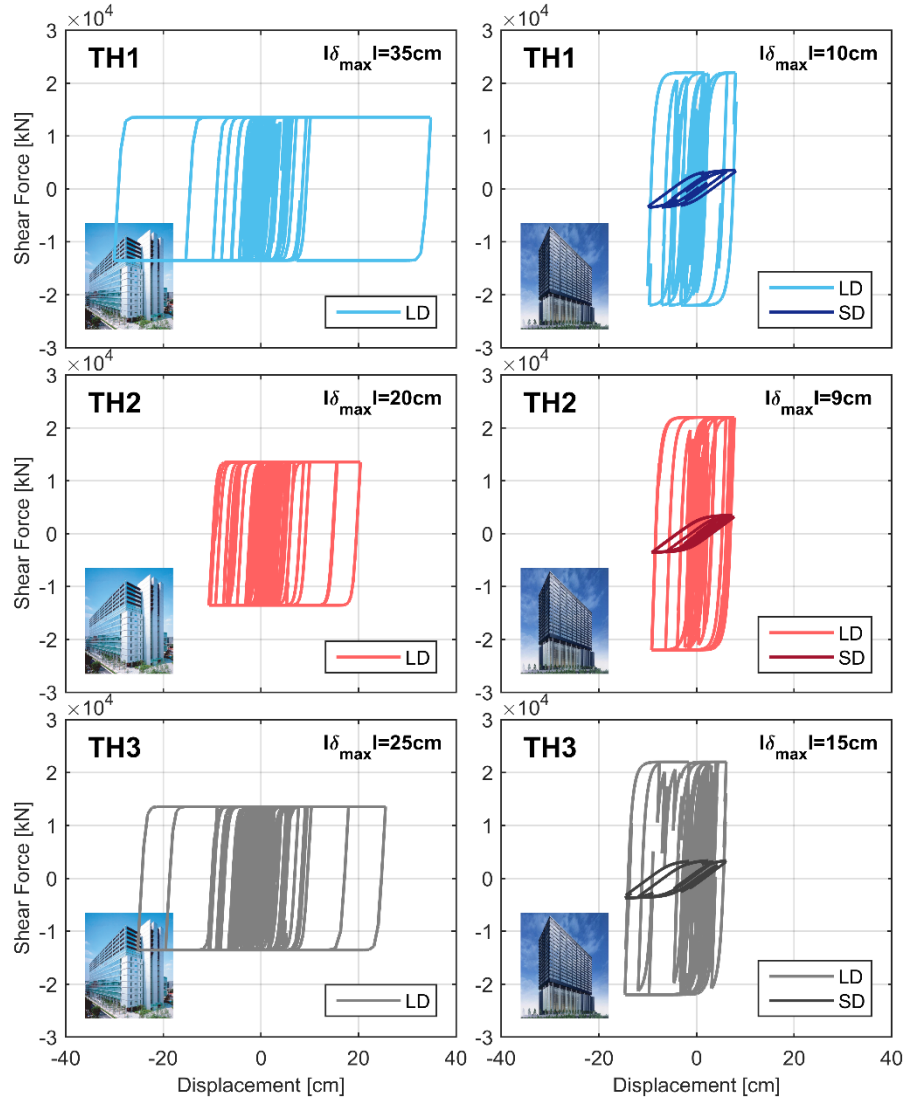


Fig. 5.15. Scaled Pseudo-Acceleration Response Spectra

### 5.6.1. Hysteresis loops

The hysteresis loops of the dampers obtained from the time history analyses of the RB+D models of the Iidabashi and Shiodome buildings are shown in Fig. 5.16.



**Fig. 5.16. Hysteretic response of dampers: (a) Iidabashi 1<sup>st</sup> Building, (b) Shiodome Sumitomo Building**

Each couple of graphs refers to the results obtained for the buildings models subjected to a specific seismic input, i.e. El Centro, Hachinohe and Taft; in each graph, the maximum displacement registered at the isolation interface during the time history is also provided.

According to the specified restoring force characteristics, the dampers in both the buildings show a bi-linear force-displacement response. In particular, in the Shiodome building (graphs on the right) the lead dampers have a larger value of the first stiffness than the steel dampers, and only the latter show a second stiffness different from zero, see Tab. 5.2. The isolation layer (rubber bearings + dampers) in the Iidabashi Building is characterized by a global initial stiffness and a global damper yield force, lower than the Shiodome building counterparts. Therefore the displacement of the isolation layer in the IB is always larger than in the SSB.

### 5.6.2. Maximum story drifts

The story drift envelopes obtained from the time history analyses of the three MDOF (RB, RB+D and FB) models of the Iidabashi and Shiodome buildings are shown in Fig. 5.17. As for the previous figure, each couple of graphs refers to the results obtained for the two buildings models, subjected to a specific seismic input.

Considering the RB models, and in particular the US and the isolation layer, the distribution of the seismic displacements is similar to the one obtained from the modal analysis described in the previous paragraphs. Furthermore, the ratio between the US relative drift and the isolation layer displacement ( $\Delta_{TOP,US}/u_{ISO}$ ) is of the same order of magnitude of the parameter  $\varepsilon$ , calculated in the previous paragraph from the modal characteristics according to the formula (5.16).

In particular, while this parameter varies with the seismic input and its energy content, it is in average equal to 0.007 for the Iidabashi and 0.205 for the Shiodome, thus remaining very close to the values obtained according to the formula (5.16), i.e. 0.008 and 0.20, for the IB and SSB, respectively.

Therefore, the linear theory of Kelly can be considered a valid approach also for a preliminary estimate of the maximum seismic response of a structure with a mid-story isolation system; in fact, despite of the dispersion of the displacement values according to the specific ground motion, the displacement amplification in the upper structure with respect to the isolation layer is almost the same of the one obtained from modal analysis, which, in turn, can be estimated through the formula (5.15), as a function of the period ratio.

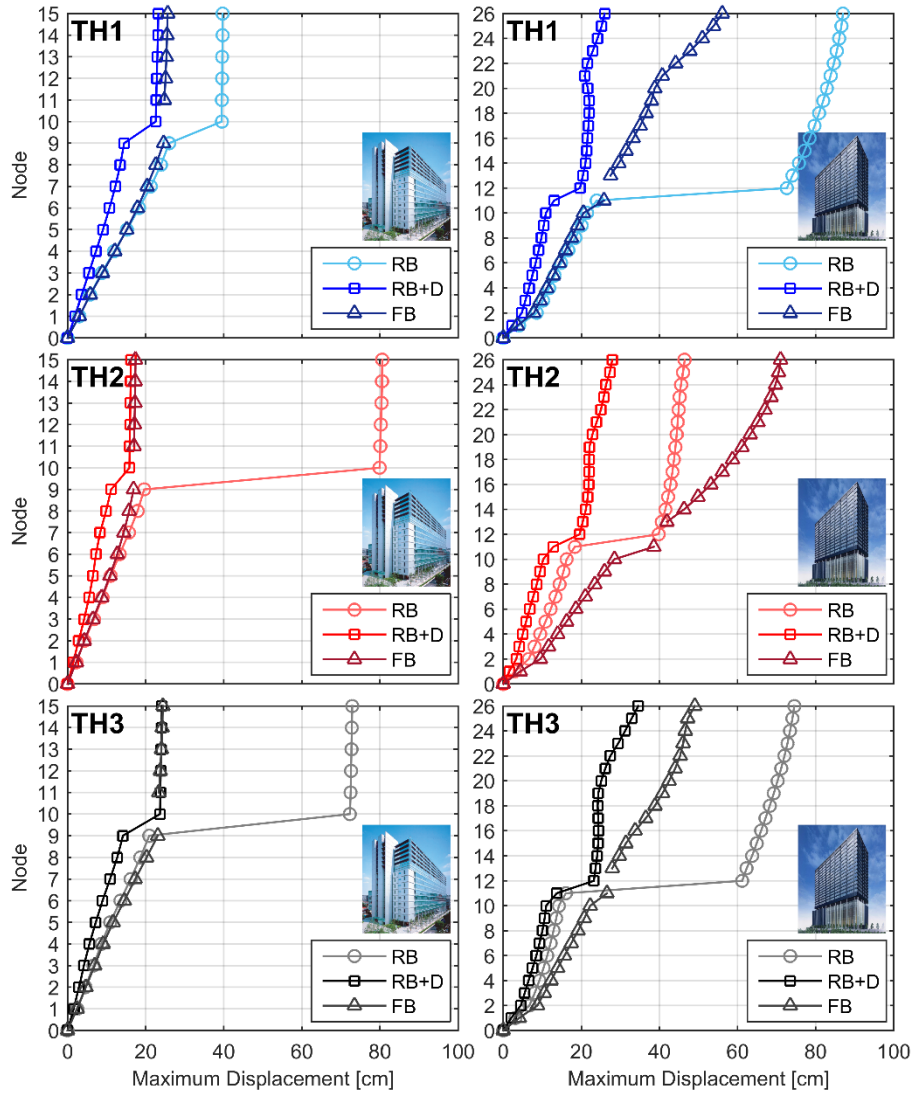


**Fig. 5.17. Peak story drift envelopes: (a) Iidabashi 1<sup>st</sup> Building, (b) Shiodome Sumitomo Building**

In order to compare the displacements of the upper and lower structures in the 3 models, relative displacements normalized to the partial heights are provided in Tabs. 5.11 – 5.12; in particular the ratio between the relative top-bottom displacement of the US (neglecting the displacement of the isolation system) and the US height,  $\Delta_{\text{TOP,US}}/H_{\text{US}}$ ; and the ratio of



LS top displacement to LS height,  $\Delta_{\text{TOP,US}}/H_{\text{LS}}$ , are shown in Tabs. 5.11 – 5.12 for the Iidabashi and Shiodome buildings, respectively. In the tables are also reported the values obtained for the fixed base structures, considering either only the degrees of freedom of the US and of the LS, or the whole structure.

**Table. 5.11. Iidabashi 1<sup>st</sup> building: normalized drift values**

	Model	El Centro S00E	Hachinohe NS	Taft S69E
$\Delta_{\text{TOT,US}}/H_{\text{US}}$	RB	1/8825	1/2520	1/2940
	RB+D	1/2635	1/4710	1/3705
	FB	1/70	1/100	1/70
$\Delta_{\text{TOT,LS}}/H_{\text{LS}}$	RB	1/145	1/195	1/180
	RB+D	1/260	1/340	1/270
	FB	1/155	1/225	1/165
$\Delta_{\text{TOP}}/H_{\text{TOT}}$	FB	1/230	1/340	1/240

**Table. 5.12. Shiodome Sumitomo building: normalized drift values**

	Model	El Centro S00E	Hachinohe NS	Taft S69E
$\Delta_{\text{TOT,US}}/H_{\text{US}}$	RB	1/525	1/1080	1/430
	RB+D	1/930	1/705	1/515
	FB	1/105	1/85	1/120
$\Delta_{\text{TOT,LS}}/H_{\text{LS}}$	RB	1/195	1/280	1/295
	RB+D	1/355	1/360	1/340
	FB	1/180	1/120	1/175
$\Delta_{\text{TOP}}/H_{\text{TOT}}$	FB	1/205	1/165	1/235

Looking at the values in Tabs. 5.11 – 5.12, it is also possible to grossly quantify both the isolation and the mass damper effects that occur in the buildings. In particular, the values  $\Delta_{\text{TOT,US}}/H_{\text{US}}$  show that the presence of isolators (RB models) produces a reduction of the displacement in the US, with respect to the FB model, of about 2 orders of magnitude (passing from  $10^{-2}$  to  $10^{-4}$ ) in the IB, and of 1 order of magnitude (passing from  $10^{-2}$  to  $10^{-3}$ ) in the SSB. Then, the presence of dampers (RB+D models) slightly modifies the US displacements, and, more remarkably, gives rise to the so-called mass damper effect, which mainly acts on the LS; this effect can also be grossly quantified by comparing the RB and RB+D models in terms of  $\Delta_{\text{TOT,US}}/H_{\text{LS}}$ .

The comparison, in the IB, reveals a reduction (from RB to RB+D models) of 80% for El Centro and of 50% for Taft; in the SSB, the behavior under El Centro is almost the same of the IB, and the displacement ratio  $\Delta_{TOP,US}/H_{LS}$  in the RB+D model decreases of 80% with respect to the RB model; on the contrary, a lower mass damper effect can be observed for the other two seismic waves, since the displacement ratios  $\Delta_{TOP,US}/H_{LS}$  decreases from the RB to the RB+D model of 30% and 15% respectively for Hachinohe and Taft ground motions.

Of course, the presence of dampers (RB+D models) dramatically decreases the displacement of the isolation layer in both buildings: over 90% for the Iidabashi, in the case of Hachinohe, and over 80% for the Shiodome, in the case of Taft.

Other results of time history analyses (maximum accelerations, shear forces, shear force coefficients) reported in the following text, confirm the above described general trends in the seismic behavior of the two buildings.

### 5.6.3. Maximum story accelerations

The story acceleration envelopes obtained from the time history analyses of the three MDOF (RB, RB+D and FB) models of the Iidabashi and Shiodome buildings are shown in Fig. 5.18. As can be seen before, each couple of graphs refers to the results obtained for the two buildings models, subjected to a specific seismic input.

Considering the RB models, only the US benefits of the isolation flexibility, leading to a reduced response with respect to the FB models; introducing the dampers, the isolation effect decreases.

Looking at the LS, comparable or greater peak story accelerations are observed in the RB+D with respect to the FB models.

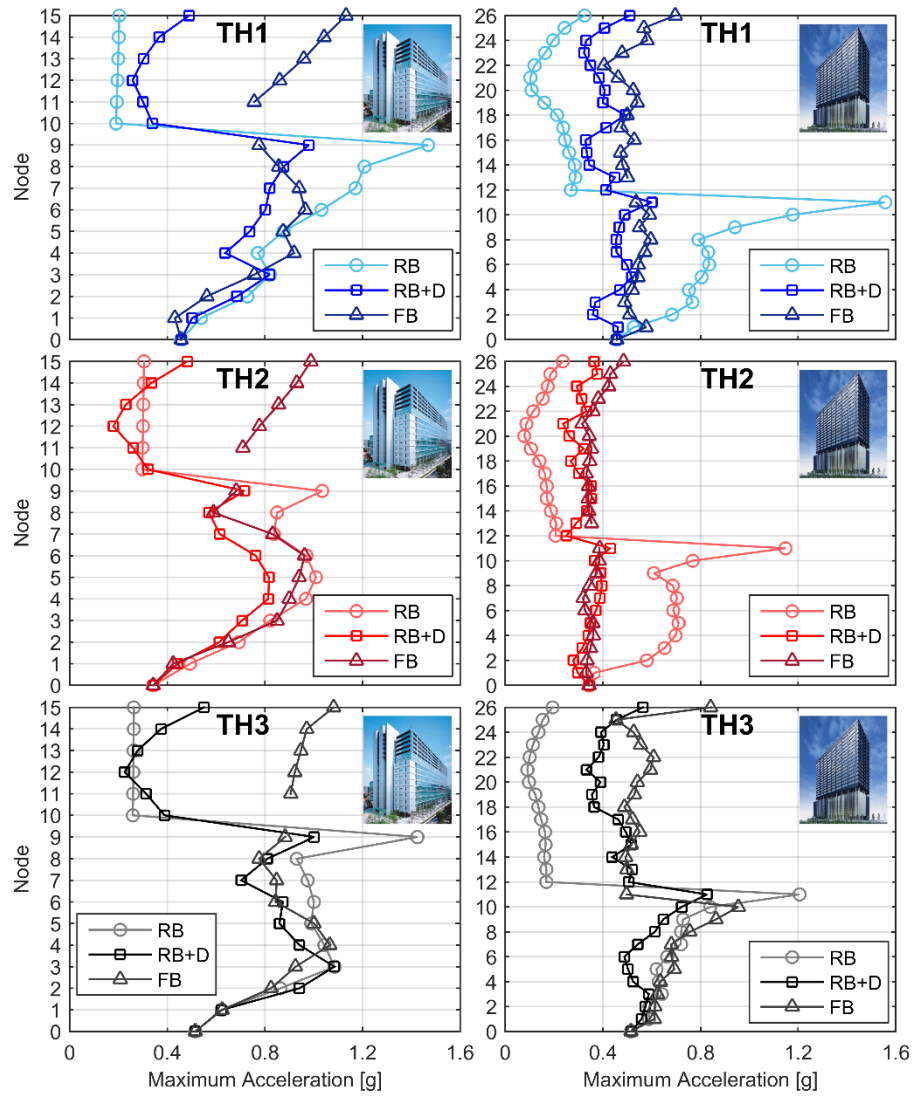


Fig. 5.18. Peak story acceleration envelopes: (a) Iidabashi 1<sup>st</sup> Building, (b) Shiodome Sumitomo Building

#### 5.6.4. Time histories of story accelerations

The story accelerations obtained from the time history analyses of the three MDOF (RB, RB+D and FB) models of the Iidabashi and Shiodome buildings are shown in Figs. 5.19 ÷ 5.21.

Each couple of graphs refers to the results obtained for the top and the stories above (ISO+1) and below (ISO-1) the isolation layer of the two buildings models, subjected to a specific seismic input. In accordance with the results shown in the previous Fig. 5.18, comparable or larger accelerations are observed in the ISO-1 story of RB and RB+D models than the FB models; otherwise, comparable or smaller accelerations are provided in the ISO+1 and top stories of the controlled models than the reference ones. It is worth noticing that, the coupling of the higher modes in SSB leads to a minor isolation effect with respect to IB.

#### 5.6.5. Maximum story shear forces

The story shear force envelopes obtained from the time history analyses of the three MDOF (RB, RB+D and FB) models of the Iidabashi and Shiodome buildings are shown in Fig. 5.22. As can be seen previously, each couple of graphs refers to the results obtained for the two buildings models, subjected to a specific seismic input.

With regards to the RB models, thanks to the isolation effect, a reduced seismic response in both US and LS is observed; considering the RB+D models, the mass damper effect allows an additional reduction of the story shear force in the LS.

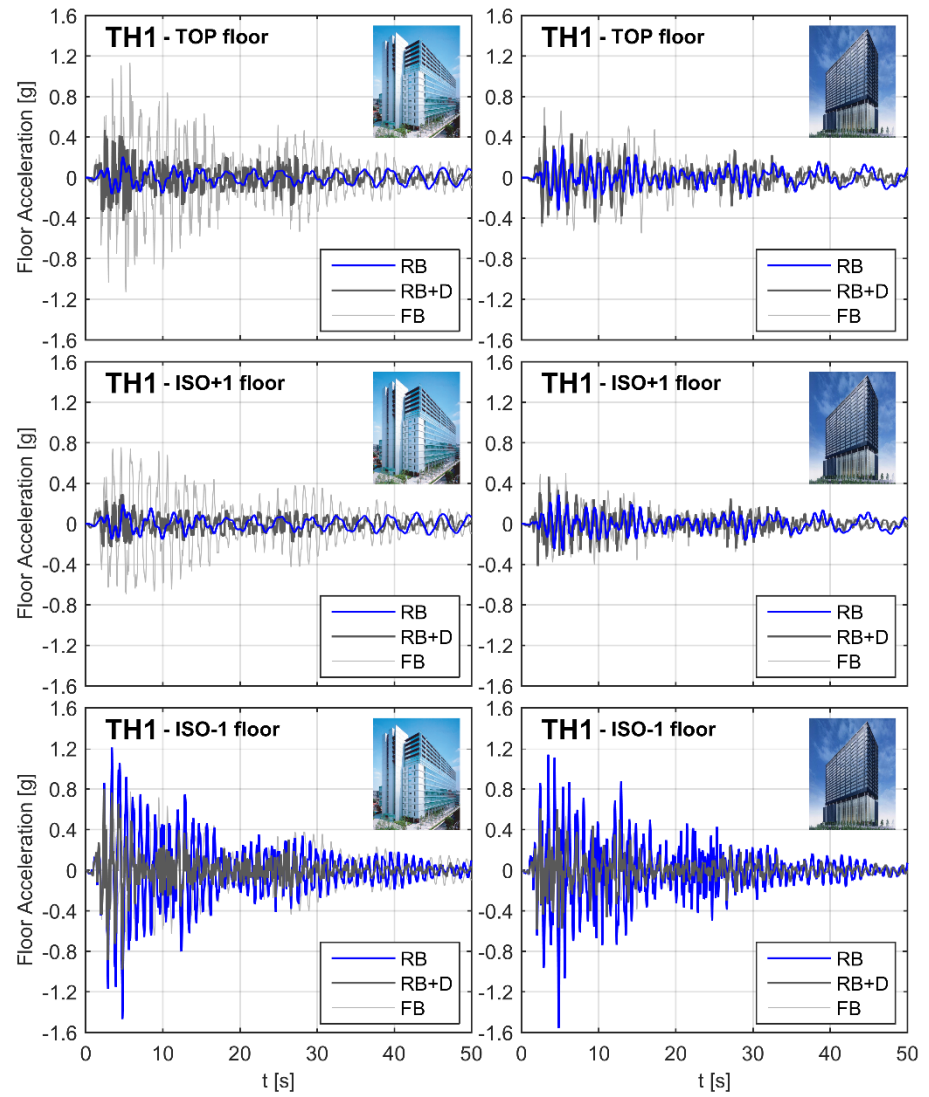
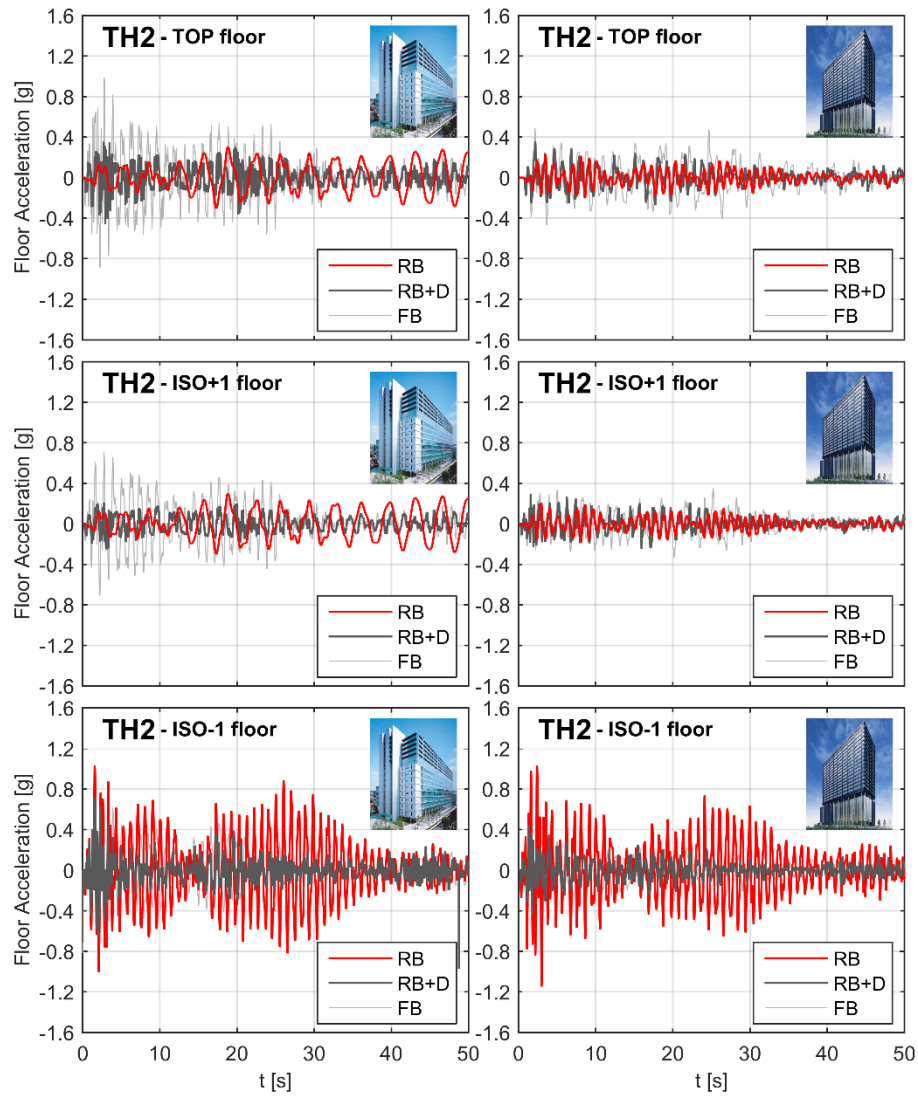


Fig. 5.19. Time histories of story accelerations under El Centro S00E 50 cm/s input wave: (a) Iidabashi 1<sup>st</sup> Building, (b) Shiodome Sumitomo Building



**Fig. 5.20.** Time histories of story accelerations under Hachinohe NS 50 cm/s input wave: (a) Iidabashi 1<sup>st</sup> Building, (b) Shiodome Sumitomo Building

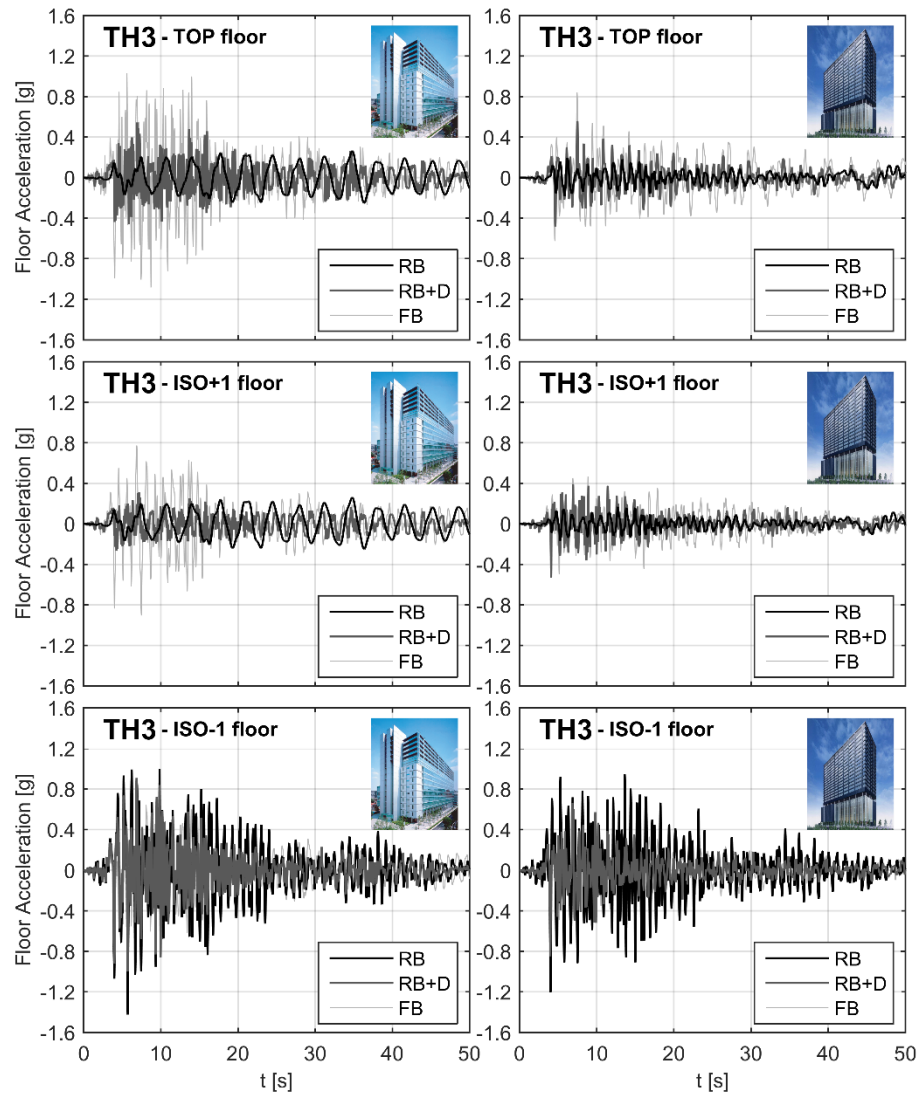


Fig. 5.21. Time histories of story accelerations under Taft S69E 50 cm/s input wave: (a) Iidabashi 1<sup>st</sup> Building, (b) Shiodome Sumitomo Building

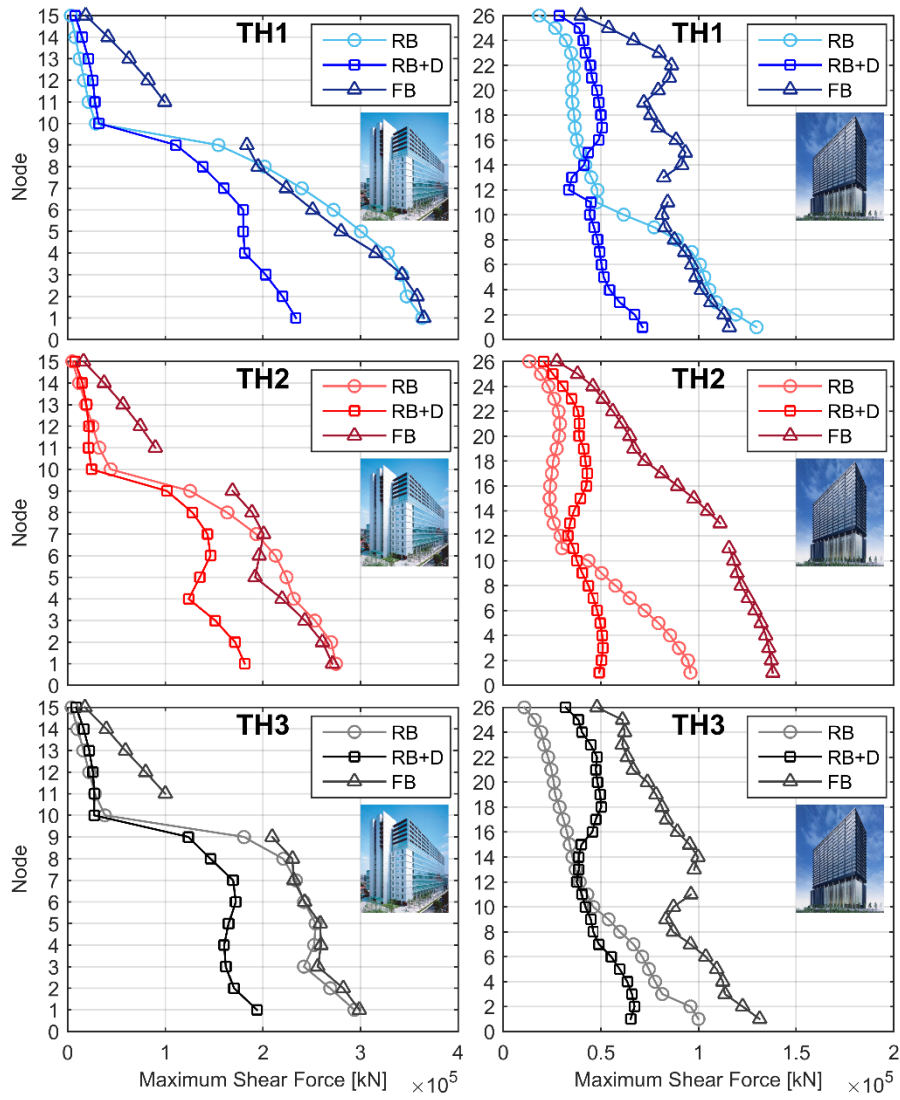


Fig. 5.22. Peak story shear force envelopes: (a) Iidabashi 1<sup>st</sup> Building, (b) Shiodome Sumitomo Building



#### 5.6.6. Seismic indices

In order to express the previous results in a synthetic way, the root mean square (rms) of the controlled response for the three input waves is normalized with respect to the corresponding one of the uncontrolled configuration.

The indices, expressed in terms of peak story drift, peak absolute accelerations, and peak story shear forces, and obtained from the time history analyses of the MDOF RB+D and FB models of the Iidabashi and Shiodome buildings, are shown in Figs. 5.23 ÷ 5.25. In particular, each couple of graphs refers to the rms results obtained for the two buildings models.

Broadly speaking, indices smaller than one indicate a reduction of the floor response in the IIS configuration as compared with the reference FB one; conversely, values greater than one imply an amplification.

Looking at the peak drift ratio, in Fig. 5.23 values less than one are obtained for both the buildings. However, in the US of Iidabashi Building, the story drift index is almost equal to one, since the US is 4.4 time stiffer than the LS (Tab. 5.4), and thus, it is already more rigid in the reference FB model.

In terms of peak acceleration ratio, in Fig. 5.24 values almost equal to, or greater than, one are observed for the LS of both the buildings; on the contrary, the US shows values smaller than one. It is worth noticing that, the major US rigidity in Iidabashi Building improves the isolation effect than in the case of Shiodome Sumitomo Building, that shows comparable values of the acceleration index between US and LS (except for the first floor below the isolation layer).

In terms of peak shear ratio, in Fig. 5.25 values lower than one are observed for both the buildings. In particular, minor values are obtained in the US of IB, thanks to the major rigidity of this structural portion with respect to the LS, and in the LS of SSB, due to a design value of the shear coefficient of dampers  $\alpha_s'$  larger than the corresponding one of IB (0.03 vs. 0.02).

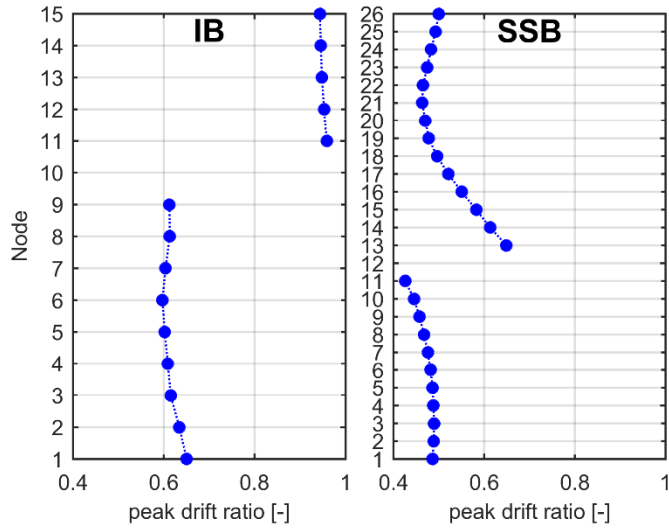


Fig. 5.23. Peak drift ratios: (a) Iidabashi 1<sup>st</sup> Building, (b) Shiodome Sumitomo Building

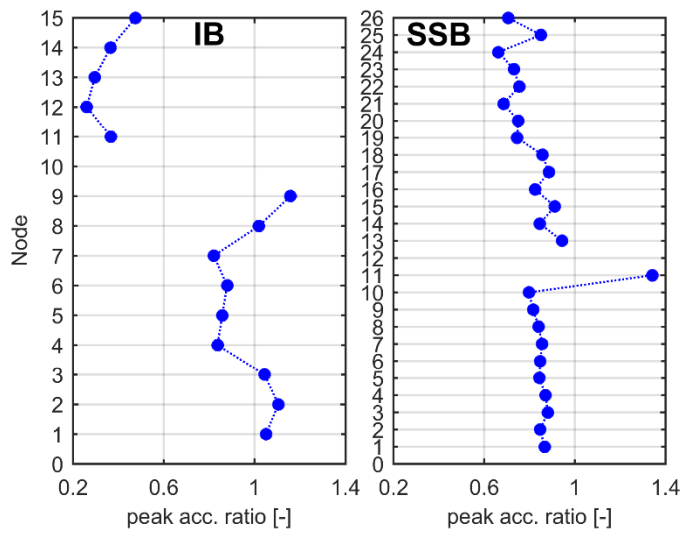


Fig. 5.24. Peak acceleration ratios: (a) Iidabashi 1<sup>st</sup> Building, (b) Shiodome Sumitomo Building

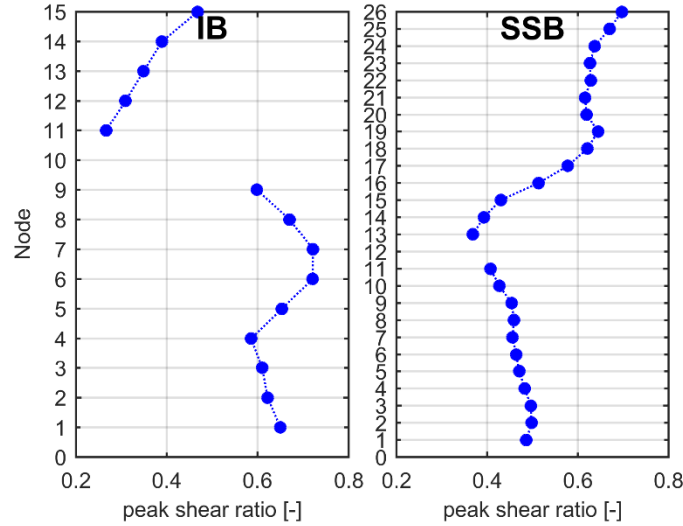


Fig. 5.25. Peak shear force ratios: (a) Iidabashi 1<sup>st</sup> Building, (b) Shiodome Sumitomo Building

#### 5.6.7. Maximum story shear coefficient

The story shear coefficient distribution represents the normalized shear force distribution with respect to the seismic weight of the building. In particular, the story shear coefficient is obtained by dividing the peak shear force of the  $i$ -th story to the seismic weight above the  $i$ -th story.

The story shear coefficient envelopes obtained from the time history analyses of the three MDOF (RB, RB+D and FB) models of the Iidabashi and Shiodome buildings are shown in Fig. 5.26. As can be seen previously, each couple of graphs refers to the results obtained for the two buildings models, subjected to a specific seismic input.

Quite trivially, from the figure can be noticed the same trend observed for the story shear force envelopes, depicted in Fig. 5.22.

Considering the RB+D models, the mean shear coefficient of the first story and of the isolation layer, respectively equal to  $0.30 - 0.19$  and  $0.08 - 0.07$  for IB and SSB, are almost within the range defined in Chapter 3 from the seismic Japanese database of more sixty IIS buildings (Fig. 3.3), i.e.  $0.1 \div 0.4$  and  $0.06 \div 0.15$ , respectively.

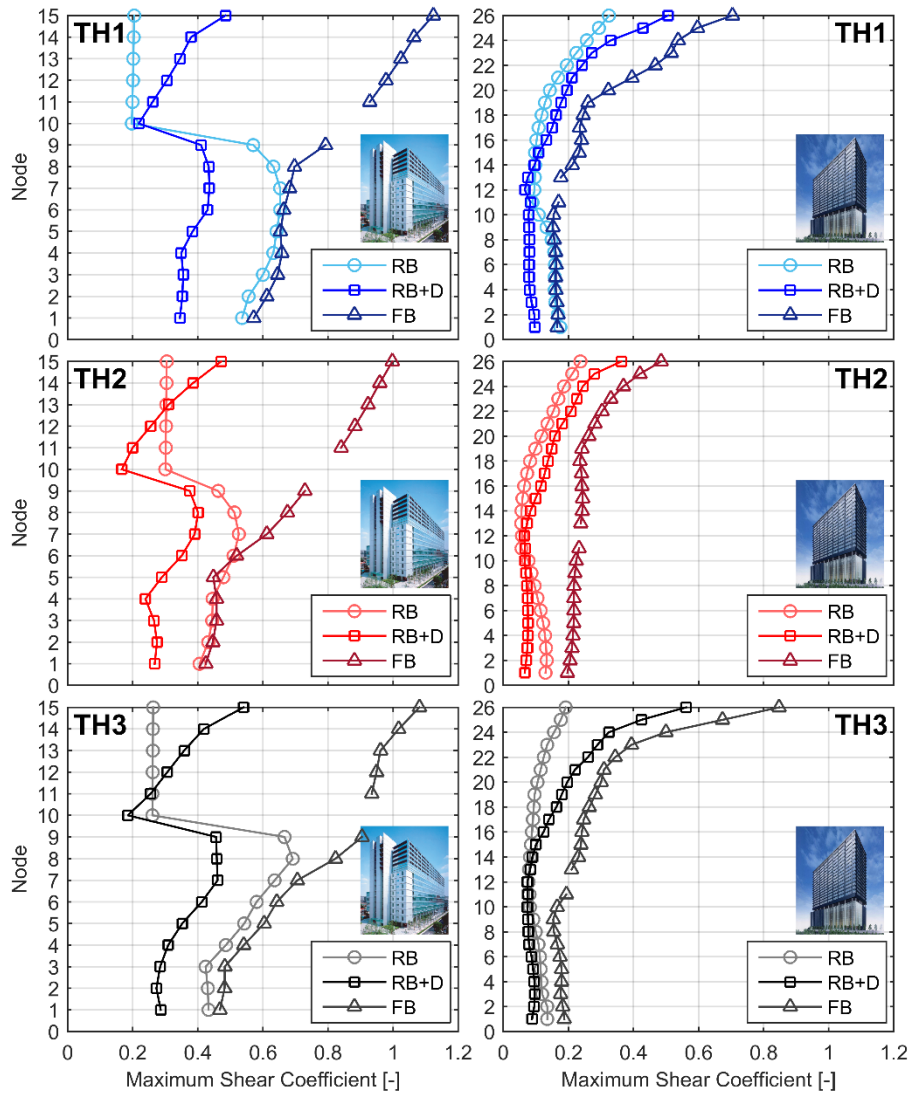


Fig. 5.26. Peak story shear coefficient envelopes: (a) Iidabashi 1<sup>st</sup> Building, (b) Shiodome Sumitomo Building

#### 5.6.8. Energy components distribution

The distributions of the energy components obtained from the time history analyses of the RB+D models of the Iidabashi and Shiodome buildings are shown in Fig. 5.27. In each graph are provided the time histories of the different energy components, i.e. Potential Energy  $E_p$ , Kinetic Energy  $E_k$ , Hysteretic Energy  $E_h$ , Internal Viscous Damping Energy  $E_d$ , normalized to the seismic input energy  $E_i$ . Each couple of graphs refers to the results obtained for the buildings models (IB and SSB) subjected to a specific seismic input (El Centro, Taft, Hachinohe).

From the figure, it is possible to notice that in both buildings a large amount of the seismic input energy is dissipated through the hysteretic response of the dampers within the isolation system; the share of hysteretic energy is between 67% and 73% for the IB and between 50% and 67% in the SSB.

This distribution confirm that the inter-story isolation system can be seen as a “concentrated type” of energy dissipation system, different from the common approach of distributed energy dissipation systems, where the dampers are spread throughout the building structure. The peculiarity of the inter-story isolation system is that the dampers are effectively engaged thanks to the large local inter-story drift generated by the isolators deformation; therefore, in this perspective the isolators work as a distinctive “amplification system” for the energy dissipation devices concentrated at the isolation level.

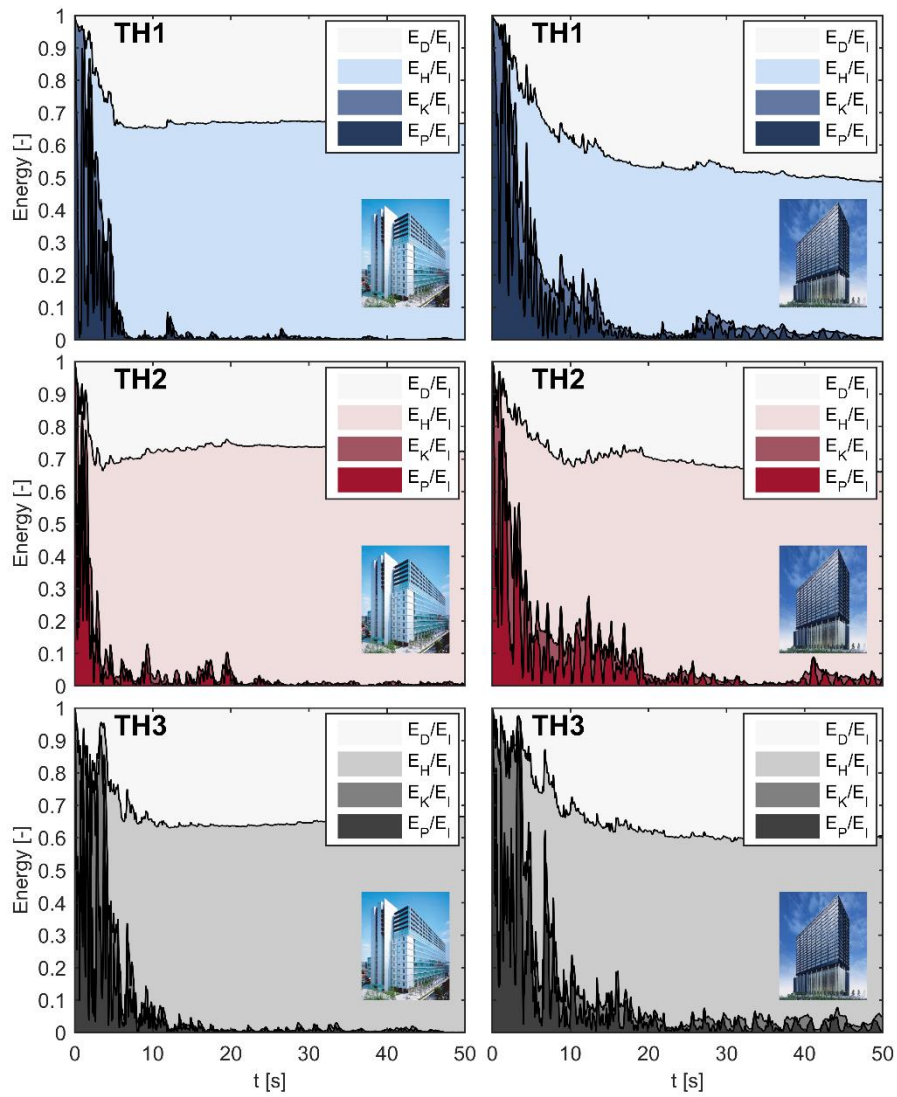


Fig. 5.27. Time histories of Energy distribution: (a) Iidabashi 1<sup>st</sup> Building, (b) Shiodome Sumitomo Building

### 5.7. THEORY AND PRACTICE: MURAKAMI ET. AL VS. IB AND SSB

[Murakami et al. 2001, Murakami & Suoeka 2004, Tasaka et al. 2008] proposed a prediction method, described in detail in Chapter 4 (§ 4.5.3), based on the balance of the enveloped-energy by retaining the actions of the isolation story and the lower story, and by using the eigen functions obtained from the modal analyses of the reduced-order 2DOF RB and RB+D models. Considering the 2DOF RB and RB+D models, in Eq. (5.1) the matrices  $\mathbf{M}$ ,  $\mathbf{C}$ ,  $\mathbf{K}$  and the vectors  $\mathbf{x}(t)$ ,  $\mathbf{r}$  have  $2 \times 2$  and  $2 \times 1$  dimensions, respectively.

In particular, the lumped masses are respectively equal to the LS mass,  $m_{LS}$ , and the total isolated mass,  $M_{ISO}$ ; the story horizontal stiffnesses are respectively equal to the LS equivalent stiffness  $k_{LS,eq}$ , defined as a function of the total mass  $M_{TOT}$  and the LS fundamental period  $T_{LS}$ , and the stiffness of the isolation story, considering only isolators, i.e.  $k_{RB}$ , or isolators and dampers at the initial stiffness,  $k_D^{(1)}$ , i.e.  $k_{RB+D}^{(1)}$ .

It is worth noticing that the equivalent reduced-order SDOF models of the LS and isolation system are the same as considered in § 5.3; the unique difference concerns the characterization of the LS equivalent stiffness, defined here as a function of the total mass and not in base of the LS mass. The authors made this assumption in order to take into account the total enveloped energy.

The values of the dynamic characteristics of the 2DOF RB and RB+D models are given in Tab. 5.13. In this table is also provided the main design parameter  $R_m$ , defined as the ratio between the total isolated mass  $M_{ISO}$  and the total mass  $M_{TOT}$ , i.e.:

$$R_m = \frac{M_{ISO}}{M_{TOT}} \quad (5.23)$$

**Table. 5.13. Lumped masses and story stiffness of the two buildings 2DOF RB and RB+D models**

Parameters	IB	SSB
$M_{ISO}$ [kN·s <sup>2</sup> /m]	14921	51558
$m_{LS}$ [kN·s <sup>2</sup> /m]	54171	23940
$M_{TOT}$ [kN·s <sup>2</sup> /m]	69092	75497
$R_m$	0.216	0.683
$k_{LS,eq}$ [kN/m]	2849168	2652652
$k_{RB}$ [kN/m]	52974	80700
$k_D^{(1)}$ [kN/m]	1625125	2117800
$k_{RB+D}^{(1)}$ [kN/m]	1678099	2198500

- Maximum deformation of the isolation story,  ${}_m\delta_{max}$  :

$${}_m\delta_{max} = \frac{-{}_mK({}_uK + \kappa {}_mK_s)M_{TOT}g\alpha'_s}{{}_mK_s \cdot {}_mK_t \cdot K_e} + \sqrt{\frac{\left\{({}_uK {}_mK + \kappa {}_mK_s^2)^2 + {}_mK_t \cdot K_e(2 {}_mK_s^2 - {}_uK {}_mK_t\psi)\right\}M_{TOT}^2g^2\alpha_s'^2 + {}_mK_s^2 {}_mK_t^2M_{TOT}^2V_D^2}{{}_mK_s \cdot {}_mK_t \cdot K_e}} \quad (4.139)$$

where

$${}_mK_f = k_{RB}, \quad {}_mK_s = k_D^{(1)}, \quad {}_mK_t = k_{RB+D}^{(1)}, \quad {}_uK_{eq} = k_{LS,eq};$$

$${}_mK_t\zeta = {}_mK, \quad {}_mK_f + {}_uK_{eq}\zeta^2 = K_e, \quad {}_uK_{eq}\psi = {}_uK;$$

$\zeta$  and  $\psi$  are drift ratios between the LS displacement and the ISO drift, obtained respectively considering only isolators and isolators and dampers, see Eqs. (4.126) and (4.127);  $\kappa$  is a damage concentration index, which depends on the characteristics of the isolation story and input seismic wave [Akiyama 1989, 1992].

- Maximum shear coefficient of the isolation story,  ${}_m\alpha$  :

$${}_m\alpha = \alpha_f + \alpha_s \quad (4.142)$$

where the shear coefficient of isolators,  $\alpha_f$ , and dampers,  $\alpha_s$ , are respectively given by:



$$\alpha_f = \frac{Q_f}{R_m M_{TOT} g} = \frac{k_{RB} \delta_{max}}{R_m M_{TOT} g} \quad (4.143)$$

$$\alpha_s = \frac{Q_{D,y}}{R_m M_{TOT} g} = \frac{k_D^{(1)} \delta_{D,y}}{R_m M_{TOT} g} \quad (4.144)$$

- Maximum shear coefficient of the lower story,  ${}_u \alpha$  :

$${}_u \alpha = \frac{\delta_{max} \zeta \cdot k_{LS,eq}}{M_{TOT} g} + \frac{k_{LS,eq} \psi \alpha'_s}{k_D^{(1)}} \quad (4.161)$$

The main parameters calculated for deriving the isolation drift and the shear coefficient of the isolation and the lower structure, are provided in Tab. 5.14.

**Table. 5.14. Parameters**

Parameters	IB	SSB
$\alpha_s$	0.02	0.03
${}_m \delta_{max}$ [m]	0.47	0.43
${}_m \alpha$	0.263	0.112
${}_l \alpha$	0.529	0.217
$\alpha_f$	0.170	0.068
$\alpha_s$	0.093	0.044
${}_0 b_s$	21.184	1.467
${}_0 a_{opt}$	1.744	2.942
$\psi$	2.019	1.023
$\zeta$	0.231	0.117
$\delta_{D,y}$ [m]	0.00834	0.0105
$\kappa$	8	8

The isolation drift and the shear coefficient of the isolation and the lower structure are plotted in Fig. 5.28 as in function of the mass ratio  $R_m$ .

Quite trivially, from this figure can be noticed that, by increasing the mass ratio  $R_m$ , for a fixed isolation period, the drift of the isolation system increases; in addition, if the mass ratio  $R_m$  is equal to, or greater than, 0.2,

the reduction of the shear coefficients gives rise to an untuned mass damper effect.

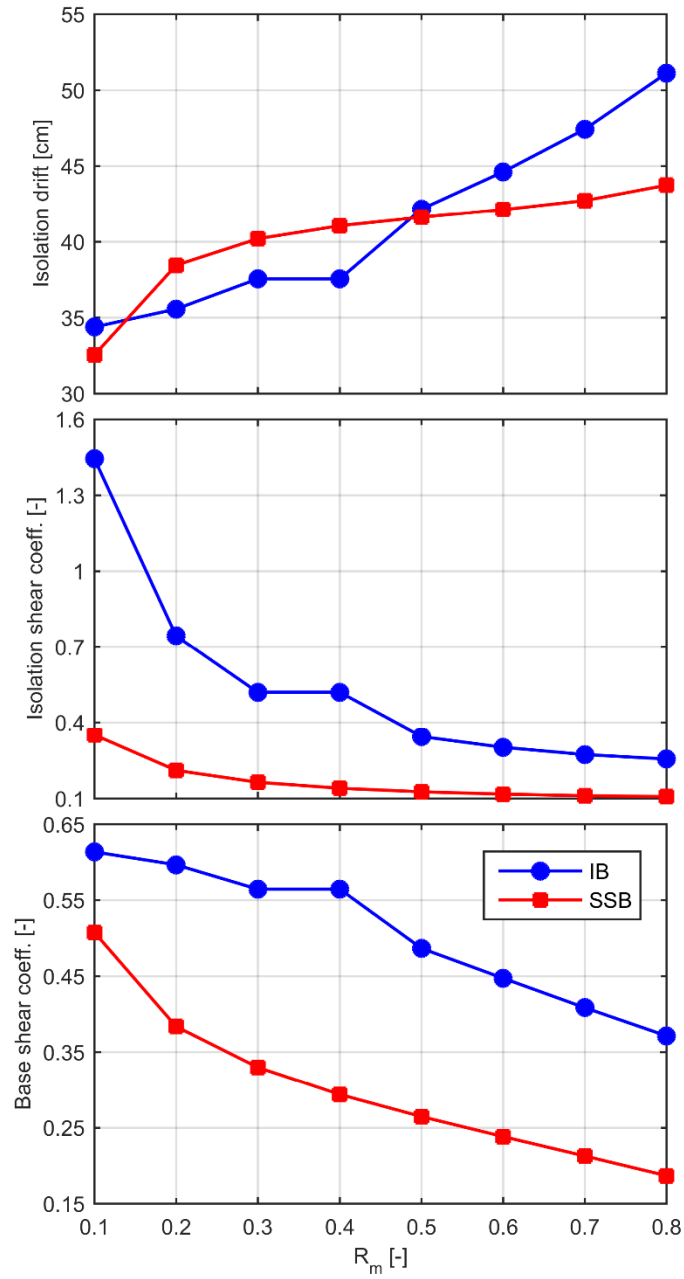


**Fig. 5.28. Untuned Mass Damper: (a) isolation drift, (b) isolation shear coefficient, (c) base shear coefficient**

It is worth noticing that, the major reduction of the response parameters in SSB is due to larger isolation period (5.02 s vs. 3.33 s) and shear coefficient of dampers (0.03 vs. 0.02) than the corresponding ones in IB. Starting from these values, it is possible to derive the enveloped energy components, depicted in Tab. 5.15, considering the equivalent damage velocity equal to  $V_D = 150$  cm/s (for the Level-II earthquake), and the equivalent input velocity equal to  $V_E = 200$  cm/s (for the Class-III ground), as prescribed by the Japanese building code, see § 4.5.3.

**Table. 5.15. Energy components and energy ratios of the two buildings**

Energy component	IB	SSB
$W_e$ [kNm]	28395	12199
$W_p$ [kNm]	49333	72736
$E_D$ [kNm]	77728	84935
$E$ [kNm]	138184	150995
$W_h$ [kNm]	60455	66060
$E_D/E$	0.56	0.56
$W_h/E$	0.44	0.44

In Tab. 5.15 are also provided the energy ratios of the damage energy,  $E_D$ , and hysteretic energy,  $W_h$ , with respect to the input energy,  $E$ , i.e.:

$$\frac{E_D}{E} = \left( \frac{V_D}{V_E} \right)^2 = 0.75^2 = 0.56$$

$$\frac{W_h}{E} = 1 - \left( \frac{V_D}{V_E} \right)^2 = 1 - 0.75^2 = 0.44$$

Having fixed the equivalent velocities  $V_D$  and  $V_E$ , the energy ratios  $E_D/E$  and  $W_h/E$  are fixed quantities; quite trivially, for a fixed  $V_D$ , increasing  $V_E$ , the ratio  $W_h/E$  increases.

The shear coefficient distribution of the MDOF RB+D models of the two buildings can be predict, by recalling the formulae written in Chapter 4.

The  $i$ -th shear coefficient of the upper structure,  ${}_0\alpha_i$ , is equal to:

$${}_0\alpha_i = \alpha_f + {}_0\alpha_{si} \quad (4.146)$$

where

$${}_0\alpha_{si} = {}_0a_i {}_0\alpha_{opt} \alpha_s \quad (4.148)$$

is the shear coefficient of the  $i$ -th story considering only dampers, where  ${}_0\alpha_{opt}$  is the optimal shear coefficient distribution ((4.149));  ${}_0a_i$  is a coefficient which increases along the height of the building with a linear distribution ((4.151));  ${}_0\alpha_{opt}$  is the optimum coefficient ((4.153) ÷ (4.155)).

The  $i$ -th shear coefficient of the lower structure is equal to:

$${}_u\alpha_i = \frac{1}{d_i} \left[ R_{m\ m} \alpha + \frac{d_i - R_{m\ m}}{1 - R_{m\ m}} {}_uA_i ({}_u\alpha - R_{m\ m} \alpha) \right] \quad (4.158)$$

with  $d_i$  ((4.157)) the normalized weight of the  $i$ -th story considering the whole structure;  ${}_uA_i$  ((4.159)) the distribution of the seismic shear coefficients ( $A_i$  distribution) of the LS only.

The story shear coefficient envelopes obtained from the time history analyses of the RB+D model of the Iidabashi and Shiodome buildings are compared with the ones derived from the analytical formulation in Fig. 5.29. As can be seen above, each couple of graphs refers to the results obtained for the two buildings models.

From Fig. 5.29 it can be noticed that the analytical formulation overestimates the shear coefficient in the LS, while it gives comparable values in the US with respect to the results of the time history analyses. It is worth noticing that, in the US of SSB, this formulation underestimates the seismic response, since the mode coupling of the higher modes is neglected using a reduced-order 2DOF prediction model.

It can be concluded that this procedure is valid only if the MCE is not expected.

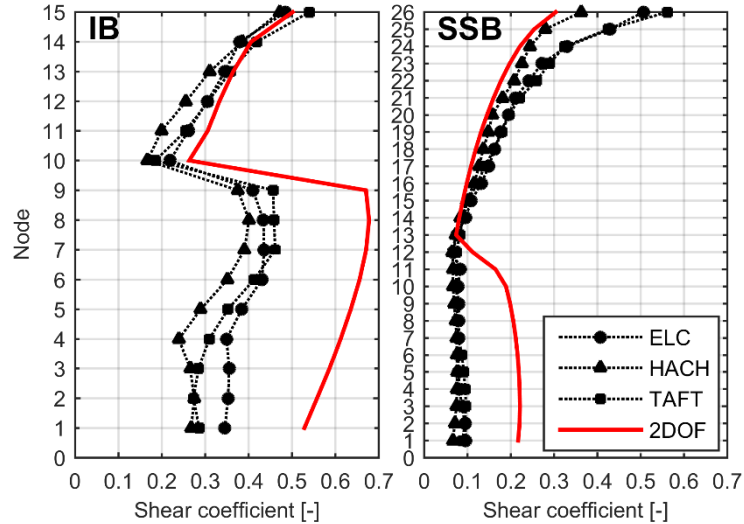


Fig. 5.29. Peak story shear coefficient envelopes, theory vs. design practice: (a) Iidabashi 1<sup>st</sup> Building, (b) Shiodome Sumitomo Building

## 5.8. CONCLUSIVE REMARKS AND DESIGN IMPLICATIONS

In this chapter the design aspects of inter-story isolation system (IIS) have been addressed by examining some case studies through the lens of research. In fact, the case of IIS appears as one where the real-world of construction moves forward much faster than the theoretical realm of research. As a matter of fact, despite of more than sixty applications realized in nearly twenty years, also trespassing in the sector of tall buildings, the conceptual framework for dealing with the design problem of IIS is not well established and a variety of approaches and design objectives can be found in the inherent scientific literature.

Starting from these considerations, an in-depth analysis of two building case-studies is proposed in this chapter; the major building data are firstly examined for an approximate guess of, and a preliminary comparative discussion on the dynamic properties of the three structural parts (i.e. isolated upper structure US, isolation system IIS, lower structure LS) of each building, and, consequently, on their expected dynamic interaction. Modal and time history analyses are then carried out on the MDOF models of the two buildings.

The analysis of the buildings and the exam of their vibration characteristics, has proved particularly interesting since the selected case studies are very different each other. One of them (the IB) is a paradigmatic example of building with inter-story isolation, with a very rigid superstructure, and frequencies of the two structural parts (upper and lower structure) well separated from the isolation frequency, which gives rise to uncoupled higher modes. The other building (the SSB) is not an ideal case of IIS, with the upper structures less rigid than the lower one, and both structural portions quite flexible, thus frequency ratios are not so high to ensure decoupling of higher modes. However, the seismic response of both buildings, assessed through nonlinear time history analyses, appears very satisfactory; the beneficial effects of isolation, dissipation, and consequent mass damping have been clearly identified thanks to the use of two analysis models, accounting for only isolators or for both isolators and dampers, respectively, and by comparing the response of such models to the reference fixed base structures.

In the authors' opinion, the peculiarity of the inter-story isolation system, and its greater design complexity with respect to base isolation, seems to come from the combination of the three above effects; in fact, depending on the values of mass ratios, frequency ratios and dampers yielding force, either the above aspects may equally and effectively contribute to the structural response, or one behavioral aspect may prevails on the others. In this perspective the isolators have the most important role: to lengthen the first period of the structural complex, to work as a distinctive "amplification system" for the energy dissipation devices concentrated at the isolation level, and to allow the upper structure moving out of phase with the lower one.

Starting from these observations and from the results obtained in this chapter, a wide parametric analysis is carried out in the next two chapters, in order to establish the ranges of different structural behavior and to propose design guidelines.

## 6. PARAMETRIC ANALYSIS

### 6.1. INTRODUCTION

In very general terms, isolation is “a means to change dynamic characteristics of a vibrating system”, while the base isolation practically reduces a multi-degree of freedom (MDOF) structure to a single-degree of freedom (SDOF) system, the mid-story isolation changes one MDOF system into another MDOF with different vibration characteristics [Ziyaeifar & Noguchi 1998]. In fact “no matter how flexible the isolation layer is, the remaining part of mass cannot directly enjoy from this additional flexibility”. Another important difference between BIS and IIS is that, while the first vibration mode of BI buildings is characterized by large mass participation with, consequently, negligible participation of the higher modes, in an IIS the first mode only activates a smaller mass fraction, and the higher modes, with considerable amount of mass, are not ineffective.

The coupling effect of these higher modes, which can produce an amplification in the seismic response of the structure, has been explicitly addressed in some papers on mid-story isolation [Wang et al. 2011, 2012, 2013; Kobayashi & Koh 2008] and the problem was formulated by means of simplified reduced-order 3DOF mid-story isolated models to examine the impact of the design parameters, mainly frequency and mass ratios.

As a result, it was recognized that the dynamics of structures with mid-story isolation is affected by the vibration characteristics of the US and LS, and that, depending on these characteristics, two different scenarios for the dynamic behavior of the global structure are found: a major influence of one of the higher modes (either the 2<sup>nd</sup> or the 3<sup>rd</sup> mode), or a coupling effect of the 2<sup>nd</sup> and 3<sup>rd</sup> modes.

However, with simplified 3DOF IIS models, only one possible combination between the higher coupled modes of the LS and US can be found. Generally, the simplified model is built up reducing the order of the degree of freedoms of the US and LS to one with respect to the fundamental mode.

Using more refined multi-degree-of-freedom IIS models, which consider the different dofs of the structural portions (US and LS), the possible coupling between more than two significant higher modes can be investigated.

In this perspective, this chapter has explored the properties of the inter-story isolation system (IIS) structures, with particular attention to the mode coupling effect (MCE) of the higher modes.

Multi-degree-of-freedom isolated models, representative of a 10-story building, have been considered, and the influence of different placements of the isolation system have been investigated; different mass and stiffness distributions, representative not only of the commonly distributions adopted for structural application but also of extreme real inter-story isolated structures, have been considered. Multi-degree-of-freedom fixed-base models are also analyzed for comparison.

For examining the effect of the higher modes, a free-free multi-degree-of-freedom IIS model, in which the stiffness of the isolation layer is assumed null (i.e. perfect isolation), is also developed. In this framework an analytical formulation for avoid MCE is derived for MDOF systems, and, then, extended to 3DOF IIS models.

## **6.2. SIMPLIFIED PARAMETRIC ANALYSIS AND DYNAMIC PROPERTIES**

### **6.2.1. Model definition**

Simplified lumped masses multi-degree of freedom (MDOF) models are developed and utilized for an in-depth analysis and discussion of the building dynamics. In particular two different MDOF models are considered, namely: FB and ISO models. The fixed-base (FB) model represents the uncontrolled structure; the isolated (ISO) model represents the controlled structure by means of high damping rubber bearings (HDRBs) in the isolation system, the mass and story stiffness are the same as fixed-base model except for the isolation layer.

A graphical representation of the FB and ISO models is shown in Fig. 6.1. As shown in Fig. 6.1, in the IIS model the isolation layer ideally divides the structure in three portions (namely: LS, ISO, US), i.e. the portion



below the isolation story (LS), the inter-story isolation system (ISO), the portion above the isolation story (US); the degrees of freedom of those portions are appointed as  $n_{US}$ ,  $n_{ISO}$ ,  $n_{LS}$ .

In the FB model the portions above and below the corresponding level of the isolation layer in the IIS model also represent the US and LS, respectively; thus, the degrees of freedom of the FB model are subdivided in the number of the US dofs,  $n_{US}$ , and in the number of the LS dofs plus one,  $n_{LS+1}$ . Therefore, the total number of dofs in the FB model ( $n_{LS+1} + n_{US}$ ) and in the IIS model ( $n_{LS} + n_{ISO} + n_{US}$ ) is equal to  $n$ .

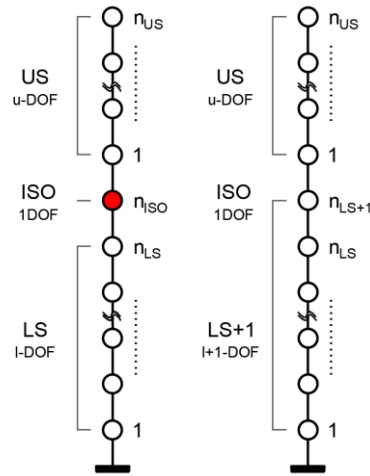


Fig. 6.1. (a) MDOF ISO model, (b) MDOF FB model

The structure horizontal stiffness at each level is represented by an equivalent linear shear spring, the stiffness of the isolation interface is represented by an elastic-plastic spring with bilinear restoring force characteristic.

Both the FB and IIS models are viscously damped systems, in particular the hysteretic damping in the isolation story is converted to equivalent viscous damping.

The MDOF FB model is representative of a 10-story residential building with a floor area about of 1850 mq; floor weight of 8 kN/mq; inter-story height of 3.4 m; total height of 34 m.

The MDOF IIS model is representative of the same 10-story building in which the isolation layer replaces the level below the first story of the US in the MDOF FB model.

In order to grasp the dynamic behavior of middle isolated structures, different ISO models, and consequentially different corresponding FB models, are considered, see Fig. 6.2.

In particular in the controlled structure the isolation interface moves from the top to the bottom story changing level by level. Therefore, ten 10DOF IIS models are obtained with extreme models related to a roof isolated structure (RIS) and a base isolated structure (BIS). Since the total number of the dofs is equal to  $n$ , changing the isolation level the number of the US and LS dofs change; in particular the couples USdof - LSdof respectively corresponding to the RIS and BIS ISO models are 0dof – 9dof and 9dof – 0dof. It is worth to notice that, taking into account the isolation story, the total dofs in these extreme models is 10 ( $0+1+9$  and  $9+1+0$ ).

The FB models corresponding to the extreme RIS and BIS ISO models present couples of US - LS+1 dofs equal to 0dof – 10dof and 9dof – 1dof for a total number of 10dof, see Fig. 6.2.

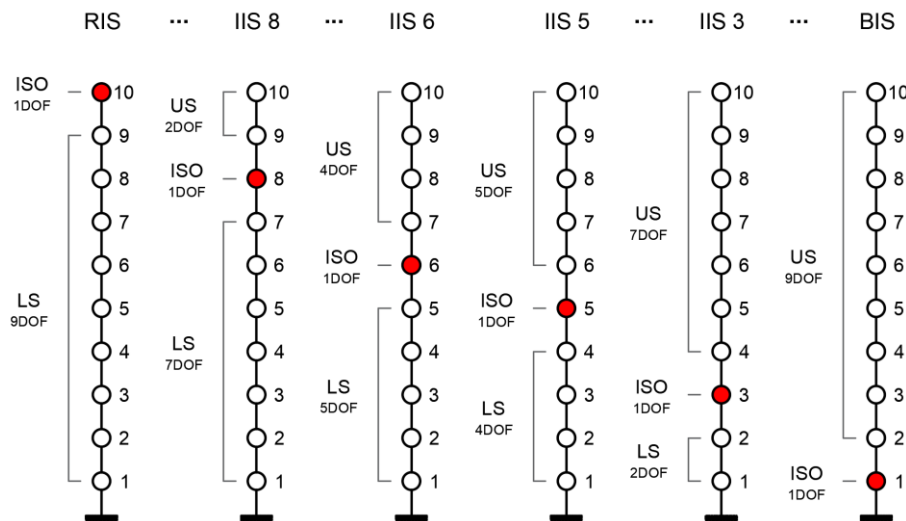


Fig. 6.2. 10DOF ISO lumped mass models

In order to grasp the dynamic behavior of middle story isolated structure different mass and stiffness distributions, not only representative of the commonly distributions adopted for structural applications but also of extreme real inter-story isolated structures [Murakami et al. 2000, Sueoka et al. 2004, Tsuneki et al. 2008-2009], are considered, see Figs. 6.3 ÷ 6.5;

the possible combinations between the mass and stiffness distributions are depicted in Fig. 6.6.

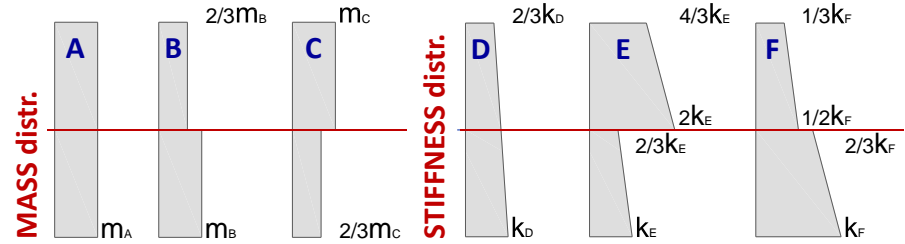


Fig. 6.3. Schematic representation of the different mass and stiffness distributions

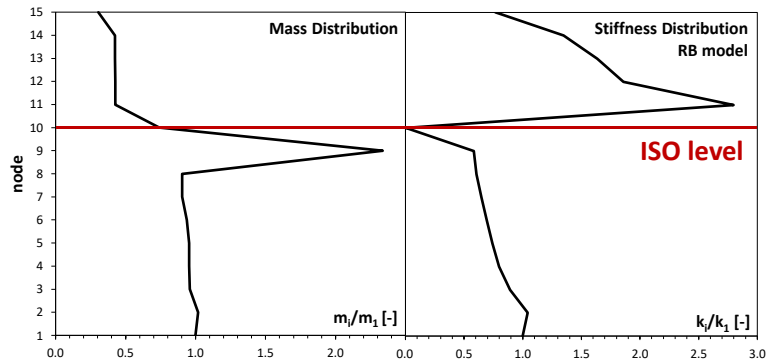


Fig. 6.4. Mass and stiffness distributions of Lidabashi 1<sup>st</sup> building

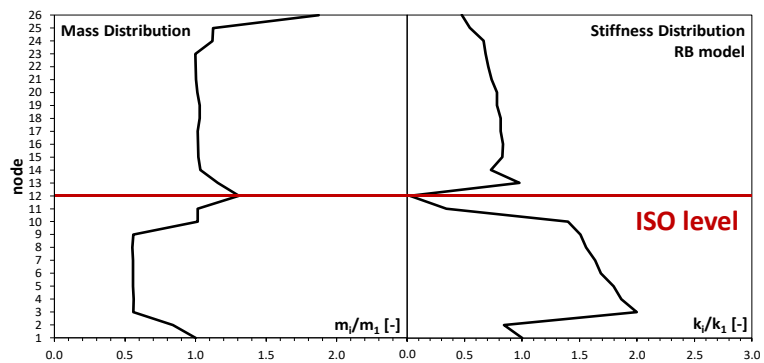


Fig. 6.5. Mass and stiffness distributions of Shiodome Sumitomo building

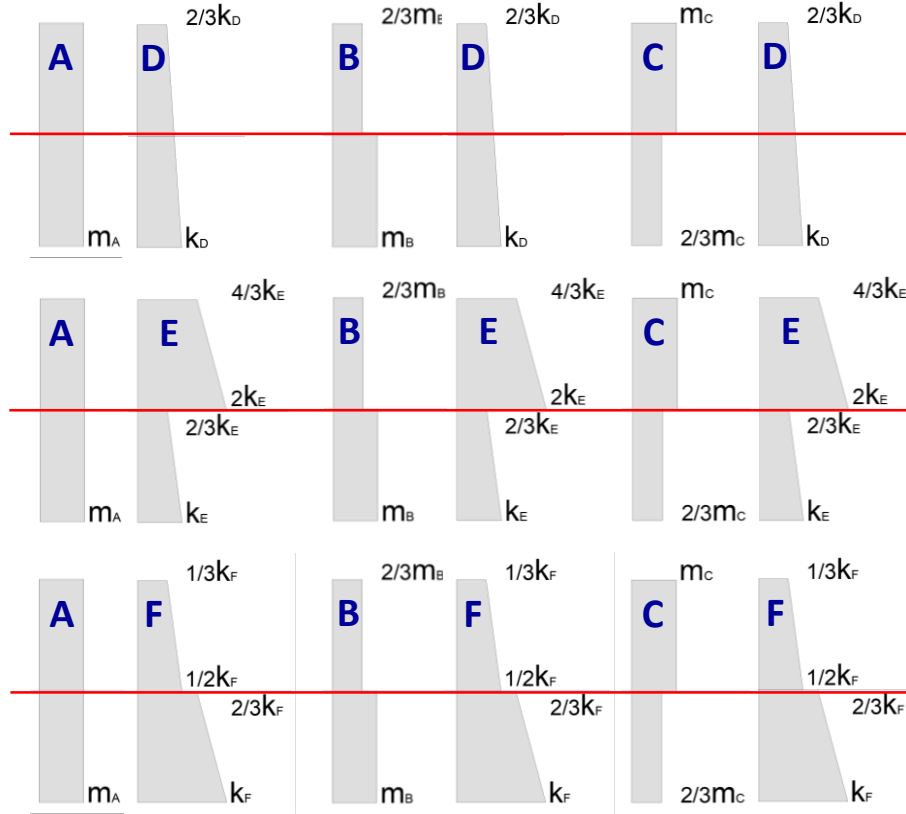


Fig. 6.6. Possible combinations between the different mass and stiffness distributions

The different mass distributions present the same total mass,  $M_{TOT}$ , obtained considering an uniform mass distribution in the 10DOF FB model. From the above assumptions, the floor mass is given by:

$$m = \frac{wA}{g} = \frac{8 \cdot 1850}{9.81} = 1509 \frac{kNs^2}{m} \cong 1500 \frac{kNs^2}{m} \quad (6.1)$$

where  $w$  is the floor weight per square meter,  $A$  is the floor area and  $g$  is the gravity acceleration.

Thus, for a floor mass equal to 1500 t and a total number  $n$  of floors, the total mass is equal to:

$$M_{TOT} = n \cdot m = 10 \cdot 1500 = 15000 \frac{\text{kNs}^2}{\text{m}} \quad (6.2)$$

The different stiffness distributions present the same global stiffness,  $k_{st}$ , equal to the ratio of the base shear,  $Q_{base}$ , to the top displacement,  $\Delta_{top}$ , i.e.:

$$k_{st} = \frac{Q_{base}}{\Delta_{top}} = \frac{S_a(T_1)\Gamma_1}{\Delta_d} = \frac{\omega_1^2 \Delta_d \Gamma_1}{\Delta_d} \cong \omega_1^2 M_{tot} = 592176.264 \text{ kN/m} \quad (6.3)$$

where  $S_a(T_1)$  is the spectral acceleration at the fundamental period  $T_1$  assumed equal to 1 s,  $\Gamma_1$  is the participating mass ratio of the fundamental mode and  $\Delta_d = \Delta_{top}$  is the target displacement. In addition, in Eq. (6.3) it is assumed a first participation factor equal to 1 (i.e. a first mode shape  $\Phi_1 = \{1 \ 1 \ 1 \ \dots \ 1\}_{n \times 1}^T$ ), leading to a first generalized modal mass equal to  $M_{tot}$ .

#### 6.2.1.1. 10DOF FB model

Three mass distributions with the same total mass,  $M_{TOT}$ , are considered, see Fig. 6.3a: the mass is uniformly distributed for the overall structure (A); the  $j$ -th mass of the US is two-third the  $i$ -th mass of the LS (B); the  $i$ -th mass of the LS is two-third the  $j$ -th mass of the US (C). Therefore, the floor mass in the three mass distributions A, B and C is respectively equal to:

$$m_A = \frac{M_{TOT}}{n} \quad (6.4)$$

$$m_B = m_A \frac{n}{(2/3)n_{US} + n_{LS+1}} \quad (6.5)$$

$$m_C = m_A \frac{n}{n_{US} + (2/3)n_{LS+1}} \quad (6.6)$$

Three linear stiffness distributions, which present the same static global stiffness,  $k_{st}$ , are considered. The static global stiffness is obtained by combining in series the shear spring constants of the relevant stories, i.e.:

$$k_{st} = \frac{1}{\sum_l \frac{1}{k_l} + \sum_u \frac{1}{k_u}} \quad (6.7)$$

where  $l = (1, \dots, n_{LS+1})$  and  $u = (n_{LS+2}, \dots, n)$  are the levels of the LS and US, respectively.

The generic stiffness distribution is described by a linear combination of the first story stiffness  $k_1$ , i.e.  $k_1, \dots, a_{n_{LS+1}}k_1, a_{n_{LS+2}}k_1, \dots, a_n k_1$ ; therefore, the generic shear spring constants of the LS and US can be written as  $k_l = a_l k_1$  and  $k_u = a_u k_1$ , with

$$a_l = a_{n_{LS+1}} + \frac{a_1 - a_{n_{LS+1}}}{n_{LS+1} - 1} (n - l) \quad \text{and} \quad a_u = a_n + \frac{a_{n_{LS+2}} - a_n}{n_{US} - 1} (n - u).$$

Fixing the shape stiffness distribution, i.e. the coefficients  $a_l$  and  $a_u$ , the first story stiffness is derived according to the following expression:

$$k_1 = k_{st} \left( \sum_l \frac{1}{a_l} + \sum_u \frac{1}{a_u} \right) \quad (6.8)$$

Varying the coefficients  $a_l$  and  $a_u$ , the three stiffness distributions considered herein are obtained, see Fig. 6.3b: continuous distribution ( $a_1 = 1$ ,  $a_n = 2/3$ ), (D); block-shape distribution with the US stiffer than the LS ( $a_1 = 1$ ,  $a_{n_{LS+1}} = 2/3$ ,  $a_{n_{LS+2}} = 2$ ,  $a_n = 4/3$ ), (E); block-shape distribution with the LS stiffer than the US ( $a_1 = 1$ ,  $a_{n_{LS+1}} = 2/3$ ,  $a_{n_{LS+2}} = 0.5$ ,  $a_n = 1/3$ ), (F).

The mass and stiffness distributions A-D are representative of the common distributions utilized in design practice; the mass distributions B-C and the stiffness distributions F-E are representative of real extreme IIS buildings, i.e. Iidabashi First Building (IB) and Shiodome Sumitomo Building (SSB) [Murakami et al. 2000, Sueoka et al. 2004, Tsuneki et al. 2008-2009]. In particular the mass and stiffness distributions B-F are representative of IB, while the mass and stiffness distributions C-E are representative of SSB.

While the mass and stiffness distributions A-D are constant for each 10DOF FB model, the mass distributions B-C and the stiffness

distributions E-F change level by level; the position of the isolation layer varies as well.

In the FB models, viscous damping equal to 2% is assumed.

#### **6.2.1.2. 10DOF ISO model**

In the IIS models the isolation mass and stiffness values replace the ones corresponding to the story below the first level of the US in the FB models.

The mass and stiffness of the isolation layer are derived as follows. Assuming a rigid superstructure, the system consisting of the US and the isolation layer is representative of a BIS, which can be characterized by means of a SDOF model, with a mass equal to the sum of the masses of the US and of the isolation story, and stiffness and damping of the isolators. In order to exploit both the isolation and mass damper effects, a range of isolation period between 1÷4 s is chosen; the mass of the isolation story is assumed equal to the corresponding story mass in the FB model; thus, the equivalent stiffness of the isolation system is derived.

$$k_{ISO} = \frac{4\pi^2(m_{US} + m_{ISO})}{T_{ISO}^2} = \frac{4\pi^2 M_{ISO}}{T_{ISO}^2} \quad (6.9)$$

Moving the isolation interface from the top to the bottom story, the ratio between the total isolated mass  $m_{US} + m_{ISO}$  and the total mass of the building  $M_{tot}$ , i.e:

$$R_m = \frac{m_{US} + m_{ISO}}{M_{tot}} = \frac{M_{ISO}}{M_{tot}} \quad (6.10)$$

varies from 0.10 (RIS) to 1.0 (BIS).

The parameter  $R_m$  determines the ratio of upper to lower mass, which, as well, strongly affects the resulting vibration characteristics and dynamic response of the single upper and lower portions, and of the structural complex.

In the IIS models, viscous damping equal to 2% is assumed for the LS and US while an equivalent viscous damping equal to 10% is assumed at the seismic isolation interface.

### 6.3. MODAL ANALYSIS

Depending on the mass distribution, it is possible to associate a mass ratio  $\alpha$ , being  $\alpha$  the ratio of the total isolated mass,  $M_{ISO}$ , to the LS mass,  $m_{LS}$ , i.e.:

$$\alpha = \frac{M_{ISO}}{m_{LS}} \quad (6.11)$$

to the position of the isolation layer along the height of the building. Therefore, considering all the RIS  $\div$  BIS MDOF AD models, the mass ratio  $\alpha$  varies in the range  $0 \div 10$ , according to the following three behavioral categories:

1.  $\alpha = 0 \div 1$ , RIS  $\div$  IIS5: TMD zone
2.  $\alpha = 1 \div 4$ , IIS6  $\div$  IIS8: IIS zone
3.  $\alpha > 4$ , IIS9  $\div$  BIS: BIS zone

In Figs. 6.7 – 6.8 are respectively depicted the distribution of the first participating mass ratio,  $\Gamma_1$ , and that of the most significant higher mode,  $\Gamma_{max,hm}$ , and of their ratio,  $\Gamma_1/\Gamma_{max,hm}$ , as a function of the mass ratio  $\alpha$ .

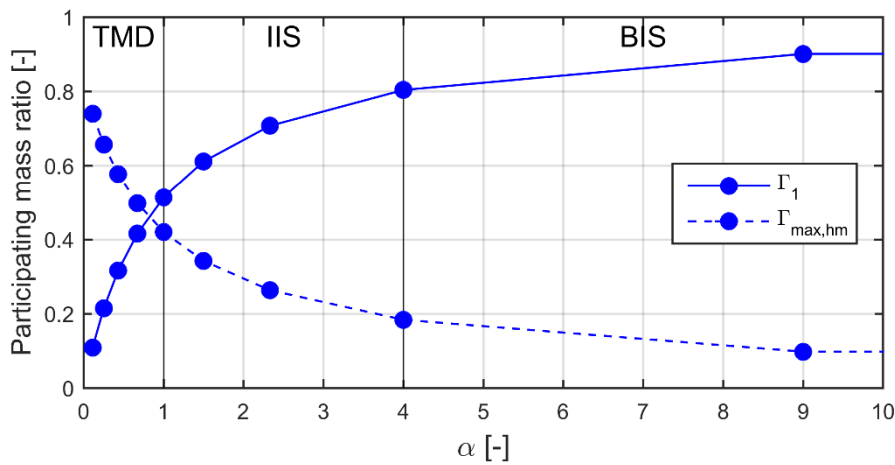


Fig.6.7. Participating mass vs. the mass ratio  $\alpha$



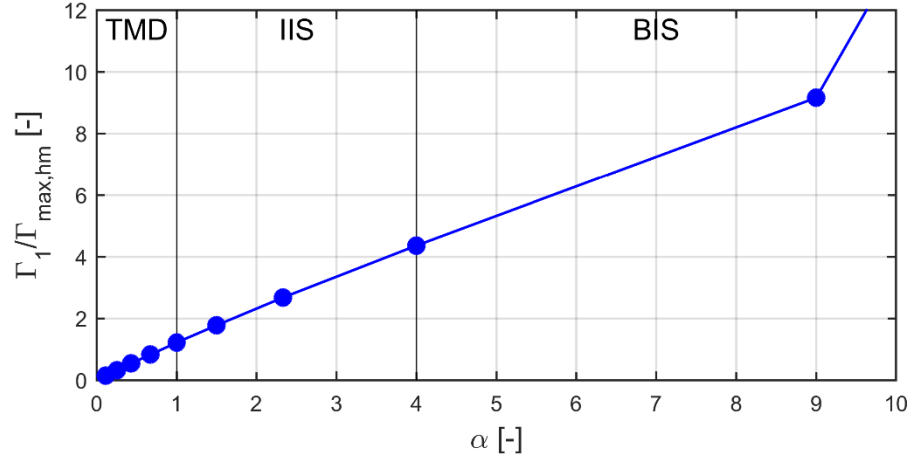


Fig.6.8. Participating mass ratio vs. the mass ratio  $\alpha$

From Fig. 6.7 it can be observed that, for a mass ratio  $\alpha$  less than 1 (TMD zone), the higher mode possesses the greater fraction of participating mass; for  $\alpha$  between  $1 \div 4$  (IIS zone) the two participating masses are comparable, but increasing  $\alpha$  the first mode provides the larger values; for  $\alpha$  larger than 4 (BIS zone), the higher mode is negligible. Consequently, by increasing  $\alpha$ , the participating mass ratio  $\Gamma_1/\Gamma_{\max, hm}$  increases almost linearly (Fig. 6.8); in the IIS area this ratio varies between 1.5 and 4.

Assuming a damping ratio of the structural portions (superstructure and substructure),  $\xi_s$ , equal to 0.02, and an equivalent viscous damping of the isolation system,  $\xi_{iso}$ , equal to 0.10, the MDOF ISO system is non-proportional viscously damped.

Considering the above modes, Fig. 6.9 shows the distribution of the damping ratios of the first mode,  $\xi_1$ , and of the higher mode that possesses the maximum fraction of participating mass,  $\xi_{\max, hm}$ . From the graph, it can be noticed that the damping ratios  $\xi_1$  and  $\xi_{\max, hm}$  reach respectively the values of  $\xi_{iso}$  and  $\xi_s$  for less values of  $\alpha$ . Increasing  $\alpha$ ,  $\xi_1$  is almost equal to  $\xi_{iso}$ , while  $\xi_{\max, hm}$  assumes values larger than  $\xi_s$ .

Since for  $\alpha$  larger than 1, the system falls in the isolation zone (from IIS to BIS), it is possible to consider the analogy with the linear theory proposed by Kelly for 2DOF base isolated structures, for which the first damping ratio is almost equal to the equivalent damping ratio of the isolation, and the damping ratio of the higher mode is larger than the structural damping ratio.

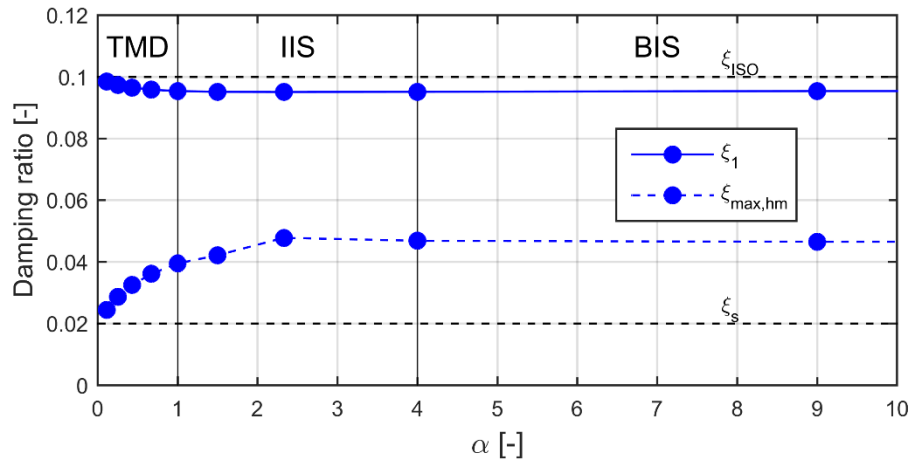


Fig.6.9. Damping ratio vs. the mass ratio  $\alpha$

The natural vibration modes obtained for the 10DOF FB and ISO models are depicted in Figs 6.10 ÷ 6.28; each tris of charts shows the first three modes of vibration corresponding to a total participating mass ratio equal to or greater than 85%. The values of periods and mass participating ratios of the isolated models are also provided in the same figures; the corresponding values of periods and masses of the fixed-base models are shown in Tab. 6.1.

Table 6.1. Natural periods and participating masses of FB IIS 5 models

Mass and stiffess distributions	1 <sup>st</sup> mode		2 <sup>nd</sup> mode		3 <sup>rd</sup> mode	
	T [s]	$\Gamma$ [%]	T [s]	$\Gamma$ [%]	T [s]	$\Gamma$ [%]
AD	0.64	83	0.22	10	0.14	3
BD	0.60	82	0.23	11	0.13	4
CD	0.68	85	0.22	8	0.14	4
AE	0.72	86	0.21	9	0.14	2
BE	0.68	85	0.22	10	0.14	2
CE	0.76	88	0.20	7	0.14	2
AF	0.59	77	0.22	13	0.14	4
BF	0.54	76	0.22	15	0.13	4
CF	0.63	80	0.22	10	0.14	4

N.B. The AD distribution is the same for all the FB models

In the following are discussed the results obtained for: (i) the same mass and stiffness distributions (AD) and different placements of the isolation

layer (from the 1<sup>st</sup> to the 10<sup>th</sup> level), see Figs 6.10 ÷ 6.19; (ii) the same position of the isolation layer (i.e. the 5<sup>th</sup> level corresponding to the 10DOF IIS 5 model), for the all the possible combinations of the mass and stiffness distributions (i.e. AD, BD, CD, AE, BE, CE, AF, BF, CF), see Figs 6.20 ÷ 6.28. The isolation period  $T_{ISO}$  is assumed equal to 3 s.

From Figs 6.10 ÷ 6.28, it is worth noticing that the first mode in the 10DOF IIS AD models involves deformation mainly concentrated at the isolation level, with almost no deformations in both US and LS. The first period  $T_1$  is very close to the isolation period  $T_{ISO}$  in all isolated models, varying between 3.03 ÷ 3.05 s, with a mean value of 3.042 s. The participating mass ratio,  $\Gamma_1$ , is close to the mass ratio  $R_m$ , and, thus, going from BIS to RIS, decreases from 1.0 to 0.1.

Comparing the first modes of the controlled and uncontrolled configurations, a reduction of displacements both in the US and LS is observed for all isolated models.

Some differences arise looking at the higher modes. The second and third periods of the 10DOF IIS AD models vary between 0.26 ÷ 0.57 s and 0.14 ÷ 0.20 s, respectively, while the higher periods in the reference FB model are 0.22 s and 0.14 s.

Looking at the higher modes of the IIS models, two different scenarios for the dynamic behavior of the global structure are found: a major influence of one of the higher modes (either the 2<sup>nd</sup> or the 3<sup>rd</sup> mode), or a coupling effect of the 2<sup>nd</sup> and 3<sup>rd</sup> modes.

The prevailing higher mode is generally the second one, with displacements mainly concentrated in the LS and isolation system and minor or almost no deformation in the US. On the contrary, the third higher mode shows displacements mainly concentrated in the US and isolation system and minor or almost no deformation in the LS. Going from BIS to RIS the participation of the LS increases up to the 74 % while the participation of the US is almost null.

It can be noticed that, for isolation layer located at the lower or upper levels, almost comparable modal displacements are observed in the controlled and uncontrolled configurations, while for isolation located around mid-height, an amplification of the displacements of the LS dofs closer to the isolation layer is shown.

In addition, from Figs 6.10 ÷ 6.28 can be seen that no coupling arises for the higher modes which are characterized by significant participant mass ratios.

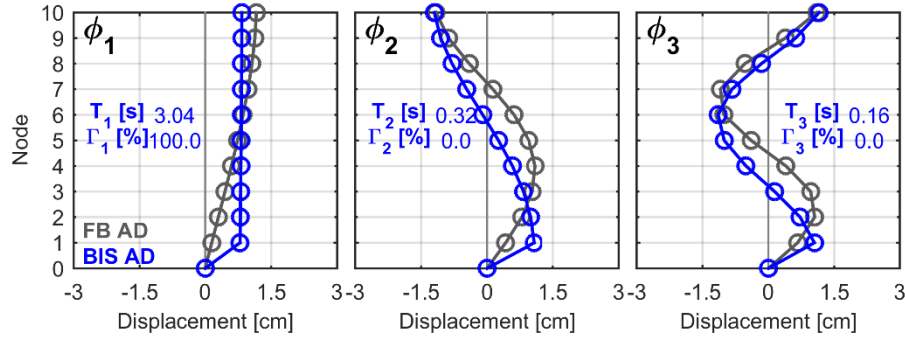


Fig. 6.10. BIS vs. FB 10DOF models: natural modes of vibration for the A-D mass and stiffness distributions

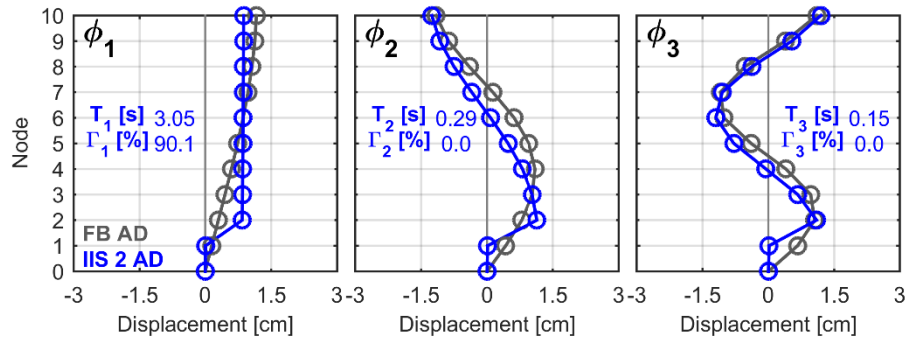


Fig. 6.11. IIS 2 vs. FB 10DOF models: natural modes of vibration for the A-D mass and stiffness distributions

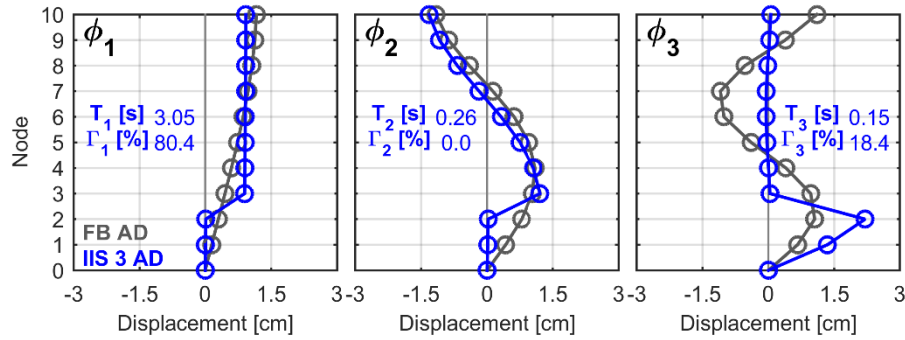


Fig. 6.12. IIS 3 vs. FB 10DOF models: natural modes of vibration for the A-D mass and stiffness distributions

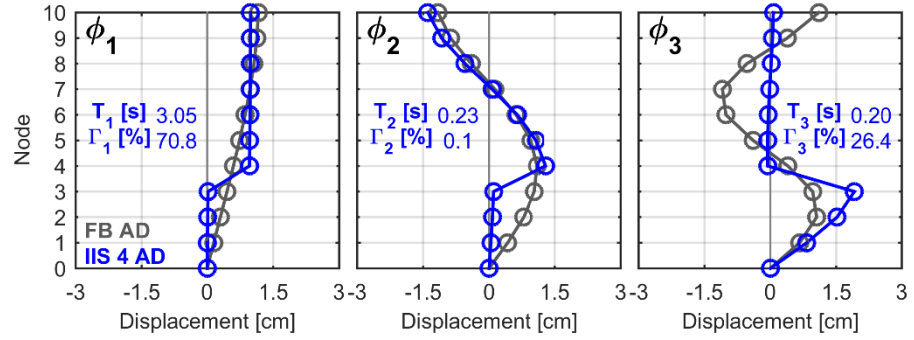


Fig. 6.13. IIS 4 vs. FB 10DOF models: natural modes of vibration for the A-D mass and stiffness distributions

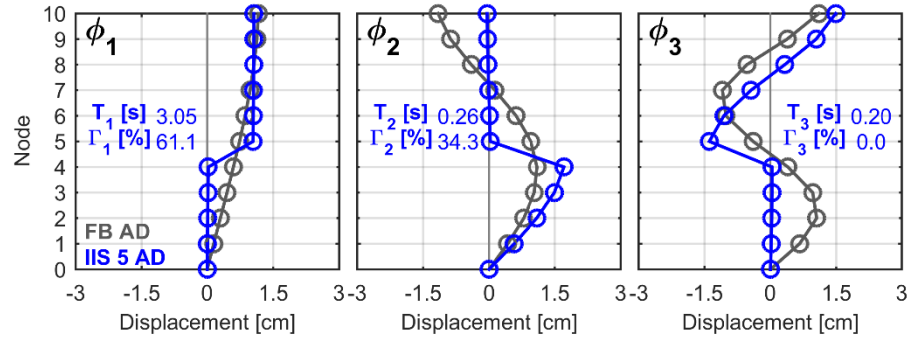


Fig. 6.14. IIS 5 vs. FB 10DOF models: natural modes of vibration for the A-D mass and stiffness distributions

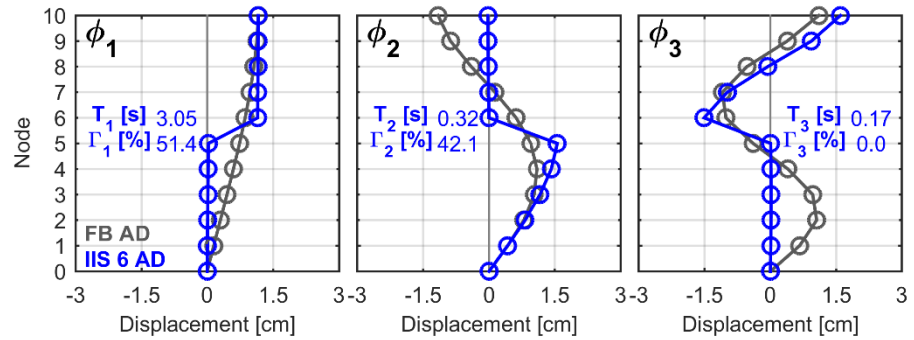


Fig. 6.15. IIS 6 vs. FB 10DOF models: natural modes of vibration for the A-D mass and stiffness distributions

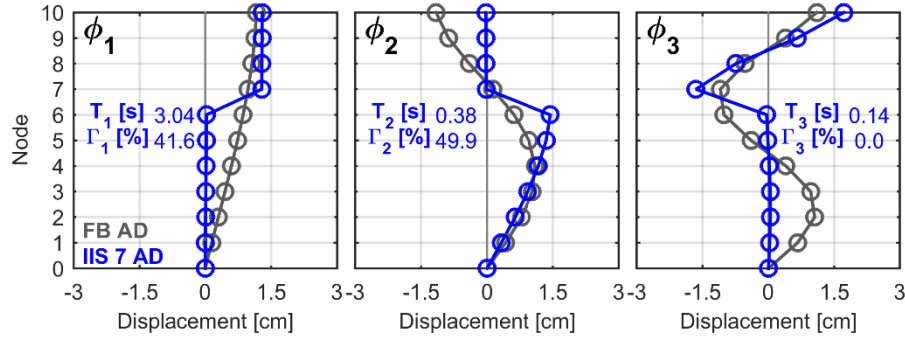


Fig. 6.16. IIS 7 vs. FB 10DOF models: natural modes of vibration for the A-D mass and stiffness distributions

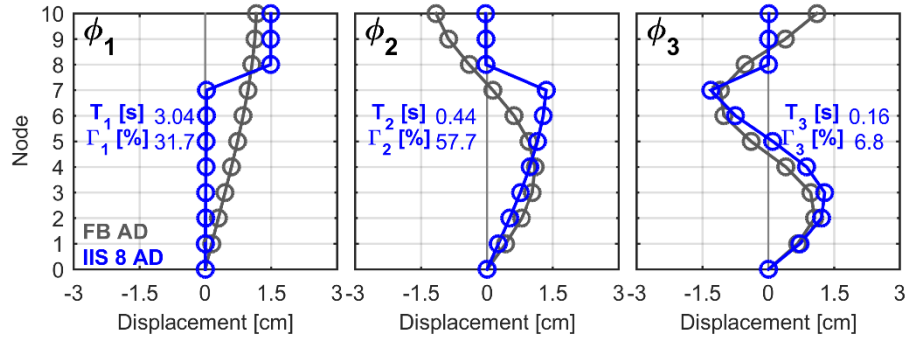


Fig. 6.17. IIS 8 vs. FB 10DOF models: natural modes of vibration for the A-D mass and stiffness distributions

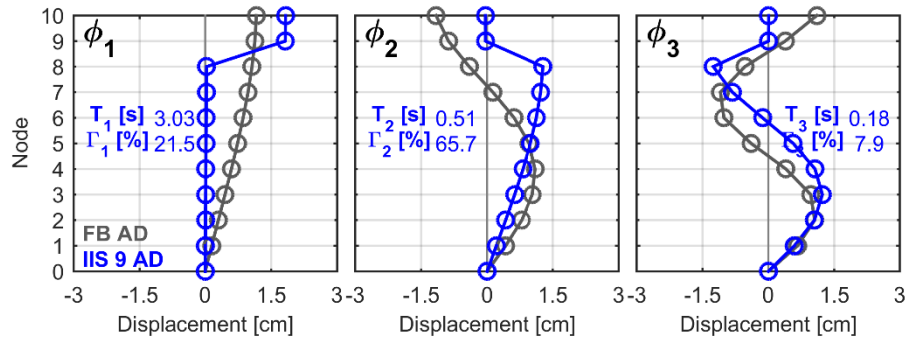
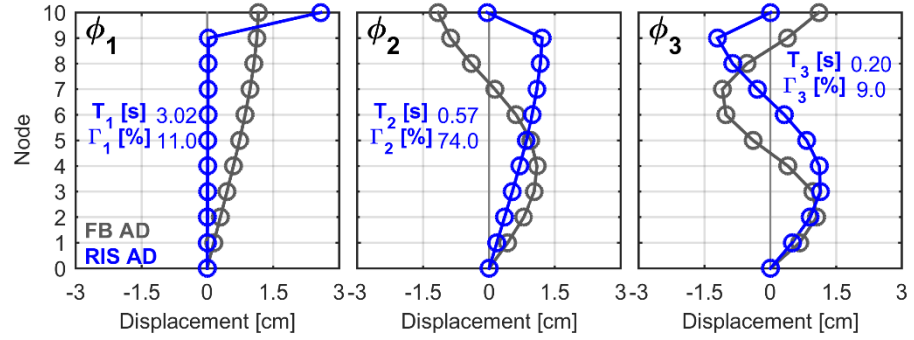


Fig. 6.18. IIS 9 vs. FB 10DOF models: natural modes of vibration for the A-D mass and stiffness distributions



**Fig. 6.19. RIS vs. FB 10DOF models: natural modes of vibration for the A-D mass and stiffness distributions**

Comparing the modal displacements of the higher modes in the 10DOF IIS 5 and FB models with different mass and stiffness distributions provided in Figs 6.20 ÷ 6.28, no significant differences arise with respect to the AD distributions, except for the stiffness distribution E. In fact, in the IIS 5 model, whatever is the mass distribution (either A, B, or C), when the US is stiffer than the LS (E), a reduction of the LS displacements with respect to the FB model counterparts can be observed.

Therefore, it seems that, the stiffness distribution affects more than the mass distribution the dynamic behavior of the controlled configuration, and a stiffer US improves the dynamic response of the overall structure. Recalling that the first participating mass is almost equal to  $R_m$ , with the mass distributions B and C the minimum and maximum values of  $\Gamma_1$  are obtained, respectively, since the former possesses the lighter US (minimum  $R_m$ ) while the latter the heavier US (maximum  $R_m$ ).

Varying the mass and stiffness distributions, the mass and stiffness ratios between the US and LS changes affecting the interaction between the structural portions. In fact, for the same placement of the isolation layer (the 5<sup>th</sup> level) only in IIS 5 AF, with a uniform mass distribution and a more flexible US than the LS, the coupling of the higher modes arises. The higher modes of the 10DOF IIS 5 AF model show equal periods (0.22 s), significant participating mass ratios (6.9% and 27.3%) and comparable displacements in US and LS. It is worth noticing that, in the second modes no significant differences arise between the IIS 5 and FB modes, since the isolation displacement is small.

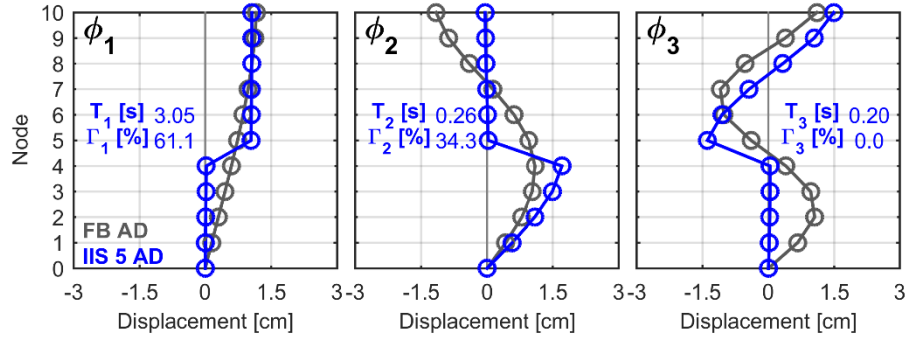


Fig. 6.20. IIS 5 vs. FB 10DOF models: natural modes of vibration for the A-D mass and stiffness distributions

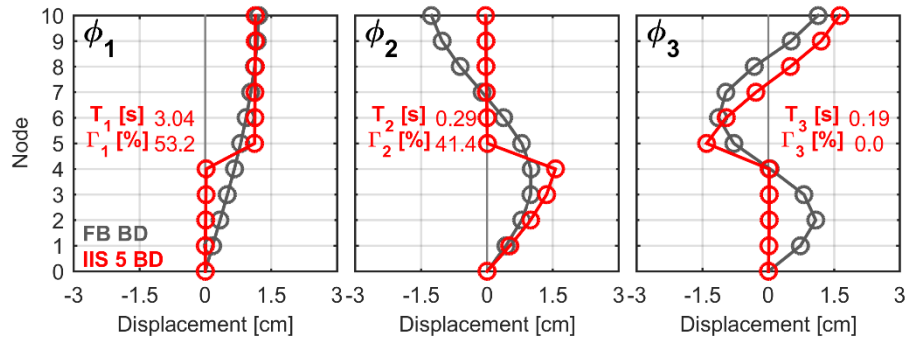


Fig. 6.21. IIS 5 vs. FB 10DOF models: natural modes of vibration for the B-D mass and stiffness distributions

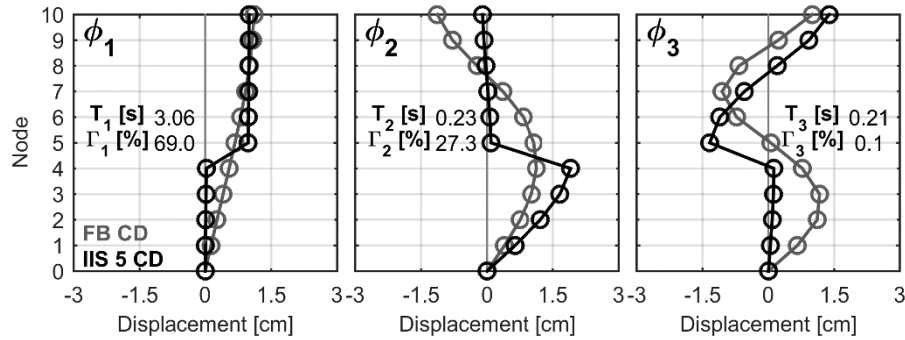


Fig. 6.22. IIS 5 vs. FB 10DOF models: natural modes of vibration for the C-D mass and stiffness distributions



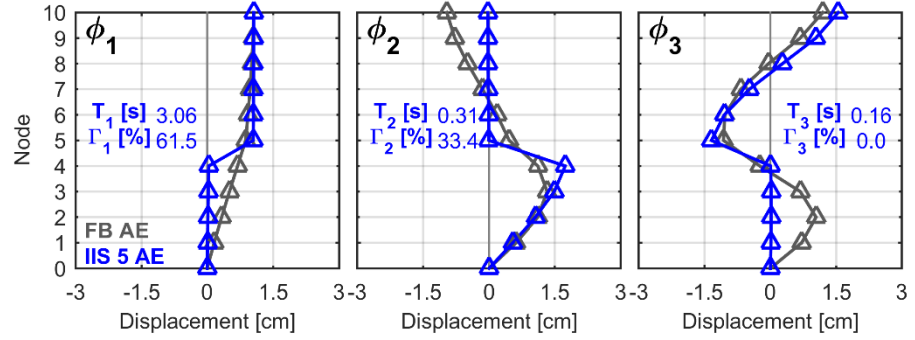


Fig. 6.23. IIS 5 vs. FB 10DOF models: natural modes of vibration for the A-E mass and stiffness distributions

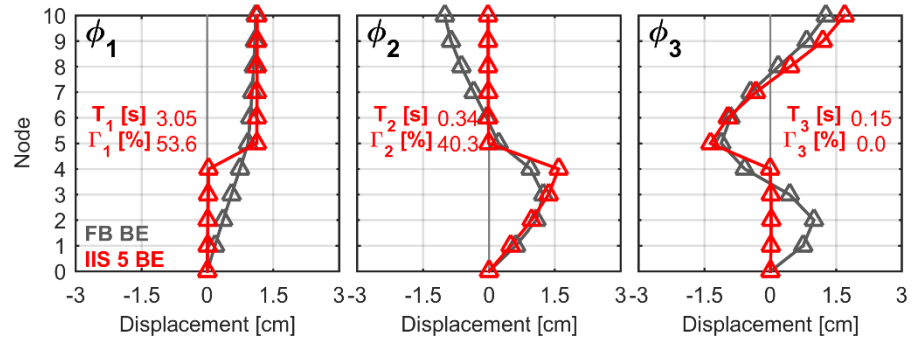


Fig. 6.24. IIS 5 vs. FB 10DOF models: natural modes of vibration for the B-E mass and stiffness distributions

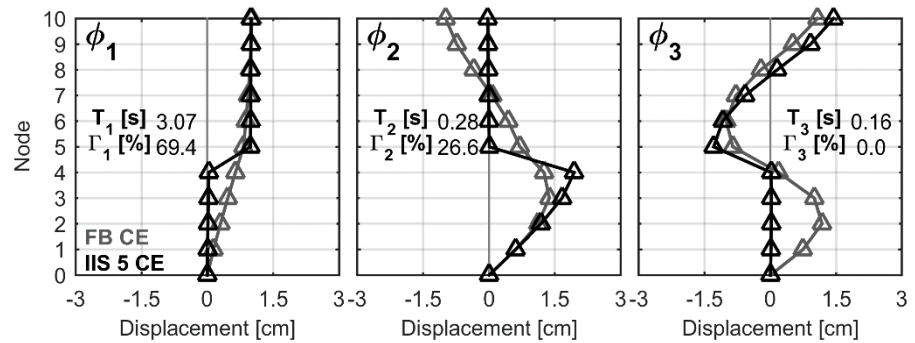


Fig. 6.25. IIS 5 vs. FB 10DOF models: natural modes of vibration for the C-E mass and stiffness distributions

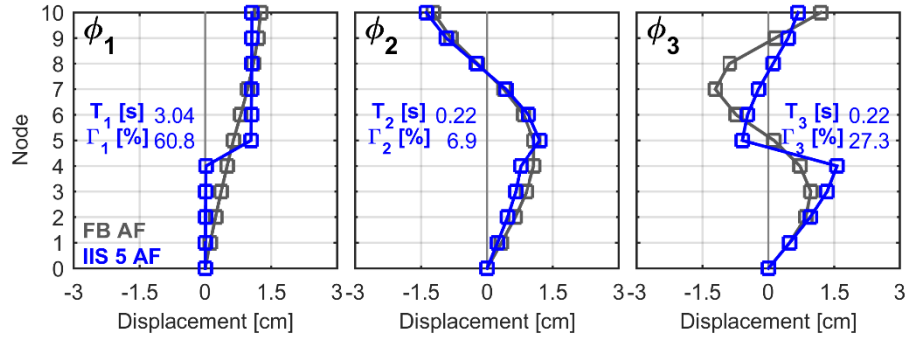


Fig. 6.26. IIS 5 vs. FB 10DOF models: natural modes of vibration for the A-F mass and stiffness distributions

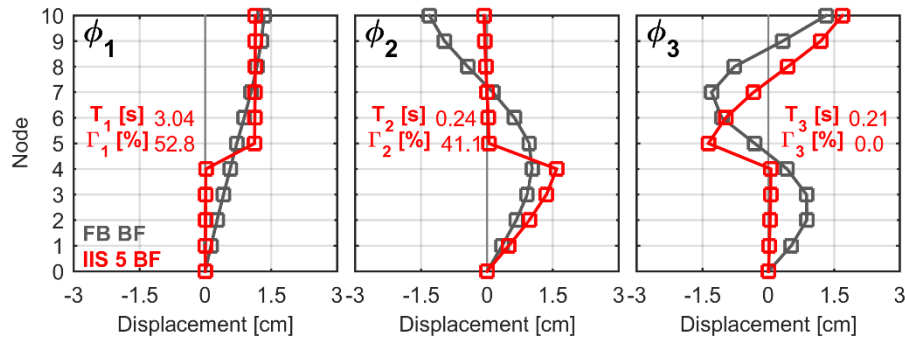


Fig. 6.27. IIS 5 vs. FB 10DOF models: natural modes of vibration for the B-F mass and stiffness distributions

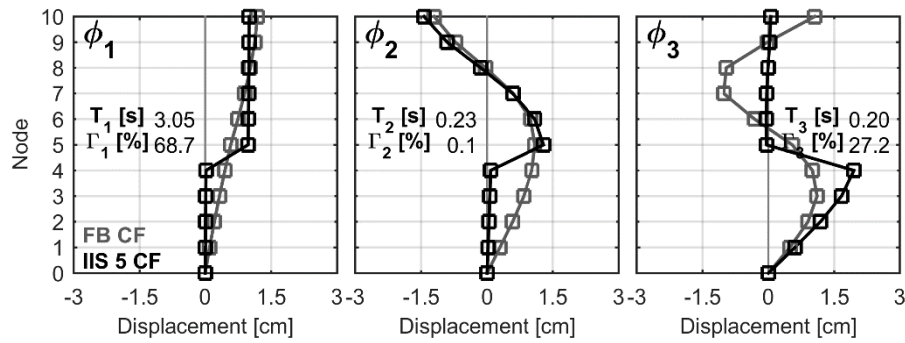


Fig. 6.28. IIS 5 vs. FB 10DOF models: natural modes of vibration for the C-F mass and stiffness distributions

### 6.3.1.1. Modal expansion of the inertial forces

Assuming the system responds linearly, the relative participation of various modes can be represented by the inertial force distribution in each mode. The  $n$ -th mode force distribution  $\mathbf{s}_n$  (with units of mass) is defined in terms of the mass matrix  $\mathbf{M}$ , mode shape  $\boldsymbol{\phi}_n$  and excitation influence vector  $\boldsymbol{\tau}$ , i.e.:

$$\mathbf{s}_n = \Gamma_n \mathbf{M} \boldsymbol{\phi}_n \quad (6.12)$$

where

$$\Gamma_n = \frac{\boldsymbol{\phi}_n^T \mathbf{M} \boldsymbol{\tau}}{\boldsymbol{\phi}_n^T \mathbf{M} \boldsymbol{\phi}_n}$$

is the participating mass of the mode  $n$ .

In a response spectrum analysis,  $\mathbf{s}_n$  is multiplied by the  $n$ -th mode spectral acceleration to obtain equivalent static forces applied to the building [Ryan & Earl 2010]. Based on these principles, the effectiveness of IIS can be predicted prior to dynamic analysis by examining the inertial forces participating in each mode and the periods of the one or more isolation modes.

For the isolation period  $T_{iso}$  equal to 3 s, in Figs. 6.29 – 6.30 are plotted the modal inertial force distributions, normalized with respect to the mass at each level, as a function of the natural periods of vibrations. In particular, in Fig. 6.29 are considered the different models for the AD distributions, in Fig. 6.30 is depicted the IIS 5 model for the different mass and stiffness distributions.

In Fig. 6.29 can be noticed that the higher modes are effective and are related to the LS only. Some differences arise looking at Fig. 6.30, in which for the same location of the isolation layer, it is observed the influence of the mass distribution. Considering the A distribution (uniform mass), the inertial forces in the higher modes are mainly attributable to the LS, with the B – C distributions (different masses for US and LS) also the US contributes to the expansion of the inertial forces. It is worth noticing that in IIS 5 AF the second and third modes possess almost equal periods and involve inertial forces in both US and LS, suggesting a coupling of the higher modes.

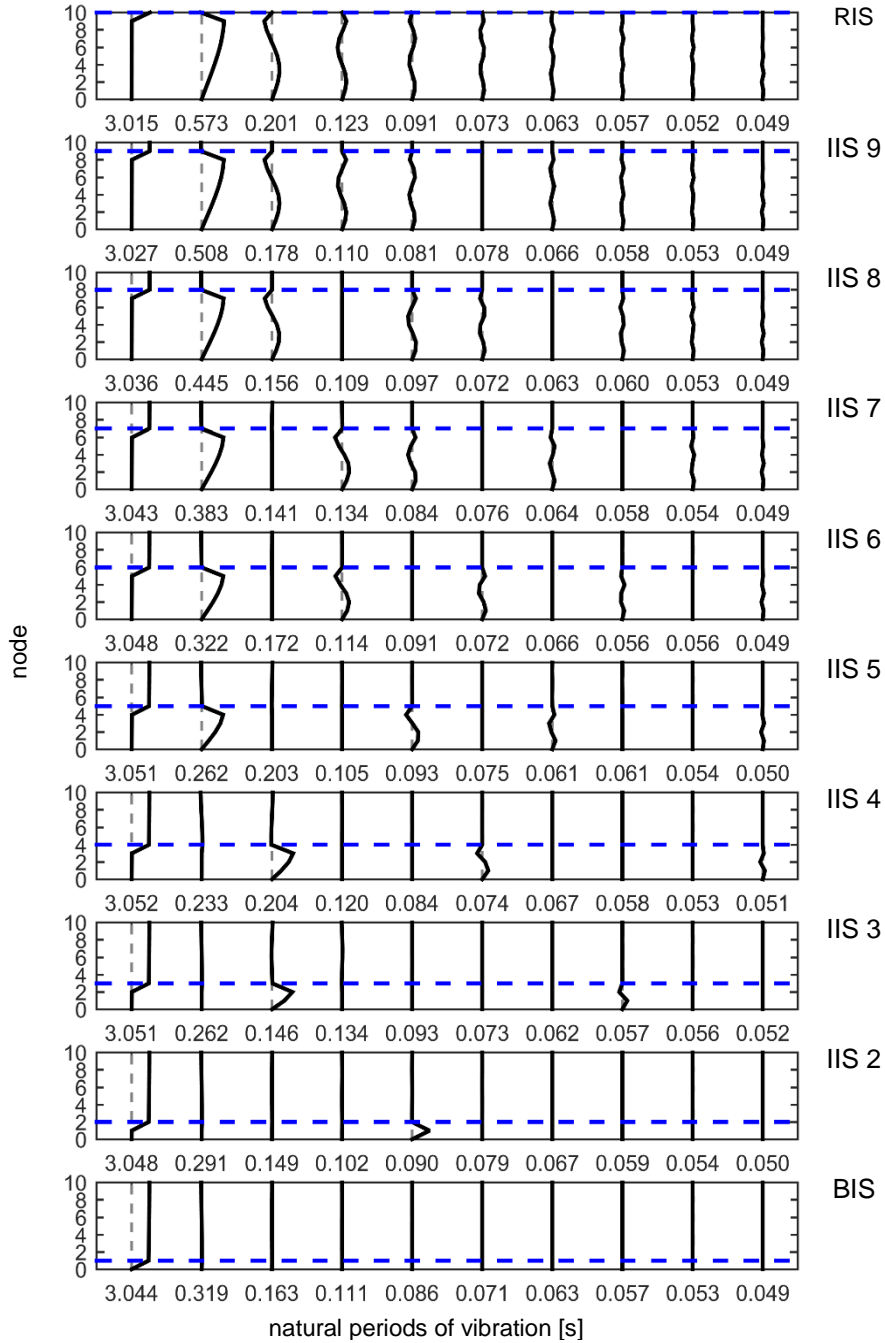
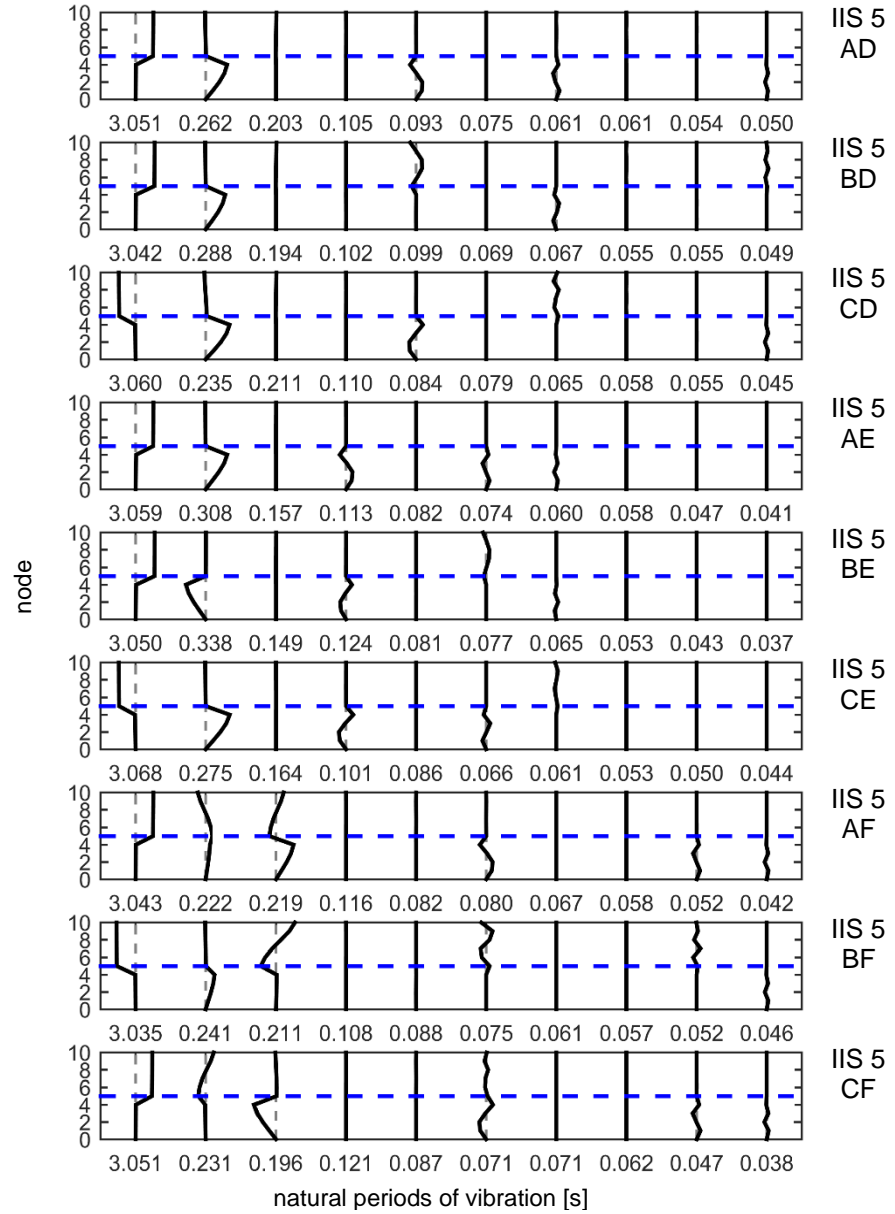


Fig. 6.29. Modal expansion of inertial force – AD,  $T_{iso} = 3$  s

Fig. 6.30. Modal expansion of inertial force – IIS 5,  $T_{ISO} = 3$  s

### 6.3.1.2. Mode Coupling Effect (MCE)

The mode coupling effect (MCE) in IIS has been addressed in literature [Wang et al. 2012a, Kobayashi & Koh 2008] (see Chapter 4).

Basically, it is recognized that the dynamics of structures with mid-story isolation is affected by the vibration characteristics of the US and LS, and that, depending on these characteristics, two different scenarios for the dynamic behavior of the global structure are found: a major influence of one of the higher modes, with a prevailing contribution of either the LS or US, or a coupling effect of the higher modes, with a contribution of both the US and LS.

For exploiting the higher modes effect, the paper by [Kobayashi & Koh 2008] employed the theory of Skinner [Skinner 1993] for defining the contribution of the higher modes in base isolated structures. Skinner has revealed the influence of the higher modes to earthquake response of base isolation buildings by sweeping the modal response with free-free mode shape vectors.

Kobayashi & Koh applied the same method to mid-story isolation buildings by means of a free-free three degree-of-freedom IIS model. The free-free 3DOF IIS model (ff-3DOF IIS) is obtained by setting the stiffness of seismic isolation layer equal to zero (i.e. ideal isolation).

Extending this method to multi-degree-of-freedom IIS model, a free-free MDOF IIS model (ff-MDOF IIS) can be defined as follows, Fig. 6.31a.

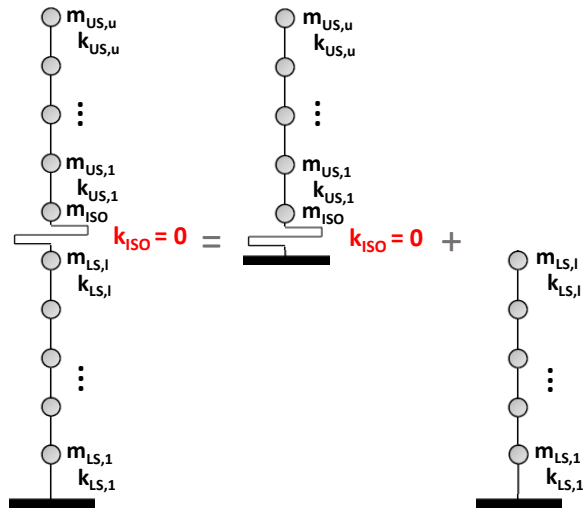


Fig. 6.31. free-free isolated models: (a) ff-MDOF IIS, (b) ff-uDOF US+ISO, (c) IDOF LS

In the ff-MDOF IIS model the free-free mode shape vectors  $\phi_0 = \{\phi_{0,1}, \dots, \phi_{0,n}\}_{n \times 1}^T$  and natural circular frequency  $\omega_{0,n}^2$ , for  $n = (1, \dots, N)$ , with  $N$  the total number of the dofs, are given by the following characteristic equations expressed in matrix form:

$$\mathbf{K}_0 \phi_0 = \omega_{0,n}^2 \mathbf{M} \phi_0 \quad (6.13)$$

where the mass matrix  $\mathbf{M}$  and the stiffness matrix  $\mathbf{K}_0$ , in which the stiffness of the isolation system is assumed equal to zero, are given by:

$$\mathbf{M} = \begin{bmatrix} \mathbf{M}_{LS, lxl} & \mathbf{0}_{lx1} & \mathbf{0}_{lxu} \\ \mathbf{0}_{1xl} & m_{ISO} & \mathbf{0}_{1xu} \\ \mathbf{0}_{uxl} & \mathbf{0}_{ux1} & \mathbf{M}_{US, uxu} \end{bmatrix}_{n \times n}; \quad \mathbf{K}_0 = \begin{bmatrix} \mathbf{K}_{LS, lxl} & \mathbf{0}_{lxu} \\ \mathbf{0}_{uxl} & \mathbf{K}_{0, US, u+1 \times u+1} \end{bmatrix}_{n \times n} \quad (6.14)$$

where  $\mathbf{M}_{LS} (lxl)$  and  $\mathbf{K}_{LS} (lxl)$  are the mass and stiffness matrices of the LS, with  $l$  the number of the dofs of the LS;  $\mathbf{M}_{US} (uxu)$  is the mass matrix of the US, with  $u$  the number of the dofs of the US;  $\mathbf{K}_{0, US} (u+1 \times u+1)$  is the stiffness matrix of the isolated upper structure with  $k_{ISO} = 0$ . Solving the eigenvalue problem, i.e. equating to zero the determinant of the matrix  $[\mathbf{K}_0 - \omega_0^2 \mathbf{M}]$ :

$$\det[\mathbf{K}_0 - \omega_{0,n}^2 \mathbf{M}] = 0 \quad (6.15)$$

the circular frequency  $\omega_{0,n}^2$  is derived.

It is worth noticing that, assuming  $k_{ISO} = 0$ , the stiffness matrix  $\mathbf{K}_0$  can be subdivided into two sub-matrices corresponding to the fixed-base lower structure,  $\mathbf{K}_{LS}$ , and the base-isolated upper structure with  $k_{ISO} = 0$ ,  $\mathbf{K}_{0, US}$ .

In lieu of the complete ff-MDOF IIS model it is possible to consider two distinct models, i.e. the  $l$  degree-of-freedom lower structure ( $l$ -DOF LS model), and the  $u$ -degree-of-freedom isolated upper structure with  $k_{ISO} = 0$  (ff- $u$ -DOF US+ISO model).

For the l-DOF LS and ff-u-DOF US+ISO models, Eqs. (6.13) and (6.15) can be respectively re-written as:

$$\mathbf{K}_{\text{LS}} \boldsymbol{\phi}_{\text{LS}} = \omega_{\text{LS},j}^2 \mathbf{M}_{\text{LS}} \boldsymbol{\phi}_{\text{LS}}; \quad \det \left| \mathbf{K}_{\text{LS}} - \omega_{\text{LS},j}^2 \mathbf{M}_{\text{LS}} \right| = 0 \quad (6.16)$$

$$\mathbf{K}_{0,\text{US}} \boldsymbol{\phi}_{0,\text{US}} = {}_{\text{ff}} \omega_{\text{US}+\text{ISO},i}^2 \mathbf{M}_{\text{US}} \boldsymbol{\phi}_{0,\text{US}}; \quad \det \left| \mathbf{K}_{0,\text{US}} - {}_{\text{ff}} \omega_{\text{US}+\text{ISO},i}^2 \mathbf{M}_{\text{US}} \right| = 0 \quad (6.17)$$

Solving the eigenvalue problem, it is possible to derive the  $j$ -th circular frequency  $\omega_{\text{LS},j}^2$  of the fixed-base LS from Eq. (6.16) and the  $i$ -th circular frequency  ${}_{\text{ff}} \omega_{\text{US}+\text{ISO},i}^2$  of the isolated upper structure with  $k_{\text{ISO}} = 0$  from Eq. (6.17), where  $i = (1, \dots, u)$  and  $j = (1, \dots, l)$  are the degree of freedoms of the US and LS, respectively.

In this framework, the MCE can be expressed by a parameter  $\beta_{i,j}$  equal to the ratio between the  $i$ -th frequency of the ff-u-DOF US+ISO model,  ${}_{\text{ff}} \omega_{\text{US}+\text{ISO},i}$ , and the  $j$ -th frequency of the l-DOF LS model,  $\omega_{\text{LS},j}$ , as follows:

$$\beta_{i,j} = \frac{{}_{\text{ff}} \omega_{\text{US}+\text{ISO},i}}{\omega_{\text{LS},j}} \quad (6.18)$$

The MCE parameter  $\beta_{i,j}$  can be easily calculated, showing that when it is equal or very close to one, the MCE occurs.

From Eq. (6.18) a simple design rule can be derived: No MCE arises if the  $i$ -th frequency of base-isolated US is far from the  $j$ -th frequency of the fixed-base LS. In general, it is sufficient that the first two-three frequencies of the free-free base-isolated US are far from the fixed-base LS counterparts.

It is worth noticing that the minimum number of degrees of freedom to grasp the coupling mode effect is three, i.e. one dof for each structural portion (US and LS) and one dof for the isolation layer. Therefore, considering the free-free three-degree-of-freedom model, ff-3DOF IIS, the sub-models become a single-degree-of-freedom fixed-base LS model, SDOF LS, and a free-free two-degree-of-freedom isolated US model, ff-2DOF US+ISO.

Solving the eigenvalue problem from Eqs. (6.16) and (6.17), the circular frequencies  $\omega_{\text{LS},j}^2$  and  ${}_{\text{ff}} \omega_{\text{US}+\text{ISO},i}^2$  become:



$$\omega_{LS,1}^2 = \omega_{LS}^2; \quad \omega_{US+ISO,2}^2 = \omega_{US}^2 \left( 1 + \frac{m_{US}}{m_{ISO}} \right) = \omega_{US}^2 (1 + r_{US}) \quad (6.19)$$

where  $r_{US} = m_{US}/m_{ISO}$  is the mass ratio defined in the previous Chapter 4. Substituting Eq. (6.19) into Eq. (6.18), the MCE parameter assumes the form already defined in Chapter 4, according to [Wang et al. 2012a, Kobayashi & Koh 2008] (see Eqs. (4.1) and (4.4)), i.e.:

$$\beta = \frac{\omega_{US+ISO,2}}{\omega_{LS}} = \frac{\omega_{US} \sqrt{1 + r_{US}}}{\omega_{LS}} \quad (6.20)$$

In this case an unique value of  $\beta$  is provided, since it is possible to couple the frequency of the LS to only one higher frequency of the free-free isolated US.

Quite trivially, the check of MCE occurrence through the parameter  $\beta$  given by Eq. (6.20) is easier than utilizing the parameter  $\beta_{i,j}$  (Eq. (6.18)). However, the formula (6.20) only account for one possible higher mode coupling, and is not able to predict the possible detrimental effect arising when more than two significant higher modes are coupled.

From the above results, it is worth noticing that the participating mass ratio corresponding to the isolation system  $\Gamma_{ISO}$  is equal to the mass ratio  $R_m$ . In fact, the first participating mass  $\Gamma_1$ , corresponding to  $\Gamma_{ISO}$ , expressed in percentage is given by:

$$\Gamma_1 = \Gamma_{ISO} = \frac{(\boldsymbol{\phi}^T \cdot \mathbf{M} \cdot \mathbf{I})^2}{(\boldsymbol{\phi}^T \cdot \mathbf{M} \cdot \boldsymbol{\phi}) \cdot M_{tot}} = \frac{\sum_{i=1}^n (m_i \phi_{i1})^2}{\sum_{i=1}^n m_i \phi_{i1}^2 \cdot M_{tot}} = \frac{M_{ISO}}{M_{tot}} = R_m \quad (6.21)$$

where the first mode shape  $\boldsymbol{\phi}^T = [\{0, \dots, 0\}_{lx1} \quad 1 \quad \{1, \dots, 1\}_{ux1}]_{nx1}^T$  shows displacement only in the isolation layer while US and LS are infinitely rigid.

In Fig. 6.32 it is shown the sensitivity of the MCE parameter  $\beta$  as a function of the mass ratio  $\alpha$ ; in the graph are considered all the possible combinations between the mass and stiffness distributions and the

positions of the isolation layer. The values of  $\beta$  for Idiabashi 1st Building (IB) and Shiodome Sumitomo Building (SSB), analyzed in the previous Chapter 5, are also provided in the graph.

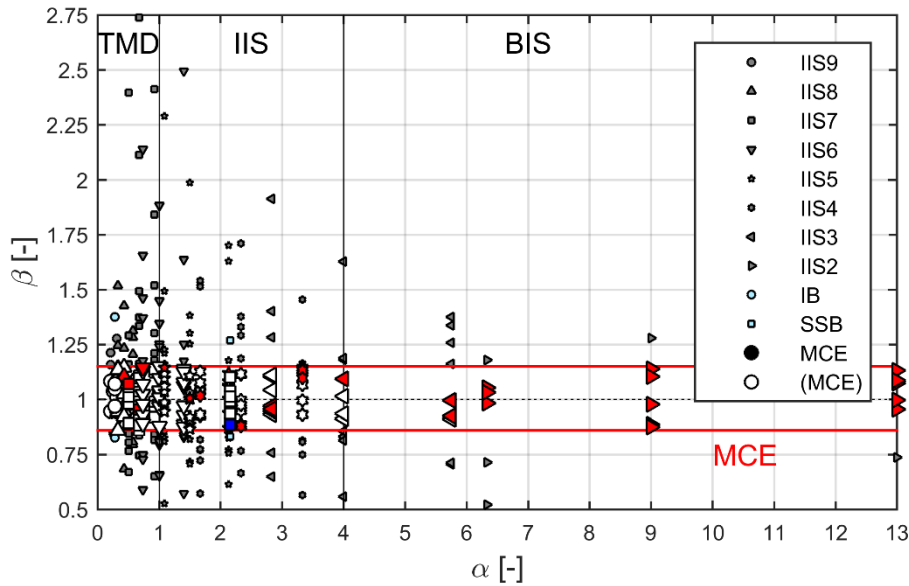


Fig.6.32.  $\beta$  vs.  $\alpha$

With continuous red lines is depicted the band of MCE, with a variation from the unit values of  $\pm 15\%$ . From Fig. 6.32 can be noticed that the larger number of values is included in the MCE band; however only the red markers possess a fraction of coupled participating mass equal to, or larger than, 5%. From the graph it is confirmed that SSB is characterized by MCE.

Considering all the mass distribution (A, B, C), for each position of the isolation layer, the mass ratio assumes three different values, as depicted in Tab. 6.2. In the table the cases of IB and SSB, and the variation of the coupled participating mass of the significant higher modes are also provided.

From Tab. 6.2 can be seen that IIS 9 does not possess significant participating mass, while IIS 5 (depicted in bold characters) shows the larger fraction of participating mass with values of  $28\% \div 42\%$ . It is worth

noticing that the minimum and maximum  $\Gamma_{\text{MCE}}$  respectively correspond to the mass distributions C and B. In fact, with the heavier US than the LS (C), the first mode is characterized by the maximum participating mass while the higher modes by the minimum fraction; on the contrary, with the lighter US than the LS (B), the first mode displays the minimum participating mass while the higher modes the maximum value.

In addition, for a mass distribution C, with  $\alpha$  and  $\Gamma_{\text{MCE}}$  respectively equal to 2.15 and 27%, SSB shows values in line with the corresponding ones of IIS 5.

**Table 6.2. Variation of  $\alpha$  and  $\Gamma_{\text{MCE}}$  as a function of the mass distribution**

Model	$\alpha$ [-]			$\Gamma_{\text{MCE}}$ [%]
	A	B	C	
IIS 9	0.25	0.21	0.31	-
IIS 8	0.43	0.33	0.57	6 ÷ 7
IIS 7	0.67	0.50	0.92	6
IIS 6	1.00	0.73	1.40	6
<b>IIS 5</b>	<b>1.50</b>	<b>1.08</b>	<b>2.13</b>	<b>28 ÷ 42</b>
IIS 4	2.33	1.67	3.33	21 ÷ 34
IIS 3	4.00	2.83	5.75	14 ÷ 24
IIS 2	9.00	6.33	13.00	7 ÷ 14
IB	0.28			-
SSB	2.15			27

Considering only the cases affected by MCE and depicted in Fig. 6.32 within the red band, the effect of the higher modes and the potential of modal coupling effect are shown in Figs. 6.33 ÷ 6.39 as a function of the higher frequencies  $\omega_{\text{LS},j}$  and  $\omega_{\text{ISO+US},i}$ ; each tris of graphs provides all the coupled higher modes for the same mass distribution (either A, B or C) by varying the stiffness distribution (D, E, F). In these figures, the participating mass ratios related to ISO ( $\Gamma_{\text{ISO}}$ ), LS ( $\Gamma_{\text{LS}}$ ), US ( $\Gamma_{\text{US}}$ ), and coupled LS+US ( $\Gamma_{\text{MCE}}$ ) are also provided.

In particular each chart is divided into three parts, which represent the two regions where either the higher modes of the LS or the isolated US prevail, and the bandwidth, marked by continuous red lines, where coupling of the higher modes of LS and US occurs; considering the great number of modes (coupled or not) of all isolated models, only the coupled modes in the bandwidth are depicted in the charts, for the sake of clarity.

For each MCE - point the number of the coupled modes and the value of the corresponding participating mass are also provided in the charts. The acronym which characterizes each MCE - point is “a - b (c)”, where: a represents the mode number of the l-DOF LS model; b the higher mode number of the ff-u-DOF US+ISO model; c is the corresponding coupled participating mass in percentage.

In particular going from the ff-10DOF IIS 2 to the IIS 9 model, the number a varies between 1 and 8 while the number b between 8 and 1 (see Fig. 6.2). Quite trivially, the ff-10DOF BIS and RIS models are excluded from this analysis, since the higher modes only concern either the US or the LS, respectively, and not the interaction between US and LS.

From the Figs. 6.33 ÷ 6.39 it can be observed that equal values of frequencies  $\omega_{LS,j}$  and  $_{ff}\omega_{ISO+US,i}$  cause a mode coupling effect, i.e. the coefficient  $\beta$  is equal to 1. According to the graph, in order to exclude a coupling effect is sufficient to have quite different values for the two frequencies  $\omega_{LS,j}$  and  $_{ff}\omega_{ISO+US,i}$ . In particular for frequencies which are at least one the half part of the other, the MCE is always avoided.

From Figs. 6.33 ÷ 6.39 it can be also noticed that coupling of higher modes arises from the ff-10DOF IIS 8 to the IIS 2 model and the number of the significant coupled higher modes (with a participating mass greater than 5%) increases going from IIS 8 to IIS 2, i.e. from the 8<sup>th</sup> to the 2<sup>nd</sup> location of isolation system. When the isolation layer is placed at the lower levels, the LS possesses few dofs with respect to the isolated US counterparts, and, thus, it is possible to combine the few modes of the LS with many modes of the isolated US; for the same reason, the coupled participating mass decreases going from the ff-10DOF IIS 8 to the IIS 2 model, since the mass ratio  $R_m$  increases.

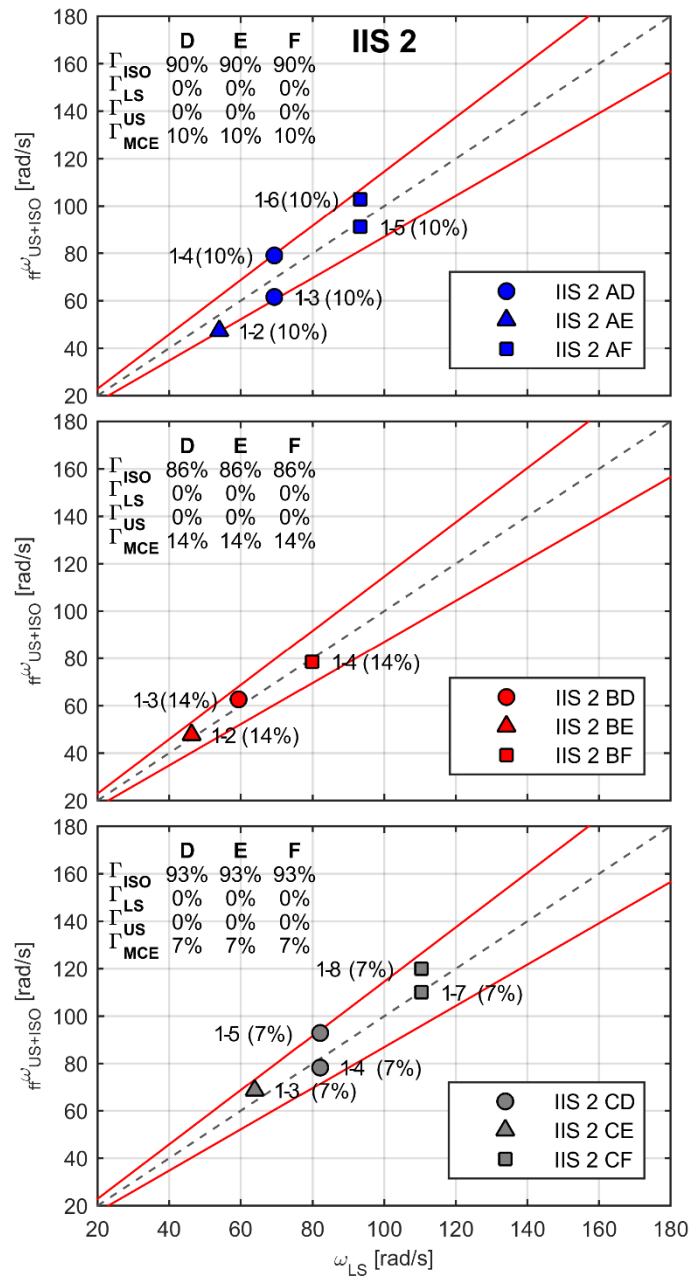


Fig. 6.33. Mode Coupling Effect – IIS 2 10DOF mode

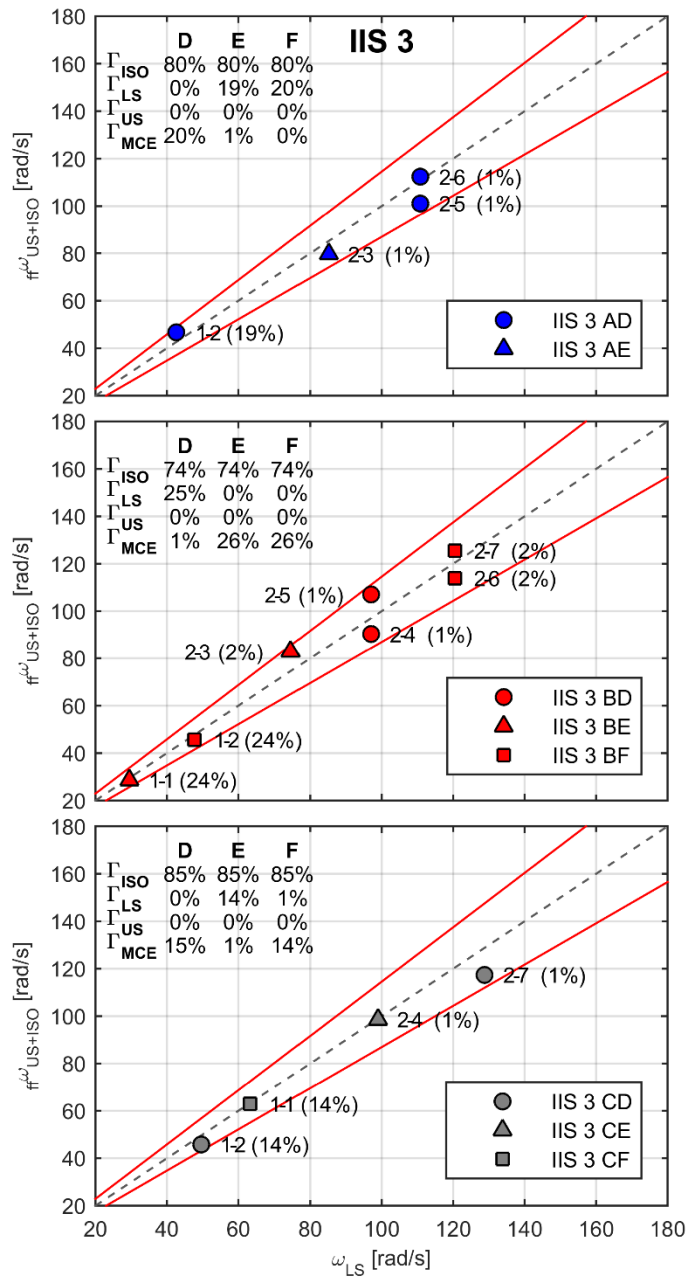


Fig. 6.34. Mode Coupling Effect – IIS 3 10DOF model

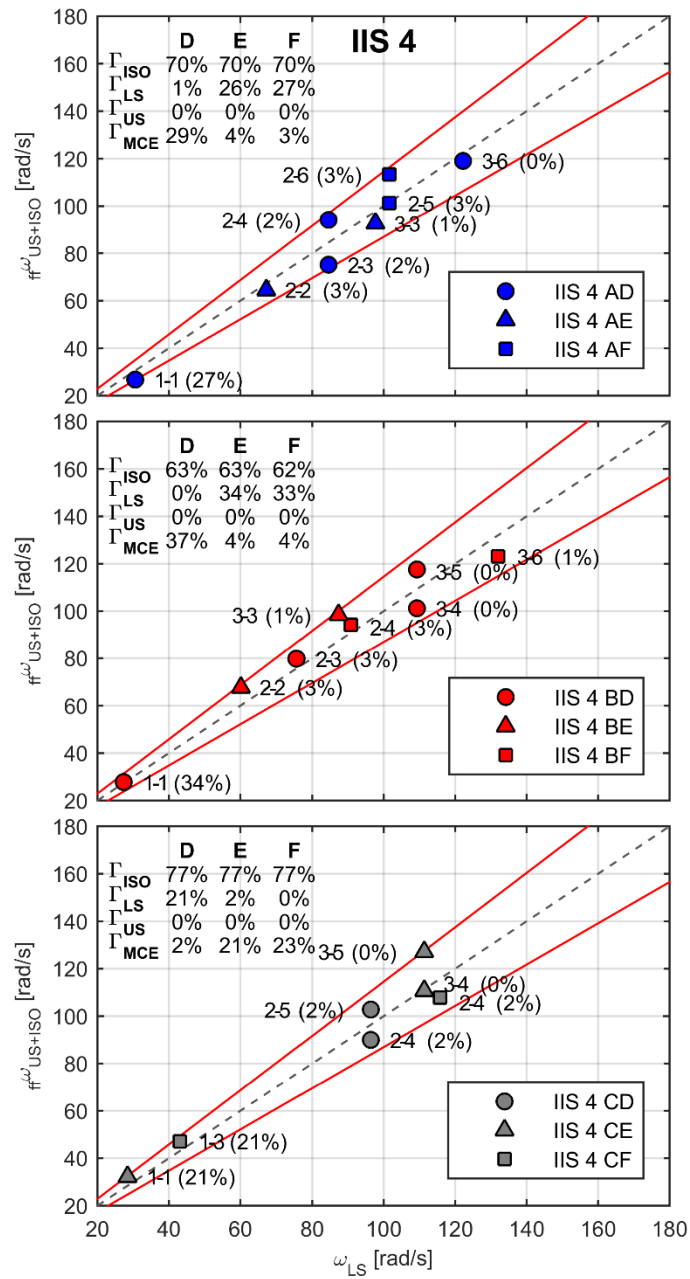


Fig. 6.35. Mode Coupling Effect – IIS 4 10DOF model

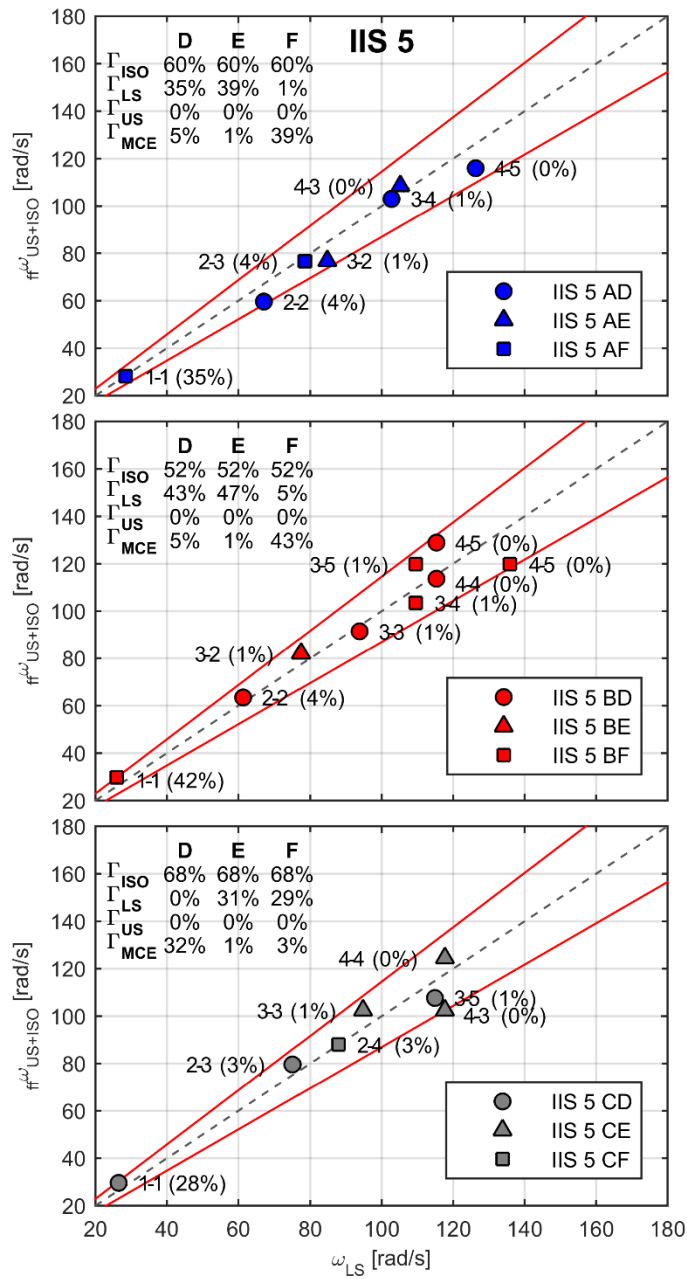


Fig. 6.36. Mode Coupling Effect – IIS 5 10DOF model



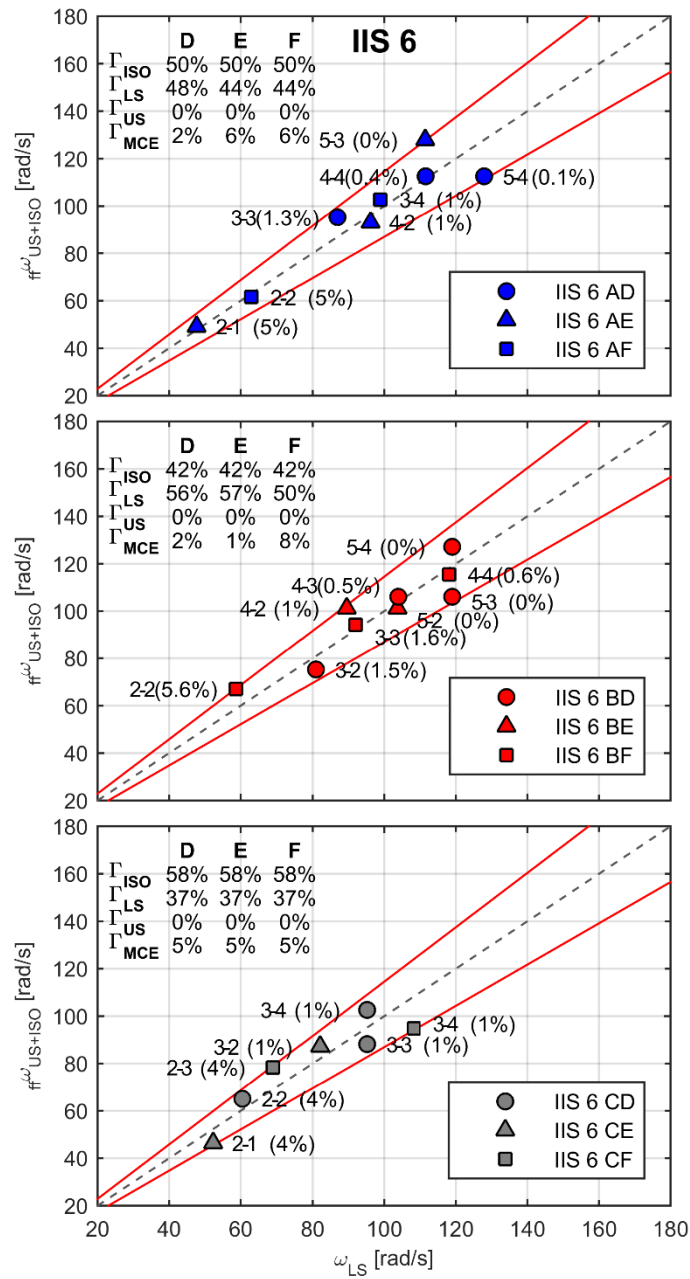


Fig. 6.37. Mode Coupling Effect – IIS 6 10DOF model

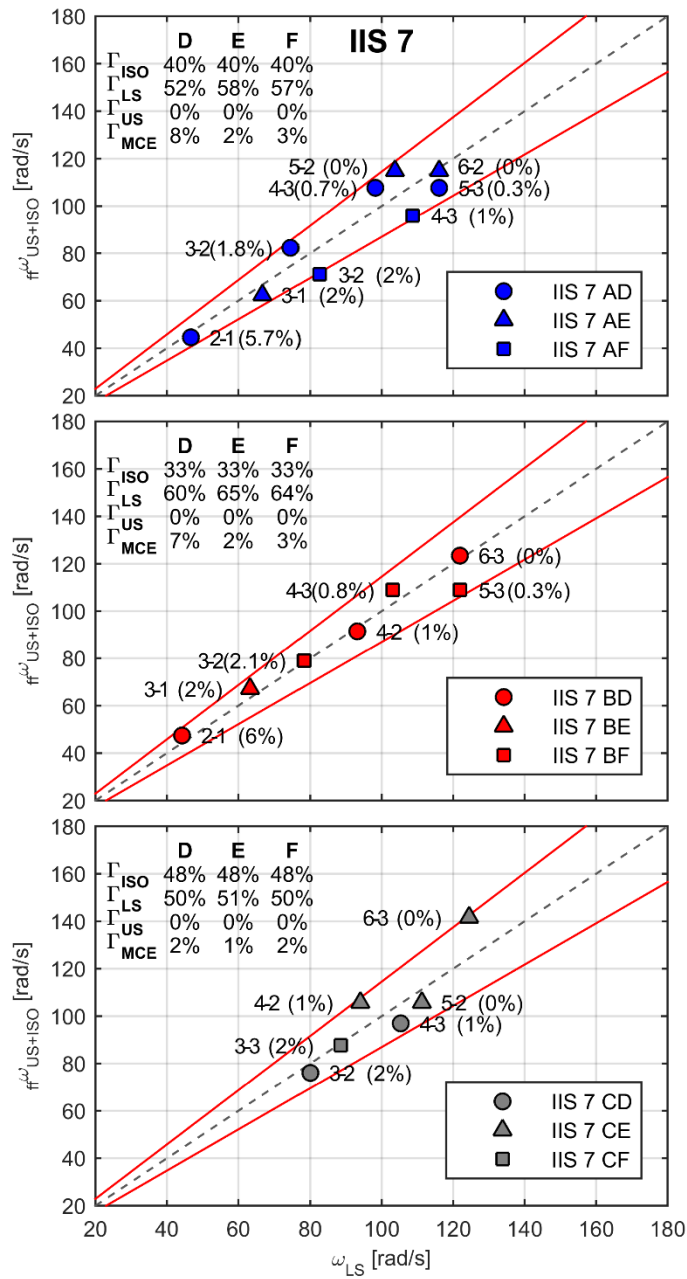


Fig. 6.38. Mode Coupling Effect – IIS 7 10DOF model

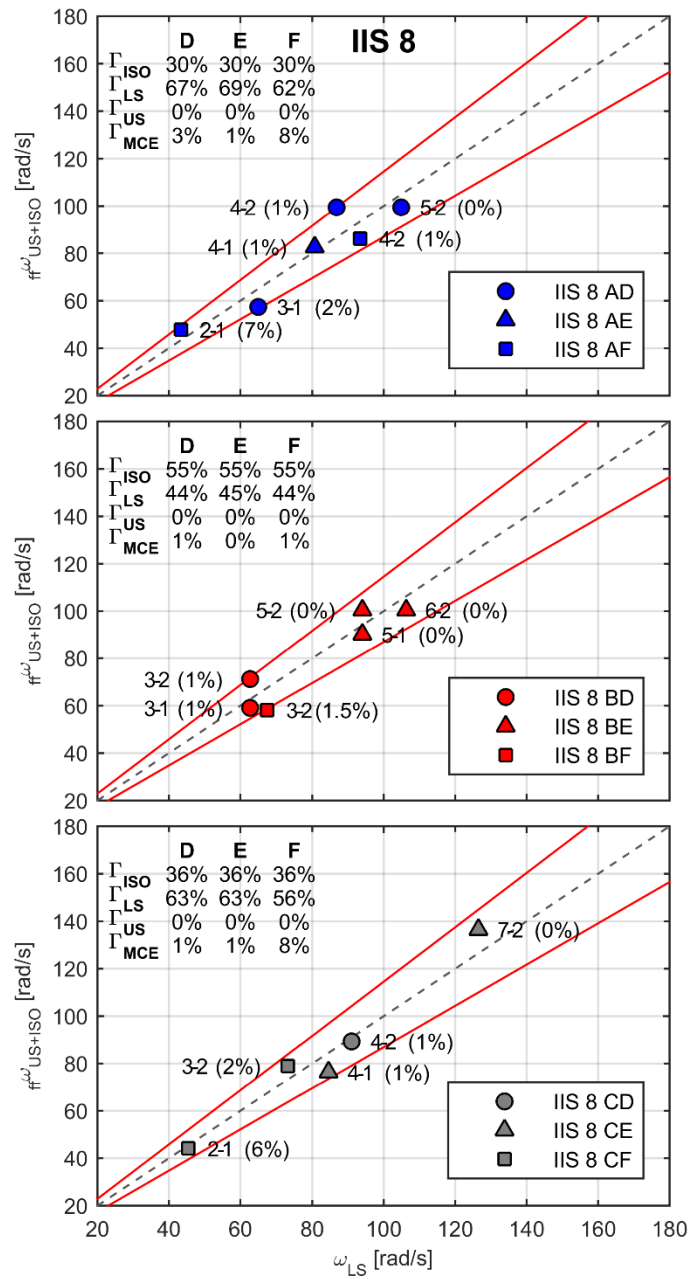


Fig. 6.39. Mode Coupling Effect – IIS 8 10DOF model

As can be seen from Figs. 6.33 ÷ 6.39, the IIS 5 model, in which the dofs of US and LS are comparable, possesses the major significant value of coupled participating mass, between 28 ÷ 42%. IIS 5 represents also a transition model between two types of behavior: for models going from IIS 4 to IIS 2 (i.e. with an isolation layer placed in the first half height of the building) the significant MCE occurs when the 1<sup>st</sup> mode of the LS is coupled to the first eight higher modes of the isolated US; on the contrary, going from IIS 6 to IIS 8 (i.e. with an isolation layer placed in the second half height of the building), the 2<sup>nd</sup> mode of the isolated US is generally coupled to the 1<sup>st</sup> mode of the LS.

The range of the significant coupled participating mass for the different contribution of the a – b coupled modes is the following: 1 – 1,  $\Gamma_{\text{MCE}} = 24 \div 42\%$ ; 1 – 2,  $\Gamma_{\text{MCE}} = 14 \div 24\%$ ; 1 – 3,  $\Gamma_{\text{MCE}} = 10 \div 14\%$ ; 1 – 4,  $\Gamma_{\text{MCE}} = 7 \div 14\%$ ; 1 – 5,  $\Gamma_{\text{MCE}} = 7 \div 10\%$ ; 1 – 6,  $\Gamma_{\text{MCE}} = 10\%$ ; 1 – 7 and 1 – 8,  $\Gamma_{\text{MCE}} = 7\%$ .

A schematic representation of the cases affected by MCE, considering all the ff-10DOF IIS models (from RIS to BIS) as well as the possible combinations of the mass and stiffness distributions (AD, BD, CD, AE, BE, CE, AF, BF, CF), is shown in Fig. 6.40; the figure shows the cases when a significant coupling of the higher modes occurs, and reports the number of the coupled modes (a – b), as well as the corresponding participating mass ratio  $\Gamma_{\text{MCE}}$  (expressed in percentage).

From Fig. 6.40 it can be observed that 31 cases are affected by MCE; subdividing these cases for the coupled modes 1-1, 1-2 (or 2-1), 1-3, 1-4, 1-5, 1-6, 1-7, 1-8, 2-2, the following classification can be drawn.

The number of each a – b coupled modes observed in the ff-10DOF IIS models is: 7 for the couple 1-1 in CD, AF, BF IIS 5 ( $\Gamma_{\text{MCE}} = 28\%$ , 35%, 42%, respectively), AD, BD, CE IIS 4 ( $\Gamma_{\text{MCE}} = 27\%$ , 34%, 21%, respectively) and BE IIS 3 ( $\Gamma_{\text{MCE}} = 24\%$ ); 6 for the couple 1-2 in CF IIS 4 ( $\Gamma_{\text{MCE}} = 21\%$ ), AD, CD, BF IIS 3 ( $\Gamma_{\text{MCE}} = 19\%$ , 14%, 24%, respectively) and AE, BE IIS 2 ( $\Gamma_{\text{MCE}} = 10\%$ , 14%, respectively); 4 for the couple 1-3 in CF IIS 3 ( $\Gamma_{\text{MCE}} = 14\%$ ) and AD, BD, CE IIS 2 ( $\Gamma_{\text{MCE}} = 10\%$ , 14%, 7%, respectively); 3 for the couple 1-4 AD, CD, BF IIS 2 ( $\Gamma_{\text{MCE}} = 10\%$ , 7%, 14%, respectively); 2 for the couple 1-5 in CD, AF IIS 2 ( $\Gamma_{\text{MCE}} = 7\%$ , 10%, respectively); 1 for the couple 1-6 in AF IIS 2 ( $\Gamma_{\text{MCE}} = 10\%$ ); 1 for the couple 1-7 in CF IIS 2 ( $\Gamma_{\text{MCE}} = 14\%$ ); 1 for the couple 1-8 in CF IIS 2 ( $\Gamma_{\text{MCE}} = 14\%$ ); 1 for the couple 2-2 in BF IIS 6 ( $\Gamma_{\text{MCE}} = 6\%$ ); 5 for the

couple 2-1 in AE IIS 6 ( $\Gamma_{\text{MCE}} = 5\%$ ), AD, BD IIS 7 ( $\Gamma_{\text{MCE}} = 6\%$ ), AF, CF IIS 8 ( $\Gamma_{\text{MCE}} = 7\%$ ).

It is worth noticing that, while in all the models only two coupled higher modes are observed, in IIS 2 model are also present three coupled higher modes in 4 cases, i.e.: AD (1-5 and 1-6), CD (1-4 and 1-5), AF (1-5 and 1-6), CF (1-7 and 1-8).

Looking at the mass (A, B, C) and stiffness (D, E, F) distributions the following considerations can be done in terms of the minimum and maximum number of coupled modes, considering either the mass distribution or the stiffness distribution, or even, taking into account both the mass and stiffness distributions.

In particular the mass distribution B shows the minimum number of coupled modes, i.e. 9, while the mass distributions A and C show the maximum number of coupled modes, i.e. 11; the stiffness distribution E shows the minimum number of coupled modes, i.e. 6, while the stiffness distribution F shows the maximum number of coupled modes, i.e. 13; the AE, BE, CE distributions show the minimum number of coupled modes, i.e. 2; otherwise, the AD and CF distributions show the maximum number, i.e. 5.

Considering both the location of the isolation level and the mass and stiffness distributions, the models AF, BF IIS 5 and BD IIS 4 show the maximum percentage of the coupled participating mass ratio  $\Gamma_{\text{MCE}}$ , respectively corresponding to 35%, 42% and 34%.

In very general terms, with a US stiffer and heavier than the LS (CE), minimum or negligible MCE is observed.

In fact, considering an isolation layer located from the 4<sup>th</sup> to the 2<sup>nd</sup> level, with CE distributions, the minimum significant coupled mass is obtained (7%); otherwise, considering an isolation layer up to the 4<sup>th</sup> level, for the same distributions no MCE arises.

The different mass and stiffness distributions can be also compared with the reference AD distributions commonly adopted in the design practice; it can be observed that: for the mass distribution A, when the US is stiffer than the LS (AE), the minimum significant MCE is observed (5%), instead, when the US is more flexible than the LS (AF), significant MCE is expected; for the stiffness distribution D, when the US is lighter than the LS (BD), significant MCE occurs; when the US is lighter and either stiffer (BE – case of the Iidabashi 1<sup>st</sup> building) or more flexible (BF) than the LS, significant MCE is expected; when the US is heavier and more

flexible than the LS (CF – case of the Shiodome Sumitomo building), significant MCE arises; however, the heavier the US, the smaller the coupled mass participating ratio.

It is worth noticing that, with the sub-models l-DOF LS and ff-u-DOF US+ISO it is possible to define the l-modes of vibrations of the LS and the u-modes of the isolated US. Hence, entering in the complete model ff-MDOF IIS, it is possible to define the order of the modes of vibration and, thus, associate each higher mode to either the LS or the isolated US.

Therefore, it is necessary to operate a simple conversion from the couples ( $a - b$ ), accounting for the sub-models, to the couples of the complete model, namely: ( $a' - b'$ ), i.e.:

the number  $a'$  is equal to the sum of  $a$  and  $b$ , i.e.  $a' = a + b$ , while the next number  $b'$  is equal to  $a'$  plus one, i.e.  $b' = a' + 1$ .

Consequently, the significant couples of numbers  $a - b$  equal to 1-1, 1-2 (or 2-1), 1-3, 1-4, 1-5, 1-6, 1-7, 1-8, 2-2, in the l-DOF LS and ff-u-DOF IIS models correspond to the significant couples of numbers  $a' - b'$  equal to 2-3, 3-4, 4-5, 5-6, 6-7, 7-8, 8-9, 9-10, 4-5, in the 10 DOF IIS models, respectively.

The coupled mode shapes of the fourteen 10DOF IIS models affected by MCE are depicted in Figs. 6.41 ÷ 6.51; in each graph the coupled participating mass ratio, indicated as  $\Gamma$  for the sake of brevity, is also provided.

In particular in Figs. 6.41 ÷ 6.46 are reported the 2<sup>nd</sup>-3<sup>rd</sup>, 3<sup>rd</sup>-4<sup>th</sup>, 5<sup>rd</sup>-6<sup>th</sup> significant coupled modes; each tris of graphs provides all the coupled higher modes for the same mass distribution (either A, B or C) by varying the stiffness distribution (D, E, F).

In Fig. 6.47 a-b and Fig. 6.47 c are reported the 4<sup>th</sup>-5<sup>th</sup> and 5<sup>th</sup>-6<sup>th</sup> significant coupled modes, respectively. In Figs. 6.48 ÷ 6.51 the 4<sup>th</sup>-6<sup>th</sup>, 5<sup>th</sup>-7<sup>th</sup>, 6<sup>th</sup>-8<sup>th</sup>, 8<sup>th</sup>-10<sup>th</sup> tris of coupled higher modes; the first, second and third graph provides the first, second and third coupled mode.

From Figs. 6.41 ÷ 6.51 it can be noticed that the coupled higher modes involve deformations both in the US and LS; however, in the 10DOF IIS 4 and IIS 5 models the displacements of the structural portions are comparable in both the coupled modes while in the other 10DOF ISO models these modes mainly involve deformations either in the LS or in the US.

m-k distr.	model	BIS	IIS 2	IIS 3	IIS 4	IIS 5	IIS 6	IIS 7	IIS 8	IIS 9	RIS
AD			1-3, 1-4 10%	1-2 19%	1-1 27%			2-1 6%			
BD			1-3 14%		1-1 34%			2-1 6%			
CD			1-4, 1-5 7%	1-2 14%		1-1 28%					
AE			1-2 10%				2-1 5%				
BE	 IB		1-2 14%	1-1 24%							
CE			1-3 7%		1-1 21%						
AF			1-5, 1-6 10%			1-1 35%			2-1 7%		
BF			1-4 14%	1-2 24%		1-1 42%	2-2 6%				
CF	 SSB		1-7, 1-8 14%	1-3 14%	1-2 21%				2-1 7%		

Legend: 1 – 1, red; 1 – 2 or 2 – 1 or 2 – 2, blue; 1 – 3, green; 1 – 4, orange; 1 – 5 ÷ 1 – 8, grey

Fig. 6.40. Schematic representation of all the 10DOF ISO models subjected to MCE

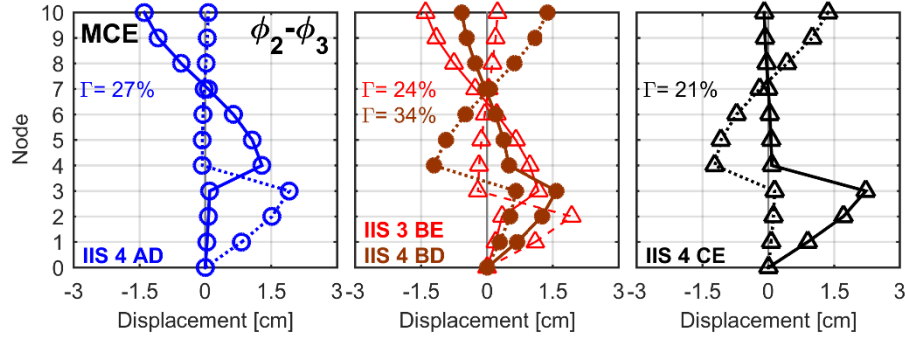


Fig. 6.41. MCE - 2<sup>nd</sup> and 3<sup>rd</sup> coupled natural modes: (a) IIS 4 AD, (b) IIS 3 BE – IIS 4 BD, (c) IIS 4 CE

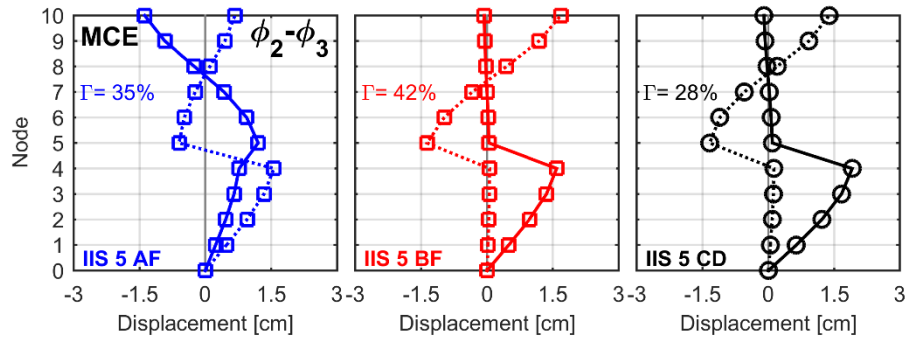


Fig. 6.42. MCE - 2<sup>nd</sup> and 3<sup>rd</sup> coupled natural modes: (a) IIS 5 AF, (b) IIS 5 BF, (c) IIS 5 CD

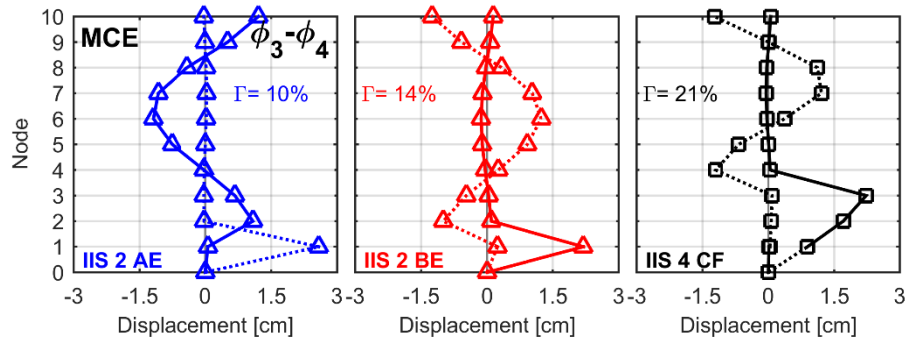


Fig. 6.43. MCE - 3<sup>rd</sup> and 4<sup>th</sup> coupled natural modes: (a) IIS 2 AE, (b) IIS 2 BE, (c) IIS 4 CF



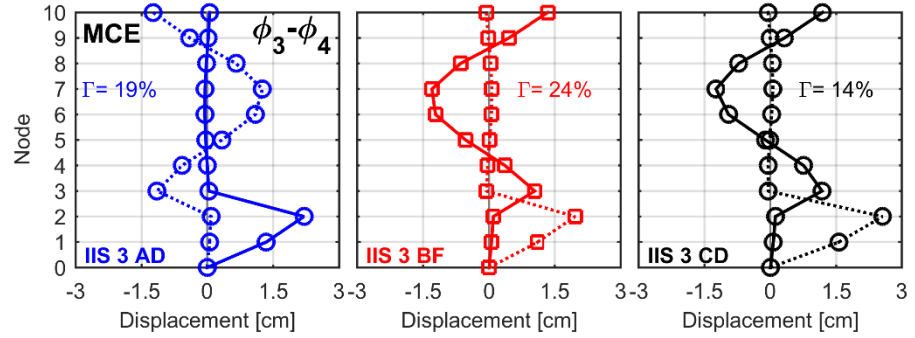


Fig. 6.44. MCE - 3<sup>rd</sup> and 4<sup>th</sup> coupled natural modes: (a) IIS 3 AD, (b) IIS 3 BF, (c) IIS 3 CF

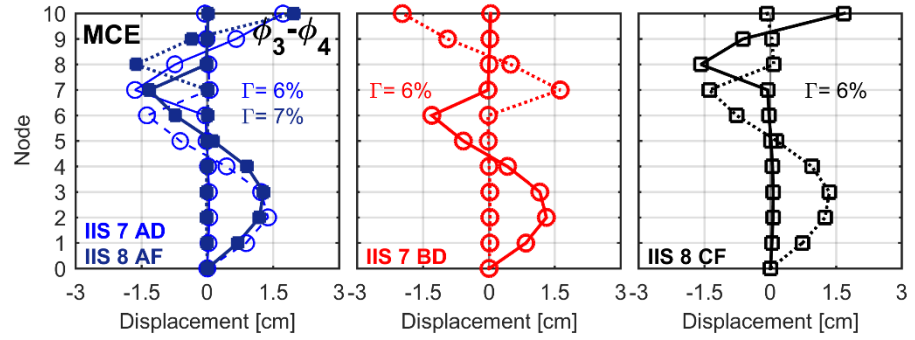


Fig. 6.45. MCE - 3<sup>rd</sup> and 4<sup>th</sup> coupled natural modes: (a) IIS 7 AD – IIS 8 AF, (b) IIS 7 BD, (c) IIS 8 CF

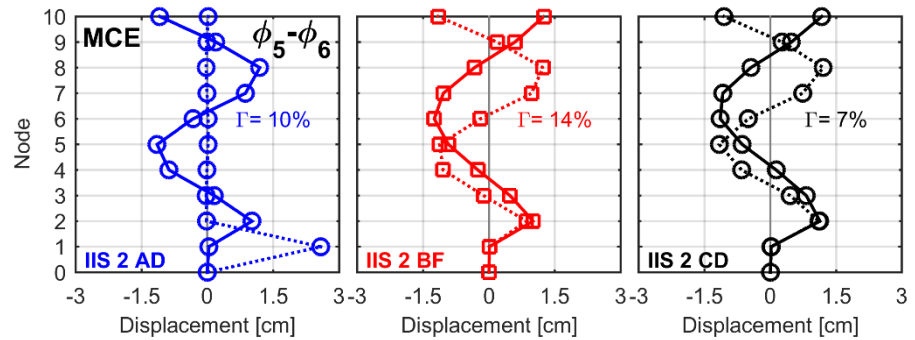


Fig. 6.46. MCE - 5<sup>th</sup> and 6<sup>th</sup> coupled natural modes: (a) IIS 2 AD, (b) IIS 2 BF, (c) IIS 2 CD

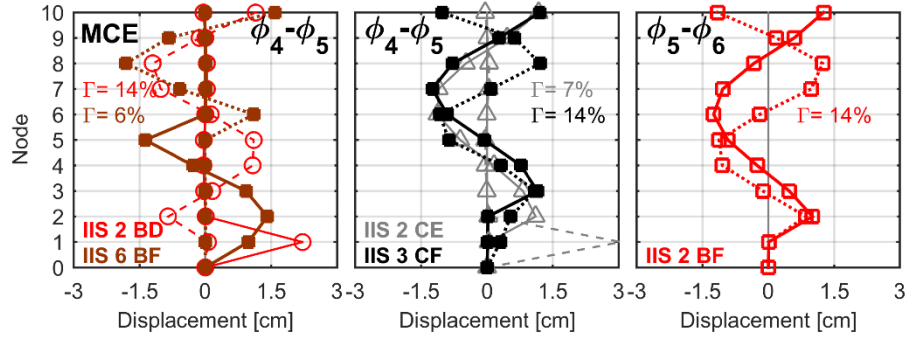


Fig. 6.47. MCE - coupled natural modes: (a) 4<sup>th</sup> and 5<sup>th</sup>: IIS 2 BD – IIS 6 BF, (b) 4<sup>th</sup> and 5<sup>th</sup>: IIS 2 CF – IIS 3 CF, (c) 5<sup>th</sup> and 6<sup>th</sup>: IIS 2 BF

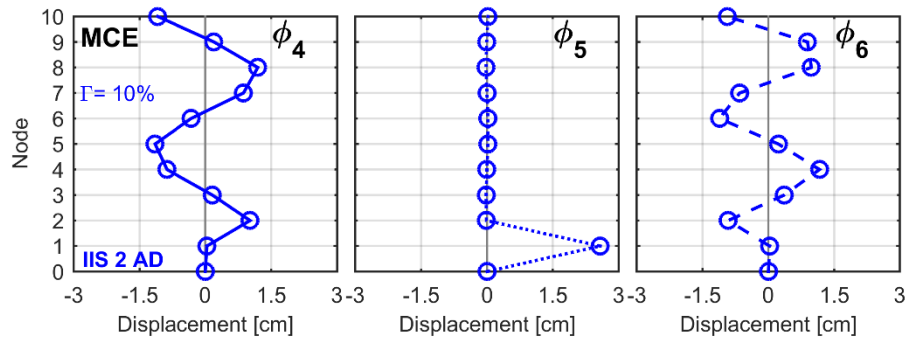


Fig. 6.48. MCE - 4<sup>th</sup> ÷ 6<sup>th</sup> coupled natural modes – IIS 2 AD: (a) 4<sup>th</sup> mode, (b) 5<sup>th</sup> mode, (c) 6<sup>th</sup> mode

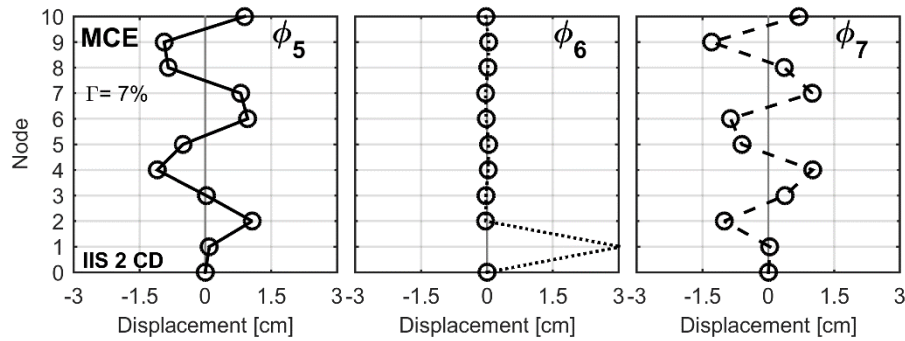


Fig. 6.49. MCE - 5<sup>th</sup> ÷ 7<sup>th</sup> coupled natural modes – IIS 2 CD: (a) 5<sup>th</sup> mode, (b) 6<sup>th</sup> mode, (c) 7<sup>th</sup> mode

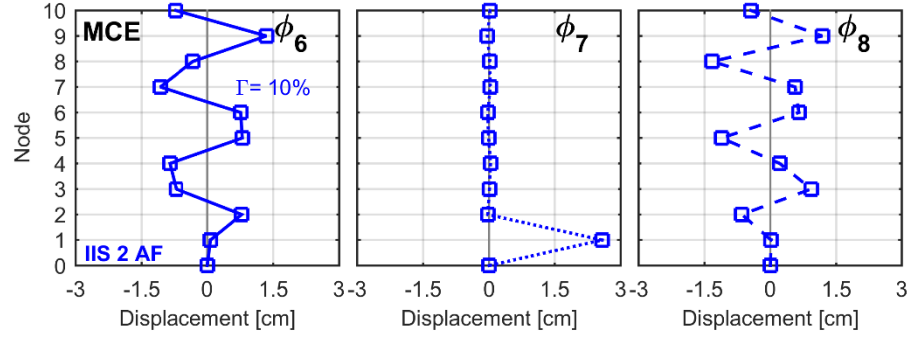


Fig. 6.50. MCE - 6<sup>th</sup> ÷ 8<sup>th</sup> coupled natural modes – IIS 2 AF: (a) 6<sup>th</sup> mode, (b) 7<sup>th</sup> mode, (c) 8<sup>th</sup> mode

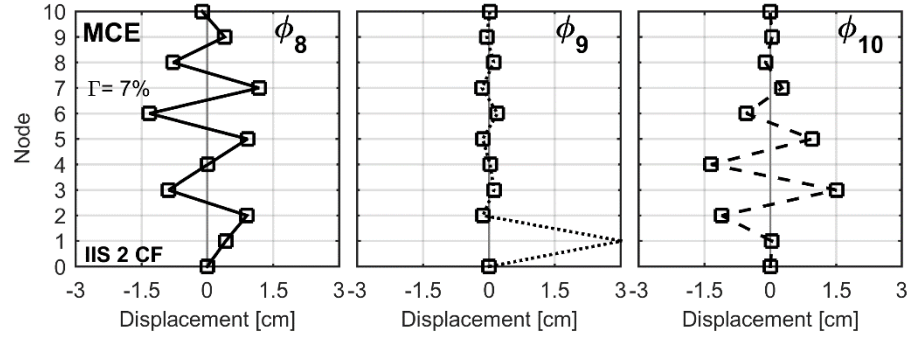
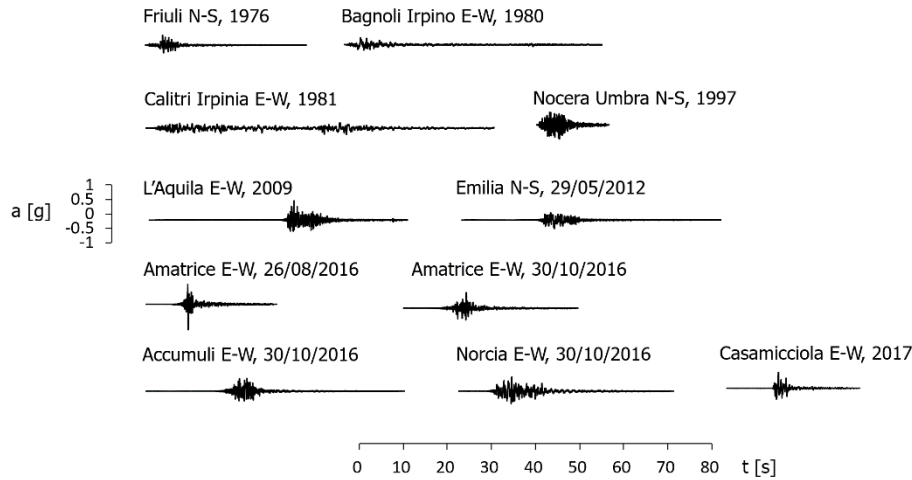


Fig. 6.51. MCE - 8<sup>th</sup> ÷ 10<sup>th</sup> coupled natural modes – IIS 2 CF: (a) 8<sup>th</sup> mode, (b) 9<sup>th</sup> mode, (c) 10<sup>th</sup> mode

#### 6.4. TIME HISTORY ANALYSIS

In order to take into account the different frequency content of earthquakes, a time history analysis is carried out considering 11 Italian natural accelerograms (Fig. 6.52), i.e.: 1976 Friuli Tolmezzo NS, 1980 Irpinia Bagnoli EW, 1980 Irpinia Calitri EW, 1997 Nocera Umbra NS, 2009 L'Aquila EW, 2012 Emilia NS, 2016 Accumuli EW (30/10), 2016 Amatrice EW (26/08), 2016 Amatrice EW (30/10), 2016 Norcia EW (30/10), 2017 Casamicciola EW.

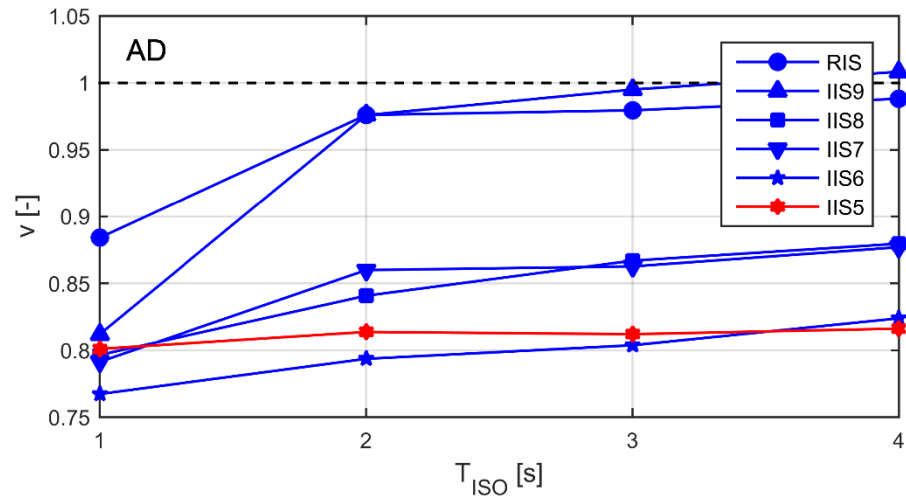
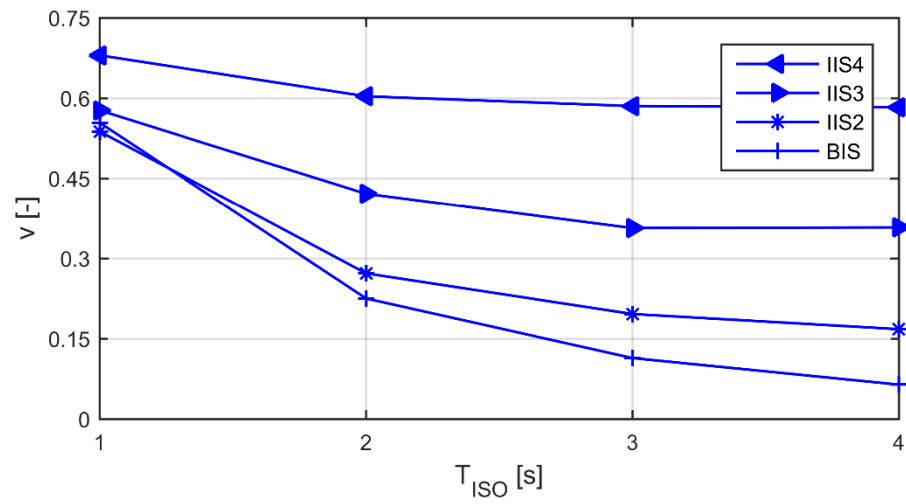


**Fig.6.52. Italian natural accelerogram (from 1976 to 2017)**

The ratio between the base share force of the controlled structure, IIS, to the uncontrolled configuration, FB, i.e.  $v = V_{b,IIS} / V_{b,FB}$ , expresses the effectiveness of the IIS design strategy in a very synthetic way.

For the AD distributions, in Figs. 6.53 – 6.54 is depicted the mean response of the 11 accelerograms in terms of the base shear ratio  $v$  as a function of the isolation period  $T_{ISO}$ ; in Fig. 6.53 are considered the models from RIS to IIS 5 and in Fig. 6.54 from IIS 6 to BIS.

As can be seen from the figures, the isolation period of 2 s represents a transition from the tuning mass zone (Fig. 6.53) to the isolation zone (Fig. 6.54); in addition, IIS 5 (depicted in red in Fig. 6.53) is the transition model from the two zones, since its response is constant for all the isolation periods. For  $T_{ISO}$  less than 2 s, in Fig. 6.53 are obtained the minimum values of  $v$ , with a reduction of the base of about 10% ÷ 25% with respect to the uncontrolled configuration; for  $T_{ISO}$  larger than 2 s, in Fig. 6.54 are obtained the minimum values of  $v$ , with a reduction of about 40% ÷ 90%. It is worth noticing that, while in the tuning zone with  $T_{ISO}$  larger than 2 s the response of the controlled configuration can be comparable or greater than the uncontrolled one, as in IIS 9, in the isolation zone a good reduction of the base shear is obtained independently on the isolation period, thanks to the major robustness of the system.

Fig.6.53.  $v$  vs.  $T_{ISO}$  : from RIS to IIS 5Fig. 6.54.  $v$  vs.  $T_{ISO}$  : from IIS 6 to BIS

## 6.5. CONCLUSIVE REMARKS AND DESIGN IMPLICATIONS

This chapter has explored the dynamic properties of the inter-story isolation system (IIS) structures, with particular attention to the mode coupling effect of the higher modes (MCE).

Eigenvalues and time history analyses are carried out on multi-degree-of-freedom isolated models, representative of a 10-story residential building, have been considered, and the influence of different locations of the isolation system, as well as, of various mass and stiffness distributions and of isolation periods have been investigated. Multi-degree-of-freedom fixed-base models are also considered for comparison.

In the controlled structure the isolation interface has been moved from the top to the bottom story changing level by level, with extreme models related to a roof isolated structure (RIS) and a base isolated structure (BIS). The different mass and stiffness distributions considered in the analysis are representative not only of the commonly distributions adopted for structural application (i.e. uniform mass distribution and linear stiffness distribution) but also of extreme real inter-story isolated structures, which show US lighter or heavier, or even, more flexible or stiffer than the LS counterparts.

The results of the eigenvalue analyses have shown that the coupling of the higher modes arises from the 10DOF IIS 8 to the IIS 2 model and the number of the coupled higher modes increases going from IIS 8 to IIS 2, i.e. from the 8<sup>th</sup> to the 2<sup>nd</sup> location of isolation system. In fact when the isolation layer is placed at the lower levels, the LS possesses few degrees-of-freedom with respect to the isolated US counterparts, and, thus, it is possible to combine the few modes of the LS with a larger number of modes of the isolated US. For the same reason, the coupled participating mass decreases going from the 10DOF IIS 8 to the IIS 2 model, since the mass ratio  $R_m$  increases.

Significant values of the coupled participating mass ratio, between 5% and 42%, is observed when only the first mode of the lower structure is coupled to the first five higher modes of the isolated upper structure.

In general, looking at the mass and stiffness distributions, when the US is heavier and stiffer than the LS, the minimum significant MCE is observed, vice versa, significant MCE is expected; however, the heavier the US, the smaller coupled mass participating ratio.

Considering both the placement of the isolation level and the mass and stiffness distributions, it is observed that, the larger values of coupled participating mass are obtained for comparable degrees of freedom between US and LS, i.e. for IIS 4 and IIS 5 models. Considering a lighter US than LS, a coupled mass of 34% is obtained for IIS 4; with a lighter and more flexible US than LS, the maximum coupled mass is reached for IIS 5, i.e. 42%.

The analyses also show that the mass ratio between the structural parts is more significant than the mass distribution; the stiffness distribution affects the dynamic behavior of the controlled configuration more than the mass distribution, and a stiffer and heavier US than the LS improves the dynamic response of the overall structure.

Even though MCE depends on the dynamic properties of the lower and upper structure, it is independent on ISO characteristics and can be successfully prevented by a careful design.

For this reason, a free-free multi-degree-of-freedom IIS model, in which the stiffness of the isolation layer is assumed null (i.e. perfect isolation), was developed. With the ff-MDOF IIS, the system can be seen as a combination of the base isolated US, with the stiffness of seismic isolation layer equal to zero (ff-u-DOF ISO+US), and the fixed-base LS (l-DOF LS).

In this framework an analytical formulation for avoiding MCE is derived for MDOF systems, and, then, extended to 3DOF IIS models. The analytical formulation can be translated in the simple design rule: no MCE arises if the  $i$ -th frequency of base-isolated US is far from the  $j$ -th frequency of the fixed-base LS. In more simplified terms, it is generally sufficient that the first two-three frequencies of the free-free base-isolated US are far from the first two frequencies of the fixed-base LS.

From the results of the eigenvalues and time history analyses, the zones of mass damping, intermediate isolation and base isolation are clearly identified. In particular, going from the mass damping to the base isolation zone, it can be observed that, the participating mass related to the higher modes is larger than, comparable to, and negligible with respect to the fundamental participating mass, respectively. In addition, in the mass damping zone, the maximum reduction of the base shear is observed for less isolation periods; on the contrary, in the isolation zones, the minimum base shear is obtained for large isolation periods. However, in the isolation

zones, due to the major robustness of the system, , a good reduction of the seismic response is reached for all the isolation periods.



## 7. IIS FOR RETROFIT

### 7.1. INTRODUCTION

By new findings in the area of seismic effects on buildings, an increasing number of existing structures are facing the necessity of seismic retrofit. There is not yet a practical method for a large number of buildings to improve their performances in the case of an earthquake incident.

In some cases, an elevation with inter-story isolation has been proved to serve as a valid retrofit strategy for existing buildings, avoiding massive retrofit interventions in the lower structure and disruption of the hosted activities. In an ideal case, it is possible to apply this technique on top of the structure simply by a vertical addition. This is considered in fact, a lucrative retrofit approach in the places in which land for new buildings is expensive [Tsuneki et al 2008, Sumnicht 2008, Dutta et al. 2009, Ziyaeifar & Noguchi 1998, Chey et al. 2013, Villaverde 2002]. IIS can also be applied in the mid-height of the existing structures by a more complicated process [Ziyaeifar & Noguchi 1998, Ming et al. 2004, Zhou et al. 2004].

The first application of seismic isolation in the world that permits the vertical expansion of an existing structure by introducing isolation bearings between the existing structure and the addition has been the China Basin Berry Street of San Francisco, see Chapter 3. In essence, the isolated addition acts more like a tuned mass damper than an isolated structure. The existing building which serves as the base for the isolated addition is about 251.5 m long and 33.5 wide with two expansion joints at approximately the third of the length. The new addition is a continuous structure that bridges over the expansion joints and utilizes concentric braced frames for its lateral strength. This is truly a unique application of the base isolation technology where the plane of isolation has been moved from the base of the building to the roof of an existing building. [Dutta et al. 2009].

The vertical addition of IIS as a retrofit strategy should be a particularly fascinating subject in Italy, given the high seismicity of almost all national territory and the need to safeguard our non-monumental masonry buildings, which possess large reserve of compression strength.

The idea is that the additional weight of the IIS elevation has a stabilizing effect with regards to the seismic action, and, if the vertical addition is well designed, the seismic base shear is not increased, or even decreased, thanks to the mass damper effect exerted by the isolated addition.

In this perspective, the effectiveness and feasibility of IIS elevation as seismic retrofit strategy for masonry buildings is here proposed. The chapter is articulated into the following steps: a) parametric dynamic analysis on a three-lumped-mass simplified model, in order to detect the optimal characteristics for the upper structure, b) choice of the actual design configuration responding to the optimal combination of isolation and upper structure, and c) seismic assessment of the three-dimensional FEM model of the design configuration including modal, elastic response spectrum and time history analyses.

## **7.2. SIMPLIFIED 3DOF MODEL**

In IIS buildings the isolation layer is introduced at an intermediate level, therefore a lower structure (LS) and an upper structure (US) can be defined. IIS building can be preliminarily analyzed through a simplified three-lumped-mass (3DOF) system [Wang et al. 2011, Moriizumi & Kobayashi 2012], the first mass  $m_{LS}$  representing the lower structure and the other two masses,  $m_{ISO}$  and  $m_{US}$ , respectively representing the upper structure (in particular,  $m_{ISO}$  is located at the floor immediately above the isolation system). Stiffness and damping constant of lower and upper structure and of isolation layer are referred to as  $k_{LS}$  and  $c_{LS}$ ,  $k_{US}$  and  $c_{US}$ ,  $k_{ISO}$  and  $c_{ISO}$  (Fig. 7.1). The stiffness of each DOF is represented by an equivalent linear shear spring. The stiffness of the isolation layer is represented by an equivalent linear elastic spring as well, describing the global behavior of the chosen isolators.

The nominal frequencies of the three portions are defined as follows:

$$\omega_{LS} = \sqrt{\frac{k_{LS}}{m_{LS}}} \quad \omega_{ISO} = \sqrt{\frac{k_{ISO}}{m_{ISO} + m_{US}}} \quad \omega_{US} = \sqrt{\frac{k_{US}}{m_{US}}} \quad (7.1)$$

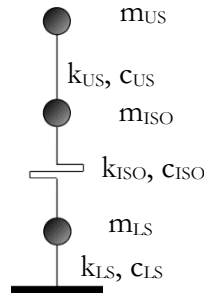


Fig. 7.1. Simplified 3DOF system used for IIS structures

### 7.3. CASE STUDY

The case study considered in this paper is a three-story masonry structure rising in Giulianova, Italy (Fig. 7.2), built probably in the 17<sup>th</sup> century and still in use nowadays to host offices. The plan has a trapezoidal shape, the maximum dimensions measured along the two main directions X and Y being 26.4 m and 19.7 m. The story height is 4.50 m. The masonry structure is in good overall conditions, apparently exhibiting no signs of the past earthquakes (such as detachments or cracks in the walls, or between walls and floors). The structure can be defined regular in elevation and also quite regular in plan. According to the technical documentation of the building, the total seismic mass (i.e. the mass of the lower structure  $m_{LS}$  as defined in the 3DOF simplified model) is equal to 2900 t.

A push over analysis with forces proportional to the equivalent static forces has been carried out to detect the lateral stiffness of the equivalent single degree-of-freedom existing structure.

The value of the equivalent lateral stiffness of the building (i.e. the stiffness of the lower structure  $k_{LS}$  as defined in the 3DOF simplified model), taken from the results of previous analyses [Gherzi et al. 2011], is equal to 175 MN/m.

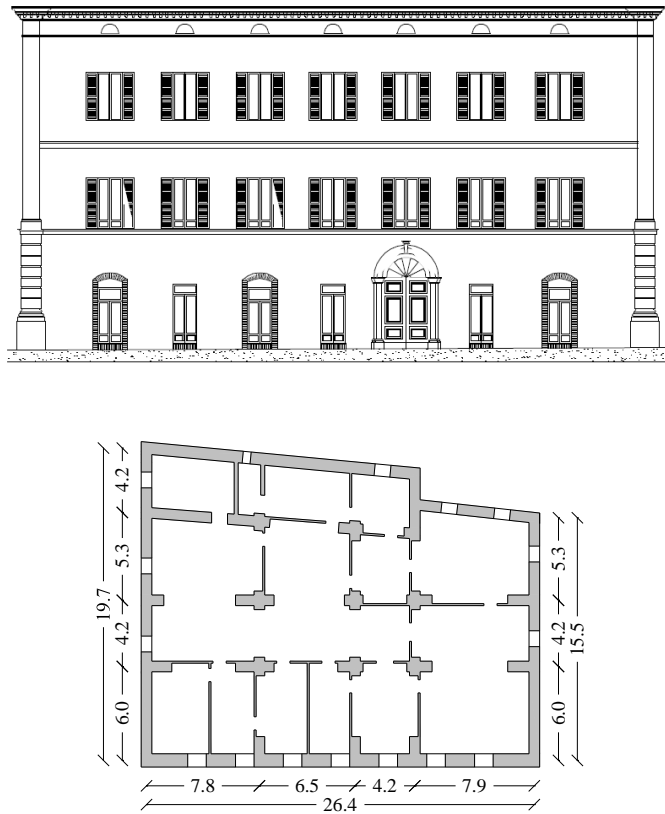


**Fig. 7.2. Case study building: (a) front view, (b) first floor plan**

In order to estimate the feasibility of a vertical addition for the case study building, a preliminary assessment of the stress state in the walls at the ground level has been carried out.

As a result, an average compressive stress due to gravity loads always less than 40% of the ultimate compression resistance has been observed for all masonry walls. Therefore, it can be concluded that the lower structure is capable of bearing the extra loads deriving from an upper addition, although not excessively heavy.

## 7.4. SIMPLIFIED PARAMETRIC ANALYSIS

In order to individuate the optimal configuration of the upper structure leading to the best overall behavior of the whole IIS building, a parametric dynamic analysis has been carried out using the 3DOF simplified model described above. In particular, the known dynamic properties of the lower structure are:  $m_{LS} = 2900$  t,  $k_{LS} = 175$  MN/m,  $T_{LS} = 0.809$  s.

The properties of the upper structure and of the isolation system will be chosen according to the results of the parametric study, for which three parameters have been adopted, namely: a) a mass ratio  $\alpha$ , defined as the total isolated mass,  $M_{ISO} = m_{ISO} + m_{US}$ , normalized to the mass of the lower structure  $m_{LS}$ ; b) a stiffness ratio  $K$ , defined as the stiffness of the upper structure  $k_{US}$  normalized to the stiffness of the lower structure  $k_{LS}$ ; c) a period ratio  $I$ , defined as the nominal period of the isolation system  $T_{ISO}$  normalized to the nominal period of the fixed-base upper structure  $T_{US}$ . The values chosen for the parameters are:

$$\alpha = \frac{M_{ISO}}{m_{LS}} = \{0.1 \div 1\} \quad (\text{from a very light to a very heavy upper structure})$$

$$K = \frac{k_{US}}{k_{LS}} = \{0.1, 0.3, 0.5, 1.0\} \quad (\text{from a very flexible to a very stiff upper structure})$$

$$I = \frac{T_{ISO}}{T_{US}} = \{3, 4, 5, 10\} \quad (\text{from a less to a more effective isolation system})$$

It must be reminded that the parameter  $I$  is actually defined for BIS buildings, an often appointed as isolation ratio. A minimum value of 3 has been chosen because it is the minimum one as recommended by many building codes (including Italian NTC2008) for base isolated structures.

### 7.4.1. Design parameters

The parameters  $\alpha$  and  $K$  respectively provide information on the amount of isolated mass and on the flexibility of the US with respect to the LS. In order to distribute the isolated mass between the US and the isolation layer and to compare the US and the LS flexibility with respect to the isolation

layer, the linear theory formulated by Kelly [Kelly 1997, Naeim & Kelly 1999] for BIS can be assumed as reference for IIS.

#### **7.4.1.1. *Distribution of the isolated mass between the US and ISO system***

The parameter  $\alpha$ , indicative of the amount of the isolated mass, does not provide information on how it is subdivided between the superstructure and the isolation system.

In Tab. 7.1, considering the  $i$ -th floor, are reported the values of the upper structural floor mass ( $m_{US,i}$ ), the mean of the floor mass,  $\bar{m}_i$ , the isolation mass,  $m_{ISO}$ , the total floor isolated mass,  $M_{ISO,i} = m_{ISO} + m_{US,i}$ , and, also, the mass ratios  $m_{US,i} / M_{ISO,i}$ ,  $m_{ISO} / \bar{m}_i$ ,  $M_{ISO,i} / m_{ISO}$  for some Japanese isolated buildings, both at the base and at an intermediate level.

In particular, the intermediate isolated buildings are the Iidabashi 1<sup>st</sup> Building [Murakami et al. 2000, Tsuneki et al. 2008-2009], and the Shiodome Sumitomo Building [Sueoka et al. 2004, Tsuneki et al. 2008-2009]; the base isolated buildings are the Main Building of the Shimizu Corporation [Nakamura et al. 2009-2011, Okada et al. 2009], the TC Building [Miyazaki et al. 1988] and the Tokyo Prada Aoyama [Nakai 2008, Nakai et al. 2009].

From Tab. 7.1 can be observed that the ratio  $m_{US,i} / M_{ISO,i}$  varies between 0.72 and 0.92 (going from 5 to 14 floors) while the ratio  $m_{ISO} / \bar{m}_i$  varies between 1.20 and 1.85 (neglecting the value provided by Tokyo Prada Aoyama building which possesses an atypical isolation floor).

In the linear theory formulated by [Naeim & Kelly 1999] for BIS, Kelly proposes a value of the mass ratios  $m_{US,i} / M_{ISO}$  in between 0.6 and 0.8, and of the mass ratio  $m_{ISO} / \bar{m}_i$  in between 1.5 and 2.0.

In line with the mean values derived by some isolated buildings (Tab. 7.1) and by the literature, assuming the mass  $m_{US,i}$  equal to two third of the corresponding mass at the  $i$ -th level in the fixed-base structure, i.e.:

$$m_{ISO} = \frac{2}{3} m_{US,i} \quad (7.2)$$

the isolated mass at the  $i$ -th level is given by:

$$M_{ISO,i} = m_{ISO} + m_{US,i} = 1.667 m_{US,i} \quad (7.3)$$

From formula (7.3) can be noticed that the presence of the isolation system increases the mass of the corresponding non-isolated floor about of the 70%.

**Tab. 7.1. Isolated mass for some real japanese isolated building**

Building	n. floors	$m_{US,i}$	$\bar{m}_i$	$m_{ISO}$	$M_{ISO,i}$	$\frac{m_{US,i}}{M_{ISO,i}}$	$\frac{m_{ISO}}{\bar{m}_i}$	$\frac{M_{ISO,i}}{m_{ISO,i}}$
	US	[t]	[t]	[t]	[t]	[t]	[t]	[t]
IB	5	10899	2180	4022	14921	0.73	1.85	3.71
SSB	14	47528	3395	4030	51558	0.92	1.19	12.79
MSC	5	5035	1007	1426	6460	0.78	1.42	4.53
TC	5	5766	1153	1778	7544	0.76	1.54	4.24
TPA	7	24456	3494	9384	33840	0.72	2.69	3.61

IB = Iidabashi Building; SSB = Shidome Sumitomo Building; MSC = Main building Shimizu Corporation; TC = TC building; TPA Tokyo Prada Aoyama

In addition, the following mass ratios can be defined: the ratio of the total mass of the upper structure to the total isolated mass,  $\gamma(n)$ ; the ratio of the upper floor mass to the mass of the isolation system,  $r_{US,i}$ ; the ratio of the total upper mass to the mass of the isolation system,  $r_{US}(n)$ .

Thus, the mass ratios  $\gamma(n)$ ,  $r_{US,i}$  and  $r_{US}(n)$  are given by:

$$\gamma(n) = \frac{m_{US}(n, \alpha, str.)}{M_{ISO}(\alpha)} = \frac{3n}{3n+2} \quad (7.4)$$

$$r_{US,i} = \frac{m_{US,i}}{m_{ISO}} \quad (7.5)$$

$$r_{US}(n) = \frac{m_{US}(n, \alpha, str.)}{m_{ISO}} \quad (7.6)$$

where the subscripts  $n$  and  $str$  indicate the total number of the US floors and the type of structure considered, respectively.

Considering a number of floor between 1 and 3, the values of the mass ratios  $\gamma(n)$ ,  $r_{US,i}$  and  $r_{US}(n)$  are given in Tab. 7.2.

The number of floors is equal to the ratio of the total US mass,  $m_{US}(n, \alpha, str.)$ , and the mass of a single floor,  $m_{US}(str)$ , which depends on the type of structure (RC: reinforced concrete structure, S: Steel structure, M: masonry structure), i.e.:

**Tab. 7.2. Mass ratios**

n. floors	$\gamma(n)$	$r_{US,i}$	$r_{US}(n)$
[-]	[-]	[-]	[-]
1	0.600	1.5	1.5
2	0.750	1.5	3.0
3	0.818	1.5	4.5

$$n^*(n, \alpha, \text{str}) = \frac{\gamma(n)M_{\text{ISO}}(\alpha)}{m_{\text{US, str}}} \quad (7.7)$$

Rounding up  $n^*(n, \alpha, \text{str})$ , in Tab. 7.3 is provided the number of floor depending on the structural type (RC, S, M) by varying the mass ratio  $\alpha$ .

**Tab. 7.3. number of US floor in base of the structural type and the mass ratio  $\alpha$** 

$\alpha$	n. floors	Structural type	$\gamma(n)$	$r_{US}$
[-]	[-]		[-]	[-]
0.1	1	S	0.600	1.5
0.2	1	RC	0.600	1.5
0.3	2	S	0.750	3.0
0.4	2	RC	0.750	3.0
0.5	3	S	0.818	4.5
0.6	3	RC	0.818	4.5
0.7	2	M	0.750	3.0
0.8	2	M	0.750	3.0
0.9	2	M	0.750	3.0
1.0	3	M	0.818	4.5

#### 7.4.1.2. Flexibility of the structural portions

According to Kelly's linear theory for the 2DOF representing the B.I. structure, a base isolated structure is mainly affected by the first mode, with a mode shape  $\phi^T = \{1, \varepsilon\}^T$ , where the parameter  $\varepsilon$  represents the amplification of the displacement in the US with respect to the isolation layer.

The parameter  $\varepsilon$  can be estimated as the square of the ratio between the frequencies of the base isolated system,  $\omega_b$ , and of the fixed base structure,  $\omega_s$ , or, equivalently, between the period  $T_s$  and  $T_b$ , i.e.:

$$\varepsilon = (\omega_b / \omega_s)^2 = (T_s / T_b)^2.$$



In the case of IIS, we can define not only the amplification of the displacement in the US with respect to the isolation layer, but also the amplification of the displacement in the LS with respect to the isolation system.

Therefore, substituting  $T_s$  and  $T_b$  with  $T_{US}$  and  $T_{ISO}$ , respectively, the parameter  $\varepsilon$  can be estimated as a function of the isolation ratio  $I$ :

$$\varepsilon_{US} = \left( \frac{T_{US}}{T_{ISO}} \right)^2 = \left( \frac{1}{I} \right)^2 \quad (7.8)$$

Analogously for the LS, the parameter  $\varepsilon$  can be expressed as

$$\varepsilon_{LS} = \left( \frac{T_{LS}}{T_{ISO}} \right)^2 = \left( \frac{T_{LS}}{I \cdot T_{US}} \right)^2 \quad (7.9)$$

It is also possible to estimate  $\varepsilon$  as a function of the modal characteristics of the first mode. Thus, two parameters, which express the flexibility of US and LS with respect to the ISO system, can be defined, i.e. the ratios of drifts of the upper and lower structure to the isolation drift  $\varepsilon_{US,IIS1}$  and  $\varepsilon_{LS,IIS1}$ :

$$\varepsilon_{US,IIS1} = \frac{\delta_{US,1}}{\delta_{ISO,1}} = \frac{\varepsilon_{US}}{1 - (1 - \gamma)\varepsilon_{US}} \cong \varepsilon_{US} \quad (7.10)$$

$$\varepsilon_{LS,IIS1} = \frac{\delta_{LS,1}}{\delta_{ISO,1}} = \frac{1}{-\frac{1}{\alpha} + \frac{\gamma}{K\varepsilon_{US}}} \neq \varepsilon_{LS} \quad (7.11)$$

It is worth to noticing that, while the drift ratios  $\varepsilon_{US,IIS1}$  and  $\varepsilon_{US}$  are almost equal, confirming that the US+ISO portion behaves as an isolated upper structure, according to Kelly's linear theory for 2DOF B.I. structure; the drift ratios  $\varepsilon_{LS,IIS1}$  and  $\varepsilon_{LS}$  are not equal since the isolated upper structure behaves as a mass damper for the lower structure.

In the parametric analysis the ratios  $\varepsilon_{US,IIS1}$  and  $\varepsilon_{LS,IIS1}$  vary in the range of order  $O(10^{-3} \div 10^{-1})$ , going from to a very stiff to a very flexible structural portion (superstructure and substructure) with respect to the isolation system. Broadly speaking, considering the fundamental mode, if both

$\epsilon_{US,IIS1}$  and  $\epsilon_{LS,IIS1}$  result equal or less than the order of magnitude  $10^{-2}$ , the isolation can be defined “perfect” involving displacements only in the isolation interface.

For all the possible combination of the parameters  $\alpha$ ,  $K$  and  $I$ , it is possible to calculate the nominal period of the superstructure and of the isolation layer. For the sake of brevity, in Tab. 7.4 are provided the period values of  $T_{US}$  and  $T_{ISO}$  for the following coupling of the parameters  $\alpha - K - I$ :  $\alpha = \{0.1, 0.6, 1.0\} - K = \{0.1, 0.3, 0.5, 1.0\} - I = \{3, 4, 5\}$ .

**Tab. 7.4. Nominal periods  $T_{US}$  and  $T_{ISO}$**

$\alpha$	$I$	$K = 0.1$		$K = 0.3$		$K = 0.5$		$K = 1.0$	
$[-]$	$[-]$	$T_{US}$ [s]	$T_{ISO}$ [s]	$T_{US}$ [s]	$T_{ISO}$ [s]	$T_{US}$ [s]	$T_{ISO}$ [s]	$T_{US}$ [s]	$T_{ISO}$ [s]
0.1	3		1.880		1.085		0.841		0.594
	4	0.627	2.506	0.362	1.447	0.280	1.121	0.198	0.792
	5		3.133		1.809		1.401		0.991
0.6	3		5.147		2.972		2.302		1.628
	4	1.716	6.863	0.991	3.962	0.767	3.069	0.543	2.170
	5		8.579		4.953		3.837		2.713
1	3		6.941		4.007		3.104		2.195
	4	2.314	9.254	1.336	5.343	1.035	4.139	0.732	2.926
	5		11.568		6.679		5.173		3.658

#### 7.4.2. Modeling of damping

In order to completely define the 3DOF model for IIS, the damping ratios of the US, LS and ISO must be defined (from which the damping constants  $c_{LS}$ ,  $c_{ISO}$  and  $c_{US}$  can be obtained). Typical values are:  $\xi_{LS} = 0.05$ ,  $\xi_{ISO} = 0.10$  and  $\xi_{US} = 0.05$ .

It is worth noticing that, assuming different values of the damping ratios for the three DOFs, the IIS model is characterized by non-proportional damping.

A *non-classical* or *non-proportional viscous damped system* is characterized by complex-valued natural modes, and does not satisfy the Caughey and O’Kelly identity:  $\mathbf{CM}^{-1}\mathbf{K} = \mathbf{KM}^{-1}\mathbf{C}$  (with  $\mathbf{M}$ ,  $\mathbf{K}$  and  $\mathbf{C}$  the mass, stiffness and damping matrices) [Veletsos & Ventura 1986].

Therefore, the common design assumption of proportional damping, which leads to real-valued natural modes of vibration identical to the ones of the associated undamped system, and allows for neglecting the off-

diagonal terms of the damping matrix  $\mathbf{C}$  (i.e. the Caughey and O' Kelly identity is satisfied) could not be adequate to grasp the actual dynamic behavior of the system.

However, for the sake of simplicity, the modal dynamic linear analyses of the simplified 3DOF IIS model are firstly carried out assuming proportional damping; then, this assumption is removed for the response spectrum and time history analyses carried out on the complete MDOF 3D model of the structure with IIS (3D IIS), see § 7.6.

### 7.4.3. Modal Analysis

Modal analyses are carried out on three different simplified lumped mass models: the 3DOF IIS structure, the fixed-base single-degree-of-freedom lower structure (SDOF LS), and the two-degree-of-freedom base isolated upper structure (2DOF ISO+US).

For the sake of brevity, only some results of the wide parametric analysis are here discussed, i.e. the ones obtained for: case A:  $\alpha = 1.0$ ,  $K = 0.1$ ,  $I = 5$ ; case B:  $\alpha = 0.1$ ,  $K = 0.5$ ,  $I = 3$ ; case C:  $\alpha = 0.6$ ,  $K = 0.1$ ,  $I = 3$ ; case D:  $\alpha = 0.1$ ,  $K = 1.0$ ,  $I = 3$ .

The case A ( $\alpha = 1.0$ ,  $K = 0.1$ ,  $I = 5$ ) is representative of an ideal IIS with a rigid superstructure, frequencies of the two structural parts well separated from each other and from the isolation frequency; the case B ( $\alpha = 0.1$ ,  $K = 0.5$ ,  $I = 3$ ) is representative of a IIS with a rigid superstructure, frequencies of the two structural parts well separated from each other and a frequency of the LS not so far from the isolation frequency; the cases C ( $\alpha = 0.6$ ,  $K = 0.1$ ,  $I = 3$ ) is representative of a IIS with both structural portions quite flexible with frequencies not well separated from each other; the case D ( $\alpha = 0.1$ ,  $K = 1.0$ ,  $I = 3$ ) is representative of a IIS with frequencies of the two structural parts well separated from each other and a frequency of the LS greater than the isolation frequency.

In the following both the natural and complex modes of vibration are considered. In particular, damping ratios equal to 0.05 and 0.10 are assumed for the structural portions and for the isolation system.

#### 7.4.3.1. *Natural modes of vibration*

The natural vibration modes obtained for the three models of the cases A ÷ D are depicted in Figs 7.3 ÷ 7.6, respectively; the  $i$ -th displacement of the  $j$ -th mode, i.e.  $\phi_i^j$ , is normalized with respect to the maximum

displacement of the  $j$ -th mode  $\phi_{\max}^j$ . The values of periods and mass participating ratios of the four simplified models are also provided in Figs 7.3 ÷ 7.6.

The first modal shape for both the cases A and C represents the first mode of the 2DOF ISO+US corresponding to the isolation, with minor deformation in the LS. Also in terms of period and mass ratio, it can be observed that the first period  $T_{1,3\text{DOF IIS}}$  is nearly coincident with the first period  $T_{1,2\text{DOF ISO+US}}$ , and the participating mass ratio,  $L_{1,3\text{DOF IIS}}$ , is very close to the ratio  $R_m = M_{\text{ISO}} / M_{\text{tot}}$ . Some differences between the two cases A and C arise looking at the higher modes. The second and the third modes of the A 3DOF IIS model are respectively corresponding to the second mode of the 2DOF ISO+US, with almost no deformation in the LS, and of the mode of the SDOF LS, with almost no deformation in the US. These correspondences of mode shapes also reflect in terms of very close values of periods and mass ratios (almost equal to zero and  $1 - L_{1,3\text{DOF IIS}}$  for the second and the third modes, respectively). On the contrary, the second and the third modes of the C 3DOF IIS model involve displacements both in the US and LS, thus suggesting higher mode coupling, which can produce an undesirable amplification effect in the seismic response of the superstructure. In addition, the higher periods of the C 3DOF IIS model are quite similar, and both the second and the third mass ratios are different from zero.

Conversely, the case B 3DOF IIS is similar to the case A 3DOF IIS; the differences between the models are the following: in B the first mode involves displacement both in the LS and in the isolation layer, suggesting a “non-perfect” isolation; the period  $T_{1,3\text{DOF IIS}}$  is slightly higher than the period  $T_{1,2\text{DOF ISO+US}}$ , and the mass ratio is greater than the ratio  $R_m = M_{\text{ISO}} / M_{\text{tot}}$ ; the second and the third modes respectively correspond to the second mode of the 2DOF ISO+US and the mode of the SDOF LS.

The Case D is an atypical IIS behaving as a FB structure, since the isolation period is less than the period of the lower structure, the order of the modes is inverted. It means that, the first mode is the mode of the existing structure while the higher modes are the modes of the isolated upper structure. However, observing the mode shapes of the isolated model it is shown that the first mode involves large displacement in the lower structure and almost the total mass of the existing structure is engaged; the second mode involves displacement in the isolation system

with almost no deformation in the LS and a quite significant mass ratio participates; the third mode shows displacement both in the isolation layer and in the lower structure.

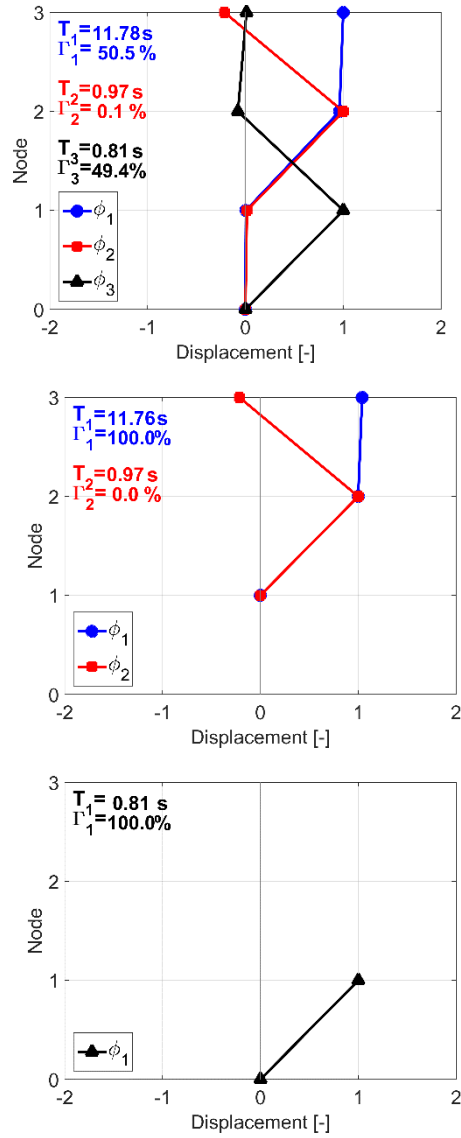


Fig. 7.3. Mode shapes for the case A: (a) 3DOF IIS, (b) 2DOF ISO+US, (c) SDOF LS

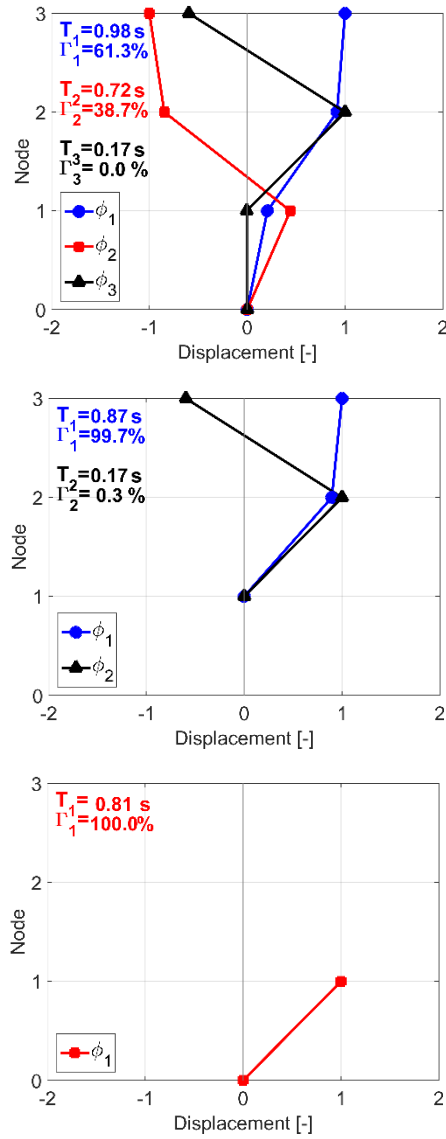


Fig. 7.4. Mode shapes for the case B: (a) 3DOF IIS, (b) 2DOF ISO+US, (c) SDOF LS

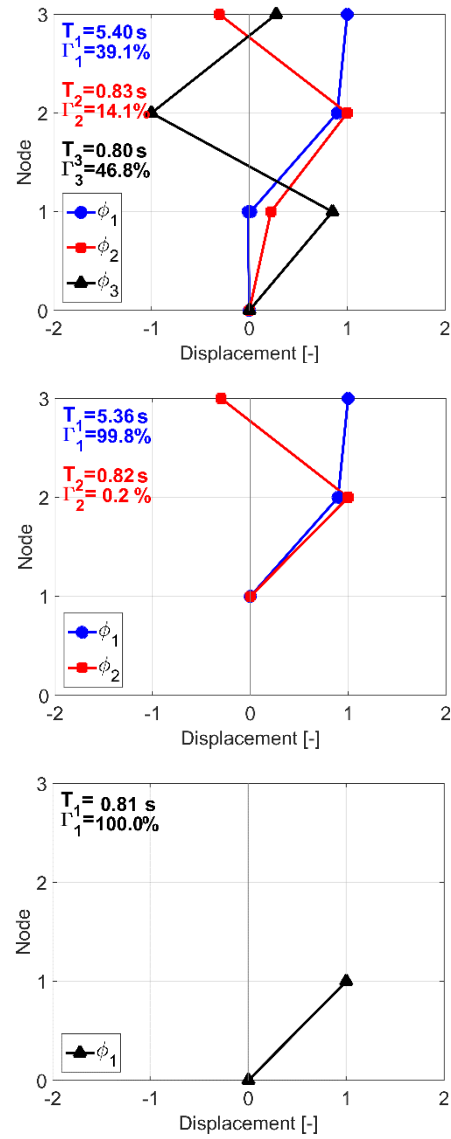


Fig. 7.5. Mode shapes for the case C: (a) 3DOF IIS, (b) 2DOF ISO+US, (c) SDOF LS

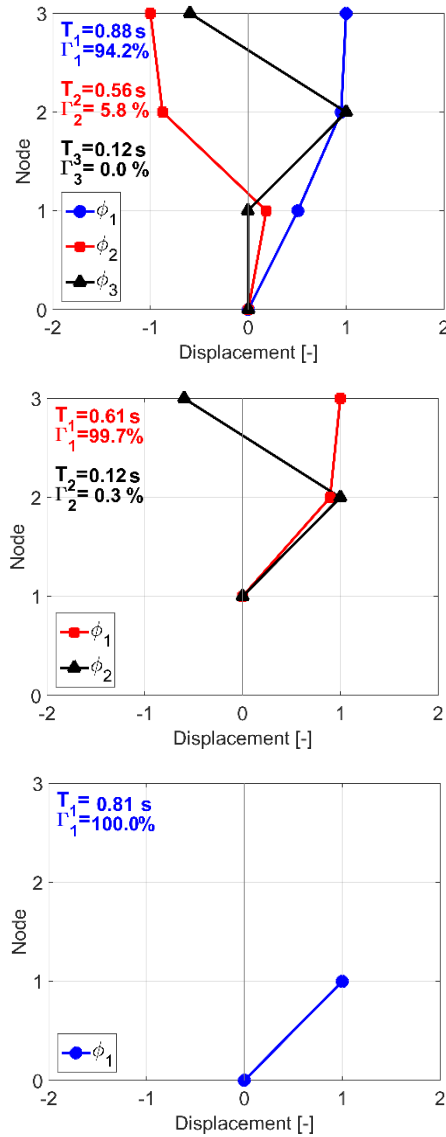


Fig. 7.6. Mode shapes for the case D: (a) 3DOF IIS, (b) 2DOF ISO+US, (c) SDOF LS

#### 7.4.3.1.1. Modal Coupling Effect (MCE)

The mode coupling effect (MCE) in IIS has been addressed in literature [Wang et al. 2012a, Kobayashi & Koh 2008] (see Chapter 6); the author, recognizing that the global dynamic behavior of the mid-story isolated



structure depends on the vibration characteristics of the US and LS, have derived a simple design rule: no MCE arises if the second frequency of base-isolated US is far from the frequency of the fixed-base LS. This statement derives from the analytical study carried out by the author on a free-free 3DOF IIS model (ff-3DOF IIS), obtained by setting the stiffness of seismic isolation layer equal to zero (i.e. ideal isolation) [Skinner et al. 1993, Kobayashi & Koh 2008]. With the ff-3DOF IIS, the system can be seen as a combination of the base isolated US, with the stiffness of seismic isolation layer equal to zero (ff-2DOF ISO+US), and the fixed-base LS (SDOF LS).

In this framework, the MCE can be expressed by a parameter  $\beta$ , being  $\beta = \omega_{\text{ff-2DOF ISO+US},2} / \omega_{\text{LS}}$ , i.e. the ratio between the second frequency of the ff-2DOF ISO+US model,  $\omega_{\text{ff-2DOF ISO+US},2}$ , and the frequency of the SDOF LS model,  $\omega_{\text{LS}}$ . The parameter  $\beta$  can be rewritten in terms of the nominal frequencies of the US and LS as follows:

$$\beta = \frac{\omega_{\text{US}} \sqrt{1 + r_{\text{US}}}}{\omega_{\text{LS}}} \quad (7.12)$$

and can be easily calculated, showing that when it is equal or very close to one, the MCE occurs.

As can be notice in Eq. (7.12), the MCE does not depend on the isolation period  $T_{\text{ISO}}$ , and consequentially on the isolation ratio  $I$ . Considering each combination of the parameters  $\alpha$  and  $K$ , for every values of  $I$ , only the cases  $\alpha = 0.6$ ,  $K = 0.1$  are affected by MCE, with  $\beta$  equal to 0.94.

However, with the free-free model the isolation is assumed perfect leading to an infinite nominal isolation period. Indeed, in the 3DOF IIS models the isolation period possesses a finite value and, thus it can influence the effect of the higher modes. As can be noticed from Tab. 7.5, even if  $\beta$  is independent from  $T_{\text{ISO}}$ , increasing the isolation period (or the parameter  $I$ ), the participation of one of the two coupled modes is reduced until it becomes negligible.

The effect of the higher modes and the potential of modal coupling effect are shown in Fig. 7.5 for all the pragmatic cases herein considered (A:  $\alpha = 1.0$ ,  $K = 0.1$ ,  $I = 5$ ; B:  $\alpha = 0.1$ ,  $K = 0.5$ ,  $I = 3$ , C:  $\alpha = 0.6$ ,  $K = 0.1$ ,  $I = 3$ , D:  $\alpha = 0.1$ ,  $K = 1.0$ ,  $I = 3$ ) as a function of the higher frequencies  $\omega_{\text{LS}}$  and  $\omega_{\text{ff-2DOF ISO+US},2}$  of the complete ff-3DOF IIS model.

In particular the graph is divided into three parts, which represent the two regions where either the 2<sup>nd</sup> or the 3<sup>rd</sup> mode prevails, and the bandwidth, marked by dashed lines, where coupling of the 2<sup>nd</sup> and the 3<sup>rd</sup> modes occurs.

**Table 7.5. Cases affect by MCE:  $\alpha=0.6 - K = 0.1$  for  $I = 3; 4; 5$**

$\alpha = 0.6$	node	$K = 0.1$	
		T [s]	$\Gamma$ [-]
I = 3	1	5.400	0.391
	2	0.831	0.141
	3	0.796	0.468
I = 4	1	7.053	0.385
	2	0.840	0.037
	3	0.804	0.578
I = 5	1	8.731	0.381
	2	0.846	0.013
	3	0.806	0.606

From the Fig. 7.7 it can be observed that equal values of both frequencies  $\omega_{LS}$  and  ${}_{ff}\omega_{US+ISO,2}$  cause a mode coupling effect, as in case C. However, according to the graph, in order to exclude a coupling effect is sufficient to have quite different values for the two frequencies  $\omega_{LS}$  and  ${}_{ff}\omega_{US+ISO,2}$ . In particular for frequencies which are at least one the half part of the other, as in case B, the MCE is always avoided.

As can be seen in Figs 7.3 ÷ 7.4 the prevailing higher mode in case A is the 3<sup>rd</sup> mode while in case B is the 2<sup>nd</sup> mode. Thus, is reasonable to assume that when  $\omega_{LS}$  is almost two times larger than  ${}_{ff}\omega_{US+ISO,2}$ , the effect of the 3<sup>rd</sup> mode is predominant, the third modal frequency is approximately equal to the frequency of the substructure, i.e.  ${}_{ff}\omega_3 \approx \omega_{LS}$ , and the participating mass ratio of the 2<sup>nd</sup> mode,  ${}_{ff}\Gamma_2$ , is equal to zero (as in case A). On the contrary, when  $\omega_{LS}$  is almost the half of  ${}_{ff}\omega_{US+ISO,2}$ , the effect of the 2<sup>rd</sup> mode is predominant, the second modal frequency is approximately equal to the frequency of the substructure, i.e.  ${}_{ff}\omega_2 \approx \omega_{LS}$ , and the participating mass ratio of the 3<sup>rd</sup> mode,  $\Gamma_3$ , is equal to zero (as in Case B). When there is a coupling effect, both frequencies  ${}_{ff}\omega_2$  and  ${}_{ff}\omega_3$  are almost equal and both participating mass ratios  ${}_{ff}\Gamma_2$  and  ${}_{ff}\Gamma_3$  are different from zero (as in case C depicted in Fig. 7.5).

It is worth to noticing that the case D, depicted in the graph for completeness, is out of meaning since the higher modes are the first and the second mode of the isolated upper structure and thus, the interaction between the structural portions is lost.

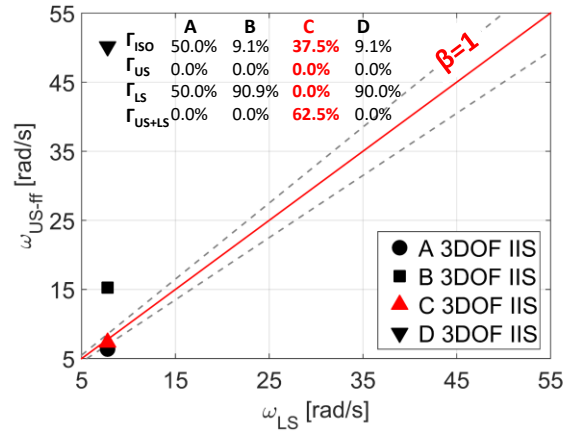


Fig. 7.7. Effect of the higher modes

#### 7.4.3.2. Complex modes of vibration

In the case of normal (real) modes, the displacement at the various DOFs reach their maximum at the same time and pass through the equilibrium position at the same time. This is not the case of complex modes, where both the maximum values and the null values of modal displacements are attained at different time instants for the various DOFs ([Rainieri & Fabbrocino 2014]). As a result, while the phase angles are all  $0^\circ$  or  $180^\circ$  for normal modes (or in general are aligned), both amplitude and phase characterize the motion of the different DOFs in the case of complex modes.

In order to define quickly the modal complexity and thus, to determine whether proportional damping could be used to satisfactorily simulate the more practical non-proportional damping, the complexity plots of the amplitudes and angles of the complex modal vectors for the cases A ÷ D are provided in Fig. 7.8.

In Fig. 7.8 each graph shows the three complex eigenvectors which are normalized with respect to the maximum amplitudes of those modes to obtain dimensionless real and imaginary components in between  $0 \div 1$ ; the periods and damping ratios of the complex modes are also provided in each chart. As can be seen in Fig. 7.8, in each graph the complex

eigenvectors are not aligned, suggesting a non-proportional damping. In particular, the case C, which is affected by MCE, provides the maximum misalignment. Looking at the complex damping ratios the following considerations can be drawn.

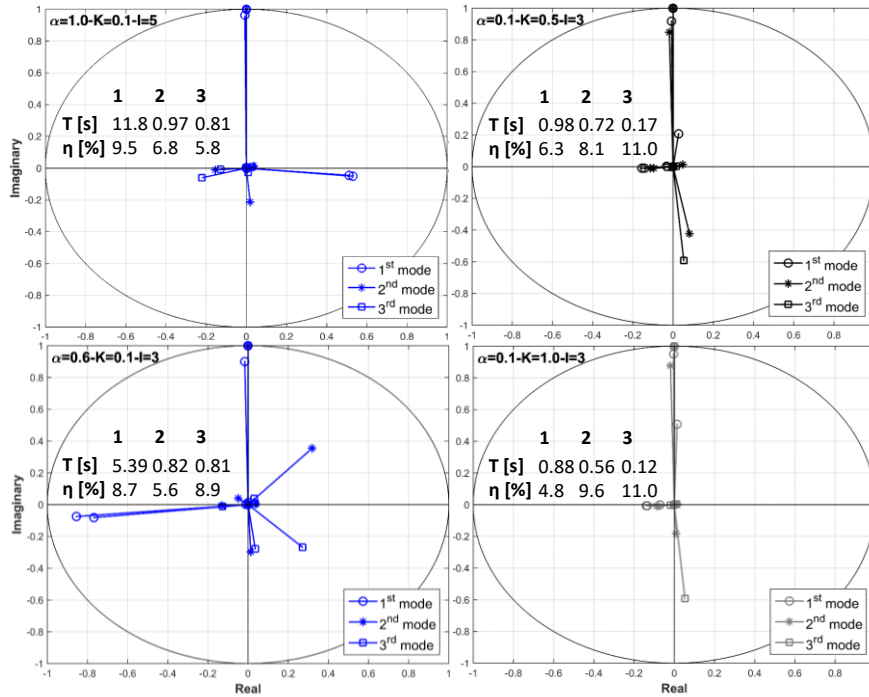


Fig. 7.8. Complexity plots: (a) Case A, (b) Case B, (c) Case C, (d) Case D

Increasing the isolation period, the first complex damping ratio  $\eta_1$  is quite less than the isolation damping ratio  $\xi_{iso}$  (Case A); on the contrary, when the fundamental period approaches the nominal period of the lower structure,  $\eta_1$  reaches the damping ratio of the lower structure  $\xi_{LS}$  (case D). The prevailing higher modes possess the lower damping ratios which are, anyway, larger than the damping ratio of the structural portions.

Therefore, in a linear dynamic analysis, the assumption of damping ratios respectively equal to 0.10 and 0.05 for the isolation system and the structural portions leads to the following situations: in cases A and C,  $\xi_1$  is less overestimated while  $\xi_2$  and  $\xi_3$  are quite underestimated; in case B,  $\xi_1$  is overestimated while  $\xi_2$  and  $\xi_3$  are underestimated; in case D all the damping ratios are overestimated.

For this reason, the assumption made is almost true for the case A and overestimate the case D. However, in order to recognize if the assumption made can still be valid, linear and non-linear analyses are carried out to clarify the influence of each mode on the overall seismic behavior of the mid-story buildings.

#### 7.4.4. Response spectrum analysis

Linear dynamic analyses have been carried out on the 3DOF IIS and the SDOF LS models, using the elastic acceleration response spectrum prescribed by the Italian NTC2008 [D.M. 14/01/2008] for the specific case study site ( $a_g = 0.162$  g,  $F_o = 2.347$ ,  $T_c^* = 0.333$  s,  $S = 1.47$ ), see Fig. 7.9.

For both the 3DOF IIS and the SDOF LS models, a constant modal damping ratio of 0.05 is set; the base shear force of the 3DOF IIS model,  $V_{b,3DOF\ IIS}$ , is evaluated through the complete quadratic combination CQC. For the sake of brevity only some results are considered herein, i.e. the ones obtained for  $I = 3$  in terms of story shear force (Figs. 7.10 ÷ 7.21), story displacement (Figs. 7.22 ÷ 7.24) and base shear (Fig. 7.25) are depicted.

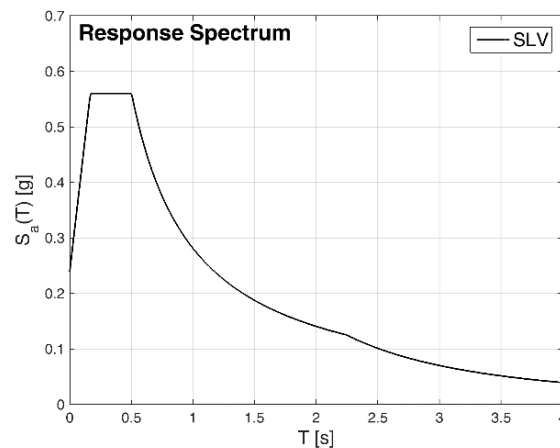


Fig. 7.9. NTC2008 elastic acceleration response spectrum ( $\xi = 0.05$ )

##### 7.4.4.1. Story Shear Force

In Figs. 7.10 ÷ 7.21, the story shear forces and the corresponding modal components are depicted as a function of the isolation period  $T_{ISO}$ ; each

curve is built up by varying the mass ratio  $\alpha$  for a fixed value of the stiffness ratio  $K$ . In particular, in Figs. 7.10 ÷ 7.13 are respectively provided the LS story shear,  $Q_{LS}$ , and the corresponding modal components,  $Q_{LS1}$ ,  $Q_{LS2}$  and  $Q_{LS3}$ ; in Figs. 7.14 ÷ 7.17 are respectively provided the ISO story shear,  $Q_{ISO}$ , and the corresponding modal components,  $Q_{ISO1}$ ,  $Q_{ISO2}$  and  $Q_{ISO3}$ ; in Figs. 7.18 ÷ 7.21 are respectively provided the US story shear,  $Q_{US}$ , and the corresponding modal components,  $Q_{US1}$ ,  $Q_{US2}$  and  $Q_{US3}$ .

Considering the LS, from Figs. 7.10 ÷ 7.13 is shown that: for  $T_{ISO}$  less than 1 s the story shear is given by the prevailing contribution of the first mode while for  $T_{ISO}$  larger than 1 s it is due to the prevailing contribution of either the 2<sup>nd</sup> mode or the 3<sup>rd</sup> mode.

Looking at the ISO and US, from Figs. 7.14 ÷ 7.21 is shown that for all the isolation periods covered, the story shear force is due to the prevailing contribution of either the 2<sup>nd</sup> mode or the 3<sup>rd</sup> mode.

However, the presence of MCE ( $\alpha = 0.6$ ,  $K = 0.1$  for each I) does not increase the response in terms of story shear force.

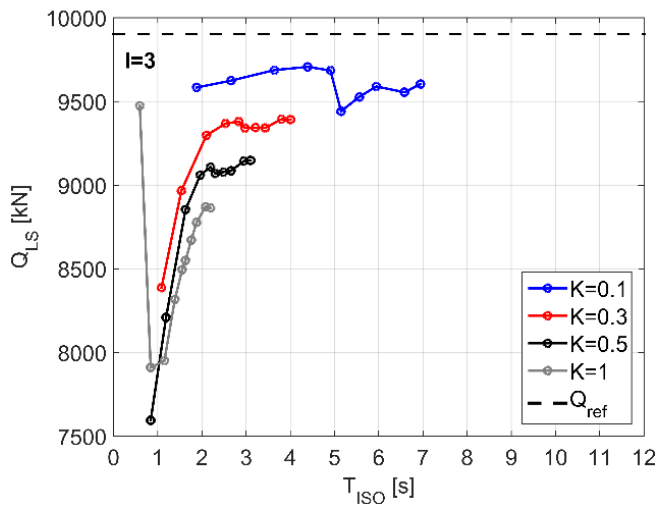


Fig. 7.10. Story shear force:  $Q_{LS}$  vs.  $T_{ISO}$

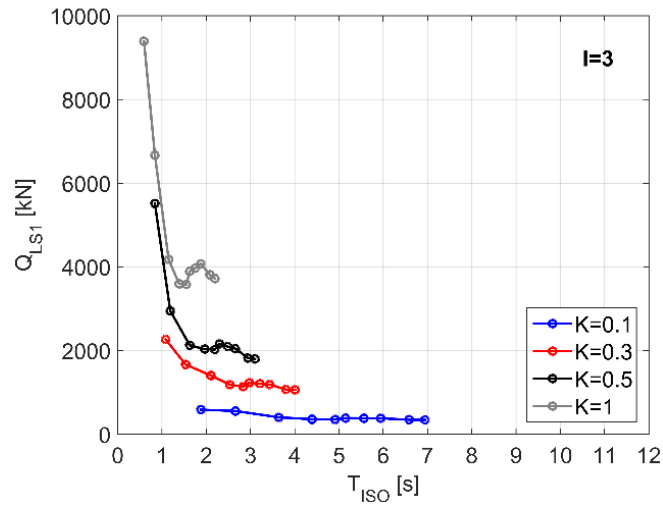


Fig. 7.11. Modal story shear force:  $Q_{LS1}$  vs.  $T_{ISO}$

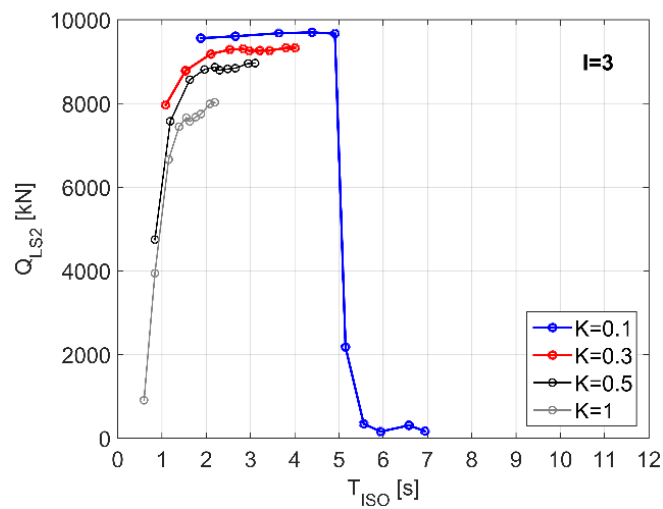


Fig. 7.12. Modal story shear force:  $Q_{LS2}$  vs.  $T_{ISO}$

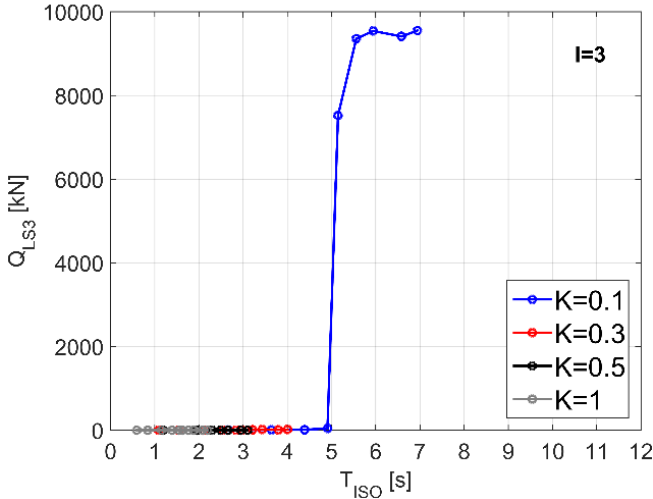


Fig. 7.13. Modal story shear force:  $Q_{LS3}$  vs.  $T_{ISO}$

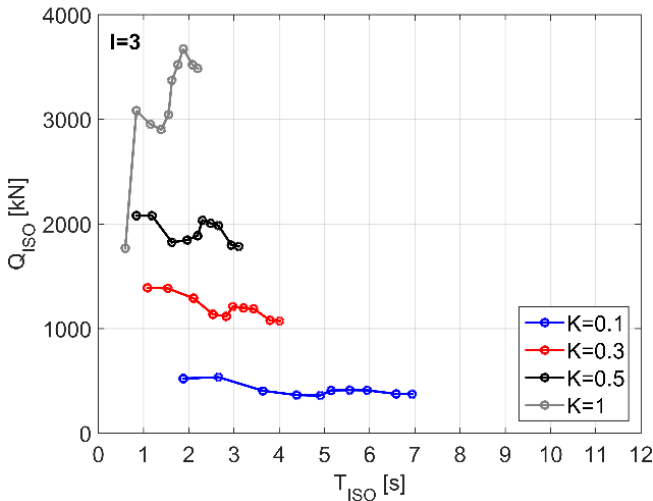
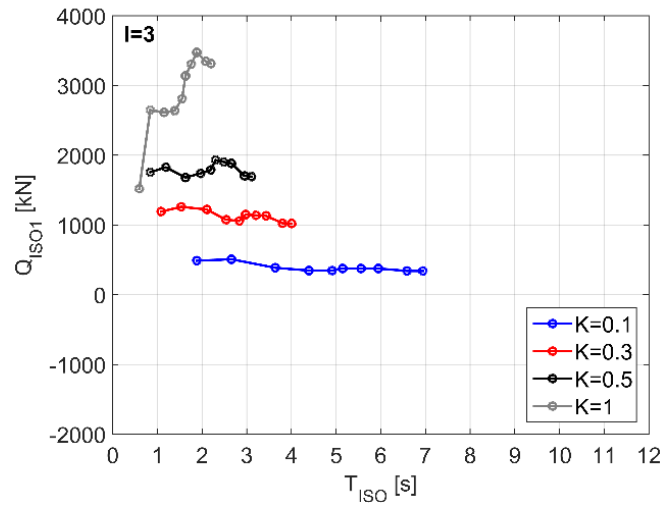
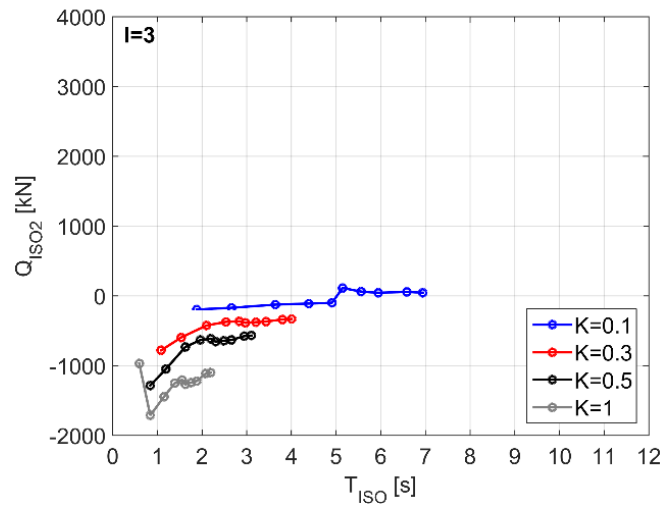


Fig. 7.14. Story shear force:  $Q_{ISO}$  vs.  $T_{ISO}$



Fig. 7.15. Modal story shear force:  $Q_{ISO1}$  vs.  $T_{ISO}$ Fig. 7.16. Modal story shear force:  $Q_{ISO2}$  vs.  $T_{ISO}$

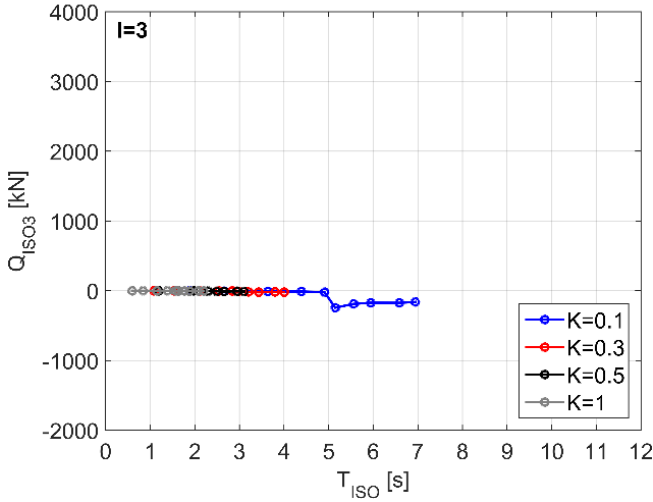


Fig. 7.17. Modal story shear force:  $Q_{ISO3}$  vs.  $T_{ISO}$

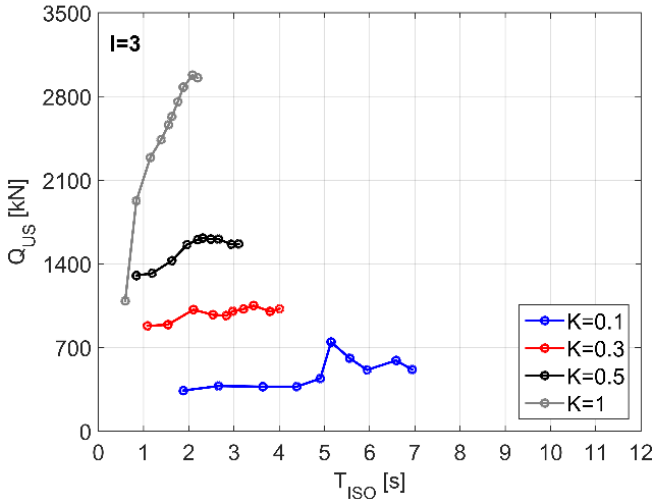
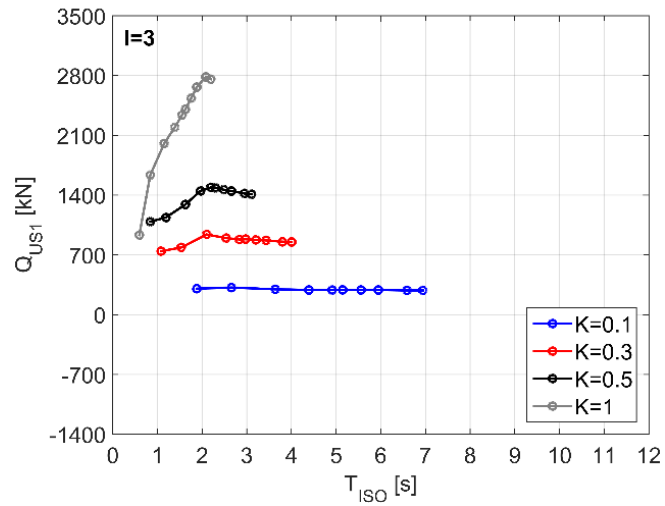
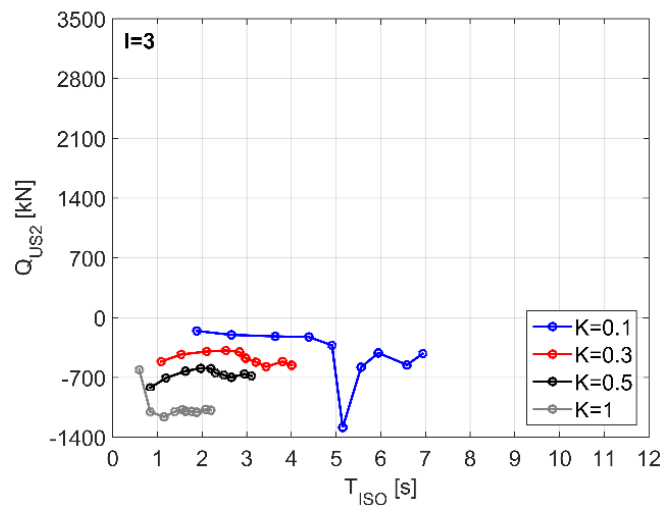


Fig. 7.18. Story shear force:  $Q_{US}$  vs.  $T_{ISO}$

Fig. 7.19. Modal story shear force:  $Q_{US1}$  vs.  $T_{ISO}$ Fig. 7.20. Modal story shear force:  $Q_{US2}$  vs.  $T_{ISO}$

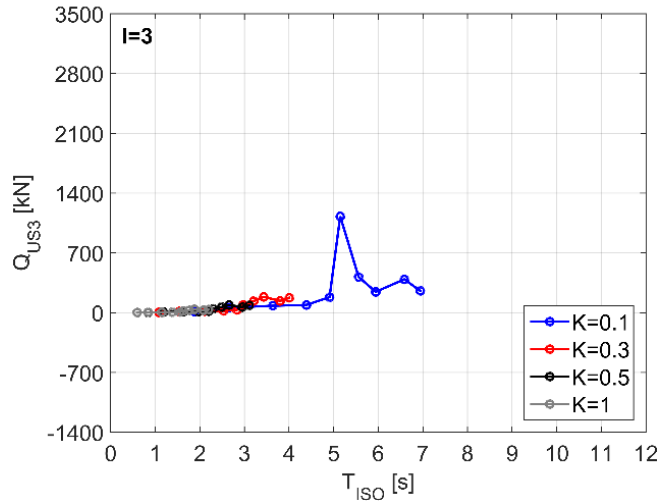


Fig. 7.21. Modal story shear force:  $Q_{US3}$  vs.  $T_{ISO}$

#### 7.4.4.2. Story displacement

In Figs. 7.22 ÷ 7.24, the story relative drifts are depicted as a function of the isolation period  $T_{ISO}$ ; in particular, each curve is built up by varying the mass ratio  $\alpha$  for a fixed value of the stiffness ratio  $K$ .

As can be seen from Figs. 7.22 ÷ 7.24, the isolation story (quite trivially) displays the larger story drifts and the upper structure shows a peak corresponding to the detrimental mode coupling effect (Case C:  $\alpha=0.6$ ,  $K=0.1$ ,  $I=3$ ).

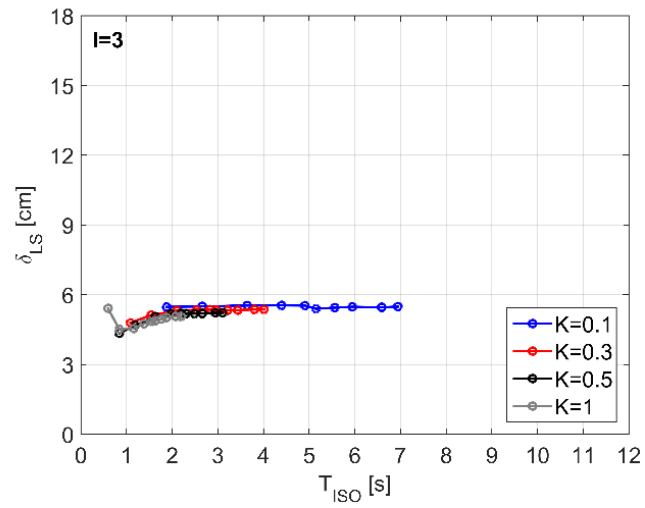


Fig. 7.22. LS - relative drift

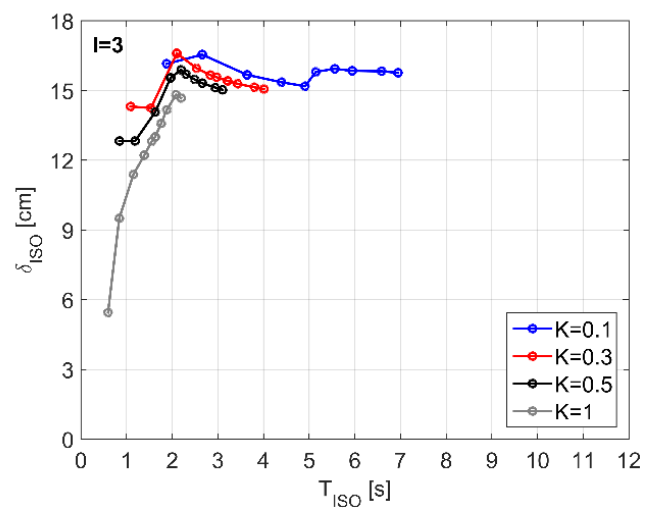


Fig. 7.23. ISO - relative drift

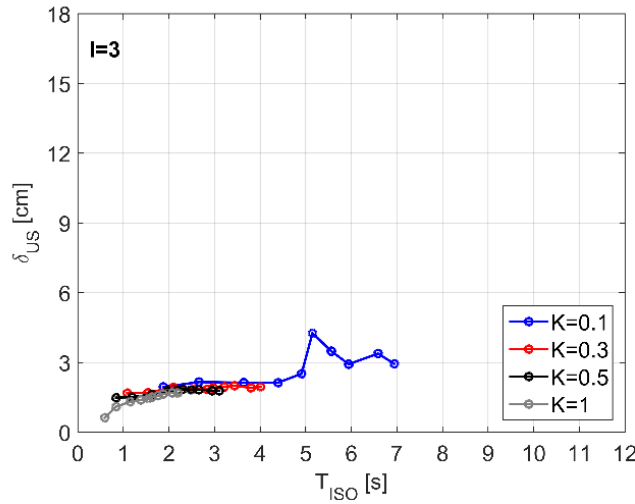


Fig. 7.24. US - relative drift

#### 7.4.4.3. Base Shear

The ratio between the base share force of the inter-story isolated structure and the fixed-base LS, i.e.  $v = V_{b,3DOF-IIS} / V_{b,SDOF-LS}$ , can be used for a preliminary guess of the effectiveness of the IIS elevation in protecting the LS from seismic actions.

In Fig. 7.25, the base shear ratio  $v$  is depicted as a function of the isolation period  $T_{ISO}$ , in particular each curve is built up by varying the stiffness ratio  $K$  for a fixed value of the mass ratio  $\alpha$ .

As can be seen from Fig. 7.25, for very low and high values of  $T_{ISO}$  the base shear ratio  $v$  is respectively, greater than, and almost equal to, one, while for values of  $T_{ISO}$  in the range of  $1.0 \div 2.5$  s the ratio  $v$  is less than one.

When  $T_{ISO}$  approaches zero, the 3DOF IIS structure behaves as a fixed-base structure with an additional mass and a global stiffness lower than the SDOF LS structure. This condition can be represented by the case D 3DOF IIS (depicted in Fig. 7.25 with a square marker) in which, as can be seen previously, the first mode is related to the LS, which possesses now larger mass than the original configuration and, consequently, the base shear becomes greater than the corresponding one in the reference model (SDOF LS).

On the other hand, when  $T_{ISO}$  tends to infinity (i.e. perfect isolation system) or more exactly is greater than 6.5 s, the flexible interface decouples the isolated US and the LS, the spectral acceleration corresponding to the first period tends to zero; no matter how flexible the isolation layer is, the LS cannot take advantage from this additional flexibility [Ziyaeifar & Noguchi 1998], thus the base shear is only given by the contribution of the LS. This condition can be represented by the case A 3DOF IIS (depicted in Fig. 7.25 with a square marker) in which the perfect isolation is provided by the fact that the parameters  $\epsilon_{US,IIS1}$  and  $\epsilon_{LS,IIS1}$  are less or equal to  $10^{-2}$ , respectively, involving a first modal displacement only at the isolation interface, see Fig. 7.3.

For values of  $T_{ISO}$  in the range of  $1.0 \div 2.5$  s the isolation can be defined “non-perfect”, the first mode involves displacement both in the LS and in the isolation interface with a high value of the first mass ratio with respect to the case of a perfect isolation; the case B 3DOF IIS (depicted in Fig. 7.25 with a square marker) describes this situation since  $\epsilon_{US,IIS1}$  and  $\epsilon_{LS,IIS1}$  are of the order  $10^{-2}$  and  $10^{-1}$ , respectively, see Fig. 7.4. Furthermore, the “non-perfect” isolation in middle-story isolation system allows an improvement in the effectiveness of IIS as a retrofit strategy for existing building with a reduction of the base shear with respect to the one of the existing structure despite of the additional mass.

In Fig. 7.25 is also depicted with a square marker the cases C 3DOF IIS affected by MCE. It is worth noticing that, the case C reaches the minimum  $v$  despite of the MCE; in fact, the “non-perfect” isolation is able to minimize the MCE reducing the coupled participating mass ratio of the higher modes.

In addition, from Fig. 7.25 can be noticed that the case B ( $\alpha = 0.1$ ,  $K = 0.5$ ,  $I = 3$ ) shows the minimum  $v$  with respect to all the possible combinations of the parameters  $\alpha - K - I$ , i.e. 0.767 at  $T_{ISO} = 0.841$  s which is almost equal to  $T_{LS}$  (scatter of 4%).

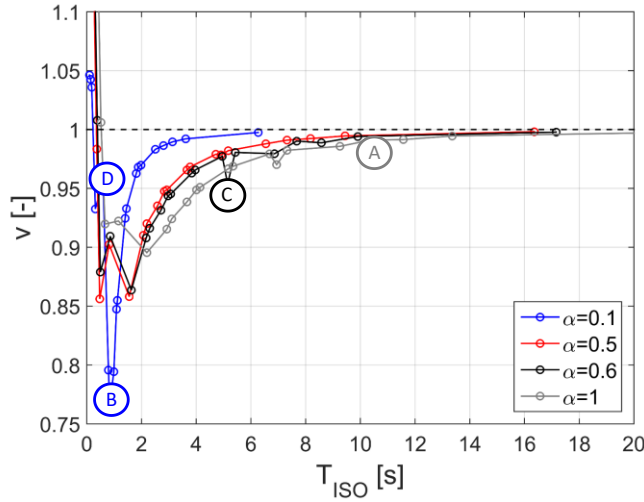


Fig. 7.25.  $v$  vs.  $T_{ISO}$  ( $I = \{0.5, 3, 4, 5, 10\}$ )

#### 7.4.5. Comparison between two 3DOF IIS models

In this section the influence of the mass ratio,  $\alpha$ , and of the isolation period,  $T_{ISO}$ , on the response of the retrofitted building is considered.

Starting from the case B, two configurations, namely: E and F, which possess the same stiffness ratio and two different mass ratios are chosen, i.e. case E:  $\alpha = 0.1$ ,  $K = 0.5$  and case F:  $\alpha = 0.5$ ,  $K = 0.5$ .

The isolation period is varied between 0.5 and 2.5; the damping ratios of both the structural portions,  $\xi_{US} = \xi_{LS} = \xi_s$ , and of the isolation period,  $\xi_{ISO}$ , are assumed equal to 0.05 and 0.10, respectively.

Response spectrum analysis (RSA) and time history - spectrum compatible ground motion (THA) are carried out on the E and F 3DOF models.

##### 7.4.5.1. Modeling of the isolators bearings by bilinear modeling

The bilinear model, which globally describes the behavior of high damping rubber bearings (HDRBs) [Naeim & Kelly 1999] is depicted in Fig. 7.26.

The design parameters which completely define the bilinear model are: the elastic stiffness  $k_1$ , the post-yield  $k_2$ , the characteristic strength  $Q$ , the design displacement  $D$ .



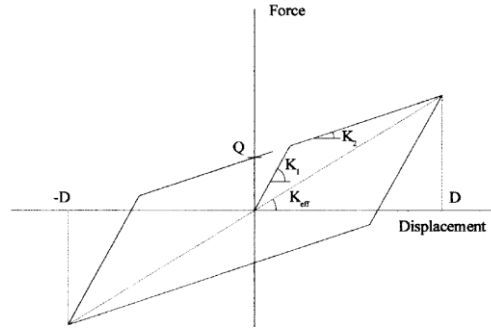


**Fig. 7.26. Bilinear HDRB model**

The effective stiffness, defined as the secant slope of the peak-to-peak values in the hysteresis loop, is given by:

$$k_{\text{eff}} = k_2 + \frac{Q}{D}, \quad D \geq D_y \quad (7.13)$$

where  $D_y$  is the yield displacement equal to

$$D_y = \frac{Q}{k_1 - k_2} \quad (7.14)$$

And the area of the hysteresis loop (the energy dissipate per cycle)  $W_D$  is equal to

$$W_D = 4Q(D - D_y) \quad (7.15)$$

The effective damping  $\xi_{\text{eq}}$  is given by:

$$\xi_{\text{eq}} = \frac{4Q(D - D_y)}{2\pi k_{\text{eq}} D^2} \quad (7.16)$$

The data for building the bilinear model are:

$$\begin{cases} \xi_{eq} = 0.10 \\ \gamma = 1.0 \\ \mathbf{D} = \mathbf{S}_d(\mathbf{T}_{ISO}, \xi_{eq}) \\ \mathbf{k}_{eq} = \omega_{ISO}^2 \mathbf{M}_{ISO} \end{cases} \quad (7.17)$$

Instead, the design unknowns are the quantities  $k_1$ ,  $k_2$  and  $D_y$ .

To build the bilinear model parametrically, it is possible to define a stiffness ratio between the post-yield and elastic stiffnesses,  $a$ , and a displacement ratio between the design and yield displacements,  $b$ . The ratios  $a$  and  $b$  are given by:

$$a = \frac{k_2}{k_1}; \quad b = \frac{D_y}{D} \quad (7.18)$$

The parameter  $a$  is generally assumed equal to 0.1 [Nacim & Kelly 1999]; the yield displacement  $D_y$  can be expressed in terms of the thickness of the rubber layer  $t_r$  through the following [Foti & Mongelli 2011]:

$$D_y = \lambda t_r = \lambda \frac{D}{\gamma} \quad (7.19)$$

In which the coefficient  $\lambda$  varies between 0.05 and 1.0, the thickness  $t_r$  is equal to the ratio  $D/\gamma$ .

From (7.18), the parameter  $b$  assumes the form:

$$b = \frac{\lambda}{\gamma} \quad (7.20)$$

Put in system the Eqs. (7.16)  $\div$  (7.20), the elastic stiffness  $k_1$  can be expressed in terms of the parameters  $a$  and  $b$  as follows:

$$k_1 = \frac{\pi \xi_{eq} k_{eq}}{2b(1-a)(1-b)} \quad (7.21)$$

#### 7.4.5.2. Response Spectrum Analysis (RSA)

Response spectrum analysis (RSA) are carried out on the E and F 3DOF models varying the isolation period between 0.5 s and 2.5 s.

The hypothesis of proportional damping is adopted and then removed; for this reason, three cases are considered: case 1:  $\xi$  equal to 0.05 for all modes (as assumed in the previous analyses); case 2:  $\xi$  equal to 0.10 for all modes; case 3:  $\xi$  interpolated as a function of the period  $T$  ( $\xi = 0.10$  at  $T = T_1$  and  $\xi = 0.05$  at  $T = T_2$ ).

The case 1 ( $\xi = 0.05$ ) underestimates the contribution of the isolation system; the case 2 ( $\xi = 0.10$ ) overestimates the contribution of the US and LS; the case 3 ( $\xi = \xi(T)$ ) grasps the global behavior of the system, associating a modal damping ratio  $\xi$  equal to 0.10 for the first mode of the isolation system and equal to 0.05 from the second mode involving the US and LS. The different response spectra under the different assumption for the damping ratios are depicted in Fig. 7.27.

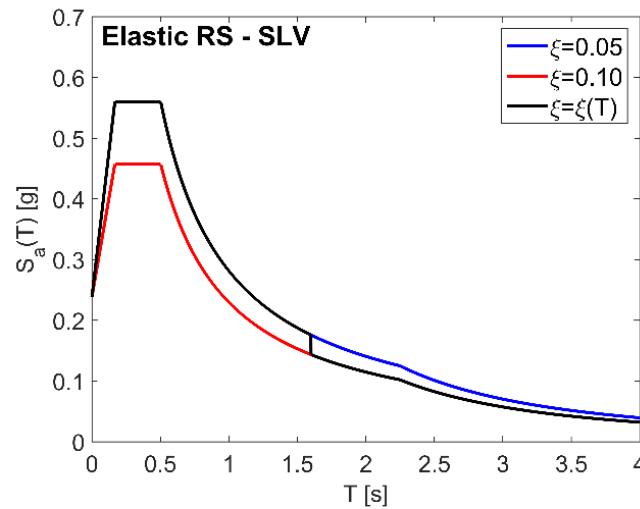


Fig. 7.27. Elastic Response Spectra

In Fig. 7.28, for all the cases 1 ÷ 3, the base shear is depicted as a function of the isolation period  $T_{ISO}$ , the base shear of the reference configuration is also shown for comparison. In particular, the chart on the left is referred to the case E ( $\alpha = 0.1$ ,  $K = 0.5$ ) while the chart on the right to the case F ( $\alpha = 0.5$ ,  $K = 0.5$ ).

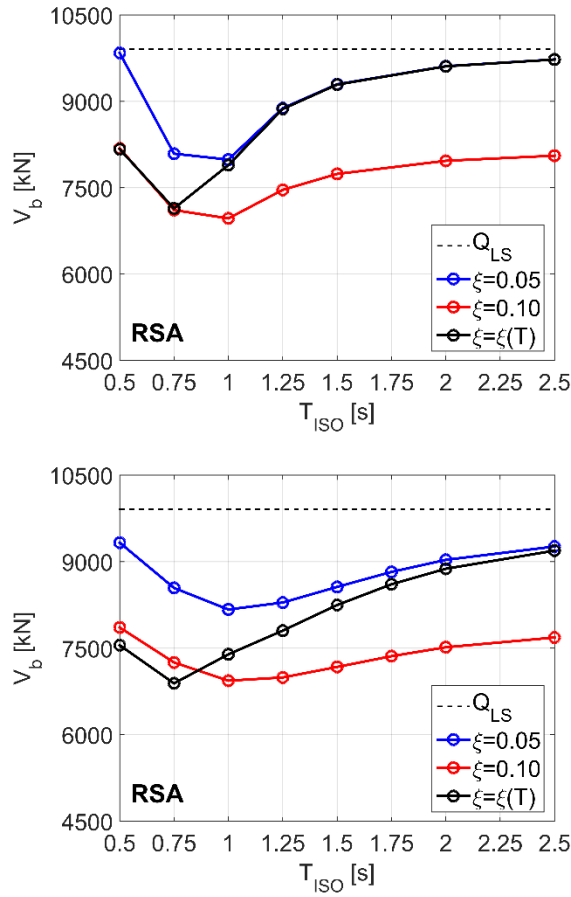


Fig. 7.28. RSA: (a)  $\alpha = 0.1, K = 0.5$ , (b)  $\alpha = 0.5, K = 0.5$

As can be seen from Fig. 7.28a (case E) almost the same results are observed for the cases 2 and 3 ( $\xi = 0.10$  and  $\xi = \xi(T)$ ) when  $T_{ISO}$  is larger than 1 s, and for the cases 1 and 3 ( $\xi = 0.05$  and  $\xi = \xi(T)$ ) when  $T_{ISO}$  is less than 0.75 s; for  $T_{ISO}$  in between  $0.75 \div 1.0$  s exists a transition zone in which the response of the case 3 is intermediate between the cases 1 and 2.

From Fig. 7.28b (case F) the same trend is observed. However, thanks to the larger mass ratio, the system is characterized by a greater robustness and, thus, for all the isolation periods the base shear in the case F is less than the corresponding counterpart in the case E. In addition, the

transition zone is more extended, with extreme values equal to 0.75 s and 2.0 s.

From the above considerations, it can be noticed that the damping ratio  $\xi$  is deeply dependent on the dynamic characteristics of the structural portions (US and LS) and on the isolation period  $T_{ISO}$ . Therefore, three behavioral situations can be considered: (a)  $T_{ISO} < T_{LS}$ ; (b)  $T_{ISO} \approx T_{LS}$ ; (c)  $T_{ISO} > T_{LS}$ .

The condition a ( $T_{ISO} < T_{LS}$ ) can be observed in cases like the case D previously described. In this situation, the mid-story isolated structure behaves as a FB structure, the base shear is due to the prevailing contribution of the first mode. For these reasons, the damping ratio  $\xi = \xi(I)$  can be interpolated as follows:  $\xi_1 = \xi_S$  and  $\xi_2 = \xi_{ISO}$ .

The condition b ( $T_{ISO} \approx T_{LS}$ ) can be observed in cases like the case B previously described. In this situation the base shear is due to the contribution of all the modes. For these reasons, the damping ratio  $\xi = \xi(I)$  can be assumed constant and equal to the mean between the damping ratios of the structural portions and the isolation system, i.e.  $\xi = (\xi_S + \xi_{ISO}) / 2$ .

The condition c ( $T_{ISO} > T_{LS}$ ) can be observed in cases like the case A previously described. In this situation the base shear is due to the prevailing contribution of the higher modes. For these reasons, the damping ratio  $\xi = \xi(I)$  can be interpolated as follows:  $\xi_1 = \xi_{ISO}$  and  $\xi_2 = \xi_S$ . Increasing the isolation period, the first complex damping ratio  $\eta_1$  is quite less than the isolation damping ratio  $\xi_{ISO}$  (Case A); on the contrary, when the fundamental period approaches the nominal period of the lower structure,  $\eta_1$  reaches the damping ratio of the lower structure  $\xi_{LS}$  (case D). The prevailing higher modes possess the lower damping ratios which are, anyway, larger than the damping ratio of the structural portions.

Therefore, in a linear dynamic analysis, the assumption of damping ratios respectively equal to 0.10 and 0.05 for the isolation system and the structural portions leads to the following situations: in cases A and C,  $\xi_1$  is less overestimated while  $\xi_2$  and  $\xi_3$  are quite underestimated; in case B,  $\xi_1$  is overestimated while  $\xi_2$  and  $\xi_3$  are underestimated; in case D all the damping ratios are overestimated.

For this reason, the assumption made is almost true for the case A and overestimate the case D. However, in order to recognize if the assumption made can still be valid, linear and non-linear analyses are carried out to clarify the influence of each mode on the overall seismic behavior of the mid-story buildings.

It is worth noticing that in the transition zone of the Case F, the assumption of a first damping ratio equal to  $\xi = (\xi_s + \xi_{ISO}) / 2$  is valid for isolation period close to the nominal period of the LS; in the other cases an estimation of the damping ratios in the complex modes of vibration is necessary. Therefore, in lieu of the average between the structural and isolation damping ratios, the values of the damping ratios in the complex modes can be assumed.

#### 7.4.5.3. Time History Analysis (THA)

Non-linear time history (THA) has been performed considering a set of 10 spectrum-compatible ground motions with the site of Pozzuoli ( $a_g = 0.162$  g,  $F_0 = 2.347$ ,  $T_C^* = 0.333$  s,  $S = 1.47$ ) [Software SIMQKE\_GR] fixing the spectral ordinate at 1.0 s, see Fig. 7.29.

The cases E and F fully account for the nonlinear behavior of the isolation devices (Fig. 7.26), while both the US and LS are considered elastic.

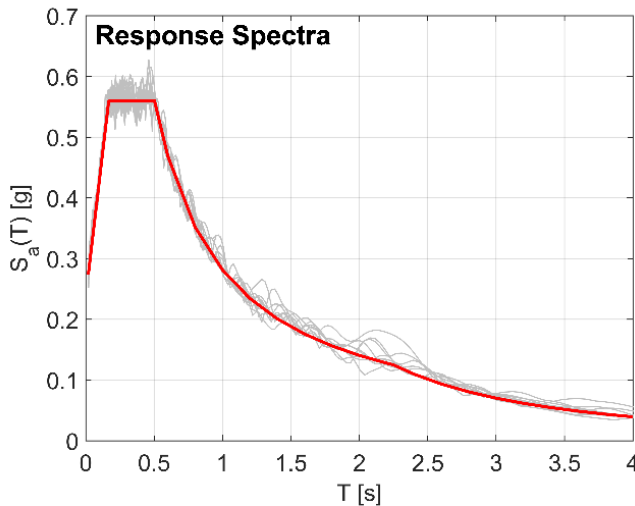


Fig. 7.29. Elastic Response spectrum – compatible ground motions

Starting from the results of the RSA in which three behavioral situations are identified, in the THA for  $T_{ISO}$  less than 1 s a constant damping is assumed, i.e.  $\xi_1 = \xi_2 = 0.05$ ; for  $T_{ISO}$  equal and larger than 1 s the interpolated damping is considered, i.e.  $\xi_1 = 0.00$  and  $\xi_2 = 0.05$  (neglecting the contribution of US and LS to the isolation mode).

The base shear obtained from the time history analyses of the two configurations, i.e.  $\alpha = 0.1 - K = 0.5$  and  $\alpha = 0.5 - K = 0.5$ , by varying the isolation period between 0.5 and 2.5 s, is shown in Fig. 7.30. Each couple of graphs refers to the results obtained for each model; the results of the RSA for the case 3 ( $\xi = \xi(T)$ ) are also depicted in the figure for comparison.

For the case E the curves of the mean THA and the RSA are almost overlapped for all the range of the isolation period; instead, some differences arise looking at the corresponding curves in the case F because of the assumptions made for  $\xi = \xi(T)$ .

Both the cases E and F display a reduction of the base shear with respect to the original configuration in a range of isolation period between  $0.75 \div 1.25$  s and  $0.75 \div 2.0$  s, respectively. In fact, the large mass ratio in the second configuration enhances the robustness of the mid-story isolation system behaving as a MD.

The peak drift and acceleration values obtained from the time history analyses of the two configurations, i.e.  $\alpha = 0.1 - K = 0.5 - T_{ISO} = 1$  s and  $\alpha = 0.5 - K = 0.5 - T_{ISO} = 2$  s, are shown in Figs. 7.31 and 7.32, respectively. Each couple of graphs refers to the results obtained for each model.

Considering the results of the mean TH, from Figs. 7.31 and 7.32 can be observed that almost equal peak values for the LS are obtained for both the configurations; in the second configuration the peak drift of the isolation system is larger than, while both the peak acceleration values of the ISO and US are less than, the corresponding counterparts in the first configuration.

Therefore, in the second configuration a mass damper effect is observed for the LS while an isolation effect is shown for US and ISO.

It means that, the second configuration, characterized by the larger mass ratio and isolation period, represents a more robust system which allows almost the same reduction of the LS response and the larger reduction of the US response with respect to the first configuration.

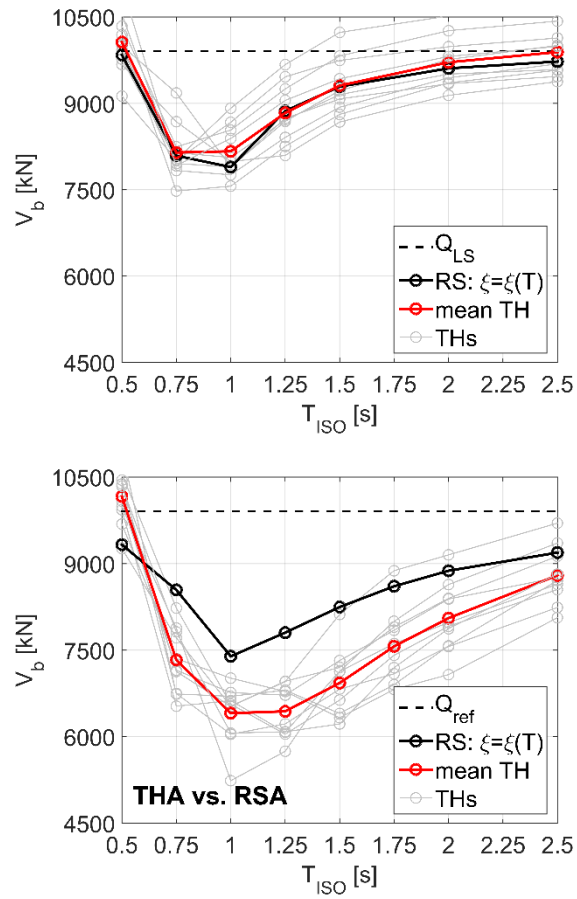


Fig. 7.30. THA vs. RSA: (a)  $\alpha = 0.1$ ,  $K = 0.5$ , (b)  $\alpha = 0.5$ ,  $K = 0.5$



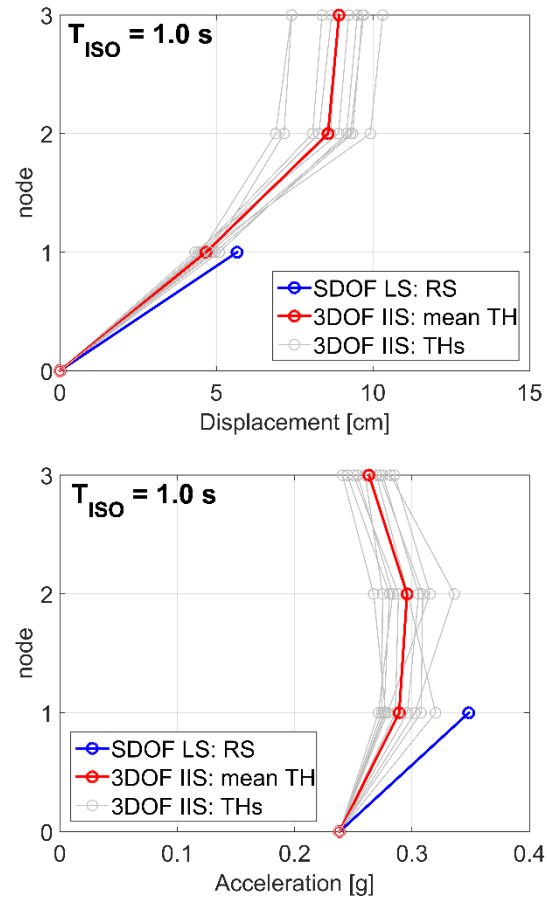


Fig. 7.31.  $\alpha = 0.1$ ,  $K = 0.5$ : (a) peak drift values, (b) peak acceleration values

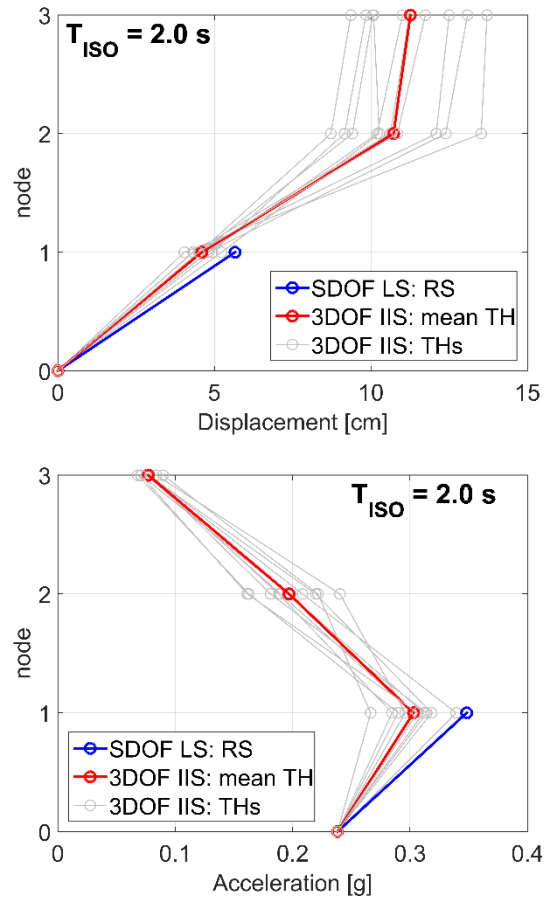


Fig. 7.32.  $\alpha = 0.5$ ,  $K = 0.5$ : (a) peak drift values, (b) peak acceleration values

## 7.5. CHOICE OF THE DESIGN CONFIGURATION FOR THE UPPER STRUCTURE AND THE ISOLATION SYSTEM

Starting from the previous results, the final design configuration has been chosen considering the following criteria: a) large reduction of the seismic base shear  $V_b$  with respect to the original configuration (i.e. the pre-existing building before the IIS elevation, b) an adequate value of  $T_{ISO}$  (around 2.0 s) in order to emphasize the isolation behavior of the IIS

system, c) prevention of MCE in order to avoid displacement amplification in the upper structure, and d) construction feasibility of the vertical addition, in terms of number of stories (not larger than three). According to the above criteria, two eligible configurations, appointed as G and H, have been individuated, and four corresponding structural solutions have been designed (Tab. 7.6).

The final choice concerns a two-story reinforced concrete frame structure, with  $30 \times 40 \text{ cm}^2$  columns and  $30 \times 60 \text{ cm}^2$  beams. For the isolation system, high damping rubber bearings of the FIP [FIP Industriale] have been used. To place the isolators, 12 positions have been individuated at the intersections between the walls of the lower structure (Fig. 7.33). The mechanical properties of the isolators have been chosen in order to reduce the eccentricity between the floor mass centroid and the stiffness centroid. Two different diameters  $D$  of the bearings have been used, respectively equal to 500 and 550 mm, with equivalent lateral stiffness  $k_{eq}$  respectively equal to 1.25 and 1.51 kN/mm. The other characteristics of the isolators are: the shear modulus,  $G = 0.80 \text{ MPa}$ ; the total thickness of the rubber,  $t = 126 \text{ mm}$ ; the equivalent damping ratio,  $\xi = 0.10$ ; the maximum horizontal displacement for lateral actions,  $\delta_{max} = 250 \text{ mm}$ . Each isolator has been verified against the vertical loads associated both to seismic and non-seismic combinations.

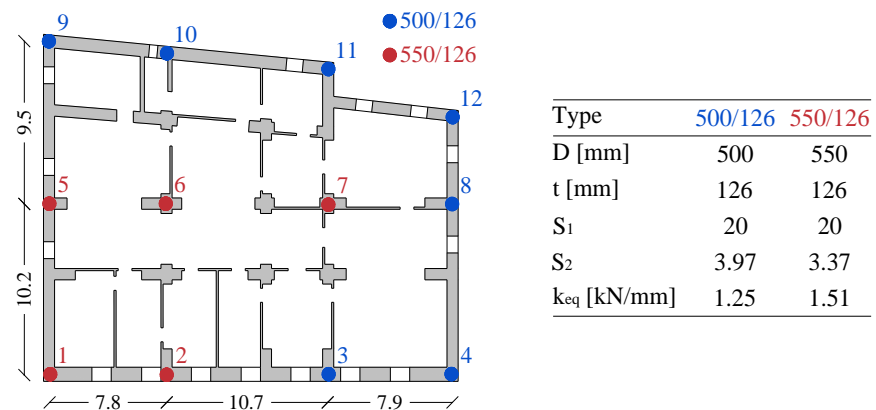


Fig. 7.33. Location in plan, typology and properties of the isolators

**Table 7.6. Structural characteristics of the two chosen configurations**

$\alpha, K, I$	$T_1$	$T_{ISO}$	$v$	Material	Structure	n. floors	Columns	Shear walls	Beams
	[s]	[s]	[-]			[-]			
0.5, 0.5, 3	2.040	1.880	0.895	Concrete	Frame	2	30 x 40	-	30 x 60
				Steel	CBF	3	HEB 260	-	IPE 550
0.5, 1, 4	1.913	1.772	0.881	Concrete	Shear w.	2	30 x 40	30 x 150	30 x 60
				Steel	CBF	3	HEB 260	-	IPE 550

## 7.6. THREE-DIMENSIONAL ANALYSIS

In order to assess the response of the inter-story isolated building, more refined three-dimensional models have been developed and used for FEM analyses through the software SAP2000. In particular, three different models are considered: the IIS structure (3D IIS), the fixed-base lower structure (3D LS), and the base isolated upper structure (3D ISO+US). The 3D IIS model is composed of lower and upper structure and the isolation layer. The 3D LS and 3D ISO+US models are defined to grasp the dynamic behavior of the two portions the 3D IIS model is composed of. The 3D models have been analyzed through modal analysis, dynamic linear analysis (elastic response spectrum analysis), and non-linear time history analysis.

### 7.6.1. Modal Analysis

The values of periods and mass participating ratios are shown in Tabs. 7.7 – 7.8; the number of the natural modes provides a total participating mass equal or greater than 85%.

The significant modes of the 3D LS model show that the prevailing directions do not coincide with the main directions X and Y, involving both the translational and the torsional contributions. The 3D ISO+US model shows the typical modes of vibrations of a base isolated structure, i.e. the first two translational modes and the third rotational mode; however, the solution adopted for the isolation system provides a slight coupling between the translational and rotation modes. As can be seen in the previous § 7.4.3, the IIS model combines the modes of vibration of the LS and the isolated US when MCE is not expected. In particular, it can be observed that the first three modes of the IIS structure correspond

to the first three modes of the isolated US in terms of period and prevailing direction of vibration. Moreover, the first period  $T_1$  of the 3D IIS model (1.97 s) is nearly identical to the one obtained by the simplified 3DOF IIS model (2.04 s), and the first two participating mass ratios  $L_{1,x-x}$  and  $L_{2,y-y}$  (0.289 and 0.304) are very close to the ratio between the isolated mass and the total mass of the building (0.330). The higher modes (beyond the third) of the 3D IIS correspond to the modes of the 3D LS and the higher modes of the 3D ISO+US, involving displacements either in the US or in the LS. However, the significant higher modes of the IIS model show displacements mainly in the LS.

**Table 7.7. Modal analysis of FEM 3D IIS models**

Mode	3D IIS			
	T [s]	$L_x$	$L_y$	$R_z$
		[-]	[-]	[-]
1	1.969	0.289	0.067	0.194
2	1.938	0.058	0.304	0.058
3	1.435	0.000	0.000	0.112
4	0.553	0.009	0.112	0.004
5	0.440	0.341	0.092	0.223
6	0.317	0.137	0.158	0.062
7	0.307	0.000	0.000	0.000
13	0.126	0.001	0.101	0.037
14	0.116	0.074	0.019	0.009
15	0.088	0.021	0.010	0.199

**Table 7.8. Modal analysis of FEM 3D ISO+US and LS models**

Mode	3D ISO+US				3D LS			
	T [s]	$L_x$	$L_y$	$R_z$	T [s]	$L_x$	$L_y$	$R_z$
		[-]	[-]	[-]		[-]	[-]	[-]
1	1.835	0.997	0.001	0.223	0.611	0.337	0.205	0.196
2	1.828	0.001	0.998	0.506	0.486	0.292	0.305	0.001
3	1.364	0.000	0.000	0.269	0.271	0.015	0.088	0.405
4	0.305	0.001	0.000	0.000	0.137	0.190	0.069	0.107
5	0.279	0.000	0.001	0.000	0.125	0.075	0.217	0.039
6	0.228	0.000	0.000	0.000	0.084	0.018	0.002	0.125
7	0.168	0.000	0.000	0.000	0.071	0.021	0.080	0.088
13								
14								
15								

### 7.6.2. Response spectrum Analysis

The dynamic linear analyses have been conducted using the same elastic response spectrum considered for the simplified 3DOF analysis (Fig. 7.27); seismic actions have been applied along the two main directions X and Y separately. For the sake of brevity, only some results are here discussed, i.e. the ones obtained for the 3D IIS and the 3D LS models; in addition, the 3DOF IIS model is considered for comparison.

The hypothesis of proportional damping adopted in the simplified dynamic analyses is verified and then removed; for this reason, three cases are considered: Case 1:  $\xi$  equal to 0.05 for all modes (as assumed for the simplified model); Case 2:  $\xi$  equal to 0.10 for all modes; Case 3:  $\xi$  interpolated as a function of the period T ( $\xi = 0.10$  at  $T = T_1$  and  $\xi = 0.05$  at  $T = T_4$ ).

The case 1 ( $\xi = 0.05$ ) underestimates the contribution of the isolation system; the case 2 ( $\xi = 0.10$ ) overestimates the contribution of the US and LS; the case 3 ( $\xi = \xi(T)$ ) grasps the global behavior of the system, associating a modal damping ratio  $\xi$  equal to 0.10 for the first of the three modes of the isolation system and equal to 0.05 from the forth mode involving the US and LS.

In Tabs. 7.9 – 7.10 for the 3D IIS model in all the cases 1 ÷ 3, for the 3D LS and 3DOF IIS models are provided: the top absolute displacement of the US and LS, i.e.  $d_{US}$  and  $d_{LS}$ , and the absolute displacement of the isolation interface  $d_{ISO}$ ; the top-bottom relative displacement of the US and LS, i.e.  $\Delta_{US}$  and  $\Delta_{LS}$ , and the relative displacement of the isolation interface  $\Delta_{ISO}$ ; the base shear along the main directions x and y, i.e.  $V_{b,x}$  and  $V_{b,y}$ .

From Table 3 can be seen that, comparing the values obtained for the case 1 with the ones of the simplified analysis, the 3DOF model offers a good prediction of the results in terms of base shear, even though the simplified model overestimates the seismic response in terms of displacements (40%). Looking at the displacements of the 3D IIS models, can be observed that: the ones of the US and the isolation system are nearly identical in the cases 2 and 3, since a BIS respectively slightly underestimates and overestimates the modal damping ratio of the isolation and the main mass; the ones of the LS are similar in the cases 1 and 3, since the lower structure cannot take advantage from the isolation flexibility.

Comparing the 3D IIS models, the values of the base shear in the cases 1 and 3 are almost equal, and are slightly larger than the ones of the case 2. However, due to the slight plan irregularity of the lower structure, a base shear component is always generated in the direction orthogonal to the applied seismic action. In addition, the case 3 shows a LS displacement slightly lower than and a base shear slightly higher than the reference 3D LS structure.

**Table 7.9. Dynamic linear analysis of FEM 3D IIS models**

Models			3D IIS					
			Case 1		Case 2		Case 3	
			$\xi = 0.05$		$\xi = 0.10$		$\xi = \xi(T)$	
			X	Y	X	Y	X	Y
Absolute displ.	$d_{US}$	[cm]	15.38	14.87	12.77	12.36	12.78	12.36
	$d_{ISO}$	[cm]	14.05	13.76	11.66	11.43	11.66	11.44
	$d_{LS}$	[cm]	3.61	2.44	3.11	2.20	3.51	2.32
Inter-story displ.	$\Delta_{US}$	[cm]	1.33	1.11	1.11	0.93	1.12	0.92
	$\Delta_{ISO}$	[cm]	10.44	11.32	8.55	9.23	8.15	9.12
	$\Delta_{LS}$	[cm]	3.61	2.44	3.11	2.20	3.51	2.32
Base shear	$V_{b,x}$	[kN]	8813	4372	7704	2955	8730	4369
	$V_{b,y}$	[kN]	5411	6656	3897	6070	5408	6548

**Table 7.10. Dynamic linear analysis of 3DOF IIS and 3D FEM LS models**

Models			3DOF IIS		3D LS	
			$\xi = 0.05$		$\xi = 0.05$	
			X	Y	X	Y
Absolute displ.	$d_{US}$	[cm]	21.87	-	-	-
	$d_{ISO}$	[cm]	20.06	-	-	-
	$d_{LS}$	[cm]	5.05	-	4.01	2.97
Inter-story displ.	$\Delta_{US}$	[cm]	1.81	-	-	-
	$\Delta_{ISO}$	[cm]	15.01	-	-	-
	$\Delta_{LS}$	[cm]	5.05	-	4.01	3.22
Base shear	$V_{b,x}$	[kN]	8851	-	7761	5693
	$V_{b,y}$	[kN]	-	-	5693	7216

#### 7.4.3. Time History Analysis

A non-linear time history analysis is carried out applying the N/S acceleration component of the 1940 El Centro earthquake record ( $PGA = 0.319\text{ g}$ ) along the two main directions X and Y separately. In particular,

the 3D IIS model fully accounts for the non-linear behavior of the isolators, while both lower and upper structures are considered elastic.

In the following are reported the results obtained for the 3D IIS and 3D LS models in terms of peak relative story displacement (Fig. 7.34a), peak absolute story acceleration (Fig. 7.34b), base shear and energy components.

From Fig. 7.34a can be seen that, moving from the top LS story (LS3) to the top US story (US2)

a reduction of the relative story displacements is observed due to the flexibility of the devices, nevertheless the drift between the lowest floor and the top of the upper structure is acceptable (around 10 mm). Analogously, in Fig. 7.34b a remarkable reduction of the absolute story acceleration from LS3 to US2 is observed, confirming the effectiveness of the isolation system in filtering the seismic actions rising towards the IIS elevation. Therefore, the peak story values of relative displacement and of the absolute acceleration along the two main directions of the 3D IIS are less or almost equal to the ones of the reference 3D LS model.

In addition, the base shear ratio  $v$  between the 3D IIS and 3D LS models, respectively correspond to 0.975 and 0.770 in X and Y directions. The distribution of the energy components obtained from the time history analysis of the 3D IIS model, not reported herein for the sake of brevity, suggests that the inter-story isolation structure can be considered as a concentrated type of energy dissipation system, differently from the common approach of distributed dissipation in which the damping capacity is spread throughout the building. In fact, it can be seen that, except the first seconds of excitation dominated by kinetic and potential energy, the energy dissipated through the hysteretic behavior of the high damping rubber bearings represents the largest fraction of the instantaneous energy balance (about 80%).



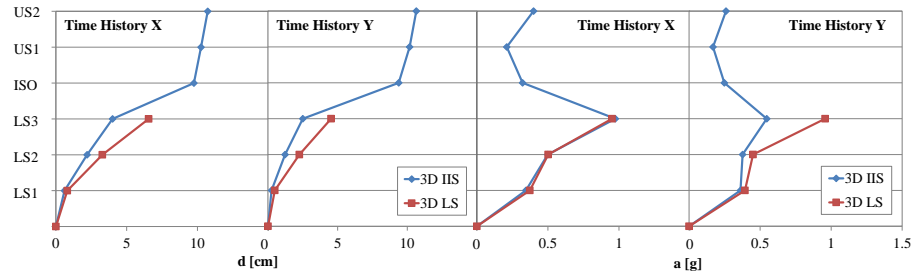


Fig. 7.34. 3D IIS vs. 3D LS: (a) peak relative story displacements, (b) peak absolute story accelerations

## 7.7. CONCLUSIVE REMARKS AND DESIGN IMPLICATIONS

This chapter has explored the properties of the inter-story isolation system (IIS) structures, with particular attention to their application as a seismic retrofit strategy through dynamic analysis of a case study building, an existing three-story masonry structure that have large safety margin with respect to gravity load condition.

For what concerns the theoretical aspect of the subject, substantial differences with respect to the base isolated (BIS) structures have been revealed: in particular, due to the connection between the lower structure and the ground, in a IIS structure higher modes are not ineffective, and cannot be neglected. For the same reasons, modal coupling (MCE) is a typical issue for IIS buildings, even though it depends on the dynamic properties of the lower and upper structure, independently on ISO characteristics, and can be successfully prevented by a careful design.

The simplified 3DOF modal analyses have shown remarkable reductions of the seismic base shear and displacements in the existing lower structure thanks to the Mass Damper Effect (MDE), and reduced accelerations in the upper structure, thanks to the Isolation Effect (IE). Seismic response is minimized for isolation periods not so large; the “perfect” isolation is not as effective as the “non-perfect” one. However, MDE arises when adequate isolation ratio is adopted, namely  $I \geq 3$ .

Modal analysis of the IIS FEM three-dimensional model and of its portions (fixed-base lower structure and base isolated upper structure) confirmed the ability of the isolation layer in keeping uncoupled the modes of vibration of the two portions when the latter are joined into a IIS configuration. Dynamic linear

analyses on the 3D models have confirmed the good level of prediction offered by the simplified 3DOF model analysis. Finally, the time history analyses have shown that the isolation system plays an important role in reducing both the absolute accelerations and the relative displacements of the upper and lower structures.

It is worth noticing that the dynamic analyses are carried out on the three-dimensional models assuming both the structural portions in the elastic range. While this assumption can be considered valid for the upper isolated structure which behaves as a base-isolated structure, for the existing masonry building it could not be valid. In fact, the post-yield behavior of masonry structure may affect the seismic performance of the overall mid-story isolated building.

However, the feasibility analysis carried out considering a real case study has demonstrated that, the IIS technology can be a valid option for the seismic retrofit of existing masonry buildings in good state of conservation and with a large safety margin with respect to the gravity loads.

## 8. CONCLUSIONS

### 8.1. SUMMARY

The Intermediate Isolation System (IIS), also appointed as inter-story or mid-story isolation, is a research topic of great relevance in the seismic risk mitigation and prevention. While IIS is currently spreading and gaining significant popularity, mainly in Japan, its potentials are not so well-known in Italy and the European countries.

The inter-story isolation is realized by placing the isolation layer at a certain level, other than the base, along the height of the building. Therefore, the flexible interface (isolation system, IS) ideally subdivides the building in two main structural portions, i.e. an upper structure (US) and a lower structure (LS) respectively above and below the isolation system.

It is quite intuitive that the presence of the LS causes a more complex dynamic behavior of IIS with respect to a base isolation system (BIS), from which the mid-story isolation derives.

In fact, the IIS combines the strategy of isolation and mass damping: on the one hand the isolation interface acts as a filter for the inertial forces rising to the upper structure, on the other the lower structure shows a reduced response thanks to the mass damping effect exerted by the isolated superstructure.

Differently from the BIS, in the IIS the higher modes not only are effective, but may possess a great fraction of participating mass, leading to an input energy which may be also greater than the corresponding one in a conventional fixed-base building. For this reason, the energy dissipation assumes an important role in the dynamics of such systems.

Furthermore, while the design concepts of base isolation and tuned mass damper (TMD) systems are well established and uniquely shared, the complexity of IIS leads to a variety of approaches both in the formulation of the problem and in the definition of the design objectives and parameters.

In the current scientific literature on this topic, three major conceptual approaches are clearly identified, each mainly focused on one single aspect

of the three ones related to IIS, i.e.: isolation, mass damping and energy dissipation.

The papers focused on the *isolation approach*, mainly investigate the impact of the dynamic interaction between the structural portions (upper and lower structures), and the effect of the higher modes and of their possible coupling (mode coupling effect, MCE).

The research contributions concerning the *mass damping* approach, start from the principle of TMD and take into account the peculiarity of IIS, i.e. the coupling of control and structural function of the US, which works as a “non-conventional” or “building” mass damper.

Finally, considering the *energy dissipation* approach, the isolation interface is designed as a concentrated ED system, quite differently from the design practice that spreads dissipation devices throughout the building elevation; in this perspective, the isolators can be seen as displacement amplification devices for triggering and activating the dissipation mechanism.

From the literature review it is observed that, also considering the same behavioral aspect, different approaches to the dynamic problem of IIS are often provided; further, all dynamic characteristics which affect the dynamic behavior of IIS, are not simultaneously considered. Finally, it is recognized that, while advanced applications of IIS have been already realized, the research mainly focuses on standard models and example of basic structures, evidencing that the real-world of construction industry moves forward much faster than the theoretical realm of research.

These considerations emphasize the need of filling some gaps in the research field, as well as between the research and the real design practice.

In this context, the aims of the present thesis are: to explore the actual and potential applications of IIS; to identify the predominant role among the three behavioral aspects of isolation, mass damping and energy dissipation effects, varying the design parameters in a wide range; and to define design criteria for benefiting from all these aspects.

Therefore, starting from the literature review and the overview of the main real-world applications of IIS, two actual buildings are chosen as case studies and thoroughly analyzed, in order to interpreting the latest design practice in the light of approaches and indications coming from the research. Modal and non-linear time history analyses are carried out on the 1D MDOF models of the two buildings, considering the presence of only

isolators and of both isolators and dampers; fixed-base MDOF models are also utilized for comparison.

From the outcomes of the analyses, two parametric analyses are carried out considering both new and existing buildings.

In the first parametric analysis, all the parameters which affect the dynamics of IIS are varied, namely: the dynamic characteristics of both structural portions; the isolation period; the location of the isolation layer; the mass and stiffness distributions of the upper and lower structures. Modal and time history analyses are carried out on 1D 10DOF IIS models, and fixed-base models are considered for comparison.

The second parametric analysis is aimed at exploring the feasibility of IIS elevation on the roof of an existing three-story masonry building as seismic retrofit strategy: the idea is to exploit the stabilizing effect of additional gravity compression, without increasing, or even decreasing, the seismic base shear, thanks to the mass damper effect exerted by the vertical IIS addition. For this purpose, a simplified 3DOF parametric analysis is proposed to detect the optimal isolated superstructure configuration that minimizes the seismic response of the overall building. Hence, a 3D FEM model is adopted for the detailed analysis of the IIS structure. Linear and non-linear analyses are carried out on both 3DOF and 3D complete models; in addition, models of the isolated upper structure and of the lower structure are considered for comparison.

From the preliminary analyses of the real-world case studies and from the two parametric analyses, the following general conclusions can be derived:

- the mass ratio (i.e. the ratio of the total isolated mass to the lower mass) and the isolation period are the main design parameters;
- the Isolation Effect (IE) on the upper structure is exploited by considering long isolation periods;
- the Mass Damper Effect (MDE) on the lower structure is obtained for shorter isolation periods;
- the Energy Dissipation Effect (EDE) is achieved by considering large mass ratios and high damping in the isolation system;
- the benefit from all the behavioral aspects of isolation, mass damping and energy dissipation are obtained with large mass ratios and adequate isolation periods;

- the improvement of IIS seismic performance is obtained with a very rigid US and a quite rigid LS with respect to the isolation system;
- the coupling of higher vibration modes (MCE) only arises when the first periods of the LS portion and one of the higher periods of the isolated US are very closed, independently on the isolation characteristics; thus, this detrimental effect can be predicted and avoided by a careful design;
- with an US heavier and stiffer than the LS, the MCE is negligible, and the seismic performance of the IIS building is improved;
- the stiffness distribution affects the response of the IIS building more than the mass distribution;
- the mass ratio is more significant than its distribution;
- the damping is strongly affected by the mass ratio, isolation period, mass and stiffness distributions, MCE;
- the IIS design strategy is effective and feasible for both new and existing buildings.

## 8.2. MAJOR RESULTS

The major conclusions already provided in each chapter are briefly recalled in the following.

### *Chapter 2: “BIS, TMD, IIS – theoretical basis”*

By writing the equations of motion of the simplified 2DOF BIS, SDOF + TMD, 3DOF IIS and 2DOF IIS models, it is recognized that, in the IIS models the isolation degree of freedom represents an isolation system for the US, and the set of the US + ISO, a mass damper system for the LS.

### *Chapter 3: “Design practice and applications”*

The IIS strategy is mainly applied in Japan, both for the seismic design of new buildings and for vertical addition in the retrofit of existing buildings. The main information derived from Japanese practice (more than 60 buildings equipped with IIS) are provided as follows:

- the height of the building is increased during the period 1995 ÷ 2007, and a maximum value of 130 m is reached for reinforced concrete buildings;

- the equivalent first period is increased of 0.09 s per year; the range of values is between  $2.5 \div 6.0$  s.
- the more frequent IIS buildings are reinforced concrete buildings;
- the isolation layer is frequently composed of natural rubber bearings and steel dampers;
- the inter-story drift of the upper and lower structures respectively corresponds to  $1/400 \div 1/200$  and  $1/1600$ , while the isolation drift is about 40 cm;
- the shear coefficient of the US and isolation is about  $0.09 \div 0.12$ , while that of the LS is about  $0.2 \div 0.3$ ;
- the mean value of the 1<sup>st</sup> natural period is 3.81 s, about 0.5 seconds longer than that of base isolated buildings;
- the maximum deformation of the isolation story is 33 cm, about 6 cm larger than that of base isolated buildings and the maximum responses of the upper structure are larger than the corresponding ones in base isolated buildings.

In addition, the overview of the main real applications of IIS has shown the wide architectural and structural flexibility as well as the effectiveness of such systems.

*Chapter 4: “Literature overview and discussion”*

The overview of the main scientific papers on intermediate isolation system has shown that:

- the dynamic of IIS is more complex than that of BIS and TMD;
- the higher modes are not negligible;
- the energy dissipation is an important aspect related to IIS;
- the IIS is characterized by not a single, fully shared design approach, but multiple approaches, each referred to one single aspect that characterizes the behavior of IIS, i.e.: isolation, mass damping and energy dissipation.

*Chapter 5: “Analysis of real IIS buildings”*

From the overview of applications provided in Chapter 3, two real-world applications of IIS are chosen as case studies. Starting from the data provided in the literature and from personal communication with the designers of the buildings, detailed numerical analyses of the case studies are carried out; the main results are summarized as follows:

- the real-world case studies are representative of the wide applicability of IIS buildings: different architectural and structural systems for US and LS, which lead to different mass ratios, mass to stiffness ratios of structural portions, irregular mass and stiffness distributions;
- the first building (Iidabashi 1st Building) is an ideal IIS case with a rigid US with respect to the LS, and frequencies of the isolated US and LS well separated from each other and from the isolation frequency, allowing for the decoupling of the higher modes;
- the second building (Shiodome Sumitomo Building) is a non-typical IIS case with a flexible US with respect to the LS, and frequencies of the isolated US and LS not so far to uncouple the higher modes.
- all three behavioral aspects have been clearly identified;
- it is observed that with a large mass ratio (mass of the isolated US to the total mass), the IIS can be designed as an untuned mass damper, since its robustness leads to a reduced response also far from the optimal configuration;
- the 60-70% of the dissipated energy is concentrated in the isolation layer, thanks to the presence of dissipation devices (steel and lead dampers);
- the results of the non-linear analyses are very satisfactory for both buildings.

*Chapter 6: "Parametric analysis"*

The parametric analysis, carried out on MDOF IIS models has shown that:

- the coupling of the higher modes (MCE) causes an amplification of the structural response of both US and LS, as well as a reduction in the isolation effect;
- the MCE depends on the frequencies of the LS and the higher frequencies of the isolated US, but the magnitude of this coupling effect is influenced by the ratio between the frequencies of the US and LS, as standalone structures, with respect to the isolation system;
- With an US stiffer than the isolation, the higher modes of the isolated US are ineffective, thus, even in presence of coupling, these modes are referred to LS only; vice versa, with a quite rigid,



- or even a flexible US than the isolation, the higher modes possess a participant mass attributable to both LS and isolated US;
- the parameter  $\beta$ , defined as the ratio of the  $i$ -th higher frequency of the isolated US and the  $j$ -th frequency of the LS, defines the MCE condition; it is recognized that values between  $0.85 \div 1.15$  lead to the coupling; this situation occurs when the first frequencies of the LS are coupled with the first higher ones of the isolated US;
  - the greatest fraction of coupled participant mass is obtained when there is comparable number of degrees of freedom in the LS and US, which also corresponds to the case in which the coupled frequencies are the first of the LS and of the isolated US;
  - the MCE occurrence decreases as the isolation period increases;
  - the stiffness distribution affects the dynamic behavior of IIS more than the mass distribution; in fact, the total mass, or rather the mass ratio, is more significant than its distribution;
  - by increasing the mass ratio, the control mechanism changes going from the mass damping, the intermediate isolation to the base isolation;
  - by increasing the mass ratio, the robustness of the system increases, leading to a reduced seismic response, regardless of the earthquake frequency content and the optimal system configuration;
  - with a stiffer and heavier US than the LS, the improvement of the seismic performance of the IIS structure is obtained.

#### *Chapter 7: "IIS for retrofit"*

The application of IIS for the vertical addition on an existing masonry three-story building has shown the effectiveness and feasibility of IIS as a seismic retrofit strategy. The main results are provided as follows:

- the simplified parametric analysis, carried out on 3DOF models, has shown that the IIS behavior is related to two main conditions, i.e.: "perfect isolation" and "non-perfect isolation"; for each of these conditions the MCE can be observed;
- in general, it is possible to link the perfect isolation to the isolation effect, and the non-perfect isolation to the mass damping effect;
- the damping can be differently defined in presence of perfect and non-perfect isolation;

- considering the IIS vertical addition as a seismic retrofit strategy for a masonry existing building, for mass ratios lower than 1 and adequate isolation periods (about of 2 s), it is observed that the non-perfect isolation reduces the seismic response more than the perfect isolation;
- the simplified 3DOF models offer a good prediction of the seismic behavior of the IIS building, compared to that of the more refined 3D models.

### 8.3. DESIGN IMPLICATIONS

The major design implications coming from the analyses carried out in the thesis are provided in the following in terms of periods, mass ratio, damping.

The periods of upper and lower portions, as standalone structures, and the isolation period, as well as their dynamic interaction, give helpful insights into the dynamic behavior of IIS structures.

While the ratio between the periods of the ISO system and US influences the local behavior of the isolated US, the ratio between the periods of the ISO system and LS affects the global behavior of IIS structures.

The set of US and ISO behaves as a BIS if the isolation ratio  $I$  between the isolation and US periods, i.e.  $I = T_{ISO}/T_{US}$ , is greater than 1. In order to consider the US rigid with respect to the isolation system,  $I$  must be greater than 3. It is worth noticing that when  $I = 1$  the participating mass of the higher modes of the isolated US is significant (say, larger than 5%); on the contrary, when  $I \geq 3$ , it is negligible, and the isolated US behaves as an ideal base isolated structure.

With regards to the interaction between the LS and ISO system, when the isolation period is at least 3 times larger than the LS period, i.e. when the LS is much stiffer than the isolation system, the first mode of the IIS structure shows displacement mainly concentrated in the isolated US, leading to the isolation effect. If the isolation period is  $1 \div 2$  times larger than the LS period, the LS is quite rigid with respect to the isolation system and participates to the IIS fundamental mode, suggesting the mass damping effect. It is worth noticing that if the isolation period is smaller than the LS period, the IIS structure behaves as a fixed-base structure.

With a stiffer US than the ISO system ( $I \geq 3$ ), considering the dynamic interaction between the three parts (LS, ISO, US), the *perfect isolation* is obtained if the ratio of the periods of US and LS are well separated from the isolation period (say,  $3 \div 15$  times); on the contrary, the *non-perfect isolation* is reached if the periods of US and LS are respectively well separated and not so far from the isolation period (say,  $1 \div 2$  times).

The main differences between the two conditions are related to the participating mass of the fundamental mode and the LS mode of vibration: with the perfect isolation these masses are almost equal to the total isolated mass and the LS mass; with the non-perfect isolation the first participating mass is larger than the total isolated mass while the mass of the LS mode is smaller than LS mass. In the latter case the LS participates to the first mode subtracting mass to the LS mode with a consequentially reduction of the base shear in the controlled configuration with respect to the uncontrolled one.

Looking at the dynamic interaction between the structural portions of the IIS (i.e. the isolated US and the LS), when one or more LS periods are almost equal to one or more higher periods of the isolated US, the mode coupling of the higher modes, MCE, occurs. For  $I \geq 3$ , the MCE can be reached in presence of either perfect isolation or non-perfect isolation. In particular, with non-perfect isolation, since the LS contributes to the first IIS mode, the participating mass of the higher modes is smaller than the case of perfect isolation. In addition, with a stiffer US than the isolation system (i.e.  $I \geq 3$ ), the participating mass of the isolated US higher modes is negligible, and thus, the participating mass of the IIS higher modes is only related to the LS contribution; on the contrary, when the US is as flexible as the isolation system, i.e.  $I \approx 1$ , the higher participating mass is referred to both US and LS.

The MCE can be predicted by a careful design, by applying the following simple design rule: “*No MCE arises if the first periods of the LS are far from one or more higher periods of the isolated US*”.

This principle can be translated in an analytical formulation through the MCE parameter  $\beta$ , defined for both MDOF IIS, see formula (6.18), and 3DOF IIS models, see formula (6.20).

If  $\beta$  is in the range  $0.85 \div 1.15$ , the mode coupling of the higher modes occurs.

The mass ratio  $\alpha$  of the total isolated mass to the LS mass, i.e.  $\alpha = M_{\text{ISO}}/m_{\text{LS}}$ , seems to be the major parameter of the IIS dynamics, since it defines the prevailing behavioral aspect, and allows to identify the

governing principle among mass damping, intermediate isolation and energy dissipation, base isolation.

A simple chart (Fig. 8.1) that can be useful for design purpose has been created, showing that, for  $\alpha \leq 1$  the mass damping effect prevails, while for  $\alpha = 1 \div 4$  the structure is affected by both isolation and energy dissipation that characterized the IIS system.

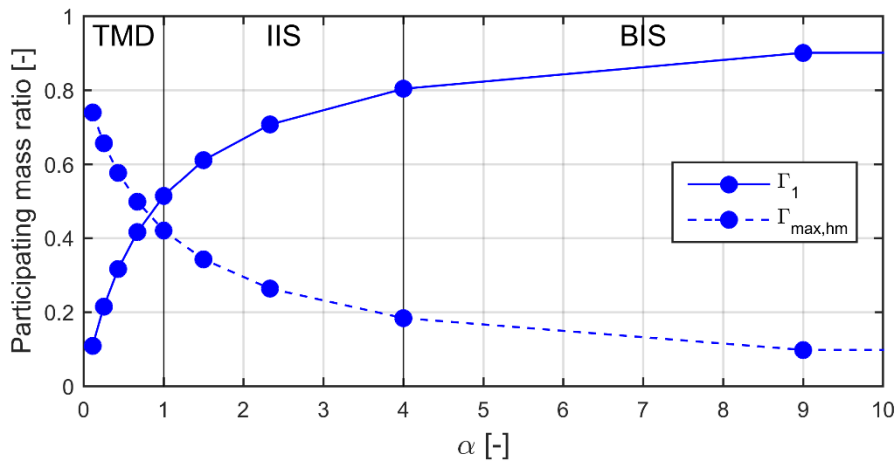


Fig. 8.1. Participating mass vs. the mass ratio  $\alpha$

It is worth observing that increasing the mass ratio, the robustness of IIS increases: a large mass ratio provides greater reduction of the structural response, the system becomes less dependent on the frequency content and on the optimal configuration. In addition, with large mass ratios the energy dissipated by the isolation system increases.

In terms of damping, the IIS structures are characterized by non-proportional damping. However, depending on the dynamic characteristics of the structural portions and the isolation system, it is possible to consider a simplified or a rigorous approach. In the simplified approach, the first damping ratio of the IIS structure can be assumed equal to the isolation counterpart while the higher damping ratios equal to the structural damping ratio; in the rigorous approach, the complex modal values should be utilized. In particular, the simplified approach can be used in presence of perfect isolation while the rigorous approach in presence of non-perfect isolation and MCE.

## REFERENCES

- Akiyama H (1985). Earthquake-Resistant Limit-State Design for Buildings; University of Tokyo Press.
- Akiyama H (1988). Earthquake Resistant design based on the energy concept. *Proceeding of the 9<sup>th</sup> World Conference on Earthquake Engineering*, August 2 – August 9. Tokyo – Kyoto, Japan; vol. V: 905-910.
- Ayorinde E, Warburton G (1980). Minimizing structural vibrations with absorbers. *Earthquake Engineering and Structural Dynamics*; 8:219–236.
- Chang KC, Hwang JS, Wang SJ, Lee BH, Chen YH (2012). Seismic Behavior of Structures with Building Mass Damper Design. *Proceedings of the 15<sup>th</sup> World Conference on Earthquake Engineering*. Lisboa; paper 1022.
- Chey M, Chase JG, Mander JB, Carr AJ (2013). Innovative seismic retrofitting strategy of added stories isolation system. *Frontiers of Structural and Civil Engineering*; 7:13-23.
- China Basin Addition (2008). Base Isolation. Earthquake Protection Technology.
- Connor J and Laflamme S (2014), *Structural Motion Engineering*, Springer.
- Consiglio Superiore Lavori Pubblici, D.M. 14/01/2008 “Norme Tecniche per le Costruzioni”, Gazzetta Ufficiale della Repubblica Italiana, Numero 29, S.O., 04/02/2008.
- De Angelis M, Perno S, Reggio A (2012). Dynamic response and optimal design of structures with large mass ratio TMD. *Earthquake Engineering and Structural Dynamics*; 41:41-60.

---

Den Hartog (1945). *Mechanical Vibrations*. New York and London. McGraw-Hill Book Company.

Dutta A, Sumnicht JF, Mayes RL, Hamburger RO, Citipitioglu A (2009). An Innovative Application of Base Isolation Technology. *ATC & SEI Conference on Improving the Seismic Performance of Existing Buildings and Other Structures*. 841-854.

Feng M, Mita A (1995). Vibration control of tall buildings using Mega Subconfiguration. *Journal of Engineering Mechanics*; 10:1082–1088.

Foti D, Mongelli M (2011). *Isolatori sismici per edifici esistenti e di nuova costruzione, Principi fondamentali – Criteri di progettazione - Dettagli costruttivi*, Dario Flaccovio Editore.

Gherzi A, Lenza P, Calderoni B (2011), *Edifici in muratura alla luce della nuova normativa sismica*, Dario Flaccovio Editore.

Hoang N, Fujino Y, Warnitchai P (2007). Optimal tuned mass damper for seismic applications and practical design formulas. *Engineering Structures*; 30:707–715.

Ishiyama Y (2011). Introduction to Earthquake Engineering and Seismic Codes in the World. Lecture note, Hokkaido University, pp. 1-115.

Kani N, Takayama M, Wada A (2006) Performance of Seismically Isolated Building in Japan. *Proceedings of the 8<sup>th</sup> U.S. National Conference on Earthquake Engineering*, San Francisco, California, USA; paper 2181.

Kelly JM (1990), Base isolation: Linear theory and design, *Earthquake Spectra*, 1990; 6(2): 223–244.

Kelly JM (1997) *Earthquake Resistant Design with Rubber*, Springer-Verlag: London.

---

Kobayashi M and Koh T (2008), Modal coupling effects of mid-story isolated buildings, *Proceedings of the 14th World Conference of Earthquake Engineering*, Beijing, China, (12-17/10).

Kobayashi M, Sasaki D (2009). Making a Seismic Design Database of Mid-story Isolated Buildings and Structural Property Evaluation based on Response Prediction Method. *Journal of Structural Construction Engineering*, AIJ; 15:65-70.

Moutinho C (2012). An alternative methodology for designing tuned mass dampers to reduce seismic vibrations in building structures. *Earthquake Engineering and Structural Dynamics*; 41:2059-2073.

Masatoshi T, Tadashi Y, Masato M, Nobuyuki A, Masataka N (2017). Structural Design and Performance Evaluation of a Mid-story Seismic Isolated High-Rise Building. *International Journal of High-Rise Buildings*. September 2017. Vol 6, 3:227-235.

Miyazaki M, Nakano K, Kitagawa Y, Shimoda I, Mitsusaka Y (1988). Design and its performance verification of a base-isolated building using Lead Ruber Bearings in Japan. *Proceedings of the 9<sup>th</sup> World Conference on Earthquake Engineering*. Tokyo-Kyoto, Japan (Vol. V), pp. 717-722.

Miyazaki M (2008). The Next Generation of Seismic Isolation Going Beyond Seismic Design Dominated by Earthquakes. *Journal of Disaster Research*. Vol.3. 6:479-502.

Moriizumi E, Kobayashi M (2012). A study on Earthquake Response Considered Vibration Characteristics of Superstructure and Substructure of Seismically Isolated Buildings. *Proceedings of the 15<sup>th</sup> World Conference on Earthquake Engineering*. Lisboa; paper 1792.

Murakami K, Kitamura H, Ozaki H, Teramoto T (2000). Design and Analysis of a Building with the Middle-story Isolation Structural System.

---

*Proceedings of the 12<sup>th</sup> World Conference on Earthquake Engineering*. Auckland, New Zealand; paper 0857.

Murakami K. (2001). A study on the Prediction for Seismic Responses of Structures with the Mid-story Isolation System. PhD Thesis, University of Tsukuba.

Murakami K & Sueoka T (2004). Proposal of a seismic design method for mid-story isolated structural system using a two-mass analysis model. *Proceeding of International Symposium of Network and Center-Based Research for Smart Structures Technologies and Earthquake Engineering*, Osaka, Japan, SE04-075.

Naeim F, Kelly J (1999) *Design of Seismic Isolated Structures: From Theory to Practice*, John Wiley and Sons, Inc.:New York, NY, USA.

Nakagawa K, Shimazaki D, Yoshida S, Okada K (2015). Application of Seismic Isolation Systems In Japanese High-Rise Buildings. *International Journal of High-Rise Buildings*. Seismic Design Issue II. 36-38.

Nakai M (2008). Unique Architectural Forms Enabled by Base-Isolation. *Proceedings of the 14<sup>th</sup> World Conference on Earthquake Engineering*. Beijing, China

Nakai M, Tanno Y, Kozuka H, Ohata M (2009). Iconic Architectural Forms Enabled by Base-Isolation. *Journal of Disaster Research*, Vol. 4 n. 3.

Nakamura Y, Saito T, Tamura K (2009). A seismic isolated long-span overhanging urban infrastructure. *Journal of Disaster Research*, Vol. 4 n. 3.

Nakamura Y, Hanzawa T, Hasebe M, Okada K, Kaneko M, Saruta M (2011). Report on the Effects of Seismic Isolation Methods from the 2011 Tohoku–Pacific Earthquake. Seismic Isolation and Protection Systems. *Journal of the Anti-Seismic Systems International Society ASSISi*; 2:57-74.



---

Nakashima M, Pan P, Zamfirescu D, Weitzmann D (2004) Post-Kobe approach for design and construction of base-isolated buildings. *Journal of Japan Association for Earthquake Engineering*; 4:259-264.

Nikken Journal (2013). Spring. 14: 1-23.

Okada K, Nakamura Y, Saruta M (2009). Application of earthquake early warning system to seismic – isolated buildings. *Journal of Disaster Research*, Vol. 4 n. 4.

Okada K, Yoshida S (2014). Structural Design of Nakanoshima Festival Tower. September 2014. Vol 4, 3:173-183.

Ping T, Zhang Y, Zhou F (2008). Optimal Design and Control Mechanism Study on Story Isolation System. *Proceedings of the 14<sup>th</sup> World Conference on Earthquake Engineering*. Beijing China; paper 0060.

Rainieri C and Fabbrocino, G (2014), *Operational Modal Analysis of Civil Engineering Structures*, Springer.

Reggio A, De Angelis M (2014). Optimization of a Non-Conventional TMD implemented via Inter-story Isolation. *Proceedings of the EUROLYN 2014 – IX International Conference of Structural Dynamics*; Porto, Portugal, June 30 – July 2.

Reggio A, De Angelis M (2015). Optimal Energy-based Seismic Design of Non-Conventional Tuned Mass Damper (TMD) implemented via Inter-story Isolation. *Earthquake Engineering and Structural Dynamics*; 44:1623–1642.

Ryan KL, Earl CL (2010). Analysis and design of inter-story isolation systems with nonlinear devices. *Journal of Earthquake Engineering*; 14:1044-1062.

---

Sadek F, Mohraz B, Taylor AW, Chung RM (1997). A method of estimating the parameters of tuned mass dampers for seismic applications. *Earthquake Engineering and Structural Dynamics*; 26:617-635.

Saito T, Iiba M, Morita K, Azuhata T, Inoue N (2013) Performance of Seismically Isolated Buildings at March 11, 2011, Tohoku Earthquake. *Proceedings of the 19<sup>th</sup> CIB World Building Congress*, Brisbane, paper 62.

Shellenberg AH, Becker TC, Mahin SA (2016). Hybrid shake table testing method: Theory, implementation and application to midlevel isolation. *Structural Control and Health Monitoring*

Skinner RI, Robinson WH, McVerry\_GH (1993), *An introduction to Seismic Isolation*, John Wiley & Sons Ltd.

Software SAP2000 CSI Italia srl, <http://www.csi-italia.eu/software/sap2000/>

Software SIMQKE\_GR.exe (versione 2.7), [http://gelfi.unibs.it/software/simqke/simqke\\_gr.htm](http://gelfi.unibs.it/software/simqke/simqke_gr.htm)

Sueoka T, Torii S, Tsuneki Y (2004). The Application of Response Control Design using Middle-story Isolation System to High-Rise Building. *Proceedings of the 13<sup>th</sup> World Conference on Earthquake Engineering*. Vancouver, B.C., Canada; paper 3457.

Sumnicht JF (2008). On the Grid. *Modern Steel Construction*.

Takayama M, Morita K (2012) Seismic Response Analysis of Seismic Isolated Buildings using Observed Records due to 2011 Tohoku Earthquake. *Proceedings of the 15<sup>th</sup> World Conference on Earthquake Engineering*. Lisboa; paper 0403.

Tasaka M, Mori N, Yamamoto H, Murakami K, Sueoka T (2008). Applying Seismic Isolation to Buildings in Japan-Retrofitting and Middle-story Isolation. *18th Analysis and Computation Specialty Conference*, ASCE.

---

Tsuneki Y, Torii S, Murakami K, Sueoka T (2008). Middle-story Isolated Structural System of High-Rise Building. *Proceedings of the 14<sup>th</sup> World Conference on Earthquake Engineering*. Beijing, China; paper S05-01-023.f

Tsuneki Y, Torii S, Murakami K, Sueoka T (2009). Middle-Story Isolated Structural System of High-Rise Building. *Journal of Disaster Research*; 4:229-238.

Veletsos AS and Ventura CE (1986), Modal Analysis of non-classically damped linear systems, *Earthquake Engineering and Structural Dynamics*, 14, 217–243.

Villaverde R (1985). Reduction seismic response with heavily-damped vibration absorbers. *Earthquake Engineering and Structural Dynamics*. 13: 33-42.

Villaverde R (2002). Aseismic Roof Isolation System: Feasibility Study with 13-story Building. *Journal of Structural Engineering*. 128 (2): 188-196.

Wang SJ, Chang KC, Hwang JS, Lee BH (2011). Simplified analysis of mid-story seismically isolated buildings. *Earthquake Engineering and Structural Dynamics*; 40: 119–133.

Wang SJ, Chang KC, Hwang JS, Hsiao JY, Lee BH, Hung YC (2012a). Dynamic Behavior of a Building Structure Tested with Base and Mid-story Isolation Systems. *Engineering Structures*; 42:420-433.

Wang SJ, Hwang JS, Chang KC, Lin MH, Lee BH (2013). Analytical and Experimental Studies on Midstory Isolated Buildings with Modal Coupling Effect. *Earthquake Engineering and Structural Dynamics*; 42:201–219.

Wang SJ, Hwang JS, Chang KC, Lin MH, Lee BH (2013). Analytical and Experimental Studies on Midstory Isolated Buildings with Modal Coupling Effect. *Earthquake Engineering and Structural Dynamics*; 42:201–219.

---

Wang SJ, Lee BH, Chang YW, Chang KC, Yu KH, Hwang JS (2017). Optimum Dynamic Characteristic Control Approach for Building Mass Damper Design. *15<sup>th</sup> World Conference on Seismic Isolation, Energy Dissipation and Active Vibration Control of Structures*. April 27 – April 29, Wellington, New Zealand.

Yamaguchi S, Akiyama H, Wada A, Nakazawa T (1993). Seismic Isolation System Design Procedure in Japan and its Comparison to the U.S.. *Proceeding of ATC-17-1 Seminar on Seismic Isolation, Passive Energy Dissipation, and Active Control*. March 11 – March 12, San Francisco, California; 435-446.

Zhou Q, Singh MP, Huang XY (2016). Model reduction of mid-story isolation systems. *Engineering Structures*; 124:36-48.

Ziayaeifar M, Noguchi T (1998). Partial mass isolation in tall buildings. *Earthquake Engineering and Structural Dynamics*; 27:49–65.

## APPENDIX A: IIS for retrofit

In Appendix A are provided insights about Chapter 7, i.e. “IIS for retrofit”, in terms of modal, response spectrum and time history analyses of the 3DOF IIS models. The main design parameters are recalled here for completeness:

- Mass ratio between the total isolated mass,  $M_{ISO}$ , and the lower structure mass,  $m_{LS}$  :

$$\alpha = \frac{M_{ISO}}{m_{LS}}$$

- Stiffness ratio between the stiffness of the upper structure,  $k_{US}$ , and the stiffness of lower structure,  $k_{LS}$  :

$$K = \frac{k_{US}}{k_{LS}}$$

- Isolation ratio between the isolation period,  $T_{ISO}$ , and the period of the upper structure,  $T_{US}$  :

$$I = \frac{T_{ISO}}{T_{US}}$$

### A.1. MODAL ANALYSIS

Figs. A.1 ÷ A.12 and Tabs. A.1 ÷ A.12 show the modal properties of both undamped and non-proportionally damped 3DOF IIS models for the cases  $\alpha = \{0.1, 0.5, 0.6, 1.0\}$  -  $K = \{0.1, 0.3, 0.5, 1\}$  -  $I = \{3, 4, 5\}$ . The non-proportionally damped systems refers to two conditions: 1) constant damping ratio,  $\xi = 0.05$ ; 2) damping ratio interpolated as a function of the period  $T$  ( $\xi_1 = \xi_{ISO} = 0.10$  at  $T = T_1$  and  $\xi_2 = \xi_{LS} = \xi_{US} = 0.05$  at  $T = T_2$ ), see § 7.4.3. In particular, Tabs. A.1 ÷ A.3 refer to the undamped 3DOF IIS models; Tabs. A.4 ÷ A.8 and Tabs. A.9 ÷ A.12 consider the damped 3DOF IIS models under condition 1 and 2, respectively. Analogously, Figs. A.1 ÷ A.4 depict the natural modes of vibrations of the cases considered

herein; Figs. A.5 ÷ A.8 and A.9 ÷ A.12 show the complexity plots of the damped 3DOF IIS models under condition 1 and 2, respectively.

**Table A.1. Undamped 3DOF IIS -  $\alpha=0.1$  –  $K=0.1; 0.3; 0.5; 1.0$  –  $I=3; 4; 5$**

$\alpha=0.1$	mode	K=0.1		K=0.3		K=0.5		K=1.0	
		T	$\Gamma$	T	$\Gamma$	T	$\Gamma$	T	$\Gamma$
		[s]	[-]	[s]	[-]	[s]	[-]	[s]	[-]
I=3	1	1.964	0.131	1.176	0.302	0.980	0.613	0.884	0.942
	2	0.801	0.869	0.772	0.698	0.718	0.387	0.563	0.058
	3	0.383	0.000	0.221	0.000	0.171	0.000	0.121	0.000
I=4	1	2.568	0.112	1.505	0.177	1.194	0.290	0.946	0.722
	2	0.804	0.888	0.792	0.823	0.774	0.710	0.690	0.278
	3	0.389	0.000	0.224	0.000	0.174	0.000	0.123	0.000
I=5	1	3.182	0.104	1.852	0.138	1.451	0.187	1.075	0.412
		0.806	0.896	0.799	0.862	0.790	0.813	0.754	0.588
	2	0.391	0.000	0.226	0.000	0.175	0.000	0.124	0.000

**Table A.2. Undamped 3DOF IIS -  $\alpha=0.5$  –  $K=0.1; 0.3; 0.5; 1.0$  –  $I=3; 4; 5$**

$\alpha=0.5$	mode	K=0.1		K=0.3		K=0.5		K=1.0	
		T	$\Gamma$	T	$\Gamma$	T	$\Gamma$	T	$\Gamma$
		[s]	[-]	[s]	[-]	[s]	[-]	[s]	[-]
I=3	1	5.163	0.350	3.021	0.385	2.373	0.422	1.746	0.520
	2	0.805	0.648	0.794	0.615	0.782	0.578	0.752	0.480
	3	0.666	0.002	0.385	0.000	0.298	0.000	0.211	0.000
I=4	1	6.735	0.343	3.918	0.363	3.059	0.384	2.209	0.439
	2	0.806	0.656	0.800	0.637	0.794	0.616	0.777	0.561
	3	0.680	0.001	0.393	0.000	0.304	0.000	0.215	0.000
I=5	1	8.333	0.340	4.835	0.353	3.764	0.366	2.696	0.400
		0.807	0.660	0.803	0.647	0.799	0.634	0.789	0.600
	2	0.686	0.001	0.396	0.000	0.307	0.000	0.217	0.000

**Table A.3. Undamped 3DOF IIS -  $\alpha=0.6$  – K=0.1; 0.3; 0.5; 1.0 – I=3; 4; 5**

$\alpha=0.6$	mode	K=0.1		K=0.3		K=0.5		K=1.0	
		T	$\Gamma$	T	$\Gamma$	T	$\Gamma$	T	$\Gamma$
		[s]	[-]	[s]	[-]	[s]	[-]	[s]	[-]
I=3	1	5.400	0.391	3.163	0.427	2.488	0.464	1.834	0.558
	2	0.831	0.141	0.792	0.573	0.780	0.536	0.749	0.442
	3	0.796	0.468	0.475	0.000	0.368	0.000	0.260	0.000
I=4	1	7.053	0.385	4.106	0.405	3.207	0.426	2.320	0.480
	2	0.840	0.037	0.799	0.595	0.792	0.574	0.775	0.520
	3	0.804	0.578	0.484	0.000	0.375	0.000	0.265	0.000
I=5	1	8.731	0.381	5.067	0.395	3.947	0.408	2.830	0.442
		0.846	0.013	0.803	0.605	0.798	0.592	0.787	0.558
	2	0.806	0.606	0.488	0.000	0.378	0.000	0.267	0.000

**Table A.4. Undamped 3DOF IIS -  $\alpha=1.0$  – K=0.1; 0.3; 0.5; 1.0 – I=3; 4; 5**

$\alpha=1.0$	mode	K=0.1		K=0.3		K=0.5		K=1.0	
		T	$\Gamma$	T	$\Gamma$	T	$\Gamma$	T	$\Gamma$
		[s]	[-]	[s]	[-]	[s]	[-]	[s]	[-]
I=3	1	7.300	0.512	4.269	0.536	3.350	0.561	2.449	0.620
	2	0.946	0.010	0.795	0.463	0.784	0.439	0.758	0.380
	3	0.802	0.478	0.544	0.001	0.422	0.000	0.298	0.000
I=4	1	9.525	0.507	5.540	0.522	4.323	0.536	3.116	0.572
	2	0.963	0.003	0.800	0.478	0.794	0.464	0.779	0.428
	3	0.805	0.490	0.555	0.000	0.430	0.000	0.304	0.000
I=5	1	11.785	0.505	6.837	0.514	5.321	0.524	3.809	0.547
		0.971	0.001	0.803	0.486	0.799	0.476	0.790	0.453
	2	0.807	0.494	0.560	0.000	0.434	0.000	0.307	0.000

**Table A.5. Damped 3DOF IIS ( $\xi=0.05$ ) -  $\alpha=0.1$  –  $K=0.1; 0.3; 0.5; 1.0$  –  $I=3; 4; 5$** 

$\alpha=0.1$	mode	K=0.1		K=0.3		K=0.5		K=1.0	
		T	$\eta$	T	$\eta$	T	$\eta$	T	$\eta$
		[s]	[-]	[s]	[-]	[s]	[-]	[s]	[-]
I=3	1	1.964	0.045	1.176	0.043	0.980	0.041	0.884	0.044
	2	0.801	0.052	0.772	0.055	0.717	0.056	0.563	0.053
	3	0.383	0.093	0.221	0.093	0.171	0.093	0.121	0.093
I=4	1	2.568	0.047	1.505	0.046	1.194	0.044	0.946	0.042
	2	0.804	0.051	0.792	0.053	0.774	0.055	0.690	0.057
	3	0.389	0.090	0.225	0.090	0.174	0.090	0.123	0.090
I=5	1	3.181	0.048	1.852	0.047	1.451	0.046	1.075	0.043
		0.806	0.051	0.799	0.052	0.790	0.053	0.754	0.056
	2	0.392	0.088	0.226	0.088	0.175	0.088	0.124	0.088

**Table A.6. Damped 3DOF IIS ( $\xi=0.05$ ) -  $\alpha=0.5$  –  $K=0.1; 0.3; 0.5; 1.0$  –  $I=3; 4; 5$** 

$\alpha=0.5$	mode	K=0.1		K=0.3		K=0.5		K=1.0	
		T	$\eta$	T	$\eta$	T	$\eta$	T	$\eta$
		[s]	[-]	[s]	[-]	[s]	[-]	[s]	[-]
I=3	1	5.161	0.044	3.020	0.042	2.373	0.041	1.745	0.044
	2	0.667	0.076	0.793	0.055	0.782	0.057	0.752	0.076
	3	0.804	0.052	0.385	0.075	0.298	0.075	0.211	0.052
I=4	1	6.734	0.046	3.917	0.045	3.058	0.044	2.209	0.046
	2	0.806	0.052	0.800	0.054	0.794	0.056	0.777	0.052
	3	0.680	0.068	0.393	0.068	0.304	0.068	0.215	0.068
I=5	1	8.332	0.047	4.834	0.047	3.763	0.046	2.696	0.047
		0.686	0.064	0.803	0.054	0.799	0.055	0.789	0.064
	2	0.807	0.052	0.396	0.063	0.307	0.063	0.217	0.052



**Table A.7. Damped 3DOF IIS ( $\xi=0.05$ ) -  $\alpha=0.6$  -  $K=0.1; 0.3; 0.5; 1.0$  -  $I=3; 4; 5$** 

$\alpha=0.6$	mode	K=0.1		K=0.3		K=0.5		K=1.0	
		T	$\eta$	T	$\eta$	T	$\eta$	T	$\eta$
		[s]	[-]	[s]	[-]	[s]	[-]	[s]	[-]
I=3	1	5.399	0.044	3.162	0.042	2.487	0.041	1.833	0.038
	2	0.830	0.050	0.792	0.056	0.780	0.058	0.748	0.062
	3	0.797	0.064	0.475	0.061	0.368	0.061	0.260	0.061
I=4	1	7.051	0.046	4.105	0.045	3.207	0.044	2.319	0.042
	2	0.839	0.051	0.799	0.055	0.792	0.057	0.775	0.060
	3	0.805	0.057	0.484	0.055	0.375	0.055	0.265	0.055
I=5	1	8.729	0.048	5.067	0.047	3.946	0.046	2.830	0.045
		0.845	0.049	0.803	0.054	0.798	0.056	0.787	0.058
	2	0.807	0.054	0.488	0.051	0.378	0.051	0.267	0.051

**Table A.8. Damped 3DOF IIS ( $\xi=0.05$ ) -  $\alpha=1.0$  -  $K=0.1; 0.3; 0.5; 1.0$  -  $I=3; 4; 5$** 

$\alpha=1.0$	mode	K=0.1		K=0.3		K=0.5		K=1.0	
		T	$\eta$	T	$\eta$	T	$\eta$	T	$\eta$
		[s]	[-]	[s]	[-]	[s]	[-]	[s]	[-]
I=3	1	7.298	0.043	4.267	0.042	3.348	0.041	2.448	0.038
	2	0.945	0.059	0.794	0.057	0.784	0.059	0.758	0.064
	3	0.803	0.058	0.545	0.064	0.422	0.064	0.298	0.063
I=4	1	9.523	0.046	5.539	0.045	4.322	0.044	3.115	0.042
	2	0.962	0.054	0.800	0.056	0.794	0.058	0.779	0.061
	3	0.806	0.055	0.555	0.056	0.430	0.056	0.304	0.055
I=5	1	11.783	0.047	6.835	0.047	5.320	0.046	3.808	0.045
		0.971	0.050	0.803	0.055	0.799	0.057	0.790	0.060
	2	0.807	0.054	0.561	0.051	0.434	0.051	0.307	0.051

**Table A.9. Damped 3DOF IIS ( $\xi_{LS} = \xi_{US} = 0.05$ ;  $\xi_{ISO} = 0.10$ ) -  $\alpha = 0.1$  -  $K = 0.1$ ;  $0.3$ ;  $0.5$ ;  $1.0$  -  $I = 3$ ;  $4$ ;  $5$** 

$\alpha = 0.1$	mode	K=0.1		K=0.3		K=0.5		K=1.0	
		T	$\eta$	T	$\eta$	T	$\eta$	T	$\eta$
		[s]	[-]	[s]	[-]	[s]	[-]	[s]	[-]
I=3	1	1.962	0.089	1.174	0.079	0.978	0.063	0.883	0.048
	2	0.801	0.055	0.773	0.065	0.718	0.081	0.562	0.096
	3	0.383	0.110	0.221	0.110	0.171	0.110	0.121	0.110
I=4	1	2.566	0.093	1.504	0.089	1.192	0.083	0.945	0.059
	2	0.804	0.053	0.793	0.058	0.775	0.065	0.691	0.089
	3	0.389	0.102	0.225	0.102	0.174	0.102	0.123	0.102
I=5	1	3.180	0.096	1.851	0.093	1.449	0.090	1.073	0.077
		0.806	0.053	0.800	0.056	0.791	0.059	0.756	0.073
	2	0.392	0.098	0.226	0.098	0.175	0.098	0.124	0.098

**Table A.10. Damped 3DOF IIS ( $\xi_{LS} = \xi_{US} = 0.05$ ;  $\xi_{ISO} = 0.10$ ) -  $\alpha = 0.5$  -  $K = 0.1$ ;  $0.3$ ;  $0.5$ ;  $1.0$  -  $I = 3$ ;  $4$ ;  $5$** 

$\alpha = 0.5$	mode	K=0.1		K=0.3		K=0.5		K=1.0	
		T	$\Gamma$	T	$\Gamma$	T	$\Gamma$	T	$\Gamma$
		[s]	[-]	[s]	[-]	[s]	[-]	[s]	[-]
I=3	1	5.155	0.086	3.016	0.083	2.369	0.080	1.742	0.072
	2	0.804	0.054	0.793	0.062	0.782	0.066	0.752	0.076
	3	0.668	0.110	0.386	0.108	0.299	0.108	0.211	0.108
I=4	1	6.729	0.092	3.914	0.090	3.055	0.088	2.206	0.083
	2	0.681	0.093	0.800	0.060	0.794	0.063	0.777	0.070
	3	0.805	0.054	0.393	0.092	0.305	0.092	0.215	0.092
I=5	1	8.328	0.095	4.831	0.093	3.760	0.092	2.693	0.089
		0.806	0.054	0.803	0.058	0.799	0.060	0.789	0.066
	2	0.687	0.084	0.397	0.083	0.307	0.083	0.217	0.083

**Table A.11. Damped 3DOF IIS ( $\xi_{LS} = \xi_{US} = 0.05$ ;  $\xi_{ISO} = 0.10$ ) -  $\alpha = 0.6$  -  $K = 0.1$ ;  $0.3$ ;  $0.5$ ;  $1.0$  -  $I = 3$ ;  $4$ ;  $5$** 

$\alpha = 0.6$	mode	K=0.1		K=0.3		K=0.5		K=1.0	
		T	$\eta$	T	$\eta$	T	$\eta$	T	$\eta$
		[s]	[-]	[s]	[-]	[s]	[-]	[s]	[-]
I=3	1	5.393	0.087	3.158	0.084	2.483	0.080	1.830	0.072
	2	0.823	0.056	0.792	0.063	0.780	0.068	0.749	0.079
	3	0.805	0.089	0.476	0.088	0.369	0.087	0.261	0.087
I=4	1	7.047	0.092	4.101	0.090	3.203	0.088	2.316	0.083
	2	0.833	0.066	0.799	0.061	0.792	0.065	0.775	0.072
	3	0.811	0.064	0.485	0.074	0.375	0.074	0.265	0.074
I=5	1	8.725	0.095	5.064	0.094	3.943	0.092	2.827	0.089
		0.843	0.063	0.802	0.059	0.798	0.062	0.787	0.068
	2	0.810	0.058	0.488	0.067	0.378	0.067	0.267	0.067

**Table A.12. Damped 3DOF IIS ( $\xi_{LS} = \xi_{US} = 0.05$ ;  $\xi_{ISO} = 0.10$ ) -  $\alpha = 1.0$  -  $K = 0.1$ ;  $0.3$ ;  $0.5$ ;  $1.0$  -  $I = 3$ ;  $4$ ;  $5$** 

$\alpha = 1.0$	mode	K=0.1		K=0.3		K=0.5		K=1.0	
		T	$\Gamma$	T	$\Gamma$	T	$\Gamma$	T	$\Gamma$
		[s]	[-]	[s]	[-]	[s]	[-]	[s]	[-]
I=3	1	7.290	0.086	4.262	0.083	3.344	0.080	2.444	0.073
	2	0.942	0.089	0.793	0.064	0.783	0.070	0.758	0.081
	3	0.806	0.066	0.546	0.098	0.423	0.097	0.299	0.096
I=4	1	9.516	0.092	5.534	0.090	4.318	0.088	3.111	0.084
	2	0.961	0.077	0.799	0.062	0.794	0.067	0.779	0.075
	3	0.807	0.060	0.557	0.081	0.431	0.080	0.305	0.080
I=5	1	11.777	0.095	6.831	0.093	5.316	0.092	3.804	0.089
		0.970	0.068	0.802	0.061	0.799	0.064	0.790	0.071
	2	0.808	0.058	0.561	0.071	0.435	0.070	0.307	0.070

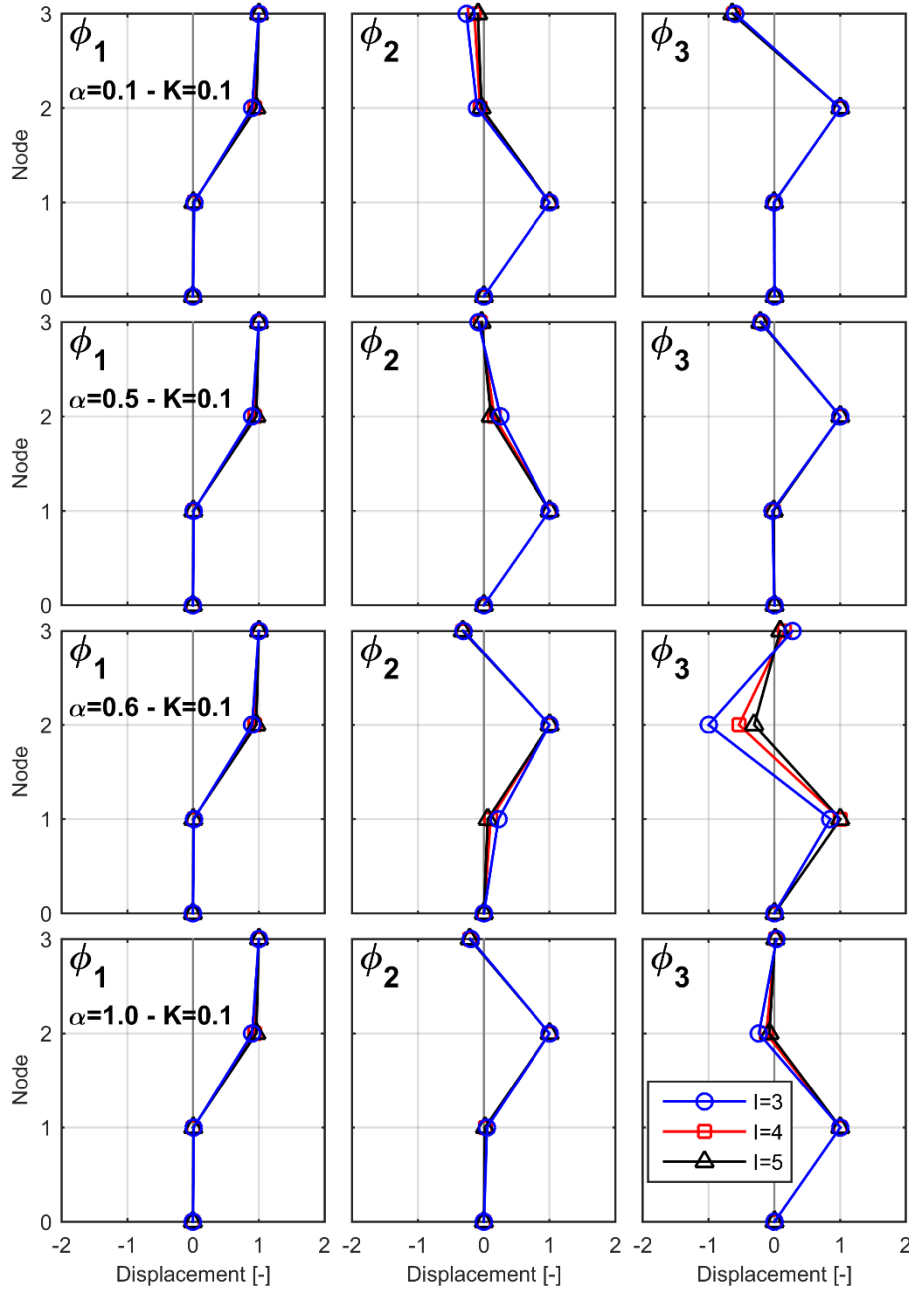


Fig. A.1. Natural modes -  $\alpha = 0.1; 0.5; 0.6; 1.0$  -  $K = 0.1$  -  $I = 3; 4; 5$

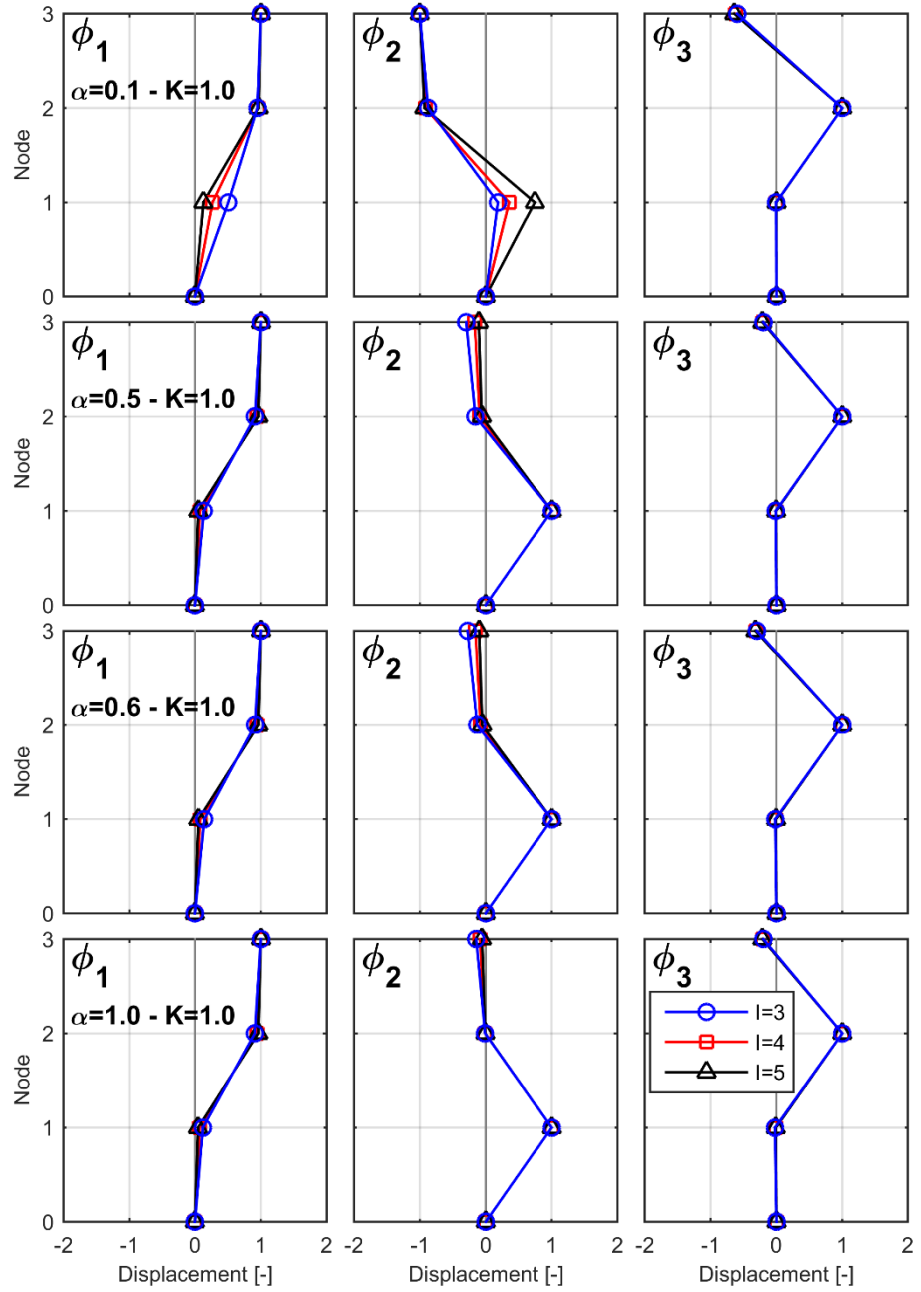


Fig. A.2. Natural modes -  $\alpha = 0.1; 0.5; 0.6; 1.0$  -  $K = 0.3$  -  $I = 3; 4; 5$

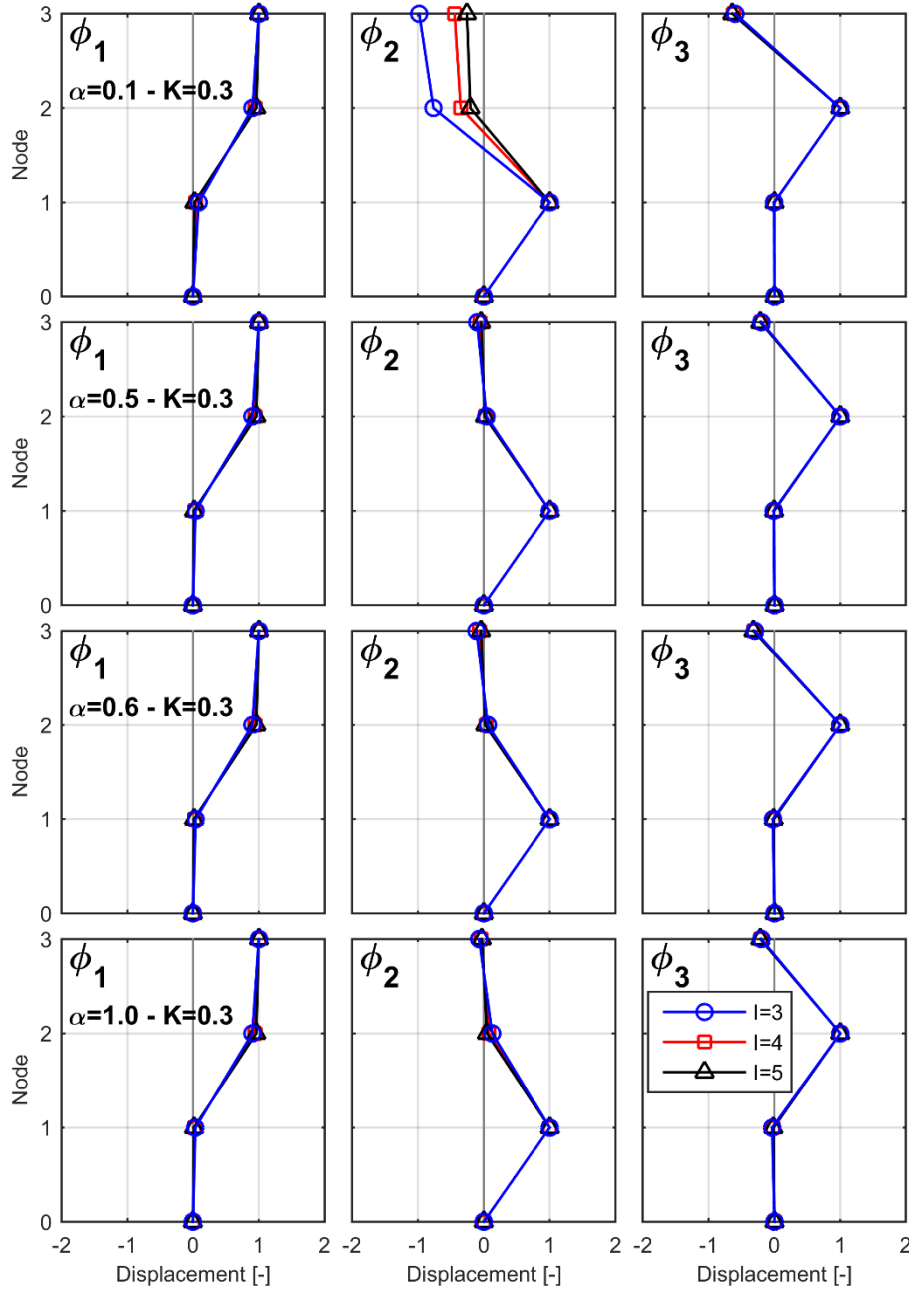


Fig. A.3. Natural modes -  $\alpha = 0.1; 0.5; 0.6; 1.0 - K = 0.3 - l = 3; 4; 5$

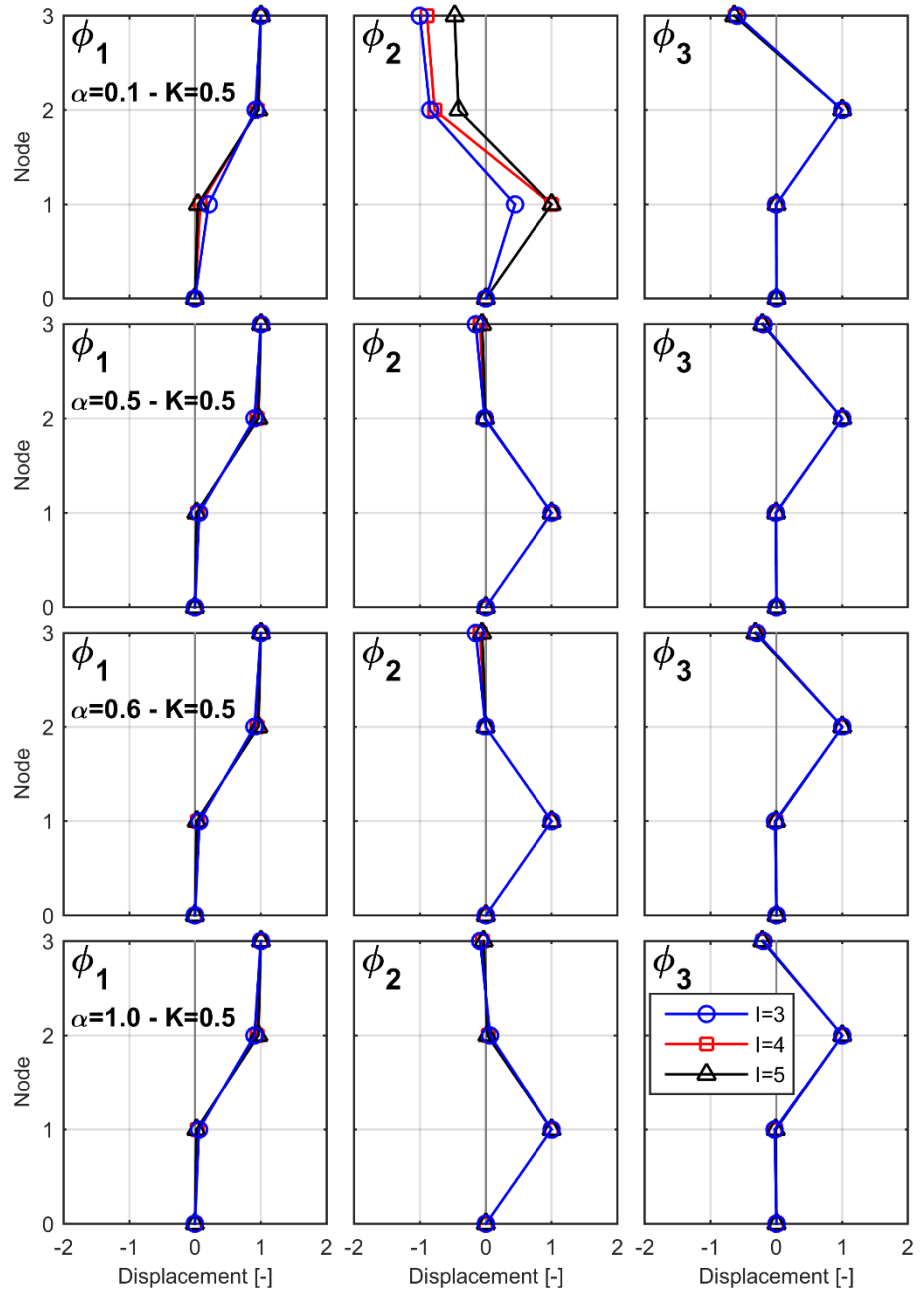


Fig. A.4. Natural modes -  $\alpha = 0.1; 0.5; 0.6; 1.0$  -  $K = 1.0$  -  $I = 3; 4; 5$

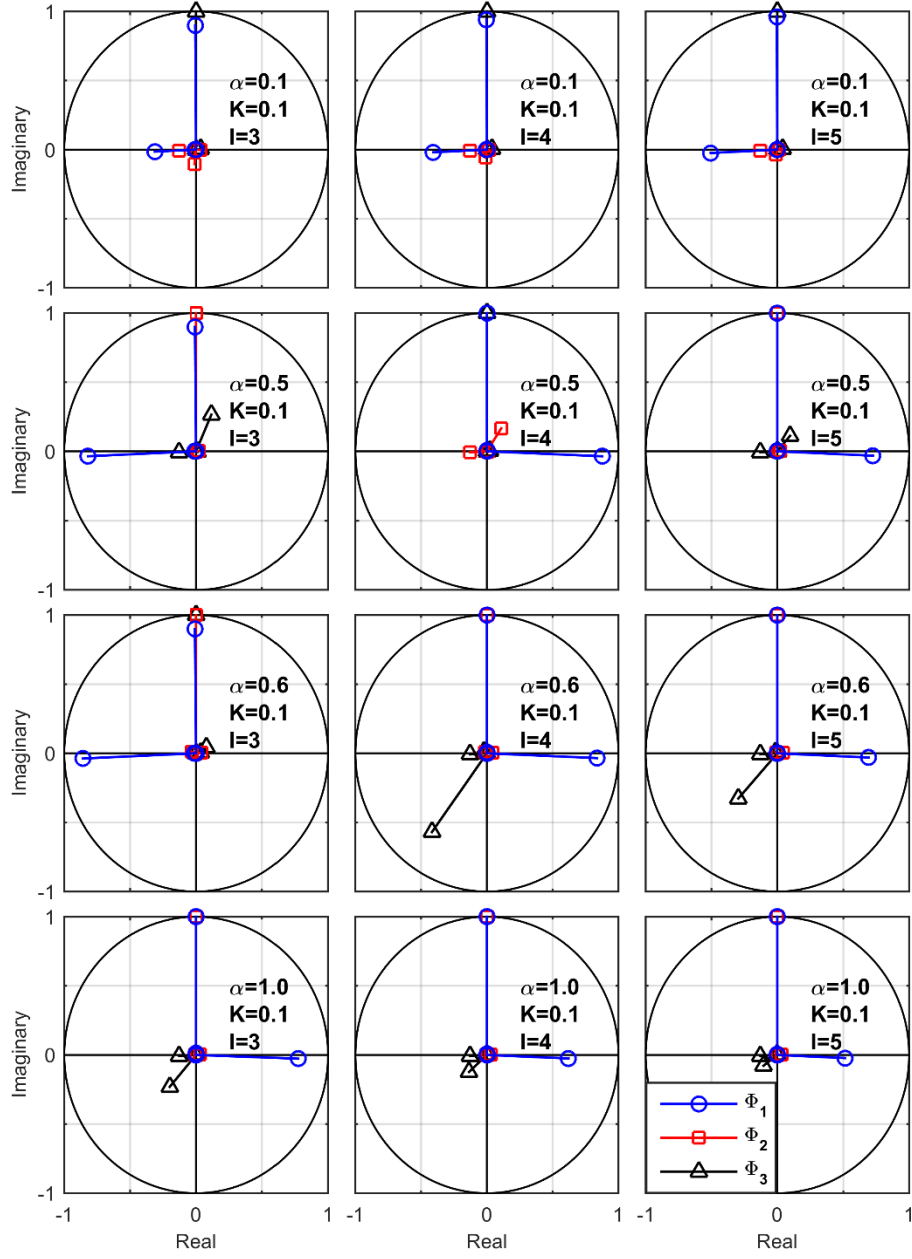


Fig. A.5. Complexity plot;  $\xi = 0.05$  -  $\alpha = 0.1; 0.5; 0.6; 1.0$  -  $K = 0.1$  -  $l = 3; 4; 5$



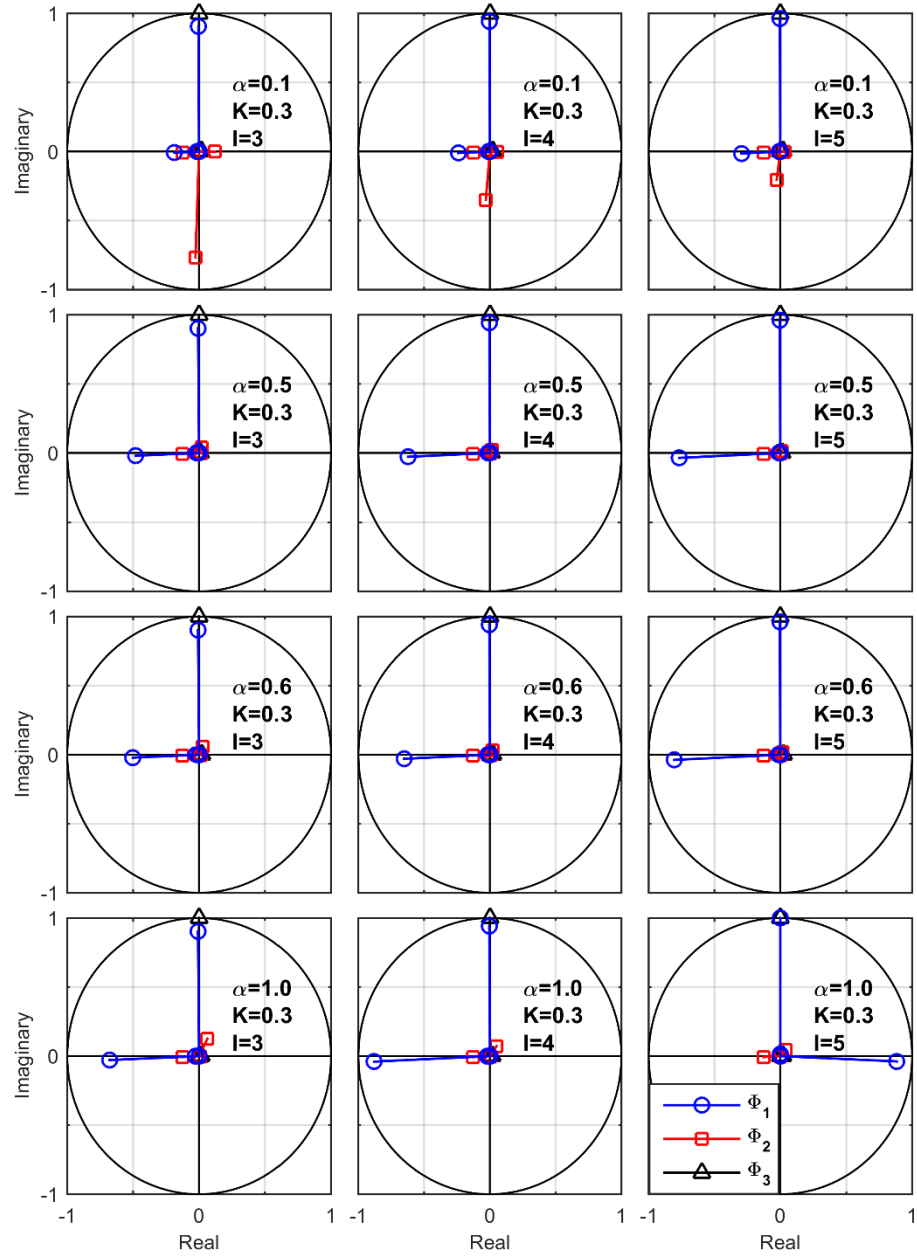


Fig. A.6. Complexity plot;  $\xi = 0.05$  -  $\alpha=0.1; 0.5; 0.6; 1.0$  -  $K=0.3$  -  $l=3; 4; 5$

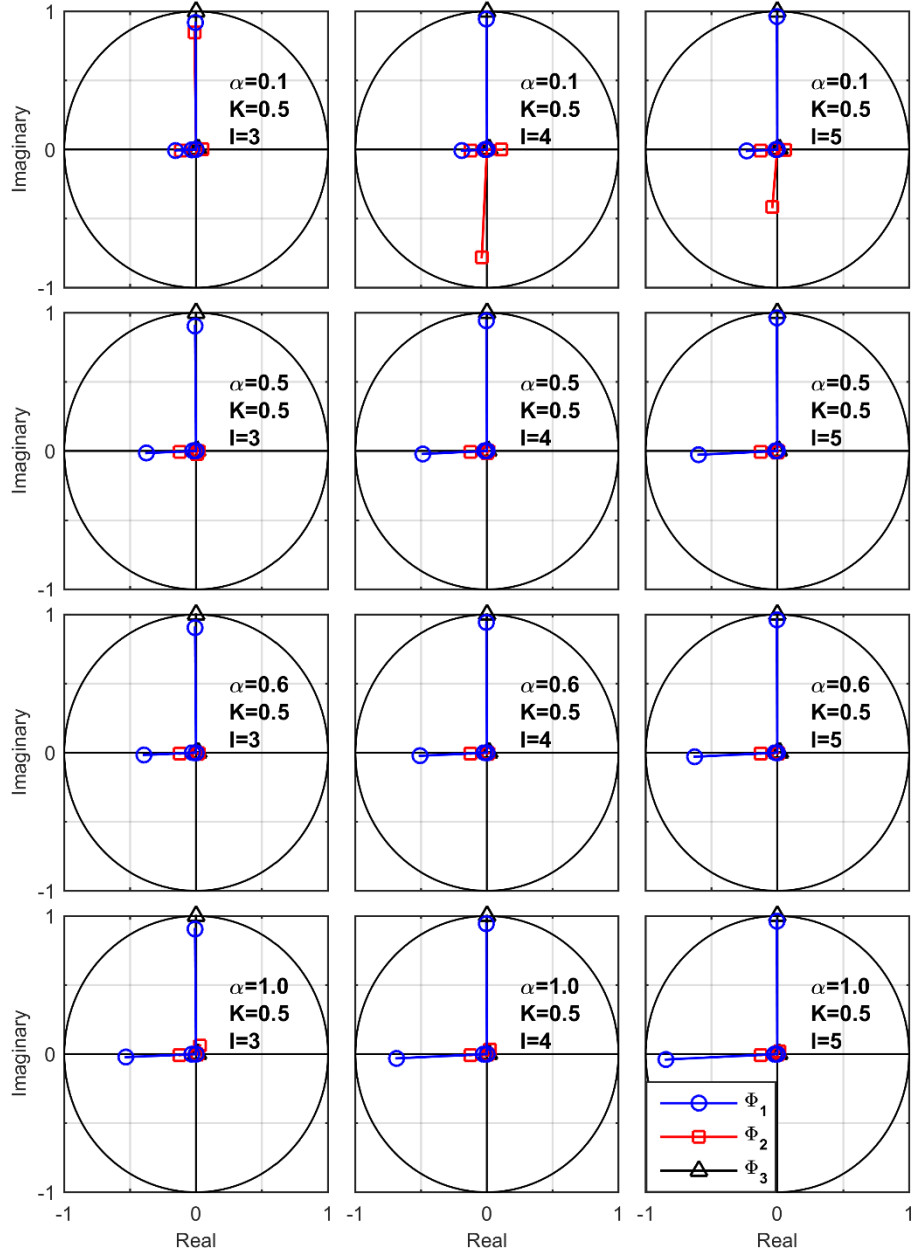


Fig. A.7. Complexity plot;  $\xi = 0.05$  -  $\alpha = 0.1; 0.5; 0.6; 1.0$  -  $K=0.5$  -  $l=3; 4; 5$

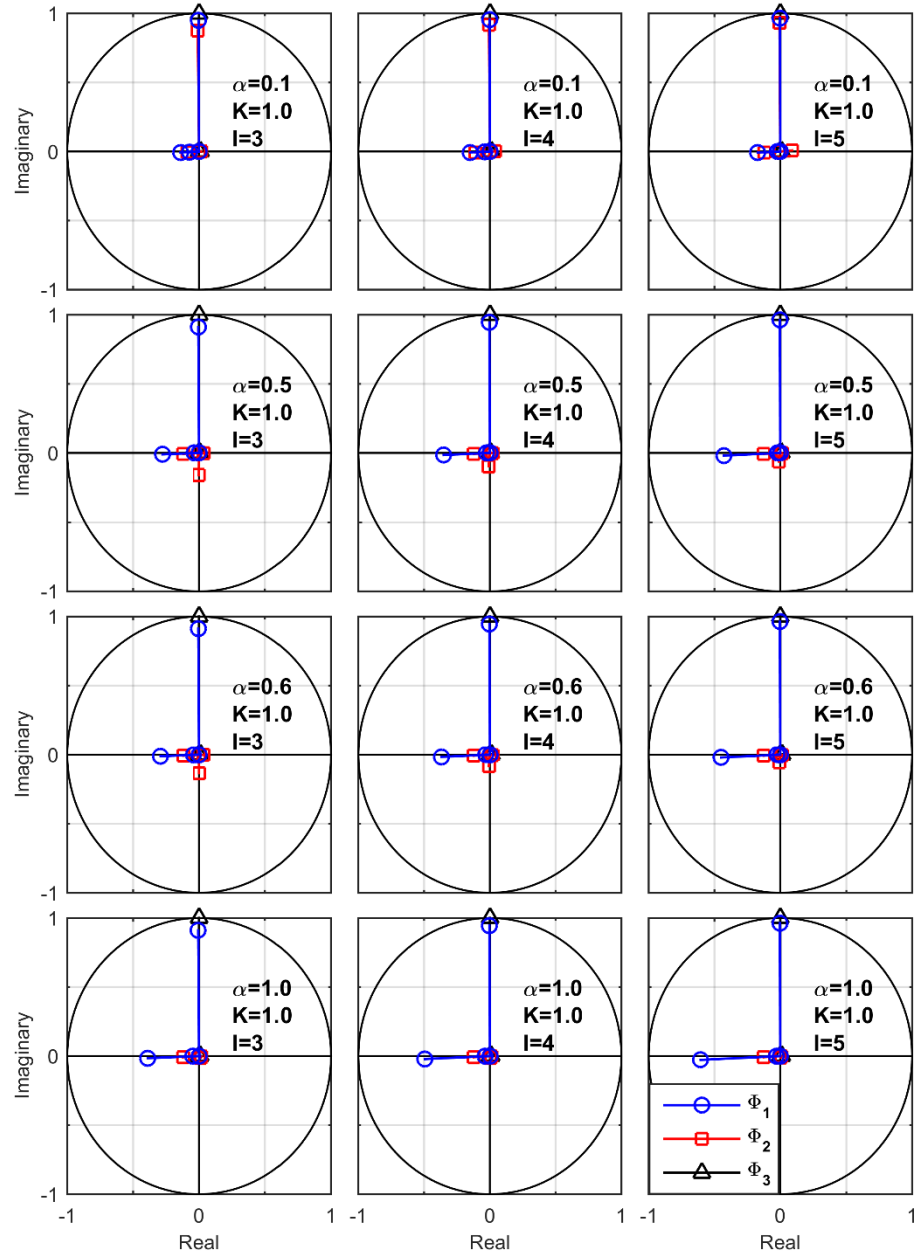


Fig. A.8. Complexity plot;  $\xi = 0.05$  -  $\alpha = 0.1; 0.5; 0.6; 1.0$  -  $K = 1.0$  -  $I = 3; 4; 5$

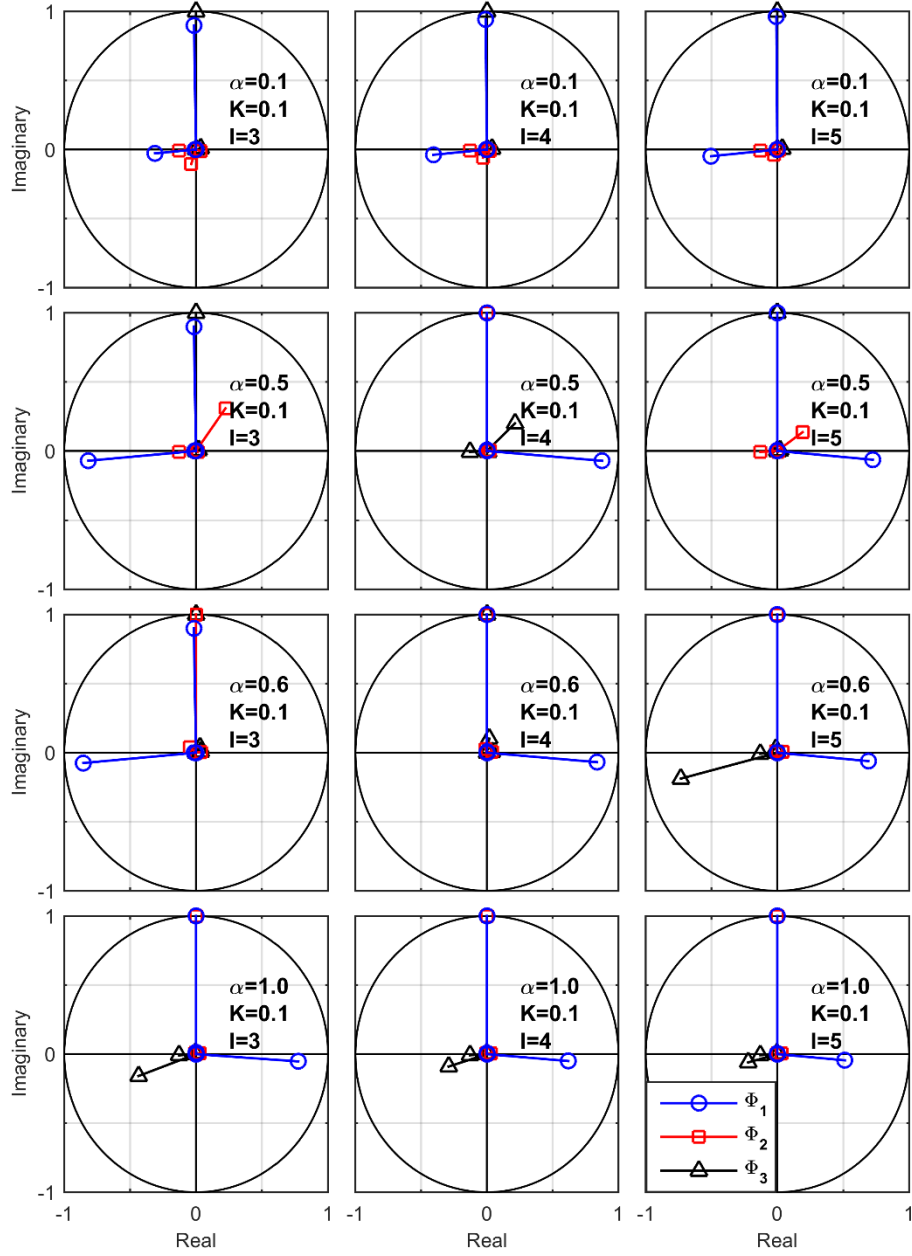


Fig. A.9. Complexity plot;  $\xi_{LS} = \xi_{US} = 0.05$ ,  $\xi_{ISO} = 0.10$  -  $\alpha = 0.1; 0.5; 0.6; 1.0$  -  $K = 0.1$  -  $l = 3; 4; 5$

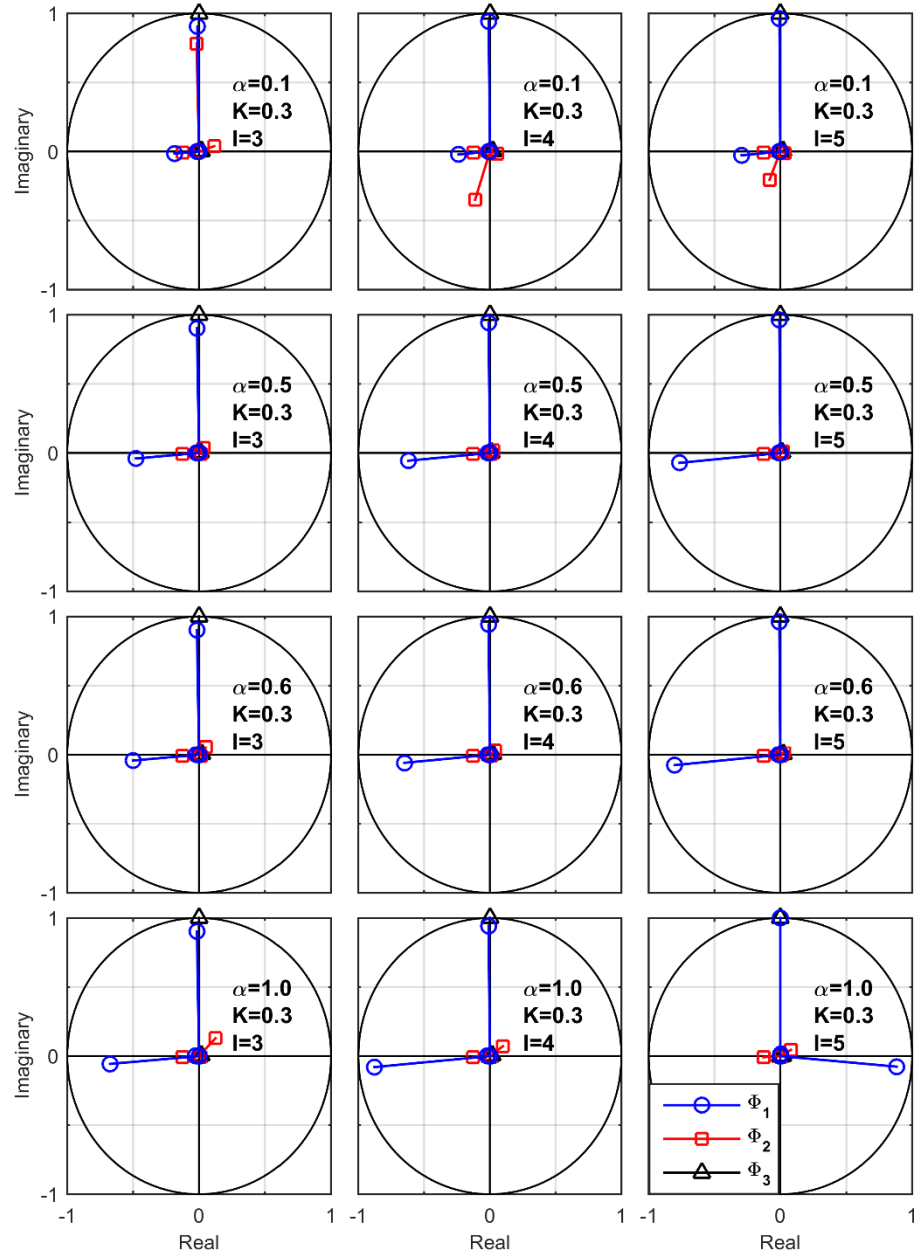


Fig. A.10. Complexity plot;  $\xi_{LS} = \xi_{US} = 0.05$ ,  $\xi_{ISO} = 0.10$  -  $\alpha=0.1; 0.5; 0.6; 1.0$  -  $K=0.3$  -  $l=3; 4; 5$

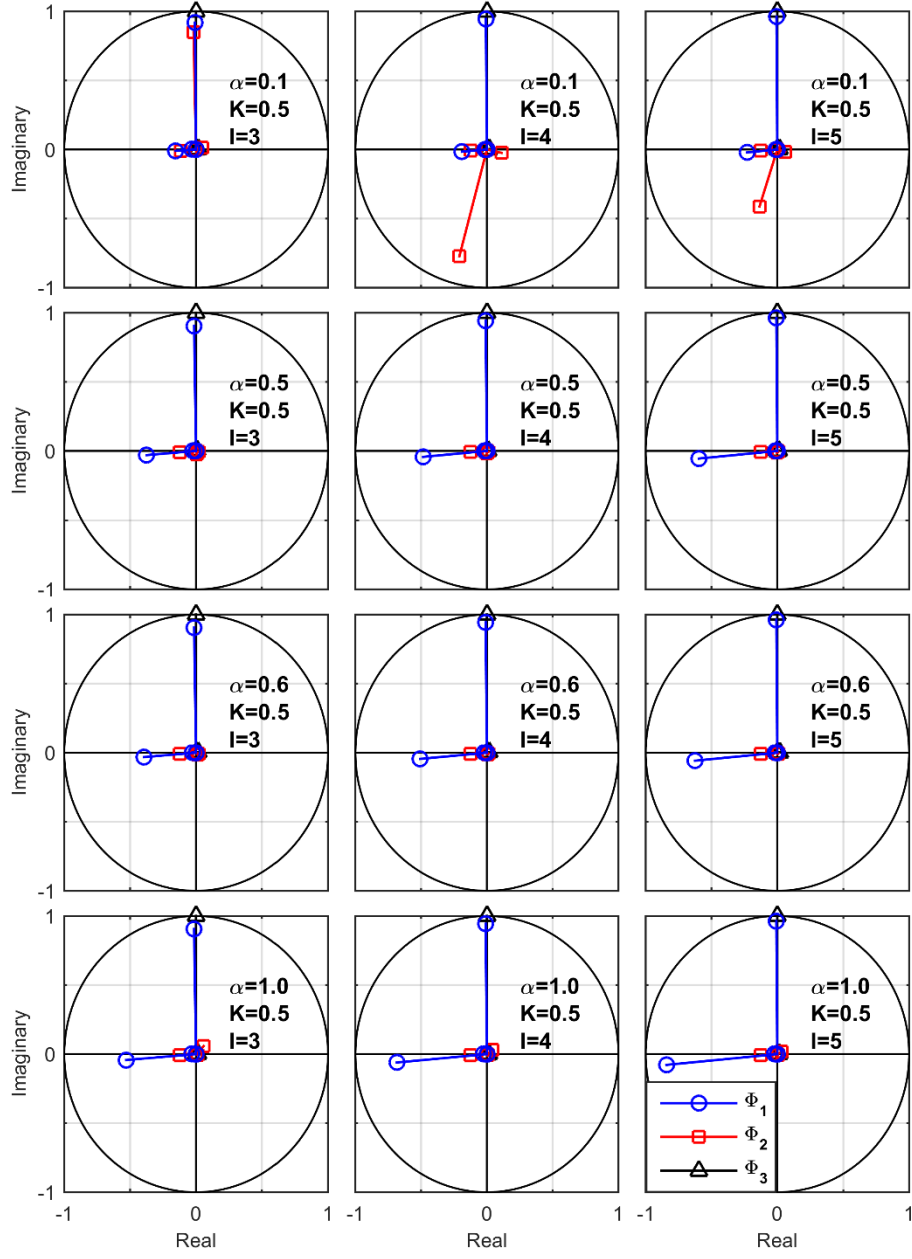


Fig. A.11. Complexity plot;  $\xi_{LS} = \xi_{US} = 0.05$ ,  $\xi_{ISO} = 0.10$  -  $\alpha = 0.1; 0.5; 0.6; 1.0$  -  $K=0.5$  -  $l=3; 4; 5$

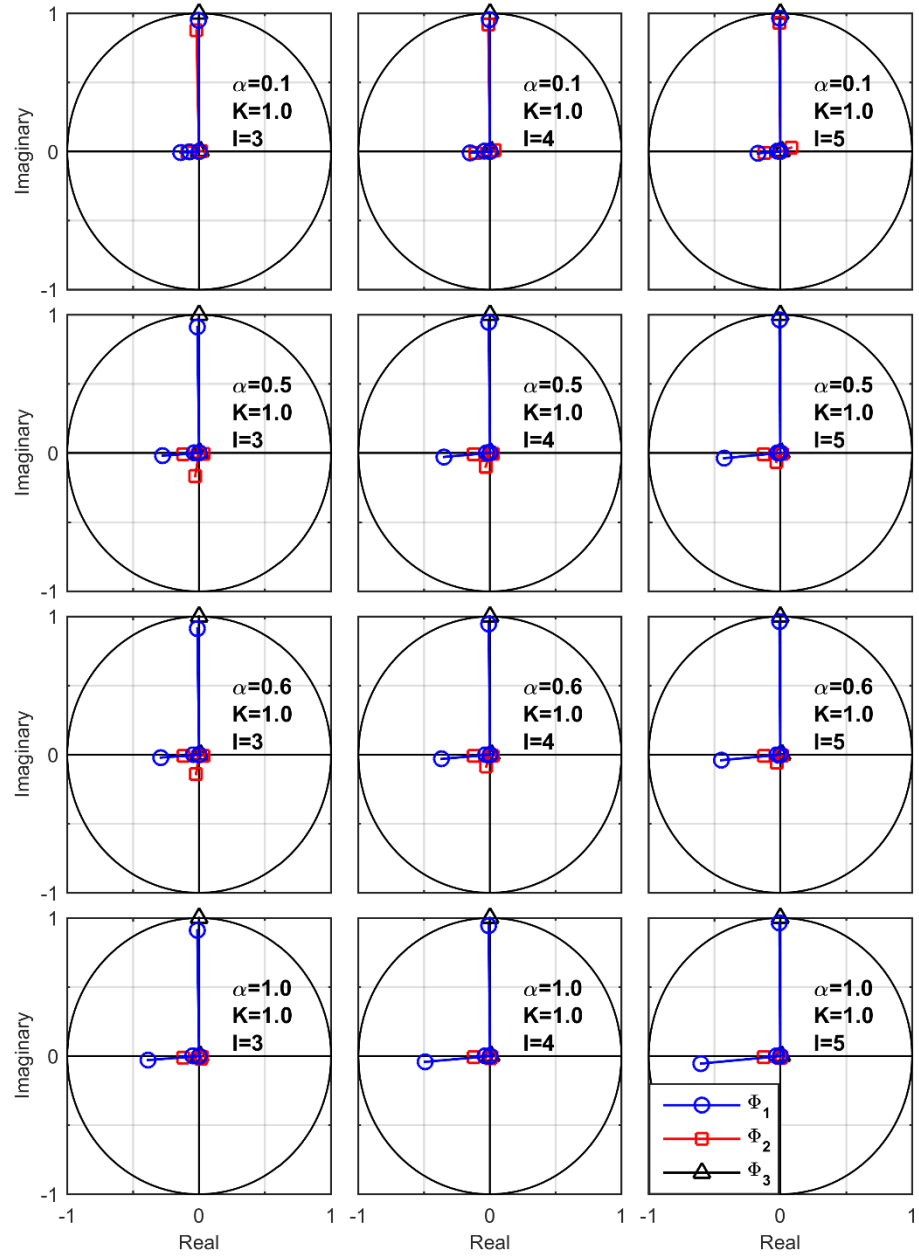


Fig. A.12. Complexity plot;  $\xi_{LS} = \xi_{US} = 0.05$ ,  $\xi_{ISO} = 0.10$  -  $\alpha = 0.1; 0.5; 0.6; 1.0$  -  $K=1.0$  -  $I=3; 4; 5$

## A.2. RESPONSE SPECTRUM ANALYSIS

Figs. A.13 ÷ A.18 show the results of the response spectrum analysis carried out considering the elastic response spectrum prescribed by the Italian NTC2008 [D.M. 14/01/2008] for the specific case study site ( $a_g = 0.162$  g,  $F_0 = 2.347$ ,  $T_c^* = 0.333$  s,  $S = 1.47$ ), see § 7.4.4.

In this section all the possible combinations of the parameters  $\alpha$  –  $K$  –  $I$  are considered, i.e.:  $\alpha = \{0.1 \div 1.0\}$  -  $K = \{0.1, 0.3, 0.5, 1\}$  -  $I = \{3, 4, 5\}$ . Considering a constant damping ratio of 0.05, the seismic response of 3DOF IIS and SDOF LS models is obtained through the complete quadratic combination CQC.

In Figs. A.13 the base shear ratio  $v$  between the controlled and uncontrolled configuration is depicted as a function of the isolation period; each curve is built up by varying the mass ratio  $\alpha$  and by fixing the stiffness ratio  $K$ , the tris of graphs refers to the three isolation ratios  $I$ .

Figs A.14 and A.15 ÷ A.17 respectively show the combined and modal shear forces of the upper and lower structures and of the isolation system as a function of the isolation periods, Fig. A.18 plots the peak drift of the three parts as a function of the isolation period; each curve is built up by varying the mass ratio  $\alpha$  and by fixing the stiffness ratio  $K$ , the tris of graphs refers to the three isolation ratios  $I$ .

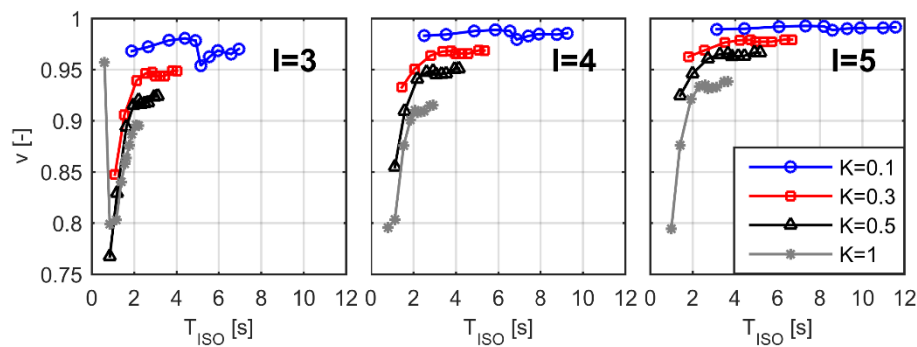


Fig. A.13.  $v$  vs.  $T_{ISO}$ : (a)  $I=3$ , (b)  $I=4$ , (c)  $I=5$



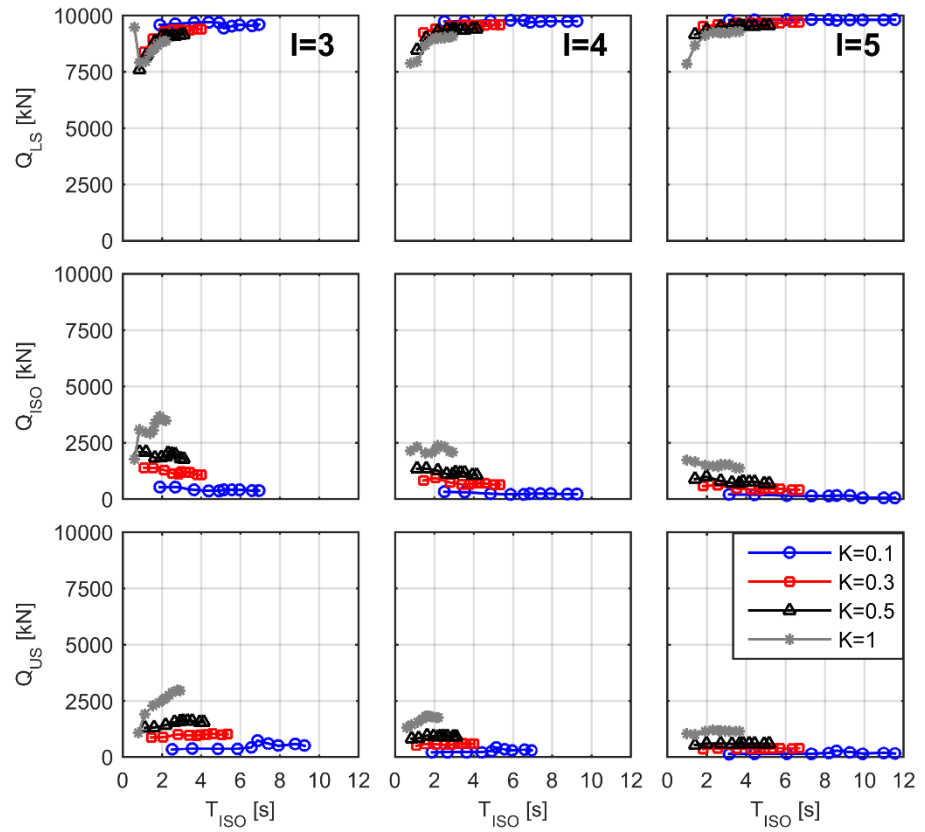


Fig. A.14. Peak Story Shear Force: (a) I=3, (b) I=4, (c) I=5

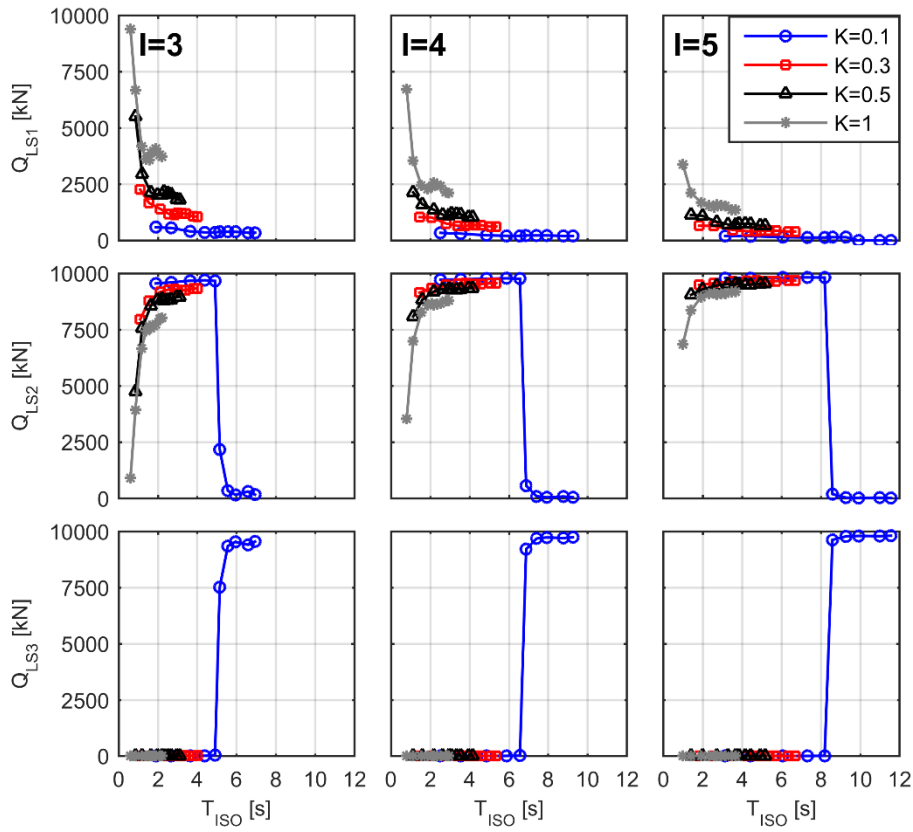


Fig. A.15. Modal Shear Force,  $Q_{LSi}$ :  $I=3; 4; 5$ : (a)  $I=3$ , (b)  $I=4$ , (c)  $I=5$

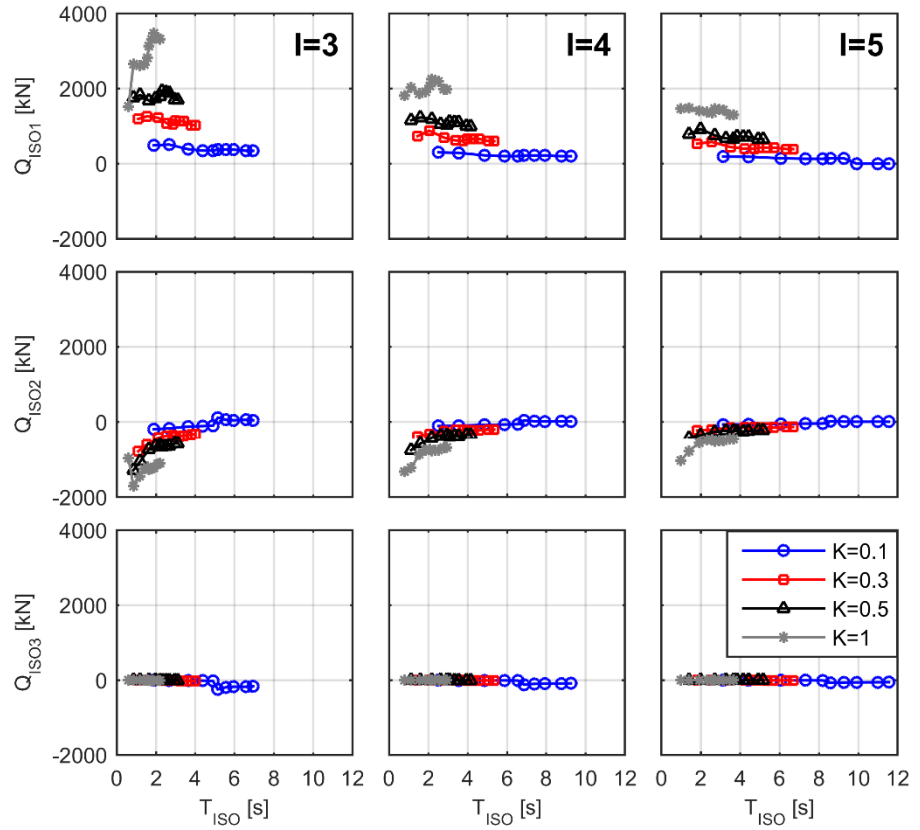


Fig. A.16. Modal Shear Force,  $Q_{ISOi}$ :  $I=3$ ; 4; 5: (a)  $I=3$ , (b)  $I=4$ , (c)  $I=5$

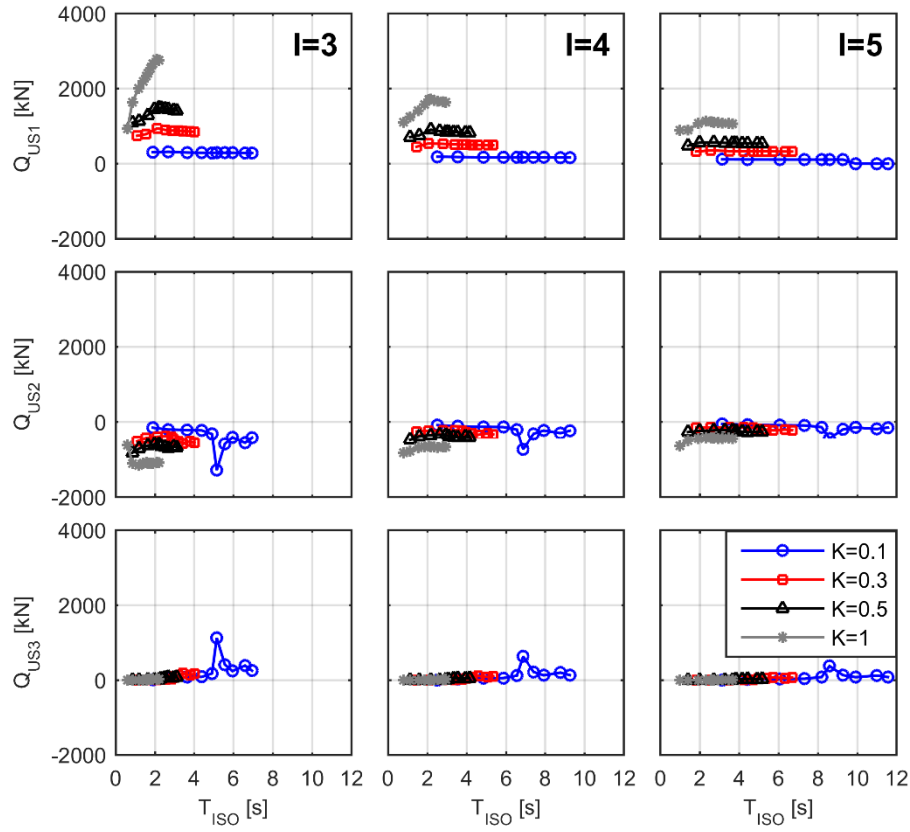


Fig. A.17. Modal Shear Force,  $Q_{USi}$ :  $I=3$ ; 4; 5: (a)  $I=3$ , (b)  $I=4$ , (c)  $I=5$

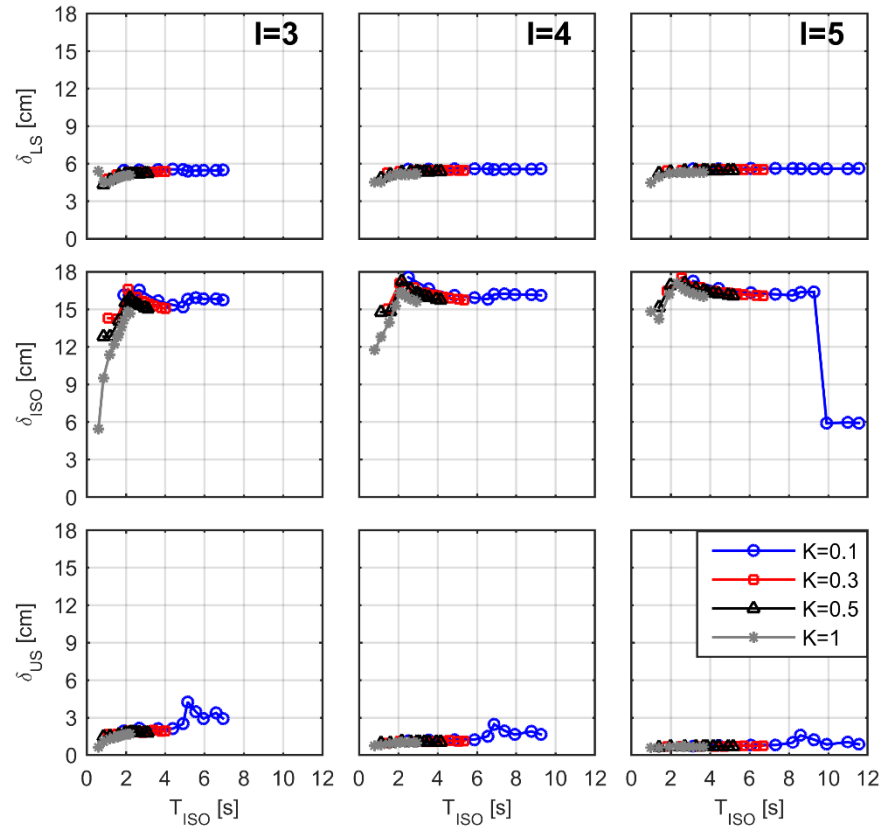


Fig. A.18. Peak Story Displacement: (a)  $I=3$ , (b)  $I=4$ , (c)  $I=5$

### A.3. TIME HISTORY ANALYSIS

Figs. A.19 ÷ A.22 show the results of the non-linear time history analysis carried out considering a set of 10 spectrum-compatible ground motions with the specific case study site of Pozzuoli (Naples, Italy) [Software SIMQKE\_GR].

The two configurations E and F (see § 7.4.5) are herein considered, respectively corresponding to  $\alpha = 0.1 - K = 0.5$  and  $\alpha = 0.5 - K = 0.5$ , by varying the isolation period between 0.5 and 2.5 s.

As can be seen in Chapter 7, considering the interpolated damping ratio as a function of the period  $T$ , for isolation periods smaller than 1 s,  $\xi_1 = \xi_{LS} = \xi_{US} = 0.05$  and at  $T=T_1$  and  $\xi_2 = \xi_{ISO} = 0.10$  at  $T=T_2$ ; for isolation periods larger than 1 s,  $\xi_1 = \xi_{ISO} = 0.10$  and at  $T=T_1$  and  $\xi_2 = \xi_{LS} = \xi_{US} = 0.05$  at  $T=T_2$ .

In Figs. A.19 - A.20 and A.20 - A.21 are respectively depicted the peak drift and the peak story acceleration for the different isolation periods; each couple of graph refers to the cases E and F. In particular, in each chart are provided the results of the mean time-history and of the 10 time histories of the compatible-spectrum ground motions of the IIS models, the response spectrum result of the SDOF LS model is considered for comparison.

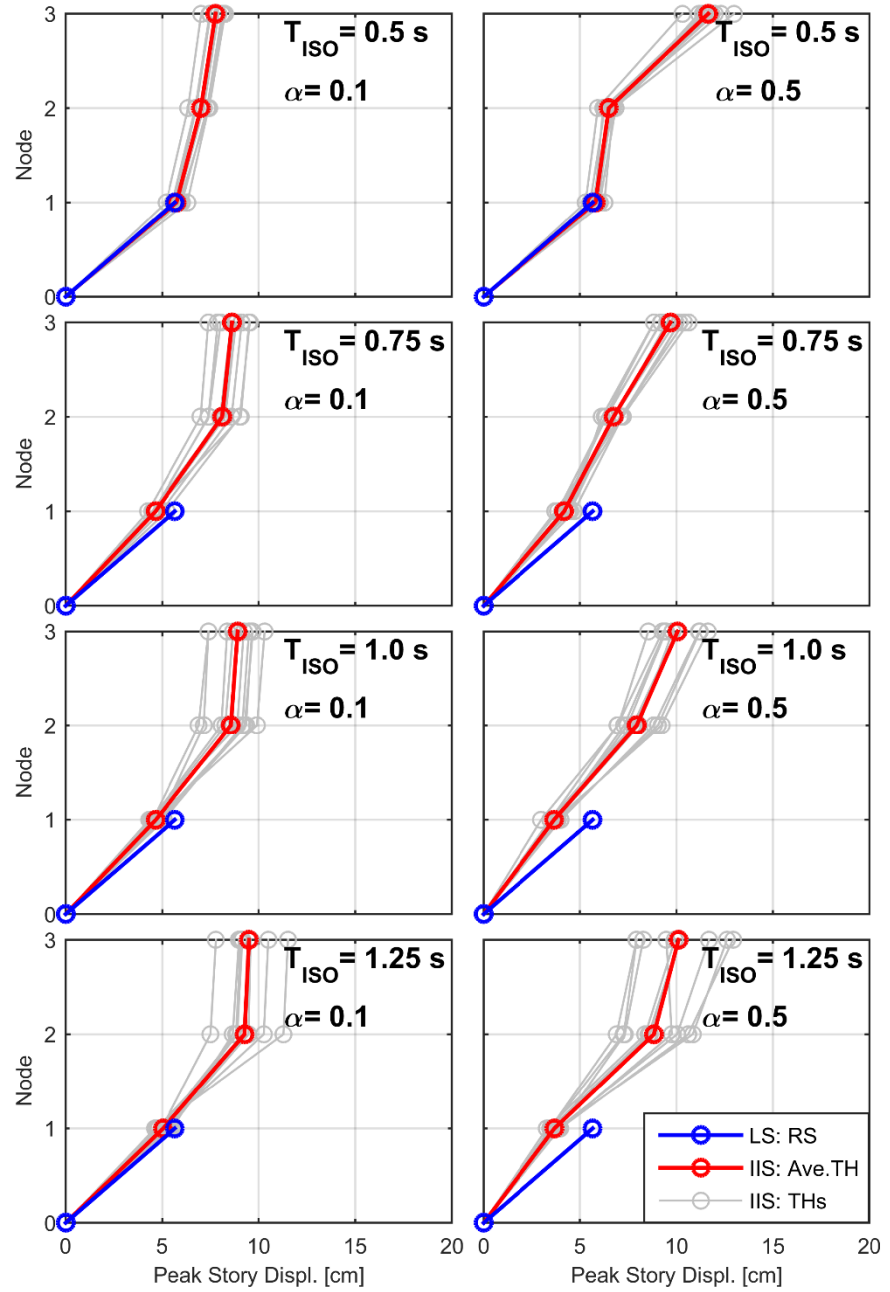


Fig. A.19. Peak Story Displacement: (a)  $\alpha = 0.1$ , (b)  $\alpha = 0.5$

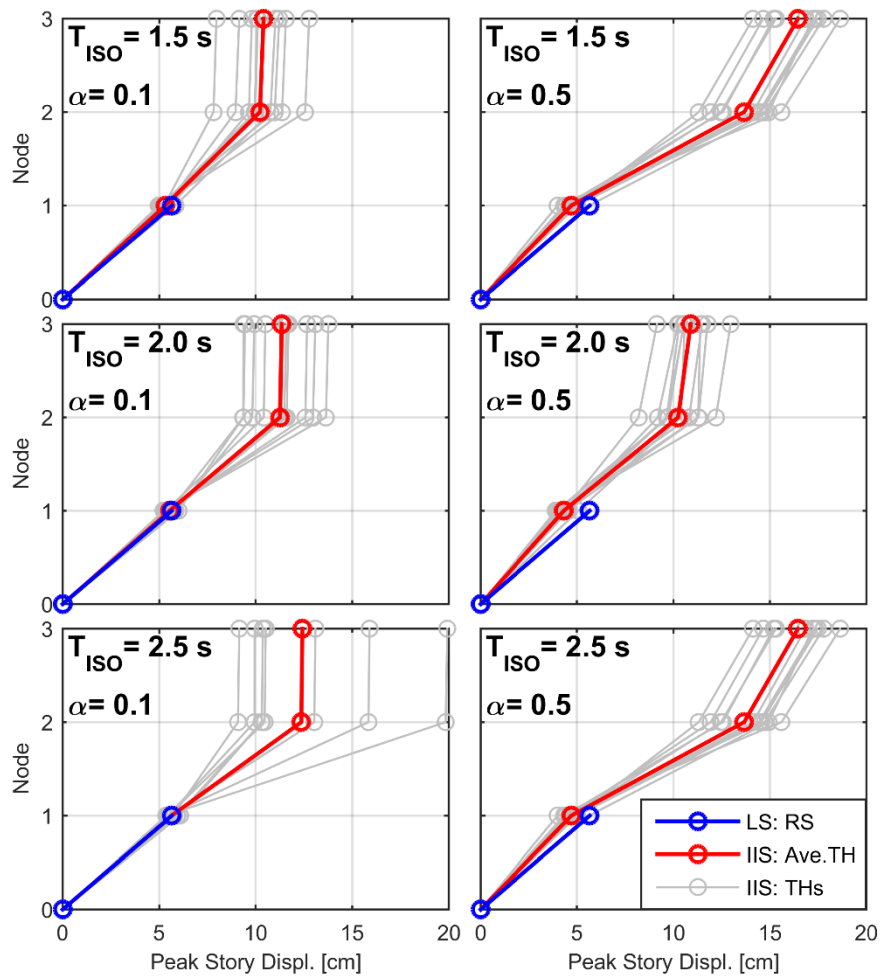
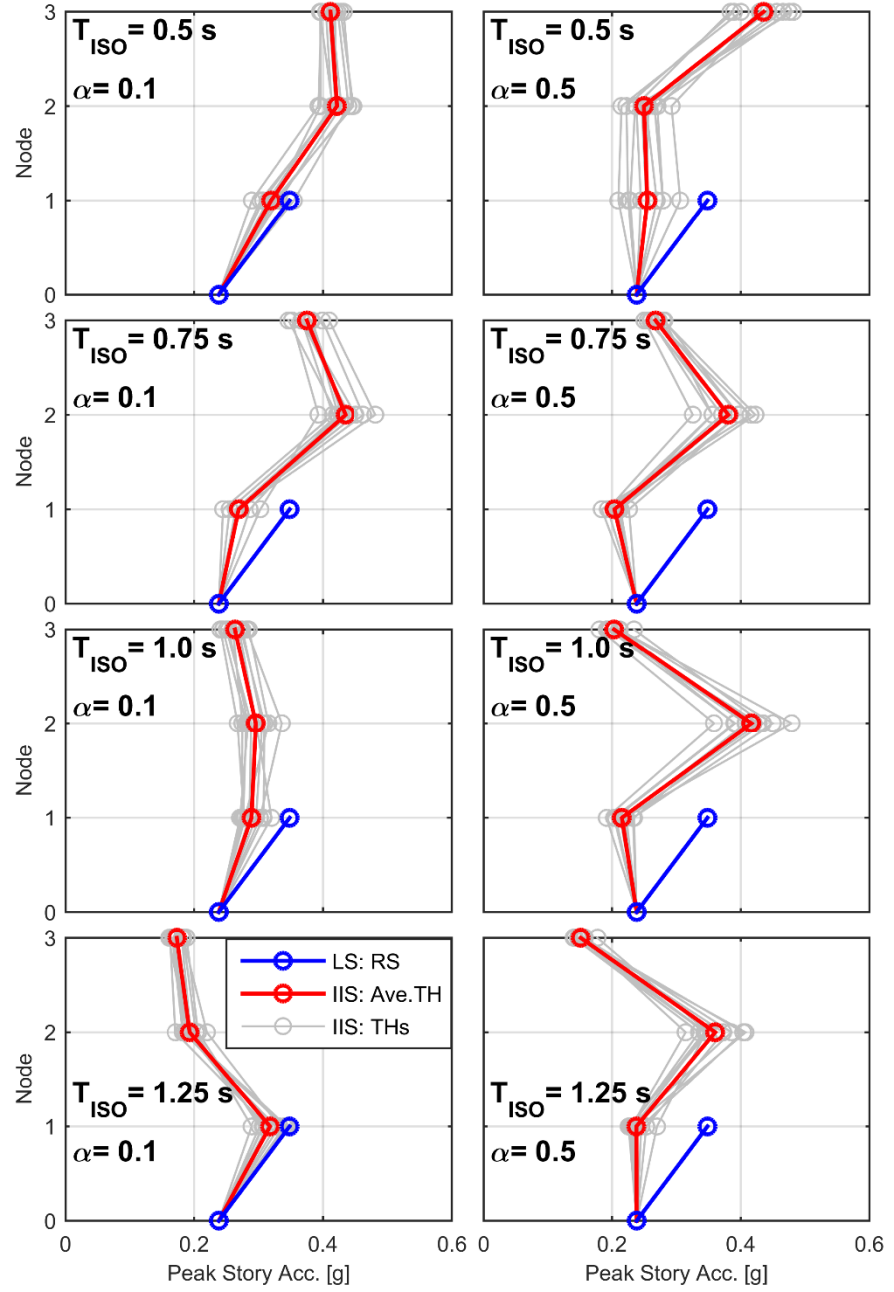


Fig. A.20. Peak Story Displacement: (a)  $\alpha=0.1$ , (b)  $\alpha=0.5$



Fig. A.21. Peak Story Acceleration: (a)  $\alpha = 0.1$ , (b)  $\alpha = 0.5$

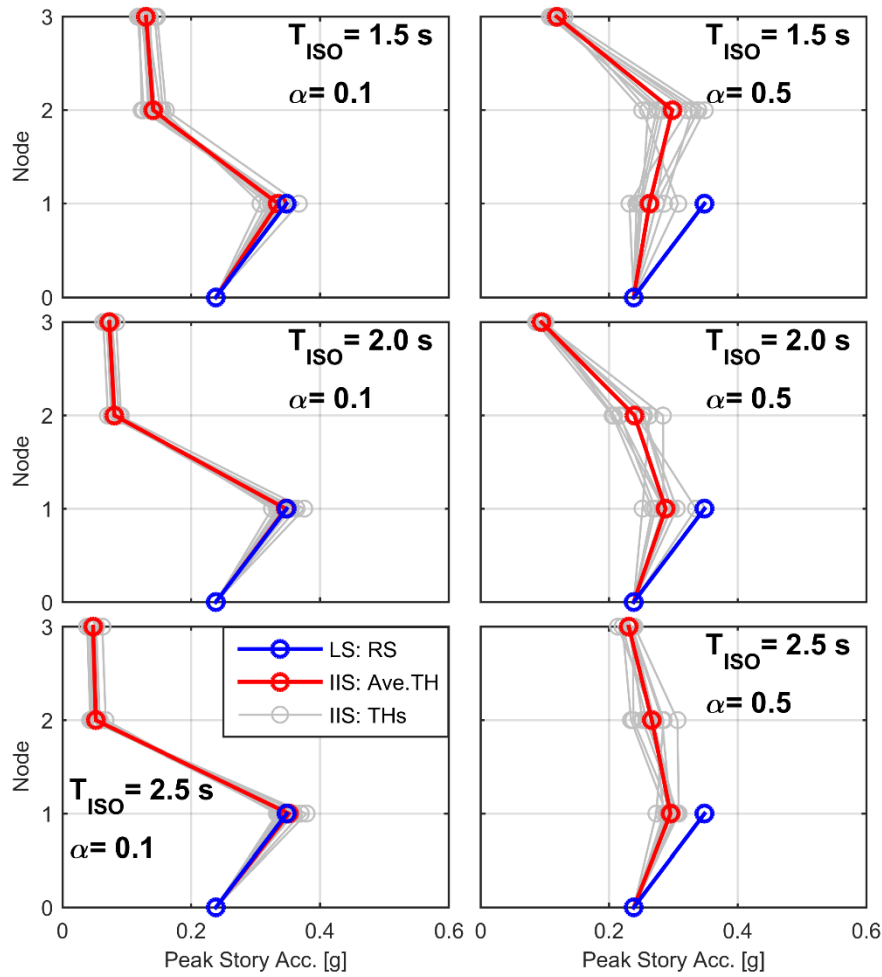


Fig. A.22. Peak Story Acceleration: (a)  $\alpha = 0.1$ , (b)  $\alpha = 0.5$

## APPENDIX B: Design Implications

### B.1. INFLUENCE OF PERIODS OF THE STRUCTURAL PORTIONS AND OF THE ISOLATION SYSTEM

Since the IIS model can be seen as a combination of the US+ISO and LS models, the isolated US and LS can be studied separately or the dynamic interaction between the two portions can be considered.

In this section, the interaction between the structural portions and the isolation, as well as between the upper and lower structures, is considered by comparing the periods of US, LS and isolation system.

#### B.1.1. $T_{ISO}$ vs. $T_{US}$

The dynamic interaction of the US and ISO system gives information about the local behavior of the isolated US. Considering the analogy between the simplified 2DOF BIS and the set of the US+ISO of the 3DOF IIS, the isolated US behaves as a base isolated structure when the period of the US,  $T_{US}$ , is almost equal to, or greater than, the isolation period,  $T_{ISO}$ ; in particular:

$$\begin{array}{ll} \text{for } T_{ISO} \gg T_{US} \leftrightarrow I \geq 3 & \varepsilon_{US} \approx \frac{\delta_{US}}{\delta_{ISO}} = O(10^{-2}) \\ \text{for } T_{ISO} > T_{US} \leftrightarrow I = 1 \div 3 & \varepsilon_{US} \approx \frac{\delta_{US}}{\delta_{ISO}} = O(10^{-1}) \\ \text{for } T_{ISO} \cong T_{US} \leftrightarrow I = 1 & \sqrt{\gamma} \approx \frac{\delta_{US}}{\delta_{ISO}} = O(10^0) \end{array}$$

where

$$I = \frac{T_{ISO}}{T_{US}} \quad \text{is the period ratio, also appointed as isolation ratio;}$$

$\epsilon_{US} = \left(\frac{1}{I}\right)^2$  is the square of the inverse of  $I$ ;

$\gamma = \frac{m_{US}}{M_{ISO}}$  is the mass ratio of the US to the total isolated mass;

$\frac{\delta_{US}}{\delta_{ISO}}$  is the US – ISO drift ratio.

Therefore, for a rigid US than the isolation system ( $I \geq 2$ ), the amplification of the US drift with respect to the ISO drift can be estimated as a function of the parameter  $\epsilon_{US}$ ; for a US as flexible as the isolation system ( $I = 1$ ), this amplification approximately corresponds to the inverse of the square root of the mass ratio  $\gamma$ .

### B.1.2. $T_{ISO}$ vs. $T_{LS}$

The dynamic interaction of the LS and ISO system gives information about the global behavior of inter-story isolated structure. Considering the 3DOF IIS with the isolated US behaving as a BIS, i.e.  $I \geq 1$ , the following cases can be considered.

for $T_{ISO} \gg T_{LS}$	$\leftrightarrow$	IS effect	$\frac{\delta_{LS}}{\delta_{ISO}} = O(10^{-3} \div 10^{-1})$
for $T_{ISO} > T_{LS}$	$\leftrightarrow$	MD effect	$\frac{\delta_{LS}}{\delta_{ISO}} = O(10^{-1})$
for $T_{ISO} \leq T_{LS}$	$\leftrightarrow$	IIS as FB	$\frac{\delta_{LS}}{\delta_{ISO}} = O(10^0)$

When the isolation period is  $1.5 \div 15$  times the LS period, the isolation (IS) effect prevails on the mass damper (MD) effect; otherwise, when the isolation period is  $1.05 \div 1.5$  times the LS period, the LS is quite rigid with respect to the isolation, the MD effect prevails on the IS effect.

It is worth noticing that when the isolation period is smaller than the LS period, i.e. the LS is more flexible than the LS, the IIS behaves as a fixed-base structure.

### B.1.3. $T_{ISO}$ vs. $T_{US}$ and $T_{LS}$

Considering the dynamic interaction between both structural portions and the isolation system, the following conditions are provided.

$$\text{for } T_{ISO} \gg T_{US}, T_{LS} \leftrightarrow \text{perfect IS - IS effect} \\ \frac{\delta_{US}}{\delta_{ISO}} = O(10^{-2}), \frac{\delta_{LS}}{\delta_{ISO}} = O(10^{-3} \div 10^{-1})$$

$$\text{for } T_{ISO} \gg T_{US}, T_{ISO} > T_{LS} \leftrightarrow \text{non-perfect IS - MD effect} \\ \frac{\delta_{US}}{\delta_{ISO}} = O(10^{-2}), \frac{\delta_{LS}}{\delta_{ISO}} = O(10^{-1})$$

As can be seen previously, when both the structural portions are assumed rigid with respect to the isolation layer, i.e. the US and LS periods are well separated from the isolation period (say,  $3 \div 15$  times), the first IIS mode involves displacement only in the isolation layer. This condition maximizes the IS effect and it can be defined as *perfect isolation*. When the periods of US and LS are respectively well separated (say,  $3 \div 5$  times) and not so far (say,  $1.05 \div 1.5$  times) from the isolation period, the US is rigid and the LS is quite rigid with respect to the isolation layer, the LS participates to the fundamental mode, thus, the MD effect is maximized. This condition can be defined as *non-perfect isolation*.

## B.2. “PERFECT” AND “NON-PERFECT” ISOLATION

### B.2.1. Perfect isolation

Considering the 3DOF IIS model, the perfect isolation is obtained when the periods of the structural portions are well separated from isolation period.

Comparing the periods and participating mass ratios of the simplified 3DOF IIS, 2DOF BIS and SDOF LS models, the following considerations can be drawn.

$$1^{\text{st}} \text{ mode: } T_{3\text{DOF IIS},1} \cong T_{2\text{DOF BIS},1}, \quad \Gamma_{3\text{DOF IIS},1} \cong R_m = M_{ISO} / m_{TOT}$$

$$\begin{aligned}
 2^{\text{nd}} \text{ mode:} \quad & T_{3\text{DOF IIS}, 2} \cong T_{\text{SDOF LS}}, \quad \Gamma_{3\text{DOF IIS}, 2} \cong m_{\text{LS}} / m_{\text{TOT}} \\
 3^{\text{rd}} \text{ mode:} \quad & T_{3\text{DOF IIS}, 3} \cong T_{2\text{DOF BIS}, 2}, \quad \Gamma_{3\text{DOF IIS}, 3} \cong 0
 \end{aligned}$$

The first modal shape represents the first mode of the 2DOF ISO+US corresponding to the isolation, with minor deformation in the LS; this results in drift ratios  $\delta_{\text{US}}/\delta_{\text{ISO}}$  and  $\delta_{\text{LS}}/\delta_{\text{ISO}}$  respectively of the order  $10^{-2}$  and  $10^{-3} \div 10^{-1}$ . The second and the third modes are respectively corresponding to the mode of the SDOF LS, with almost no deformation in the US, and the second mode of the 2DOF ISO+US, with almost no deformation in the LS.

With the perfect isolation the flexible interface decouples the isolated US and the LS, the spectral acceleration corresponding to the first period tends to zero; since the LS cannot take advantage from this additional flexibility, the base shear is only given by the contribution of the LS.

### B.2.2. Non-perfect isolation

Considering the 3DOF IIS model, the non-perfect isolation is obtained when the US period is well separated from the isolation period and the isolation period is not so far from the LS period.

Comparing the periods and participating mass ratios of the simplified 3DOF IIS, 2DOF BIS and SDOF LS models, the following considerations can be drawn.

$$\begin{aligned}
 1^{\text{st}} \text{ mode:} \quad & T_{3\text{DOF IIS}, 1} > T_{2\text{DOF BIS}, 1}, \quad \Gamma_{3\text{DOF IIS}, 1} > R_m = M_{\text{ISO}} / m_{\text{TOT}} \\
 2^{\text{nd}} \text{ mode:} \quad & T_{3\text{DOF IIS}, 2} \cong T_{\text{SDOF LS}}, \quad \Gamma_{3\text{DOF IIS}, 2} < m_{\text{LS}} / m_{\text{TOT}} \\
 3^{\text{rd}} \text{ mode:} \quad & T_{3\text{DOF IIS}, 3} \cong T_{2\text{DOF BIS}, 2}, \quad \Gamma_{3\text{DOF IIS}, 3} \cong 0
 \end{aligned}$$

The first modal shape represents the first mode of the 2DOF ISO+US corresponding to the isolation, involving deformation both in the LS and in the isolation layer; this results in drift ratios  $\delta_{\text{US}}/\delta_{\text{ISO}}$  and  $\delta_{\text{LS}}/\delta_{\text{ISO}}$  of order  $10^{-2}$  and  $10^{-1}$ , respectively. The second and the third modes are respectively corresponding to the mode of the SDOF LS, with almost no deformation in the US, and the second mode of the 2DOF ISO+US, with almost no deformation in the LS.

Since the mode of the isolation is characterized by a participating mass larger than  $R_m$ , and the isolation is able to filter the inertial forces rising to the US, the contribution of this mode to the base shear is negligible. Furthermore, the mode of the LS possesses a comparable period, and a lower participating mass, than those of the LS as a standalone structure; the resulting base shear is reduced with respect to the one of the fixed-base LS. This situation suggests that with the non-perfect isolation, the IIS behaves as a mass damper.

### B.3. MODE COUPLING EFFECT (MCE)

Considering the 3DOF IIS model, the mode coupling effect (MCE) is obtained when one or more periods of the LS are not well separated from one or more higher periods of the isolated US. With a rigid US than the ISO system ( $I \geq 3$ ), the MCE can arise both in presence of perfect and non-perfect isolation.

#### B.3.1. MCE + perfect isolation

Comparing the periods and participating mass ratios of the simplified 3DOF IIS, 2DOF BIS and SDOF LS models, the following considerations can be drawn.

$$\begin{aligned} 1^{\text{st}} \text{ mode:} \quad & T_{3\text{DOF IIS},1} \cong T_{2\text{DOF BIS},1}, \quad \Gamma_{3\text{DOF IIS},1} \cong R_m = M_{\text{ISO}} / m_{\text{TOT}} \\ 2^{\text{nd}} \text{ and } 3^{\text{rd}} \text{ modes:} \quad & T_{3\text{DOF IIS},2} \cong T_{3\text{DOF IIS},3}, \quad \Gamma_{3\text{DOF IIS},2} \neq 0, \Gamma_{3\text{DOF IIS},3} \cong 0 \end{aligned}$$

The first modal shape represents the first mode of the 2DOF ISO+US corresponding to the isolation, with minor deformation in the LS. The second and third modes involve displacements both in the US and LS. When MCE occurs, the detrimental effect is mainly shown in terms of amplification of the US drift.

### B.3.2. MCE + non-perfect isolation

Comparing the periods and participating mass ratios of the simplified 3DOF IIS, 2DOF BIS and SDOF LS models, the following considerations can be drawn.

$$\begin{aligned} 1^{\text{st}} \text{ mode:} \quad & T_{3\text{DOF IIS},1} \cong T_{2\text{DOF BIS},1}, \quad \Gamma_{3\text{DOF IIS},1} \cong R_m = M_{\text{ISO}} / m_{\text{TOT}} \\ 2^{\text{nd}} \text{ and } 3^{\text{rd}} \text{ modes:} \quad & T_{3\text{DOF IIS},2} \cong T_{3\text{DOF IIS},3}, \quad \Gamma_{3\text{DOF IIS},2} \neq 0, \Gamma_{3\text{DOF IIS},3} \cong 0 \end{aligned}$$

The first modal shape represents the first mode of the 2DOF ISO+US corresponding to the isolation, with minor deformation in the LS. The second and third modes involve displacements both in the US and LS. When MCE occurs, the detrimental effect is mainly shown in terms of amplification of the US drift. Instead, it is able to slightly reduced the base shear and this reduction is more evident in presence of non-perfect isolation.

### B.3.3. MCE parameter: $\beta$

The MCE can be prevented by a careful design and a simple design rule can be utilized, i.e.: “*No MCE arises if one or more periods of the LS are far from one or more higher periods of the isolated US*”.

Recognizing that the MCE is independent on the isolation characteristics, an analytical formulation can be derived by setting the stiffness of the isolation system equal to zero, i.e. following MCE parameter  $\beta_{ij}$  :

$$\beta_{ij} = \frac{\omega_{\text{US+ISO},i}^{\text{ff}}}{\omega_{\text{LS},j}}$$

where  $\beta_{ij}$  is the MCE parameter, equal to the ratio of the  $i$ -th higher frequency of the isolated US in the free-free MDOF IIS model (null isolation stiffness) to the  $j$ -th frequency of the LS.

For a 3DOF IIS model the MCE parameter can be rewritten as:

$$\beta = \frac{\omega_{\text{US}} \sqrt{1 + m_{\text{US}} / m_{\text{ISO}}}}{\omega_{\text{LS}}}$$



When the MCE parameter is close to 1 ( $0.85 \div 1.15$ ) the mode coupling effect occurs.

#### B.3.4. 3DOF IIS vs. MDOF IIS

The minimum number of degrees of freedom necessary to estimate MCE is three, i.e. one for the US, LS and the isolation system. However, considering a 3DOF IIS model, the coupling of only two modes can be predicted. If more than two significant coupled modes are present (i.e. the participating coupled mass is equal to, or larger than, 5%), MDOF IIS model must be considered.

The number of degrees of freedom can be preliminary defined taking into account the position of the isolation layer,  $h_{ISO}$ , with respect to the total height of the building,  $H$ , i.e:

$\frac{h_{ISO}}{H} = 0.5$	3DOF IIS,
$\frac{h_{ISO}}{H} = 0.2 \div 0.4$	MDOF IIS (1dof LS + 1dof ISO + u-DOF US), u=1÷4
$\frac{h_{ISO}}{H} = 0.6 \div 0.9$	MDOF IIS (l-dof LS + 1dof ISO + u-DOF US), l=1÷2, u=1÷2

Starting from the MDOF IIS model, the reduced-order 3DOF IIS can be obtained as follows.

$\frac{h_{ISO}}{H} = 0.5$	sdof LS:	1 <sup>st</sup> mode of MDOF LS;
	sdof ISO:	1 <sup>st</sup> mode of 2DOF ISO;
	sdof US:	1 <sup>st</sup> mode of MDOF US;
$\frac{h_{ISO}}{H} = 0.2 \div 0.4$	sdof LS:	1 <sup>st</sup> mode of MDOF LS;
	sdof ISO:	1 <sup>st</sup> mode of 2DOF ISO;

	sdof US:	mode n of MDOF US (function of $T_{US}/T_{LS}$ );
$\frac{h_{ISO}}{H} = 0.6 \div 0.9$	sdof LS:	2 <sup>nd</sup> mode of MDOF LS;
	sdof ISO:	1 <sup>st</sup> mode of 2DOF ISO;
	sdof US:	mode n of MDOF US (function of $T_{US}/T_{LS}$ ).

In the case of  $h_{ISO}/H = 0.2 \div 0.4$  the number of the coupled higher mode of the isolated US can be defined in function of the period ratio between US and LS as standalone structures, i.e.  $T_{US}/T_{LS}$ , see Tab. B.1.

**Table B.1. n-th mode of MDOF US as a function of  $T_{US}/T_{LS}$  for  $h_{ISO}/H = 0.2 \div 0.4$**

$T_{US}/T_{LS}$	1.5÷2	3÷4	5÷5.5	6÷6.5
u	1	2	3	4

In the case of  $h_{ISO}/H = 0.6 \div 0.9$  the number of the coupled higher mode of the isolated US can be defined in function of the period ratio between US and LS as standalone structures, i.e.  $T_{US}/T_{LS}$ , see Tab. B.2.

**Table B.1. n-th mode of MDOF US as a function of  $T_{US}/T_{LS}$  for  $h_{ISO}/H = 0.2 \div 0.4$**

$T_{US}/T_{LS}$	$\leq 0.6$	$\approx 1.0$
u	1	2

It is worth noticing that, in this section the cases in which more than 2 higher modes are coupled are neglected. In fact, for such cases it is necessary to consider a MDOF IIS model.

#### B.4. MASS RATIO, IIS ROBUSTNESS, UNTUNED IIS EFFECT

The mass ratio  $\alpha$  between the total isolated mass,  $M_{ISO}$ , and the LS mass,  $m_{LS}$ , represents one of the main parameters for designing inter-story isolated structures. In fact, it defines the prevailing behavioral aspect, and allows to identify the governing principle among mass damping, intermediate isolation and energy dissipation, base isolation; in particular:

for $\alpha \leq 1$	mass damping effect	$\frac{h_{ISO}}{H} = 0.1 \div 0.5$
for $\alpha = 1 \div 4$	inter-story isolation and energy dissipation effects	$\frac{h_{ISO}}{H} = 0.6 \div 0.8$
for $\alpha \geq 4$	base isolation	$\frac{h_{ISO}}{H} = 0.9 \div 1.0$

Therefore, for  $\alpha \leq 1$  the mass damping effect prevails on the isolation effect; on the contrary, for  $\alpha > 1$  the isolation effect prevails on the mass damping effect.

In addition, the mass ratio  $\alpha$  is indirectly related to the position of the isolation layer,  $h_{ISO}$ , with respect to the total height of the building,  $H$ . Therefore, when the structural portions (upper and lower structures) possess comparable degrees of freedom or the LS shows few dofs with respect to the US, the isolation effect prevails; when the US is composed of few dofs with respect to the LS, the mass damping effect prevails.

Excluding the cases in which the isolation layer is placed at the top and bottom stories, the position of the isolation layer can be indirectly taken into account by considering the mass ratio  $\alpha$  and the period ratio between the upper and lower structures as follows.

for $\alpha \leq 1$	and	$\frac{T_{US}}{T_{LS}} = 0.2 \div 1.0 :$	$\frac{h_{ISO}}{H} = 0.2 \div 0.5$
for $\alpha = 1 \div 4$	and	$\frac{T_{US}}{T_{LS}} = 1.3 \div 2.0 :$	$\frac{h_{ISO}}{H} = 0.6 \div 0.8$
for $\alpha \geq 4$	and	$\frac{T_{US}}{T_{LS}} = 3.0 :$	$\frac{h_{ISO}}{H} = 0.9$

Increasing the mass ratio  $\alpha$ , the robustness of IIS increases. This large mass ratio provides greater reduction of the structural response, the system becomes less dependent on the frequency content and on the optimal configuration. Therefore, for large mass ratios the IIS can be seen as an untuned mass damper; in addition, the energy dissipated by the isolation system increases.

### B.5. MASS AND STIFFNESS DISTRIBUTIONS

Considering the same global mass and static stiffness, the stiffness distribution influences the overall behavior of IIS buildings more than the mass distribution.

An improvement of the seismic performance of the building is expected with an upper structure stiffer than both the lower structure and the isolation layer, and heavier than the lower structure. Since the higher modes are affected by the dynamic characteristics of both upper and lower structures, the mass and stiffness distributions influence the interaction of these structural portions. When the upper structure is stiffer and heavier than the lower structures, the coupling of the higher modes can be negligible; on the contrary, with a US more flexible and lighter than the LS, the MCE is significant.

### B.6. DAMPING

The IIS structures are characterized by non-proportional damping. However, depending on the dynamic characteristics of the structural portions and the isolation system, it is possible to consider a simplified or a rigorous approach.

Considering a simplified 3DOF IIS system, for damping ratios  $\xi_{\text{ISO}}$  and  $\xi_s = \xi_{\text{LS}} = \xi_{\text{US}}$  respectively corresponding to the isolation system and the structural portions, in presence of perfect and non-perfect isolation, the following situations can be obtained.

$$\textit{Perfect Isolation:} \quad \xi_1 \leq \xi_{\text{ISO}} ; \xi_2, \xi_3 \geq \xi_{\text{LS}}, \xi_{\text{US}}$$

$$\textit{Non-perfect Isolation:} \quad \xi_1 < \xi_{\text{ISO}} ; \xi_2, \xi_3 > \xi_{\text{LS}}, \xi_{\text{US}}$$

assuming modal damping ratios  $\xi_1 = \xi_{\text{ISO}}$  and  $\xi_1 = \xi_2 = \xi_s$ , with  $\xi_s = \xi_{\text{LS}} = \xi_{\text{US}}$ .

Therefore, in perfect isolation the first modal damping ratio  $\xi_1$  underestimates, or it is at least almost equal to, the isolation damping ratio  $\xi_{\text{ISO}}$ ; the higher damping ratios  $\xi_2$  and  $\xi_3$  overestimate, or they are at least almost equal to, the structural damping ratio. In non-perfect isolation the first damping ratio  $\xi_1$  underestimates the isolation damping ratio  $\xi_{\text{ISO}}$  while the higher damping ratios,  $\xi_2$  and  $\xi_3$ , overestimate the structural damping ratio.

For these reasons, such simplified approach is adequate only in presence of perfect isolation with isolation periods larger than 2 s). In the other cases a complex analysis is needed.

